

ISSN 0911-5730

UVSOR-50

August 2023

# UVSOR ACTIVITY REPORT

# 2022

UVSOR Synchrotron Facility  
Institute for Molecular Science  
National Institutes of Natural Sciences



## Preface



This Activity Report covers scientific and technological activities carried out using the UVSOR-III Synchrotron in FY2021 (April 2021 - March 2022). We present scientific examples of how the users study at the UVSOR Synchrotron Facility.

The present UVSOR-III Synchrotron is one of the most advanced low-energy SR facilities of the 3<sup>rd</sup> generation SR in the world and is now one of the critical resources to accelerate the investigation of molecular science. The UVSOR-III Synchrotron has a small electron storage ring but has powerful 6-undulator beamlines (3 VUV and 3 in-vacuum soft X-ray undulators) with 8-dipole beamlines. We continue improving and upgrading our micro- and nano-scale photoabsorption and photoemission approaches and in situ/operando measurements in the IR, VUV, and soft X-ray regions, based on our strategic international collaboration program in molecular

science. We are grateful to all the people who use our facility and support our efforts.

UVSOR operates for 40 weeks/year (ca. 2,200 h user time for 36 weeks), accepts ~230 proposals, about ~600 individual researchers counting total ~5,000 people\*day/year. Most users stay for one or two weeks for experimenting. To continue high-level achievements in science and technology at the UVSOR-III Synchrotron, our in-house staff is constantly committed to maintaining and improving high-performance accelerators and beamlines.

In terms of personnel, Assistant professor, K. Sugita left UVSOR. The support technical staff, T. Horigome retired, who has been dedicated manufacturing and equipment development for a long time since the early days of UVSOR. A senior researcher, beamline scientist, T. Araki joined to UVSOR from January 2022. He will promote life science and biology field using BL4U and BL3U.

On the experimental side, technological development never stops, hence we will make a progress on the operando and/or imaging-related techniques to inspire advanced molecular science. We have started to construct the new endstation at the undulator-based soft X-ray beamline BL6U since 2020. The new instrumentation of the photoelectron momentum microscope (PMM) is developing and you may find the final whole picture of the apparatus in FY2022, which consists of a double-hemispherical analyzer with spin detector. In FY2023, it will be connected to another beamline BL7U for doing normal-incident geometry experiments. In the beamline BL1U, we have conducted in developing the novel light sources, including novel experiments using twin-Undulator configuration to demonstrate atto-second interference experiments. The advanced SR-related instrument will offer opportunities in characterizing the electronic structure of surface atomic sites, thin films, molecular adsorbates, bulk crystals, and so on.

We have discussed to construct the post-UVSOR-III as a long-term plan for sustainable development since 2019. The idea would partly be seen in the IOP journal we submitted, a special issue of Electron Structure. We look forward to receiving your feedback and suggestions on the continuing evolution of the UVSOR Synchrotron Facility. In the FY2023, the UVSOR conglutinates the 40<sup>th</sup>-year ceremony, hence the cover design of Activity Report is revised as a memorial issue of 50th. We hope many users will perform excellent work by fully utilizing the UVSOR-III Synchrotron as a unique international hub for the SR research in advanced molecular science.

April 2023

Satoshi Kera

Director of the UVSOR Synchrotron Facility

## The 10th JSSRR Achievement Award Given to Mr. Eiken Nakamura

Mr. Eiken Nakamura, Chief Engineer in UVSOR, has been awarded “the 10th Achievement Award” from the Japanese Society for Synchrotron Radiation Research (JSSRR). The award is given by JSSRR to persons who made a significant contribution to support for synchrotron radiation research and technology for many years.

Among his many achievements, Mr. Nakamura’s development of an L-shaped water-cooled four-quadrant slit drive mechanism is worthy of special mention. He developed a drive mechanism that can control an aperture in both vertical and horizontal directions, while the pulse motor shafts for the drive are all located in the vertical direction, achieving the same performance as conventional systems at a fraction of the size. This technology is indispensable for a compact synchrotron light source such as UVSOR.

The award was presented in the award ceremony in the 36th Annual Meeting of JSSRR in January, 2023.



# UVSOR ACTIVITY REPORT 2022

## Preface

S. Kera

## News

### I Organization and Staff List

1

### II Current Status of Light Sources and Beamlines

9

Light Source in 2022 (Y. Taira)

11

Beamlines in 2022 (F. Matsui)

14

### III Research Activities

#### III-1 Accelerators and Instruments

33



Spectral Phase Interferometry for Direct Electric-field Reconstruction of Undulator Radiation [1U]

T. Fuji, T. Kaneyasu, M. Fujimoto, Y. Okano, E. Salehi, M. Hosaka, Y. Takashima, A. Mano, Y. Hikosaka, S. Wada and M. Katoh

35

Construction of Laser Transport Line and Light Measurement Setup for Coherent Harmonic Generation Experiment at BL1U [1U]

F. Sakamoto, H. Zen, T. Tanikawa, Y. Taira, Y. Okano, H. Ohta, J. Yamazaki, K. Hayashi, Y. Takashima, A. Mano and M. Katoh

36

Impact of the Temperature on the Non-Destructive Nuclide Assay in the Transmission NRF Method [1U]

M. Omer, T. Shizuma, M. Koizumi, Y. Taira, H. Zen, H. Ohgaki and R. Hajima

37

Basic Study on Compton Camera for Detection of Polarized gamma-rays [1U]

K. Shimazoe, M. Uenomachi, T. Ueki, Q. Shu, A. Takeda, K. Magata, K. Nagayanagi and Y. Taira

38

Development of gamma-ray-induced Positron age-momentum Correlation [1U]

Y. Taira, Y. Okano and T. Hirade

39

Study on Generation of F-LCS Gamma-rays for Absolute Cross-section Measurement of NRF using BL1U Undulator [1U] H. Ohgaki, H. Zen, T. Kii, T. Hayakawa, T. Shizuma, M. Fujimoto and Y. Taira	<b>40</b>
Double-Pulsed Light Wave Packets Emitted from a Tandem Undulator [1U] T. Kaneyasu, M. Hosaka, A. Mano, Y. Takashima, M. Fujimoto, E. Salehi, H. Iwayama, Y. Hikosaka and M. Katoh	<b>41</b>
Progress in Single Electron Storage Experiment [1U] A. Asai, M. Shimada, H. Miyauchi and M. Katoh	<b>42</b>
Calibration of the Soft X-ray Response Matrix of CMOS Detector Used in Sounding Rocket Experiment FOXSI-3 [2A] N. Narukage, R. Shimizu, Y. Sato and S. Kashima	<b>43</b>
Development of a Transfer Vessel for NEXAFS Spectroscopy [2A] E. Kobayashi and A. Inoishi	<b>44</b>
Soft X-ray Transmission Measurements of Polymer Films for Soft X-ray Absorption Spectroscopy of Liquids in Low-Energy Regions [3U] M. Nagasaka, S. Fujikawa, H. Takaya and Y. Uozumi	<b>45</b>
Dissociation Channels of Molecules for a Use of Plasma Etching Processes [3B] T. T. Nguyen, K. Ishikawa and H. Iwayama	<b>46</b>
Study of Luminescence Characteristics of Diamond Scintillator for Dark Matter Search [3B] A. Umemoto	<b>47</b>
Current Photon Flux and Focus Size of BL4B [4B] H. Iwayama	<b>48</b>
Low Radiation Damage XAFS Measurements at BL4B [4B] H. Iwayama	<b>49</b>
Transmission Characteristics of an Optical Filter for UV Observations [5B] A. Yamazaki, K. Goda, T. Matsumoto, S. Teramoto and K. Yoshioka	<b>50</b>
Evaluation of the Pressure Dependence of the Krypton Absorption Cell [5B] M. Kuwabara, K. Kato, K. Arakawa and M. Taguchi	<b>51</b>
XUV Polarization Measurement using Visible Fluorescence from Neon Atoms [5B] T. Kaneyasu, K. Hosaka and J. Adachi	<b>52</b>
A Position-sensitive Microchannel Plate Detector with Resistive Anode [5B] S. Matoba, S. Kanda, H. Ohshita, K. Hirata, H. Iwayama and T. Kaneyasu	<b>53</b>
Progress of Photoelectron Momentum Microscopy for Revealing Complex and Detailed Electronic Structures of Materials [6U] S. Suga and F. Matsui	<b>54</b>

Low-frequency Photocarrier Response in Semiconductors Based on ns-visible-pump broadband-infrared-probe Spectroscopy [6B] J. Nishida and T. Kumagai	55
Study on the Reflective Properties of Black Coatings Used in UV Observation Equipment. [7B] T. Matsumoto, K. Goda, A. Yamazaki, K. Inoue, S. Liu and K. Yoshioka	56
Complex Refractive Index Measurement by Reflectance Spectra in Different Polarization Configurations (II) [7B] K. Shinkai, K. Fukui, K. Yamamoto and T. Saito	57
Performance of the Refreshable Large Crystal Nuclear Emulsion for the NINJA Experiment [Others] T. Fukuda, H. Kobayashi, Y. Hirobe, Y. Morimoto and M. Nakamura	58
Lattice Design of the UVSOR-IV Storage Ring [Accelerators] E. Salehi, Y. Taira, M. Fujimoto and M. Katoh	59
<b>III-2 Material Sciences</b>	<b>61</b>
 Observation of Charge Separation Reaction in a Ti-Mn Electrolyte for Redox Flow Batteries by STXM [4U] E. Hosono, D. Asakura, A. Ohira, H. Yuzawa and T. Ohgashi	63
 Temperature-dependent Electronic Band Structure of Organic Molecular Semiconductor [7U] K. Fukutani, F. Nishino, P. I. Jaseela, D. Okaue, K. Fukui, S. Makita, K. Tanaka and S. Kera	64
Gamma-induced Positron Annihilation Lifetime Spectroscopy of $\beta$ -SiAlON:Eu Phosphor [1U] M. Kitaura, S. Watanabe, H. Masai, Y. Taira, K. Takahashi, T. Takeda, N. Hirotsuki, M. Tansho, K. Deguchi, S. Ohki and A. Ohnishi	65
In-situ Measurement of Defects Dynamics in Stress Applied Bulk Iron by Means of Gamma Ray Induced Positron Annihilation Spectroscopy [1U] F. Hori, S. Araki, S. Hirayama and Y. Taira	66
Gamma-ray Induced Positron Annihilation Lifetime Measurement of CeO <sub>2</sub> Catalyst Placed in a Quartz Tube [1U] S. Dohshi, K. Maeda, Y. Taira and T. Hirade	67
Formation of the stress-induced Vacancies in Iron by <i>in situ</i> Positron Annihilation Lifetime Spectroscopy [1U] M. Fujinami, R. Awaji, A. Yabuuchi, T. Hirade, N. Oshima and Y. Taira	68
In-situ Measurements of Vacancies Formed in Pure Iron by Electrolytic Hydrogen Charging using gamma-ray-induced Positron Annihilation Lifetime Spectroscopy [1U] A. Yabuuchi, T. Hirade, M. Fujinami, R. Awaji, N. Oshima, K. Takai and Y. Taira	69

Formation of Catalytically Active Mo <sub>2</sub> C Species on H-MFI for Methane Aromatization Studied by Mo L-edge XANES [2A] K. Kuramochi, Y. Sonobe, H. Shimura, Y. Kinoshiro, R. Yamazaki, Y. Uchimura and H. Aritani	70
Local Environment of Dopants in (M, Nb) co-doped TiO <sub>2</sub> (M=Fe, Ni) [2A] H. Murata, T. Nishio, Y. Nagatomo and A. Nakahira	71
XAFS Study of MgAl <sub>2</sub> O <sub>4</sub> - MgGa <sub>2</sub> O <sub>4</sub> Solid Solutions [2A] S. Yoshioka, K. Yasuda, E. Kobayashi and K. Okudaira	72
NEXAFS Spectroscopy of Battery Materials Using a Transfer Vessel [2A] A. Inoishi and E. Kobayashi	73
Direct Observation of Electrochemically Generated High Valent Iron-Oxo Species of $\mu$ -Nitrido-Bridged Iron Phthalocyanine Dimer Deposited on Graphite Surface by Soft X-ray Absorption Spectroscopy [3U] Y. Yamada and M. Nagasaka	74
Structural Analysis of fluoro-polymers Using Resonant Soft x-ray Scattering [3U] K. Yamanoi, M. Yamashita, Y. Yamamoto, H. Iwayama and M. Noumi	75
Structure Analysis on Chiral Dark Conglomerate of Achiral Liquid Crystal Trimers by Resonant Soft X-ray Scattering (RSoXS) at UVSOR [3U] Y. Takanishi, F. Araoka and H. Iwayama	76
Measurements of Fluorescence Lifetimes of Scintillators Adopted for a New in-beam Detector of the $K_L^0$ Rare Decay Experiment at J-PARC [3B] K. Shintate, R. Abe, Y. Hayashi, T. Naito, S. Sakano, J. Ohashi, Y. Tajima and H.Y. Yoshida	77
Material Search of Li-Containing Halide Scintillators for Neutron Detection [3B] C. Fujiwara, S. Kurosawa and A. Yamaji	78
Optical Properties of Cs <sub>2</sub> IrCl <sub>6</sub> -CsCl Composite Phosphor [3B] S. Kodama, S. Omiya, N. Shimoyama, T. Saito, I. Yanase and H. Takeda	79
Visible-to-Ultraviolet Spectral Change with the Current-Induced Local-to-Nonlocal Transition of SmS [3B, 6B] H. Watanabe, S. Tatsukawa, K. Imura, H. S. Suzuki, N. K. Sato and S. Kimura	80
Exciton States of Cesium Silver Iodide Crystals [3B] S. Ibuki and T. Kawai	81
Temperature Dependence of Excitation Spectra in Er-doped La <sub>2</sub> Zr <sub>2</sub> O <sub>7</sub> [3B] M. Yoshino and M. Ito	82

Analysis of Cathode Materials for Li-Ion Batteries by STXM [4U] E. Hosono, D. Asakura, H. Yuzawa, T. Ohigashi, W. Zhang, M. Kobayashi, H. Kiuchi and Y. Harada	83
Unraveling the Origin of Irreversibility between the First and Second Charging Process in Primary Conversion Anode Particle [4U] J. Kim, J. Chung, T. Ohigashi, H. Yuzawa and J. Lim	84
Chemical Bonding Structures of SBR/BR Interfaces [4U] T. Ejima and Y. Tamura	85
Observation of Distribution of Sulfur and cross-linking Reagent in Vulcanized Rubber by Using STXM [4U] T. Ohigashi, F. Kaneko, H. Yuzawa and H. Kishimoto	86
Scanning Transmission X-ray Microscopy of Hydrogen Evolution Electrocatalysts on Graphene Oxide Membranes [4U] C. O. M. Mariano, J. S. D. Rodriguez, R. H. Clemente, T. Ohigashi, H. Yuzawa, W. H. Hsu, J. Shiue and C. H. Chuang	87
Examination of Methods for Inner Structures of Magnetic Thin Films at UVSOR BL4B by Reflection XMCD Measurement Setup [4B] K. Yamamoto, H. Iwayama, O. Ishiyama and T. Yokoyama	88
L <sub>2,3</sub> -edge X-ray Absorption Spectra of Transition Metal in Wurtzite-AlN [4B] S. Imada	89
C K-edge XAFS Measurement of Carbon Containing Porous Silica [4B] S. Dohshi	90
Evolution of the Electronic States by Electron Doping in a Kagome Superconductor KV <sub>3</sub> Sb <sub>5</sub> [5U] T. Kato, K. Nakayama, Y. Li, Z. Wang, S. Souma, K. Tanaka, T. Takahashi, Y. Yao and T. Sato	91
Evolution of Electronic Correlations and Excitonic Properties Near semiconductor-excitonic Insulator Transition [5U] K. Fukutani, K. Kiyosawa, C.I. Kwon, J.S. Kim, K. Tanaka and S. Kera	92
Polarization-dependent Angle-resolved Photoemission Study of MAX Phase Compound Zr <sub>3</sub> SnC <sub>2</sub> [5U] M. Mita, D. Pinek, M. Nakatake, K. Tanaka, T. Ouisse and T. Ito	93
Electronic Structure of a Layered Magnetic Semiconductor CeTe <sub>1.83</sub> Sb <sub>0.17</sub> [5U, 7U] T. Nakamura, H. Murakawa, Y. Chen, H. Sugihara, K. Tanaka, N. Hanasaki and S. Kimura	94
Synchrotron ARPES Study of Nodal Dirac Semimetal Candidate LaTeBi [5U] R. Saitou, N. Kataoka, H. Kageyama, R. Kondo and T. Yokoya	95
Re-examination of the Phase Diagram of the high-T <sub>c</sub> Cuprate Superconductor Bi <sub>2</sub> Sr <sub>2</sub> CaCu <sub>2</sub> O <sub>8+δ</sub> Studied by ARPES [5U, 7U] Y. Tsubota, Y. Miyai, S. Nakagawa, S. Ishida, S. Kumar, K. Tanaka, H. Eisaki, T. Kashiwagi, M. Arita, K. Shimada and S. Ideta	96

Alkaline-metal-dependent Electronic States in V-based Kagome Metals [5U] T. Kato, K. Nakayama, Y. Li, Z. Wang, S. Souma, K. Tanaka, T. Takahashi, Y. Yao and T. Sato	97
Verification of the Intrinsic Electron Doping Effect in T'-type Cuprate high-temperature Superconductors [5U] M. Miyamoto, M. Horio, K. Moriya, A. Takahashi, K. Tanaka, Y. Koike, T. Adachi and I. Matsuda	98
Polarization Dependent Orbital States in Mn <sub>3-x</sub> Ga Studied by angle- resolved Photoemission Spectroscopy [5U] J. Okabayashi, Y. Miura, K. Tanaka, K. Z. Suzuki and S. Mizukami	99
Impact of Electron Scattering on Seebeck Coefficient [5U] K. Kandai, K. Kuga, M. Matsunami and T. Takeuchi	100
Temperature Dependence of the Band Folding in TiSe <sub>2</sub> [5U] S. Tanaka, K. Ueno, K. Fukutani and K. Tanaka	101
Doping-Dependent ARPES Study of Nodal Dirac Semimetal Candidate LaTeSb and LaTeBi [5U] R. Saitou, N. Kataoka, T. Wakita, H. Kageyama, R. Kondo and T. Yokoya	102
Symmetry Reduction of the Electronic Structure in Heavily Overdoped Pb-Bi2201 Observed by Angle-resolved Photoemission Spectroscopy [5U, 7U] Y. Miyai, T. Kurosawa, M. Oda, M. Arita, K. Tanaka, S. Ideta and K. Shimada	103
Far- and Mid-infrared Absorption on the Single-crystal Pentacene [6B] Y. Nakayama, K. Yamauchi, Y. Baba and J. Miyamoto	104
ARPES Study of a chalcopyrite-type Topological Insulator Candidate [7U] T. Iwaya, A. Honma, K. Nakayama, K. Sugawara, S. Souma, K. Tanaka, T. Takahashi, K. Segawa and T. Sato	105
Electronic Structure of the five-fold oxygen-coordinated Cuprate Superconductor [7U] M. Horio, M. Miyamoto, X. Peiao, K. Tanaka, T. Taniguchi, M. Fujita and I. Matsuda	106
Angle-Resolved Photoemission Study of Solid Electrolytes Li <sub>3x</sub> La <sub>2/3-x</sub> TiO <sub>3</sub> Bulk Single Crystal [7U] S. Koyama, M. Nakatake, S. Takakura, K. Tanaka, Y. Fujiwara, T. Taishi, H. Moriwake, Y. Iriyama and T. Ito	107
Electronic Structure of Layered Nitride Chloride ZrNCl by ARPES [7U] N. Kataoka, R. Saitou, M. Tanaka and T. Yokoya	108
Low-Energy ARPES Study on the Electronic Structure of Cr <sub>2</sub> Se <sub>3</sub> [7U] C.-W. Chuang, T. Kawakami, T. Kato, K. Sugawara, K. Nakayama, S. Souma, K. Tanaka, A. Chainani, T. Takahashi, K. Segawa and T. Sato	109
Polarization-Dependent Photoemission from the Folded Band of TiSe <sub>2</sub> [7U] S. Tanaka, K. Ueno, K. Fukutani and K. Tanaka	110

Momentum Dependence of the Spectral Weight in the Single Layer High- $T_c$ Cuprate $\text{Bi}_2\text{Sr}_2\text{CuO}_{6+\delta}$ Studied by ARPES [7U]	111
Y. Onishi, Y. Miyai, Y. Tsubota, S. Kuma, M. Atira, K. Tanaka, H. Eisaki, S. Ishida, K. Shimda and S. Ideta	
Excitation Spectra of Plastic Scintillators in the Vacuum Ultraviolet Region [7B]	112
M. Koshimizu, Y. Fujimoto and K. Asai	
Mineral Analysis for Resource Exploration by Deep Ultraviolet Spectroscopy [7B]	113
T. Shimizu, K. Shinohara, K. Yamanoi and N. Sarukura	
Optical Reflectivity Study of Au-Al-Yb Quasicrystals [7B]	114
H. Okamura, A. Kamiki, K. Namba, S. Hirokawa and K. Deguchi	
<b>III-3 Chemistry</b>	117
 Ligand Field in Fe-based spin-crossover Coordination Polymer Revealed by Soft x-ray Absorption Spectroscopy [4B]	119
K. Yamagami	
Monitoring Phase Difference between Magnetic Substates in Helium Atom [1U]	120
T. Kaneyasu, Y. Hikosaka, M. Fujimoto, H. Iwayama and M. Katoh	
High-Resolution Measurement of State-Resolved Photoelectron Circular Dichroism with Varied Photoionization Energies [1U]	121
H. Kohguchi, Y. Hikosaka, T. Kaneyasu, S. Wada, H. Ota, M. Katoh and Y.-I. Suzuki	
$M_{4,5}$ -edge XANES Spectra of La and Nd Complex Oxides [2A]	122
H. Asakura, M. Konno and K. Nanakarage	
O K-edge XAS of Photoreactions in Dissolved Oxygen on Lipid Bilayer [3U]	123
F. Kumaki, M. Nagasaka, Y. Kinjo, R. Tero, Y. Okano, M. Fujimoto and J. Adachi	
Carbon K-edge X-ray Absorption Spectra of Liquid Ethanol Reproduced by Quantum Chemical Calculations and Molecular Dynamics Simulations [3U]	124
M. Nagasaka	
Observation of the Behavior of Sumanene in Organic Solvents by C K-edge XAS Experiment [3U]	125
Y. Uetake, K. Sugimura, R. Ihsan, M. Nagasaka and H. Sakurai	
Operando Observation of Adsorbed Anions on the Surface of Nickel Catalysts by Soft X-ray Absorption Spectroscopy [3U]	126
A. Sakai, Z. Li, K. Harada, S. Tsunekawa, M. Nagasaka and M. Yoshida	
Temperature Effects on the X-ray Absorption Spectrum of Aqueous $\text{Ca}(\text{NO}_3)_2$ Recorded at the Ca L-edge [3U]	127
D. Céolin, T. Saisopa, Y. Rattanachai, H. Yuzawa and N. Kosugi	

Self-Assembled Hierarchical Nanosegregated Chiral Intermediate Phases Composed of Two Different Achiral Bent-Core Molecules [3U] F. Araoka, Y. Takanishi, S-W. Choi and H. Iwayama	128
X-ray Absorption Spectra of Metal Carbonyl Solutions [3U] T. Sasaki and H Xu	129
Soft X-ray Absorption of Photocatalysts for Artificial Photosynthesis: Ultraviolet Light Irradiation in Water [3U] H. Onishi, Yi Hao Chew, K. Matsui, N. Ichikuni and T. Yoshida	130
Hydration of Dimethyl Sulfoxide Probed by Liquid-Phase Soft X-ray Absorption Spectroscopy [3U] C. Sugahara, K. Okada and H. Iwayama	131
Multielectron-ion Coincidence Spectroscopy of I 4d inner-shell Photoionization of CH <sub>3</sub> I and CH <sub>2</sub> I <sub>2</sub> Molecules [4B] M. Fushitani, Y. Hikosaka and A. Hishikawa	132
Quadruple Auger Decay from Xe 4s Core-Hole State Studied by Multi-Electron-Ion Coincidence Spectroscopy [4B] Y. Hikosaka	133
Metastable OCS <sup>3+</sup> States Investigated by Multi-Electron-Ion Coincidence Spectroscopy [4B] Y. Hikosaka	134
Soft X-ray Absorption Study of Semiconductor Photocatalysts for Highly Efficient Oxidation of Water [4B] T. Yoshida, N. Ichikuni, H. Onishi and Yi Hao Chew	135
High-Resolution Photoelectron Spectroscopy of Unexplored Chiral Systems for Demonstration of the Photoelectron Circular Dichroism [7B] H. Kohguchi, Y. Hikosaka, T. Kaneyasu, S. Wada and Y-I. Suzuki	136
The Challenge of Photoionization Plasma Generation Using Synchrotron Radiation Source for Study of Plasmas in Interstellar Space and in Nuclear Fusion Devices [7B] M. Kobayashi, H. Iwayama, J. Takahashi, S. Yoshimura, H. Ota, K. Kobayashi, M. Katoh, H. Nakamura, I. Sakon, K. Sawada and Y. Kebukawa	137
<b>III-4 Surface, Interface and Thin Films</b>	<b>139</b>
 Fermiology of a Kagome Superconductor Cs(V <sub>1-x</sub> Nb <sub>x</sub> ) <sub>3</sub> Sb <sub>5</sub> Revealed by Momentum Microscope [6U] T. Kato, K. Nakayama, Y. Li, Z. Wang, S. Souma, F. Matsui, T. Takahashi, Y. Yao and T. Sato	141
Mg K-edge NEXAFS of MgO, Mg(OH) <sub>2</sub> and MgCO <sub>3</sub> [2A] E. Kobayashi, S. Yoshioka and K. K. Okudaira	142
Structural Analyses of Silicon Atoms in a Zero-dimensional Metal-atom Encapsulating Silicon Cage Clusters by X-ray Absorption Spectroscopy [2A] A. Nakajima and T. Inoue	143

Annealing Effects on Surface Electronic Structure of MoO <sub>3</sub> Nanoparticles by UPS [2B] K. K. Okudaira and S. Ishii,	144
X-ray Absorption Spectroscopy Study of 4-MBA and Cysteine on Gold Surfaces [3U] F. Sato, I. Sakaida, S. Ohno and M. Nagasaka	145
Evaluation of Growth Orientation and Crystallinity of Deep UV Emitting Zinc Aluminate Thin Films [3B] H. Kominami, K. Inoue, N. Uesugi, K. Nie, A. Adachi, R. Isihara, K. Yabe, J. Kamikawa, T. Sadamori, D. Takeya, N. Miyazaki, A. Dorokhina and S. Kurosawa	146
Application of atomically-thin Graphene to X-ray Astronomy: Soft X-ray Transmission Measurements [4U] I. Mitsuishi, K. Kashiwakura, Y. Niwa, T. Ogawa, M. Hirota, Y. Tawara, R. Kitaura, H. Yuzawa, T. Ohigashi and K. Tanaka	147
Tuning Magnetic Properties of Atomic Layer Materials by organic-inorganic Interfacial Magnetic Coupling [4B (XMCD)] H. Ono, Y. Umeda, K. Yamamoto, O. Ishiyama, T. Yokoyama, M. Mizuguchi and T. Miyamachi	148
X-ray Magnetic Circular Dichroism Study of Chiral Antiferromagnetic Co <sub>2-x</sub> Pd <sub>x</sub> Mo <sub>3</sub> N Thin Films [4B (XMCD)] B. Qiang, M. Togashi, T. Fukasawa, T. Hajiri, M. Kuwahara, H. Asano and T. Ito	149
Controlling Magnetic Anisotropy of Magnetic Thin Film Heterostructures [4B (XMCD)] Y. Umeda, H. Ono, K. Yamamoto, O. Ishiyama, T. Yokoyama, M. Mizuguchi and T. Miyamachi	150
X-ray Photoemission Spectroscopy and X-ray Absorption Spectroscopy Measurement of the Chiral Molecule on the Metal Substrate [4B] F. Nishino, K. Fukutani, P. I. Jaseela, H. Iwayama, S. Makita and S. Kera	151
Observation of Heat Treatment Effects of Amorphous Selenium Thin Film by Vacuum Ultraviolet Transmission Spectrum [4B] K. Hayashi	152
UV-X-ray Transmission Measurements of Atomically Thin Graphene Astronomical Applications [4B] I. Mitsuishi, K. Kashiwakura, Y. Niwa, T. Ogawa, R. Kitaura, E. Nakamura, M. Nagasaka and K. Tanaka	153
Si L-edge NEXAFS Spectra of Native Oxide Si Wafer with Different Crystal Surface [4B] K. K. Okudaira, S. Yoshioka and E. Kobayashi	154
ARPES from Si{111} $\sqrt{3} \times \sqrt{3}$ -Ag ultra-thin Film on Artificially Designed three-dimensional Si facet-line Structure with {111} Facet Surfaces on Si(001) Substrates [5U] K. Hattori, Ni'matil Mabarroh, Juharni, Y. Ida, W. Imayama, Y. Kimoto, Y. Kitagawa, S. Tanaka, A. N. Hattori, S. Suga and K. Tanaka	155

Sizable Rigid Shift of the Valence Band of h-BN by Cs-doping [5U] S. Ichinokura, A. Hemmi, H. Cun, K. Tanaka, T. Greber and T. Hirahara	156
Growth of Transition Metal Phosphide Thin Film on Au(111) [5U] N. Maejima, K. Inaoka and K. Edamoto	157
Heavy-Fermion in a Mono-Atomic Layer YbCu <sub>2</sub> /Cu(111) [5U, 7U] H. Sugihara, T. Nakamura, Y. Chen, K. Nishihara M. F. Lubis, K. Tanaka and S. Kimura	158
Region and Element-specific Surface Observation of CVD Graphene on Ir(111)/ $\alpha$ -Al <sub>2</sub> O <sub>3</sub> (0001) by Photoelectron Momentum Microscopy [6U] E. Hashimoto, Y. Onuma, F. Matsui and S. Koh	159
High-resolution angle-resolved Photoemission Study on MnBi <sub>2</sub> Te <sub>4</sub> / MnBi <sub>2</sub> Te <sub>4</sub> /Bi <sub>2</sub> Te <sub>3</sub> Heterostructure [7U] K. Ishihara, H. Nishimichi, K. Ide, S. Ichinokura, K. Tanaka and T. Hirahara	160
Electrochemical Attenuated Total Reflectance Ultraviolet (EC-ATR-UV) Spectroscopy Applied for Organic Semiconductor / Ionic Liquids Interface [7B] I. Tanabe, Y. Hanamori and K. Fukui	161
<b>III-5 Life, Earth and Planetary Sciences</b>	<b>163</b>
 X-ray Absorption Spectra of Lipid Bilayer Membranes in Aqueous Solutions [3U] R. Tero, Yu Kinjo and M. Nagasaka	165
Study on Chirality Emergence of Amino Acid Molecules Induced by Circularly Polarized Lyman- $\alpha$ Light Irradiation [1U] M. Kobayashi, J. Takahashi, H. Ota, G. Fujimori, K. Kobayashi, K. Matsuo, Y. Taira, M. Katoh, H. Nakamura and Y. Kebukawa	166
Attempts at Structural Analysis of Biological Macromolecules Using Resonant Soft X-ray Scattering [3U] Y. Sugimoto and H. Iwayama	167
Water-Ion Interactions in Natural Lake Brines [3U] Y. Hao, N. Fauré, Y. Qiu, M. Nagasaka, E. Thomson, S. Wang and X. Kong	168
Drug Administration Concepts Involving Redox Nanocarriers Affect the Spatial Distribution of Topically Applied Formulations in Human Skin [4U] G. Germer, T. Ohigashi, H. Yuzawa, K. Rajes, R. Haag, F. Rancan, A. Vogt and E. Rühl	169
Absorption- Image and Spectra of Apoptosis Nuclei in P-L Edge [4U] T. Ejima and S. Tone	170

Embracing Natural and Anthropogenic Aerosol Particle Complexity [4U] P. A. Alpert, L. Li, L. F. Escusa Dos Santos, F. Mahrt, M. Ammann, L. Wu, W. Hu, P. Fu, M. Hallquist, E. Thomson and X. Kong	171
STXM in Characterizing Lysosomal Storage Materials in a Mouse Model [4U] T. Mansikkala, T. Ohigashi, H. Yuzawa, I. Miinalainen, S. M. Kangas, M. Salo, N. Kosugi, J. Uusimaa, M. Huttula, R. Hinttala and M. Patanen	172
Determination of Spectral Changes in NEXAFS of Biomolecules Caused by Radiation Effects for Molecular Mapping of Biological Specimens [4U] A. Ito, K. Shinohara, A. Matsuura, S. Toné, K. Tohya, H. Yuzawa and T. Ohigashi	173
Attempt to Constrain the Initial Condition of Aqueous Alteration on Cometary Organic Matter [4U] H. Yabuta, N. Nishii, T. Araki and H. Yuzawa	174
Organics in Asteroid Ryugu Samples: Analytical Approach Utilizing Micro and Multi Beam Techniques. [4U] M. Ito, N. Tomioka, M. Uesugi, A. Yamaguchi, N. Imae N. Shirai, T. Ohigashi, M. Kimura, M-C. Liu, R.C. Greenwood, K. Uesugi, A. Nakato, K. Yogata, H. Yuzawa, Y. Kodama, A. Tsuchiyama, M. Yasutake, R. Findlay, I.A. Franchi, J.A. Malley, K.A. McCain, N. Matsuda, K.D. McKeegan, K. Hirahara, A. Takeuchi, S. Sekimoto, I. Sakurai, I. Okada, Y. Karouji, T. Yada, M. Abe, T. Usui, S. Watanabe and Y. Tsuda	175
Chemical Morphology of Biomass-Burning Particles Generated from Different Fuels under Varied Burning Conditions [4U] J. Chen, N. Faure, Y. Hao, Z. Kanji, E. S. Thomson, S. Wang and X. Kong	176
Heat Resistance of SiC/Mo/Si Multilayer Mirrors at 30.4nm [5B] S. Teramoto, K. Inoue, A. Yamazaki, T. Matsumoto, S. Liu, K. Yoshioka and I. Yoshikawa	177
Synchrotron-radiation Infrared Microspectroscopy Analysis of Persistent Organic Compounds [6B] T. Kawasaki, F. Teshima and K. Tanaka	178
Development of an Infrared Spectro-Microtomography Using a Mid-IR Supercontinuum Laser: Preliminary Report [6B] H. Yabuta, Y. Ikemoto, F. Teshima and K. Tanaka	179

## IV List of Publications

181

<b>V Workshops</b>	<b>187</b>
UVSOR Symposium 2022	189
The 5 <sup>th</sup> workshop on prospects and construction plan of the next generation synchrotron radiation facility: Cooperation between facilities II	191
IMS Symposium “Resonant Soft X-ray Scattering and Reflectivity”	192
IMS Symposium “Symposium on Generation and Advanced Use of Various Quantum Beams in UVSOR-III”	193
<b>Facts and Figures</b>	<b>197</b>



# Organization and Staff List

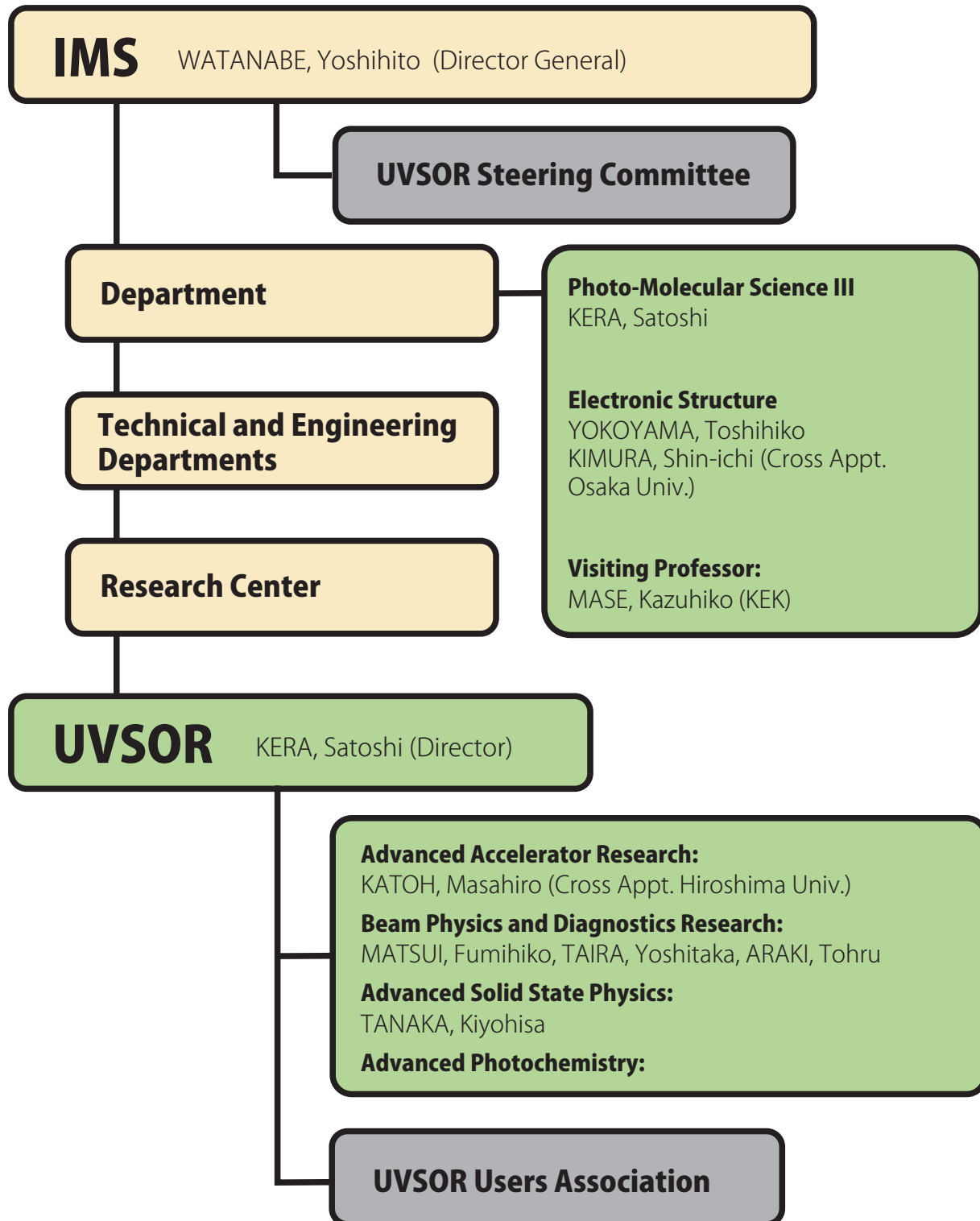




## UVSOR Synchrotron Facility Organization

Mar. 2023

I



## Staff List

Mar. 2023

### UVSOR Staff

#### Director

KERA, Satoshi                      Professor                      kera@ims.ac.jp

#### Division of Advanced Accelerator Research

KATOH, Masahiro                      Project Professor                      mkatoh@ims.ac.jp  
(Cross Appt. Hiroshima Univ.)

SALEHI, Elham                      Project Research Staff                      elham@ims.ac.jp

#### Division of Beam Physics and Diagnostics Research

TAIRA, Yoshitaka                      Associate Professor                      yostaira@ims.ac.jp

OHIGASHI, Takuji                      Associate Professor (Cross Appt. KEK)                      (until Mar. 2023)

SUGITA, Kento                      Assistant Professor                      ysugimoto@ims.ac.jp                      (until Feb. 2023)

MATSUDA, Hiroyuki                      Project Research Staff                      hmatsuda@ims.ac.jp

#### Division of Advanced Solid State Physics

MATSUI, Fumihiko                      Professor                      matui@ims.ac.jp

TANAKA, Kiyohisa                      Associate Professor                      k-tanaka@ims.ac.jp

HAGIWARA, Kenta                      Project Research Staff                      k-hagiwara@ims.ac.jp                      (since Nov. 2022)

#### Division of Advanced Photochemistry

ARAKI, Tohru                      Senior Researcher                      araki@ims.ac.jp                      (since Jan. 2023)

IWAYAMA, Hiroshi                      Assistant Professor                      iwayama@ims.ac.jp

#### Research Cooperative Staff

KANEYASU, Tatsuo                      (Concurrent Appt. SAGA-LS)                      (since Apr. 2022)

SUGIMOTO, Yasunobu                      Specially Appointed Senior Specialist                      (since May 2022)

#### Technical Staff

HAYASHI, Kenji                      Engineer (Unit Leader)

NAKAMURA, Eiken                      Chief Engineer

MAKITA, Seiji                      Engineer

YAMAZAKI, Jun-ichiro                      Chief Technician

SAKAI, Masahiro                      Chief Technician

YANO, Takayuki                      Chief Technician

OKANO, Yasuaki                      Chief Technician

TESHIMA, Fumitsuna                      Chief Technician

KONDO, Naonori                      Chief Technician

YUZAWA, Hayato                      Technician

OTA, Hiroshi	Technician	
HORIGOME, Toshio	Technical Fellow	(until Mar. 2023)
MIZUKAWA, Tetsunori	Technical Fellow	
MINAKUCHI, Aki	Technical Fellow	

### Secretary

ISHIHARA, Mayumi  
KAMO, Kyoko

## Departments in IMS (\*Group Leader)

### Division of Photo-Molecular Science III

KERA, Satoshi*	Professor	
NAGASAKA, Masanori	Assistant Professor	
FUKUTANI, Keisuke	Assistant Professor	

### Division of Photo-Molecular Science IV

MASE, Kazuhiko                      Visiting Professor (KEK)

### Division of Electronic Structure

YOKOYAMA, Toshihiko*	Professor	
KIMURA, Shin-ichi	Professor (Cross Appt. Osaka Univ.)	
KOITAYA, Takanori	Assistant Professor	(until Jul. 2022)
YAMAMOTO, Kohei	Assistant Professor	(until Mar. 2023)
KURAHASHI, Naoya	Assistant Professor	(since Dec. 2022)

## Graduate Students

KOYAMA, Shotaro	Nagoya University	(until Mar. 2023)
MITA, Manaya	Nagoya University	(until Mar. 2023)
OZAWA, Shunnosuke	Nagoya University	(until Mar. 2023)
SEMA, Ryota	Nagoya University	(until Mar. 2023)
SHIOHARA, Keisuke	Nagoya University	(until Mar. 2023)
YAMAUCHI, Saki	Nagoya University	(until Mar. 2023)

## UVSOR Steering Committee (\*Chair)

KERA, Satoshi*	UVSOR, IMS	Chair
MATSUI, Fumihiko	UVSOR, IMS	
KATOH, Masahiro	UVSOR, IMS	
TANAKA, Kiyohisa	UVSOR, IMS	
TAIRA, Yoshitaka	UVSOR, IMS	
MASE, Kazuhiko	UVSOR, IMS (KEK)	(since Apr. 2022)

KANEMITSU, Yoshihiko	Kyoto University	
KIMURA, Shin-ichi	Osaka University	
HARADA, Yoshihisa	University of Tokyo	
FUKUSHIMA, Takanori	Tokyo Institute of Technology	
NAKAMURA, Tetsuya	Tohoku University	(since Apr. 2022)
YABASHI, Makina	RIKEN	(since Apr. 2022)
ITO, Takahiro	Nagoya University	(since Apr. 2022)
WATANABE, Yoshihito	IMS, Director General	(since Apr. 2022)
YOKOYAMA, Toshihiko	IMS	
IINO, Ryota	IMS	(since Apr. 2022)
SEGAWA, Yasutomo	IMS	(since Apr. 2022)
KURAMOCHI, Hikaru	IMS	(since Apr. 2022)
SHIGEMASA, Eiji	IMS	
HAYASHI, Kenji	IMS	
NAKAMURA, Toshikazu	IMS	

### UVSOR Users Association (\*Chair)

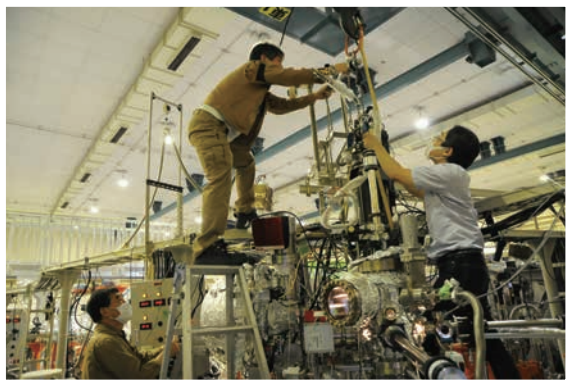
KITAURA, Mamoru*	Yamagata University	
HIKOSAKA, Yasumasa	Toyama University	
ITO, Takahiro	Nagoya University	(since Apr. 2022)
MIYAMACHI, Toshio	Nagoya University	(since Apr. 2022)
HIRAHARA, Toru	Tokyo Institute of Technology	(since Apr. 2022)

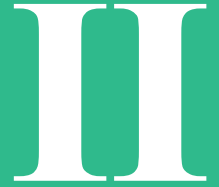
### Visiting Scientists

MANSIKKALA, Leo	Oulu University	Jul. 2022
PATANEN, Minna	Oulu University	Jul. 2022
SILLY, Mathieu	Synchrotron Soleil	Aug. 2022
ALPERT, Peter	Paul Scherrer Institute	Aug. 2022
CEOLIN, Denis	Synchrotron Soleil	Aug. 2022
<b>ESCUSA DOS SANTOS, Luis Filipe</b>		
	University of Gothenburg	Aug. 2022
LI, Linjie	University of Gothenburg	Aug. 2022
MAHRT, Fabian	Paul Scherrer Institute	Aug. 2022
SAISOPA, Thanit	Rajamangala University of Technology Isan	Aug. 2022
RATTANACHAI, Yuttakarn	Rajamangala University of Technology Isan	Aug. 2022
KONG, Xiangrui	University of Gothenburg	Aug. 2022, Feb. 2023, Mar. 2023
CHUANG, Cheng-Hao	Tamkang University	Sep. 2022
HUANG, Wun-Cin	Tamkang University	Sep. 2022
<b>RODRIGUEZ, Jan Sebastian Dominic</b>		
	Tamkang University	Sep. 2022
RÜHL, Eckart	Free University of Berlin	Sep. 2022, Mar. 2023
Chien-Lin Pan	Tamkang University	Dec. 2022

Chung-Li Dong	Tamkang University	Dec. 2022
TA THỊ THÚY NGA	National Yang Ming Chiao Tung University	Dec. 2022
Huang Hou-Yi	Tamkang University	Dec. 2022
Mannu Pandian	Tamkang University	Dec. 2022
CHEN, Jie	ETH	Feb. 2023
FAURE, Nicolas	University of Gothenburg	Feb. 2023, Mar.2023
HAO, Yuxin	Northwest University, China	Feb. 2023, Mar.2023

*Staff*





# Current Status of Light Sources and Beamlines





## Light Source in 2022

Yoshitaka Taira

UVSOR Synchrotron Facility, Institute for Molecular Science, Okazaki 444-8585, Japan

In FY2022, UVSOR-III was operated for users as scheduled for 36 weeks from end of May 2022 to March 2023. Monthly statistics of operation time and integrated beam current are shown in Fig. 1. From April 1 to May 6 was a shutdown period, during which periodic inspections were conducted. The two weeks following the shutdown were allocated to the adjustment of the accelerator and beamlines.

The weekly operation schedule is as follows. Mondays are assigned to machine studies from 9:00 AM to 9:00 PM. User operation is assigned Tuesday through Friday, with Tuesday and Wednesday operating from 9:00 AM to 9:00 PM, and Thursday from 9:00 AM to 9:00 PM on Friday for 36 continuous hours. Thus, the user's beam time per week is 60 hours.

July to August is the period when attention should be paid to instantaneous voltage drops caused by lightning strikes. Beam dumps due to instantaneous voltage drops occurred frequently, resulting in loss of operation time. High voltage application errors in the klystron pulse modulator had been occurring since the fall of 2021 and were still occurring frequently in 2022. The cause of this event is unknown, but it is not occurring now. It is possible that the error was corrected accidentally during an inspection. Regarding vacuum-related issues, vacuum leakage from the bellows duct of the bending magnet of the booster synchrotron has occurred frequently. The vacuum level has deteriorated due to the formation of pinholes in the ducts, but this has been addressed each time by applying repair materials. Failures of the beam position monitor module and the RF frequency signal generator were addressed by replacing them with alternatives or repairing them.

APPLE-II type tandem undulators are in operational at BL1U. Until now, they were used only on machine study days as the standard orbit of the electron beam for user operation did not pass through the central axis of these undulators. From April 2022, the standard orbit has been changed to one that passed through the center axis. This improvement allows some users to conduct experiments on the BL1U undulators during normal user operation.

We started a design study for the future plan of UVSOR-IV. As a first step, we have analyzed the present magnetic lattice, seeking a possibility to reduce the emittance more [1]. Although, we did not find a solution to drastically reduce emittance, we have found a few interesting solutions that achieved lower emittance than the current situation. As the second step, we have started designing a totally new storage ring, which is close to the diffraction limit in the VUV range

[2].

The steep rise in electricity prices is a global problem. Although the rate of increase in electricity prices in Japan is lower than in Europe, the impact is still enormous. UVSOR's electricity rates typically range between 50 - 60 million yen per year, but the estimated amount for FY2022 is over 80 million yen. The power consumption of the electron accelerator and beamline during non-operating periods is 50 kW and 150 kW, respectively. These are mainly the power used to maintain a high vacuum, such as vacuum pumps. During accelerator operation, these increase to 390 kW and 250 kW, respectively. As power saving measures, we have begun shortening operation hours outside of normal user operation, such as weekend operation, turning off unused equipment, and shutting down vacuum pumps at beamlines with low user utilization.

The light source development and utilization beamline BL1U, constructed under the support of Quantum Beam Technology Program by MEXT/JST, continue to develop new light source technologies and their applications such as free electron laser, coherent harmonic generation, coherent synchrotron radiation, coherent control [3], laser Compton scattered gamma rays [4], and optical vortices.

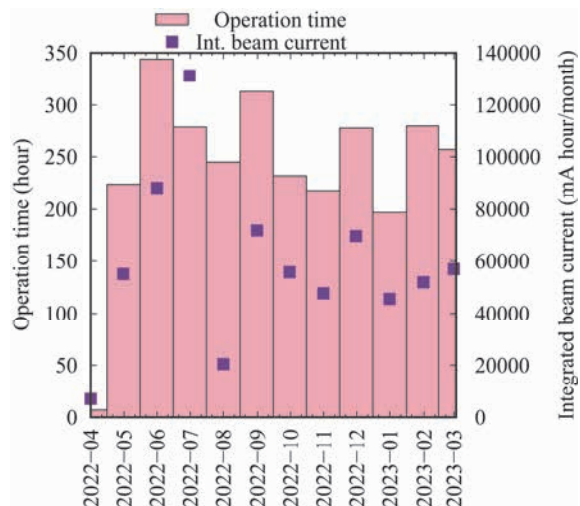


Fig. 1. Monthly statistics in FY2022.

[1] E. Salehi and M. Katoh, Proceedings of IPAC2021 (2021) 3970.

[2] E Salehi, Y Taira, M Fujimoto, L Guo, M. Katoh, J. Phys.: Conf. Ser. **2420** (2023) 012062.

[3] T. Kaneyasu *et al.*, Sci. Rep. **13** (2023) 6142.

[4] Y. Taira *et al.*, Rev. Sci. Instr. **93** (2022) 113304.

# UVSOR Accelerator Complex

## Injection Linear Accelerator

Energy	15 MeV
Length	2.5 m
Frequency	2856 MHz
Accelerating RF Field	$2\pi/3$ Traveling Wave
Klystron Power	1.8 MW
Energy Spread	$\sim 1.6$ MeV
Repetition Rate	2.6 Hz

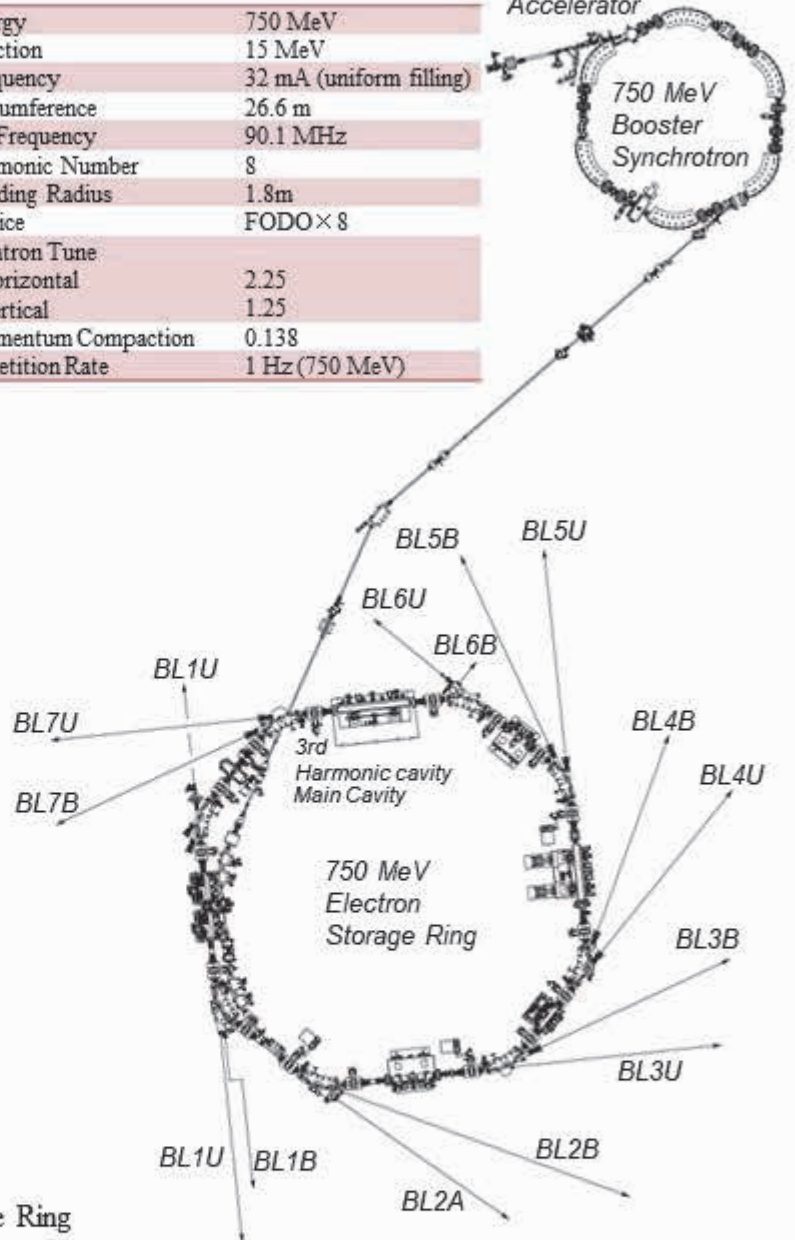
## UVSOR-III Storage-Ring

Energy	750 MeV
Injection Energy	750 MeV
Maximum Storage Current	500 mA (multi bunch) 100 mA (single bunch)
Normal operation current (Top-up mode)	300 mA (multi bunch) 50 mA (single bunch)
Natural Emittance	17.5 nm-rad
Circumference	53.2 m
RF Frequency	90.1 MHz
Harmonic Number	16
Bending Radius	2.2 m
Lattice	Extended DBA $\times 4$
Straight Section	$(4\text{ m} \times 4) + (1.5\text{ m} \times 4)$
RF Voltage	120 kV
Betatron Tune	
Horizontal	3.75
Vertical	3.20
Momentum Compaction	0.030
Natural Chromaticity	
Horizontal	-8.1
Vertical	-7.3
Energy Spread	$5.26 \times 10^{-4}$
Coupling Ratio	1%
Natural Bunch Length	128 ps

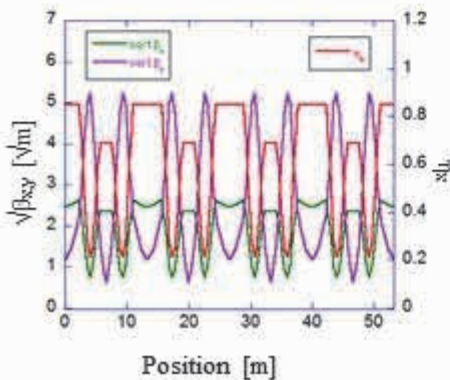
## Booster Synchrotron

Energy	750 MeV
Injection	15 MeV
Frequency	32 mA (uniform filling)
Circumference	26.6 m
RF Frequency	90.1 MHz
Harmonic Number	8
Bending Radius	1.8m
Lattice	FODO $\times 8$
Betatron Tune	
Horizontal	2.25
Vertical	1.25
Momentum Compaction	0.138
Repetition Rate	1 Hz (750 MeV)

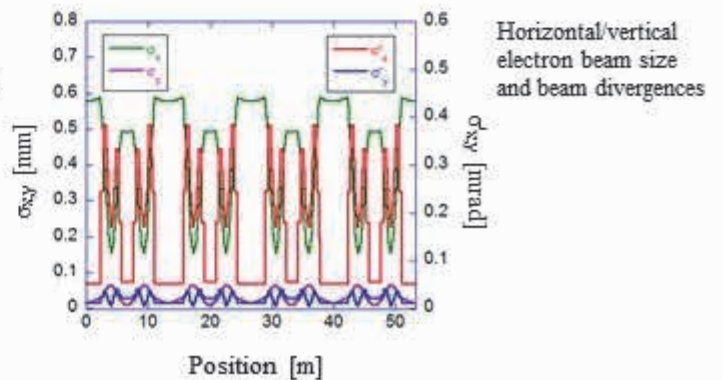
15 MeV  
Linear  
Accelerator



## Electron Beam Optics of UVSOR-III Storage Ring

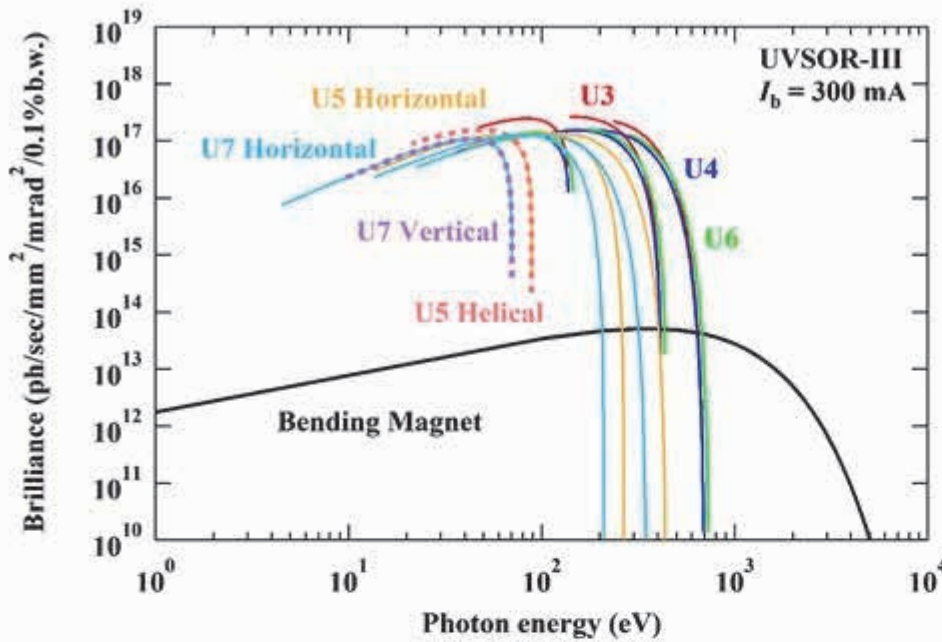


Horizontal/vertical betatron functions and dispersion function



Horizontal/vertical electron beam size and beam divergences

## Insertion Device



Brilliance of radiation from the insertion devices (U3, U4, U5, U6 and U7) and a bending magnet of UVSOR-III

### U1 Apple-II Undulator /

#### Optical Klystron

Number of Periods	10+10
Period length	88 mm
Pole Length	0.968 m + 0.968 m
Pole Gap	24-200 mm
Deflection Parameter	7.36 (Max. Horizontal) 4.93 (Max. Vertical) 4.06 (Max. Helical)

### U3 In-vacuum Undulator

Number of Periods	50
Period length	38 mm
Pole Length	1.9 m
Pole Gap	16.5-40 mm
Deflection Parameter	1.8-0.24

### U4 In-vacuum Undulator

Number of Periods	26
Period length	38 mm
Pole Length	0.99 m
Pole Gap	13-40 mm
Deflection Parameter	2.4-0.19

### U5 Apple-II

#### Variable Polarization Undulator

Number of Periods	38
Period length	60 mm
Pole Length	2.28 m
Pole Gap	24-190 mm
Deflection Parameter	3.4 (Max. Horizontal) 2.1 (Max. Vertical) 1.8 (Max. Helical)

### U6 In-vacuum Undulator

Number of Periods	26
Period length	36 mm
Pole Length	0.94 m
Pole Gap	13-40 mm
Deflection Parameter	1.78 - 0.19

### U7 Apple-II

#### Variable Polarization Undulator

Number of Periods	40
Period length	76 mm
Pole Length	3.04 m
Pole Gap	24-200 mm
Deflection Parameter	5.4 (Max. Horizontal) 3.6 (Max. Vertical) 3.0 (Max. Helical)

### Bending Magnets

Bending Radius	2.2 m
Critical Energy	425 eV

## Beamlines in 2022

Fumihiko Matsui

*UVSOR Synchrotron Facility, Institute for Molecular Science*

UVSOR is one of the highest-brilliance light sources in the extreme-ultraviolet region among the synchrotron radiation facilities with electron energies of less than 1 GeV. The low natural emittance of the UVSOR-III storage ring, 17.5 nm-rad, was accomplished after the successful completion of the storage ring upgrade project (the UVSOR-III project) in 2012. Eight bending magnets and six insertion devices are available as synchrotron light sources at UVSOR. There are a total of fourteen operational beamlines. Twelve of them are the so-called “Public beamlines”, which are open to scientists from universities and research institutes belonging to the government, public organizations, private enterprises and also those from foreign countries. The beamline BL6U is the “In-house beamlines”, and are dedicated to the use of research groups within Institute for Molecular Science (IMS). The beamline BL1U is a partially “Public” and partially “In-house” beamline. There is one tender X-ray (TX) station equipped with a double-crystal monochromator, seven extreme ultraviolet (EUV) and soft X-ray (SX) stations with grazing incidence monochromators, three vacuum ultraviolet (VUV) stations with normal incidence monochromators, two infrared (IR) stations equipped with Fourier Transform interferometers, and one direct radiation station located after two tandem undulators, as shown in the appended table (next page) for all available beamlines at UVSOR in 2022. The details of the updates for undulator beamlines are the followings.

- In **BL1U**, the development of a new light source and the utilization of gamma-rays are being carried out. This beamline is equipped with a tandem undulators with a buncher section, which can be used for free electron laser in the range from visible to deep UV, VUV coherent harmonic generation, and generation of spatiotemporal structured light such as an optical vortex beam, a vector beam and double-pulsed wave packets. It is also equipped with a femto-second laser system synchronized with the accelerator, which is used for the generation of Compton scattered gamma-rays. Users are provided with gamma-ray induced positron annihilation spectroscopy that can analyze nanometer-order defects in bulk materials. To increase the counting rate of annihilation gamma rays, an array detector with eight BaF<sub>2</sub> scintillators was developed. The measurement can be completed in a few hours for metal samples.
- In **BL3U**, the ultrathin-liquid cell for low-energy XAS has been developed. The studies of local structures of several aqueous solutions and various chemical processes in solution such as catalytic and electrochemical reactions, and laminar flows in microfluidics by using operando XAS in C, N, and O K-edges were demonstrated. Moreover, an argon gas window that is effective from 60 to 240 eV with the removal of high-order X-rays, which will develop chemical research since it includes K-edges of Li and B and L-edges of Si, P, S, and Cl was established.
- Resonant soft X-ray scattering (RSoXS) for soft materials is also applicable. RSoXS is similar to small angle X-ray scattering (SAXS) and can provide information on the mesoscopic structure (1-100nm) of sample. This method has selectivity of elements, functional groups and molecular orientation. Since soft X-ray region include K—edge energies of light element (C, N, O), RSoXS is a powerful tool to investigate soft matters.
- **BL4U**, which is equipped with a scanning transmission soft X-ray microscope (STXM), is actively used not only by academic users but also by many industrial users. The STXM can be applied to wide range of sciences, such as polymer science, material science, cell biology, environmental science, and so on. In FY2020, it became possible to image the lithium K-edge with a spatial resolution of 72 nm. Final adjustments for the airtight sample transport system and the sample transport container were carried out for the organic substance analysis of the Hayabusa2 returned samples for the summer of FY2021.
- In **BL5U**, high energy resolution angle-resolved photoemission spectroscopy (ARPES) is available. Users can now use so-called “deflector mapping” for all kinetic energies and lens modes by using the latest version of ARPES analyzer. Users can also obtain spatial-dependence of the electronic structure of solid surfaces using micro-focused beam (50 μm). An alkali-metal deposition system has been installed. Potassium for example can be deposited while the sample is still mounted on the manipulator at low temperatures. As part of the development of spin-resolved ARPES, a two-dimensional image of the spin-resolved spectrum of the Rashba splitting of Au(111) surface has been successfully obtained.
- At **BL6U**, one of the In-house beamlines, photoelectron momentum microscope (PMM), which is a new-concept multi-modal electronic structure analysis system with high resolution in real space and momentum space, has been installed and is in operation. A key feature of the PMM is that it can very effectively reduce radiation-induced damage by directly projecting a single photoelectron constant energy contour in

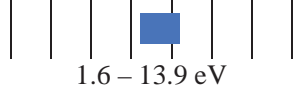
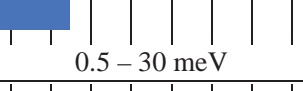
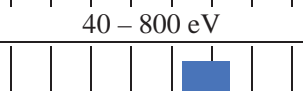
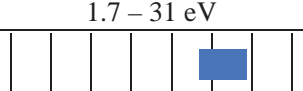
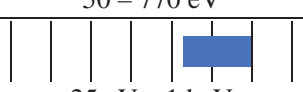
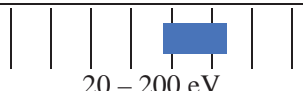
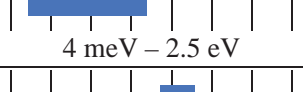
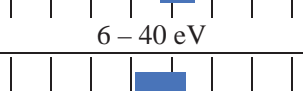
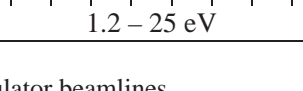
reciprocal space with a radius of a few  $\text{\AA}^{-1}$  or real space with a radius of a few hundred  $\mu\text{m}$  onto a 2D detector. Experiments such as valence band photoelectron spectroscopy on the micrometer scale and resonance photoelectron diffraction by soft X-ray excitation are performed. In FY2023, we plan to further expand PMM's capabilities by introducing an additional 2D spin filter. In addition to grazing-incidence soft X-ray excitation, normal-incidence vacuum ultraviolet (VUV) beam with variable polarizations (horizontal/vertical/circular) became also available at the same focal position of the PMM via a newly added branch from the next BL7U. This highly symmetrical measurement geometry completely eliminates the p-polarized linear dichroism effect in the circular dichroism measurements of valence band, making transition matrix element analysis much simpler and reliable.

- At **BL7U**, high-energy resolution ARPES is

available with extremely low energy of photons (6 eV~) using the low-temperature 6-axis manipulator with a sample temperature 4.5-350 K. In FY2021, the deflector-type detector for the hemispherical analyzer was installed to realize an effective 2D measurement with the automated manipulator control. Users can perform the measurement of the bulk sensitive electronic structure of solids and the high-throughput measurement for molecular materials using high-photoionization cross-section using low-excitation photon energy.

Those wishing to use the open and in-house beamlines are recommended to contact the appropriate beamline contact persons (see next page). Applications can be submitted at NOUS ([https:// nous.nins.jp/user/signin](https://nous.nins.jp/user/signin)). All users are required to refer to the beamline manuals and the UVSOR guidebook, on the occasion of conducting the actual experimental procedures. For updated information on UVSOR, please see <http://www.uvsor.ims.ac.jp>.

## Beamlines at UVSOR

Beamline	Monochromator / Spectrometer	Energy Range	Targets	Techniques	Contact
BL1U	Free electron laser	 1.6 – 13.9 eV		(Irradiation)	Y. Taira yostaira@ims.ac.jp
BL1B	Martin-Puplett FT-FIR	 0.5 – 30 meV	Solid	Reflection Absorption	K. Tanaka k-tanaka@ims.ac.jp
BL2A	Double crystal	 585 – 4 keV	Solid	Reflection Absorption	F. Matsui matui@ims.ac.jp
BL2B	18-m spherical grating (Dragon)	 23 – 205 eV	Solid	Photoemission	S. Kera kera@ims.ac.jp
BL3U	Varied-line-spacing plane grating (Monk-Gillieson)	 40 – 800 eV	Gas Liquid Solid	Absorption Photoemission Photon-emission	H. Iwayama iwayama@ims.ac.jp
BL3B	2.5-m off-plane Eagle	 1.7 – 31 eV	Solid	Reflection Absorption Photon-emission	F. Matsui matui@ims.ac.jp
BL4U	Varied-line-spacing plane grating (Monk-Gillieson)	 50 – 770 eV	Gas Liquid Solid	Absorption (Microscopy)	T. Ohigashi ohigashi@ims.ac.jp
BL4B	Varied-line-spacing plane grating (Monk-Gillieson)	 25 eV – 1 keV	Gas Solid	Photoionization Photodissociation Photoemission	H. Iwayama iwayama@ims.ac.jp
BL5U	Spherical grating (SGM-TRAIN <sup>+</sup> )	 20 – 200 eV	Solid	Photoemission	K. Tanaka k-tanaka@ims.ac.jp
BL5B	Plane grating	 6 – 600 eV	Solid	Calibration Absorption	K. Tanaka k-tanaka@ims.ac.jp
BL6U*	Variable-included-angle varied-line-spacing plane grating	 40 – 500 eV	Gas Solid	Photoionization Photodissociation Photoemission	F. Matsui matui@ims.ac.jp
BL6B	Michelson FT-IR	 4 meV – 2.5 eV	Solid	Reflection Absorption IR microscope	K. Tanaka k-tanaka@ims.ac.jp
BL7U	10-m normal incidence (modified Wadsworth)	 6 – 40 eV	Solid	Photoemission	K. Tanaka k-tanaka@ims.ac.jp
BL7B	3-m normal incidence	 1.2 – 25 eV	Solid	Reflection Absorption Photon-emission	F. Matsui matui@ims.ac.jp

Yellow columns represent undulator beamlines.

\* In-house beamline.

# BL1U

## Light Source Development Station

### ▼ Description

BL1U is dedicated for developments and applications of novel light sources. This beamline is equipped with a dedicated tandem undulator for variable polarization with a buncher section, which can be used for free electron laser in the range from visible to deep UV, VUV coherent harmonic generation (CHG), and generation of spatiotemporal structured light such as an optical vortex beam, a vector beam and double-pulse wave packets. It is also equipped with a femto-second laser system synchronized with the accelerator, which is used for the generation of CHG, laser Compton scattered gamma-rays, and coherent THz radiation. Nowadays, material analysis by positron annihilation spectroscopy using laser Compton scattered gamma rays is actively used.

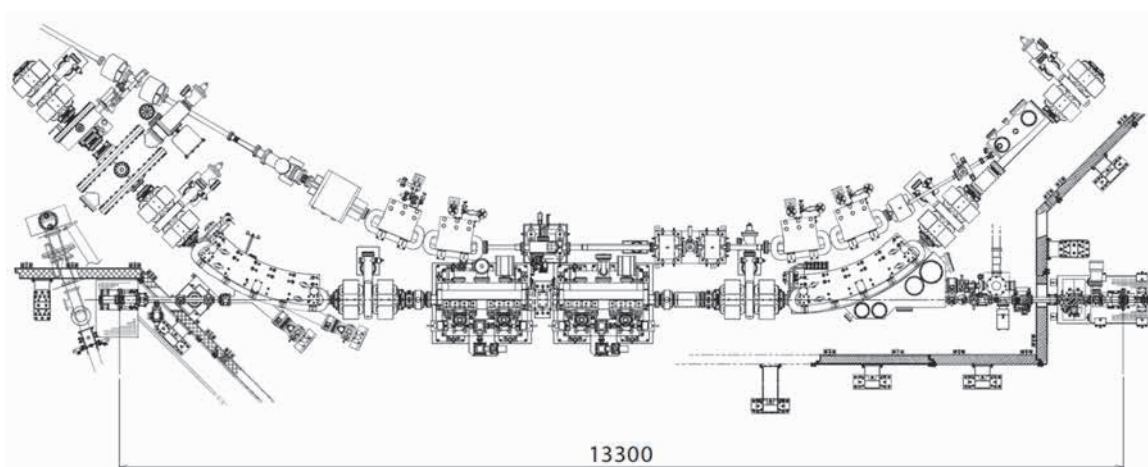


Fig. 1. Configuration of the free electron laser

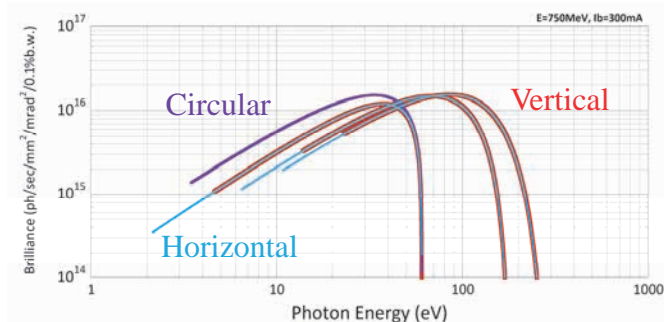


Fig. 2. Brilliance of BL1U Apple-II Undulator

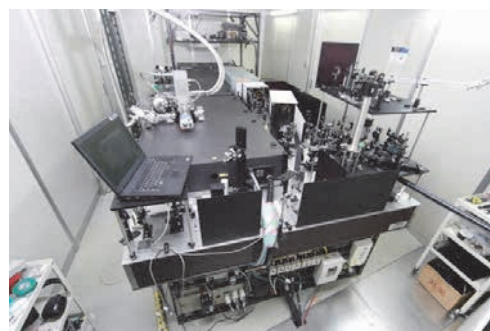


Fig. 3. Accelerator synchronized Laser System

### ▼ Technical Data of FEL

Wave Length	199-800 nm
Spectral Band Width	~10 <sup>-4</sup>
Polarization	Circular/Linear
Pulse Rate	11.26 MHz
Max. Ave. Power	~1 W

### ▼ Technical Data of Ti:Sa Laser

Wave Length	800 nm
Pulse Length	130 fsec
Oscillator	90.1 MHz
Pulse Energy	2.5 mJ    10 mJ    50 mJ
Repetition Rate	1 kHz    1 kHz    10 Hz

# BL1B

## Terahertz Spectroscopy Using Coherent Synchrotron Radiation

### ▼ Description

Coherent synchrotron radiation (CSR) is a powerful light source in the terahertz (THz) region. This beamline has been constructed for basic studies on the properties of THz-CSR. However, it can be also used for measurements of reflectivity and transmission spectra of solids using conventional synchrotron radiation.

The emitted THz light is collected by a three-dimensional magic mirror (3D-MM, M0) of the same type as those already successfully installed at BL43IR in SPring-8 and BL6B in UVSOR-II. The 3D-MM was installed in bending-magnet chamber #1 and is controlled by a 5-axis pulse motor stage ( $x, z$  translation;  $\theta_x, \theta_y, \theta_z$  rotation). The acceptance angle was set at 17.5-34 degrees (total 288 mrad) in the horizontal direction. The vertical angle was set at  $\pm 40$  mrad to collect the widely expanded THz-CSR.

The beamline is equipped with a Martin-Puplett type interferometer (JASCO FARIS-1) to cover the THz spectral region from 4 to 240  $\text{cm}^{-1}$  ( $h\nu = 500 \mu\text{eV}$ -30 meV). There is a reflection/absorption spectroscopy (RAS) end-station for large samples ( $\sim$  several mm). At the RAS end-station, a liquid-helium-flow type cryostat with a minimum temperature of 4 K is installed.

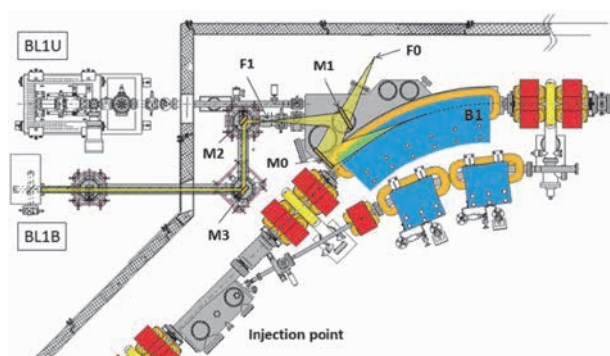


Fig. 1. Schematic top view of the beam extraction part of the THz-CSR beamline, BL1B. The three-dimensional magic mirror (3D-MM, M0) and a plane mirror (M1) are located in the bending-magnet chamber. A parabolic mirror (M2) is installed to form a parallel beam. The straight section (BL1U) is used for coherent harmonic generation (CHG) in the VUV region.

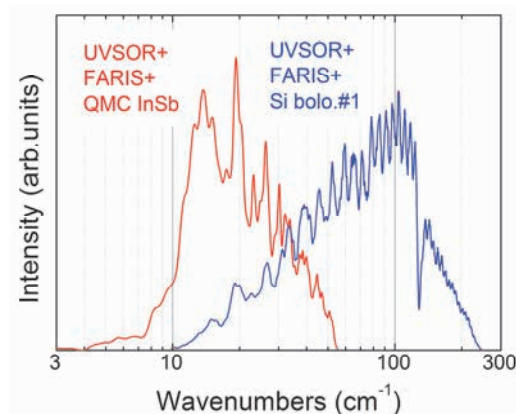


Fig. 2. Obtained intensity spectra with the combination of a light source (UVSOR), interferometer (FARIS-1), and detectors (Si bolometer and InSb hot-electron bolometer).

### ▼ Technical Data

Interferometer	Martin-Puplett (JASCO FARIS-1)
Wavenumber range (Energy range)	4-240 $\text{cm}^{-1}$ (500 $\mu\text{eV}$ -30 meV)
Resolution in $\text{cm}^{-1}$	0.25 $\text{cm}^{-1}$
Experiments	Reflection/transmission spectroscopy
Miscellaneous	Users can use their experimental system in this beamline.

# BL2A

## Soft X-Ray Beamline for Photoabsorption Spectroscopy

### ▼ Description

BL2A is a soft X-ray beamline for photoabsorption spectroscopy. The beamline is equipped with a pre-focusing mirror and a double-crystal monochromator [1]. The monochromator serves soft X-rays in the energy region from 585 to 4000 eV using several types of single crystals, such as beryl, KTP (KTiOPO<sub>4</sub>), and InSb. The throughput spectra measured using a Si photodiode (AXUV-100, IRD Inc.) are shown in Fig. 1. The typical energy resolution ( $E/\Delta E$ ) of the monochromator is approximately 1500 for beryl and InSb.

There is a small vacuum chamber equipped with an electron multiplier (EM) detector. Photoabsorption spectra for powdery samples are usually measured in total electron yield mode, with the use of the EM detector. In addition, a hemispherical electron analyzer for photoelectron spectroscopy is equipped.

Recently, a new omnidirectional photoelectron acceptance lens (OPAL) has been developed aiming to realize  $2\pi$ -steradian photoelectron spectroscopy and photoelectron holography [2]. By combining OPAL and the existing hemispherical electron analyzer, a photoelectron spectrometer with high energy resolution can be realized, and a full range ( $\pm 90^\circ$ ) 1D angular distribution can be measured at once. This upgrade is currently in the commissioning phase.

[1] Hiraya *et al.*, Rev. Sci. Instrum. **63** (1992) 1264.

[2] H. Matsuda and F. Matsui, Jpn. J. Appl. Phys. **59** (2020) 046503.

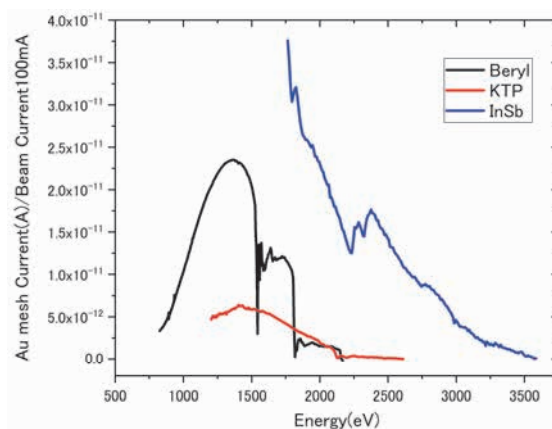


Fig. 1. Throughput spectra of the double-crystal monochromator at BL2A.

### ▼ Technical Data

Monochromator	Double crystal monochromator
Monochromator crystals: (2d value, energy range)	beryl (15.965 Å, 826–2271 eV), KTP (10.95 Å, 1205–3310 eV), InSb (7.481 Å, 1764–4000 eV), Ge (6.532 Å, 2094–4000 eV)
Resolution	$E/\Delta E = 1500$ for beryl and InSb
Experiments	Photoabsorption spectroscopy (total electron yield using EM and partial fluorescence yield using SDD)

# BL2B

## Photoelectron spectroscopy of molecular solids

### ▼ Description

This beamline previously dedicated for experiments in the field of gas phase photoionization and reaction dynamics. Then, the beamline has been reconstructed for photoelectron spectroscopy of molecular solids with a new end station, and experiments can be performed from May 2014. The monochromator is a spherical grating Dragon type with 18-m focal length. High throughput ( $1 \times 10^{10}$  photons  $s^{-1}$ ) and high resolution ( $E/\Delta E = 2000 - 8000$ ) are achieved simultaneously under the condition of the ring current of 100 mA [1]. The optical system consists of two pre-focusing mirrors, an entrance slit, three spherical gratings (G1 - G3), two folding mirrors, a movable exit slit, and a refocusing mirror [2]. The monochromator is designed to cover the energy range of 23–205 eV with the three gratings: G1 (2400 lines  $mm^{-1}$ ,  $R = 18$  m) at 80–205 eV; G2 (1200 lines  $mm^{-1}$ ,  $R = 18$  m) at 40–100 eV; G3 (2400 lines  $mm^{-1}$ ,  $R = 9.25$  m) at 23–50 eV. The percentage of the second-order light contamination at  $h\nu = 45.6$  eV is 23 % for G2 or 7 % for G3.

A UHV chamber is placed downstream of the refocusing mirror chamber and equipped silicon photodiode, sapphire plate Au mesh and filters for absolute photon flux measurement, monitor the photon-beam position, relative photon flux measurements and attenuate higher order light, respectively.

The new end station consists of a main chamber with a hemispherical analyzer (SCIENTA R3000) and a liquid-He-cooled cryostat (temperature range of 15-400 K) with 5-axis stage, a sample preparation chamber with a fast-entry load-lock chamber and a cleaning chamber with LEED, ion gun for sputtering and IR heating unit.

[1] M. Ono, H. Yoshida, H. Hattori and K. Mitsuke, Nucl. Instrum. Meth. Phys. Res. A **467-468** (2001) 577.

[2] H. Yoshida and K. Mitsuke, J. Synchrotron Radiation **5** (1998) 774.

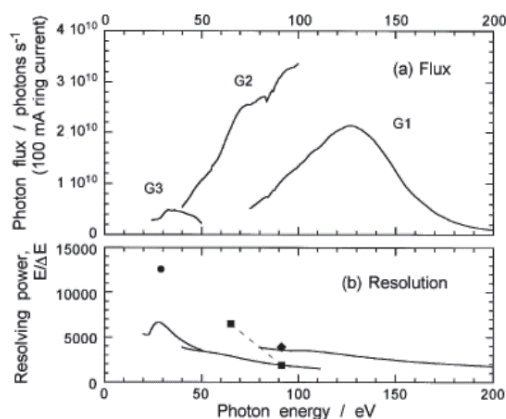


Fig. 1. Throughput from Dragon monochromator.

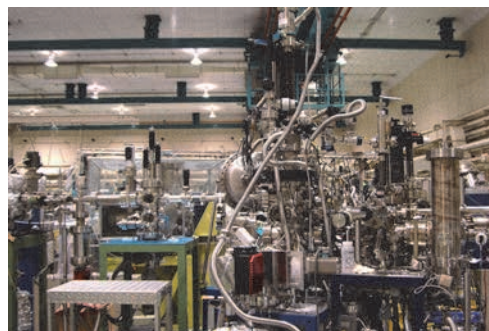


Fig. 2. End station of BL2B for photoelectron spectroscopy of molecular solids.

### ▼ Technical Data

Monochromator	18 m spherical grating Dragon-type
Wavelength Range	23-205 eV
Resolution	2000–8000 depending on the gratings
Experiments	Angle-resolved ultraviolet photoelectron spectroscopy

# BL3U

## Varied-Line-Spacing Plane Grating Monochromator for Molecular Soft X-Ray Spectroscopy

### ▼ Description

The beamline BL3U is equipped with an in-vacuum undulator composed of 50 periods of 3.8 cm period length. The emitted photons are monochromatized by the varied-line-spacing plane grating monochromator (VLS-PGM) designed for various spectroscopic investigations in the soft X-ray range. Three holographically ruled laminar profile plane gratings are designed to cover the photon energy range from 40 to 800 eV. The beamline has liquid cells for soft X-ray absorption spectroscopy (XAS) in transmission mode as shown in Fig. 1. The liquid cell is in the atmospheric helium condition, which is separated by a 100 nm thick  $\text{Si}_3\text{N}_4$  membrane with the window size of  $0.2 \times 0.2 \text{ mm}^2$  from the beamline in an ultrahigh vacuum condition. The thin liquid layer is assembled by using two 100 nm thick  $\text{Si}_3\text{N}_4$  membranes. The thickness of the liquid layer is controllable from 20 to 2000 nm by adjusting the helium pressures around the liquid cell in order to transmit soft X-rays. Liquid samples are exchangeable *in situ* by using a tubing pump. The liquid cell has two types of windows: one is the liquid part to obtain the soft X-ray transmission of liquid ( $I$ ), and the other is the blank part to obtain the transmission without liquid ( $I_0$ ). We can obtain the reliable XAS spectra based on the Lambert-Beer law  $\ln(I_0/I)$ . Since the liquid cell is in the atmospheric condition, we can measure XAS of liquid samples in the real environment. *Operando* XAS observation of several chemical reactions such as catalytic, electrochemical reactions are also possible by using our liquid cells developed for these purposes.

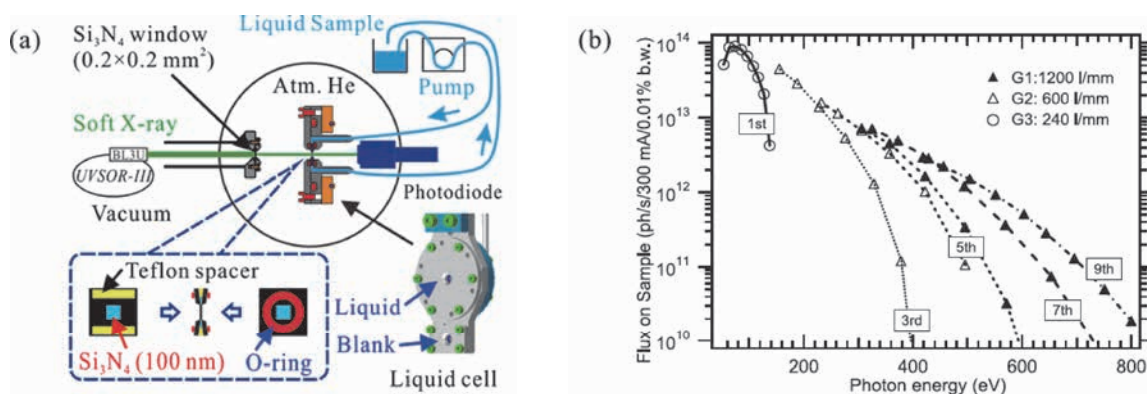


Fig. 1. (a) Schematics of a liquid cell for XAS in transmission mode settled in BL3U. The blowup shows a thin liquid layer assembled by two  $\text{Si}_3\text{N}_4$  membranes with the thickness of 100 nm. (b) Flux at the sample position with the resolving power of  $\lambda/\Delta\lambda=10^4$ .

### ▼ Technical Data

Monochromator	Varied-line-spacing plane grating monochromator
Energy Range	40-800 eV
Resolution	$E / \Delta E > 10\ 000$
Experiments	Soft X-ray absorption spectroscopy of liquid in transmission mode

# BL3B (HOTRLU)

## VIS-VUV Photoluminescence and Reflection/Absorption Spectroscopy

### ▼ Description

BL3B has been constructed to study photoluminescence (PL) in the visible (VIS) to vacuum ultraviolet (VUV) region. This beamline consists of a 2.5 m off-plane Eagle type normal-incidence monochromator, which covers the VUV, UV, and VIS regions, i.e., the energy (wavelength) region of 1.7-31 eV (40-730 nm), with three spherical gratings having constant grooving densities of 1200, 600, and 300 l/mm optimized at the photon energies of ~20, ~16, and ~6 eV, respectively. The schematic side view and top view layouts are shown in Figs. 1(a) and 1(b), respectively. The FWHM of the beam spot at the sample position is 0.25 mm (V) × 0.75 mm (H). Low energy pass filters (LiF, quartz, WG32, OG53) can be inserted automatically to maintain the optical purity in the G3 (300 l/mm) grating region (1.7~11.8 eV). Figure 2 shows the throughput spectra (photon numbers at a beam current of 300 mA) for each grating with entrance and exit slit openings of 0.1 mm (resolving power  $E / \Delta E$  of ~2000 (G3, ~6.8 eV)). Since both slits can be opened up to 0.5 mm, a monochromatized photon flux of  $10^{10}$  photons/s or higher is available for PL measurements in the whole energy region.

The end station is equipped with a liquid-helium-flow type cryostat for sample cooling and two detectors; one of which is a photomultiplier with sodium salicylate and the other a Si photodiode for reflection/absorption measurement. For the PL measurements in the wide energy region from VIS to VUV, two PL monochromators, comprising not only a conventional VIS monochromator but also a VUV monochromator with a CCD detector, are installed at the end station.

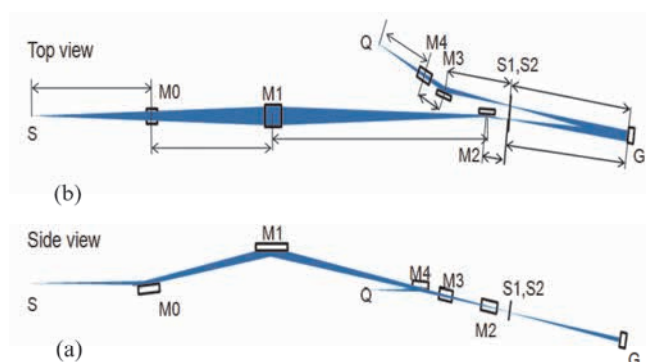


Fig. 1. Schematic layout of the BL3B (a) side view and (b) top view.

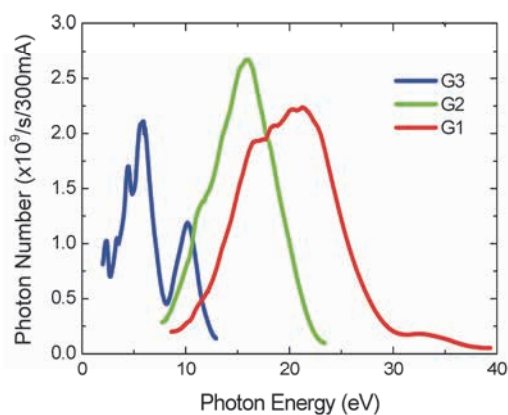


Fig. 2. Throughput spectra for each grating (G1:1200 l/mm, G2:600 l/mm and G3:300 l/mm) with  $S1 = S2 = 0.1$  mm.

### ▼ Technical Data

Monochromator	-2.5 m normal-incidence monochromator
Energy range	1.7-31 eV (40~730 nm)
Resolution ( $\Delta h\nu / h\nu$ )	$\geq 12000$ (at ~ 6.9 eV, 0.02 mm slits, G1 (1200 l/mm))
Experiments	Photoluminescence, reflection, and absorption spectroscopy, mainly for solids

# BL4U

## Scanning Transmission X-ray Microscopy in the Soft X-ray Region

### ▼ Description

In the soft x-ray region, there are several absorption edges of light elements and transition metals. The near edge X-ray absorption fine structure (NEXAFS) brings detailed information about the chemical state of target elements. A scanning transmission X-ray microscope (STXM) in the soft X-ray region is a kind of extended technique of the NEXAFS with high spatial resolution. The STXM has a capability of several additional options, for example, in-situ observations, 3-dimensional observation by computed tomography and ptychography, by utilizing the characteristics of the X-rays. The STXM can be applied to several sciences, such as polymer science, material science, cell biology, environmental science, and so on.

This beamline equips an in-vacuum undulator, a varied-line-spacing plane grating monochromator and a fixed exit slit. The soft X-ray energy range from 50 to 770 eV with the resolving power ( $E/\Delta E$ ) of 6,000 is available. The aperture size of the fixed exit slit determines not only the resolving power but also the size of a microprobe. A Fresnel zone plate is used as a focusing optical device through an order select aperture and its focal spot size of ~30 nm is available at minimum. An image is acquired by detecting intensities of the transmitted X-rays by a photomultiplier tube with scintillator with scanning a sample 2-dimensionally. By changing the energy of the incident beam, each 2-dimensional NEXAFS image is stacked. A main chamber of STXM is separated from the beamline optics by a silicon nitride membrane of 50-nm thickness; therefore, sample folders can be handled in vacuum or in helium.

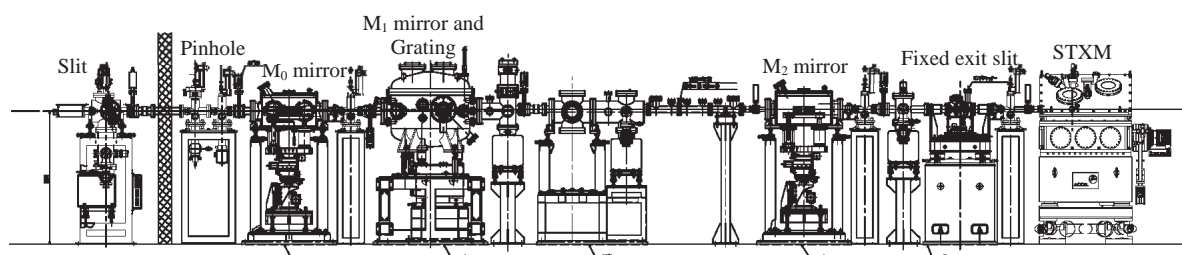


Fig. 1. Schematic image of BL4U

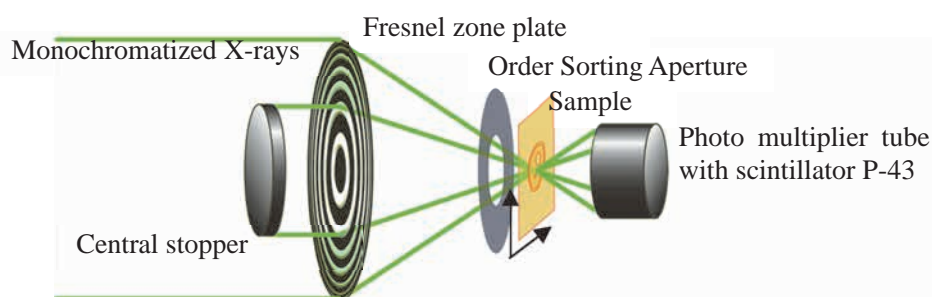


Fig. 2. Schematic image of STXM

### ▼ Technical Data

Energy range (E)	50 -770 eV
Resolving power ( $E/\Delta E$ )	~6,000
Photon flux on a sample (photons/s)	~ $2 \times 10^7$ @400 eV
Focusing optical element	Fresnel zone plate
Spatial resolution	~30 nm
Experiments	2-dimensional absorption spectroscopy
Measurement environment	standard sample folder in vacuum or in helium, specially designed sample cell in ambient condition

# BL4B

## Varied-Line-Spacing Plane Grating Monochromator for Molecular Soft X-Ray Spectroscopy

### ▼ Description

The beamline BL4B equipped with a varied-line-spacing plane grating monochromator (VLS-PGM) was constructed for various spectroscopic investigations in a gas phase and/or on solids in the soft X-ray range. Three holographically ruled laminar profile plane gratings with SiO<sub>2</sub> substrates are designed to cover the photon energy range from 25 to 800 eV. The gratings with groove densities of 100, 267, and 800 l/mm cover the spectral ranges of 25–100, 60–300, and 200–1000 eV, respectively, and are interchangeable without breaking the vacuum. Figure 1 shows the absolute photon flux for each grating measured using a Si photodiode (IRD Inc.), with the entrance- and exit-slit openings set at 50 and 50 μm, respectively. The maximum resolving power ( $E/\Delta E$ ) achieved for each grating exceeds 5000.

There is no fixed endstation on this beamline. A small vacuum chamber equipped with an electron multiplier (EM) detector is available. Soft X-ray absorption spectra of solid samples are usually measured by means of the total electron yield method using EM, and the partial fluorescence yield method using a silicon drift detector (SDD).

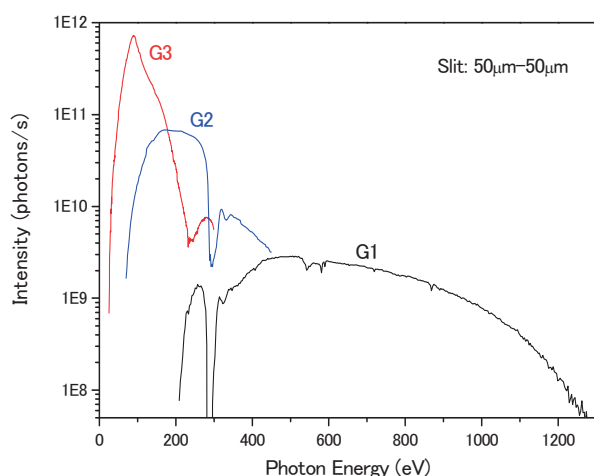


Fig. 1. Throughput from the VLS-PGM monochromator on BL4B.



Fig. 2. Photo of BL4B.

### ▼ Technical Data

Monochromator	Varied-line-spacing Plane Grating Monochromator
Energy range	25-1000 eV
Resolution	$E / \Delta E > 5000$ (at maximum)
Experiments	Soft X-ray spectroscopy (mainly, photoabsorption spectroscopy for solid targets by means of total electron yield method using EM and partial fluorescence yield method using SDD)

# BL5U

## Photoemission Spectroscopy of Solids and Surfaces

### ▼ Description

Since the monochromator of BL5U was an old-style spherical grating type SGMTRAIN constructed in 1990s and the throughput intensity and energy resolution were poor, the whole beamline has been replaced to state-of-the-art monochromator and end station. The new beamline has been opened to users from FY2016 as high-energy resolution ARPES beamline. Samples can be cooled down to 3.8 K with newly developed 5-axis manipulator to perform high energy resolution measurements. Users can also obtain spatial-dependence of the electronic structure of solids using micro-focused beam ( $\sim 50 \mu\text{m}$ ). The new electron lens system makes it possible to obtain ARPES spectra without moving samples. This beamline will also have new capability to perform high-efficient spin-resolved ARPES in the future.

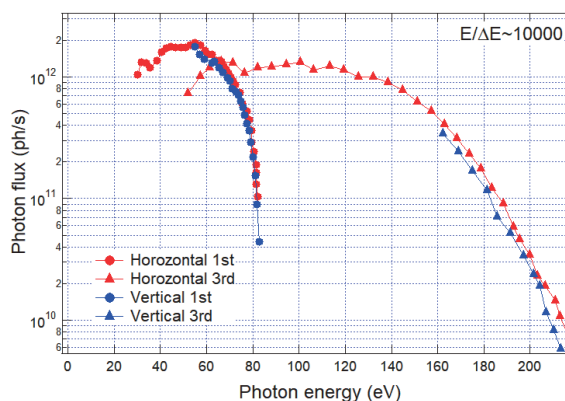


Fig. 1. Picture and photon flux of BL5U.

### ▼ Technical Data (Expected Performance)

Light source	APPLE-II type undulator ( $\lambda_u = 60 \text{ mm}$ , $N = 38$ ) vertical/horizontal, right/left circular (depending on $h\nu$ )
Monochromator	Monk-Gillieson VLS-PGM
Energy Range	20-200 eV
Resolution	$h\nu / \Delta E > 10,000$ for $< 10 \mu\text{m}$ slits
Experiment	ARPES, Space-resolved ARPES, Spin-resolved ARPES
Flux	$< 10^{12}$ photons/s for $< 10 \mu\text{m}$ slits (at the sample position)
Beam spot size	23 (H) x 40 (V) $\mu\text{m}$
Main Instruments	Hemispherical photoelectron analyzer with deflector scan (MBS A-1 Lens#4), Liq-He flow cryostat with 5-axis manipulator (3.8 K-350 K)

# BL5B

## Calibration Apparatus for Optical Elements and Detectors

### ▼ Description

BL5B has been constructed to perform calibration measurements for optical elements and detectors. This beamline is composed of a plane grating monochromator (PGM) and three endstations in tandem. The most upstream station is used for the calibration measurements of optical elements, the middle one for optical measurements for solids, and the last for photo-stimulated desorption experiments. The experimental chamber at the most downstream station is sometimes changed to a chamber for photoemission spectroscopy. The calibration chamber shown in Fig. 2 is equipped with a goniometer for the characterization of optical elements, which has six degrees of freedom, X-Y translation of a sample, and interchanging of samples and filters. These are driven by pulse motors in vacuum. Because the polarization of synchrotron radiation is essential for such measurements, the rotation axis can be made in either the horizontal or vertical direction (s- or p-polarization).

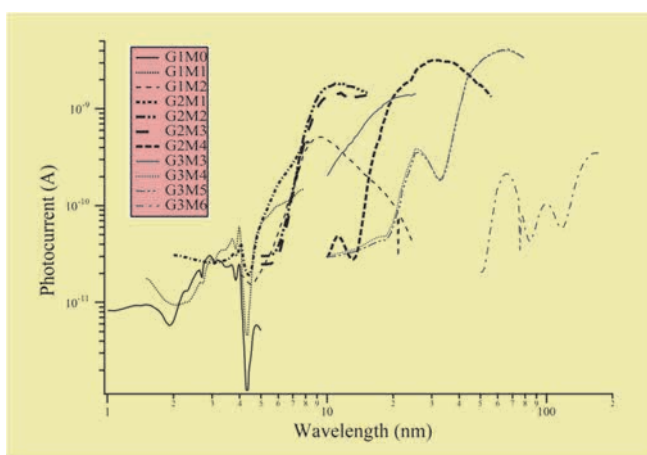


Fig. 1. Throughput spectra for possible combinations of gratings and mirrors at BL5B measured by a gold mesh.

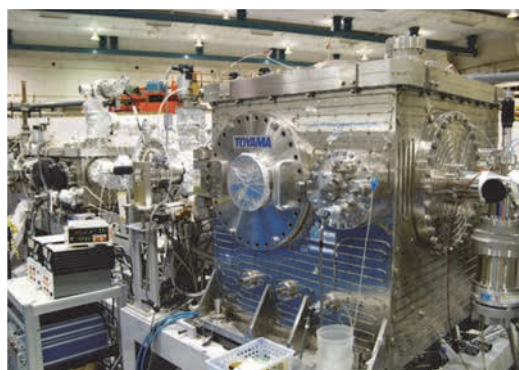


Fig. 2. A side view of the experimental chamber for calibration measurements.

### ▼ Technical Data

Monochromator	Plane Grating Monochromator
Energy range	6-600 eV (2-200 nm)
Resolution	$E / \Delta E \sim 500$
Experiments	Calibration of optical elements, reflection and absorption spectroscopy mainly for solids

# BL6U

## Variable-Included-Angle / Variable-Line-Spacing Plane Grating Monochromator for Soft X-Ray photoelectron Spectroscopy

### ▼ Description

The beamline BL6U equipped with a variable-included-angle Monk-Gillieson mounting monochromator with a varied-line-spacing plane grating was constructed for various spectroscopic investigations requiring high-brilliance soft X-rays on solid surfaces. Through a combination of undulator radiation and sophisticated monochromator design (entrance slit-less configuration and variable-included-angle mechanism), using a single grating, the monochromator can cover the photon energy ranging from 40 to 500 eV, with resolving power of greater than 10000 and photon flux of more than  $10^{10}$  photons/s. Figure 1 shows an example of the monochromator throughput spectra measured using a Si photodiode, with the exit-slit opening set at 30  $\mu\text{m}$ , which corresponds to the theoretical resolving power of 10000 at 80 eV.

A new Momentum Microscope experimental station for photoelectron spectroscopy resolved in 3D momentum space with a microscopic field of view has been built at BL6U (SPECS KREIOS 150 MM). A momentum resolution of  $0.01 \text{ \AA}^{-1}$  in  $k_x/k_y$ , as well as  $k_z$  is achieved. A spatial resolution of 50 nm, an energy resolution of 20 meV at 9 K, and a field of view of 2  $\mu\text{m}$  for ARPES are successfully demonstrated. This experimental station specializes in characterizing the electronic structure of surface atomic sites, thin films, molecular adsorbates, and bulk crystals. This method opens the door to direct observation of the Fermi surface of  $\mu\text{m}$ -sized crystals, which was difficult with conventional ARPES-type hemispherical analyzers.

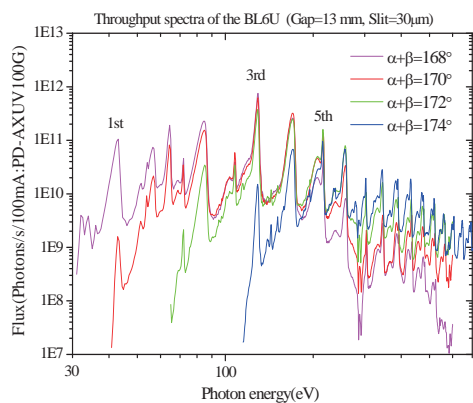


Fig. 1. Throughput spectra of the BL6U monochromator at various included angles.

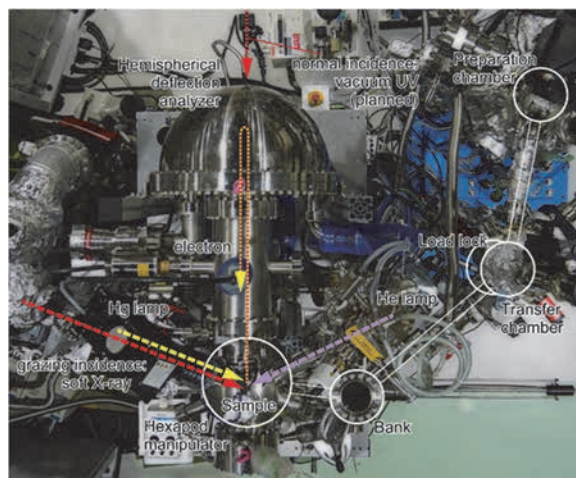


Fig. 2. Photograph of BL6U end station

### ▼ Technical Data

Monochromator	Variable-included-angle Varied-line-spacing Plane Grating Monochromator
Energy range	40-500 eV(practical)
Resolution	$E / \Delta E > 10000$ (at maximum)
Experiments	High-resolution soft X-ray spectroscopy (photoelectron spectroscopy for solid surfaces)

# BL6B

## Infrared and Terahertz Spectroscopy of Solids

### ▼ Description

Synchrotron radiation (SR) has good performance (high brilliance and high flux) not only in the VUV and soft X-ray (SX) regions but also in the infrared (IR) and THz regions. BL6B covers the IR and THz regions. The previous beamline, BL6A1, which was constructed in 1985, was the pioneer in IRSR research. The beamline was deactivated at the end of FY2003 and a new IR/THz beamline, BL6B (IR), was constructed in FY2004. The front-end part including bending duct #6 was replaced with a new part having a higher acceptance angle ( $215 \text{ (H)} \times 80 \text{ (V)} \text{ mrad}^2$ ) using a magic mirror, as shown in Fig. 1.

There are two Michelson type interferometers in this endstation; with first one (Bruker Vertex70v), which covers a wide spectral region from  $30$  to  $20,000 \text{ cm}^{-1}$  ( $h\nu = 4 \text{ meV}-2.5 \text{ eV}$ ), reflection/absorption spectroscopy measurements of large samples (up to several mm) and IR/THz microscopy measurements of tiny samples (up to several tens of  $\mu\text{m}$ ) can be performed. For reflection/absorption spectroscopy measurements, a liquid-helium-flow type cryostat with a minimum temperature of  $4 \text{ K}$  is installed. The other interferometer (Jasco FT/IR-6100), which covers  $350$  to  $15,000 \text{ cm}^{-1}$  ( $h\nu = 45 \text{ meV}-1.8 \text{ eV}$ ), has been available for IR microscopy imaging measurements from FY2014. One can also perform ATR measurements using diamond ATR prism.

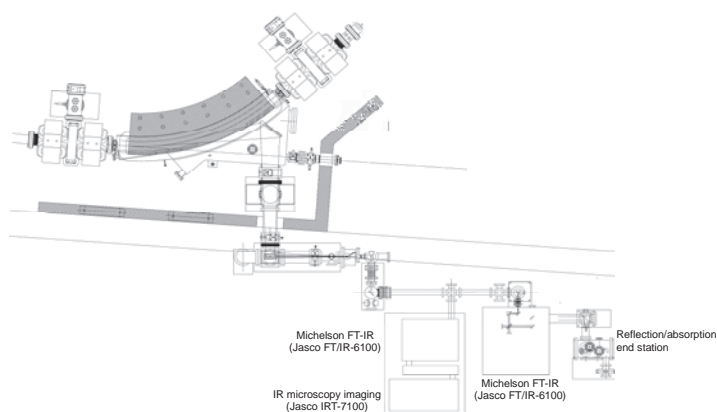


Fig. 1. Schematic top view of BL6B.

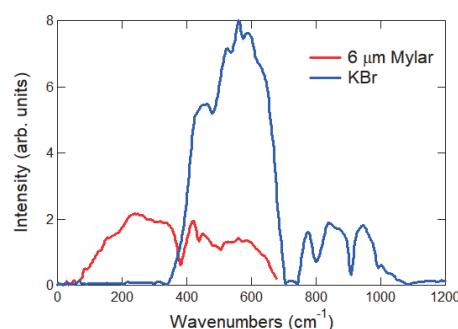


Fig. 2. Obtained intensity spectra with the combination of a light source (UVSOR), detector (Si bolometer), and interferometer (Bruker Vertex70v) with different beamsplitters ( $6 \mu\text{m}$  Mylar and KBr). (Only low energy side is shown).

### ▼ Technical Data

Interferometer	Michelson (Bruker Vertex70v)	Michelson (Jasco FT/IR-6100)
Wavenumber Range (Energy range)	$30-20,000 \text{ cm}^{-1}$ ( $4 \text{ meV}-2.5 \text{ eV}$ )	$350-15,000 \text{ cm}^{-1}$ ( $45 \text{ meV}-1.8 \text{ eV}$ )
Resolution in $\text{cm}^{-1}$	$0.1 \text{ cm}^{-1}$	$0.5 \text{ cm}^{-1}$
Experiments	Reflectivity and transmission spectroscopy THz Microspectroscopy	IR microscopy imaging (JASCO IRT-7000) ATR spectroscopy

# BL7U (SAMRAI)

## Angle-Resolved Photoemission of Solids in the VUV Region

### ▼ Description

Beamline 7U, named the Symmetry- And Momentum-Resolved electronic structure Analysis Instrument (SAMRAI) for functional materials, was constructed to provide a photon flux with high energy resolution and high flux mainly for high-resolution angle-resolved photoemission spectroscopy, so-called “ARPES”, of solids [1]. An APPLE-II-type variable-polarization undulator is installed as the light source. The undulator can produce intense VUV light with horizontal/vertical linear and right/left circular polarization. The undulator light is monochromatized by a modified Wadsworth type monochromator with three gratings (10 m radius; 1200, 2400, and 3600 lines/mm optimized at  $h\nu = 10, 20,$  and  $33$  eV). The energy resolution of the light ( $h\nu/\Delta h\nu$ ) is more than  $10^4$  with a photon flux of  $10^{11}$ - $10^{12}$  ph/s or higher on samples in the entire energy region. The beamline has a photoemission end-station equipped with a 200 mm-radius hemispherical photoelectron analyzer (MB Scientific AB, A-1 analyzer) with a wide-angle electron lens and a liquid-helium-cooled cryostat with 6-axis pulse motor control. The main function of the beamline is to determine the electronic structure of solids and its temperature dependence in order to reveal the origin of their physical properties.

[1] S. Kimura, T. Ito, M. Sakai, E. Nakamura, N. Kondo, K. Hayashi, T. Horigome, M. Hosaka, M. Katoh, T. Goto, T. Ejima and K. Soda, Rev. Sci. Instrum. **81** (2010) 053104.

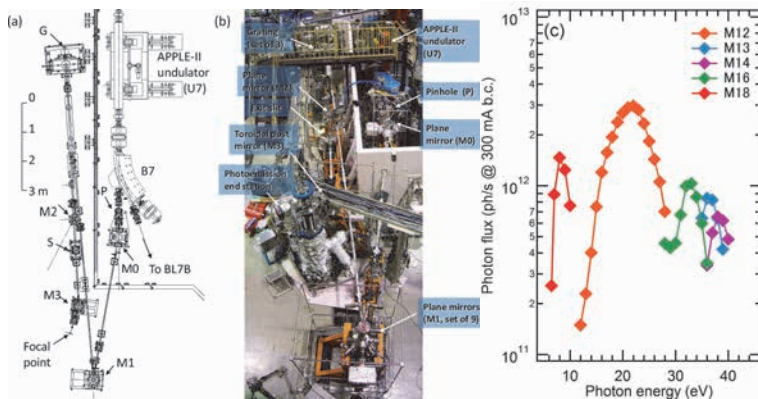


Fig. 1. SAMRAI beamline [(a), (b)] consisting of an APPLE-II type undulator (U7), a modified Wadsworth type monochromator (M0-S), and a high-resolution photoemission analyzer at the focal point. The monochromator has five major optical components: two plane mirrors (M0 and M1) with water cooling, one set of three spherical gratings (G), an exit slit (S), and one toroidal refocusing mirror (M3). (c) Example of flux intensity *versus* photon energy [1]

### ▼ Technical Data

Light source	APPLE-II type undulator ( $\lambda_u = 76$ mm, $N = 36$ ) vertical/horizontal, right/left circular (depending on $h\nu$ )
Monochromator	10 m normal-incidence monochromator (modified Wadsworth type)
Photon energy range	6 – 40 eV ( $\lambda = 30 - 200$ nm)
Resolution ( $h\nu/\Delta h\nu$ )	$E / \Delta E > 10000$ - $50000$
Photon flux on sample	$\geq 10^{11}$ - $10^{12}$ ph/s (depending on $h\nu$ )
Beam size on sample	$200$ (H) $\times$ $50$ (V) $\mu\text{m}^2$
Experiments	Angle-resolved photoemission of solids (MV Scientific A-1 analyzer, acceptance angle: $\pm 18$ deg)

# BL7B

## 3 m Normal-Incidence Monochromator for Solid-State Spectroscopy

### ▼ Description

BL7B has been constructed to provide sufficiently high resolution for conventional solid-state spectroscopy, sufficient intensity for luminescence measurements, wide wavelength coverage for Kramers–Kronig analyses, and minimum deformation to the polarization characteristic of incident synchrotron radiation. This beamline consists of a 3-m normal incidence monochromator, which covers the vacuum ultraviolet, ultraviolet, visible, and infrared, i.e., the wavelength region of 50–1000 nm, with three gratings (1200, 600, and 300 l/mm). Two interchangeable refocusing mirrors provide two different focusing positions. For the mirror with the longer focal length, an LiF or a MgF<sub>2</sub> window valve can be installed between the end valve of the beamline and the focusing position. Figure 1 shows the absolute photon intensity for each grating with the entrance and exit slit openings of 0.5 mm. A silicon photodiode (AXUV-100, IRD Inc.) was utilized to measure the photon intensity and the absolute photon flux was estimated, taking the quantum efficiency of the photodiode into account.

The cooling system for the pre-focusing mirror has been removed, resulting in longer beam settling times. Currently, BL7B is opened during single bunch mode, but limited use is possible during multi bunch mode.

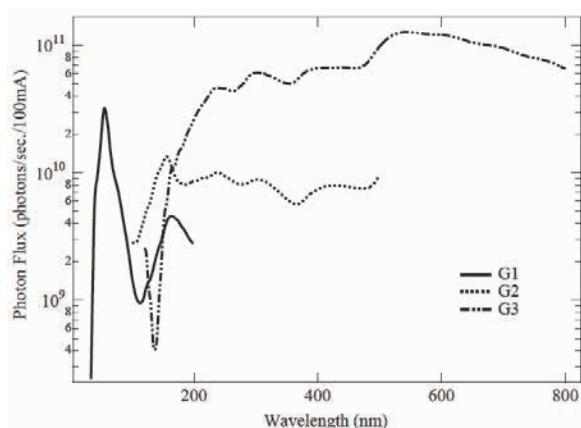


Fig. 1. Throughput spectra of BL7B measured using a silicon photodiode.

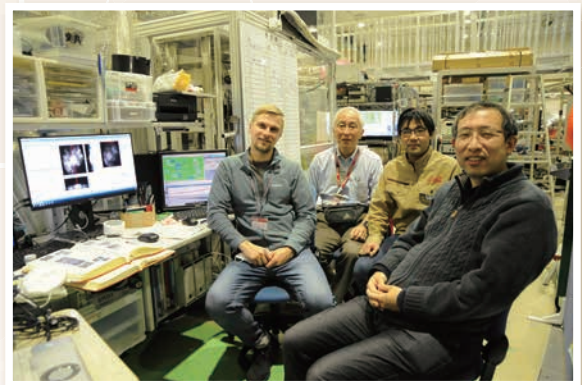
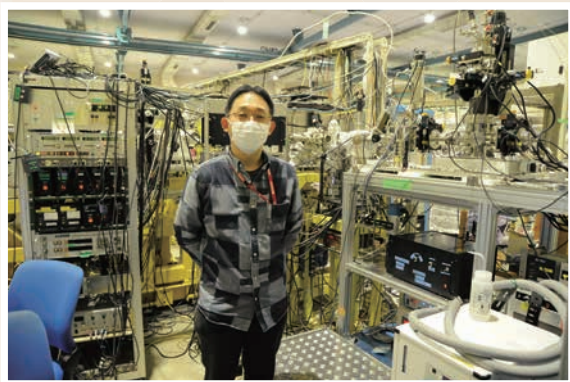
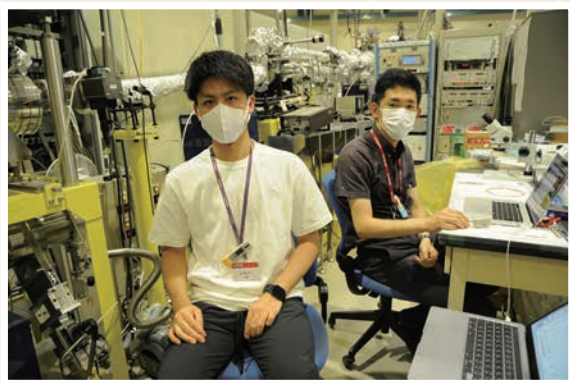
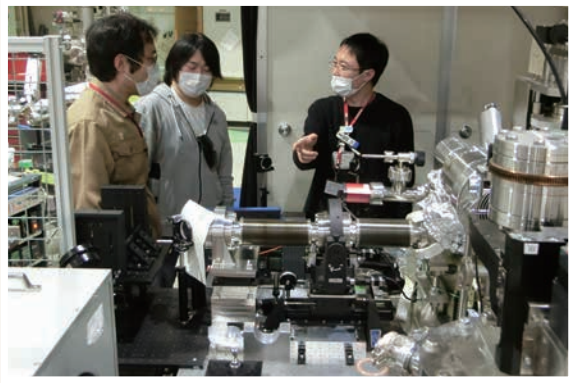


Fig. 2. Photo of BL7B.

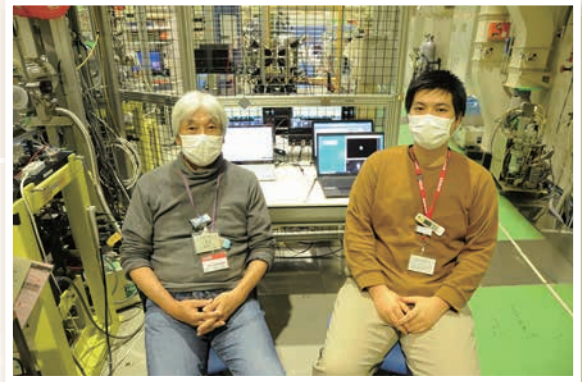
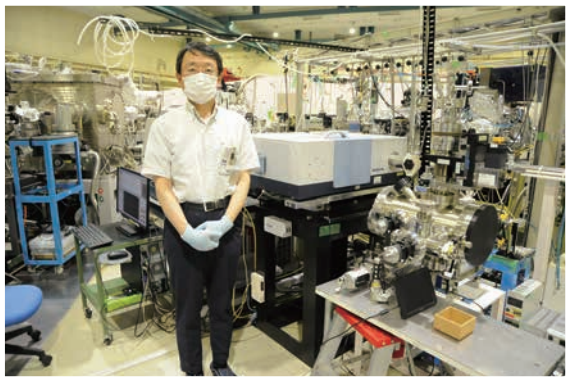
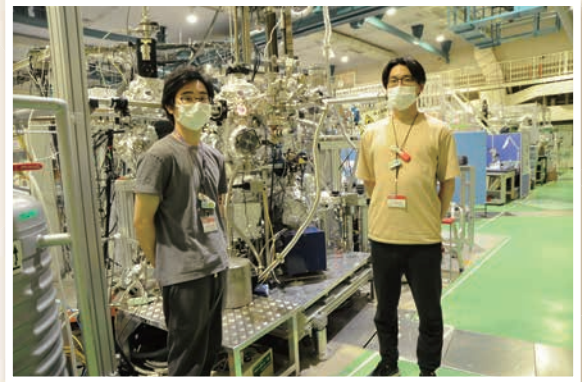
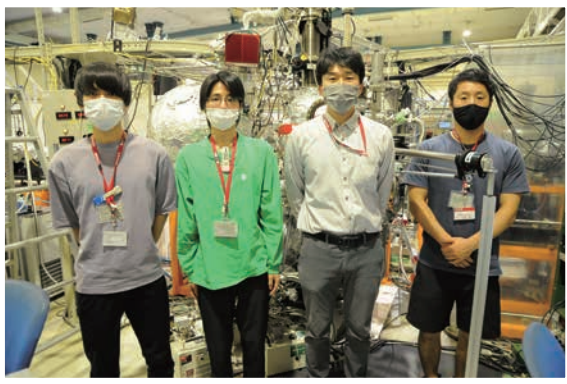
### ▼ Technical Data

Monochromator	3 m Normal-Incidence Monochromator
Wavelength Range	50-1000 nm (1.2-25 eV)
Resolution	$E / \Delta E = 4000-8000$ for 0.01 mm slits
Experiments	Absorption, reflection, and fluorescence spectroscopy, mainly for solids

# *UVSOR User 1*

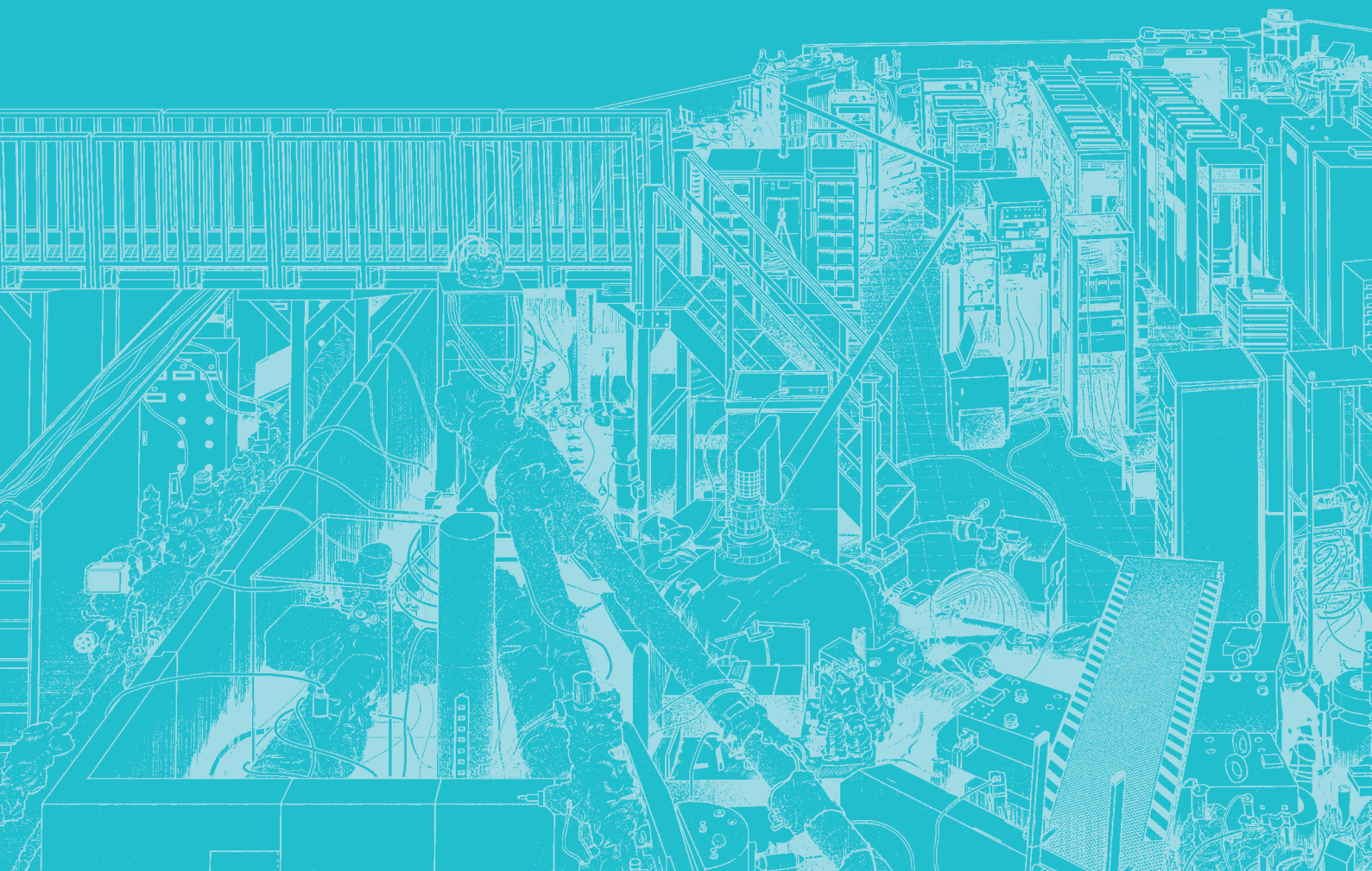


# UVSOR User 2



# III-1

Accelerators and  
Instruments





BL1U

## Spectral Phase Interferometry for Direct Electric-field Reconstruction of Undulator Radiation

T. Fuji<sup>1</sup>, T. Kaneyasu<sup>2</sup>, M. Fujimoto<sup>3</sup>, Y. Okano<sup>3</sup>, E. Salehi<sup>3</sup>, M. Hosaka<sup>4,5</sup>, Y. Takashima<sup>4</sup>,  
A. Mano<sup>4</sup>, Y. Hikosaka<sup>6</sup>, S. Wada<sup>7</sup> and M. Katoh<sup>8,3</sup>

<sup>1</sup>Laser Science Laboratory, Toyota Technological Institute, Nagoya 468-8511, Japan

<sup>2</sup>SAGA Light Source, Tosu 841-0005, Japan

<sup>3</sup>Institute for Molecular Science, Okazaki 444-8585, Japan

<sup>4</sup>Synchrotron Radiation Research Center, Nagoya University, Nagoya, 464-0814, Japan

<sup>5</sup>National Synchrotron Radiation Laboratory, University of Science and Technology of China, Hefei 230029, China

<sup>6</sup>Institute of Liberal Arts and Sciences, University of Toyama, Toyama 930-0194, Japan

<sup>7</sup>Graduate School of Advanced Science and Engineering, Hiroshima University, Higashi-Hiroshima 739-8526, Japan

<sup>8</sup>Hiroshima Synchrotron Radiation Center, Hiroshima University, Higashi-Hiroshima 739-0046, Japan

An undulator is a device widely used in modern synchrotron light sources to produce quasi-monochromatic light. The waveform of the electric field produced by a relativistic electron in the undulator is primarily determined by the number of magnets and the gap between them. Although a simple electromagnetic theory predicts a square-shaped waveform, it has never been measured due to the lack of a suggested method. Therefore, it is crucial to characterize the electric field produced by the undulator for the development of synchrotron sources.

SPIDER is a femtosecond pulse characterization method that has been widely used since its invention in 1998 [1]. It involves retrieving the spectral phase by analyzing the fringes of the interferogram between a test pulse and a spectrally sheared replica. At the UVSOR-III synchrotron light source, a tandem undulator produces two wave packets whose wavelengths can be individually adjusted by changing the gap between the permanent magnets of each undulator. A phase shifter consisting of three pairs of electromagnets forms a small chicane for the electron beam and controls the delay between the wave packets in the femtosecond regime with attosecond accuracy.

The twin tandem undulator produces a pair of wavelength-shifted wave packets with a delay, and the interferogram between them can be regarded as a “SPIDER” interferogram. Consequently, we can use the same algorithm as SPIDER to analyze the interferogram and reconstruct the electric field generated by the undulator [2].

The experiment took place at the 750-MeV UVSOR-III storage ring, where a tandem undulator was installed as shown in Figure 1. The undulator consisted of twin APPLE-II type variable polarization devices that operated in the horizontal linear polarization mode, with 10 magnetic periods and a period length of 88 mm. The central photon energy of the fundamental radiation

was adjusted to 35 eV. Figure 2 displays the retrieved electric field, which shows 10-cycle field oscillations with a rectangular envelope of the wave packet that are accurately reproduced.

This method is advantageous for shorter wavelength synchrotron radiation, including soft and hard x-rays, as it does not require nonlinear wavelength conversion. Additionally, it holds potential for the characterization of FEL pulses.

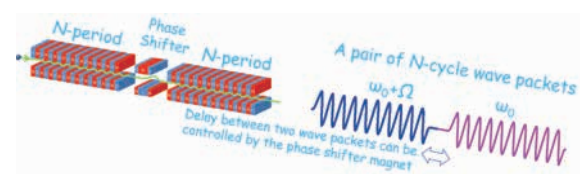


Fig. 1. Conceptual diagram of the tandem undulator.  $\omega_0$  and  $\omega_0 + \Omega$  represent the carrier frequencies of the upstream and downstream wave packets, respectively.

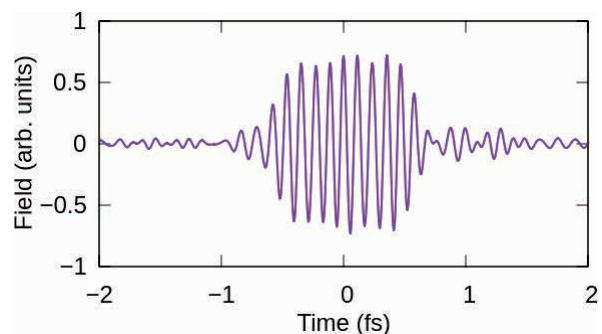


Fig. 2. Waveform of the wave packet retrieved using the SPIDER algorithm.

[1] C. Iaconis and I. A. Walmsley, *Opt. Lett.* **23** (1998) 792.

[2] T. Fuji *et al.*, *Optica* **10** (2) (2023) 302.

## Construction of Laser Transport Line and Light Measurement Setup for Coherent Harmonic Generation Experiment at BL1U

F. Sakamoto<sup>1</sup>, H. Zen<sup>2</sup>, T. Tanikawa<sup>3</sup>, Y. Taira<sup>4</sup>, Y. Okano<sup>4</sup>, H. Ohta<sup>4</sup>,  
J. Yamazaki<sup>4</sup>, K. Hayashi<sup>4</sup>, Y. Takashima<sup>5</sup>, A. Mano<sup>5</sup> and M. Katoh<sup>4,6</sup>

<sup>1</sup>National Institute of Technology, Akita College, Akita 011-8511, Japan

<sup>2</sup>Institute of Advanced Energy, Kyoto University, Kyoto 611-0011, Japan

<sup>3</sup>Innovation Center for Applied Superconducting Accelerators (iCASA), High Energy Accelerator Research Organization (KEK) Ibaraki 305-0801, Japan

<sup>4</sup>UVSOR Synchrotron Facility, Institute for Molecular Science, Okazaki 444-8585, Japan

<sup>5</sup>Synchrotron Radiation Research Center, Nagoya University, Nagoya 464-8603, Japan

<sup>6</sup>HiSOR, Hiroshima University, Higashi-Hiroshima 739-0046, Japan

Coherent Harmonic Generation (CHG) is a method to imprint external laser information to an electron beam and generate temporally coherent and short VUV radiations from it [1]. Since the properties of the CHG such as polarization, temporal and spectral distribution are completely dependent on the external laser [2], they can be optimized by changing the laser and electron beam conditions. These features of the CHG have possibilities for some applied experiments. So far, some experiments on CHG have been performed at UVSOR-II and important features of CHG were observed [3, 4].

We plan to resume detailed studies of CHG using an optical klystron and an ultrashort Ti:Sapphire laser pulse at BL1U. The optical klystron of BL1U consists of two APPLE-II variable polarization undulators and a buncher magnet which is located between the undulators [5]. The laser pulse is injected into the first undulator and an energy exchange between the laser pulse and electron beam that circulates in the storage ring occurs. This leads to an energy modulation inside the electron beam. In the buncher magnet, the energy modulation is converted to a density modulation with a period of the laser wavelength (micro-bunching). Temporally coherent radiations are generated from the micro-bunched electrons in the second undulator.

In order to perform the CHG experiment, we have newly constructed a laser transport line and light measurement setup at BL1U. Schematics of the setup are shown in Fig. 1. The laser pulse is transported about 10 m from laser hutch and injected to the vacuum tube connected to the storage ring. The polarization state is controlled by a  $\lambda/2$  waveplate and a polarization beam splitter (PBS). We also set a monitoring system to adjust spatial and temporal overlaps between the laser and electron beam using CMOS and streak cameras. After the construction of the setup, we have performed the first CHG experiment at BL1U.

The experiment was performed with an electron beam energy of 600 MeV. A resonant wavelength of the undulators was set to 800 nm which corresponds to the wavelength of Ti:Sapphire laser. Figure 2 shows the streak camera images. From these images, we can confirm the laser pulse of 1 ps was well overlapped on the undulator radiation (i.e., electron beam) of 100 ps.

We also observed the spatial overlap by using CMOS camera that was focused in the first undulator. The first target wavelength for the observation was set to 267 nm which was 3rd harmonics of the radiation from the micro-bunching. For the purpose, CHG and Ti:Sapphire pulses were separated by using a dichroic mirror and a band pass filter (BPF) at a downstream of undulators. A photo-multiplier tube (PMT) was used to monitor an intensity of the CHG signals but unfortunately no CHG signals was observed. We are considering the spatial overlap between the laser pulse and electron beam in the first undulator was not good enough. For the next experiment, we plan to remodel the alignment optics for the spatial overlap.

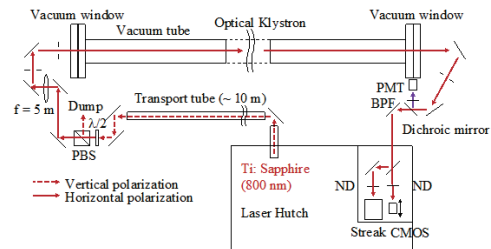


Fig. 1. Schematics of laser transport line and light measurement setup.

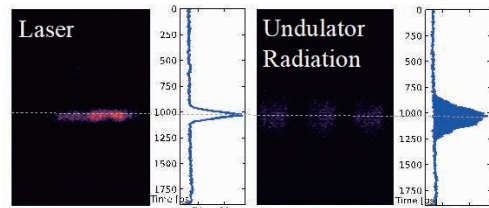


Fig. 2. Streak camera images of laser pulse and undulator radiation. The vertical scale corresponds between right and left images and is synchronized with RF signal of accelerator.

[1] G. Vingola *et al.*, Nucl. Instrum. Methods Phys. Res., Sect. A **239** (1985) 43.

[2] H. Zen *et al.*, Proc. FEL2010 TUPB16 (2010) 286.

[3] M. Labat *et al.*, Eur. Phys. J. D **44** (2007) 187.

[4] T. Tanikawa *et al.*, Appl. Phys. Express **3** (2010) 122702.

[5] Y. Uematsu *et al.*, Proc. PASJ 2012 WEPS066 (2012) 551.

BLIU

## Impact of the Temperature on the Non-Destructive Nuclide Assay in the Transmission NRF Method

M. Omer<sup>1</sup>, T. Shizuma<sup>2</sup>, M. Koizumi<sup>1</sup>, Y. Taira<sup>3</sup>, H. Zen<sup>4</sup>, H. Ohgaki<sup>4</sup> and R. Hajima<sup>2</sup>

<sup>1</sup>Japan Atomic Energy Agency, Tokai 319-1195, Japan

<sup>2</sup>National Institutes for Quantum Science and Technology, Kizugawa 619-0215, Japan

<sup>3</sup>UVSOR Synchrotron Facility, Institute for Molecular Science, Okazaki 444-8585, Japan

<sup>4</sup>Institute of Advanced energy, Kyoto University, Uji 611-0011, Japan

Nuclear resonance fluorescence (NRF) is the photoexcitation of a nuclide using high energy  $\gamma$ -rays. The resonating levels excited by NRF are a fingerprint of each nucleus. Therefore, NRF can be employed as a non-destructive assay technique for nuclear materials such as fissile isotopes. There are two schemes for NRF measurement. The first one is scattering NRF measurement, by which the sample is irradiated by a  $\gamma$ -ray beam, and the scattered NRF photons are measured. The second scheme is the transmission NRF measurement, by which the absorption of NRF photons by the sample is measured. To realize absorption measurement, a second target (witness target of the same sample located downstream the sample target) is used to estimate the amount of  $\gamma$ -ray absorption in the sample. In transmission NRF,  $\gamma$ -ray detector is positioned close to the witness target. So, the measurement is possible without the shadow of background radiation from the sample target. [1].

The emission and absorption rate of NRF  $\gamma$ -rays depend on the temperature of the scattering and witness targets via the Doppler broadened widths of NRF levels. Therefore, the temperature of the scattering and witness targets may affect the time and sensitivity of the measurement. Based on the level widths, many isotopes are possible candidates to study the effect of temperature on transmission NRF, such as <sup>27</sup>Al, <sup>48</sup>Ti, <sup>51</sup>V, <sup>206</sup>Pb, and <sup>208</sup>Pb. In the present measurement, <sup>208</sup>Pb target was irradiated with laser Compton scattering (LCS)  $\gamma$ -ray beam at BLIU of UVSOR. LCS  $\gamma$ -rays of maximum energy of 5.54 MeV were produced from the collision of 746-MeV electrons with laser photons of a wavelength of 1.98  $\mu$ m. A lead collimator with 20-cm thickness and 3-mm aperture size was used to confine the generated  $\gamma$ -rays energy width to approximately 8% (FWHM). Three 140% HPGe detectors, located horizontally, were used to detect NRF  $\gamma$ -rays. Two of them were positioned at a scattering angle of 135° and the third at a scattering angle of 70° with respect to the incident  $\gamma$ -ray direction, as shown in Fig. 1.

A typical  $\gamma$ -ray spectrum measured using <sup>208</sup>Pb is shown in Fig. 2. NRF peaks of <sup>208</sup>Pb were observed as indicated in Fig. 2. We also observed substantial background lines at energies higher than the maximum energy of the LCS  $\gamma$ -ray beam. These lines probably originate from the neutron capture interactions with materials surrounding the experimental setup. The

neutron capture background affects the accuracy of NRF peaks. We applied a 10-cm thickness lead shield around one detector to decrease the background. As shown in Fig. 2 (green spectrum), the background was effectively suppressed. The shielding configuration will be applied in the planned transmission NRF experiments. This work is a contribution of the JAEA to the International Atomic Energy Agency (IAEA) under the agreement of the coordinated research program (CRP), J02015 (Facilitation of Safe and Secure Trade Using Nuclear Detection Technology - Detection of RN and Other Contraband).



Fig. 1. Photo of the experimental setup used for the cryo-NRF experiment at BLIU.

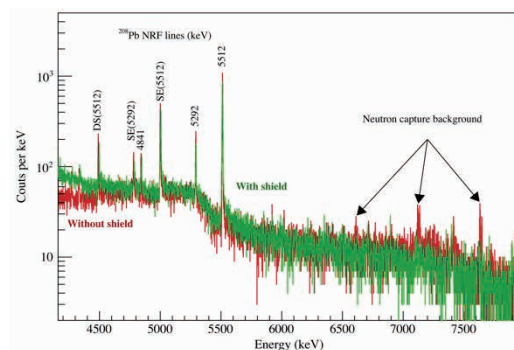


Fig. 2. Typical  $\gamma$ -ray spectra observed for <sup>208</sup>Pb before (red) and after (green) heavy shield. NRF levels are labeled with resonance energies. Also, single and double escape peaks are labeled. The high energy background was effectively suppressed.

[1] C.T. Angell *et al.*, Nucl. Instrum. Methods Phys. Res. B **347** (2016) 11.

## Basic Study on Compton Camera for Detection of Polarized gamma-rays

K. Shimazoe<sup>1</sup>, M. Uenomachi<sup>2</sup>, T. Ueki<sup>1</sup>, Q. Shu<sup>1</sup>, A. Takeda<sup>3</sup>, K. Magata<sup>3</sup>,  
K. Nagayanagi<sup>3</sup> and Y. Taira<sup>4</sup>

<sup>1</sup>Graduate School of Engineering, The University of Tokyo, Tokyo 113-8656, Japan

<sup>2</sup>Space Unit, Kyoto University, Kyoto 606-8502, Japan

<sup>3</sup>Miyazaki University, Miyazaki 889-2192, Japan

<sup>4</sup>UVSOR Synchrotron Facility, Institute for Molecular Science, Okazaki 444-8585, Japan

Compton imaging is a promising technology visualizing the distribution of gamma-rays by using the Compton kinetics principle. Measuring the energies in scatterer and absorber determines the scattering angle of gamma-rays and enables the localization of radiation source. Compton imaging is now widely investigated for the application of astronomy, medical imaging [1] and environmental monitoring [2]. Although the gamma-ray imaging is possible through Compton imaging, but the information of polarization in gamma-ray is not well utilized till now. The polarization information can be used to improve the image quality in positron emission tomography (PET) scanners with its quantum entanglement nature [3].

In the previous research, we have been working on developing silicon on insulator (SOI) based monolithic sensor integrating the silicon sensor and readout electronics in one chip [4]. SOI device can be used to detect the track of Compton recoil electrons for the advanced Compton imaging. In this research we investigated the possibility of extracting the polarization information of incoming linearly or circularly polarized gamma-rays through the pattern of electron tracks and Compton scattering angles.

Figure 1 shows the experimental setup for detecting the polarization of gamma-rays. Two SOI pixel sensor are used as scatterers and Compton electron trackers. Eight 8×8 GAGG arrays (pixel size is 3.2 mm and thickness is 9 mm) coupled with SiPM array are used as absorber. All the detectors are synchronized for detecting the coincidence events between detectors.

Figure 2 shows the picture of detector setup aligned to the beam. In this setup 31-47 degree and 45-61 degree scattering events can be acquired for SOI1/GAGG and SOI2/GAGG coincidence respectively.

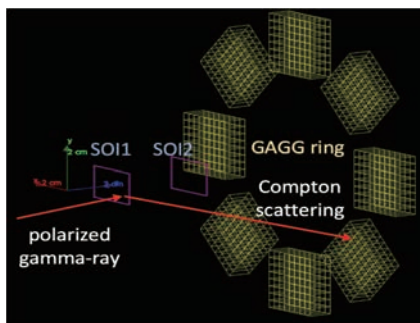


Fig. 1. Two SOI sensors and eight GAGG arrays are used to detect polarized gamma-rays.

Figure 3 shows the expected scattering angle of polarized photon with a Monte Carlo simulation code (GEANT4).

In the first analysis, the coincidence events are successfully acquired between laser trigger and SOI and between laser trigger and GAGG as shown in Figure 4. The more detail analysis is ongoing.

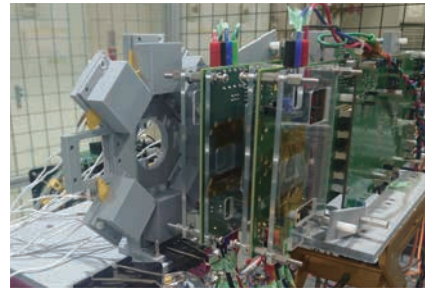


Fig. 2. the detector setup in the beamline BLIU

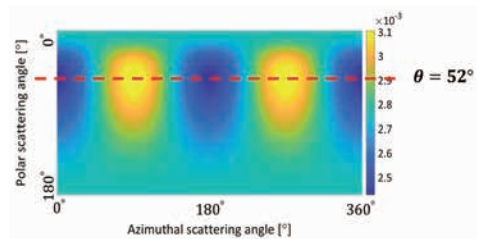


Fig. 3. Simulated scattering angle of polarized photon

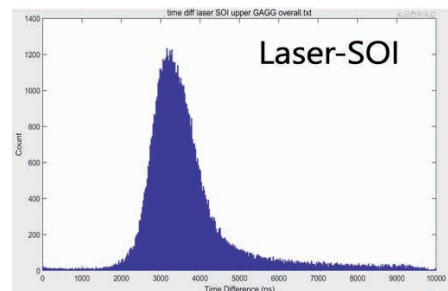


Fig. 4. time difference histogram of SOI and laser

[1] M. Uenomachi, M. Takahashi, K. Shimazoe, *et al.*, *Sci Rep* **11** (2021) 17933 .

[2] Jianyong Jiang, *et al.*, *Journal of Nuclear Science and Technology* **53.7** (2016) 1067.

[3] D. P. Watts, *et al.*, *Nature Communications* **12.1** (2021) 2646.

[4] Y. Yoshihara, *et al.*, *Journal of Instrumentation* **12.01** (2017) C01045.

BLIU

## Development of gamma-ray-induced Positron age-momentum Correlation

Y. Taira<sup>1,2</sup>, Y. Okano<sup>1</sup> and T. Hirade<sup>3</sup>

<sup>1</sup>UVSOR Synchrotron Facility, Institute for Molecular Science, Okazaki 444-8585, Japan

<sup>2</sup>School of Physical Sciences, The Graduate University for Advanced Studies (SOKENDAI), Okazaki 444-8585, Japan

<sup>3</sup>Nuclear Science and Engineering Center, Japan Atomic Energy Agency, Tokai, 319-1195, Japan

In UVSOR-III, gamma-ray-induced positron annihilation spectroscopy using the ultra-short pulsed gamma rays is developed. The ultra-short pulsed gamma rays with a pulse width of ps range are generated via inverse Thomson scattering with 90 degree collisions between an electron beam and a laser pulse at BLIU [1]. Gamma-ray-induced positron annihilation lifetime spectroscopy (GiPALS) is currently available to users. In addition to GiPALS, gamma-ray-induced age-momentum correlation (GiAMOC) is being developed. GiAMOC is an approach to measure the emission time and the energy shift of annihilation gamma rays with an energy of 0.511 MeV simultaneously for observing the time-resolved momentum distribution of an electron, which is the annihilation counterpart of a positron. For that, one of the two annihilation gamma rays produced from a sample is detected using a barium fluoride ( $\text{BaF}_2$ ) detector with high time resolution and the other is detected by a high purity germanium detector (Mirion Technologies, GC4018, 40% relative efficiency) with high-energy resolution. A  $\text{BaF}_2$  detector comprises a  $\text{BaF}_2$  scintillator and a photomultiplier tube (Hamamatsu Photonics K.K., H3378-51). GiAMOC using one detector pair was presented in Ref. [2]. In this report, we present the results of quartz measurements using two detector pairs.

The GiAMOC measurement system is shown in Figure 2 of Ref. [2]. Two sets of this system were used to improve the counting rate by a factor of two, as shown in the picture in Fig. 1. The measured time evolution of a fraction of low-momentum annihilation ( $S$ -parameter) of synthetic silica glass (Tosoh SGM Corp., ED-C) is shown in Fig. 2. As shown in Fig. 2,  $S$ -parameter decreased with time. Around time 0, the annihilation process of para-positronium, which has a short annihilation lifetime and a small energy spread, is dominant, and as time passes, the annihilation processes of free positrons and ortho-positronium, which have longer lifetimes and larger energy spreads than the para-positronium, is dominant. The time evolution of the measured  $S$ -parameter is consistent with that measured using a slow positron beam at AIST [3].

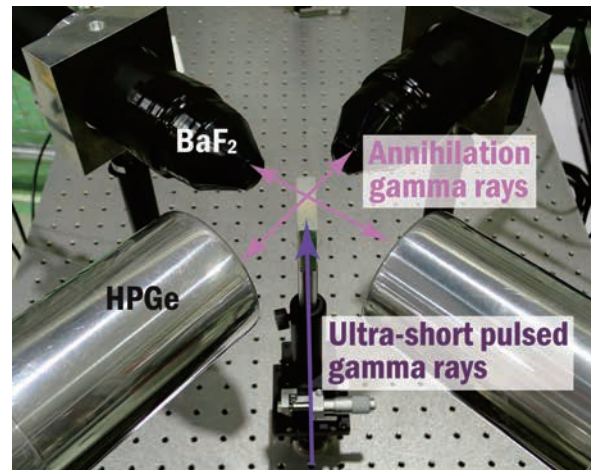


Fig. 1. Detector arrangement of GiAMOC.

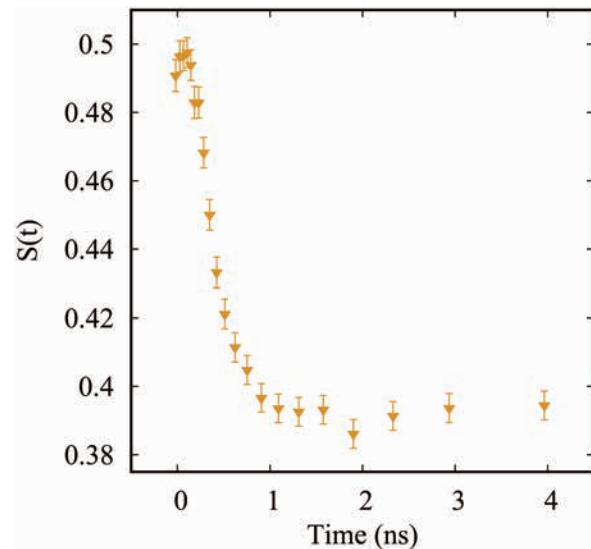


Fig. 2. The time evolution of  $S$ -parameter for synthetic silica glass.

[1] Y. Taira *et al.*, Nucl. Instr. Meth. A **652** (2022) 696.

[2] Y. Taira *et al.*, Rev. Sci. Instr. **93** (2022) 113304.

[3] Y. Komuro *et al.*, Rad. Phys. Chem. **76** (2007) 330.

## Study on Generation of F-LCS Gamma-rays for Absolute Cross-section Measurement of NRF using BL1U Undulator

H. Ohgaki<sup>1</sup>, H. Zen<sup>1</sup>, T. Kii<sup>1</sup>, T. Hayakawa<sup>2</sup>, T. Shizuma<sup>2</sup>, M. Fujimoto<sup>3</sup> and Y. Taira<sup>3</sup>

<sup>1</sup>*Institute of Advanced Energy, Kyoto University, Kyoto 611-0011, Japan*

<sup>2</sup>*Tokai Quantum Beam Science Center, National Institutes for Quantum and Radiological Science and Technology, Ibaraki 319-1106, Japan*

<sup>3</sup>*UVSOR Synchrotron Facility, Institute for Molecular Science, Okazaki 444-8585, Japan*

Laser Compton Scattering Gamma-ray beam (F-LCS), which has a flat distribution in the energy spectrum and the spatial distribution with a few mm diameter beam size, has been developed to study an isotope selective CT Imaging application in the beamline BL1U in UVSOR. By using a circular motion of the electron beam which is excited by a helical undulator installed in a storage ring, and collision with an intense laser beam, an F-LCS beam can be generated. The principle is that the electron beam divergence could be enlarged by the undulator field that enlarges the beam divergence of the Compton backscattered gamma-ray (LCS) beam. At the same time, the LCS beam energy is also spread.

An Electron Gamma Shower version 5 (EGS5) [1] simulation study assumed in the LCS beamline BL1U (Fig.1) with the collimator diameter of 2 mm  $\phi$ . has been carried out. Figure 2 shows the energy spectra of the LCS beams with K-values from 0 to 0.4. The boarder energy spread peak is observed with a larger K-value. The energy spread is widened from 2.7 to 22% (FWHM), and the peak energy is shifted from 5.53 MeV to 5.01 MeV by increment of the K-value from 0 to 0.4. On the other hand, the F-LCS beam yield at the top energy region decreases with the increase of the undulator field. Therefore, K-value of 0.2 could be recommended for practical applications in BL1U.

A POP experiment was carried out at the BL1U in UVSOR. The experimental setup was the same as that shown in Fig. 2 except for a high-purity germanium (Ge) detector with a relative efficiency of 120% was added after the 2-mm $\phi$  collimator. The stored electron with an energy of 746 MeV and a current of about 6 mA was used. The laser beam from a Tm-fiber laser system (TLR-50-AC-Y14, IPG Laser GmbH) whose wavelength was 1.896  $\mu\text{m}$  with random polarization was used at around 1 W CW power. The spectra of the LCS beams were measured for different K-values from K=0 to 0.3. Although the Ge detector response made complicated energy spectra, we observed peak the shift toward lower energy according to larger K value, as shown in Fig. 3.

As a result, the larger K-value, the broader energy bandwidth of the LCS was observed as predicted by EGS5 simulation. This result supports the successful generation of the F-LCS beam.

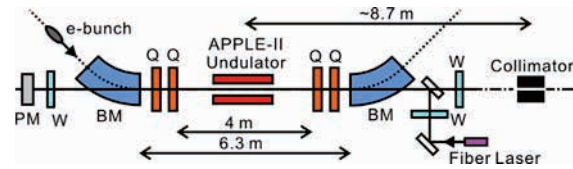


Fig. 1. Schematic drawing of the LCS beamline BL1U, UVSOR. PM: power meter, W: window, SM: Spherical Mirror. A Ge detector was added after the collimator in the POP experiment.

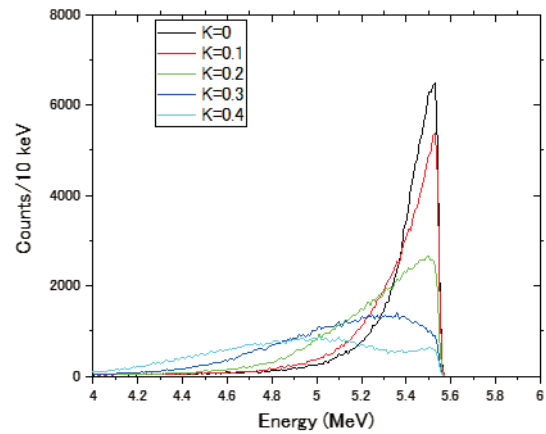


Fig. 2. LCS gamma-ray energy distribution in the vertical axis with the undulator K-value of K=0.2.

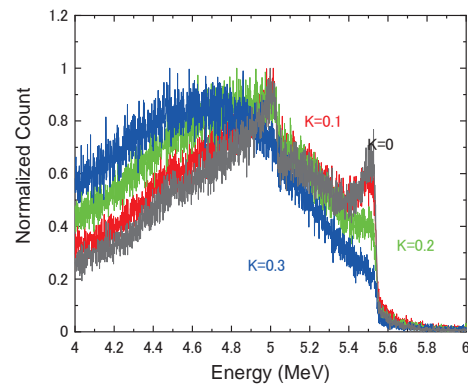


Fig. 3. Measured LCS beam spectra with the undulator K-value of 0, 0.1, 0.2, and 0.3.

[1] H. Hirayama, Y. Namito, A.F. Bielajew, S.J. Wilderman and W.R. Nelson, The EGS5 code system, SLAC Report number: SLAC-R-730, KEK report number: 2005-8 (2005).

BL1U

## Double-Pulsed Light Wave Packets Emitted from a Tandem Undulator

T. Kaneyasu<sup>1,2</sup>, M. Hosaka<sup>3,4</sup>, A. Mano<sup>4</sup>, Y. Takashima<sup>4</sup>, M. Fujimoto<sup>2,4</sup>, E. Salehi<sup>2</sup>,  
H. Iwayama<sup>2,5</sup>, Y. Hikosaka<sup>6</sup> and M. Katoh<sup>2,4,7</sup>

<sup>1</sup>SAGA Light Source, Tosu 841-0005, Japan

<sup>2</sup>Institute for Molecular Science, Okazaki 444-8585, Japan

<sup>3</sup>University of Science and Technology of China, Hefei 230029, China

<sup>4</sup>Synchrotron Radiation Research Center, Nagoya University, Nagoya, 464-8603, Japan

<sup>5</sup>Sokendai (The Graduate University for Advanced Studies), Okazaki 444-8585, Japan

<sup>6</sup>Institute of Liberal Arts and Sciences, University of Toyama, Toyama 930-0194, Japan

<sup>7</sup>Hiroshima Synchrotron Radiation Center, Hiroshima University, Higashi-Hiroshima 739-0046, Japan

The waveform of electromagnetic radiation from an ultra-relativistic electron reflects the motion of the electron. We report on a fully-optical characterization of double-pulsed wave packets emitted by individual relativistic electrons passing through a tandem undulator in a synchrotron light source [1]. The experiment was carried out at the undulator beamline BL1U. The light source of BL1U consists of two identical APPLE-II undulators, between which a three-pole electromagnetic phase shifter is installed (Fig. 1). The period length and number of periods for each undulator were 88 mm and 10, respectively. A relativistic electron passing through the undulators emits a wave packet with a waveform expected to be characterized by time-separated 10-cycle oscillations. The time delay between the double-pulsed components can be controlled by adjusting the length of electron orbit between the undulators using the phase shifter magnet.

Using a Mach-Zehnder interferometer [2] operating at ultraviolet wavelengths, we measured the autocorrelation trace for the spontaneous radiation from the tandem undulator. The double-pulsed wave packets were randomly distributed within the overall 300 ps radiation pulse corresponding to the length of the electron bunch. Figure 2(a) shows the interferograms obtained by setting the field strength of the phase shifter magnet to four different values. The central wavelength of the radiation was 357 nm for both undulators. The interferograms measured at a phase shifter current of 10.0 A or more show approximately 20-cycle oscillations with triangular envelopes in the range of  $-12 - +12$  fs, as well as weaker 20-cycle oscillations lying on both sides. The side oscillation structures approach the central structure as the phase shifter current decreases, and they are unified at a phase shifter current of 0 A.

The observed interferograms can be understood as autocorrelation traces of double-pulsed wave packet. The calculated autocorrelation traces for a double-pulsed 10-cycle sinusoidal wave packet at 357 nm wavelength are shown in Fig. 2(b). Over the whole range of phase shifter currents, one finds excellent agreement between the experiments and calculations.

This fact confirms that each of the relativistic electron emits a double-pulsed 10-cycle wave packet which well reflects the magnetic field in the tandem undulator.

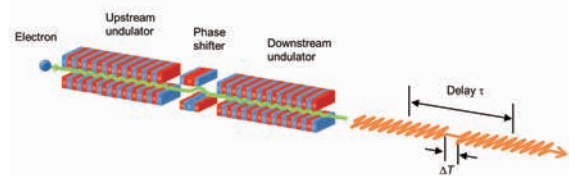


Fig. 1. Schematic illustration of the tandem undulator. A relativistic electron passing through the undulators emits a wave packet with a waveform expected to be characterized by time-separated 10-cycle oscillations.

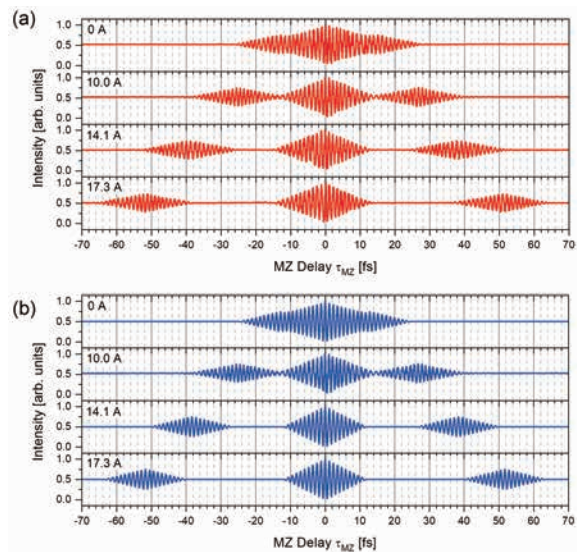


Fig. 2. Autocorrelation measurements of spontaneous radiation from the tandem undulator at various values of the phase shifter current. The wavelength of the fundamental undulator radiation was set to 357 nm. (a) Measurement. (b) Calculation.

[1] T. Kaneyasu *et al.*, *Sci. Rep.* **12** (2022) 9.

[2] A. Mano *et al.*, *UVSOR Activity Report 2020*, **48** (2020) 38.

## Progress in Single Electron Storage Experiment

A. Asai<sup>1</sup>, M. Shimada<sup>2,3</sup>, H. Miyauchi<sup>2,3</sup> and M. Katoh<sup>3,1,4,2</sup>

<sup>1</sup>*School of Science, Hiroshima University, Higashi-hiroshima 444-8585, Japan*

<sup>2</sup>*High Energy Accelerator Research Organization (KEK), Tsukuba 305-0801, Japan*

<sup>3</sup>*Hiroshima Synchrotron Radiation Research Center, Hiroshima University, Higashi-hiroshima 739-0046, Japan*

<sup>4</sup>*UVSOR Synchrotron Facility, Institute for Molecular Science, Okazaki 444-8585, Japan*

Single electron storage has been achieved at several electron synchrotrons, aiming to investigate electron dynamics in a synchrotron [1,2,3], to investigate electromagnetic radiation from an electron [4], or to utilize the radiation as a primary standard [5,6,7]. In FY2021, we have started an experimental study on single electron storage at UVSOR-III and successfully demonstrated it [8, 9]. In FY2022, we continued improving the operation technique for the single electron storage and also have started some basic studies on undulator radiation [10]. Here, we report some preliminary results. The final results will be published elsewhere in future.

We have established the following procedure for the single electron storage. First, we accumulate an electron beam with very low current, typically 0.1 mA. Indeed, this current corresponds to one shot of the injector. At this low beam current, we could observe and adjust the optical axis by eye from the undulator at BL1U, which is tuned at 355 nm wavelength. Then, we reduce the beam lifetime to several minutes by using beam scraper. We use a photomultiplier tube (PMT) to measure the synchrotron radiation intensity. The PMT signal was analyzed with a counting unit and recorded by a PC. Single electron storage corresponds to about 1 pA beam current. Therefore, we have to observe very wide range of the intensity for many orders of magnitudes. Therefore, we set ND filters in front of the PMT to adjust the radiation intensity and remove them as the intensity reduces. To make the operation simpler, we examined an ultra-wide range PMT and obtained a good result. The details will be described elsewhere in future.

We could observe step function like changes in the intensity as shown in Figure 1, which corresponds to a loss of one electron. We also observed the timing of the PMT output relative to the revolution signal provided by the RF system, as also shown in Figure 1. We could observe in which RF bucket the electrons exists. We confirmed that the last electron survives for more than 2 hours after we pulled out the beam scraper to the original position. This allows us to observe some basic properties of synchrotron radiation. An example is presented in Figure 2, which shows that the photon statistics is well represented by Poisson distribution. Other interesting results will be presented somewhere in future.

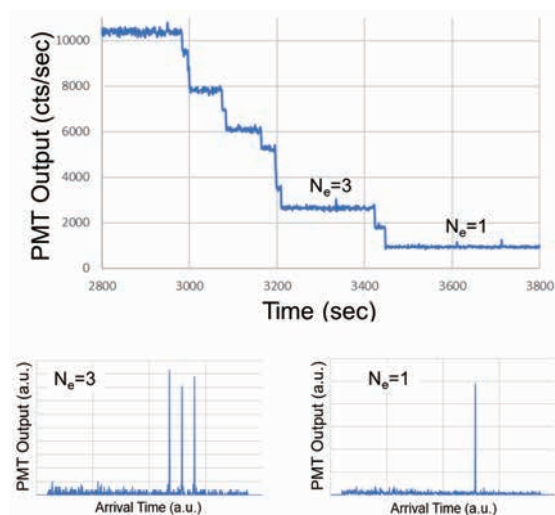


Fig. 1. Synchrotron radiation intensity

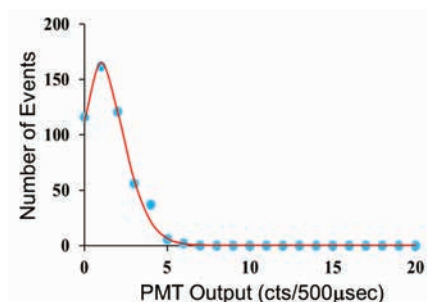


Fig. 2. Photon Statistics observed at BL1U

- [1] A. N. Aleshaev *et al.*, NIM A **359** (1995) 80.
- [2] I. V. Pinayev *et al.*, NIM A **375** (1996) 71.
- [3] A. Romanov *et al.*, 2021 JINST **16** (2021) P12009.
- [4] I. V. Pinayev *et al.*, NIM A **341** (1994) 17.
- [5] R. Klein *et al.*, Phys. Rev. STAB **11** (2008) 110701.
- [6] R. Klein *et al.*, 2010 Metrologia **47** (2010) R33.
- [7] T. Saito *et al.*, Bulletin of the Electrotechnical Laboratory (in Japanese) (1985) 431.
- [8] R. Shinomiya *et al.*, UVSOR Activity Report 2021, (2022) 39.
- [9] R. Shinomiya, Bachelor Thesis (Hiroshima University) (in Japanese) (2022).
- [10] Y. Asai, Bachelor Thesis (Hiroshima University) (in Japanese) (2023).

BL2A

## Calibration of the Soft X-ray Response Matrix of CMOS Detector Used in Sounding Rocket Experiment FOXSI-3

N. Narukage<sup>1,2</sup>, R. Shimizu<sup>2,3</sup>, Y. Sato<sup>1,2</sup> and S. Kashima<sup>3</sup>

<sup>1</sup>National Astronomical Observatory of Japan (NAOJ), Mitaka, 181-8588, Tokyo, Japan

<sup>2</sup>The Graduate University for Advanced Studies, SOKENDAI, Hayama, 240-0193, Kanagawa, Japan

<sup>3</sup>Institute of Space and Astronautical Science (ISAS), Japan Aerospace Exploration Agency (JAXA), Sagami-hara, 252-5210, Kanagawa, Japan

The solar corona is full of dynamic phenomena such as solar flares. The understandings of these phenomena have been progressing step-by-step with the evolution of the observation technology in EUV and X-rays from the space. But there are fundamental questions remain unanswered or haven't even addressed so far. Our scientific objective is to understand underlying physics of the dynamic phenomena in the solar corona, covering some of the long-standing questions in solar physics such as particle acceleration in flares and coronal heating. To achieve this objective, we identify the imaging spectroscopy (the observations with spatial, temporal and energy resolutions) in the soft X-ray range (from  $\sim 0.5$  keV to  $\sim 10$  keV) is a powerful approach for the detection and analysis of energetic events [1]. This energy range contains many lines emitted from below 1 MK to beyond 10 MK plasmas plus continuum component that reflects the electron temperature.

The soft X-ray imaging spectroscopy is realized with the following method. We take images with a short enough exposure to detect only single X-ray photon in an isolated pixel area with a fine pixel Silicon detector. So, we can measure the energy of the X-ray photons one by one with spatial and temporal resolutions. When we use a high-speed soft X-ray camera that can perform the continuous exposure with a rate of more than several hundred times per second, we can count the photon energy with a rate of several 10 photons / pixel / second. This high-speed exposure is enough to track the time evolution of spectra generated by dynamic phenomena in the solar corona, whose lifetimes are about from several ten seconds to several minutes. For the first imaging spectroscopic observation of the solar corona in soft X-ray range, we launched a NASA's sounding rocket (FOXSI-3) on September 7<sup>th</sup>, 2018 and successfully obtained the unprecedented data [2] using a high-speed X-ray camera [3] with a back-illuminated CMOS detector [4].

Calibration of CMOS detectors is essential for scientific data analysis. For this purpose, a completely monochromatic X-ray light source is needed. In addition, the flux must be adjusted so that individual X-ray photons can be isolated. Therefore, we have developed a mirror-based reflective-type flux reduction system [5].

In this time, using this system, the response of the CMOS detector aboard the FOXSI-3 sounding rocket is

completely calibrated in the energy range of 840 eV to 4500 eV in 20 eV intervals (see Fig. 1).

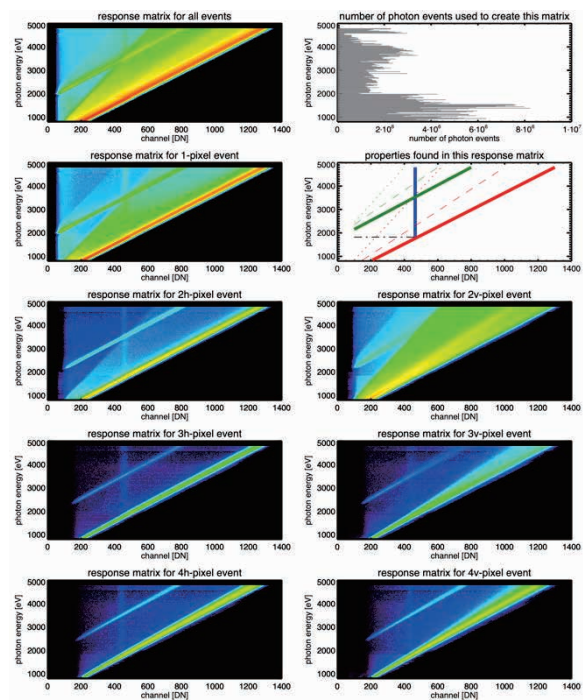


Fig. 1. Measured response matrix of the FOXSI-3 CMOS detector from 840 eV to 4500 eV. In the color maps, the horizontal axis shows the values of output signals from the detector, when the detector detects the monochromatic X-ray photons with the energy shown in the vertical axis. The colors indicate, in log scale, how frequently each signal value is output. The top-right panel shows the number of monochromatic X-ray photons used to create this matrix.

- [1] N. Narukage *et al.*, White paper of the “soft X-ray imaging spectroscopy”, arXiv:1706.04536 (2017).
- [2] N. Narukage and S. Ishikawa, *UVSOR Activity Report 2018* **46** (2018) 36.
- [3] S. Ishikawa *et al.*, *Nucl. Instrum. Methods Phys. Res., Sect. A* **912** (2018) 191.
- [4] N. Narukage *et al.*, *Nucl. Instrum. Methods Phys. Res., Sect. A* **950** (2020) 162974.
- [5] N. Narukage, *UVSOR Activity Report 2022*, **49** (2021) 42.

## Development of a Transfer Vessel for NEXAFS Spectroscopy

E. Kobayashi<sup>1</sup> and A. Inoishi<sup>2</sup>

<sup>1</sup> *Kyushu Synchrotron Light Research Center, 8-7 Yayoigaoka, Tosu, Saga 841-0005, Japan*

<sup>2</sup> *Institute for Materials Chemistry and Engineering, Kyushu University 6-1 Kasuga-koen, Kasuga-Shi 816-8580, Japan*

Battery materials are contaminated with oxygen, carbon dioxide and water when exposed to the atmosphere. Therefore, we developed a sample transfer vessel that can transport the sample to the analyzer without exposing it to the atmosphere [1, 2]. Furthermore, in order to perform more precise analysis, we developed a transfer vessel with a small ion pump [3]. In recent years, analysis of battery materials using soft X-ray absorption spectroscopy has been performed. However, it was difficult to analyze across the beamline without atmospheric exposure. This is because the sample holders are different depending on the beamline. Therefore, we have developed a transfer vessel that can measure the soft X-ray absorption spectrum across the beamline without exposing the sample to the atmosphere, based on the apparatus that we have developed.

The ZrO<sub>2</sub> powders was attached to the transfer vessel in a glove box under an argon atmosphere. NEXAFS spectra of the ZrO<sub>2</sub> powders using both total electron yield (TEY) and partial fluorescence yield (PFY) modes were measured at the beamline 2A of the UVSOR in the Institute of Molecular Science. For TEY, the drain current of the sample was measured. For PFY, fluorescence X-rays were collected using an energy dispersible silicon drift detector (SDD). All experiments were performed at room temperature.

Fig. 1 shows a photograph of the developed transfer vessel. The sample is fixed to the lower part of the vessel using carbon tape. The sample current is measured using the Bayonet Neill-Concelman (BNC) connector on the upper part of the vessel. Fig. 2 shows the Zr *L*-edge NEXAFS spectra of ZrO<sub>2</sub> powder obtained from TEY and PFY. The shape of the spectrum measured in the TEY mode was almost the same as that measured in the PFY mode. The TEY is surface-sensitive whereas the PFY is sensitive to the bulk. The result indicates that the sample could be transported without air contamination.



Fig. 1. Photograph of the transfer vessel.

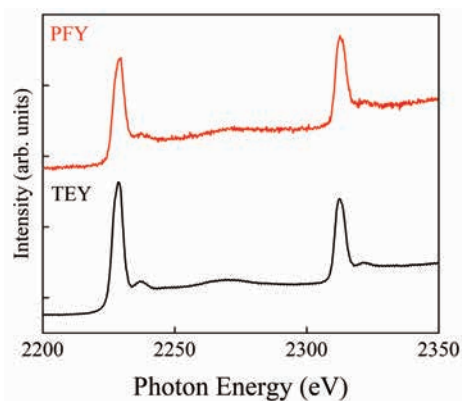


Fig. 2. Zr *L*-edge NEXAFS spectra of ZrO<sub>2</sub> powder obtained from TEY and PFY.

[1] E. Kobayashi, J. Meikaku, T. Okajima, and H. Setoyama, Japanese Patent No. 5234994.

[2] E. Kobayashi, J. Meikaku, H. Setoyama, T. Okajima, *J. Surf. Anal.*, **19** (2012) 2.

[3] E. Kobayashi, S. Tanaka, T. Okajima. *J. Vac. Soc. Jpn.* **59** (2016) 192.

BL3U

## Soft X-ray Transmission Measurements of Polymer Films for Soft X-ray Absorption Spectroscopy of Liquids in Low-Energy Regions

M. Nagasaka<sup>1,2</sup>, S. Fujikawa<sup>3</sup>, H. Takaya<sup>1,4</sup> and Y. Uozumi<sup>1,2</sup>

<sup>1</sup>*Institute for Molecular Science, Okazaki 444-8585, Japan*

<sup>2</sup>*The Graduate University for Advanced Studies (SOKENDAI), Okazaki 444-8585, Japan*

<sup>3</sup>*International Institute for Carbon-Neutral Energy Research (WPI-I2CNER) and Research Center for Negative Emissions Technologies, Kyushu University, 744 Moto-oka, Nishi-ku, Fukuoka 819-0395, Japan*

<sup>4</sup>*Department of Life Science, Faculty of Life & Environmental Sciences, Teikyo University of Science, Main Buld #15-05, 2-2-1 Senjyusakuragi, Adachi-ku, Tokyo 120-0045, Japan*

Soft X-ray absorption spectroscopy (XAS) is an element-specific method to investigate electronic structures of liquids. The soft X-ray regions below 2 keV have chemically and biologically absorption edges such as K-edges of C, N, and O and L-edges of transition metals such as Mn, Fe, Co, and Ni. Recently, we have developed a transmission-type liquid cell, where a liquid layer is sandwiched between two Si<sub>3</sub>N<sub>4</sub> membranes with the thickness of 100 nm, and measured XAS spectra of several liquid samples in transmission mode by adjusting the liquid thicknesses precisely from 20 nm to 2000 nm [1].

The low-energy regions below 200 eV include absorption edges for the investigation of chemical and biological phenomena in solutions such as K-edges of Li and B and L-edges of Si, P, S, and Cl. Since soft X-ray transmission in the low-energy region is extremely lower than that in the high-energy region above 200 eV [2], transmitted soft X-rays below 200 eV include many high-order X-rays. Recently, we have used an argon gas window for removing high-order X-rays by using the Ar L-edge (240 eV) [3] and developed the soft X-ray detector that removes high-order X-rays [4]. However, the XAS measurements in the low-energy regions are still difficult since soft X-rays are strongly absorbed by Si<sub>3</sub>N<sub>4</sub> membranes with the Si L-edges (100 eV). In this study, we have synthesized polymer films that include no Si atoms with the thickness of 100 nm and evaluated the soft X-ray transmission of the polymer film.

The experiments were performed at BL3U. The polymer film was settled under an ultrahigh vacuum condition, which directly connected to the beamline. The transmitted soft X-rays through the polymer film were measured by using a photodiode detector.

Figure 1 shows the soft X-ray transmission of the polymer film in the soft X-ray region from 50 eV to 560 eV. Since the polymer film includes the C=C and C=N groups, the sharp absorption peaks such as the transition from C 1s electrons to C=C  $\pi^*$  orbitals at the C K-edge and the transition from N 1s electrons to C=N  $\pi^*$  orbitals at the N K-edge are observed. Note that the soft X-ray beamline BL3U includes three monochromatic gratings for covering wide photon energy regions. The

photon intensities are also maximized by adjusting the undulator gap. That is why several photon energy regions are not continuous due to the different gratings and the orders of the undulator gap. Since the polymer film includes no Si atoms, there is no peaks at the Si L-edge. Soft X-ray transmission of the polymer film shows a still high value below 200 eV, indicating the present polymer film is suitable to measure XAS of liquids in the low-energy region.

In the present, we have developed an ultrathin liquid cell to reduce the optical pass length of Ar gas. We will include the present polymer films to the ultrathin liquid cell for improving the soft X-ray transmission of liquid samples in the low energy region below 200 eV.

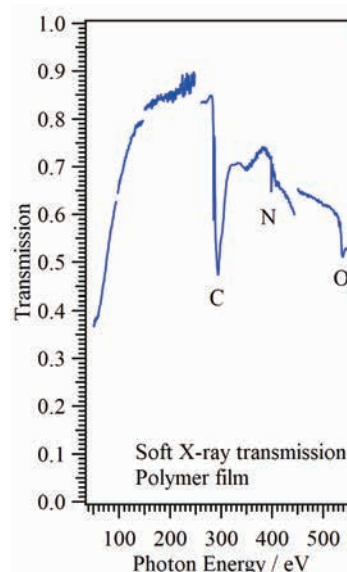


Fig. 1. Soft X-ray transmission of the polymer film.

- [1] M. Nagasaka and N. Kosugi, *Chem. Lett.* **50** (2021) 956.  
 [2] C. T. Chantler, *J. Phys. Chem. Ref. Data* **29** (2000) 597.  
 [3] M. Nagasaka, *J. Synchrotron Rad.* **27** (2020) 959.  
 [4] M. Nagasaka and H. Iwayama, *Rev. Sci. Instrum.* **91** (2020) 083103.

## Dissociation Channels of Molecules for a Use of Plasma Etching Processes

T. T. Nguyen<sup>1</sup>, K. Ishikawa<sup>1</sup> and H. Iwayama<sup>2</sup>

<sup>2</sup>Nagoya University Center for low-temperature plasma sciences, Nagoya 464-8601,

<sup>1</sup>UVSOR Synchrotron Facility, Institute for Molecular Science, Okazaki 444-8585, Japan

Plasma etching is indispensable for the fabrication of semiconductor devices. In recent years, there has been an urgent need to develop etching gases that meet the requirements for manufacturing three-dimensional devices and high aspect ratio structures. For the plasma-etching, hydrofluorocarbon molecules are used. Plasma dissociates and ionizes gas molecules. The plasma-related reactions are complicated significantly, however these reactions of dissociated and ionized fragments of molecules should be controlled on the basis of scientific understanding. First, we predicted dissociation and ionization channels of gas molecules using computational chemistry. As the results, we calculated precisely the excited state of perfluorocarbon, *c*-C<sub>4</sub>F<sub>8</sub> [1]. In order to improve the accuracy of the reaction prediction, experimental verification of photodissociation is required.

In this study, experimental verification of dissociation of perfluorocarbons, which are not in the database for plasma-etching gases, mainly hydrofluorocarbon molecules, has been performed with precision and accuracy using beamlines owned by the Institute for Molecular Science (IMS). Through this study, we will pioneer the future development of the world's best plasma etching gas by combining coincidence spectroscopy and computational chemistry.

This study conducted coincidence spectroscopy experiments on photoionization and photodissociation using vacuum ultraviolet light region from 40 nm to 400 nm from beamlines of BL3B in the IMS. This light source is the only facility in Japan.

In the etching process plasmas, abundances for dissociated ions are reported by C<sub>3</sub>F<sub>5</sub><sup>+</sup> > CF<sub>3</sub><sup>+</sup> > CF<sup>+</sup> > C<sub>2</sub>F<sub>4</sub><sup>+</sup>, which are different C<sub>2</sub>F<sub>4</sub><sup>+</sup> > C<sub>3</sub>F<sub>5</sub><sup>+</sup> > CF<sup>+</sup> > CF<sub>3</sub><sup>+</sup> in mass spectra taken at 70 eV electron energy. The calculation results showed that a secondary process of *c*-C<sub>4</sub>F<sub>8</sub><sup>+</sup> to C<sub>2</sub>F<sub>4</sub> + C<sub>2</sub>F<sub>4</sub><sup>+</sup> dissociation route is a potential barrier of 12.05 eV (Fig. 1, Table 1), which is well corresponded with the calculated energy barrier of 12.0 eV along the C<sub>2</sub>F<sub>4</sub><sup>+</sup> dissociation route [1]. The C<sub>3</sub>F<sub>5</sub><sup>+</sup> ion production channel is the lowest energy barrier due to intramolecular rearrangement reaction, that is *c*-C<sub>4</sub>F<sub>8</sub><sup>+</sup> → C<sub>3</sub>F<sub>5</sub><sup>+</sup> + CF<sub>3</sub> and additionally *c*-C<sub>4</sub>F<sub>8</sub><sup>+</sup> ions C<sub>2</sub>F<sub>4</sub><sup>+</sup> channel is the second lowest energy barrier. The other fragments such as C<sub>3</sub>F<sub>5</sub><sup>+</sup>, CF<sub>3</sub><sup>+</sup>, CF<sup>+</sup>, are produced by intermolecular rearrangement reactions.

Consequently, the ionization process of C<sub>3</sub>F<sub>5</sub><sup>+</sup> channel is abundant due to the lowest potential barrier.

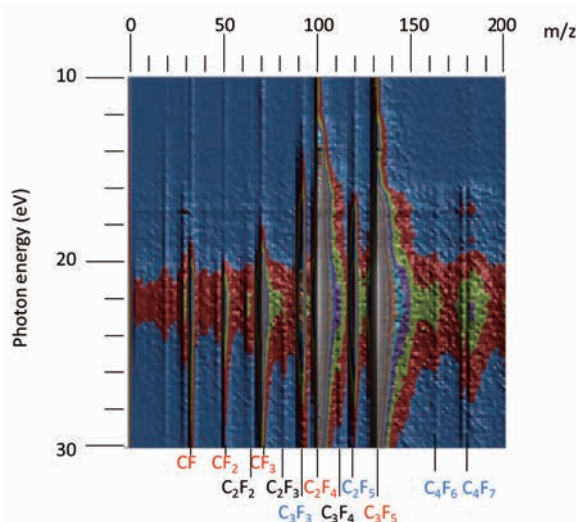


Fig. 1. Typical mass spectral intensities by photoionization of *c*-C<sub>4</sub>F<sub>8</sub> measured vacuum ultraviolet ranges from 10 to 30 eV.

Table 1. Ionization potential (IP) and appearance potentials (AP) for *c*-C<sub>4</sub>F<sub>8</sub>.

	Ions	Potential Calc. [1]	(eV) Exp.	References
IP	<i>c</i> -C <sub>4</sub> F <sub>8</sub> <sup>+</sup>	11.5	<b>11.55</b>	This study
AP	<i>c</i> -C <sub>4</sub> F <sub>7</sub> <sup>+</sup>	15.1	<b>15.45</b>	This study
	C <sub>3</sub> F <sub>5</sub> <sup>+</sup>	12.0	12.1 <b>11.85</b>	Lifshitz[2] This study
	C <sub>2</sub> F <sub>4</sub> <sup>+</sup>	12.4 12.0*	12.35 <b>12.05</b>	Lifshitz[2] This study
	CF <sub>3</sub> <sup>+</sup>	12.5	14.4 <b>16.6</b>	Lifshitz[2] This study
	CF <sub>2</sub> <sup>+</sup>	14.8	17.9	This study
	CF <sup>+</sup>	13.6	18.4 <b>17.1</b>	Lifshitz[2] This study

\* vertical ionization potential

[1] T. Hayashi, *et al.* Jpn. J. Appl. Phys. **61** (2022) 106006.

[2] C. Lifshitz, *et al.* Int. J. Mass Spectrum Ion Phys. **10** (1972) 25.

BL3B

## Study of Luminescence Characteristics of Diamond Scintillator for Dark Matter Search

A. Umemoto

*Division of Physics, University of Tsukuba, Tennoudai, Tsukuba, Ibaraki, 305-8571, Japan*

Direct detection of dark matter is one of the highest priorities in astroparticle physics. The dark matter in Milky Way Galaxy can be detected via elastic scattering from nuclei in a detector on the earth. For the direct dark matter search, diamond is one of the promising detector. The highest Debye temperature among crystals (2200 K) and optical centers due to defects and impurities are unique physical properties of diamond, and they might make good performance of a diamond scintillating bolometer [1][2].

With the goal of developing a diamond scintillating bolometer for dark matter search, we constructed an experimental system to measure a photoluminescence property of synthetic diamond at BL3B in UVSOR. Usually, the measurements at BL3B are conducted by the following setup: the excitation light is incident on a sample surface at an angle of  $45^\circ$ , and fluorescence is detected with a CCD placed at right angles to the excitation light. But this measurement setup will not work well for diamond due to the total internal reflection because the refractive index of diamond ( $n = 2.42$ ) is much larger comparing with that of air (also vacuum). Therefore, a measurement system using a right angle prism as shown in the schematic diagram of Fig.1 was designed. The excitation deviated a light path by  $90^\circ$  by entering one side of the prism will be made incident on the diamond attached on the other side of the prism by vacuum grease. The system makes it possible for the CCD to detect the photoluminescence of diamond emitted in a direction perpendicular to the diamond surface. We used a UV fused silica right angle prism with length of 10 mm manufactured by Thorlabs, which transmits more than 90% of light with wavelengths more than 185 nm.

Fig.2 shows a photoluminescence spectrum of a diamond excited by ultra violet light with wavelength of 200 nm. The diamond is a commercially available synthetic crystal with a size of  $3 \times 3 \times 0.3$  mm manufactured by a method of high-pressure high-temperature. Nitrogen impurities of the diamond is less than 200 ppm. Although a peak due to the second-order diffraction of the excitation light was also observed, the shape of the spectrum detected in the wavelength of

$500 < \lambda < 700$  nm was consistent with our previous result of X-ray radio luminescence spectrum. It was demonstrated that the measurement system is useful for detecting a photoluminescence of diamond. In FY2023, we plan to perform low-temperature measurements with this setup to quantify the luminescence properties of diamond scintillators.

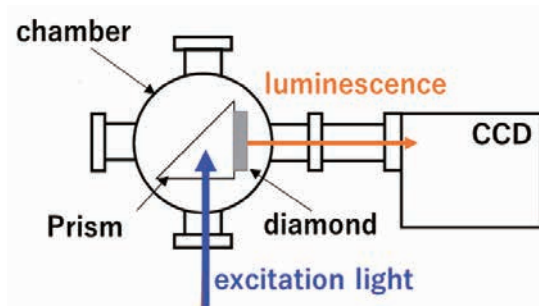


Fig. 1. A design of the experimental setup for photoluminescence measurement of diamond.

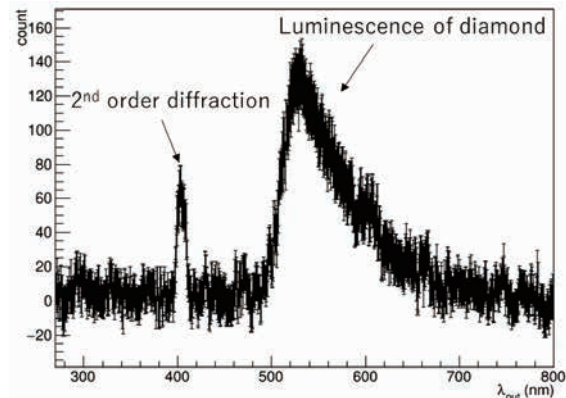


Fig. 2. Photoluminescence spectrum of a commercially available HPHT diamond measured by using the system shown as Fig.1. Ultra violet light with wavelength of 200 nm was used for photoluminescence excitation.

[1] T.L. Nam *et al.*, *Appl. Radiat. Isot.* **40** (1989) 8.

[2] L. Canonica *et al.*, *J. Low. Temp. Phys.* **189** (2020) 606.

## Current Photon Flux and Focus Size of BL4B

H. Iwayama<sup>1,2</sup>

<sup>1</sup>UVSOR Synchrotron Facility, Institute for Molecular Science, Okazaki 444-8585, Japan

<sup>2</sup>School of Physical Sciences, The Graduate University for Advanced Studies (SOKENDAI), Okazaki 444-8585, Japan

Beamline BL4B has three holographically ruled laminar profile plane gratings (G1: 800 lines/mm, G2: 267 lines/mm, G3: 100 lines/mm) and covers soft X-ray regions ranging from 40 eV to 1000 eV. This soft x-ray region includes K-edge energies of light elements such as C, N, and O and L-edge energies of transition metals such as Mn, Fe, and Co. Since an endstation of BL4B is not fixed for specific equipment, users can bring in their equipment and connect them to BL4B. The main experiments at BL4B are X-ray magnetic circular dichroism (XMCD), angular resolved photoemission spectroscopy (ARPES), and X-ray absorption fine structure (XAFS) measurements.

The BL4B uses synchrotron radiation from a bending magnet, and its photon flux and focus size are weak and large compared to undulator beamlines. While BL4B is difficult to measure in tiny samples, it is suitable for organic molecules, which are fragile against radiation damage. Thus photon density is an important parameter for estimating radiation damage on the sample.

This work measured photon flux and focus image at the focus point. We use a photodiode and Ce:YAG scintillator for photo flux and focus image measurements.

Figure 1 shows photon flux curves for each grating. Entrance and exit slits of the beamline are set to 50  $\mu\text{m}$ . The photon flux is almost the same as the previous one measured in 2005, and a photon flux is higher than the previous one for a high photon energy region of more than 400 eV. In 2012, our facility improved the optics of electron storage ring, such as bending magnets, and upgraded from UVSOR-II to UVSOR-III. While electron trajectories in the storage ring were significantly changed after the major update of UVSOR synchrotron, the photon flux curves measured this time indicate that beamline optics were optimized well and the throughput and photon flux of the beamline was maintained.

Figure 2 shows a photo of measurement equipment for a focus image. The equipment comprises Ce:YAG scintillator, ultra-long working distance lens, and CMOS camera. The scintillator is in a vacuum chamber and irradiated by soft X-ray beam of BL4B. The irradiated scintillator emits  $\sim 550$  nm fluorescence, and we observed them by the ultra-long working distance lens and CMOS camera. This lens's working distance and optical magnification are 305 mm and 0.37  $\sim$  4.48, respectively. The highest space resolution is 7  $\mu\text{m}$ .

Figure 3 shows a typical focus image. Photon energy and flux are 400 eV and  $8 \times 10^9$  photons/s. An exposure

time is 30 seconds. This image exhibits a focus size of  $\phi \sim 500$   $\mu\text{m}$ .

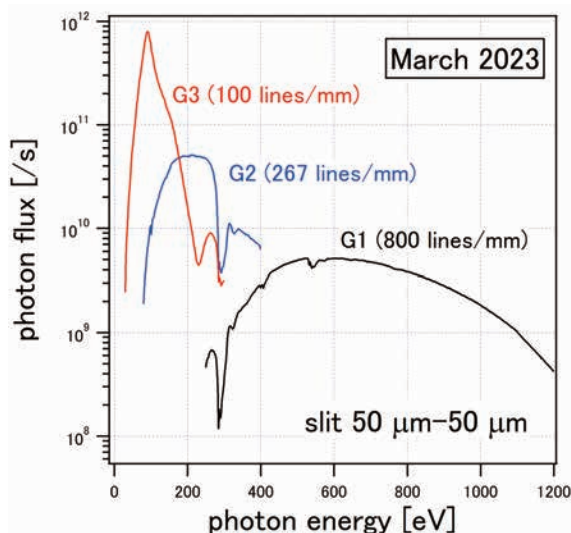


Fig. 1. Photon flux curves for G1, G2 and G3. Entrance and exit slits are set to 50  $\mu\text{m}$ .

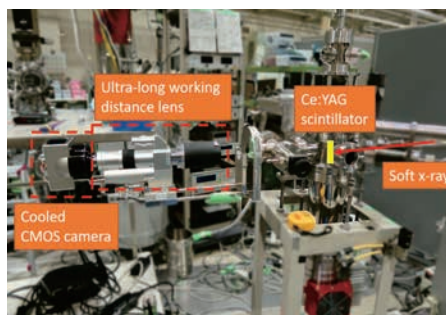


Fig. 2. Photo of focus image measurement equipment at an endstation of BL4B.

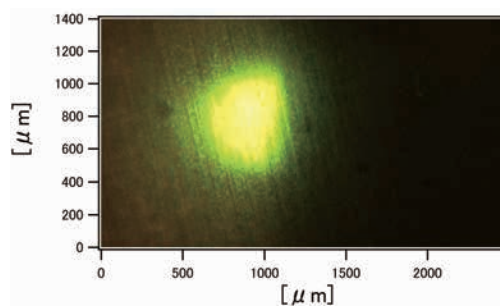


Fig. 3. Focus image at the Ce:YAG scintillator. The photon energy is 400 eV.

BL4B

## Low Radiation Damage XAFS Measurements at BL4B

H. Iwayama<sup>1,2</sup>

<sup>1</sup>UVSOR Synchrotron Facility, Institute for Molecular Science, Okazaki 444-8585, Japan  
<sup>2</sup>School of Physical Sciences, The Graduate University for Advanced Studies (SOKENDAI), Okazaki 444-8585, Japan

Recent developments in synchrotron radiation and focusing optics technologies yield highly brilliant light sources. This high bright synchrotron radiation enables us to measure tiny samples and perform nano-structure analysis such as scanning transmission x-ray microscope (STXM) and photoemission electron microscope (PEEM). In addition, photon-hungry experiments such as resonant inelastic x-ray scattering benefit from the recent higher brightness of synchrotron radiations.

However, the higher brightness causes severe problems of radiation damage to the samples. In particular, soft X-rays has weak penetration power, and only a several-100 nm thickness of the sample almost absorbs them. Thus radiation damage problem for soft X-ray regions is much more severe than that for hard X-ray regions. If a photon flux, focus size, and photon energy are  $10^{13}$  photons/s,  $10\ \mu\text{m}$ , and  $300\ \text{eV}$ , the corresponding dose is estimated to be at  $10\ \text{GGy/s}$  for samples mainly composed of carbon. Critical dose for chemical change are 80, 280, and  $1230\ \text{MGy}$  for polymethyl methacrylate, fibrinogen, and polystyrene, respectively [1]. It means that irradiation of such brilliant synchrotron radiation destroys soft matter samples in a moment.

Low photon flux measurements are also important to avoid radiation damage on fragile samples such as soft matter. In this case, signals of XAFS measurements are weak in proportion to the photon flux. For good SN ratio data, noise levels should be pretty small. A total electron yield (TEY) measurement is one of the most popular X-ray absorption fine structure analysis methods. In the TEY measurements, we measure currents in the sample irradiated by soft X-rays. The current means the total electrons ejected from the sample, corresponding to absorption cross sections. Thus we measure the sample current for each photon energy by using a pico-amperemeter. In this case, the noise of signals mainly comes from electric noise. In particular, noise from the ground level of the experimental hall is critical.

In this work, we estimate radiation damages for XAFS measurements and verify the lower limit of photon flux, which is enough to obtain XAFS spectra with good SN ratios. Our TEY equipment at BL4B is simple. A sample is fixed on a sample holder of an aluminum board in a vacuum chamber using carbon tape. We connect a current output terminal of the vacuum chamber to a pico-amperemeter (Keythley electrometer 617) with a low-noise BNC cable. The sample is  $\text{FePO}_4$  powders.

Figure 1 shows (a) sample currents and (b) the histogram of our TEY equipment when no soft X-ray irradiates the sample. The Full-width half maximum (FWHM) is  $2\ \text{fA}$ . In this measurement, we observe an offset of  $6\ \text{fA}$ . It may be because the ground voltages of the pico-amperemeter and sample holder are slightly different. When we use a standard BNC cable instead of the low-noise cable, the FWHM of noise levels becomes  $2\ \text{fA}$ .

Figure 2 shows TEY spectra of  $\text{FePO}_4$  powders at different photon fluxes. The resolution of photon energies is set to  $E/\Delta E$  of 2000, and it takes 8 minutes to obtain one spectrum. When photon flux is more than  $4 \times 10^7$  photons/sec, SN ratios are enough to find fine structure of XAFS spectra. However, at the photon flux of  $8 \times 10^6$  photons/sec, while we observe the prominent peak at the photon energy of  $710\ \text{eV}$ , sample current intensities are about  $10\ \text{fA}$ , and their fine structures around  $723\ \text{eV}$  are drowned in noise. From this, a lower limit of photon flux is around  $4 \times 10^7$  photons/sec at the Fe L edge, and the corresponding dose is only  $20\ \text{kGy}$ . This work demonstrates that our TEY system enables us to perform low radiation damage XAFS measurements.

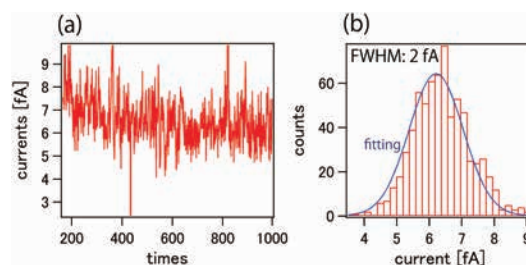


Fig. 1. Noise levels of our TEY equipment at BL4B.

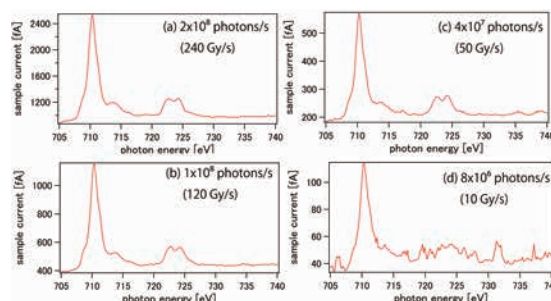


Fig. 2. TEY spectra of  $\text{FePO}_4$  powders for various photon fluxes.

[1] J. Wang *et al.*, J. Electron Spectrosc. Relat. Phenom. **170** (2009) 25.

## Transmission Characteristics of an Optical Filter for UV Observations

A. Yamazaki<sup>1</sup>, K. Goda<sup>1</sup>, T. Matsumoto<sup>2</sup>, S. Teramoto<sup>2</sup> and K. Yoshioka<sup>2</sup>

<sup>1</sup>*Department of Earth and Planetary Science, Graduate School of Science,  
The University of Tokyo, Tokyo 113-0033, Japan*

<sup>2</sup>*Department of Complexity Science and Engineering, Graduate School of Frontier Sciences,  
The University of Tokyo, Chiba 277-8561, Japan*

The hydrogen absorption cell is a unique type of filter that functions as an optical band-stop filter for hydrogen Lyman- $\alpha$ . The Lyman- $\alpha$  is absorbed by hydrogen contained in the cell when thermally dissociated into the atomic state. The shape of this cell is cylindrical ( $\phi 35$  mm, L40 mm), and the windows on each side are made of magnesium fluoride (MgF2) for UV light transmission. Therefore, the cell simply acts as an MgF2 filter without hydrogen gas. Overall, the cell is known for its narrow bandwidth, lightweight, small size, and thus suited to mount on a small spacecraft. We plan to use this filter in the ongoing Comet Interceptor Mission, in which the filter is used to observe the atomic hydrogen coma of the target comet remotely.

However, there is a difficulty regarding this filter: the degradation of MgF2 transmittance. The transmittance of MgF2 drops over time as it alters by UV light irradiation, and this filter is no exception. Since we have been using this filter in past experiments, the center of the MgF2 window is more altered compared to the edges. To better understand the characteristic, in this experiment, we mainly focused on evaluating the position dependence of the MgF2 transmittance and the change in the transmittance after polishing the surface with ethanol. The latter aims to retrieve the transmittance lost due to alteration. Since the experiments aim to understand the characteristics of the filter window, we did not fill hydrogen gas in the cell and thus was not functioning as a band-stop filter.

In the experiment, we measured the position dependence of the filter transmittance. The cell was set on a motorized stage, and the transmittance was measured at multiple incident positions by moving it vertically against the beam. Microchannel plates and a resistive anode encoder were used for the detector. For each measurement, a wavelength scan was performed using the G3M5 grating system with the range of 110-135 nm at an interval of 1 nm. Later, the same measurement was done after polishing the MgF2 surface with ethanol.

Figure 1 shows the transmittance of the cell filter.

The solid and dashed lines show the result before and after polishing the surface with ethanol. The plots' colors describe the different incident positions as shown in the upper right illustration. The area below 116 nm is shaded since the data in this range has a low S/N ratio due to the MgF2 cutoff wavelength at 115 nm.

The result implies that the transmittance increases from the center towards the edge, and also increases by polishing the MgF2 surface with ethanol. However, the increase in transmittance varies significantly among the incident positions. At the center of the cell, the transmittance increases no more than a few percent, but around the edges, it increases by  $\sim 20\%$ . One possible explanation is that polishing the surface is effective for surface dust and smears, but not for degradation caused by intensive UV light irradiation. Since the center of the cell has suffered irradiation throughout the past experiments, the alteration is discernible. Polishing the cell surface proved effective in increasing the transmissions, but we could not fully retrieve those lost due to UV-induced alteration.

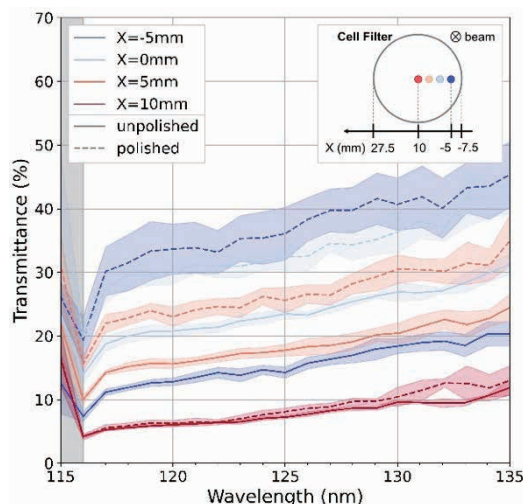


Fig. 1. Transmission spectra of MgF2 windows on a hydrogen absorption cell.

BL5B

## Evaluation of the Pressure Dependence of the Krypton Absorption Cell

M. Kuwabara<sup>1</sup>, K. Kato<sup>1</sup>, K. Arakawa<sup>1</sup> and M. Taguchi<sup>1</sup>

<sup>1</sup>Department of Physics, College of Science, Rikkyo University, Tokyo 171-8501, Japan

In planetary upper atmospheres, hydrogen atoms originating from hydrogen molecules in lower atmospheres expand to an altitude equivalent to several planetary radii. These hydrogen atoms resonantly scatter the solar Lyman-alpha radiation (121.567 nm), forming planetary hydrogen coronae. Since the brightness of the hydrogen coronae depends on the number density of hydrogen atoms, the spatial structures can be obtained by imaging the coronae.

A hydrogen absorption cell is efficient tool for remote sensing of the density and temperature distribution of the exospheric hydrogen atoms. Additionally, this technique has advantages over other techniques in terms of geometrical size, weight, and simplicity. Therefore, this technique is expected to be effectively used for exploration using ultra-small spacecraft and other applications [1].

One of the drawbacks of the absorption cell technique is the difficulty of calibration. Since the absorption linewidth of the hydrogen absorption cell is a few pm at most, the calibration system must have high wavelength stability. However, it is revealed that the measurement wavelength of BL5B beam line drifts as the temperature of the mirror changes, so it is necessary to know the correct wavelength for each measurement. This

problem can be overcome by placing a krypton absorption cell in front of the hydrogen absorption cell. This is because krypton has a strong absorption line at 123.584 nm, which is close to the Lyman-alpha line of the hydrogen atom. By measuring the light transmitted through both cells, the peak of the absorption of the hydrogen Lyman-alpha line can be determined.

In this experiment, we evaluate the pressure dependence of the absorption line profile of the krypton cell to establish a calibration method for the hydrogen absorption cell. Figure 1 shows the result of the experiment. The absorption line of krypton is 123.584 nm, but the measurement wavelengths of the calibration system are off, and the peaks are seen a little beyond 124 nm. In addition, the positions of the peak vary in each measurement. Regarding the pressure dependence, as the pressure of krypton gas increases, both the depth and the width of absorption also increase. The result will be used to determine the optimum pressure for the krypton absorption cell needed for the BL5B calibration system in the future.

[1] M. Kuwabara *et al.*, Rev. Sci. Instrum. **89** (2018) 023111.

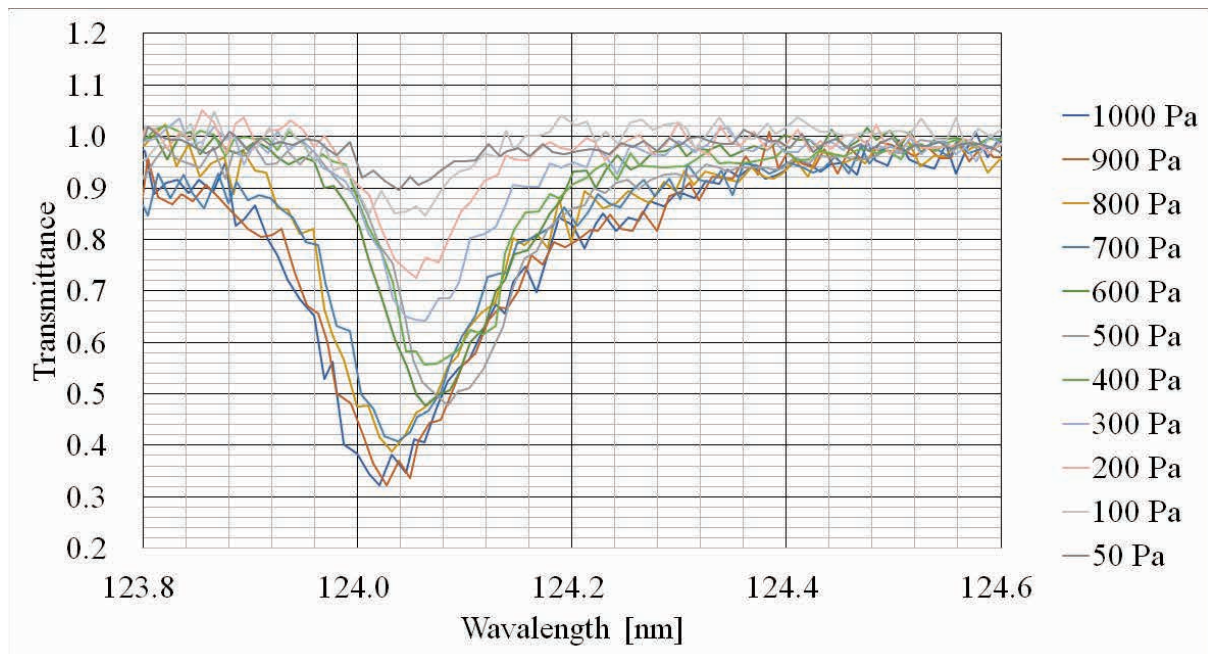


Fig. 1. Pressure dependence of the krypton cell absorption.

## XUV Polarization Measurement using Visible Fluorescence from Neon Atoms

T. Kaneyasu<sup>1,2</sup>, K. Hosaka<sup>3</sup> and J. Adachi<sup>4,5</sup>

<sup>1</sup>SAGA Light Source, Tosu 841-0005, Japan

<sup>2</sup>Institute for Molecular Science, Okazaki 444-8585, Japan

<sup>3</sup>National Institutes for Quantum Science and Technology, Takasaki 370-1292, Japan

<sup>4</sup>Institute of Materials Structure Science, KEK, Tsukuba 305-0801, Japan

<sup>5</sup>The Graduate University for Advanced Studies (SOKENDAI), Tsukuba 305-0801, Japan

Polarization is one of the most important characteristics of synchrotron radiation. For accurate measurements using the polarization properties of synchrotron radiation, it is essential to evaluate the polarization state of light at a sample point. Fluorescence polarimetry is a useful technique to determine the polarization state of the extreme ultraviolet (XUV) radiation. This method is based on the conversion of XUV radiation to visible light on the atomic resonance [1,2]. The fluorescence preserves the polarization state of the excitation light when it is observed along the light propagation axis. Comparing with the optical polarimeters [3,4], this method has advantages in its simple apparatus and easy operation. Up to the present, however, this method has been only applied to helium atoms [2,4,5], and the wavelength range is restricted to around 50 nm. In this study, we show that neon atoms can be used to measure the polarization state of XUV radiation at 60 nm wavelength.

The experiment was performed at the bending magnet beamline BL5B. Figure 1 shows the experimental layout of the present study. The wavelength of monochromatized synchrotron radiation was set to 59.6 nm. Neon atoms were provided by an effusive beam. The XUV radiation resonantly excites the neon atom to the  $4d^1[3/2]_1$  state. This state decays to the  $3p[1/2]_1$  state with the emission of 511.4 nm fluorescence photon. The fluorescence photons emitted parallel to the light propagation axis ( $z$ -axis) were detected by a photomultiplier tube equipped with a polarizer and a bandpass filter. The fluorescence photon basically preserves the polarization state of the XUV radiation. The only difference between them is that the polarization angle of the fluorescence photon is expected to rotate by 90 degrees with respect to the polarization angle of the incident XUV radiation.

Figure 2 shows the fluorescence intensity measured as a function of the polarizer angle which is defined by the angle of the polarization axis with respect to the horizontal axis ( $x$ -axis). In accordance with the expectation, the fluorescence intensity shows a sinusoidal modulation reflecting the vertically linear polarization of the fluorescence photon. Assuming an elliptical polarization, the experimental data points are

fitted by a theoretical curve. The linear polarization degree and polarization angle of XUV radiation are evaluated to be  $0.67 \pm 0.02$  and  $10 \pm 2$  degrees, respectively. This is roughly in agreement with the results obtained by helium atoms [5, 6], suggesting the capability of fluorescence polarimeter using neon atoms.

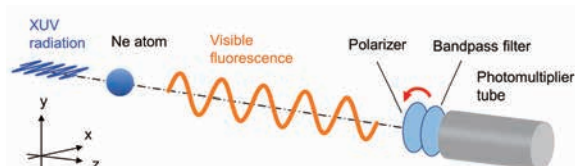


Fig. 1. Experimental setup. The visible fluorescence photon emitted along the light propagation axis was detected.

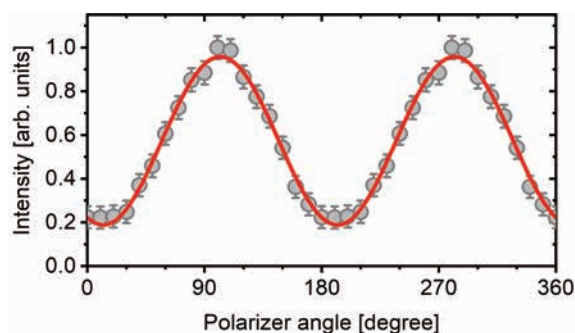


Fig. 2. Fluorescence intensity measured as a function of the polarizer angle. The experimental data points are fitted by a theoretical curve.

[1] V. Bobahev and O. S. Vasyutinskii, *Rev. Sci. Instrum.* **63** (1992) 1509.

[2] C. J. Latimer *et al.*, *J. Electron Spectroscopy Relat. Phenom.* **101-103** (1999) 875.

[3] D. Cubric *et al.*, *Meas. Sci. Technol.* **10** (1999) 554.

[4] E. Allaria *et al.*, *Phys. Rev. X* **4** (2014) 041040.

[5] T. Kaneyasu, K. Hosaka and J. Adachi, *UVSOR Activity Report 2020* **49** (2021) 46.

[6] Y. Hiosaka, H. Iwayama and T. Kaneyasu, *J. Synchrotron Rad.* **27** (2020) 675.

BL5B

## A Position-sensitive Microchannel Plate Detector with Resistive Anode

S. Matoba<sup>1</sup>, S. Kanda<sup>1</sup>, H. Ohshita<sup>1</sup>, K. Hirata<sup>2</sup>, H. Iwayama<sup>3,4</sup> and T. Kaneyasu<sup>5</sup>

<sup>1</sup>*Institute of Materials Structure Science, KEK, Tsukuba 305-0801, Japan*

<sup>2</sup>*National Metrology Institute of Japan, National Institute of Advanced Industrial Science and Technology, 1-1-1 Higashi, Tsukuba, Ibaraki 305-8565, Japan*

<sup>3</sup>*Editorial Board, UVSOR Synchrotron Facility, Institute for Molecular Science, Okazaki 444-8585, Japan*

<sup>4</sup>*School of Physical Sciences, The Graduate University for Advanced Studies (SOKENDAI), Okazaki 444-8585, Japan*

<sup>5</sup>*SAGA Light Source, Tosu 841-0005, Japan*

A microchannel plate (MCP) is a lead glass detector with a two-dimensional array of electron-multiplying pores of about 10  $\mu\text{m}$  in diameter. When charged particles or short-wavelength photons collide with the inner wall of the pore, secondary electrons are generated and amplified in the pore to be detected as electron pulses. MCPs are used in a very wide range of fields from basic research to industry because of their large area, high spatial resolution, and high-speed detection capability.

We are developing a system that enables easy measurement of imaging techniques using quantum beams regardless of the beam type and location, which can be used for trial experiments prior to the use of advanced devices. The most common method of two-dimensional detectors for MCP anodes is optical detection of emission from fluorescent anodes using a CCD camera or the like. However, the difficulty of inserting a detector in the middle of the beamline and the upper limit of the frame rate of the camera limit the use of this method for accelerator beamlines. Another major method, the delay-line anode[1], requires a high-speed circuit that can detect time differences between wires, making it expensive and difficult to implement in small-scale experiments.

We are developing a position-sensitive detector using resistive anodes as a two-dimensional detector for various particles such as neutrons, ultraviolet light, muons, and ions. The advantages of this system are that position detection can be easily performed by using a 4-channel waveform analyzer and that the resistive anodes are only about 2 mm thick, so they can be assembled into a compact assembly. Resistive anodes as two-dimensional detector elements have been developed for a long time[2], but there is no simple system that can be used by researchers who are not detector experts, and we are developing one.

In this experiment, the “solid chamber” of BL5B was removed and a pinhole, a four-quadrant slit, and a light-reducing filter made of aluminum foil and tungsten mesh were installed to detect the incident position of

the MCP with a wavelength of 130 nm UV light of approximately 1 mm in diameter. The charge of the electron pulses generated by the MCP, which has an effective diameter of 40 mm and consists of two stages, is dispersed and transferred to the electrodes at the four corners of the resistive anode. The two-dimensional position information is calculated from the current flowing to each electrode as  $x/d = (I_1 + I_4) / I$ ,  $y/d = (I_1 + I_2) / I$  (where  $d$  is the full width or height of one side of the resistive anode and  $I = I_1 + I_2 + I_3 + I_4$ ). The current flowing to each electrode was measured with a 4-channel amplifier, shaper and waveform analyzer.

Figure 1 shows an example of the measured light positions. In this experiment, the measurement system was verified and confirmed to be capable of sound position detection. In the future, the position resolution and detection efficiency distribution will be investigated using patterns, etc.

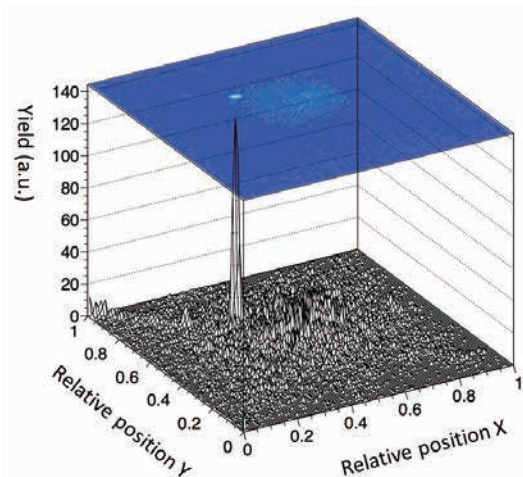


Fig. 1. Position reconstruction on the resistive anode.

[1] S. E. Sobottka and M. B. Williams, *IEEE Trans. Nucl. Sci.*, **35** (1988) 348.

[2] M. Lampton and R. F. Malina, *Rev. Sci. Instrum.*, **47** (1976) 1360.

## Progress of Photoelectron Momentum Microscopy for Revealing Complex and Detailed Electronic Structures of Materials

S. Suga<sup>1,2</sup> and F. Matsui<sup>3,4</sup>

<sup>1</sup>SANKEN, Osaka University, Osaka, 567-0047, Japan

<sup>2</sup>PGI-6, Jülich Research Center, Germany

<sup>3</sup>UVSOR Synchrotron Facility, Institute for Molecular Science, Okazaki 444-8585, Japan

<sup>4</sup>The Graduate University for Advanced Studies (SOKENDAI), Okazaki 444-8585, Japan

The photoelectron momentum microscope (often abbreviated as 2D-PMM) is installed already in 2020 at BL6U of UVSOR in the form of single hemispherical deflection electron energy analyzer (HDA) behind the PEEM type objective lens, which can easily be switched between the real space to the momentum space detection mode.  $E_B(x,y)$  or  $E_B(kx,ky)$  constant energy contour (CEC) can be simultaneously detected by a 2D detector behind the focusing lens optics installed after the exit of the HDA[1]. The detection efficiency of the  $E_B(kx,ky)$  is very high in comparison with the conventional HDA detection due to the simultaneously covered wide acceptance angle owing to the use of PEEM, where the sample rotation is not necessary for  $E_B(kx,ky)$  detection and excitation light focusing is not necessary to probe micro-nano regions. Then very reliable gigantic data set is obtained by this instrument in rather short measuring time [2–4]. Temperature down to 10 K can be measured.

Since the best quality sample surface region down to  $\sim 10 \mu\text{m}$  can be selected by the proper sized field aperture in the objective lens, high quality and reproducible data can be obtained by this instrument. The beam focusing is not necessary in this system by using the PEEM and several tens of nm resolution can be realized without noticeable radiation damage.

Detailed behaviors of CECs of graphite are shown in Fig.1 [3]. Resolutions are  $\Delta E \sim 40 \text{ meV}$  and  $\Delta k \sim 0.01 \text{ \AA}^{-1}$ . Band dispersions along any  $kx$ - $ky$  direction can be immediately derived from the big data.

Since 2022 upgrading is progressing. In addition to  $68^\circ$  incidence of light from the surface normal direction,  $0^\circ$  incidence is soon available. HDA is upgraded to 2 HDAs to realize this configuration. 2D spin filter will be installed within a few months to realize the multichannel figure of merit  $\text{FoM} \sim 10^2$ . Then the spin detection efficiency becomes  $10^4$  times higher than the single channel spin detection and  $10^2$  times higher than using the W (tungsten) 2D spin filter.

Various additional upgrading of the SP-2D-PMM system in UVSOR will be made in the next few years, producing the world best heavy data on micro-nano regions of exotic and/or functional materials supporting the new device development.

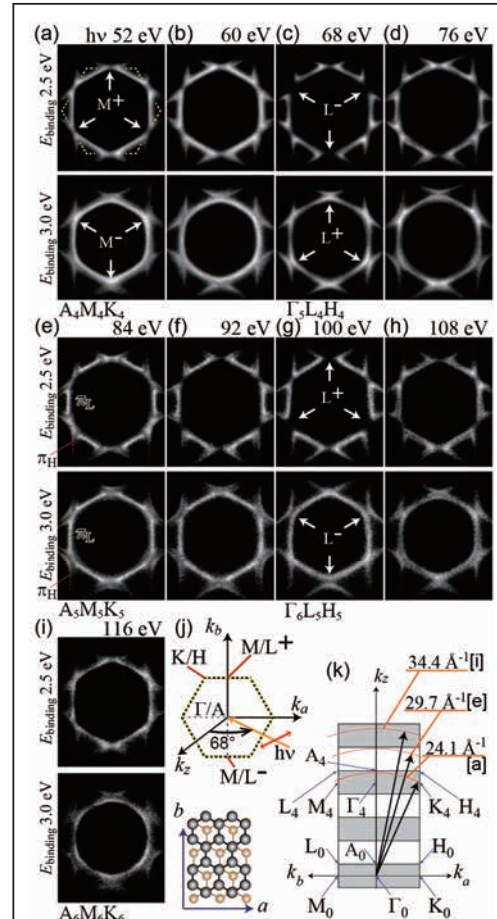


Fig.1. CECs of graphite (0001) at various  $h\nu$  reproduced from Ref.[3]. Thus  $E_B(kx,ky,kz)$  as well as band dispersions along any  $kx$ - $ky$  directions can be easily derived from gigantic data.

[1] S. Suga, A. Sekiyama, C. Tusche, Photoelectron Spectroscopy, Springer, Springer Series of Surface Science **72** (2021) 1–503.

[2] F. Matsui, S. Makita, H. Matsuda, T. Yano, E. Nakamura, K. Tanaka, S. Suga, and S. Kera, Jpn. J. Appl. Phys. **59** (2020) 067001.

[3] F. Matsui and S. Suga, Phys. Rev. B **105** (2022) 235126.

[4] F. Matsui, Y. Okano, H. Matsuda, T. Yano, E. Nakamura, S. Kera and S. Suga, J. Phys. Soc. Jpn. **91** (2022) 094703.

BL6B

## Low-frequency Photocurrent Response in Semiconductors Based on ns-visible-pump broadband-infrared-probe Spectroscopy

J. Nishida<sup>1\*</sup> and T. Kumagai<sup>1</sup><sup>1</sup>Institute for Molecular Science, National Institutes of Natural Sciences, Okazaki 444-8585, Japan

Optical responses of photoinduced carriers in mid- to far-infrared encode their scattering times as well as trap and polaronic states, which are all directly relevant to the mobility of the carriers. Yet, due to the spectrally broad nature of such responses, the time-resolved study of such photoinduced carriers is often difficult and requires advanced laser sources for ultrafast experiments [1]. While mid-infrared thermal light source with fast electronics covers important subsets of the spectral range and time resolution [2], the full characterization of the low-frequency carrier response has remained elusive.

An extremely broadband output of a synchrotron provide unique opportunities to tackle such problems. With the combination of broad spectrum extending from mid- ( $\sim 100$  meV) to far-infrared ( $\sim$  meV), as well as a reasonable pulse duration of  $< 1$  ns, it may be possible to address the scattering and polaronic stabilization of photoinduced carriers on the nanosecond time scale. Such an information is particularly relevant to address the photoinduced carrier responses in lead halide perovskites, where the interaction of carriers with surrounding lattice has been intensely debated [3].

We thus attempted to combine the mid-infrared synchrotron output at BL6B beam line as a probe pulse with a 10s-ns visible laser as a pump pulse (Fig. 1a). We mainly focused on the application in the single-bunch operation ( $\sim 5$  MHz) to enforce the relaxation of photoinduced carriers as much as possible. The TTL output synchronized with the synchrotron laser is used to trigger our commercial and duration-tunable (6 – 40 ns) pulsed nanosecond laser. In collaboration with Equipment Development Center, we developed time-delay generator and modulator to control the timing between the visible and broadband mid-infrared pulse, as well as to modulate the visible pump pulse intensity. The modulation frequency is used for the lock-in detection of the photoinduced change in the intensity that transmits a sample. We implemented a Michelson interferometer for spectral measurements.

We first demonstrated the photo-modulation absorption spectroscopy on the low-frequency response of silicon. In Fig. 1b, we show an acquired interferogram in the ground-state ( $I$ ), and its photoinduced change ( $\Delta I$ ). With the average time of  $\sim 30$  min, we demonstrated the sensitivity of  $\Delta I/I \sim 10^{-3}$ . The Fourier transform (Fig. 1c) shows the divergent response toward the low-frequency side, consistent with the Drude-like behavior

expected for the photo-carriers in silicon.

We then attempted to extend the approach to perovskite quantum dots dispersed in solution. While we observed a photoinduced change in the transmitted intensity, the response was strongly dependent on the modulation frequency (Fig. 1d), likely pointing to a thermal effect. Such a thermal contribution can be alleviated by modulating the pump pulse rapidly at 100 kHz. We scanned the pump-probe delay to identify any relaxation processes related to the photoinduced carriers, but so far could not identify any such responses (Fig. 1d, inset; 5 min average each point).

To observe photoinduced carriers in a broad range of semiconductor materials, we estimate another order of magnitude improvement is necessary for the signal-to-noise ratio. We confirmed that the current signal-to-noise level is limited by the HgCdTe detector, potentially due to the large element size. With the optimization of the electronics, we may attain enough sensitivity to be combined with the time resolution and spectral range that we demonstrated.

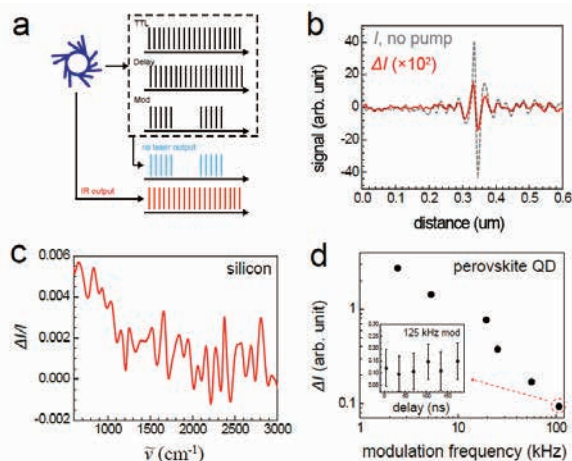


Fig. 1. (a) Timing scheme, (b) photo-modulated interferogram and (c) spectrum on silicon, (d) modulation-frequency dependence of photo-induced modulation.

[1] T. T. Yeh *et al.*, *Sci. Rep.* **7** (2017) 1.

[2] K. Furuhashi *et al.*, *J. Phys. Chem. C* **117** (2013) 19101.

[3] K. Munson T. *et al.*, *Chem*, **4** (2018) 2826.

## Study on the Reflective Properties of Black Coatings Used in UV Observation Equipment.

T. Matsumoto<sup>2</sup>, K. Goda<sup>1</sup>, A. Yamazaki<sup>1</sup>, K. Inoue<sup>1</sup>, S. Liu<sup>2</sup> and K. Yoshioka<sup>2</sup>

<sup>1</sup>Department of Earth and Planetary Science, Graduate School of Science,

The University of Tokyo, Tokyo 113-0033, Japan

<sup>2</sup>Department of Complexity Science and Engineering, Graduate School of Frontier Sciences,

The University of Tokyo, Chiba 277-8561, Japan

The emission angle dependence of scattered light intensity (Experiment 1) and reflectance (Experiment 2) were measured for three different, black-coated aluminum plates (Samples A, B, and C) and a mirror. The reflectance of the samples was determined based on their relative reflectance to the mirror. This experiment aimed to optimize the black coating to be applied to the optics of the hydrogen imager (HI) on board the Comet Interceptor (CI) mission to be launched in 2029. To do this, we quantitatively determine the black coating that minimizes stray light caused by reflections inside the equipment. These measurements are also crucial for the quantitative estimation of the expected performance of CI/HI.

The setup for both Experiment 1 and Experiment 2 was the same. Samples A, B, and C and a mirror were mounted on the inner rotating stage, while the detector was mounted on the outer rotating stage (Fig. 1). The detector used was a photodiode with an effective area of 10 mm × 10 mm. The slit width was adjusted to prevent saturation of the measured values at each incident angle. A G3 diffraction grating was used.

The following 12 measurements were performed.

$$\begin{array}{|c|} \hline 4 \text{ targets} \\ \hline (A, B, C, \text{Mirror}) \\ \hline \end{array} \times \begin{array}{|c|} \hline 3 \text{ incident angles} \\ \hline (30^\circ, 45^\circ, 60^\circ) \\ \hline \end{array}$$

In Experiment 1, the wavelength was set to 121.4 nm. The detector was positioned with the direction of the incoming beam as 0° and rightward as positive. Angle scans were performed from 45° to 180° with an interval of about 13.5°, followed by angle scans near the peak with an interval of about 2°. In Experiment 2, the detector was fixed, and wavelength scans were performed from 112 nm to 133 nm with an interval of 1 nm without summing.

Experiments 1 and 2 are summarized below with their results (Fig. 2 and Fig. 3).

The results found that, at any incident angle, the reflectance was A, B, and C from the lowest to the highest, with Sample A being the most optimal. However, the reflectance of Samples A and B was negative only at 45° incident angle, which might have been due to the dark noise and the positional accuracy of the detector. Further experiments are needed to confirm reproducibility and evaluate the consistency of the incident angle dependence of reflectance with theoretical values.

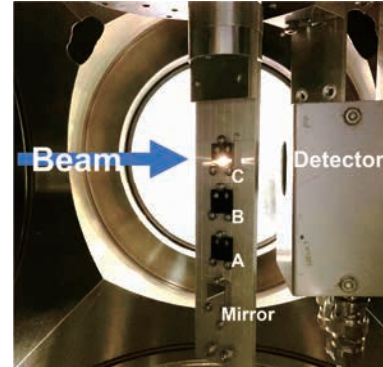


Fig. 1. The setup of the measurements.

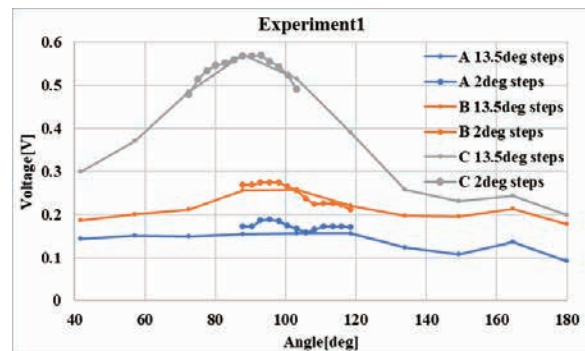


Fig. 2. Experiment 1: The emission angle dependence of the scattered light intensity

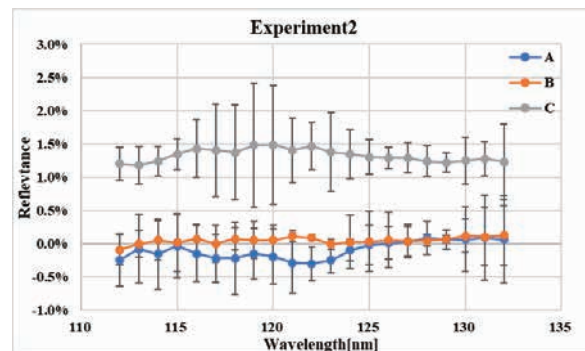


Fig. 3. Experiment 2: Reflectance

BL7B

## Complex Refractive Index Measurement by Reflectance Spectra in Different Polarization Configurations (II)

K. Shinkai<sup>1</sup>, K. Fukui<sup>1</sup>, K. Yamamoto<sup>1</sup> and T. Saito<sup>2</sup>

<sup>1</sup>Department of Electrical and Electronics Engineering, University of Fukui, Fukui 910-8507, Japan

<sup>2</sup>Department of Electrical and Electronic Engineering, Tohoku Institute of Technology, Sendai 982-8577, Japan

Based on the basic design of the instrument by a group at AIST [1], a combined refractive index spectrum measurement system (CRIMS-VUV) [2] has been developed specifically for BL7B, which can continuously measure from the visible region (VIS) at 2 eV to the vacuum ultraviolet (VUV) region at 20 eV. CRIMS-VUV is composed of two measurement modes (spectroscopic ellipsometry measurement (SE) mode and reflection spectrum measurement (OR) mode), both of which can be performed in the same environment.

SE mode has the advantage of measuring the complex refractive index with high accuracy. However, this mode has the disadvantage that, due to its measurement principle, it takes time to measure at each measurement point (photon energy), making it difficult to measure a continuous spectrum. In this respect, OR mode is suitable for measuring continuous spectrum. The well-known Kramers - Kronig analysis (KKA) method is used to determine the complex refractive index spectrum from the reflectance spectrum. However, as mentioned our previous work [2], KKA method is useful, for example, for obtaining qualitative complex refractive index spectrum for limited photon energy region around the absorption edge, but is not well suited for obtaining quantitative complex refractive index spectrum over a wide photon energy region. Therefore, we decided to use the method for determining the complex refractive index from the reflectance in *p*- and *s*-polarization configurations (PS method) as a method for determining the complex refractive index from the reflectance for each photon energy. This method requires the linear polarization of the incident light (Stokes parameter  $S_1$ ), which can be measured from the SE mode of the system. The  $S_1$  can be measured from the SE mode of the system, and the polarization

configuration can be easily changed with the system. These features make the PS method suitable for this system. The following are the intermediate results of complex refractive index measurements of fused silica glass substrate using this PS method.

Figure 1 shows reflectance spectra both in *p*- and *s*-polarization configurations. The dots are reference points which represent the reflectance calculated from the complex refractive index obtained from the ES mode, and the lines are reflection spectra of the OR mode in *p*- and *s*- polarization configurations corrected for the reference points. Note that the effect of surface roughness is taken into account in the optical model of the ES mode and reflectance calculations. The dispersion after the band edge is well shown by the continuous spectrum.

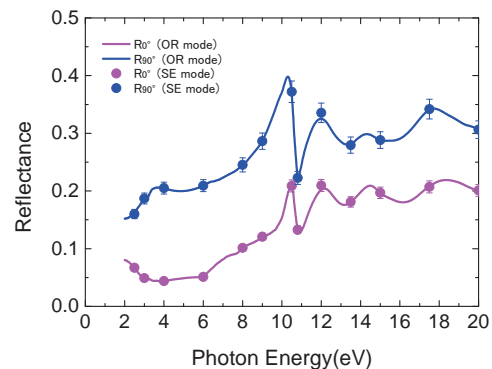


Fig. 1. Reflectance spectra in *p*- and *s*-polarization configurations of fused quartz glass

[1] T. Saito, M. Yuri and H. Onuki, Rev. Sci. Instrum. **66** (1995) 1570.

[2] M. Horiba *et al.*, UVSOR Activity Report 2021 **49** (2022) 49.

## Performance of the Refreshable Large Crystal Nuclear Emulsion for the NINJA Experiment

T. Fukuda<sup>1,2</sup>, H. Kobayashi<sup>2</sup>, Y. Hirobe<sup>2</sup>, Y. Morimoto<sup>2</sup> and M. Nakamura<sup>1,3</sup>

<sup>1</sup>*F-lab., Graduate School of Science, Nagoya University, Nagoya 464-8602, Japan*

<sup>2</sup>*Institute for Advanced Research, Nagoya University, Nagoya 464-8601, Japan*

<sup>3</sup>*Institute of Materials and Systems for Sustainability, Nagoya University, Nagoya 464-8601, Japan*

In neutrino oscillation studies, it is important to detect short-range hadrons in the energy range of about 1 GeV in order to understand neutrino-nucleus interactions. The Emulsion Cloud Chamber (ECC) is a sandwich structure consisting of a special photographic film nuclear emulsion film with sensitivity to minimum ionizing particles, with a thickness of several hundred microns (composed of two sensitive emulsion gel layers each tens of microns thick and plastic base layer), and a thin target material with a thickness of several hundred microns to several millimeters, stacked alternately. The NINJA experiment, which uses ECC as the main detector, has been publishing measurement data on low-energy hadrons for neutrino-iron and neutrino-water interactions since 2014, while expanding the scale of the experiment.

This autumn to winter, we plan to conduct a large-scale statistical experiment on neutrino-H, O, C, and Fe nuclear interactions using about 250 square meters of nuclear emulsion films. The tracks on the nuclear emulsion films are automatically scanned by the track selecting device HTS, but 250 square meters is twice the amount of the previous experimental run that took approximately 20 months for track scanning, and we are developing the track selecting device HTS2, which has five times the scanning speed of HTS. With the expansion of the field of view, the pixel size of HTS2 has been increased, and it is necessary to increase the size of the developed silver grains compared to the conventional nuclear emulsion.

We have created a nuclear emulsion with AgBrI crystal size of 320 nm, which is larger than the conventional 240 nm, and added a group of chemicals that have a proven effect in suppressing latent image fading and fogging. After irradiating the emulsion films with electron beams using UVSOR, we performed a refresh process to eliminate unwanted tracks by exposing it to high temperature and humidity conditions (30°C, 95%RH). We have newly discovered that the refresh which removes unwanted tracks is insufficient (Fig. 1.). The left image of Fig. 1. has a grain density of  $53.5 \pm 1.5$  grains/100  $\mu\text{m}$  and has not undergone a refresh process. The image on the right of Fig. 1. has undergone a refresh process with a grain density of  $29.8 \pm 1.7$ , but the disappearance of tracks due to the refresh process is insufficient.

Based on our experience in the OPERA experiment, we conducted experiments to determine the appropriate

amount of 5-methylbenzotriazole (5-MBT, Fig. 2.), which promotes refreshment by oxidizing latent image nuclei in high humidity conditions. The results of comparing the GD of emulsion film samples with varying amounts of 5-MBT added, using UVSOR to apply an electron beam and comparing with and without refresh processing, are shown in Fig. 3. The initial sensitivity decreased depending on the amount of 5-MBT added to the emulsion. However, when 5-MBT was added at  $1.0 \times 10^{-3}$  or more moles per mole of silver in the emulsion, the refresh effect was enhanced. A suitable amount of balance between the refresh effect and initial sensitivity was found through this addition.

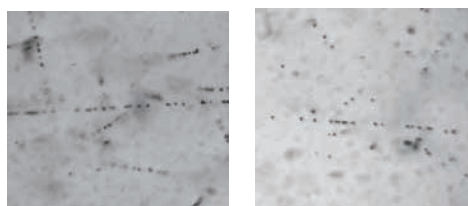


Fig. 1. Microscopic images of large crystal emulsion films. (left) unrefreshed film. (right) refreshed film.

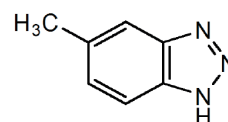


Fig. 2. The chemical formula of 5-MBT.

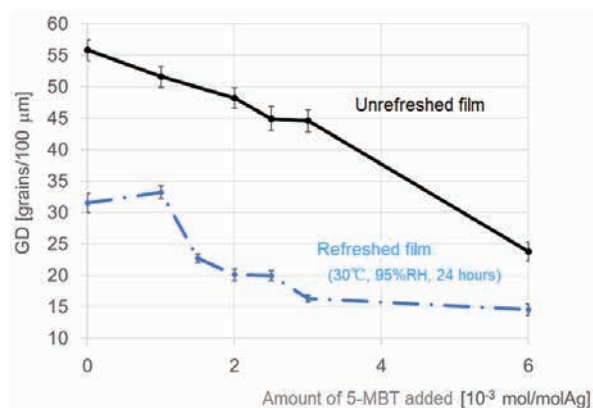


Fig. 3. GD of electron beam tracks. The solid and dashed lines show the data of unrefreshed films and refreshed films, respectively.

## Lattice Design of the UVSOR-IV Storage Ring

E. Salehi<sup>1</sup>, Y. Taira<sup>1</sup>, M. Fujimoto<sup>1,3</sup> and M. Katoh<sup>1,2</sup>

<sup>1</sup>UVSOR Synchrotron Facility, Institute for Molecular Science, Okazaki 444-8585, Japan

<sup>2</sup>Hiroshima Synchrotron Radiation Center, Hiroshima University, Higashi-hiroshima 739-0046, Japan

<sup>3</sup>NUSR, Nagoya University, Nagoya, Japan

In this study, we have designed a new lattice for UVSOR storage ring to provide diffraction-limited light in the vacuum ultraviolet range which requires a small emittance at least a few nm. UVSOR is a low energy synchrotron light source. After some major upgrades [1-4], it is now called UVSOR-III, which has a moderately small emittance of about 17 nm and provide vacuum ultraviolet light of high brightness.

In order to provide diffraction-limited light, at the first step, we have analyzed the present magnetic lattice of UVSOR based on tie diagram to explore the possibility to get a lower emittance with some minor changes in the configuration of magnets. We have found a few optics which has smaller emittance around 10 nm than the present value [5]. To reach the low emittance around a few nm, we have designed a new storage ring of 1 GeV electron energy, which is higher than the present value, 750 MeV. The magnetic lattice is based on a compact double bend achromat cell. This cell consists of two bending magnets and four focusing magnets, all of which are of combined function magnets. In this lattice two sextupole families are located in between two combined dipoles for the chromaticity correction and two harmonic sextupole families are also employed to correct the high order geometric aberrations. The circumference is 82.5 m. This lattice has twelve DBA cells with six long straight sections about 4 m and six short straight sections around 1.5 m long. Among 12 straight sections, two sections will be used for the injection and RF cavity, and ten sections will be used for insertion devices. These lengths are same as those of UVSOR-III. This may enable us to use the undulators at UVSOR\_III in the new ring. The undulators can radiate nearly diffraction-limited light in VUV.

A tune survey was performed to optimize the magnet arrangement and the working point by ELEGANT [6]. We found an optic with a small natural emittance around 4.2 nm in the achromatic condition, which becomes lower in the non-achromatic condition. Occupying three short straight sections with 2T multipole wigglers in symmetry can reduce the emittance to 3.6 nm-rad. Moreover, these wigglers provide intense tender X-rays. Figure 1 shows (left) the lattice functions in the achromatic condition and (right) the dynamic aperture for on- and off energy particles at the straight section after optimizing the strengths of the harmonic sextupoles.

Intra-beam and Touschek scattering which dominate the lifetime in low emittance storage rings, particularly of low energy has been studied. Figure 2 shows that IBS effect increases the Touschek lifetime, while the

emittance is increased. One possible technique to decrease the IBS effect is lengthening the bunches by using harmonic cavity which is routinely used at UVSOR-III. Our simulation shows that the increasing of the bunch length by 80 mm can reduce IBS effect on the emittance to an acceptable level with to  $\epsilon_0 = 4.3 \text{ nm}$  [7].

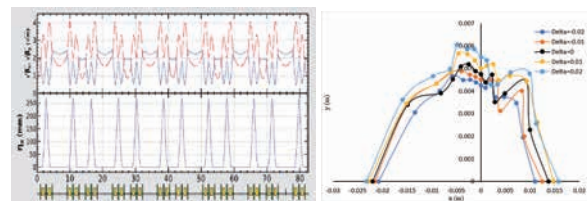


Fig. 1. (Left) Lattice function of 1 GeV storage ring with a small emittance of 4.2 nm for UVSOR-IV, (right) dynamic aperture of optic for different energy deviation.

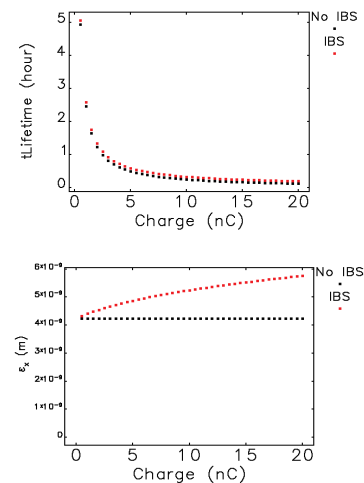


Fig. 2. IBS effect on Touschek lifetime (top) and longitudinal emittance (bottom) versus bunch charge.

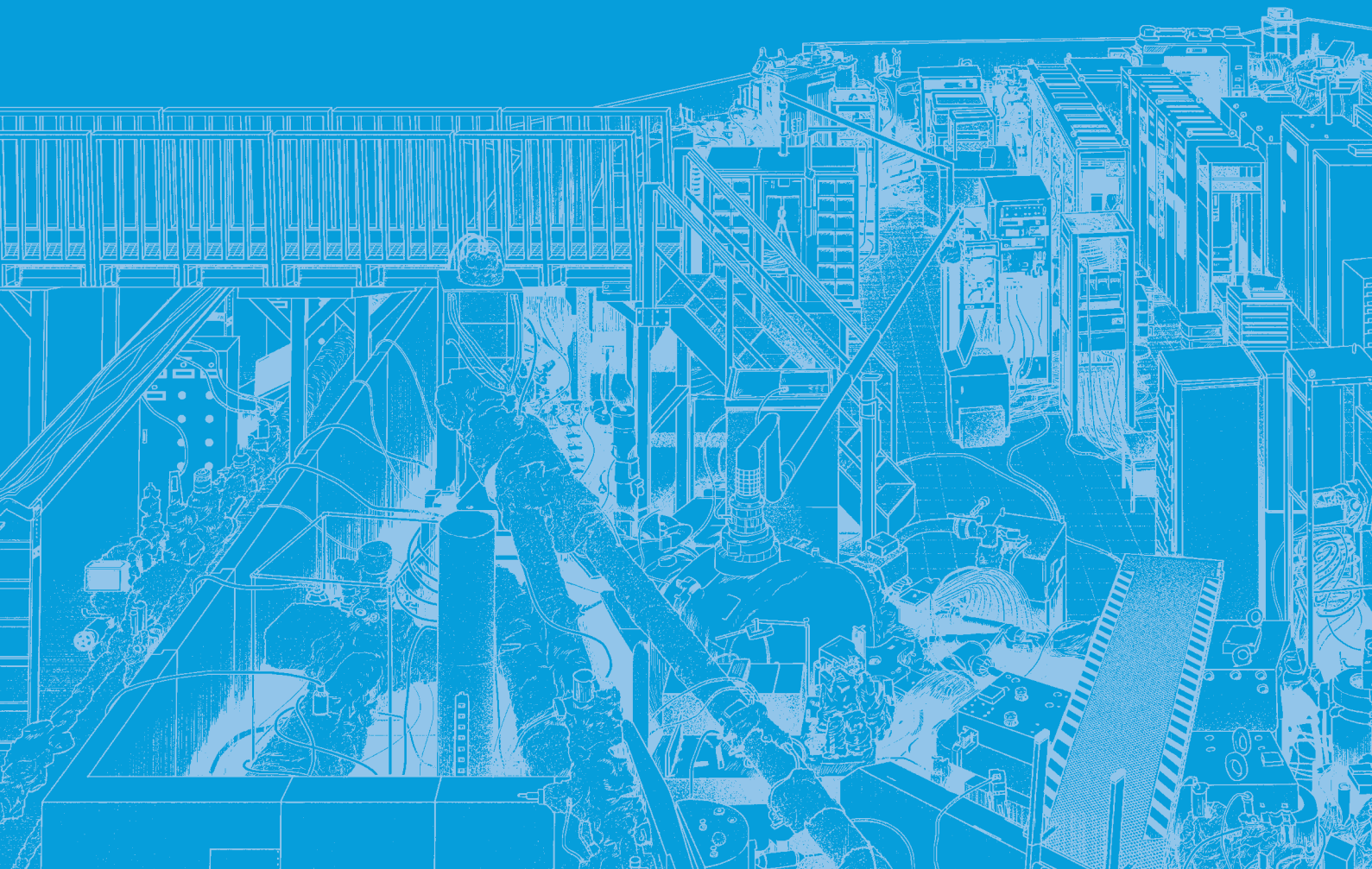
- [1] M. Katoh, K. Hayashi, *et al.*, *Nucl. Instr. Meth. A* **467** (2001) 68.
- [2] M. Katoh, M. Hosaka, *et al.*, *AIP Conf. Proc.* **705** (2004) 49
- [3] M. Adachi, H. Zen, *et al.*, *J. Phys. Conf. Ser.* **425** (2013) 042013.
- [4] M. Katoh, M. Adachi, *et al.*, *AIP Conf. Proc.* **1234** (2010) 531.
- [5] E. Salehi and M. Katoh, in *Proc. IPAC'21*, Campinas, Brazil, May 2021, 3970.
- [6] M. Borland, APS LS-287 (2000). <https://www.aps.anl.gov/Accelerator-Operations-Physics/Software>
- [7] E. Salehi, Y. Taira, *et al.*, *J. Phys. Conf. Ser.* **2420** (2023) 012062.

# UVSOR User 3



# III-2

Material Sciences





BL4U

## Observation of Charge Separation Reaction in a Ti-Mn Electrolyte for Redox Flow Batteries by STXM

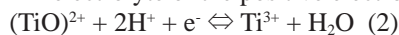
E. Hosono<sup>1,2,3</sup>, D. Asakura<sup>1,2,3</sup>, A. Ohira<sup>1,2</sup>, H. Yuzawa<sup>4</sup> and T. Ohgashi<sup>4,5</sup><sup>1</sup>Global Zero Emission Research Center, National Institute of Advanced Industrial Science (AIST), Tsukuba, Ibaraki 305-8569, Japan<sup>2</sup>Research Institute for Energy Conservation, AIST, Tsukuba, Ibaraki 305-8565, Japan<sup>3</sup>AIST-UTokyo Advanced Operando Measurement Technology Open Innovation Laboratory (Operando-OIL), Kashiwa, Chiba 277-8565, Japan<sup>4</sup>UVSOR Synchrotron Facility, Institute for Molecular Science, Okazaki 444-8585, Japan<sup>5</sup>School of Physical Sciences, The Graduate University for Advanced Studies (SOKENDAI), Okazaki 444-8585, Japan

Redox flow battery (RFB) is one of the candidates of large-scale energy storage device to utilize renewable energy. RFBs use the redox reaction of electrolytes [1], which is different from lithium-ion batteries using the redox reaction of the solid-state electrodes. To enhance the performances of RFBs such as cyclability, charge-discharge capacity, and cost, understanding the redox reaction is of particular importance. Electronic-structure analysis by synchrotron X-ray spectroscopy is essential to reveal the redox reaction.

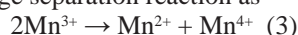
In this study we focus on Ti-Mn RFB which involves sulfuric acid aqueous solution electrolyte with Ti and Mn ions [2]. The same Ti-Mn electrolyte is used for both positive and negative electrodes. The redox reaction has been thought to be



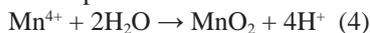
in the Ti-Mn electrolyte of the positive electrode and



in the Ti-Mn electrolyte of the negative electrode [2]. Besides, it has been reported that the  $\text{Mn}^{3+}$  ions in the charged electrolyte of the positive electrode (Eq. (1)) exhibits charge separation reaction as



during the charge process [2]. Moreover, the  $\text{Mn}^{4+}$  ions are changed to  $\text{MnO}_2$  which precipitates in the electrolyte of the positive electrode.



This reaction is less reversible that is problematic for the cyclability. To further understand those reactions in Ti-Mn RFB, we demonstrate STXM measurements of the electrolytes [3]. The high spatial resolution of STXM is helpful to clarify the formation of precipitation.

To conduct soft X-ray spectroscopic measurements of liquid samples, we have developed a special cell as shown in Fig. 1 [3]. The  $\text{Si}_3\text{N}_4$  thin-film window (100 nm) and UV curable resin bond separate liquid sample from the vacuum. A Ti-Mn electrolyte of the positive electrode was investigated by STXM at BL4U of UVSOR. The electrolyte had been charged up to 50 % of state of charge. The spatial resolution was around 100 nm.

Figure 2(a) shows the STXM image at the Mn  $L_3$ -edge. The bright area corresponds to a precipitate

whose size is approximately  $4 \mu\text{m} \times 4 \mu\text{m}$ . The Mn  $L_3$ -edge absorption spectrum of the white area (I) shown in Fig. 2(b) is mostly attributed to  $\text{Mn}^{4+}$  state as compared with spectra of reference materials [4]. The surrounding area in Fig. 2(a) corresponds to the solution whose spectrum (area (II)) is attributed to  $\text{Mn}^{2+}$  state (Fig. 2(b)). Therefore, the charge separation reaction of Eq. (3) was successfully confirmed by STXM. Similar STXM experiments of different electrolytes will be performed to obtain strategies to suppress the formation of precipitations.

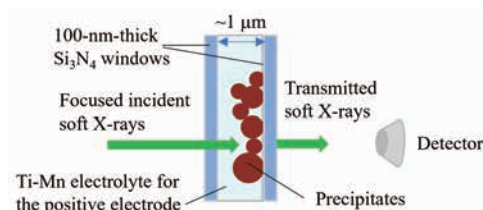


Fig. 1. A schematic image of the cell for the STXM measurements [3].

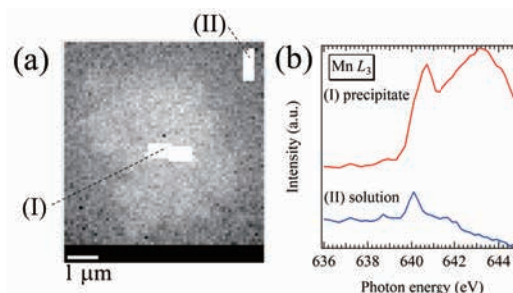


Fig. 2. (a) Mn  $L_3$ -edge STXM image and (b) spectra of selected area in the charged Ti-Mn electrolyte of the positive electrode [3].

[1] For example, T. Shigematsu, *Curr. Opin. Electrochem.* **18** (2019) 55.

[2] Y. R. Dong *et al.*, *ECS Trans.* **69** (2015) 59.

[3] D. Asakura *et al.*, *Chem. Asian J.* **18** (2023) e202201047.

[4] For example, R. Qiao *et al.*, *Nano Energy* **16** (2015) 186.

## Temperature-dependent Electronic Band Structure of Organic Molecular Semiconductor

K. Fukutani<sup>1,2</sup>, F. Nishino<sup>2</sup>, P. I. Jaseela<sup>2</sup>, D. Okaue<sup>3</sup>, K. Fukui<sup>1,3</sup>, S. Makita<sup>1</sup>,  
K. Tanaka<sup>1,2</sup> and S. Kera<sup>1,2</sup>

<sup>1</sup>Institute for Molecular Science, Okazaki 444-8585, Japan

<sup>2</sup>The Graduate University for Advanced Studies (SOKENDAI), Okazaki 444-8585, Japan

<sup>3</sup>Graduate School of Engineering Science, Osaka University, Osaka 560-8531, Japan

The organic molecular semiconductors are among the very promising materials in shaping the future of our electronic device applications in various aspects, including their physical flexibility, low cost of fabrication, high biodegradability in the environment, and the abundance of the constituent elements (mostly carbon and hydrogen) that are, in principle, inexhaustive. In fact, the organic molecular semiconductor crystals already play indispensable roles in our industry, and the continuing extensive researches have been ceaselessly improving their performances.

However, despite the success of organic molecular semiconductor devices, the knowledge of their electronic structure, one of the most fundamental building blocks for understanding and controlling their properties, is far from complete. Among such organic molecular semiconductors, single crystalline rubrene ( $C_{42}H_{28}$ ) is known to exhibit exceptionally high carrier mobility ( $40 \text{ cm}^2/\text{Vs}$  [1]) and is considered one of the most promising organic semiconductor materials for the next-generation electronics.

In this regard, we have been extensively investigating the electronic band structure of rubrene for the purposes of not only elucidating their band structures, but also for understanding the vibrational effects, arising from the intra-molecular and inter-molecular (phonon) degrees of freedom.

It is well known that many organic semiconductors exhibit a dual nature in their electronic transport properties, namely the (coherent) band transport and (polaronic) hopping transport, assisted by the electronic coupling to the aforementioned vibrations. Rubrene indeed falls into this category and its transport properties are believed to originate from the ‘mixture’ of both the band and the hopping transports. Since the respective contributions from each mechanism are believed to depend on temperature, it is clear that the direct experimental elucidations of the temperature-dependent band structure are essential for the full understanding of the origin of carrier transport in organic semiconductors.

However, there are very limited number of such direct measurements as with angle-resolved photoemission spectroscopy (ARPES) [2], most likely due to the numerous experimental difficulties, including the fabrication of large single crystals, removing of the sample charge-up effects and molecular damages caused by light irradiations.

In our experiments, we have successfully overcome these obstacles by utilizing BL7U at UVSOR and revealed the high-resolution temperature-dependent band structure of rubrene by ARPES. Figure 1 shows the band structure of rubrene observed at  $T = 300$ , 180, and 80 K along the  $\pi$ -stacking ( $\Gamma$ -Y) direction. Our data clearly shows the change in the band dispersion width as the temperature decreases. These data points towards the discernable change in the carrier effective masses, which play an important role in the determining the carrier mobilities. Furthermore, the band dispersion width appears to be ‘locked’ above  $T \sim 200$  K, which is the temperature at which the structural anomaly [3] is observed. Our researches with these experimental results are expected to provide a key insight into the transport mechanisms of organic semiconductors.

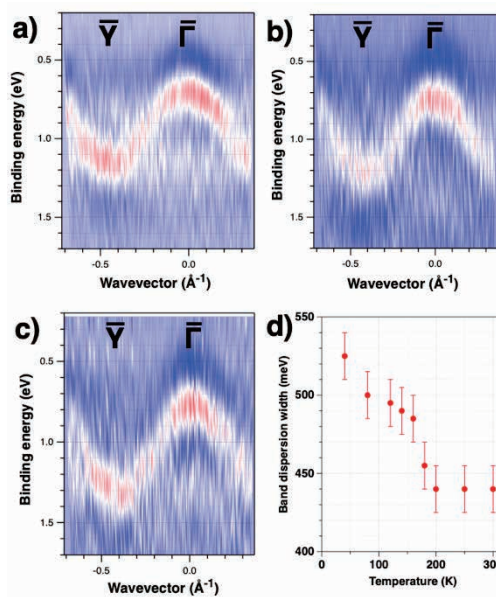


Fig. 1. Temperature-dependent ARPES data (second derivative plots) obtained along the  $\Gamma$ -Y direction at (a)  $T = 300$  K, (b) 180 K and (c) 80 K. (d) shows the band dispersion widths as a function of temperature extracted from our measurements.

[1] J. Takeya *et al.*, Appl. Phys. Lett. **90** (2007) 102120.

[2] F. Bussolotti *et al.*, Nat. Commun. **8** (2017) 173.

[3] A. van der Lee *et al.*, J. Phys. Chem. Lett. **13** (2022) 406.

BLIU

## Gamma-induced Positron Annihilation Lifetime Spectroscopy of $\beta$ -SiAlON:Eu Phosphor

M. Kitaura<sup>1</sup>, S. Watanabe<sup>2</sup>, H. Masai<sup>3</sup>, Y. Taira<sup>4,5</sup>, K. Takahashi<sup>6</sup>, T. Takeda<sup>6</sup>, N. Hirosaki<sup>6</sup>,  
M. Tansho<sup>7</sup>, K. Deguchi<sup>7</sup>, S. Ohki<sup>7</sup> and A. Ohnishi<sup>1</sup>

<sup>1</sup>Faculty of Science, Yamagata University, Yamagata 990-8560, Japan

<sup>2</sup>Institute of Innovative Research, Tokyo Institute of Technology, Tokyo 152-8550, Japan

<sup>3</sup>Department of Materials and Chemistry, National Institute of Advanced Industrial Science and Technology, Ikeda 563-8577, Japan

<sup>4</sup>UVSOR Synchrotron Facility, Institute for Molecular Science, Okazaki 444-8585, Japan

<sup>5</sup>School of Physical Sciences, The Graduate University for Advanced Studies, Okazaki 444-8585, Japan

<sup>6</sup>Research Center for Functional Materials, National Institute for Materials Science, Tsukuba, Ibaraki 305-0044, Japan

<sup>7</sup>High field NMR group, National Institute for Materials Science, Tsukuba, Ibaraki 305-0003, Japan

Eu-doped  $\beta$ -SiAlON ( $\text{Si}_{6-z}\text{Al}_z\text{O}_z\text{N}_{8-z}$ ;  $0 \leq z \leq 4.2$ ) is well-known to be a green-emitting phosphor with high brightness, narrow line width, and excellent resistance to thermal quenching [1]. These features are indispensable for the development of next-generation phosphors to fabricate advanced wide gamut backlighting device. For this purpose, it is important to investigate the nature of lattice imperfections such as vacancies, interstitials, and unexpected impurities, because they affect adversely as so-called “killer” or “trap” responsible for luminescence quenching and afterglow.

Positron annihilation lifetime spectroscopy (PALS) is a unique experimental method that can probe vacancy-type defects with negative charge. In the present study, we investigated such vacancy-type defects in  $\beta$ -SiAlON:Eu phosphors by gamma-ray induced PALS (GiPALS) experiment [2]. GiPALS experiment was performed at the BLIU of UVSOR synchrotron facility. Positron annihilation lifetimes and relative intensities were analyzed using the software LT10 [3]. Positron annihilation lifetimes at the bulk and defect states were calculated by two-component density-functional-theory (TCDFT) calculations [4,5].

Figure 1 shows the GiPALS spectrum of a  $\beta$ -SiAlON:Eu phosphor. The composition was  $\text{Si}_{5.97}\text{Al}_{0.03}\text{O}_{0.03}\text{N}_{7.97}\text{Eu}_{0.01}$ . The data were obtained at room temperature. The GiPALS spectrum reproduced three exponential decay components indicated by broken lines. The first and second component with short and middle lifetime are attributed to the positron annihilation at the bulk and defect states in  $\beta$ -SiAlON, respectively. The third component with long lifetime originates in the formation of positronium, which may arise from amorphous layer covering phosphor particles [6]. The relative intensity of the third component was negligibly small compared to other two. To estimate bulk lifetimes using experimental lifetimes and relative intensities, we adopted two-state trapping model, where the long lifetime component was not considered. The experimental bulk lifetime was estimated to be  $265 \pm 18$

ps. This value agreed with the bulk lifetime (= 271 ps) calculated for the relaxed lattice of a  $\beta$ -SiAlON ( $\text{Si}_{95}\text{Al}_1\text{O}_1\text{N}_{127}$ ). This fact indicates the validation of our experiment and calculation. On the other hand, the lifetime of the middle lifetime component was not reproduced by DFT calculations for monovacancies at silicon and nitrogen sites. We suppose that the second component originates in defect complexes of multiple vacancies. The origin of the second component is now in investigation.

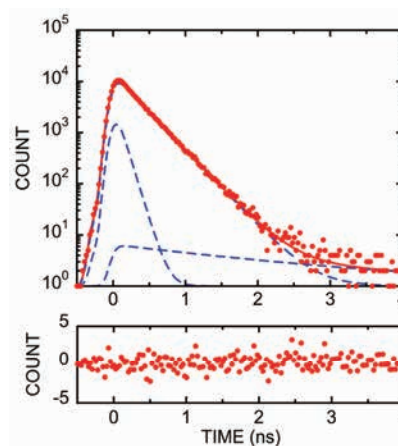


Fig. 1. (Upper) GiPALS spectrum of a  $\beta$ -SiAlON:Eu phosphor. (Lower) Residual between the results of experiment and curve fit analysis.

- [1] X. Zhang *et al.* Chem. Mater. **29** (2017) 6781.
- [2] Y. Taira *et al.*, Rev. Sci. Instrum. **84** (2013) 053305.
- [3] D. Giebal and J. Kansy, Phys. Procedia **35** (2012) 122.
- [4] P. Giannozzi *et al.* J. Phys.: Condens. Matter **21** (2009) 395502.
- [5] X. Gonze *et al.*, Comput. Phys. Commun. **248** (2020) 107042.
- [6] N. Hirosaki *et al.*, Appl. Phys. Lett. **86** (2005) 211905.

## In-situ Measurement of Defects Dynamics in Stress Applied Bulk Iron by Means of Gamma Ray Induced Positron Annihilation Spectroscopy

F. Hori<sup>1</sup>, S. Araki<sup>1</sup>, S. Hirayama<sup>1</sup> and Y. Taira<sup>2</sup>

<sup>1</sup>Dept. of Quantum and Radiation Eng., Osaka Metropolitan University, Sakai, Osaka 599-8570, Japan

<sup>2</sup>UVSOR Synchrotron Facility, Institute for Molecular Science, Okazaki 444-8585, Japan

The behavior of hydrogen atoms is attracting attention in a wide range of research fields such as high-strength structural materials and hydrogen storage materials. In such materials, hydrogen atom diffuses and has various interaction with defects, consequently it makes serious characteristic change. In particular, in the corrosion of metallic materials, it is known that the presence or absence of lattice defects in the material affects mechanical and physical properties of materials. On the point of view, positron annihilation techniques are useful to detect and estimate the behavior of vacancy type micro defects in materials. However, in order to investigate the dynamics of the internal defect behavior without destructing materials, more than mega electron volts positron is needed. Recently, the development of high-energy Gamma-ray induced positron spectroscopy (GiPS) has developed at some photon factories. Especially, direct incidence of high-energy gamma rays with the energy more than 1.022 MeV into the target material produces positrons in it and annihilated there. High-energy gamma rays from laser Compton scattering at synchrotron radiation facilities enables positron experiments to detect defects in bulk materials without sample destruction. In this study, in-situ positron annihilation lifetime measurement while applying stress to a bulk specimen have performed on the beam line BL1U at UVSOR.

Positron lifetime measurement has performed on pure iron bulk specimens processed into JIS standard tensile specimens, irradiated with 8 MeV electron, and irradiated with electron and then hydrogen introduced. Electron irradiation have done by linear accelerator at Kyoto University Reactor Research. Hydrogen was introduced into the sample by immersion in a 20% ammonium thiocyanate solution at 318 K for 14 days.

Figure 1 shows the results of the stress change after applying a stress of 88 MPa, corresponding to 90% of the yield stress, for all samples. It is clear that stress relaxation is suppressed by the presence of hydrogen and vacancies. In addition, the sample without defects relaxes greatly in a short period of time and almost no change can be confirmed after that, but the sample with vacancy and hydrogen shows a small amount of relaxation, but it relaxes slowly over a long period of time. Figure 2 shows the change of positron lifetimes and their relative intensities during relaxation after initial stress applied. The long lifetime of positron  $\tau_2$  increase to more than 170 ps after stress application in all samples, indicating that vacancies were formed even at stresses below the yield point. Also,  $\tau_2$  for

hydrogen introduced sample slightly higher than that of pure Fe. This indicates the formation of vacancy clusters, such as di-vacancy, and the presence of hydrogen may facilitate the aggregation of vacancies. However, this is considered that the  $\tau_2$  slightly decreases taking long time afterwards indicates that these initially formed di-vacancies dissociate. Also, it found that the relative intensity  $I_2$  corresponds to the defect concentration of  $\tau_2$  component, and the concentration change after stress addition also shows a slight decrease with relaxation time.

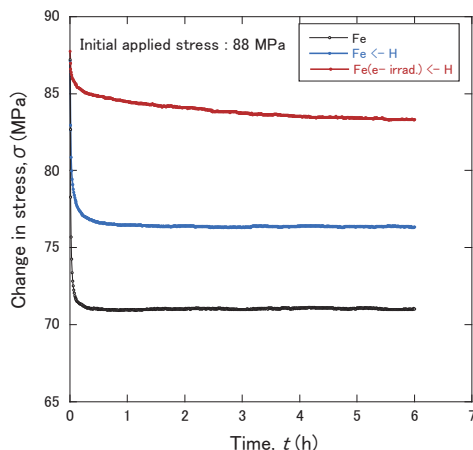


Fig. 1. Stress change after initial stress applied.

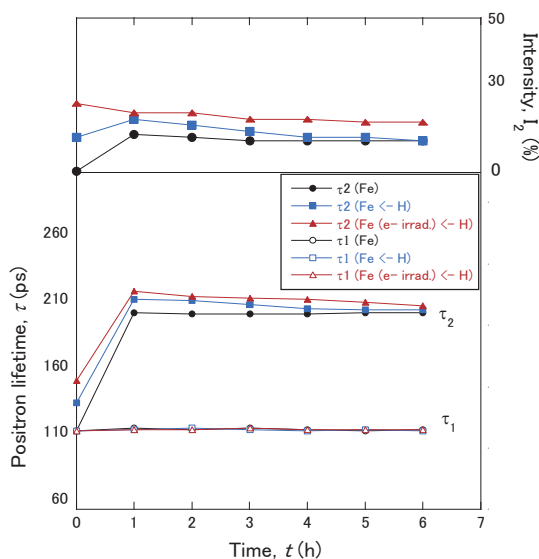


Fig. 2. Positron lifetimes and relative intensity  $I_2$  change after initial stress applied.

BL1U

## Gamma-ray Induced Positron Annihilation Lifetime Measurement of CeO<sub>2</sub> Catalyst Placed in a Quartz Tube

S. Dohshi<sup>1</sup>, K. Maeda<sup>1</sup>, Y. Taira<sup>2</sup> and T. Hirade<sup>3</sup>

<sup>1</sup>Osaka Research Institute of Industrial Science and Technology

2-7-1, Ayumino, Izumi, Osaka 594-1157, Japan

<sup>2</sup>UVSOR Synchrotron Facility, Institute for Molecular Science, Okazaki 444-8585, Japan

<sup>3</sup>Japan Atomic Energy Agency, Ibaraki 319-1195, Japan

In situ observation of the catalyst during catalytic reactions is very important for elucidating the reaction mechanism and preparing the highly active catalyst. Recently, it has been reported that the presence of oxygen vacancies in CeO<sub>2</sub> catalysts affect their catalytic activity [1]. Therefore, it becomes more and more important to analyze the behavior of oxygen vacancies of CeO<sub>2</sub> with high sensitivity during catalytic reactions.

Positron annihilation lifetime measurement is a powerful tool for the detection of lattice defects such as oxygen vacancies with high sensitivity. However, there have been no examples of positron annihilation lifetime measurements with controlling gas atmosphere and temperature. Typically, the catalytic reaction is performed in a quartz or alumina tube with controlling gas atmosphere and temperature. When gamma-ray induced positron annihilation lifetime measurement is performed under the same conditions as the catalytic reaction, positrons generated in the sample can be annihilated not only in the sample but also in the quartz tube, because of the presence of the quartz tube between the sample and the detector.

In this study, the effect of quartz tube on the positron annihilation lifetime of CeO<sub>2</sub> was investigated.

The pellet sample with 20 mm in diameter and 10 mm in thickness were prepared using CeO<sub>2</sub> nanoparticles with a primary particle size of ca. 2 nm.

We have set up a gamma-ray spectroscopy system at the laser-Compton scattering (LCS) beamline of BL1U at UVSOR-III [2], and measured the lifetime of the

annihilation gamma-rays at room temperature using BaF<sub>2</sub> scintillation detector. We used the software Lifetime9 (LT9) to analyze the spectra.

Table 1 shows the positron annihilation lifetimes and relative intensities of CeO<sub>2</sub> catalyst with various measurement conditions. In case of the measurement without quartz tube, the positron annihilation lifetime was composed of two components ( $\tau_1$  and  $\tau_2$ ). These lifetimes were attributed to the positron annihilation in CeO<sub>2</sub> bulk and surface. On the other hand, in case of the measurement with quartz tube, the positron annihilation lifetime was composed of three components ( $\tau_1$ ,  $\tau_2$  and  $\tau_3$ ). The longest lifetime component ( $\tau_3$ ) can be attributed to the annihilation in the quartz tube, with a relative intensity ( $I_3$ ) of about 1%, regardless of the gamma-ray beam diameter. Furthermore, the lifetimes and relative intensities of the other two components derived from CeO<sub>2</sub> ( $\tau_1$  and  $\tau_2$ ) did not change significantly when measured using quartz tubes. These results suggest that positron annihilation lifetime measurements can be performed in a quartz tube while controlling the gas atmosphere and temperature.

Next fiscal year, gamma-ray induced positron annihilation lifetime measurement will be performed with controlling the gas atmosphere and temperature to clarify the behavior of oxygen vacancies in CeO<sub>2</sub>.

[1] X. Liu *et al.*, J. Am. Chem. Soc. **131** (2009) 3140.

[2] Y. Taira *et al.*, Rev. Sci. Instr. **84** (2013) 053305.

Table 1 Positron annihilation lifetimes and relative intensities of CeO<sub>2</sub> catalyst with various measurement conditions.

measurement conditions	$\tau_1$ (ps)	$I_1$ (%)	$\tau_2$ (ps)	$I_2$ (%)	$\tau_3$ (ps)	$I_3$ (%)
without quartz tube	155±17	6.5±1.0	388.2±1.5	93.5±1.0	-	-
with quartz tube (γ-ray beam: 2 mm)	159±42	3.8±1.1	367.8±1.9	95.0±1.1	1386±46	1.2±0.1
with quartz tube (γ-ray beam: 3 mm)	142±44	4.2±1.7	362.5±4.0	94.4±1.7	1290±120	1.4±0.3

## Formation of the stress-induced Vacancies in Iron by *in situ* Positron Annihilation Lifetime Spectroscopy

M. Fujinami<sup>1</sup>, R. Awaji<sup>1</sup>, A. Yabuuchi<sup>2</sup>, T. Hirade<sup>3</sup>, N. Oshima<sup>4</sup> and Y. Taira<sup>5</sup>

<sup>1</sup>Department of Applied Chemistry and Biotechnology, Chiba University, Chiba 263-8522, Japan

<sup>2</sup>Institute for Integrated Radiation and Nuclear Science, Kyoto University, Kumatori 590-0494, Japan

<sup>3</sup>Nuclear Science and Engineering Center, Japan Atomic Energy Agency, Tokai 319-1195, Japan

<sup>4</sup>National Institute of Advanced Industrial Science and Technology, Tsukuba 305-8568, Japan

<sup>5</sup>UVSOR Synchrotron Facility, Institute for Molecular Science, Okazaki 444-8585, Japan

Investigating the formation process of atomic vacancies by mutual cutting of dislocations is essential to understand the role of vacancies in the mechanical properties of metals. However, such vacancies have yet to be directly observed. The reason is that vacancies have a significant diffusion coefficient and are unstable.

Positron annihilation lifetime spectroscopy is the only method that allows direct observation of atomic vacancies. However, the conventional method using a radioactive isotope such as <sup>22</sup>Na as a positron source is difficult to measure *in situ* under various conditions due to the risk of radioactive contamination. If it becomes possible to measure the vacancies while applying stress, it will be possible to detect transient vacancies, which leads to the first detection of transient vacancy formation. It also provides essential fundamental knowledge for discussing the behavior of vacancy stabilization by impurities, including hydrogen. In this study, we attempted to directly detect vacancies formed in pure iron during tensile deformation *in situ* using the BLIU beamline, where positrons are created in the sample directly.

A 3-mm-thick tensile sample was mounted on a small tensile tester. The sample was subjected to tensile deformation up to a nominal strain of over 7% with a strain rate of  $2.2 \times 10^{-5} \text{ s}^{-1}$ . Ten samples were measured under the same tensile deformation conditions to obtain enough counts of positron lifetime spectra.

Figure 1 shows the positron lifetime spectra of pure iron before and after tensile deformation. A longer lifetime component is observed in the positron lifetime spectrum when the sample is elongated to a nominal strain of  $\sim 7.3\%$ . Figure 2 shows the change in mean positron lifetime during tensile deformation. The mean positron lifetime increases with increasing nominal strain. However, the change in mean positron lifetime obtained in this study differs significantly from the trend reported in an earlier study using the conventional method [1]. One possible reason for this difference is the difference between the conventional method, which observes a depth of about 0.1 mm from the sample surface, and this method, which observes the entire sample, including the deeper region. Further detailed analysis is currently underway.

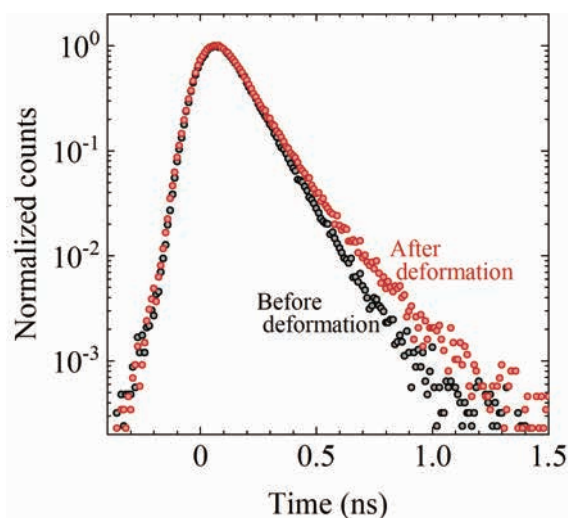


Fig. 1. Positron lifetime spectra of pure iron before and after tensile deformation with a nominal strain of  $\sim 7.3\%$ .

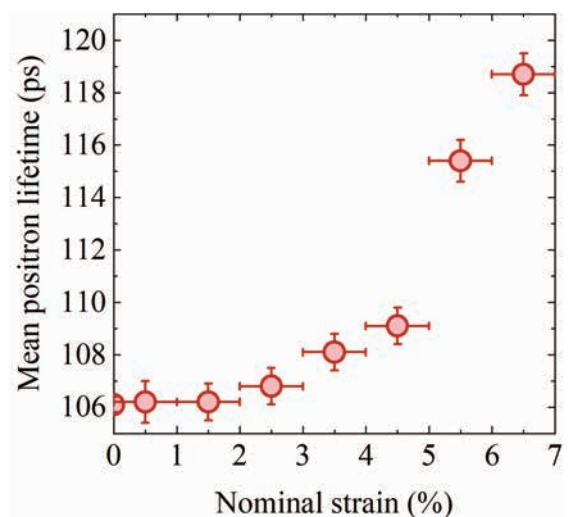


Fig. 2. Change in mean positron lifetime during tensile deformation.

[1] B. Somieski *et al.*, NDT & E Int. **27** (1994) 235.

BLIU

## In-situ Measurements of Vacancies Formed in Pure Iron by Electrolytic Hydrogen Charging using gamma-ray-induced Positron Annihilation Lifetime Spectroscopy

A. Yabuuchi<sup>1</sup>, T. Hirade<sup>2</sup>, M. Fujinami<sup>3</sup>, R. Awaji<sup>3</sup>, N. Oshima<sup>4</sup>, K. Takai<sup>5</sup> and Y. Taira<sup>6</sup>

<sup>1</sup>*Institute for Integrated Radiation and Nuclear Science, Kyoto University, Kumatori 590-0494, Japan*

<sup>2</sup>*Nuclear Science and Engineering Center, Japan Atomic Energy Agency, Tokai 319-1195, Japan*

<sup>3</sup>*Department of Applied Chemistry and Biotechnology, Chiba University, Chiba 263-8522, Japan*

<sup>4</sup>*National Institute of Advanced Industrial Science and Technology, Tsukuba 305-8568, Japan*

<sup>5</sup>*Department of Engineering and Applied Sciences, Sophia University, Tokyo 102-8554, Japan*

<sup>6</sup>*UVSOR Synchrotron Facility, Institute for Molecular Science, Okazaki 444-8585, Japan*

Recently, a fracture mechanism involving vacancies has been proposed as a new model to explain the hydrogen embrittlement of steels [1]. Therefore, many studies on hydrogen embrittlement have been performed using positron annihilation spectroscopy, a vacancy detection technique. However, the conventional positron annihilation technique is challenging to measure during hydrogen dosing in a liquid. The high-energy pulsed gamma-rays obtained at UVSOR make it possible to produce positrons directly inside a sample placed in a fluid and perform positron annihilation measurements. In this study, we attempted in-situ positron annihilation lifetime measurements during hydrogen charging in liquid to investigate hydrogen-induced vacancies in pure iron.

Six well-annealed pure iron plates with a purity of 99.99% and a thickness of 2 mm were arranged in the beam axis direction with a gap of 2 mm between them. This measurement geometry was chosen to achieve sufficient hydrogen introduction throughout the sample and still obtain a sufficient count rate of annihilation gamma-rays. For electrolytic hydrogen charging, the sample was immersed in 0.1 N NaOH solution containing 5 g/L  $\text{NH}_4\text{SCN}$ . A pulsed gamma-ray beam with a maximum energy of 6.6 MeV was injected to measure the positron lifetime.

Figure 1 shows the positron lifetime spectra of pure iron plate samples placed in air and the electrolyte solution. The spectrum obtained from the in-air measurement shows almost no lifetime component of positrons annihilated outside the sample. In contrast, a longer lifetime component originating from positron annihilation in the electrolyte solution appears in the spectrum obtained from the sample placed in the electrolyte solution. The change in positron lifetime in iron during hydrogen charging was investigated by analyzing such spectra. However, it was concluded that eliminating the electrolyte solution component from the spectra is essential for a detailed analysis of the iron sample components.

Figure 2 shows the calculated positron flux distribution when a gamma-ray beam is injected into an iron plate in water. Positrons are mainly produced in iron, which has a high specific gravity, but they are also produced to some extent in water. In addition, some of

the positrons produced in iron are emitted out of iron and annihilated in water. Therefore, we consider improving the measurement geometry for the next beamtime.

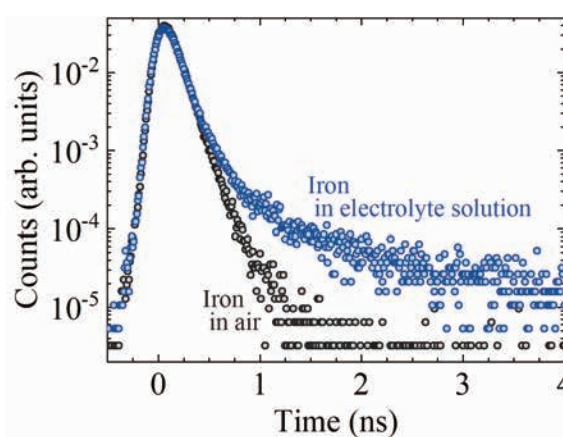


Fig. 1. Positron lifetime spectra of well-annealed pure iron measured in air or an electrolyte solution.

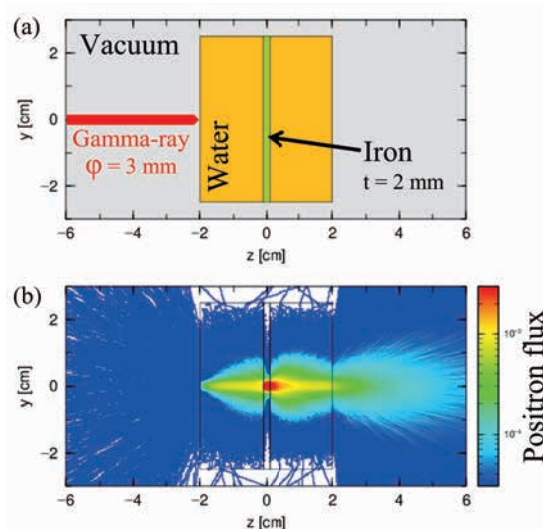


Fig. 2. (a) Geometry of the simulation model. (b) Calculated positron flux distribution.

[1] M. Nagumo, Mater. Sci. Technol. **20** (2004) 940.

## Formation of Catalytically Active Mo<sub>2</sub>C Species on H-MFI for Methane Aromatization Studied by Mo L<sub>III</sub>-edge XANES

K. Kuramochi<sup>1</sup>, Y. Sonobe<sup>2</sup>, H. Shimura<sup>2</sup>, Y. Kinoshiro<sup>2</sup>, R. Yamazaki<sup>1</sup>, Y. Uchimura<sup>2</sup> and H. Aritani<sup>2</sup>

<sup>1</sup>Advanced Science Research Laboratory, Saitama Institute of Technology, Fukaya 369-0293 Japan

<sup>2</sup>Graduate School of Engineering, Saitama Institute of Technology, Fukaya 369-0293 Japan

As a typical GTL (Gas-To-Liquid) catalyst, supported molybdenum on H-MFI zeolites show catalytically high and selective activity to convert methane to benzene directly. Although the GTL process is extremely innovative, it is an important subject to suppress deactivation as well as increase the yield of aromatics. For the Mo/H-MFI catalysts, definite deactivation due to coke deposition has been a major problem for enhancement of MTB reactivity. A cause of the deactivation strongly depends on both coke deposition onto strong acid sites over H-MFI and structural deactivation of carbonized Mo species. One of the most important subjects for catalytically high and durable activity is the elucidation of active Mo carbide (MoC<sub>x</sub>) species and their structural stability. In this study, Mo L<sub>III</sub>-edge XANES is applied to characterize the active MoC<sub>x</sub> species on Mo/H-MFI during the methane aromatization.[1] The change of active Mo species during the reaction was investigated as a time course of XANES spectra.

Mo/H-MFI (Si/Al<sub>2</sub>=23-30 in H-MFI, 5.0 wt% as MoO<sub>3</sub>-loading) catalysts were prepared as described in the previous paper.[2] The methane dehydroaromatization reactivity was evaluated at 1023 K. Mo L<sub>III</sub>-edge XANES spectra were obtained in BL2A of UVSOR-IMS in a total-electron yield mode using the InSb double-crystal monochromator. A REX-2000 (Rigaku) software was used for normalization of each XANES spectra. The edge energy was obtained from the maximum of the first derivative of XANES.

Figure 1 shows the L<sub>III</sub>-edge XANES of reference Mo compounds. The energy of the absorption edge becomes higher according to the higher oxidation state of molybdenum. For Mo-carbides, the edge energy in α-Mo<sub>2</sub>C (fcc: 2526.55 eV) is significantly larger than that in β-Mo<sub>2</sub>C (orthorhombic: 2524.45 eV). Since the difference of energy value should be due to the coordination number in Mo-C shells, the edge energy of XANES can be applied to characterize the local structure of Mo<sub>2</sub>C species.

For evaluation of catalytic activity for methane aromatization at 973 K, it is concluded that Mo/H-MFI(Si/Al<sub>2</sub>=30) shows the maximum benzene yield in 30 minutes as an initial streaming range. On the Mo/H-MFI catalysts, time course of L-edge XANES spectra are shown in Figure 2. Before the reaction (at 0 min.), the Mo/H-MFI catalyst has been pre-reduced with CO(2%)-He at 1023 K. At this time, Mo species have already reduced to form Mo<sup>4+</sup> (due to MoO<sub>2</sub>) and/or Mo<sup>2+</sup> (α-Mo<sub>2</sub>C). The edge of XANES shifts to the low

energy side after the reaction for 10 minutes, indicating that further reduction of Mo proceeds to form β-Mo<sub>2</sub>C like species with low crystallinity. Since the edge energy is kept on after 90 minutes (in the maximum activity) is exhibited, β-Mo<sub>2</sub>C like species are possibly act as a highly active one for methane dehydrogenation. As the reaction time progresses, only a slight shift of the edge to the lower energy side can be seen. Therefore, it is presumed that the deactivation of reactivity after 30 minutes is caused mainly by carbon deposition on H-MFI support rather than excess reduction of Mo species.

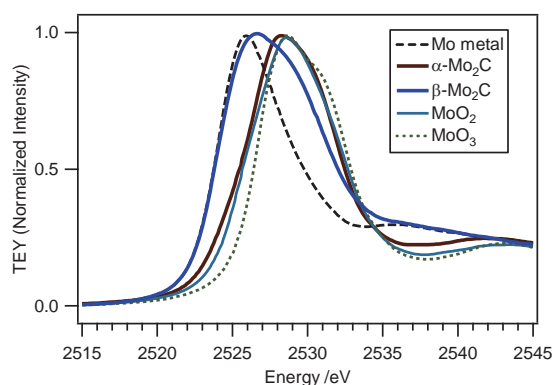


Fig. 1. Mo L<sub>III</sub>-edge XANES spectra of reference Mo compounds.

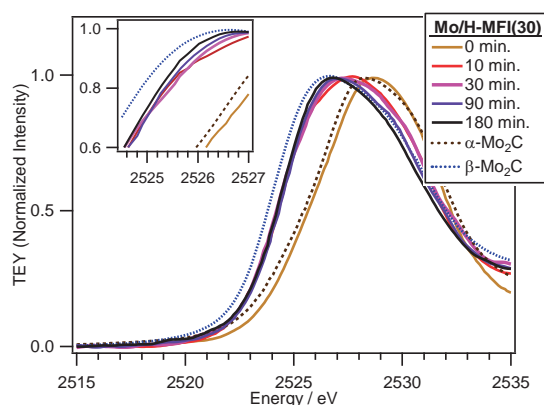


Fig. 2. Mo L<sub>III</sub>-edge XANES spectra of Mo/H-MFI (Si/Al<sub>2</sub>=30) catalyst after the reaction for each time (0 – 180 minutes).

[1] H. Aritani *et al.*, *UVSOR Activity Report 2021* **49** (2022) 58.

[2] H. Aritani *et al.*, *J. Environm. Sci.*, **21** (2009) 736.

BL2A

## Local Environment of Dopants in (M, Nb) co-doped TiO<sub>2</sub> (M=Fe, Ni)

H. Murata<sup>1,2</sup>, T. Nishio<sup>2</sup>, Y. Nagatomo<sup>2</sup> and A. Nakahira<sup>1,2</sup>

<sup>1</sup>Department of Materials Science, Osaka Metropolitan University, Sakai 599-8531, Japan

<sup>2</sup>Department of Materials Science, Osaka Prefecture University, Sakai 599-8531, Japan

Titanium dioxide (TiO<sub>2</sub>) is a typical fine ceramic material used in a wide range of applications, such as photocatalysts, pigments and transparent conductors. TiO<sub>2</sub> has several polymorphs with wide band gaps and absorb only UV light. Numerous studies have been carried out on cation and anion doping into TiO<sub>2</sub> to utilize visible light. However, most of them induce weak visible light absorption due to their small solid solubility limits. Co-doping into TiO<sub>2</sub> has been investigated [1] and combinations of dopants such as (Fe, Nb) and (Ni, Nb) significantly increase solid solubility limits [2-4]. However, local environments of the co-doped dopants in TiO<sub>2</sub> and their light absorption mechanism have not been clarified. In this study, local environments and electronic structures of (Fe, Nb) and (Ni, Nb) co-doped TiO<sub>2</sub> were investigated.

(Fe, Nb) and (Ni, Nb) co-doped TiO<sub>2</sub> samples were prepared by a conventional solid-state reaction method using TiO<sub>2</sub>, Fe<sub>2</sub>O<sub>3</sub>, NiO and Nb<sub>2</sub>O<sub>5</sub> as starting materials. The starting materials were ground and mixed by an alumina mortar and pestle. They were calcined in an alumina crucible at 1200 °C for 6 h. The samples were ground and mixed by the mortar and pestle again. Then, they were calcined in an alumina crucible at 1200 °C for 6 h.

Samples were characterized using X-ray diffraction (XRD), UV-Vis, <sup>57</sup>Fe Mössbauer spectroscopy, and X-ray absorption near edge structure (XANES). Ni-L<sub>3</sub> and Nb-L<sub>3</sub> XANES spectra were collected using the total electron yield method with a sample current at BL2A in UVSOR (Okazaki, Japan). The X-ray beam was monochromated using beryl and InSb double crystals for Ni-L<sub>3</sub> and Nb-L<sub>3</sub>, respectively. NiO and Nb<sub>2</sub>O<sub>5</sub> was used as reference materials.

XRD patterns of the samples can be assigned to rutile-type TiO<sub>2</sub> with peak shifts. They confirmed that (Fe, Nb) and (Ni, Nb) co-doped TiO<sub>2</sub> has large solubility limit over 50 cation%, where the dopants ratios are 1:1 and 1:2 for (Fe, Nb) and (Ni, Nb), respectively. Note that their lattice parameters increased linearly with the concentration of dopants.

<sup>57</sup>Fe Mössbauer spectroscopy and Ni-L<sub>3</sub> XANES show that Fe and Ni in the samples are high-spin Fe<sup>3+</sup> and Ni<sup>2+</sup> in octahedral coordination, respectively. Nb-L<sub>3</sub> XANES of the samples have typical features of Nb<sup>5+</sup> in octahedral coordination [5], as shown in fig. 1. These results indicate that large solid solubility limit of the co-doped TiO<sub>2</sub> is due to charge compensation between dopants.

Both of the co-doped TiO<sub>2</sub> samples exhibited visible light absorption. Based on the spin and valence states of dopants, the visible light absorptions are induced at different origins. The (Fe, Nb) co-doped TiO<sub>2</sub> has a narrowed band gap and weak spin forbidden d-d transitions. On the other hand, the (Ni, Nb) co-doped TiO<sub>2</sub> has a strong spin-allowed d-d transition. These different origins of visible light absorption fundamentally influence behaviors of excited carriers and chromaticity. These results lead to a comprehensive understanding of the visible light applications such as photocatalyst and pigments.

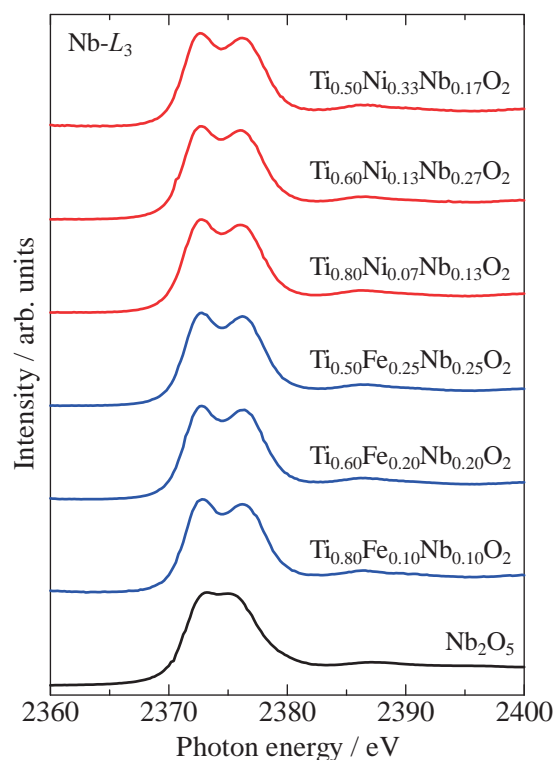


Fig. 1. Nb-L<sub>3</sub> XANES spectra of (Fe, Nb) and (Ni, Nb) co-doped TiO<sub>2</sub>.

[1] A. S. M. Nur *et al.*, J. Water Process. Eng. **47** (2022) 102728.

[2] M. A. Tena *et al.*, Mater. Res. Bull. **27** (1992) 1301.

[3] B. Balzer and H. Langbein, Cryst. Res. Technol. **31** (1996) 93.

[4] M. Wenger and T. Armbruster, Neues Jahrb. Mineral. Monatsh. **5** (1993) 225.

[5] Y. Kubouchi *et al.*, X-ray Spectrom. **41** (2012) 259.

## XAFS Study of $\text{MgAl}_2\text{O}_4$ - $\text{MgGa}_2\text{O}_4$ Solid Solutions

S. Yoshioka<sup>1</sup>, K. Yasuda<sup>1</sup>, E. Kobayashi<sup>2</sup> and K. Okudaira<sup>3</sup>

<sup>1</sup>*Department of Applied Quantum Physics and Nuclear Engineering, Kyushu University, Fukuoka, 819-0395, Japan*

<sup>2</sup>*Kyushu Synchrotron Light Research Center, Saga 841-0005, Japan*

<sup>3</sup>*Graduate school of Advanced Integration Science, Chiba University, Chiba, 263-8522, Japan*

Spinel oxides with the general formula  $\text{AB}_2\text{O}_4$  can be formed with various kinds of divalent A and trivalent B cations. Owing to their unique mechanical, electronic, and magnetic properties, the spinel oxides have gained considerable attention not only from the fundamental research fields but also from the industrial application point of view. Some spinel compounds accommodate a large degree of cationic disorder. The cationic disordering naturally affects the structural properties of the spinels. For example, magnesium aluminate ( $\text{MgAl}_2\text{O}_4$ ) and magnesium gallate ( $\text{MgGa}_2\text{O}_4$ ) are generally known as normal and inverse spinel structures, respectively. However, their inversion degrees for synthetic specimens were also reported to be fluctuating between 0 and 1, respectively, due to the cationic disordering. Recently, the structure of  $\text{MgAl}_{2-x}\text{Ga}_x\text{O}_4$  was reported using first principles calculations and X-ray diffraction [1]. X-ray absorption spectroscopy (XAS) is a powerful structure characterization method that uses an X-ray probe to reveal local atomic coordination and electronic structures. In this study, we focus on the local structures in  $\text{MgAl}_2\text{O}_4$  -  $\text{MgGa}_2\text{O}_4$  solid solutions, particularly cationic-disordered structures.

The polycrystalline samples of  $\text{MgAl}_{2-x}\text{Ga}_x\text{O}_4$  ( $x = 0, 0.5, 1.0, 1.5,$  and  $2.0$ ) were synthesized by a solid-state reaction. They were sintered in air at  $1500^\circ\text{C}$  for 10 h followed by furnace. Mg and Al  $K$ -edge XANES measurements were performed on BL2A beamline at UVSOR Synchrotron Facility, Okazaki, Japan, using the partial fluorescence yield method. A  $\text{KTiOPO}_4$  double-crystal monochromator gives Mg and Al  $K$ -absorption edges in the energy regions 1290–1340 eV and 1540–1610 eV, respectively. The measurements of Mg and Al  $K$ -edge XANES spectra were carried out in vacuum at a pressure and temperature of  $1 \times 10^{-4}$  Pa and  $20^\circ\text{C}$ , respectively. Fluorescence X-rays of Mg  $K_\alpha$  and Al  $K_\alpha$  were collected utilizing an energy-dispersible silicon drift detector.

The Mg  $K$ -edge XANES spectra for  $\text{MgAl}_2\text{O}_4$  and  $\text{MgGa}_2\text{O}_4$  are shown in Fig. 1. The intensity of each spectrum was normalized to a value of 1 at the photon

energy of 1330 eV after the removal of the background intensity. The Mg  $K$ -edge XANES of  $\text{MgGa}_2\text{O}_4$  were clearly different from that of  $\text{MgAl}_2\text{O}_4$ . The spectrum difference between  $\text{MgAl}_2\text{O}_4$  and  $\text{MgGa}_2\text{O}_4$  suggests local structure difference between two specimens. Previous study using diffraction technique reported octahedral location of Mg in  $\text{MgGa}_2\text{O}_4$  as an inverse spinel, whereas tetrahedral location of Mg in normal spinel of  $\text{MgAl}_2\text{O}_4$ . Detailed analyses on the local environment of Mg and Al in the  $\text{MgAl}_{2-x}\text{Ga}_x\text{O}_4$  are in progress by combined use of the XANES and the first principles band structure calculations.

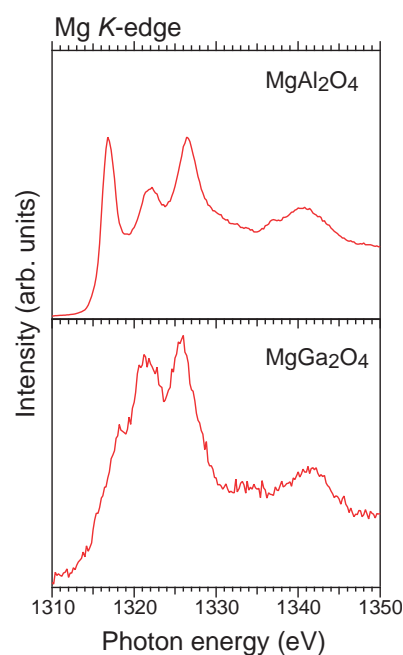


Fig. 1. Mg  $K$ -edge XANES spectra of  $\text{MgAl}_2\text{O}_4$  and  $\text{MgGa}_2\text{O}_4$

[1] G. Pilania, V. Koczekski, J. A. Valdez, C. R. Keller and B. P. Uberuaga, *Commun. Mater.* **1**, Article number: 84 (2020).

BL2A

## NEXAFS Spectroscopy of Battery Materials Using a Transfer Vessel

A. Inoishi<sup>1</sup> and E. Kobayashi<sup>2</sup>

<sup>1</sup>*Institute for Materials Chemistry and Engineering, Kyushu University  
6-1 Kasuga-koen, Kasuga-Shi 816-8580, Japan*

<sup>2</sup>*Kyushu Synchrotron Light Research Center, 8-7 Yayoigaoka, Tosu, Saga 841-0005, Japan*

To increase capacity in all solid-state lithium-ion batteries, it is better to remove as much of the solid electrolyte and conductive carbon contained in the electrode as possible. Recently, we reported the all-solid-state lithium batteries using electrochemical lithium insertion in some anode materials. We reported  $\text{Mg}(\text{BH}_4)_2$  and  $\text{MgH}_2$  anode materials.[1,2] In these conversion-type electrodes,  $\text{LiBH}_4$  and  $\text{LiH}$  are generated as lithium salt during lithiation and ionic conduction paths are formed during the electrochemical reaction. Solid electrolyte is not required in these electrode mixture and reasonable battery performances were observed with the electrode composed of active material ( $\text{Mg}(\text{BH}_4)_2$  or  $\text{MgH}_2$ ) and acetylene black, without electrolyte powder. We call this new concept as “*in-situ* forming of solid electrolyte”. Recently, we newly focused on  $\text{MgCl}_2$  as a new anode active material. For the case of  $\text{MgCl}_2$ , it is assumed that  $\text{LiCl}$  is formed after lithiation as “*in-situ* formed electrolyte”. In this study, we evaluated the mechanism of electrochemical reaction of  $\text{MgCl}_2$  anode by X-ray adsorption spectroscopy.

Composite powder containing  $\text{MgCl}_2$  was prepared by mechanical milling of  $\text{MgCl}_2$  with acetylene black (AB) in a 70:30 mass ratio at 400 rpm for 30 min. Each all-solid-state cell ( $\text{Li}/\text{LiBH}_4/\text{MgCl}_2$ , AB) was assembled using an insulating cell die (Poly Ether Ether Ketone) sandwiched between two stainless steel rods under Ar. Discharge/charge measurements were conducted in a vacuum at a current density of  $0.05 \text{ mAcm}^{-2}$  and at  $120^\circ\text{C}$ . *Ex-situ* X-ray absorption spectroscopy (XAS) data for Mg K-edge and Cl K-edge were acquired at the BL2A of UVSOR Synchrotron Facility, Institute for Molecular Science. For the transportation to XAS, a sample transfer vessel was used.[3,4]

Initial lithiation capacity and delithiation capacity of the  $\text{Li}/\text{LiBH}_4/\text{MgCl}_2$  cell were  $465 \text{ mAhg}^{-1}$  and  $321 \text{ mAhg}^{-1}$ , respectively. The initial lithiation capacity was 82 % of the theoretical capacity of  $\text{MgCl}_2$ . In this electrode, solid electrolyte is not required in the electrode mixture. This indicates that lithium conduction path is formed from  $\text{MgCl}_2$  by the electrochemical reaction. Mg K-edge X-ray adsorption spectroscopy for the  $\text{MgCl}_2$  electrode before and after the discharge-charge were measured.  $\text{MgCl}_2$  showed sharp peaks at 1310 eV. “Initial state” just after cell fabrication was similar spectrum with  $\text{MgCl}_2$  chemical,

indicating that “initial state” is still  $\text{MgCl}_2$ . After the initial lithiation, adsorption at 1302 eV was newly observed. This is also observed in Mg metal.[5] Therefore,  $\text{MgCl}_2$  is reduced to form Mg metal during lithiation process. After the following delithiation, similar spectrum with initial state was observed, indicating that  $\text{MgCl}_2$  is reversibly formed after the delithiation process. Cl K-edge X-ray adsorption spectroscopy for the  $\text{MgCl}_2$  electrode before and after the discharge-charge were also measured. Initial state and delithiated state were similar spectra with that of  $\text{MgCl}_2$ . After lithiation, the main intense peak was slightly shifted to higher energy. This corresponds to the adsorption observed in  $\text{LiCl}$ .[6] From these results, it was confirmed that following reaction is occurred in the  $\text{MgCl}_2$  anode as shown in Fig. 1.

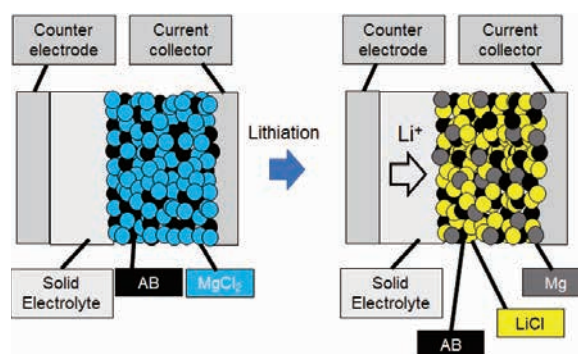
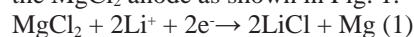


Fig. 1. Schematic view of “*in-situ* forming of solid electrolyte” in  $\text{MgCl}_2$  electrode using  $\text{Li}/\text{LiBH}_4/\text{MgCl}_2$  cell.

- [1] H. Sato, R. Sakamoto, H. Minami, H. Izumi, K. Ideta, A. Inoishi, S. Okada, *Chem. Commun*, **57** (2021) 2605.
- [2] A. Inoishi, H. Sato, Y. Chen, H. Saito, R. Sakamoto, H. Sakaebe, S. Okada, *RSC Advances*, **12** (2022) 10749.
- [3] E. Kobayashi, J. Meikaku, T. Okajima, and H. Setoyama, Japanese Patent No. 5234994.
- [4] E. Kobayashi, J. Meikaku, H. Setoyama, T. Okajima, *J. Surf. Anal.*, **19** (2012) 2.
- [5] J. W. Chiou, H. M. Tsai, C. W. Pao, K. P. Krishna Kumar, S. C. Ray, F. Z. Chien, W. F. Pong, *App. Phys. Lett.* **89** (2006) 043121.
- [6] H. S. Lee, X. Q. Yang, J. McBreen, L. S. Choi, Y. Okamoto, *J. Electrochem. Soc.* **143** (1996) 3825.

# Direct Observation of Electrochemically Generated High Valent Iron-Oxo Species of $\mu$ -Nitrido-Bridged Iron Phthalocyanine Dimer Deposited on Graphite Surface by Soft X-ray Absorption Spectroscopy

Y. Yamada<sup>1,2</sup> and M. Nagasaka<sup>3</sup>

<sup>1</sup>Department of Chemistry, Graduate School of Science, Nagoya University, Furo-cho, Chikusa-ku, Nagoya 464-8602, Japan

<sup>2</sup>Research Center for Materials Science, Nagoya University, Furo-cho, Chikusa-ku, Nagoya 464-8602, Japan

<sup>3</sup>Institute for Molecular Science, Myodaiji, Okazaki 444-8585, Japan

CH<sub>4</sub> is expected as a next generation carbon resource because it is abundant in nature as natural gas or methane hydrate. Therefore, development of novel catalysts that convert CH<sub>4</sub> into valuable raw chemicals efficiently is strongly desired. However, high chemical stability of CH<sub>4</sub> makes it highly challenging. We recently reported that a  $\mu$ -nitrido-bridged iron phthalocyanine dimer closely stacked on a graphite surface **1**/G (Fig. 1a) efficiently convert CH<sub>4</sub> into methanol, formaldehyde, and formic acid in an acidic aqueous solution containing excess H<sub>2</sub>O<sub>2</sub> at a temperature below than 100 °C. It was demonstrated that **1**/G showed especially potent CH<sub>4</sub> oxidation catalyst among a variety of molecule-based CH<sub>4</sub> oxidation catalysts and its catalytic activity was almost comparable to that of a natural particulate methane monooxygenase (pMMO)[1].

In order to advance the chemistry of **1**/G, we next attempted to develop the method for electrochemical generation of **1**<sub>oxo</sub>/G. It is expected that **1**<sub>oxo</sub>/G could be generated by oxidation of coordinating H<sub>2</sub>O on the iron center of **1**(H<sub>2</sub>O)/G in an aqueous solution (Fig. 1b). This method is expected to provide a more economically favored approach for CH<sub>4</sub> oxidation.

We first prepared a SiN membrane tip modified by **1**/G. A SiN membrane tip modified with 20 nm thickness of carbon membrane (cmSiN) was treated with a pyridine solution of **1**, followed by washing with trifluoroacetic acid and H<sub>2</sub>O to give a SiN membrane tip modified by **1**/G (**1**/cmSiN). It was confirmed that **1** was successfully deposited on the carbon surface of cmSiN (Fig. 2a) by using cyclic voltammogram in an CH<sub>3</sub>CN solution containing 100 mM <sup>n</sup>Bu<sub>4</sub>N<sup>+</sup>·PF<sub>6</sub><sup>-</sup>.

Electrochemical generation of the high-valent iron-oxo species from **1**(H<sub>2</sub>O)/cmSiN (Fig. 2b) was monitored by O K-edge XAS spectra in a 100 mM phosphate buffer (pH = 7.0) by using a beamline equipped with a transmission-type liquid flow cell in BL3U of UVSOR [2]. The measurements were performed by changing the applied voltage to **1**(H<sub>2</sub>O)/cmSiN. The spectra were obtained by the Lambert-Beer law,  $\ln(I_0/I)$ , where  $I_0$  is the transmission signals of the cmSiN in buffer and  $I$  is those of **1**(H<sub>2</sub>O)/cmSiN at different applied voltage in buffer.

It was found that the broad peak around 532 eV was apparently appeared when applying the voltage of 1.8

V vs. Ag/AgCl (Fig. 2c). Taking that DFT calculation indicated that the peak of O1s –  $\pi^*$  of Fe=O for **1**<sub>oxo</sub> should appear at around 529 eV, whereas the peaks for **1** having a coordinating H<sub>2</sub>O should be observed at higher energy than 534 eV, it is considered that the peak appeared at around 532 eV is assignable to the excitation of O1s –  $\pi^*$  of Fe=O of electrochemically generated high-valent iron-oxo species of **1**(H<sub>2</sub>O)/cmSiN (**1**<sub>oxo</sub>/cmSiN). We are going to check the CH<sub>4</sub> oxidation activity of electrochemically generated **1**<sub>oxo</sub>/cmSiN.

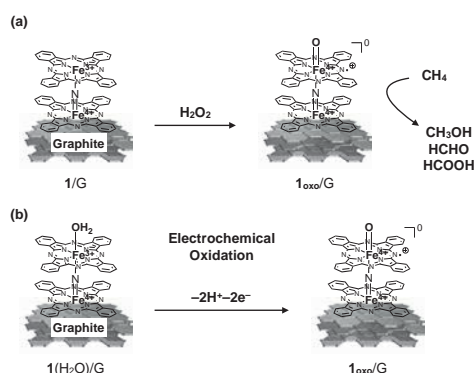


Fig. 1. Generation of **1**<sub>oxo</sub>/G from **1**/G (a) by using H<sub>2</sub>O<sub>2</sub> or (b) by electrochemical oxidation.

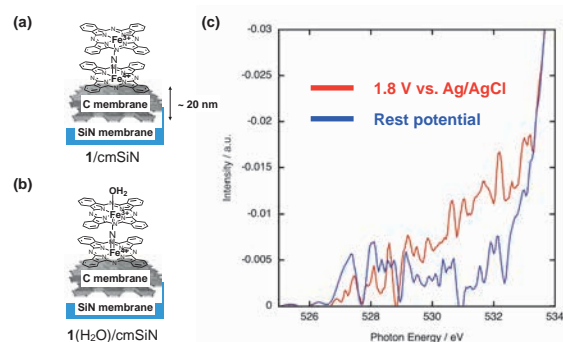


Fig. 2. Structures of (a) **1**/cmSiN and (b) **1**(H<sub>2</sub>O)/cmSiN. (c) Comparison of O K-edge XAS spectra of **1**(H<sub>2</sub>O)/cmSiN at rest potential (blue) and **1**(H<sub>2</sub>O)/cmSiN at the applied potential of 1.8 V vs. Ag/AgCl.

[1] Y. Yamada, M. Nagasaka *et al.*, *JACS Au*. DOI : 10.1021/jacsau.2c00618.

[2] M. Nagasaka and N. Kosugi, *Chem. Lett.* **50** (2021) 956.

BL3U

## Structural Analysis of fluoro-polymers Using Resonant Soft x-ray Scattering

K. Yamanoi<sup>1,2</sup>, M. Yamashita<sup>1</sup>, Y. Yamamoto<sup>1</sup>, H. Iwayama<sup>3</sup> and M. Noumi<sup>2</sup>

<sup>1</sup>*Institute of Laser Engineering, Osaka university, Suita, Osaka, 565-0871, Japan*

<sup>2</sup>*DAIKIN Industries Ltd, Settsu, Osaka, 566-8585, Japan*

<sup>3</sup>*UVSOR Synchrotron Facility, Institute for Molecular Science, Okazaki 444-8585, Japan*

Fluoropolymers or sometimes referred to as fluororesins have been widely used for chemical, electrical, and medical applications because of their high chemical resistance, mechanical strength, hydrophobicity, heat resistance, low surface energies, low coefficients of friction, and low dielectric constants [1-3]. These favorable properties stem from the electronic structure of the fluorine (F) atom, the stable carbon-fluorine (C-F) covalent bond, and the unique intramolecular and intermolecular interactions between the polymers' fluorinated segments and main chains [4]. Based on their structure and composition, fluoropolymers can be classified as partially fluorinated polymers or perfluoropolymers. Partially fluorinated polymers contain F and hydrogen (H) atoms in their structures, while perfluoropolymers only contain F atoms, i.e., the H atoms are replaced with F atoms. For example, polyvinylidene fluoride (PVdF) is a very processable and mechanically strong partially fluorinated polymer, whereas polytetrafluoroethylene (PTFE) is a chemically strong and heat-resistant perfluoropolymer.

Among their different applications, modified PTFE which includes oxygen component in the polymer is used to fuel injectors and as packing and linings of high-pressure vessels. Consequently, the ability to directly observe the oxygen related microscopic morphology is very important in revealing polymer function. As PTFE is known to have semi-crystalline, lamellar structures consisting of both amorphous and crystal phases [5], small-angle x-ray scattering (SAXS) technique is the most appropriate method to study the internal morphologies of these fluoropolymers within the 10 to 100-nm range. Additionally, the Resonant Soft X-ray Scattering (RSoXS) is attractive method to observe the structure related with specific chemical bond in mesoscopic region.

Previously, SAXS has been used to investigate the morphology of PTFE and their co-polymers under supercritical carbon dioxide condition [6]. In this research the RSoXS method was used in BL3U, UVSOR facility on the modified PTFE sample.

The sample was sliced to 1  $\mu\text{m}$  thickness and sandwiched with  $\text{Si}_3\text{N}_4$  membrane. Soft x-ray is irradiated on the sample through the  $\text{Si}_3\text{N}_4$  membrane and the scattered soft x-ray is monitored by camera at the position of  $2\theta=7.5$  and  $30^\circ$ . The x-ray energy is

tuned at 540 eV which is resonant with oxygen bonding in polymer.

Figure 1 shows the results of scattering patterns of 540 eV comparing with the 528 eV which is not resonant with oxygen bonding.

We could observe the difference around the higher angle corresponding to smaller structure between resonant and non-resonant x-rays. This result shows the oxygen bonding related structure has the smaller crystal structure compared with others, however the scattered x-ray signal was weak since the sample was much thick. For the detailed discussion of oxygen bonding related structure, more thinner sample is required.

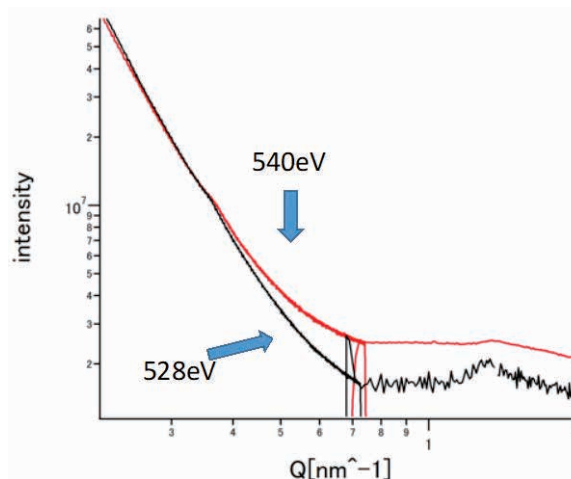


Fig. 1. Scattering patterns of RSoXS with 540 eV and 528 eV

- [1] S. Ebnesajjad, P. R. Khaladkar, Fluoropolymer applications in the chemical processing industries (Second Edition), William Andrew Publishing (2017).
- [2] Z. Cui, E. Drioli, Y. M. Lee, Prog. Polym. Sci. **39** (2014) 164.
- [3] G. Eberle, H. Schmidt, W. Eisenmenger, IEEE Trans. Dielectr. Electr. Insul. **3** (1996) 624.
- [4] H. Teng, Appl. Sci **2** (2012) 496.
- [5] A. Marigo, C. Marega, R. Zannetti, G. Ajroldi, Macromolecules **29** (1996) 2197.
- [6] K. Yamanoi, S. Shibuta, A. Shiro, M. Noumi, M. J. F. Empizo, M. Cadatal-Raduban, N. Sarukura, K. Nishikawa, and T. Morita, J. Supercrit. Fluids, May 2022 vol. **184** (2022) 105555.

## Structure Analysis on Chiral Dark Conglomerate of Achiral Liquid Crystal Trimers by Resonant Soft X-ray Scattering (RSoXS) at UVSOR

Y. Takanishi<sup>1</sup>, F. Araoka<sup>2</sup> and H. Iwayama<sup>3,4</sup>

<sup>1</sup>Faculty of Science, Kyoto University, Kitashirakawa-oiwake, Sakyo, Kyoto, 606-8502, Japan

<sup>2</sup>RIKEN Center for Emergent Matter Science, Hirosawa 2-1, Wako, Saitama 351-0198, Japan

<sup>3</sup>UVSOR Synchrotron Facility, Institute for Molecular Science, Okazaki 444-8585, Japan

<sup>4</sup>School of Physical Sciences, The Graduate University for Advanced Studies (SOKENDAI), Okazaki 444-8585, Japan

Spontaneous chiral symmetry breaking in soft matter is one of most attractive topics. Liquid crystal (LC) is a typical one of soft matter, and bent-core molecules show unique LC phases. The B4 phase is the lowest temperature phase observed in the bent-core liquid crystals, and it shows spontaneously chiral separated domains despite of achiral molecules. Recently it is reported that some kinds of rod-like LC trimers also show similar DC phase caused by unique molecular packing by designing intermolecular interactions. Yoshizawa's group studied intensively achiral LC trimers exhibiting DC phase. They systematically synthesized LC trimers, and reported that the DC phase is stabilized in (a) equimolecular mixture of nematic and smectic trimers, (b) binary mixtures of a nematic trimer with biphenyl units at the center and cyano-biphenyl compound and (c) a single asymmetric trimer.

In resonant X-ray scattering, using X-ray whose energy is coincident with a certain atom absorption edge, the structure factor becomes a tensor instead of the scalar in conventional X-ray diffraction. Carbon K-edge resonant soft x-ray scattering (RSoXS) has been applied to study, and successful in obtaining the precise structures of polymer blends, block copolymer, and LCs. Recently one of authors (YT) studied the binary system between a rod-like cholesteric LC mixture and a bent-core LC showing B4, and found a new smectic structure that does not appear in only constituent molecules with wide temperature range was unexpectedly discovered. Last year, the structure of helical nano-filament of B4 phase in the nano phase separation of cholesteric liquid crystal mixture and a bent-core molecule was analyzed using RSoXS to study the effect on the nano-helical filament in this mixture. We summarized that the pitch of helical filament decreases and coherence of helical structure increases, which would be caused by the interaction between bent-core and rod-like molecules.[1]

In this study, we report the local nano-structure analysis of DC conglomerate phase in achiral LC trimer using resonant soft-X-ray scattering (RSoXS) technique. Small angle and wide angle scattering were measured and alkyl chain length dependence of rod-like molecules was discussed.

The experiment was performed at BL3U of UVSOR. Used achiral liquid crystal trimers are I-(m,n), as shown in Fig. 1. In this study, m is fixed to 9, and n changes

from 7~11. Samples used were filled in the isotropic phase between two pieces of 100 nm-thick Si<sub>3</sub>N<sub>4</sub> membranes (Norcada). The scattering was detected by CCD (ANDOR DO940P-BN). Incident X-ray beam was tuned between 270~300eV. In these compounds, carbon K-edge energy was 284.5 eV.

Figure 2 shows 2D small-angle RSoXS images of (a) I-(9,7), (b)I-(9,9) and (c)I-(9,11). Resonant scattering peaks are clearly observed, and with the increase of spacer chain length n, the long-range periodicity corresponding to the peak increases from ca. 900~1300 nm. In I-(9,9), tubercle structures are seen by STEM observation, but its diameter was about 200 nm, and hence our results suggest the existence of the longer-range periodic structure.

Figure 3 shows 2D wide-angle RSoXS images of (a) I-(9,7), (b)I-(9,9) and (c)I-(9,11). Even in these images, clear sharp peaks are observed, and the corresponding periodicity are ca. 70~80Å, which increases with the increase in the spacer chain length n. Since the layer thickness by conventional X-ray scattering are ca.40Å, these results indicate that LC trimers form intercalated bilayer structure.

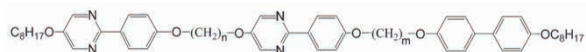


Fig. 1. Chemical structure of I-(m,n).

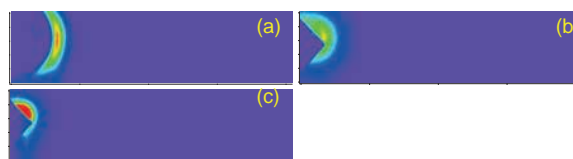


Fig. 2. 2D small-angle RSoXS images of (a)I-(9,7), (b) I-(9,9) and (c)I-(9,11).

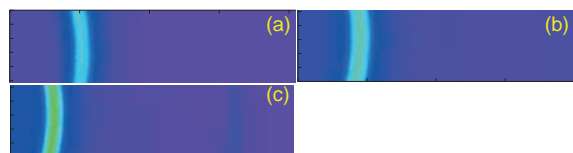


Fig. 3. 2D wide-angle RSoXS images of (a)I-(9,7), (b) I-(9,9) and (c)I-(9,11).

[1] Y. Takanishi, *Soft Matter*, **17** (2021) 563.

BL3B

## Measurements of Fluorescence Lifetimes of Scintillators Adopted for a New in-beam Detector of the $K_L^0$ Rare Decay Experiment at J-PARC

K. Shintate, R. Abe, Y. Hayashi, T. Naito, S. Sakano, J. Ohashi, Y. Tajima and H.Y. Yoshida  
*Department of Physics, Yamagata University, 990-8560, Japan*

J-PARC E-14 KOTO [1] is the experiment of searching for the direct CP violating decay  $K_L \rightarrow \pi^0 \nu \bar{\nu}$ . This decay mode is considered to be sensitive to new physics beyond the Standard Model (SM), and its branching ratio is predicted to be  $3.0 \times 10^{-11}$  in the SM with about 2% theoretical uncertainty.

The cross-sectional view of the KOTO detector is shown in Fig.1. The upper limit currently obtained on the branching fraction of  $K_L \rightarrow \pi^0 \nu \bar{\nu}$  decay is  $3.0 \times 10^{-9}$  at the 90% confidence level [2].

One of the main backgrounds is caused by  $K^\pm$  decays in the beam. To reduce this background by detecting  $K^\pm$ , we are planning to install an in-beam charged particle detector with a scintillator of 0.2 mm thickness named UCV (Upstream Charged Veto, Fig.2). The scintillator used for UCV is required to have sufficient light yield and short fluorescence lifetime. We measured fluorescence spectra and decay curves of the scintillator to evaluate the performance of UCV as a particle detector.

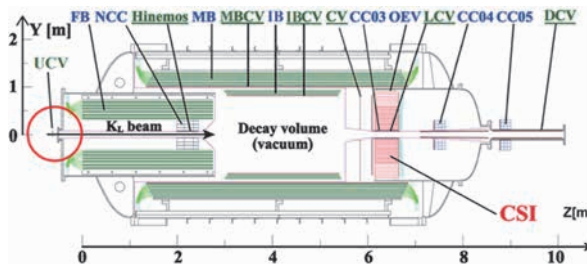


Fig. 1. Cross-sectional view of the KOTO detector. The beam enters from the left. Detector components with their abbreviated names written in blue (in green and underlined) are photon (charged-particle) veto counters. The UCV detector is installed at the upstream (left) end of the KOTO detector.

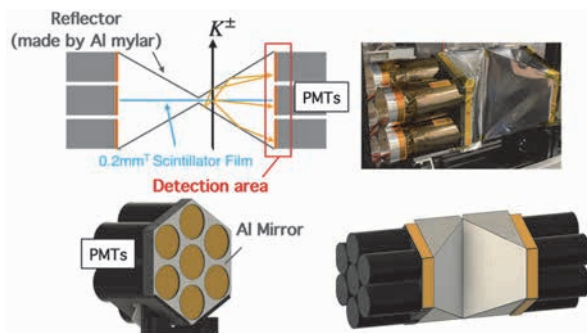


Fig. 2. The UCV detector. To install in the beam line, the scintillators are made as thin as 0.2mm thick and scintillating lights are detected by photomultiplier tubes (PMTs) using reflector sheets.

Fig. 3 shows the 2D fluorescence spectra of the UCV scintillator. Fig. 4 shows the decay curve for the 432 nm band under excitation at 284 nm. The blue line indicates experimental data. The red line is the fitting curve consists of two fluorescence lifetimes and reproduces the experimental data. The fitting results analyzed by using the data analysis framework named “ROOT” [3] are summarized in Table 1.

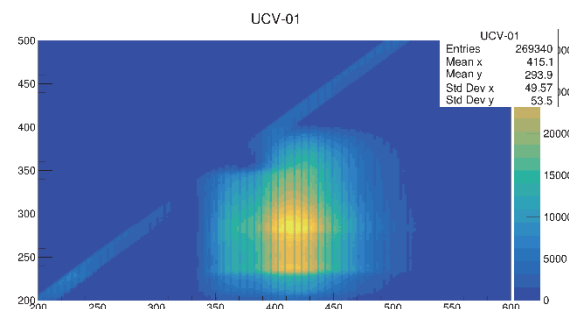


Fig. 3. 2D fluorescence spectra of the UCV scintillator. Y-axis is excitation wave length (nm), and x-axis is emission wave length (nm).

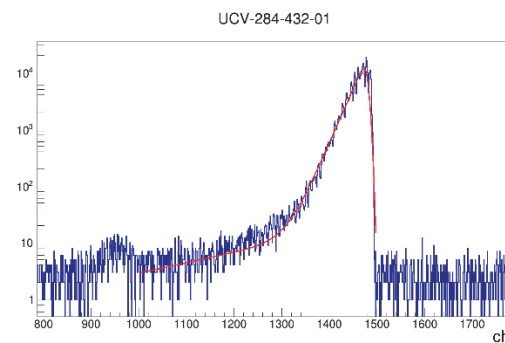


Fig. 4. Decay curve of the UCV scintillator for the 432 nm band under excitation at 284 nm.

Table 1. Fluorescence lifetimes of the UCV scintillator, determined from our data analysis.

Sample	$\lambda_{EX}$ [nm]	$\lambda_{EM}$ [nm]	$\tau_1$ [ns] (Ratio)	$\tau_2$ [ns] (Ratio)
UCV	284	432	1.9 (91.4%)	20.3 (8.6%)

[1] J. Comfort *et al.*, Proposal for  $K_L \rightarrow \pi^0 \nu \bar{\nu}$  Experiment at J-PARC (2006).

[2] J. Ahn *et al.* (KOTO Collaboration), Phys. Rev. Lett. **122** (2019) 021802.

[3] R. Brun and F. Rademakers, Nucl. Instrum. Methods Phys. Res. A **389** (1997) 81.

## Material Search of Li-Containing Halide Scintillators for Neutron Detection

C. Fujiwara<sup>1,2</sup>, S. Kurosawa<sup>2,3,4</sup> and A. Yamaji<sup>2,3</sup>

<sup>1</sup>Department of Materials Science, Graduate School of Engineering, Tohoku University, Sendai, Japan

<sup>2</sup>Institute for Materials Research (IMR), Tohoku University, Sendai, Japan

<sup>3</sup>New Industry Creation Hatchery Center (NICHe), Tohoku University, Sendai, Japan

<sup>4</sup>Institute of Laser Engineering, Osaka University, Osaka, Japan

A remote real-time radiation detector consisting of a scintillator and optical fiber is required to achieve the decommissioning of the Fukushima Daiichi Nuclear Power Plant[1]. The scintillator for this application is required to have an emission wavelength of 550 nm or longer and high light output from the viewpoint of transmission efficiency in the optical fiber and reduction of optical fiber-derived noise[2][3]. In addition, neutrons-emitting debris is expected to be present inside the reactor, and neutron-sensitive scintillation materials are needed. Due to the above reason, we have developed  $\text{Li}_2\text{HfI}_6$  as a candidate material [4], while  $\text{Li}_2\text{HfI}_6$  contains a heavy element, Hf with a high detection efficiency for gamma rays. Therefore, in this study,  $\text{Li}_2\text{ZrX}_6$  (X=Cl, Br, I) was prepared by replacing Hf with Zr, and its luminescence properties were investigated.

$\text{Li}_2\text{ZrX}_6$  crystal specimen was synthesized by the vertical Bridgman growth method in our laboratory using 99.9%-pure LiCl, LiBr and LiI powders, and 99%-pure  $\text{ZrCl}_4$ ,  $\text{ZrBr}_4$  and  $\text{ZrI}_4$  powders were used. We measured the photoluminescence excitation and emission spectrum from 50 to 300K at UVSOR BL3B beam line.

As shown in Fig.1(a),  $\text{Li}_2\text{ZrCl}_6$  showed broad luminescence with a peak at 570 nm at an excitation wavelength of 300 nm at 50K. Although the luminescence intensity decreased as the temperature increased, no significant change in both the excitation and emission wavelengths were observed. The emission wavelength was 580 nm at the excitation wavelength of 300 nm at room temperature. This wavelength range satisfies the above requirement, and  $\text{Li}_2\text{ZrCl}_6$  can be a candidate material for neutron detection with optical fiber.

Fig.1(b) showed the emission spectrum of  $\text{Li}_2\text{ZrBr}_6$  as a function of temperatures.  $\text{Li}_2\text{ZrBr}_6$  shows a broad emission with a peak at 580 nm at an excitation wavelength of 305 nm at 50 K. When the temperature is increased, the emission intensity decreases, and the emission wavelength became shorter.

Fig. 1(c) shows the emission spectrum of  $\text{Li}_2\text{ZrI}_6$ , and  $\text{Li}_2\text{ZrI}_6$  had red and near-infrared emission with the emission wavelength of 670 nm at an excitation wavelength of 430 nm at 50 K. However, the emission intensity decreases significantly as the temperature increases, and no emission is observed at room temperature.

From these results,  $\text{Li}_2\text{ZrCl}_6$  was found to be a

candidate material for neutron detection using an optical fiber. In the future, we plan to investigate the light output by neutron excitation and conduct a detection test by connecting the optical fiber.

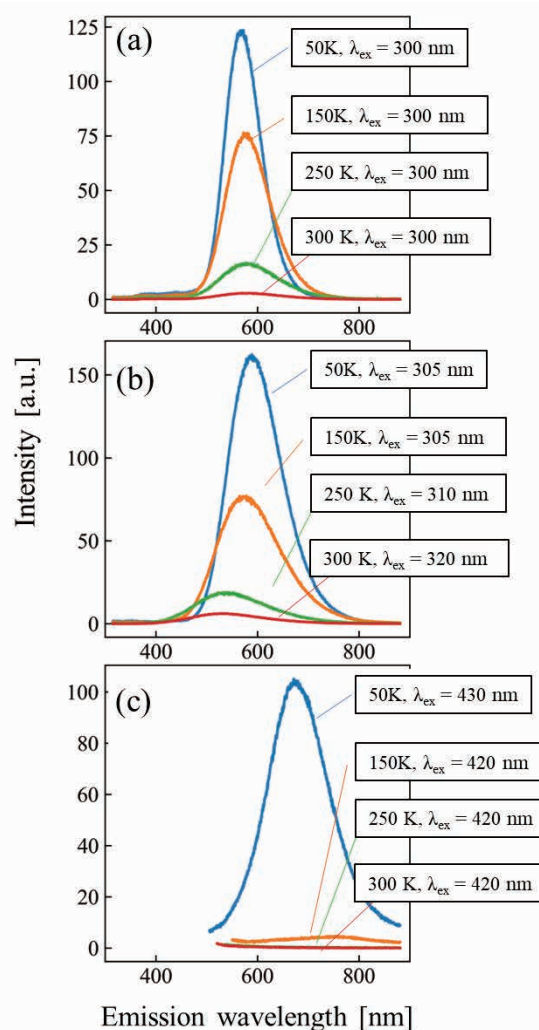


Fig. 1. Photoluminescence spectrum at each temperature for (a)  $\text{Li}_2\text{ZrCl}_6$ , (b)  $\text{Li}_2\text{ZrBr}_6$ , (c)  $\text{Li}_2\text{ZrI}_6$

- [1] I. Wakaida, Topic. Fukushima **70** (2015) 1.
- [2] C. and H. Ltd, Opt. Quantum Electron **13** (1981) 85.
- [3] H. Liu *et al.*, Rev. Sci. Instrum. **89** (2018) 083302.
- [4] C. Fujiwara, K. Shunsuke, and Y. Akihiro, UVSOR Activity Report **49** (2021) 84.

BL3B

## Optical Properties of Cs<sub>2</sub>IrCl<sub>6</sub>-CsCl Composite Phosphor

S. Kodama, S. Omiya, N. Shimoyama, T. Saito, I. Yanase and H. Takeda  
Saitama University, Saitama 338-8570, Japan

Cs<sub>2</sub>HfCl<sub>6</sub> was reported as the novel single-crystalline inorganic scintillator with a high light output and a good energy resolution [1]. Cs<sub>2</sub>HfCl<sub>6</sub> exhibits the strong intrinsic luminescence at the blue region. Several luminescence origins were suggested for Cs<sub>2</sub>HfCl<sub>6</sub> [2-3], however, the detailed mechanism was still unclear.

In this study, we focused on the charge transition transfer (CT) phenomena. Inorganic crystals which consist an isolated anion complex show the CT luminescence. In order to occur the CT luminescence, the peripheral electron orbital of the center metal ion in the anion complex should be empty. The crystal structure of Cs<sub>2</sub>HfCl<sub>6</sub> consists Cs<sup>+</sup> ions and isolated [HfCl<sub>6</sub>]<sup>2-</sup> anion complexes. In addition, the electron orbital of Hf<sup>4+</sup> of [HfCl<sub>6</sub>]<sup>2-</sup> anion complex is empty, thus we assumed that the intrinsic luminescence of Cs<sub>2</sub>HfCl<sub>6</sub> can be attributed to be CT luminescence.

To distinguish the CT luminescence from other luminescence origins such as the self-trapped luminescence or the defect luminescence, therefore in this study, we synthesized Cs<sub>2</sub>IrCl<sub>6</sub> and compared the optical properties with Cs<sub>2</sub>HfCl<sub>6</sub>. Although Cs<sub>2</sub>IrCl<sub>6</sub> has the same crystal structure as Cs<sub>2</sub>HfCl<sub>6</sub>, the peripheral electron orbital of Ir<sup>4+</sup> of [IrCl<sub>6</sub>]<sup>2-</sup> is not empty, therefore, Cs<sub>2</sub>IrCl<sub>6</sub> must not exhibit the CT luminescence. If some luminescence was observed in Cs<sub>2</sub>IrCl<sub>6</sub>, the CT luminescence should not occur in Cs<sub>2</sub>HfCl<sub>6</sub>.

Cs<sub>2</sub>IrCl<sub>6</sub> was synthesized from the starting powders of CsCl and IrCl<sub>4</sub>. The melted specimen included Cs<sub>2</sub>IrCl<sub>6</sub> and CsCl phases, thus we represent the obtained specimen to be Cs<sub>2</sub>IrCl<sub>6</sub>-CsCl composite. Additionally, in order to compare the optical properties, non-doped CsCl and Ir:CsCl crystals were grown.

Figure 1 shows the photoluminescence spectra of Cs<sub>2</sub>IrCl<sub>6</sub>-CsCl composite, CsCl and Ir:CsCl. At 300K, all specimens showed the single emission peak at ~310 nm excited by 254 nm. In addition to ~310 nm band, all specimens showed another emission peak at ~420 nm at 300K. The emission peaks of Cs<sub>2</sub>IrCl<sub>6</sub>-CsCl composite and Ir:CsCl well corresponded to that of CsCl, therefore, Cs<sub>2</sub>IrCl<sub>6</sub> was concluded to show no luminescence originated from the self-trapped excitons or defects. Based on the obtained results, the luminescence origin of Cs<sub>2</sub>HfCl<sub>6</sub> might be assumed to be the CT luminescence.

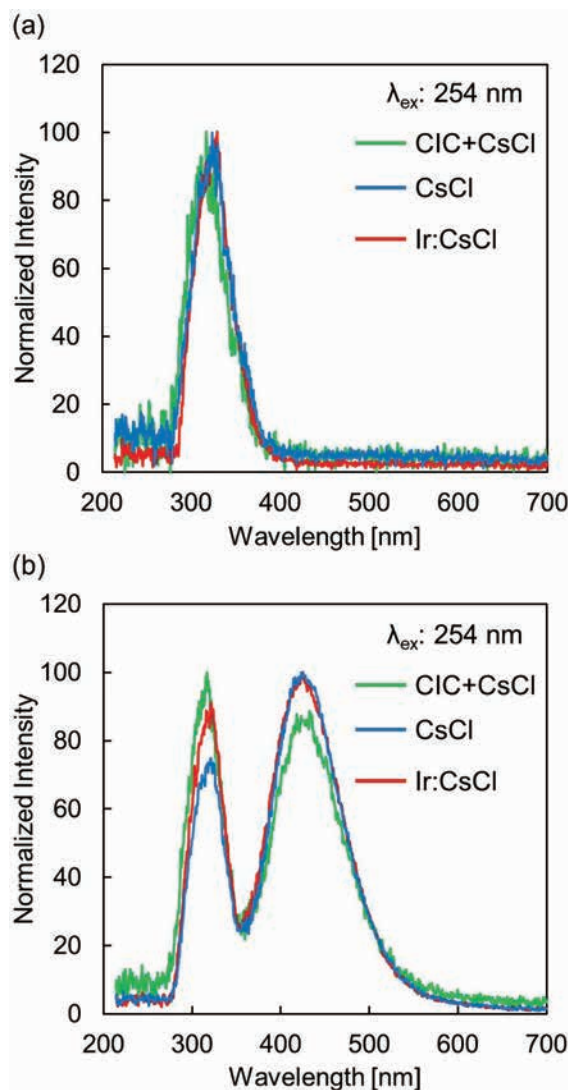


Fig. 1. Photoluminescence spectra of Cs<sub>2</sub>IrCl<sub>6</sub>-CsCl composite (represented as CIC+CsCl), CsCl and Ir:CsCl at (a) 300K and (b) 10K.

- [1] A Burger *et al.*, Appl. Phys. Lett **107** (2015) 34.  
[2] B. Kang and K. Biswas, J. Phys. Chem. C **120** (2016) 12187.  
[3] R. Král *et al.*, J. Phys. Chem. C **121** (2017) 12375.

## Visible-to-Ultraviolet Spectral Change with the Current-Induced Local-to-Nonlocal Transition of SmS

H. Watanabe<sup>1,2</sup>, S. Tatsukawa<sup>2</sup>, K. Imura<sup>3</sup>, H. S. Suzuki<sup>4</sup>, N. K. Sato<sup>5</sup> and S. Kimura<sup>1,2,6</sup>

<sup>1</sup>Graduate School of Frontier Biosciences, Osaka University, Suita 565-0871, Japan

<sup>2</sup>Department of Physics, Graduate School of Science, Osaka University, Toyonaka 560-0043, Japan

<sup>3</sup>Institute of Liberal Arts and Sciences, Nagoya University, Nagoya 464-8602, Japan

<sup>4</sup>Institute for Solid State Physics, The University of Tokyo, Kashiwa 277-8581, Japan

<sup>5</sup>Center for General Education, Aichi Institute of Technology, Toyota, 470-0392 Japan

<sup>6</sup>Institute for Molecular Science, Okazaki 444-8585, Japan

Samarium monosulfide SmS exhibits the phase transition from a black-colored semiconductor to a golden-colored metal (BGT) by applying pressure above 0.7 GPa [1,2]. The origin of the BGT is now still under debate. Among the possible origins, the transition between Bose-Einstein condensation and BCS state of excitons is currently being discussed [3,4], but no definitive evidence has been obtained. Recently, Ando *et al.* reported the nonlinear relation between the voltage ( $V$ ) and electric current ( $I$ ) with increasing current at lower temperatures than 100 K, which suggests a drastic change in the electrical resistivity [5]. It is unclear whether the nonlinear  $V/I$  relation is related to pressure-induced BGT. To clarify the origin of the nonlinear  $V/I$  curve and its relation to the BGT, we have investigated the current and temperature dependencies of the reflectivity spectrum in the THz and IR regions. We have already reported the carrier character change from the high increasing rate ( $dN/dI$ ) and the high relaxation time ( $\tau$ ) of carriers at the region of low temperature and low current to low  $dN/dI$  and low  $\tau$  at high temperature or high current regions [6,7].

The origin of the character change of carriers can be attributed to an electron delocalization, in which the localized electrons trapped at Sm sites start moving by the applied current. In this case, the electronic structure is modified, and finally, the band gap is expected to be closed, but it has not been revealed. In the visible-ultraviolet region, there are excitations from occupied  $4f$  states to the unoccupied  $5d$  states. It is expected to be able to observe changes in the reflectivity spectrum due to the modification in the electronic structure, such as a band gap narrowing. To observe the current-induced spectral change in SmS, we measured the current dependence of the visible-ultraviolet reflectance at BL3B.

Single crystalline SmS with a typical sample size of  $1 \times 1 \times 1$  mm<sup>3</sup> was sandwiched by the electrodes connected to the current source. The sample was cooled down to 30 K during the experiment.

Figure 1 shows the applied current dependence of the visible-ultraviolet reflectivity spectrum. With increasing applied current, the intensity of a peak at 3 eV decreases, and a shoulder at about 6 eV shifts to low energy. In

addition to the spectral change, an oscillation in reflectivity appeared between 4 to 6 eV, which is expected to be due to a change in the surface condition, but the exact origin is not clarified. From these results, although we observed a slight change in the reflectivity spectrum in the visible-ultraviolet region due to the current application, these could not suggest a drastic change in the electronic structure, such as a shift in the overall band structure due to a change of the band gap.

In summary, the application of electric current gives energy to the electrons, causing delocalization. However, the results suggest that the applied current does not influence the electronic structure far from the Fermi level.

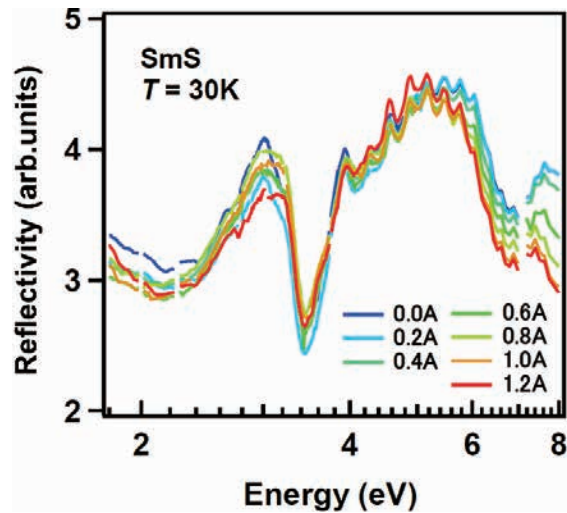


Fig. 1. Current dependence of the visible-to-ultraviolet reflectivity spectrum of SmS at 30 K.

- [1] A. Jayaraman *et al.*, PRL **25** (1970) 1430.
- [2] T. Mizuno *et al.*, JPSJ **77** (2008) 113704.
- [3] B. I. Halperin and T. M. Rice, RMP **40** (1968) 755.
- [4] S. Watanabe, JPSJ **90** (2021) 023706.
- [5] H. Ando *et al.*, JPS Conf. Proc. **30** (2020) 011132.
- [6] H. Watanabe *et al.*, UVSOR Activity Report 2021 (2022) 92.
- [7] S. Kimura *et al.*, arXiv: 2302.12998 (2023).

BL3B

## Exciton States of Cesium Silver Iodide Crystals

S. Ibuki and T. Kawai

Graduate School of science, Osaka Metropolitan University, Sakai 599-8531, Japan

In the past decade, ternary lead halides have attracted wide interest in the field of applications, including scintillator materials, photodetectors, and solar cells [1]. However, the environmental toxicity of the lead is among the significant concerns in this field. Therefore, considerable efforts have been devoted to developing alternative eco-friendly lead-free ternary metal halide. In this study, we focused on ternary silver iodides such as  $\text{CsAg}_2\text{I}_3$ .

$\text{CsAg}_2\text{I}_3$  compounds were obtained by the Bridgman method from high purity CsI and AgI powders, which were mixed in a stoichiometric ratio. The thin crystals of  $\text{CsAg}_2\text{I}_3$  were prepared by a cell method [2]. The quartz-cells with the narrow gap are made of a pair of two quartz plates. The melt of  $\text{CsAg}_2\text{I}_3$  compounds was percolated into the gap of the quartz-cells through capillary action and the thin crystals were grown in the gap by natural cooling.

Figure 1 shows the reflection spectrum of the  $\text{CsAg}_2\text{I}_3$  crystal at 12 K in the energy region of 3.5 ~ 6.5 eV. The sharp dispersion-like structures due to band-edge excitons are observed around 3.8 eV. Furthermore, the broad reflection peaks are observed around 4.6 and 5.1 eV. The energy values are consistent with those of the absorption bands reported in a previous paper [3].

Now, we confine one's attention to the dispersion-like structures due to the band-edge excitons around 3.8 eV. The reflection spectrum magnified around the dispersion-like structures is shown in Fig.2. Two dispersion-like structures are confirmed. We attempted to fit the reflection structures by using the simple oscillators model with two close-lying resonances. Then, the dielectric function is represented by the following expression:

$$\begin{aligned}\varepsilon(\omega) &= \varepsilon_r + i\varepsilon_i \\ &= \varepsilon_b + \frac{f_1}{\omega_{ex1}^2 - \omega^2 - i\omega\gamma_1} \\ &\quad + \frac{f_2}{\omega_{ex2}^2 - \omega^2 - i\omega\gamma_2}\end{aligned}$$

where  $\varepsilon_r$  and  $\varepsilon_i$  are the real and imaginary parts of the dielectric constant, respectively,  $\omega_{ex1,2}$  is the resonance frequency of the excitons,  $\varepsilon_b$  the background dielectric constant,  $f_{1,2}$  oscillator strength, and  $\gamma$  the damping constant. The reflectance  $R$  is given by

$$R = \frac{1 + |\varepsilon| - \sqrt{2(|\varepsilon| + \varepsilon_r)}}{1 + |\varepsilon| + \sqrt{2(|\varepsilon| + \varepsilon_r)}}$$

where  $|\varepsilon| = (\varepsilon_r^2 + \varepsilon_i^2)^{1/2}$ . From the best-fitting analysis,

which is shown by the broken curve in Fig.2, the resonance energies of the excitons were estimated to be 3.78 and 3.87 eV.

As future works, we are planning to investigate the optical properties of ternary silver iodides such as  $\text{Cs}_2\text{AgI}_3$ .

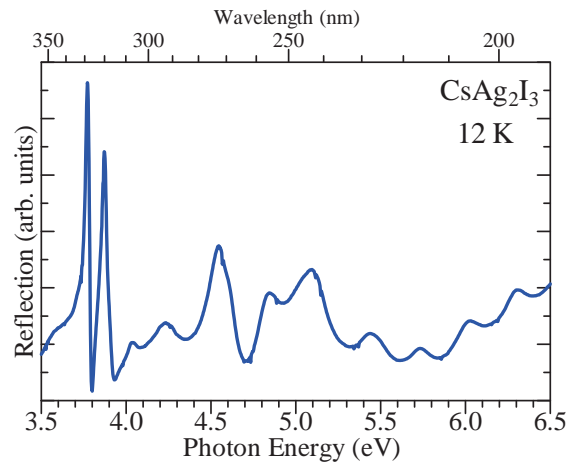


Fig. 1. Reflection spectrum of the  $\text{CsAg}_2\text{I}_3$  crystal at 12K.

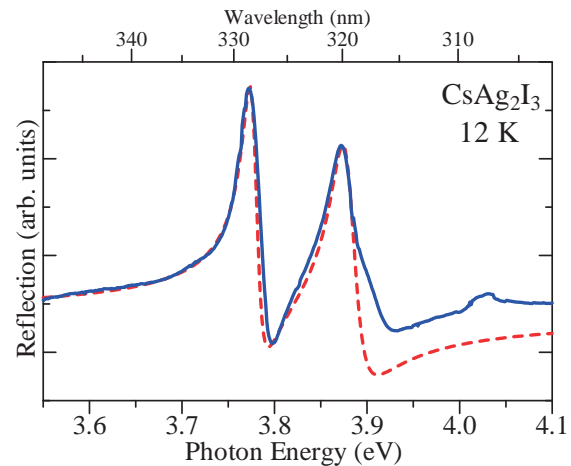


Fig. 2. Reflection spectrum of the  $\text{CsAg}_2\text{I}_3$  crystals in the band-edge exciton region at 12 K. Broken curve is the fitting result calculated with the two-oscillator model.

[1] J. Yuan, *et. al*, *Joule* **4** (2020)1160.

[2] S. Hashimoto and M. Itoh, *Jpn. J. Appl. Phys.* **27** (1988) 726.

[3] V. K. Miloslavskii, *et. al*, *Solid State Spectro.* **80** (1996) 577.

## Temperature Dependence of Excitation Spectra in Er-doped $\text{La}_2\text{Zr}_2\text{O}_7$

M. Yoshino and M. Ito

Graduate School of Engineering, Nagoya University, Nagoya 464-8603, Japan

Based on our first-principles calculations, Er substituted for La in pyrochlore-type oxide,  $\text{La}_2\text{Zr}_2\text{O}_7$  (LZO) has multiple stable positions with significant displacements from the original La position, and is expected to spread in a disc shape at room temperature. This combination of static and dynamic disorder produces diversity in the Er coordination environment, and the transition spectrum of  $\text{Er}^{3+}$  is expected to have a broad shape due to the overlap of each environment case. At low temperatures, the transition spectra become sharper due to the decrease in the dynamic disorder. Therefore, we measured the excitation spectra of Er-doped LZO from low temperature to room temperature. For comparison, we also measured Er-doped  $\text{Y}_2\text{Ti}_2\text{O}_7$  (YTO) with pyrochlore-type structure,  $\text{Y}_{0.5}\text{Zr}_{0.5}\text{O}_{1.75}$  (YZO) with defect fluorite structure, and  $\text{Y}_3\text{Ga}_5\text{O}_{12}$  (YGG) with garnet-type structure. Er in YTO and YGG have small displacements, and Er in YZO has static disorder but less dynamic disorder, so the

temperature dependence of their spectral shapes is expected to be small. Fig. 1 shows the excitation spectrum of LZO with emission wavelength of 560 nm. Results from 20 K to 100 K are shown here, but measurements were also performed up to 300 K. To examine the temperature dependence of the spectral shape, we normalized the spectra using the peak with the maximum intensity at 20 K. Fig. 2 and Fig. 3 show the results for YZO and YTO, respectively. In each case, the spectral shape becomes broader with increasing temperature. To compare their temperature dependences, we estimated the change in the height of the valley between peaks around 380 nm with respect to the 20 K case as shown in Fig. 4. It was found that LZO tends to have a larger change in the height of the valley than the other samples, resulting in broad spectra. This indicates that the temperature dependence is larger for LZO.

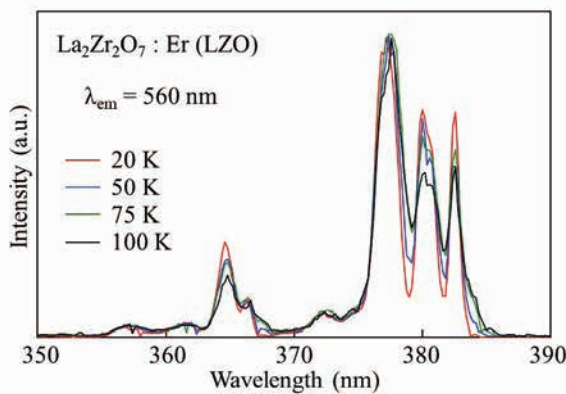


Fig. 1. Excitation spectra of  $\text{La}_2\text{Zr}_2\text{O}_7$ : Er ( $\lambda_{\text{em}} = 560$  nm).

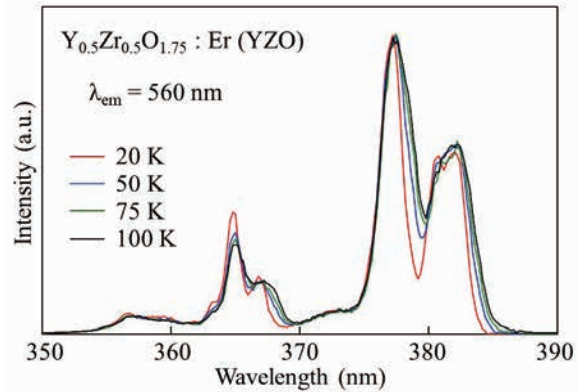


Fig. 2. Excitation spectra of  $\text{Y}_2\text{Zr}_2\text{O}_7$ : Er ( $\lambda_{\text{em}} = 560$  nm).

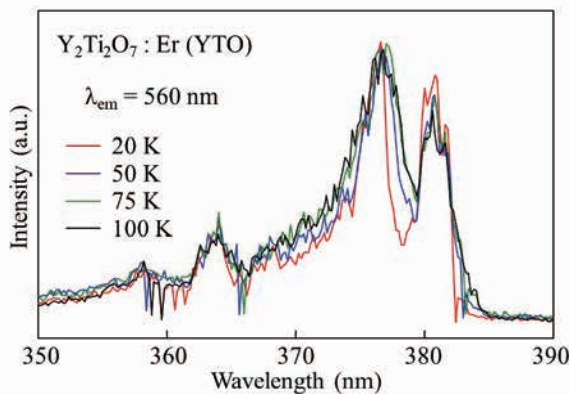


Fig. 3. Excitation spectra of  $\text{Y}_2\text{Ti}_2\text{O}_7$ : Er ( $\lambda_{\text{em}} = 560$  nm).

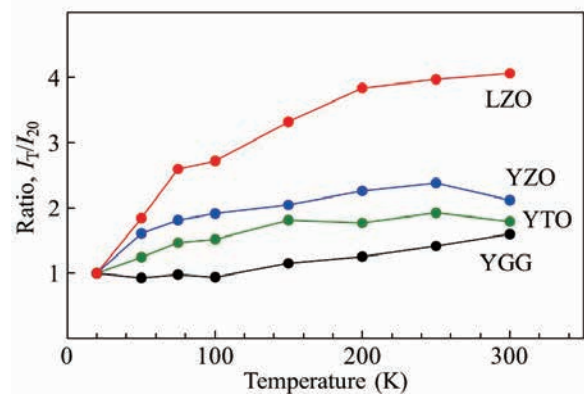


Fig. 4. Change in the height of the valley between peaks around 380 nm.

BL4U

## Analysis of Cathode Materials for Li-Ion Batteries by STXM

E. Hosono<sup>1,2,3</sup>, D. Asakura<sup>1,2,3</sup>, H. Yuzawa<sup>4</sup>, T. Ohigashi<sup>4,5</sup>, W. Zhang<sup>6</sup>, M. Kobayashi<sup>7,8</sup>,  
H. Kiuchi<sup>6</sup> and Y. Harada<sup>3,6,9</sup>

<sup>1</sup>Global Zero Emission Research Center, National Institute of Advanced Industrial Science and Technology (AIST),  
Tsukuba, Ibaraki 305-8569, Japan

<sup>2</sup>Research Institute for Energy Conservation, AIST, Tsukuba, Ibaraki 305-8565, Japan

<sup>3</sup>AIST-UTokyo Advanced Operando Measurement Technology Open Innovation Laboratory (Operando-OIL),  
Kashiwa, Chiba 277-8565, Japan

<sup>4</sup>UVSOR Synchrotron Facility, Institute for Molecular Science, Okazaki 444-8585, Japan

<sup>5</sup>School of Physical Sciences, The Graduate University for Advanced Studies (SOKENDAI),  
Okazaki 444-8585, Japan

<sup>6</sup>Institute for Solid State Physics (ISSP), The University of Tokyo,  
5-1-5 Kashiwanoha, Kashiwa, Chiba 277-8581, Japan

<sup>7</sup>Department of Electrical Engineering and Information Systems, The University of Tokyo,  
7-3-1 Hongo, Bunkyo-ku, Tokyo 113-8656, Japan

<sup>8</sup>Center for Spintronic Research Network, The University of Tokyo, 7-3-1 Hongo, Bunkyo-ku, Tokyo

<sup>9</sup>Synchrotron Radiation Research Organization, The University of Tokyo,  
7-3-1 Hongo, Bunkyo-ku, Tokyo, 113-8656, Japan

The development of clean energy devices is attracting attention toward the realization of a low-carbon society for preventing global warming. Since lithium ion batteries (LIBs) are expected to be broadly used for such as electric vehicles and stationary types for home use, their devices are the most actively investigated in both industry and academia fields. However, the market demand for improved performance of LIBs is still extremely high, and the development of innovative materials for LIBs is essential to exceed significantly the current performance. To solve this difficult problem, characterization of component materials for LIBs is crucially important.

We have been analyzing electrode active materials by absorption and emission spectroscopy using synchrotron soft X-rays in order to clarify the detailed electronic states of the materials. In addition, we have also been analyzing them by microscopic photoelectron spectroscopy using synchrotron soft X-rays. The LIBs are devices that stores energy by the insertion and diffusion of Li into the host crystal, which is strongly dependent on the local environment of the active materials. Therefore, local analysis can provide important information for understanding the charge-discharge mechanism. Photoelectron spectroscopy is a surface-sensitive method, while scanning transmission X-ray microscopy (STXM) is a bulk-sensitive method because of its transmission.

In this study, we applied STXM analysis to most famous LIB cathode material, LiCoO<sub>2</sub> (LCO). Figure 1 shows the Co L<sub>3</sub>-edge X-ray absorption spectra (XAS) of the initial (dotted line) and charged (solid line) conditions of LCO. By using STXM, we were able to obtain XAS spectra of selected areas and visualize the distribution of the oxidation state of LCO. The details were reported in ref. [1].

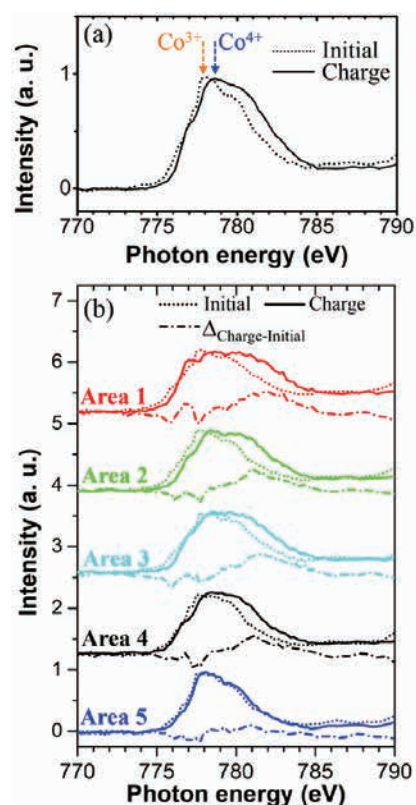


Fig. 1. Co L<sub>3</sub>-edge XAS of the initial (dotted line) and charged (solid line) conditions of LCO. Panel (a) shows average spectra of selected particles including area 1-5 (circle areas: 300 nm diameter). Panel (b) shows extracted spectra from area 1-5, which exhibit different charging states (oxidation states) from each other.

[1] W.X. Zhang *et al.*, *Sci. Rep.* **13** (2023) 4639.

## Unraveling the Origin of Irreversibility between the First and Second Charging Process in Primary Conversion Anode Particle

J. Kim<sup>1</sup>, J. Chung<sup>1</sup>, T. Ohigashi<sup>2</sup>, H. Yuzawa<sup>2</sup> and J. Lim<sup>1</sup>

<sup>1</sup>Department of Chemistry, Seoul National University; 1 Gwanak-ro, Gwanak-gu, Seoul 08826, Republic of Korea

<sup>2</sup>UVSOR Synchrotron Facility, Institute for Molecular Science, Okazaki 444-8585, Japan

Among the various candidates for rechargeable lithium-ion battery anode, alpha-hematite ( $\alpha\text{-Fe}_2\text{O}_3$ ) has been actively investigated due to its high theoretical capacity (1007 mA·h/g), low processing cost, abundant remaining source, and nontoxicity. Despite these advantages, commercialization of  $\alpha\text{-Fe}_2\text{O}_3$  anode is challenging due to the fast capacity fading, particularly occurring in first and second charging process. A previous report proposed the three reaction pathways in the first charging process of  $\alpha\text{-Fe}_2\text{O}_3$  [1]. First step: monophasic insertion reaction; (1)  $\text{Fe}_2\text{O}_3 + x\text{Li}^+ \rightarrow \text{Li}_x\text{Fe}_2\text{O}_3$ . Subsequent second and third steps: biphasic conversion reaction; (2)  $\text{Li}_x\text{Fe}_2\text{O}_3 + (2-x)\text{Li}^+ \rightarrow 2\text{FeO} + \text{Li}_2\text{O}$  and (3)  $2\text{FeO} + 4\text{Li}^+ \rightarrow 2\text{Fe} + 2\text{Li}_2\text{O}$ . From our electrochemistry data (Fig. 1), it shows that the voltage plateau in the first charging is attributed to (2) and (3) distinct conversion reactions. Since this conversion reaction produces an (ir)reversible reaction product (i.e.,  $\text{Li}_2\text{O}$ ), we hypothesize that the local reaction pathway of subsequent electrochemical cycles could be influenced by the site-specific  $\text{Li}_2\text{O}$  formation in first cycle. The  $\text{Li}_2\text{O}$ , well-known insulating material, increases reaction overpotential which allows the sluggish reaction kinetics of the host material.

To reveal this degradation mechanism, we note that the nanoscale chemical distribution of  $\alpha\text{-Fe}_2\text{O}_3$  single particle at first charged/discharged states should be identified. The compositional heterogeneity within the intraparticle in first charging process allows us to investigate non-uniform intraparticle distribution of  $\text{Li}_2\text{O}$ , which insulates the subsequent electrochemical reaction. Furthermore, to unravel reaction hysteresis in first battery cycle in Fig. 1, it is essential for capturing the chemical distribution of  $\alpha\text{-Fe}_2\text{O}_3$  at first discharged state which are entangled with the first charging process. Thus, we conducted ex-situ STXM measurement of first charged/discharged states of  $\alpha\text{-Fe}_2\text{O}_3$  at UVSOR BL4U.

Fig. 2 shows chemical composition maps at pristine, first charged state, and first discharged state, revealing that chemical distribution of Fe phases is inhomogeneous within the single particle. In Fig 2b, fully charged Fe phase ( $\text{Fe}^0$ ) was partially formed and randomly distributed, suggesting that insulating  $\text{Li}_2\text{O}$  species was generated in the first charge regardless of any specific location. In Fig. 2c, the discharging end phase was not

fully recovered to the pristine state ( $\text{Fe}^{3+}$ ). This observation correlates with some previous reports [2, 3], claiming that existence of various discharging reaction pathways; (4)  $2\text{Fe} + 3\text{Li}_2\text{O} \rightarrow \text{Fe}_2\text{O}_3 + 6\text{Li}^+$ , (5)  $\text{Fe} + \text{Li}_2\text{O} \rightarrow \text{FeO} + 2\text{Li}^+$  and (6)  $3\text{Li}_2\text{O} + 2\text{Fe} \rightarrow 1.5\text{LiFeO}_2 + 0.5\text{Fe}$ . From our results, we conclude that intraparticle heterogeneity evolves in first charging process (conversion reaction) and this inhomogeneity could be affected by the distribution of the reaction product ( $\text{Li}_2\text{O}$ ), resulting in irreversibility of (dis)charging process.

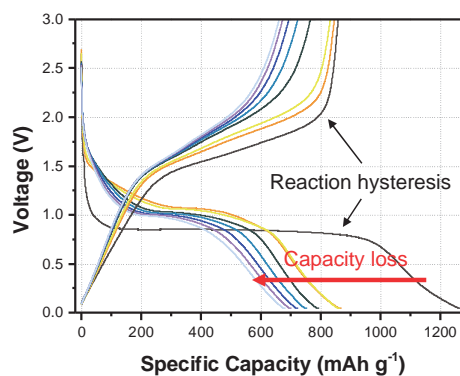


Fig. 1. Charge/discharge profiles of the synthesized  $\alpha\text{-Fe}_2\text{O}_3$  at 0.1 C current rate. (Unpublished)

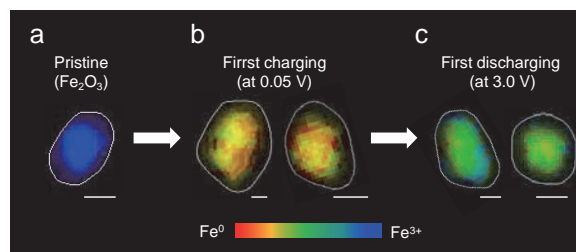


Fig. 2. Chemical composition maps at **a.** pristine, **b.** first charged state (0.05 V vs.  $\text{Li}/\text{Li}^+$ ), and **c.** first discharged state (3.0 V vs.  $\text{Li}/\text{Li}^+$ ). Scale bars below each image are 1  $\mu\text{m}$ .

- [1] A. Banerjee, *et al.*, *Nano Energy* **2** (2013) 890.  
 [2] T. C. Christie, *et al.*, *Journal of Materials Chemistry* **22** (2012) 12198.  
 [3] Su. Qingmei, *et al.*, *ACS Nano* **7** (2013) 9115.

BL4U

## Chemical Bonding Structures of SBR/BR Interfaces

T. Ejima<sup>1</sup> and Y. Tamura<sup>2</sup>

<sup>1</sup>SRIS, Tohoku University, Sendai 980-8577, Japan

<sup>2</sup>ENEOS Materials Corp., Yokkaichi 510-0871, Japan

Rubber materials used in tires often have multiple elastomers to achieve desired properties. Combining styrene-butadiene rubber (SBR) and butadiene rubber (BR) can enhance skid and rolling resistance, but increasing styrene content can reduce low-temperature performance. By using high cis-1,4 BR instead of BR and adding it to SBR, the glass transition temperature ( $T_g$ ) can be controlled, and low-temperature performance can improve [1-3]. The study used SBR and BR to fabricate interface structures with NEXAFS spectra, clarifying chemical bonding states. Understanding these states can clarify complex elastomer properties.

The preparation of the samples involved compounding SBR-A, SBR-B, and BR with a 75 ml plast mill (Toyo Seiki). The difference of the types of SBR is the difference of the crosslink density: The A type SBR (SBR-A) is normal one and the B type has a high crosslink density (SBR-B). The prepared samples were then cut into sheet shapes, and these sheets were subsequently laminated together to form a SBR-A/BR interface sheet and a SBR-B/BR interface sheet. Furthermore, a sample SBR-B/BR was kneaded by compounding SBR-B and BR at a ratio of 70:30. The resulting SBR-A/BR and SBR-B/BR interface sheets and kneaded SBR-B/BR sheet were sliced using an ultramicrotome, placed on an electron microscope grid, fixed to a dedicated STXM sample holder. The thickness of the sample was fixed at 100 nm.

The soft X-ray image of the SBR-B/BR interface sample shows the existence of a region near the interface that exhibits a spectral structure different from that of the SBR-B and BR used to prepare the sample. The two-dimensional (2D) soft X-ray absorption distributions of the SBR-B phase, the BR phase, and the residual phase are shown in Fig. 1(a). In the figure, the absorption intensity of the BR phase is shown in red, the SBR-B phase in blue, and the residual phase in green. The respective absorption intensities are represented by the respective color gradations. The simultaneously obtained spectra of the BR phase, the SBR-B phase, and the residual phase are shown in Fig. 1 (b). The color of the spectra corresponds to the color in the soft X-ray image of Fig. 1(a). The spectral intensities are normalized by the background before and after the absorption edge.

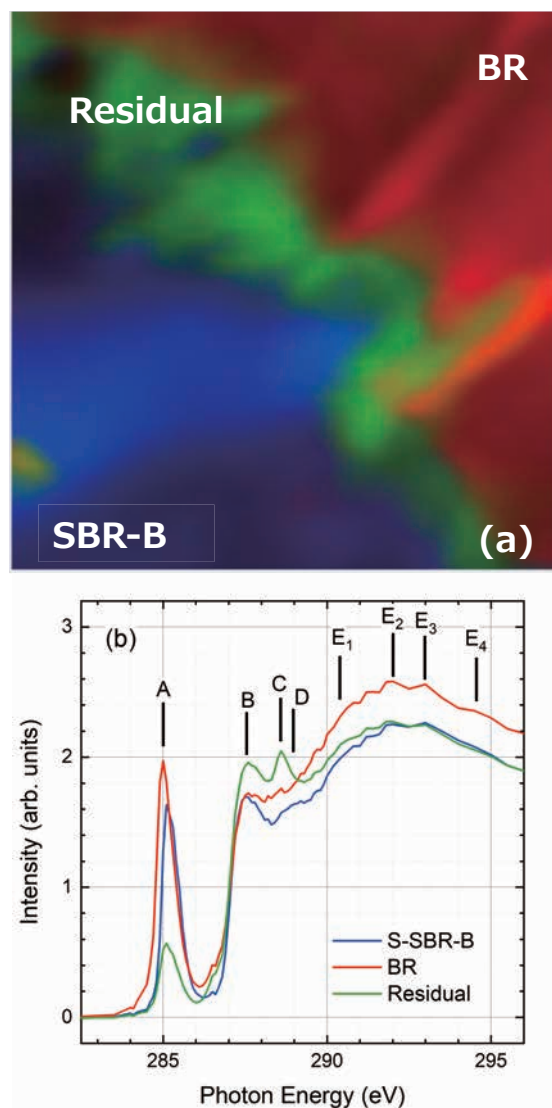


Fig. 1. (a) Material separation image of S-SBR-B/BR interface sample, (b) NEXAFS spectra of each material obtained in (a).

- [1] A. J. Marzocca, *et al.*, *Polym. Int.* **49** (2000) 216.  
 [2] J. M. Massie, *et al.*, *Rubber Chem. Technol.* **66** (1993) 276.  
 [3] H. H. Le, *et al.*, *Macromol. Mater. Eng.* **298** (2013) 1085.

## Observation of Distribution of Sulfur and cross-linking Reagent in Vulcanized Rubber by Using STXM

T. Ohigashi<sup>1,2,3</sup>, F. Kaneko<sup>4</sup>, H. Yuzawa<sup>2</sup> and H. Kishimoto<sup>4</sup>

<sup>1</sup>*Institute of Material Structure Science, High Energy Accelerator Research Organization, Tsukuba 305-0801, Japan*

<sup>2</sup>*UVSOR Synchrotron Facility, Institute for Molecular Science, Okazaki 444-8585, Japan*

<sup>3</sup>*School of Physical Sciences, The Graduate University for Advanced Studies (SOKENDAI), Tsukuba 305-0801, Japan*

<sup>4</sup>*Sumitomo Rubber Industries Ltd., Kobe 651-0072, Japan*

In recent years, SDGs (Sustainable Development Goals) is a keyword to represent attitude of our daily life. Especially, reduction of mass consumption is a critical issue. Rubber is one of the important resources and its demand is assumed to increase especially according to growth of car industries. To reduce its consumption, establish of LCA (Life Cycle Assessment) of rubber industrialization and further improvement of functionality of rubbers, such as wear- and destruction-resistant, are essential.

Rubber is generally heterogeneous network structure, which is produced by rubber polymer and cross-linking agent (vulcanization). Since the remained cross-linking reagent in this structure is heterogeneously distributed, it gathers internal stress of rubber deformation to cause the destruction. Therefore, dispersion of a cross-linking reagent in the rubber is an important parameter to determine mechanical character of rubber. However, it is not easy to observe the dispersion because the cross-linking reagent in rubber is so small amount and is consisted of light elements.

We have been characterized rubber by using scanning transmission X-ray microscopy (STXM) at BL4U [1,2]. STXM is a powerful tool to obtain 2-dimensional X-ray absorption spectroscopy by near edge X-ray absorption fine structure (NEXAFS) with high spatial resolution around 30 nm. Moreover, STXM gives much less radiation damage to the sample than by electron microscopy. Therefore, STXM is the best approach for this study. In this report, the distribution of cross-linking reagent in vulcanized rubber is investigated by STXM.

The sample is styrene-butadiene rubber with zinc oxide, sulfur, N-cyclohexyl-2-Benzothiazolylsulfenamide (CBS), 3-diphenylguanidine (DPG) as cross-linking reagents. The rubber was cut as 200 nm-thick by ultramicrotome and was placed on a TEM grid. As reference samples, CBS, DPG and 2-mercaptobenzothiazole (MBT) were dispersed in acetone and were drop-casted onto TEM grids with support membrane. X-ray absorption images of unvulcanized and vulcanized rubbers taken at 400 eV are shown in Fig. 1. In these images, dark spots show higher absorption than matrix and are considered as distribution of cross-linking reagents. By comparing Figs. 1(a) and 1(b), dark spots decrease in size and

become more dispersive through a vulcanization process. Normalized N *K*-edge NEXAFS spectra of reference samples of CBS (blue), DPG (green), MBT (red) and the dark spot (black; shown by an arrow in Fig. 1(b)) are shown in Fig. 2. Although the signal of the dark spot is quite low, the dark spot seems to be consisted of mixture of CBS, DPG and MBT. Especially, the sharp peak of MBT at 400.8 eV contributes to that of the dark spot. MBT was produced by vulcanization process and contributed to the distribution of cross-linking reagent.

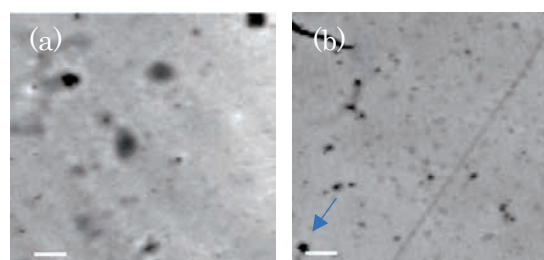


Fig. 1. X-ray absorption image of (a) unvulcanized and (b) vulcanized rubbers taken at 400 eV. Scale bars are 5  $\mu\text{m}$ .

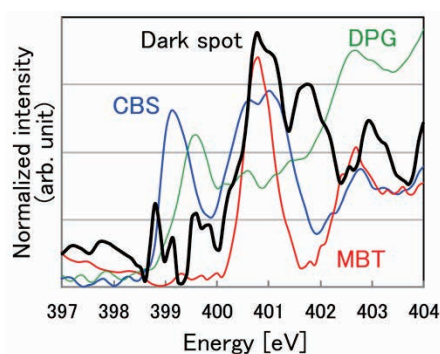


Fig. 2. N *K*-edge NEXAFS spectra of CBS (blue), DPG (green), MBT (red) and a dark spot (shown in Fig. 1 by an arrow). The spectra are normalized by max and minimum.

[1] T. Ohigashi, F. Kaneko, H. Yuzawa and H. Kishimoto, *UVSOR Activity Report 2021*, **49** (2022) 73.

[2] T. Ohigashi, *et al.*, *J. Electron Spectrosc. Relat. Phenom.* **266** (2023) 147356.

BL4U

## Scanning Transmission X-ray Microscopy of Hydrogen Evolution Electrocatalysts on Graphene Oxide Membranes

C. O. M. Mariano<sup>a</sup>, J. S. D. Rodriguez<sup>a,b</sup>, R. H. Clemente<sup>a</sup>,

T. Ohigashi<sup>c,d</sup>, H. Yuzawa<sup>c</sup>, W. H. Hsu<sup>e</sup>, J. Shiue<sup>f</sup> and C. H. Chuang<sup>a,\*</sup>

<sup>a</sup>Department of Physics, Tamkang University, Tamsui, New Taipei City 251301, Taiwan

<sup>b</sup>Institute of Chemistry, Leiden University, Leiden, 2300 RA, The Netherlands

<sup>c</sup>Institute for Molecular Science, Okazaki 444-8585, Japan

<sup>d</sup>Photon Factory, Institute of Materials Structure Sciences, High Energy Accelerator Research Organization, Tsukuba 305-0801, Japan

<sup>e</sup>Institute of Physics, Academia Sinica, Nankang, Taipei 11529, Taiwan

<sup>f</sup>Institute of Atomic and Molecular Sciences, Academia Sinica, Daan, Taipei 106319, Taiwan

The oxygen functional groups present in GO have effects on the HER activity of cobalt catalyst ( $\text{Co}_x\text{O}_y$ ) and should be studied for its specific role thoroughly. GO has several oxygen functional groups, i.e., carboxyl (-COOH), carbonyl (C=O), hydroxyl (-OH), and epoxide groups (C-O-C). These functional groups are important because they can interact with the cobalt ions, which increases the catalytic activity for the HER. The oxygen functional groups of GO can be identified using such as fourier-transform infrared spectroscopy, raman spectroscopy, and X-ray photoelectron spectroscopy, but to acquire additional information about the spatial distribution of these functional groups, scanning transmission X-ray microscopy (STXM) must be used [1].

This study aims to understand the relationship between the oxidation state of  $\text{Co}_x\text{O}_y$  supported on GO membranes (called as Co/GO), for their catalytic activities. Fig. 1(a) shows the surface morphology of the dropcast GO membranes measured using the tapping mode of AFM. The vertical difference along the line profile (red arrow) was noted as 46 nm because a random flake stacking of the GO on the Au mesh behaves like a rough surface after drying. Fig. 1(b) exhibits a SEM image for the  $\text{Co}_x\text{O}_y$  grown on GO membranes, and Fig. 1(c) shows a high magnification image of Co/GO to display the 3D wrinkle flower structure of electrodeposited (ED) Co.

To identify the nanoscale distribution of these heterogeneous materials, STXM was measured in the energy regions of C *K*-edge, O *K*-edge, and Co *L*-edge XANES. The area-selected spectra are marked as “1”, “2”, and “3” owing to the prominent contrast in the OD image at C/O *K*-edges and Co *L*-edge, as for the total absorbance amount of Co/GO membranes. From the C *K*-edge XANES of Fig.1(d), the oxygen functional groups (C-O-C, C=O of COOH, and C=O) in the GO membranes were assigned based on our previous result [1]. The feature at 284.9 eV was assigned to the formation of doubly coordinated carbon, because of the ring opening and modifying  $\pi^*$  bond [2]. The intensive feature at 288.4 eV is known as HO-C=O ( $\pi^*$ )/defect state and its low-energy shoulder nearby at 287.4 eV is assigned to C-O-C ( $\pi^*$ ) state; furthermore, the most intensive feature and its shoulder are identified as O-C(O)-O/C=O ( $\pi^*$ ) of the GO edge at 290.2 eV and HO-C=O ( $\sigma^*$ ) state at 289.5 eV [1,2,3]. C-OH ( $\pi^*$ ) at 286.5 eV appears in the raw GO membranes [1] but is absent in Co/GO membranes.

Fig. 1(e) exhibits the area-selected O *K*-edge XANES spectra of Co/GO and GO. Compared the spectrum Co/GO with that of GO, the signal of O *2p*-Co *3d* ( $\pi^*$ ) and

Co-4s ( $\sigma^*$ ) newly centered at PE of 531.5 eV and 539.5 eV [3,4]. The surface oxidation (i.e., C=O and C-O-C) of the GO membranes also emerges among the feature centered at 531.5 eV [1]. Furthermore, it is critical to see one shoulder at the 534.4 eV, mainly considered a water signal[5]. Fig. 1(f) shows Co *L*-edge XANES spectra, which are composed of spectral components of  $\text{Co}^0$ ,  $\text{Co}^{2+}$ , and  $\text{Co}^{3+}$  states. The octahedral (Oct.) symmetrical  $\text{Co}^{2+}$  state composes of two features at 775.0 and 776.2 eV. The metal species of cobalt has one primary absorption at 776.2 eV because its energy levels are continuous. The Oct. symmetrical  $\text{Co}^{3+}$  state offers two additional features at 777.3 and 779.6 eV, with a higher energy range than the other cobalt species[3]. The rising shoulder shows the gains of metal cobalt and Oct.  $\text{Co}^{3+}$  states due to the chemical reduction and growth along the continuous electrodeposition process, consistent with the result on the G membranes (Co/G) in Fig. 1(f) [3].

The Co/GO membranes became a great variety in the oxidation state and lattice structure at the interface, compared to the raw GO surface. The mapping and spectroscopic information at different positions helps us to understand the chances of ED  $\text{Co}_x\text{O}_y$  growth on the confirmed GO membranes.

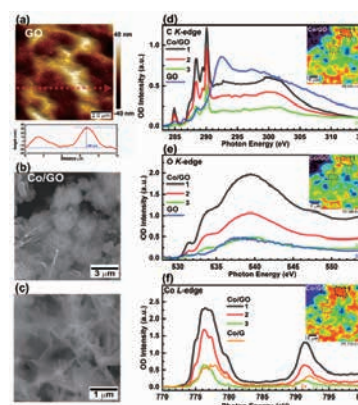


Fig. 1. (a) AFM image of GO membranes and certain curve of its height line profile along the red dotted arrow. (b)(c) SEM image of electrodeposited Co-GO membranes. (d)-(f) XANES spectra of selected areas at C *K*-edge, O *K*-edge, and Co *K*-edge.

- [1] J.S.D. Rodriguez *et al.*, Carbon N Y. **185** (2021) 410.
- [2] J.J. Vélez *et al.*, Electrochem. Soc. **160** (2013) C445.
- [3] J.-J.V. Vélez *et al.*, Chin. J. Phys. **76** (2022) 135.
- [4] J. Wang *et al.*, Energy Environ. Sci. **6** (2013) 926.
- [5] J.W. Smith *et al.*, Chem. Rev. **117** (2017) 13909.

## Examination of Methods for Inner Structures of Magnetic Thin Films at UVSOR BL4B by Reflection XMCD Measurement Setup

K. Yamamoto, H. Iwayama, O. Ishiyama and T. Yokoyama  
*Institute for Molecular Science, Okazaki 444-8585, Japan*

Complex depth-structured magnetic thin films/multilayers exhibit a wide range of magnetic phenomena due to interlayer interactions[1]. In addition, multilayer structures are used to achieve useful properties in recording media, an application area of great importance for magnetic materials. It has been possible to elucidate the evolution mechanism of the magnetic structure of thin films by directly observing the magnetic distribution in the depth direction of these magnetic multilayers.

We have installed an experimental setup for the reflection X-ray magnetic circular dichroism (XMCD) method [2] in the soft X-ray region at BL4B, and experiments have been performed on test samples. The sample and detector can be rotated independently to obtain the reflectivity. The magnetic field was about 0.35T and the measurements were performed at room temperature. The magnetic field was applied by two pairs of opposing Nd magnets. The magnets can be rotated and the relative position between the magnetic field and the sample was kept constant. The setup is shown schematically in Fig. 1. We used a photodiode (AXUV100G, Optodiode inc.) for our measurements last year. In order to measure the lower signals in the higher angle regions and to eliminate the fluorescence of oxygen from the substrates, we introduced a silicon drift detector (FASTSDD, Amptek). The detector temperature was controlled by water cooling and the noise level was kept constant at lower levels and the detector and samples can be rotated arbitrary in the vacuum chamber shown in Fig. 2.

We used off-axis components of X-rays from the bending magnet to obtain circularly polarised light. The X-rays are elliptically polarised. The intensity of the XMCD was measured by changing the direction of the magnetic field.

When measurements were performed on a reference sample, a vibrational structure was observed due to interference between the cap layer and the underlying layer. By changing the direction of the magnetic field, differences corresponding to XMCD were observed. The same measurements were also made near the absorption edge and spectroscopic information was extracted. However, structural information is not well obtained compared to hard x-rays. Using an X-ray tube light source, we also performed hard x-ray reflectometry.

Both soft and hard X-ray results could be reproduced by simulations based on a full-matrix algorithm, taking into account the magneto-optical effects of elliptically polarized X-rays. Although there have been previous studies using XMCD of reflectance, few have extended this method to obtain spectroscopic information. In order to analyze depth-resolved magnetization information, spectroscopic measurements were performed to obtain the photon energy dependence and the reflection angle dependence.

Combining this study with a light source that can arbitrarily modulate polarization would provide a method to reveal more detailed properties.

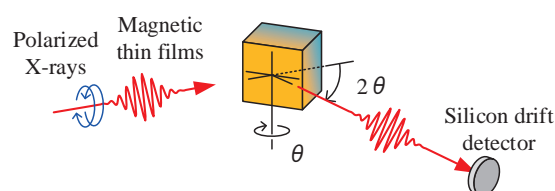


Fig. 1. The illustration for the XMCD reflectivity measurements.

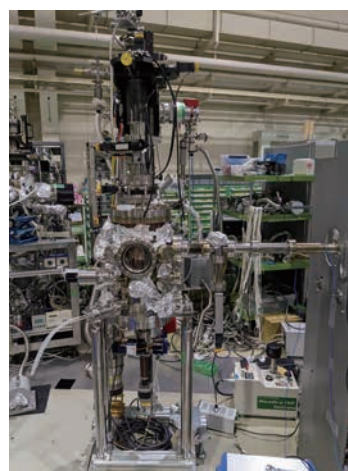


Fig. 2. The vacuum chamber for the measurements in UVSOR BL4B.

[1] F. Hellman *et al.*, *Rev. Mod. Phys.* **89** (2017) 025006.

[2] S. Macke and E. Goering, *J. Phys. Condens. Matter.* **26** (2014) 363201.

BL4B

## L<sub>2,3</sub>-edge X-ray Absorption Spectra of Transition Metal in Wurtzite-AlN

S. Imada

Faculty of Electrical Engineering and Electronics, Kyoto Institute of Technology, Kyoto 606-8585, Japan

3d-TM doped AlN (Al<sub>1-x</sub>TM<sub>x</sub>N) is promising for light-emitting, spintronic, and photoelectric conversion materials [1,2]. For these applications, it is indispensable to reveal the electric structure, including ligand field and charge transfer multiplets. For this purpose, TM L<sub>2,3</sub>-edge X-ray absorption structure (XAS) and resonant X-ray emission scattering (RIXS) spectroscopies are powerful tools. So far, however, a comprehensive and systematic study of these important systems still needs to be included.

We synthesised and investigated the band structures of Al<sub>1-x</sub>TM<sub>x</sub>N using Al and N K-edge XAS [2-4]. This study investigated TM L<sub>2,3</sub>-edge XAS structures of Al<sub>1-x</sub>TM<sub>x</sub>N films with various TM concentrations (0.02 < x < 0.08), focusing on Ti, V and Mn for the first time. For example, with low concentrations x < 0.05, the average distance between TMs is larger than 7.5 Å; we expect to observe a well-localised electronic structure. Looking ahead, we can even prepare films including other TMs with concentrations well above 0.1 (< 6 Å) to reveal interactions between TMs, which are necessary to understand for spintronic and photoelectric conversion use.

Here we show an example of the TM concentration dependence of the XAS structure for Al<sub>1-x</sub>Ti<sub>x</sub>N. Our previous study [2] revealed that the Al<sub>1-x</sub>Ti<sub>x</sub>N films with x ≥ 0.083 showed photoconductivity under blue-green light irradiation, while the film with x < 0.083 did not. The Ti L<sub>2,3</sub>-edge XAS spectra of Al<sub>1-x</sub>Ti<sub>x</sub>N films showed structural change at x = 0.083 (Fig.1). Our previous study on Ti K-edge extended X-ray absorption fine structure (EXAFS) did not show any evidence of local crystallographic structure change at the concentration. Thus, we tentatively conclude that the observed change

in L<sub>2,3</sub>-edge XAS implies delocalisation of Ti 3d electrons starts at around x = 0.083. To reveal the origins of the spectral change in detail, we will conduct L-edge RIXS measurements and partial RIXS yield (PRIXS) analyses, which will give us new insights into XAS structure interpretation.

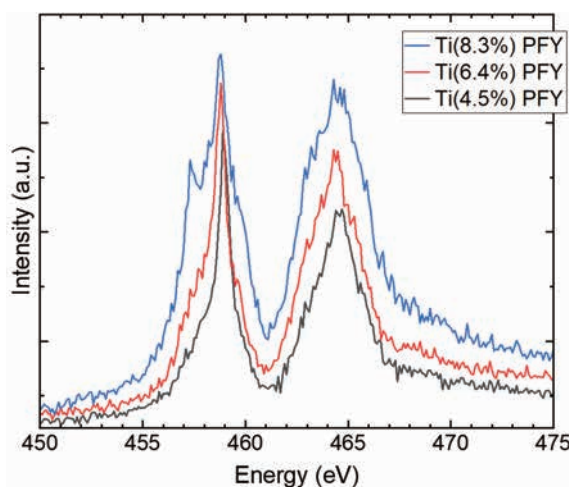


Fig. 1. Ti L<sub>2,3</sub>-edge X-ray absorption spectra of Al<sub>1-x</sub>Ti<sub>x</sub>N films (x = 0.083, 0.064, and 0.045). These spectra were measured in partial fluorescence yield (PFY) mode.

- [1] S. S. Khludkov *et al.*, Russian Physics Journal **63** (2020) 2013.
- [2] N. Tatemizo *et al.*, J. Mater. Chem. A **5** (2017) 20824.
- [3] N. Tatemizo *et al.*, Sci. Rep. **10** (2020) 1819.
- [4] S. Imada *et al.*, Matr. Adv. **2** (2021) 4075.

## C K-edge XAFS Measurement of Carbon Containing Porous Silica

S. Dohshi

*Osaka Research Institute of Industrial Science and Technology  
2-7-1, Ayumino, Izumi, Osaka 594-1157, Japan*

Porous silica with only micropores of less than 1 nm in diameter has been successfully synthesized by using collagen fibers or denatured collagen as a template [1]. As a result of a detailed study of the process of removing collagen as a template by calcination, we found that the porous silica with a small amount of carbon (hereafter denoted as carbon containing porous silica) showed white luminescence under UV light irradiation [2]. The emission spectrum of the prepared carbon containing porous silica under UV excitation shows a continuous spectrum over the visible light region, and this carbon containing porous silica is expected to be used as a white light source material with high color rendering property. The author investigated the mechanism of white luminescence of carbon-containing porous silica. Since porous silica without carbon does not show white light luminescence property under UV light irradiation, it is clear that carbon in porous silica contributes to luminescence property. However, the local structure of carbon in porous silica has not yet been elucidated because the carbon content is very low, about 0.1%. Therefore, in this study, we attempted to elucidate the local structure of carbon in porous silica by C K-edge XAFS measurement using BL4B of UVSOR III. We optimized the sample preparation method and measurement conditions.

Fig. 1 shows the experimental setup at BL4B and the sample holder for C K-edge XAFS measurement. The powder sample was fitted onto carbon tape or indium foil. The measurement was performed by fluorescence mode (using SDD detector).

When the sample was fixed on the carbon tape, the spectra derived from the carbon tape were observed, and almost no spectra derived from the sample were observed. On the other hand, when the sample was fixed on indium foil, the spectra derived sample was obtained. It was also found that the X-ray irradiation angle to the sample had a significant effect on the intensity of the spectra.

In the next fiscal year, we will measure the C K-edge XAFS measurement using pelletized sample under the optimized conditions.

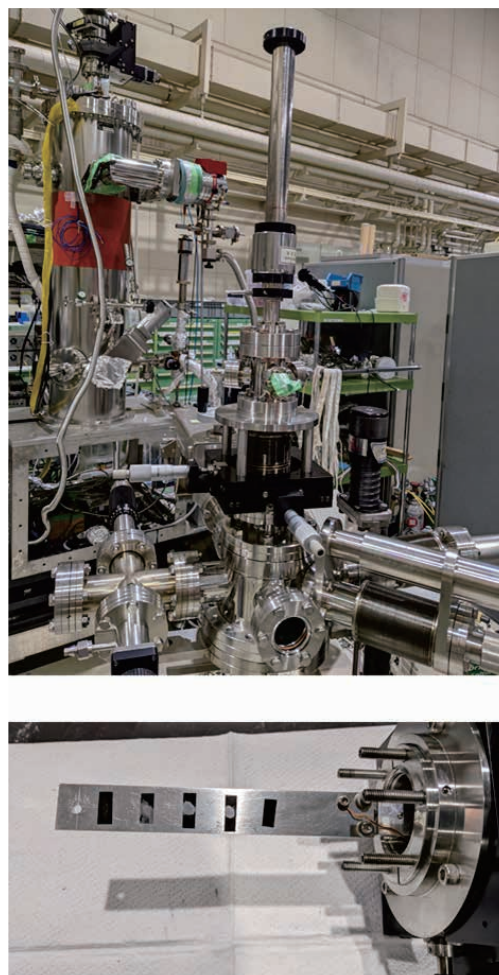


Fig. 1. The experimental setup at BL4B and the sample holder for C K-edge XAFS measurement.

[1] S. Dohshi, *J. Soc. Leather Technol. Chem*, **95** (2011) 200.

[2] S. Dohshi *et al.*, *J. Soc. Mater. Sci., Jpn.*, **68** (2019) 549.

BL5U

## Evolution of the Electronic States by Electron Doping in a Kagome Superconductor $KV_3Sb_5$

T. Kato<sup>1</sup>, K. Nakayama<sup>1</sup>, Y. Li<sup>2,3,4</sup>, Z. Wang<sup>2,3,4</sup>, S. Souma<sup>5,6</sup>, K. Tanaka<sup>7,8</sup>, T. Takahashi<sup>1</sup>, Y. Yao<sup>2,3</sup> and T. Sato<sup>1,5,6,9</sup>

<sup>1</sup>Department of Physics, Graduate School of Science, Tohoku University, Sendai 980-8578, Japan

<sup>2</sup>Centre for Quantum Physics, Key Laboratory of Advanced Optoelectronic Quantum Architecture and Measurement (MOE), School of Physics, Beijing Institute of Technology, Beijing 100081, P. R. China

<sup>3</sup>Beijing Key Lab of Nanophotonics and Ultrafine Optoelectronic Systems, Beijing Institute of Technology, Beijing 100081, P. R. China

<sup>4</sup>Material Science Center, Yangtze Delta Region Academy of Beijing Institute of Technology, Jiaxing, 314011, P. R. China

<sup>5</sup>Advanced Institute for Materials Research (WPI-AIMR), Tohoku University, Sendai 980-8577, Japan

<sup>6</sup>Center for Science and Innovation in Spintronics (CSIS), Tohoku University, Sendai 980-8577, Japan

<sup>7</sup>UVSOR Synchrotron Facility, Institute for Molecular Science, Okazaki 444-8585, Japan

<sup>8</sup>School of Physical Sciences, The Graduate University for Advanced Studies (SOKENDAI), Okazaki 444-8585, Japan

<sup>9</sup>International Center for Synchrotron Radiation Innovation Smart (SRIS), Tohoku University, Sendai 980-8577, Japan

Recent discovery of a new kagome-lattice material  $AV_3Sb_5$  ( $A = K, Rb,$  and  $Cs$ ) is attracting great attention. While most of the kagome-lattice materials studied so far have been magnetic,  $AV_3Sb_5$  is unique in that it is paramagnetic and shows superconductivity with  $T_c$  of 0.93-2.5 K.  $AV_3Sb_5$  also undergoes a charge-density wave (CDW) transition below  $T_{CDW} = 78$ -103 K, accompanied by the unit-cell doubling with the  $2 \times 2 \times 2$  periodicity. This CDW state shows an intriguing interplay with the superconductivity and hosts exotic properties such as strong anomalous Hall effect, possible time-reversal symmetry breaking, and nematicity. From the electronic structure point of view,  $AV_3Sb_5$  is a multiband/multi-orbital superconductor characterized by the formation of multiple Fermi surfaces originating from Dirac-cone, saddle-point, and free-electron-like bands. Given the multiband character, it is essential to understand which bands/orbitals are responsible for the CDW and superconductivity. A useful means to clarify this point is to control the energy position of bands relative to the Fermi level ( $E_F$ ) by carrier doping [1] because the CDW and superconductivity would be sensitive to the band filling.

In this study, we have performed an angle-resolved photoemission spectroscopy (ARPES) study on K-dosed  $KV_3Sb_5$ . We have successfully controlled electron doping level by K dosing and determined the doping-induced evolution of the band structure.

High-quality single crystals of  $KV_3Sb_5$  were grown by the self-flux method. K dosing was carried out by using K dispenser (SAES Getters) in an ultrahigh vacuum. High-resolution ARPES measurements were performed by using a MBS-A1 spectrometer at BL5U with linearly-polarized energy-tunable photons.

A comparison of Fermi surfaces in pristine [2] and

K-dosed  $KV_3Sb_5$  [Figs. 1(a) and 1(b), respectively] shows that a circular-shaped electron pocket at the  $\Gamma$  point expands with the K dosing, indicative of the electron doping. We have estimated the amount of energy shift for each band and found band/orbital-dependent electron doping effect. In addition, we determined the evolution of CDW gap size with electron doping. Our results suggest an important role of the saddle-point band for the occurrence of CDW.

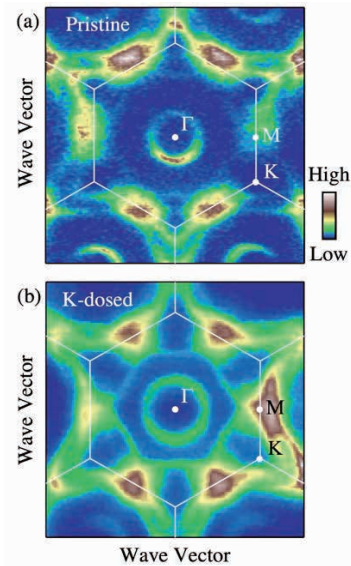


Fig. 1. (a), (b) ARPES intensity plots at  $E_F$  in freshly cleaved and K-dosed  $KV_3Sb_5$ , respectively

[1] K. Nakayama *et al.*, Phys. Rev. X **12** (2022) 011001.

[2] T. Kato *et al.*, Commun. Mater. **3** (2022) 30.

## Evolution of Electronic Correlations and Excitonic Properties Near semiconductor-excitonic Insulator Transition

K. Fukutani<sup>1,2</sup>, K. Kiyosawa<sup>3</sup>, C.I. Kwon<sup>4,5</sup>, J.S. Kim<sup>4,5</sup>, K. Tanaka<sup>1,2</sup> and S. Kera<sup>1,2,3</sup>

<sup>1</sup>Institute for Molecular Science, Okazaki 444-8585, Japan

<sup>2</sup>The Graduate University for Advanced Studies (SOKENDAI), Okazaki 444-8585, Japan

<sup>3</sup>Graduate School of Science and Engineering, Chiba University, Chiba 263-8522, Japan

<sup>4</sup>Center for Artificial Low-Dimensional Electronic Systems, Institute for Basic Science, Pohang, Korea

<sup>5</sup>Pohang University of Science and Technology, Pohang, Korea

In semiconductors, external stimuli, such as light irradiations are known to create bound pair of an electron and a hole. This quasi-particle is known as excitons, and are known to play principal roles in various quantum devices, including solar cells, light emitting diode (LED), and excitonic lasers etc. The efficient creation of excitons and the manipulations of their properties are among the central interest in the current semiconductor industry.

Recently, what is called an *excitonic insulator* has been experimentally identified. This new class of materials is either a narrow-gap semiconductor or a shallow-overlap semimetal in their normal phase and, at sufficiently low temperature, the electrons and holes are spontaneously paired into excitons via quantum condensation process.

$\text{Ta}_2\text{NiSe}_5$  is one of the most extensively studied excitonic insulators [1], along with  $1T\text{-TiSe}_2$ . What differentiates  $\text{Ta}_2\text{NiSe}_5$  from  $1T\text{-TiSe}_2$  is the fact that the former exhibits a direct band gap and does not accompany the change in the structural periodicities (charge density wave transition). Thus, from the point of view of excitonic instability,  $\text{Ta}_2\text{NiSe}_5$  is ideal platform to study the nature of excitonic insulator and the transition to/from the normal phase.

The recent extensive researches have revealed that  $\text{Ta}_2\text{NiSe}_5$  is classified into Bose-Einstein condensate (BEC)-type excitonic insulator, while it is near the crossover regime between BEC and BCS transitions.

Theoretically, in the BEC-type excitonic insulator, the excitons are created *above* the transition temperature ( $T_c$ ) and as they cool down below  $T_c$ , those “preformed excitons” undergo the condensation and acquire the macroscopic coherence [2]. The temperature (and band gap) regime where such steady-state excitons exist without forming a condensate is called “preformed exciton phase” and its existence has been recently verified [3].

Such phase of steady-state excitons represents the inverted ground state from the normal semiconductors (i.e., the excitons are formed in the *ground state*, while the external stimuli are required to dissociate them into free carriers) and provides a particularly unique playground for future electronics applications.

The purpose of this research project is to explore the excitonic insulator phase diagram both in terms of temperature and the bandgap to evaluate the properties of the steady-state excitons, including its binding

energy, Bohr radius and their relative density (compared to the free carriers), in order to understand the formation process of this new ground state.

With these goals, we have performed high-resolution angle-resolved photoemission spectroscopy (ARPES) at BL5U for the chalcogen-substituted compounds  $\text{Ta}_2\text{Ni}(\text{Se}_{1-x}\text{S}_x)_5$  with particular focus at the composition  $x \sim 0.6$ , where the material is believed to be very close to the transition between a BEC-type excitonic insulator and a normal semiconductor. Figure 1 shows the temperature-dependent ARPES spectra for this composition. It can be seen that at  $T \sim 120$  K, the material exhibits a flat-top valence band, characteristic of excitonic insulator phase. As the temperature rises, at  $T \sim 200$  K, the clear signature of exciton appears near the valence band maximum and at  $T \sim 350$  K, the valence band maximum is no longer flat, reminiscent of the normal semiconductor  $\text{Ta}_2\text{NiS}_5$ , and the weakened exciton signal moves towards the Fermi level with the valence band. These observations possibly indicates that as the temperature increases, the electronic correlations, which are keeping the excitons bound, are weakening at the same time as the exciton binding energy decreases. The experimental results obtained here are expected to give new insights into the formation path of excitons.

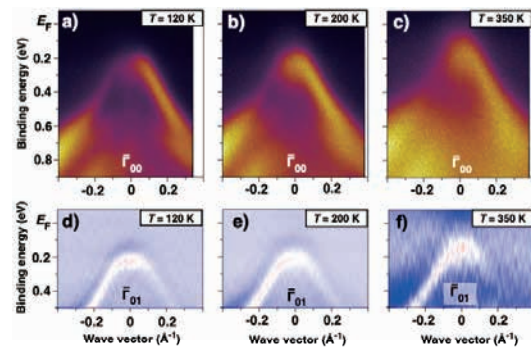


Fig. 1. Temperature-dependent ARPES data from  $\text{Ta}_2\text{Ni}(\text{Se}_{1-x}\text{S}_x)_5$  at  $x \sim 0.6$  measured at (a)  $T \sim 120$  K, (b) 200 K and (c) 350 K. The second derivative plots from  $\Gamma_{01}$  are shown on the bottom panel (d-f).

[1] Y. Wakasaka *et al.*, Phys. Rev. Lett. **102** (2009) 026402.

[2] Y.F. Lu *et al.*, Nat. Commun. **8** (2017) 14408.

[3] F.X. Bronold *et al.*, Phys. Rev. B **74** (2006) 165107.

[4] K. Fukutani *et al.*, Nat. Phys. **17** (2021) 1024.

BL5U

## Polarization-dependent Angle-resolved Photoemission Study of MAX Phase Compound $Zr_3SnC_2$

M. Mita<sup>1</sup>, D. Pinek<sup>2</sup>, M. Nakatake<sup>3</sup>, K. Tanaka<sup>4,5</sup>, T. Ouisse<sup>2</sup> and T. Ito<sup>1,6</sup>

<sup>1</sup>Graduate School of Engineering, Nagoya University, Nagoya 464-8603, Japan

<sup>2</sup>Grenoble Alpes, CNRS, Grenoble INP, LMGP, F-38000 Grenoble, France

<sup>3</sup>Aichi Synchrotron Radiation Center, Seto, 489-0965, Japan

<sup>4</sup>UVSOR Facility, Institute for Molecular Science, Okazaki 444-8585, Japan

<sup>5</sup>The Graduate University for Advanced Studies, Okazaki 444-8585, Japan

<sup>6</sup>Synchrotron radiation Research center, Nagoya University, Nagoya 464-8603, Japan

MAX phase compounds, i.e.,  $M_{n+1}AX_n$  where M is a transition metal, A belongs to groups 13-16 and X is the C or N element, have recently been attracted much attention due to their possible application for new class of two-dimensional systems called MXenes by removing A atoms [1]. On the other hand, the bulk electronic structure of MAX phase has been studied mostly by calculations, mainly because of lack of well-established single crystalline samples. In this study, we have performed angle-resolved photoemission spectroscopy (ARPES) on MAX phase compound  $Zr_3SnC_2$ , in which relatively higher two-dimensionality than 211 phase due to the thicker MX layer as well as the strong spin-orbit coupling effect due to the 4d transition metal Zr were expected.

ARPES measurements were performed at the UVSOR-III BL5U. Data were acquired at  $T = 30$  K with  $h\nu = 76$  eV which enables us to trace around the  $\Gamma$ KM plane with inner potential of  $V_0=17.7$  eV estimated from the photon energy dependent measurement (not shown). With using linear horizontally (LH), vertically (LV) and circularly right (CR), left (CL) polarized photons, we have obtained the orbital and orbital-angular-momentum (OAM) dependent ARPES images. It should be noted that each ARPES images were obtained without changing the photon incident angle relative to the sample surface by utilizing two-dimensional mapping lens mode of MBS A-1 analyzer.

Figure 1 shows the obtained Fermi surface (FS) image on the  $\Gamma$ KM plane. The band structure along the  $\Gamma$ M line is shown in Fig. 2 (a) together with the DFT calculation of Sn-terminated surface. Six-fold symmetry of hole-pockets  $\alpha$  and  $\beta$  has clearly been observed in consistent with the DFT calculation. In addition, three-fold symmetry around the K point of the small triangular-shape FS  $\gamma$  formed by so-called saddle-like surface state (SS) at the M point also has been elucidated in Fig.1. With respect to this SS, even orbital symmetry has been recognized with almost the same circular dichroism (Fig. 2(b) and (c)). On the other hand, opposite OAM sign without changing orbital symmetry with respect to the MK line has been

observed at the high-binding energy region. The results might suggest the change of chirality of OAM at the high-energy bound states at the Sn-terminated surface of  $Zr_3SnC_2$ . To elucidate the relation between the observed anomalies and the spin-orbit coupling effect, further studies are intended.

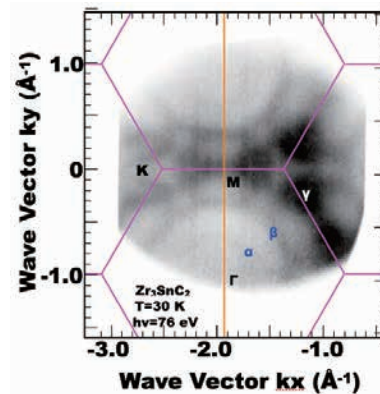


Fig. 1. (a) Fermi surface (FS) image on  $\Gamma$ KM plane of  $Zr_3SnC_2$ .

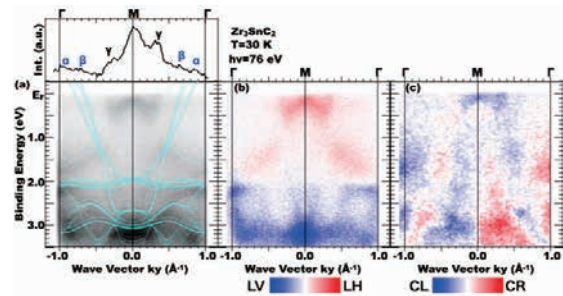


Fig. 2. (a) Band structure along the  $\Gamma$ M line of  $Zr_3SnC_2$  obtained by LH polarized photons. Solid lines are DFT calculation for Sn-terminated surface. (b,c) orbital (b) and OAM (c) dependent ARPES image of  $Zr_3SnC_2$  along the  $\Gamma$ M line, which is obtained by subtracting the ARPES results of linearly (LH–LV) and circularly (CR–CL) polarized photons, respectively.

[1] M. Basoum, *MAX phases* (Wiley, Weinheim 2013).

## Electronic Structure of a Layered Magnetic Semiconductor $\text{CeTe}_{1.83}\text{Sb}_{0.17}$

T. Nakamura<sup>1,2</sup>, H. Murakawa<sup>2</sup>, Y. Chen<sup>2</sup>, H. Sugihara<sup>2</sup>, K. Tanaka<sup>3</sup>,  
N. Hanasaki<sup>2</sup> and S. Kimura<sup>1,2,3</sup>

<sup>1</sup>Graduate School of Frontier Biosciences, Osaka University, Suita 565-0871, Japan

<sup>2</sup>Department of Physics, Graduate School of Science, Osaka University, Toyonaka 560-0043, Japan

<sup>3</sup>Institute for Molecular Science, Okazaki 444-8585, Japan

The metal-insulator transition through charge density wave (CDW) formation has been a central topic of solid-state physics. While many materials have been reported to exhibit CDW,  $\text{CeTe}_2$ , a family of rare-earth dichalcogenide, has attracted considerable interest due to its high transition temperature that reaches 1000 K [1,2] as well as magnetic ordering below 4 K [3]. Recently,  $\text{CeTe}_{1.83}\text{Sb}_{0.17}$ , which shows a huge anisotropic magnetoresistance ratio as high as 7500 thanks to the extremely low carrier density, has been synthesized by a chemical vapor transport technique [4]. Due to the partial substitution of Te with Sb, an extra charge carrier removes by hole doping. However, the detail of the electronic band structure of this sample has not been observed yet. In this study, we have measured the angle-resolved photoelectron spectroscopy (ARPES) of the  $\text{CeTe}_{1.83}\text{Sb}_{0.17}$  to investigate the electronic structure.

The single-crystalline  $\text{CeTe}_{1.83}\text{Sb}_{0.17}$  was cleaved under ultra-high vacuum conditions. Due to the difficulty of cleavage, the ARPES measurable domain size was less than  $100 \times 100 \mu\text{m}^2$ . However, the micro-focused beam from UVSOR-III BL5U made it possible to observe the electronic structure in a piece of domains.

Figure 1 shows the resonant angle-integrated photoelectron spectra of  $\text{CeTe}_{1.83}\text{Sb}_{0.17}$ , taken with the energy of 122 eV, corresponding to the resonant energy of the Ce  $4d-4f$  absorption. In contrast to the non-resonant condition ( $h\nu = 110 \text{ eV}$ ), the sharp peak at a binding energy of 1.7 eV originates from the Ce  $4f^0$  final states after photoexcitation was observed in the resonant condition, indicating that the Ce  $4f$  states are fully localized.

Figure 2 shows the ARPES intensity plot along  $\Gamma$ -M at 15 K. Several hole bands near the  $\Gamma$  point are observed. Among them, the apex of band H1, which is at the outermost part of the measurement range, seems to be in an unoccupied state, indicating that it exhibits metallic properties even though extremely low carrier densities are confirmed in the transport measurements. Further experimental studies such as polarization dependence and bulk sensitive measurement using higher energy photons would help to elucidate the orbital character of bands in the electronic structure of  $\text{CeTe}_{1.83}\text{Sb}_{0.17}$ .

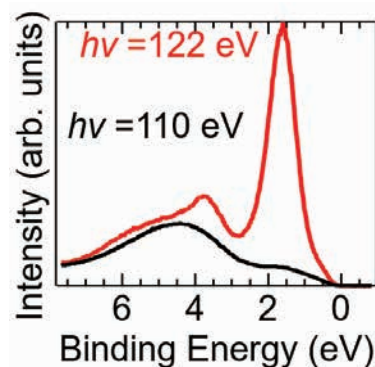


Fig. 1. Resonant angle-integrated photoelectron spectra of  $\text{CeTe}_{1.83}\text{Sb}_{0.17}$  at 15 K. The excitation energies of 110 and 122 eV correspond to the off- and on-resonance conditions at the Ce  $4d-4f$  absorption edge.

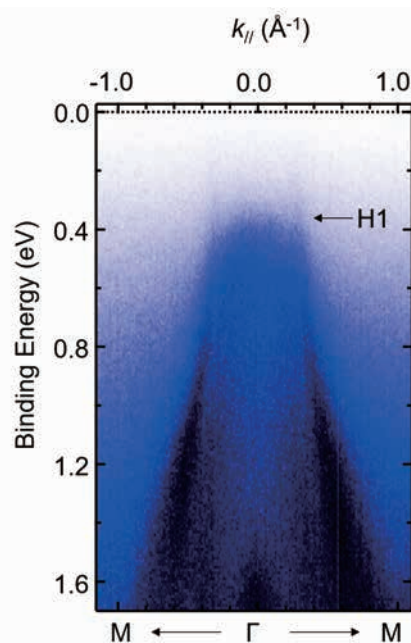


Fig. 2. ARPES intensity plot of  $\text{CeTe}_{1.83}\text{Sb}_{0.17}$  along  $\Gamma$ -M taken with 103 eV at 15 K.

- [1] J. G. Park *et al.*, *Physica B* **241-243** (1998) 684.
- [2] M. H. Jung *et al.*, *J. Phys. Soc. Jpn.* **69** (2000) 937.
- [3] M. H. Jung *et al.*, *Phys. Rev. B* **67** (2003) 212504.
- [4] H. Murakawa *et al.*, *Phys. Rev. Mater.* **6** (2022) 054604.

BL5U

## Synchrotron ARPES Study of Nodal Dirac Semimetal Candidate LaTeBi

R. Saitou<sup>1</sup>, N. Kataoka<sup>1</sup>, H. Kageyama<sup>1</sup>, R. Kondo<sup>1</sup> and T. Yokoya<sup>1,2</sup>

<sup>1</sup>Graduate School of Natural Science and Technology, Okayama University, Okayama 700-8530, Japan

<sup>2</sup>Research Institute for Interdisciplinary Science, Okayama University, Okayama 700-8530, Japan

LnTe<sub>1-x</sub>Sb<sub>1-x</sub> (Ln: lanthanides) is a layered material consisting of alternative stack of a layer of LnTe and a layer of a single Sb square lattice. It is theoretically predicted as a nodal line semimetal [1]. In addition, by selecting a magnetic element as Ln, it is possible to break the time-reversal symmetry. Therefore, it is a material that has the potential to access novel topological phases [2-5]. Our research group are making an effort to control the physical properties of related materials by introducing magnetic elements, substituting Sb with Bi, and changing carrier concentration [6] for the purpose of observing the exotic transport properties peculiar to Dirac electrons. In the present study, we have performed synchrotron angle-resolved photoemission spectroscopy (ARPES) to clarify the electronic structure of the non-magnetic phase and check the relative energy relationship between the Fermi energy ( $E_F$ ) and Dirac nodes in a related material, LaTe<sub>1-x</sub>Bi<sub>1-x</sub>, which possesses single square lattices composed of Bi atoms, having a stronger spin-orbit interaction than Sb.

LaTe<sub>1-x</sub>Bi<sub>1-x</sub> single crystal samples ( $x = 0.025$ ) were prepared by a self-flux method. ARPES measurements were performed at BL5U of UVSOR III. Linear polarized light of 32-124 eV energies were used. The energy resolution was set to  $\sim 40$  meV. All samples were cleaved in situ on the (001) plane in an ultrahigh vacuum of less than  $5.0 \times 10^{-9}$  Pa and were measured at 20 K.

Figure 1 shows the valence band dispersion of LaTe<sub>1-x</sub>Bi<sub>1-x</sub> along the  $\Gamma$ -X direction in the Brillouin zone (BZ), measured with the photon energy of 94 eV. White regions, which are the higher-intensity regions, correspond to band dispersions. The band dispersions are symmetric with respect to the high symmetry points:  $\Gamma$  and X of the bulk BZ of LaTe<sub>1-x</sub>Bi<sub>1-x</sub>. This indicates that the band dispersions reflect intrinsic electronic structure of the sample. Importantly, one can observe weak structures near  $E_F$  on both sides of the X points, where Dirac nodal lines are expected to be located theoretically. To look at the electronic structures more in detail, an energy and momentum enlarged intensity map is shown in Fig. 2. We now clearly observe two electron-pockets-like structures. These band dispersions are consistent with the calculated band dispersions. However, at the X point, the intensity at  $E_F$  is very small, indicating that the starting point of the theoretically expected Dirac nodal line at the X point is not located below  $E_F$  for the measured sample. The energy position of the Dirac nodal line at the X

point with respect to  $E_F$  is found to be calculation dependent. However, an implication from this study is that the electron concentration is not enough. To achieve the interesting physical properties originating from the topological electronic structure in the sample, further electron doping is necessary.

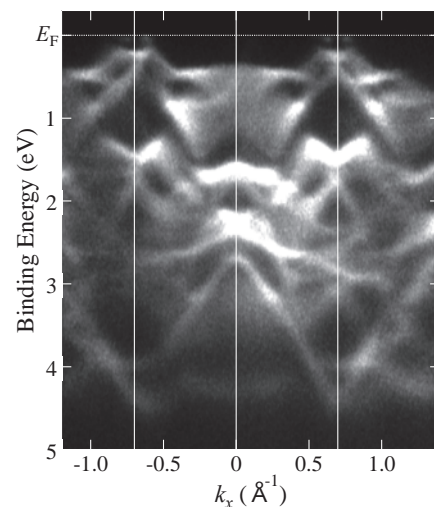


Fig. 1. ARPES intensity map of LaTe<sub>1-x</sub>Bi<sub>1-x</sub> measured with 94 eV photons and at 20 K.

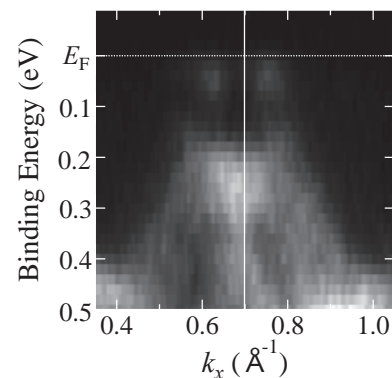


Fig. 2. Enlargement of Fig. 1 for the region near  $E_F$  and the X point.

- [1] A. Weiland *et al.*, APL Mater. **7** (2019) 101113.
- [2] Y. Wang *et al.*, Phys. Rev. B **103** (2021) 125131.
- [3] S. Yue *et al.*, Phys. Rev. B **102** (2020) 155109.
- [4] P. Gebauer *et al.*, Chem. Mater. **33** (2021) 2420.
- [5] L. M. Schoop *et al.*, Sci. Adv. **4** (2018) eaar2317.
- [6] R. Kondo, in preparation.

## Re-examination of the Phase Diagram of the high- $T_c$ Cuprate Superconductor $\text{Bi}_2\text{Sr}_2\text{CaCu}_2\text{O}_{8+\delta}$ Studied by ARPES

Y. Tsubota<sup>1</sup>, Y. Miyai<sup>2</sup>, S. Nakagawa<sup>5</sup>, S. Ishida<sup>4</sup>, S. Kumar<sup>2</sup>, K. Tanaka<sup>3</sup>, H. Eisaki<sup>4</sup>,  
T. Kashiwagi<sup>5</sup>, M. Arita<sup>2</sup>, K. Shimada<sup>1,2</sup> and S. Ideta<sup>1,2</sup>

<sup>1</sup>Graduate School of Advanced Science and Engineering, Hiroshima Univ., Japan

<sup>2</sup>Hiroshima Synchrotron Radiation Center (HiSOR), Hiroshima Univ., Japan

<sup>3</sup>UVSOR-III Synchrotron, Institute for Molecular Science, Japan

<sup>4</sup>National Institute of Advanced Industrial Science and Technology (AIST), Japan

<sup>5</sup>Graduate School of Science and Technology, Tsukuba Univ., Japan

It has been known that the cuprate superconductors show a high superconducting (SC) transition temperature ( $T_c$ ) and exotic physical properties. However, the SC mechanism has been unclear yet. In order to understand the mechanism of high- $T_c$  cuprates,  $\text{Bi}_2\text{Sr}_2\text{CaCu}_2\text{O}_{8+\delta}$  (Bi2212) is one of the promising candidates to study the electronic structure and reveal the physical properties. Bi2212 has two  $\text{CuO}_2$  planes in the unit cell and shows the high  $T_c$  around 95 K at the optimally doped sample. Superconductivity occurs upon hole doping into the  $\text{CuO}_2$  plane and the amount of hole doping can control  $T_c$ , and therefore, carrier doping (hole/electron concentration) plays an important key parameter in cuprates [1, 2]. The electronic phase diagram of hole-doped high- $T_c$  cuprate superconductors plotted as a function of temperature and carrier concentration has been reported as an empirical and universal phase diagram which is a dome-like shape centered at  $\sim 0.16$  of hole concentration [1]. However, previous ARPES experiments suggest that its empirical phase diagram is not universal and shifted toward overdoped region [2-4]. Therefore, in the present study, we have performed an angle-resolved photoemission spectroscopy (ARPES) measurements to study whether the phase diagram changes depending on sample compositions and hole concentration or not.

In this study, we have performed ARPES measurements systematically to directly investigate the electronic structure of the underdoped, optimally doped, and overdoped Bi2212. ARPES experiments were carried out at BL5U and BL7U. We measured overdoped sample:  $\text{Bi}_{2.1-x}\text{Pb}_x\text{Sr}_2\text{CaCu}_2\text{O}_{8+\delta}$  ( $x = 0.66$ ,  $T_c \sim 70$  K) in the SC and the normal states at BL7U and 5U. We measured underdoped, optimally doped, and overdoped samples: underdoped  $\text{Bi}_2\text{Sr}_2\text{CaCu}_2\text{O}_{8+\delta}$  ( $T_c \sim 75$  K), optimally doped  $\text{Bi}_2\text{Sr}_2\text{CaCu}_2\text{O}_{8+\delta}$  ( $T_c \sim 92$  K), overdoped  $\text{Bi}_2\text{Sr}_2\text{CaCu}_2\text{O}_{8+\delta}$  ( $T_c \sim 74$  K) and optimally doped  $\text{Bi}_{2.1-x}\text{Pb}_x\text{Sr}_2\text{CaCu}_2\text{O}_{8+\delta}$  ( $x = 0.66$ ,  $T_c \sim 97$  K) in the SC and the normal states. High quality single crystals of Bi2212 were cleaved *in-situ* in the ultrahigh vacuum  $\sim 5 \times 10^{-9}$  Pa.

Figure 1 (a) shows the Fermi surface taken at  $h\nu = 17.8$  eV and  $T = 30$  K in the SC state for optimally doped  $\text{Bi}_2\text{Sr}_2\text{CaCu}_2\text{O}_{8+\delta}$ . Fermi surface is clearly observed in wide momentum space.

We have analyzed the ARPES spectra from the nodal to the antinodal region for each sample and determined the Fermi momentum ( $k_F$ ) for each Fermi surface by fitting of momentum-distribution curves (MDCs) with single Lorentzian or double Lorentzian. Around the nodal region,  $k_F$  is defined at Fermi level ( $E_F$ ) by single Lorentzian. In the offnodal to the antinodal region,  $k_F$  is defined at the momentum which shows the gap minimum by double Lorentzian. The  $k_F$  points are plotted as shown by red dots (Fig. 1. (a)). We have fitted Fermi surface shape (red dots) by tight binding model (white curve) and estimated the hole concentration of each sample from the Fermi surface area and compared them quantitatively. Figure 1 (b) shows the new phase diagram re-examined by the present ARPES study. As a result, the phase diagram (Fig. 1. (b)) is different from the previous one which was reported by Tallon *et al* [1]. We have figured out that the phase diagram changes depending on sample compositions and hole concentration. As a future work, we continue to study the electric structure of underdoped and overdoped samples to make an entire phase diagram of Bi2212.

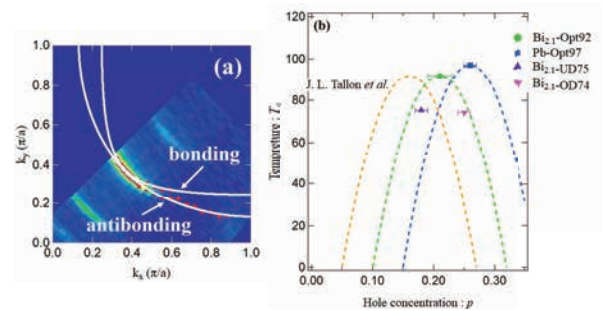


Fig. 1. (a) Fermi surface of optimally doped  $\text{Bi}_2\text{Sr}_2\text{CaCu}_2\text{O}_{8+\delta}$  in the superconducting state (30 K). (b) The new phase diagram of Bi2212 in the present ARPES study.

- [1] J. L. Tallon *et al.*, Phys. Rev. B **51** (1995) 12911.  
[2] I. M. Vishik *et al.*, Proc. Nat. Acad. Sci. **6** (2012) 18332-18337.  
[3] R. Sobota *et al.*, J. Phys. Soc. Jpn. **88** (2019) 064711.  
[4] H. Sakamoto *et al.*, J. Phys. Soc. Jpn. **85** (2016) 104710.

BL5U

## Alkaline-metal-dependent Electronic States in V-based Kagome Metals

T. Kato<sup>1</sup>, K. Nakayama<sup>1</sup>, Y. Li<sup>2,3,4</sup>, Z. Wang<sup>2,3,4</sup>, S. Souma<sup>5,6</sup>, K. Tanaka<sup>7,8</sup>, T. Takahashi<sup>1</sup>, Y. Yao<sup>2,3</sup> and T. Sato<sup>1,5,6,9</sup>

<sup>1</sup>Department of Physics, Graduate School of Science, Tohoku University, Sendai 980-8578, Japan

<sup>2</sup>Centre for Quantum Physics, Key Laboratory of Advanced Optoelectronic Quantum Architecture and Measurement (MOE), School of Physics, Beijing Institute of Technology, Beijing 100081, P. R. China

<sup>3</sup>Beijing Key Lab of Nanophotonics and Ultrafine Optoelectronic Systems, Beijing Institute of Technology, Beijing 100081, P. R. China

<sup>4</sup>Material Science Center, Yangtze Delta Region Academy of Beijing Institute of Technology, Jiaxing, 314011, P. R. China

<sup>5</sup>Advanced Institute for Materials Research (WPI-AIMR), Tohoku University, Sendai 980-8577, Japan

<sup>6</sup>Center for Science and Innovation in Spintronics (CSIS), Tohoku University, Sendai 980-8577, Japan

<sup>7</sup>UVSOR Synchrotron Facility, Institute for Molecular Science, Okazaki 444-8585, Japan

<sup>8</sup>School of Physical Sciences, The Graduate University for Advanced Studies (SOKENDAI), Okazaki 444-8585, Japan

<sup>9</sup>International Center for Synchrotron Radiation Innovation Smart (SRIS), Tohoku University, Sendai 980-8577, Japan

Kagome lattice offers a fertile playground to explore exotic quantum phases such as Weyl semimetals, density-wave orders, fractional charge, and superconductivity, owing to the interplay between electron correlation effects and unique band structures such as flat bands, Dirac cone bands, and van Hove singularities. Recently-discovered  $AV_3Sb_5$  ( $A =$  alkali metal), in which V atoms form an ideal two-dimensional kagome lattice, provides an excellent opportunity to investigate charge-density wave (CDW) in the kagome lattice. The CDW state of  $AV_3Sb_5$  is characterized by three-dimensional lattice distortions with  $2 \times 2 \times 2$  or  $2 \times 2 \times 4$  periodicity depending on the  $A$  element. The transition temperature  $T_{CDW}$  varies with the  $A$  element from 78 K to 103 K.  $AV_3Sb_5$  also exhibits superconductivity in the CDW phase ( $T_c = 0.92\text{--}2.5$  K). Besides the CDW and superconductivity in the bulk,  $AV_3Sb_5$  shows an  $A$ -element-dependent charge order at the surface. To clarify the origin of these  $A$ -element dependent physical properties, elucidation of the bulk and surface band structures is urgently required.

In this study, we have performed high-resolution angle-resolved photoemission spectroscopy (ARPES) measurements of a series of  $AV_3Sb_5$  ( $A =$  K, Rb, and Cs). High-quality single crystals of  $KV_3Sb_5$ ,  $RbV_3Sb_5$ , and  $CsV_3Sb_5$  were grown by the self-flux method. High-resolution ARPES measurements were performed by using a MBS-A1 spectrometer at BL5U with linearly-polarized energy-tunable photons of 90-150 eV.

Figures 1(a) and 1(b) show the ARPES intensity plots measured along the high-symmetry line of the bulk Brillouin zone in  $KV_3Sb_5$  [1] and  $CsV_3Sb_5$ , respectively. While the band dispersions show overall similarity between the two compounds, a closer look reveals  $A$ -element dependence in the energy positions of the electron-like band at the  $\Gamma$  point and the Dirac point at

the K point. High-resolution measurements at low temperatures show doubling of some energy bands, indicative of CDW-induced electronic reconstruction. We performed first-principles band calculations to understand the origin of  $A$ -element-dependent band structures and their relationship with physical properties in  $AV_3Sb_5$ .

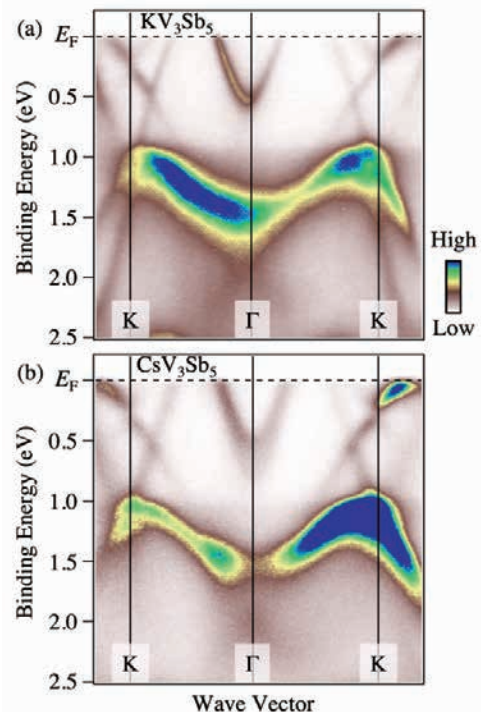


Fig. 1. (a) ARPES intensity along the  $\Gamma$ K cut in  $KV_3Sb_5$  plotted as a function of binding energy and wave vector. (b) Same as (a) but for  $CsV_3Sb_5$ .

[1] T. Kato *et al.*, Commun. Mater. **3** (2022) 30.

## Verification of the Intrinsic Electron Doping Effect in T'-type Cuprate high-temperature Superconductors

M. Miyamoto<sup>1</sup>, M. Horio<sup>1</sup>, K. Moriya<sup>2</sup>, A. Takahashi<sup>3</sup>, K. Tanaka<sup>4</sup>,  
Y. Koike<sup>3</sup>, T. Adachi<sup>2</sup> and I. Matsuda<sup>1</sup>

<sup>1</sup>Institute for Solid State Physics, The University of Tokyo, Kashiwa, Chiba 277-8581, Japan.

<sup>2</sup>Department of Engineering and Applied Sciences, Sophia University, Tokyo 102-8554, Japan.

<sup>3</sup>Department of Applied Physics, Tohoku University, Sendai 980-8579, Japan.

<sup>4</sup>UVSOR Facility, Institute for Molecular Science, Okazaki 444-8585, Japan.

It is believed that in cuprate high-temperature superconductors, superconductivity appears when the carrier is doped by elemental substitution. However, in the electron-doped cuprates  $R_{2-x}Ce_xCuO_4$  (R: rare earth) with a T'-type structure, As-grown samples don't show superconductivity and reduction annealing is essential for it, regardless of Ce doping level [1,2]. This is probably due to the presence of excess oxygen on the apical site from the  $CuO_2$  plane in As-grown samples. A crucial role of this reduction annealing has been thought to remove the apical oxygen [3]. In thin-film samples with large surface area relative to volume, the apical oxygen was reduced more efficiently, resulting in a non-doped superconductor [4]. On the other hand, ARPES measurement performed on  $Pr_2CuO_4$  thin films revealed that the carrier concentration was comparable to that of Ce-doped superconductor samples [5]. Therefore, the nature of the electronic structure in T'-type cuprates remains elusive. And it is important to investigate the carrier concentration dependence in isolation from the actual crystal structure degrees of freedom.

In recent years, several studies have shown that the carrier concentration in cuprate high-temperature superconductors can be controlled by alkali metal adsorption [6,7,8]. And our group has previously used a similar technique for a Mott insulator  $Ca_3Ru_2O_7$  with successful carrier dosing [9]. This method can dope electrons on the sample's surface without changing its crystal structure, Ce concentration, and oxygen amount. That is, if this method is effective enough, we can distinguish the effects of apical oxygens from that of carrier concentration.

We have carried out the ARPES measurement on  $Pr_{1.22}La_{0.7}Ce_{0.08}CuO_4$  As-grown samples at BL5U at 8 K and dosed K on them. To verify the K deposition, we recorded the core level peaks of K 3p and O 2s (Fig.1). The figure shows K was dosed effectively. Fig.2 shows the energy distribution curves at the nodal cut before and after dosing of K. After 10 minutes of dosing, the quasi-particle spectrum around the Fermi level enhanced, and the nodal gap looks closing. After experimenting with various deposition times and deposition counts, we currently concluded that fewer

and longer depositions lead to more electron electrons being doped.

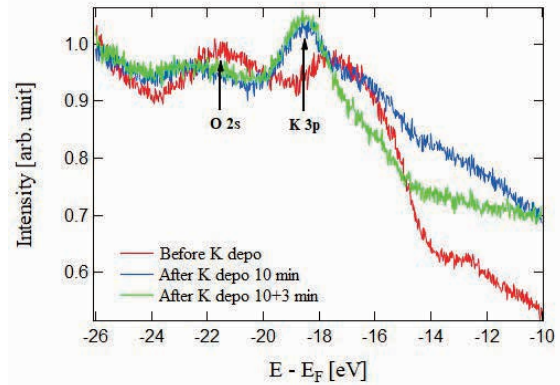


Fig. 1. Energy distribution curves around the K core level

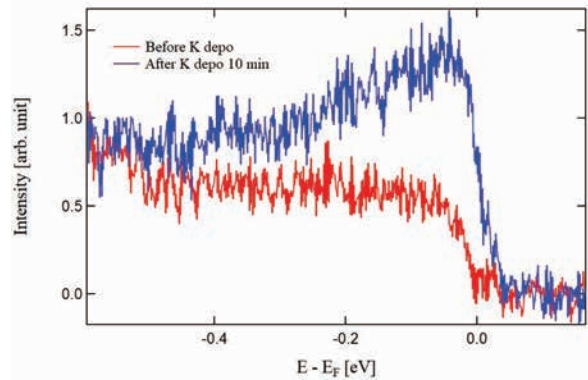


Fig. 2. Energy distribution curves at nodal cut

- [1] Y. Tokura, *et al.* Nature **337** (1989) 345.
- [2] H. Takagi *et al.* Phys. Rev. Lett. **62** (1989) 10.
- [3] M. Horio *et al.* Nat. Commun. **7** (2016) 10567.
- [4] O. Matsumoto *et al.* Physica C **469** (2009) 924.
- [5] M. Horio *et al.* Phys. Rev. B **98** (2018) 020505(R)
- [6] Q. Gao *et al.* Chinese Phys. Lett. **37** (2020) 087402.
- [7] S. Kunisada *et al.* Science **369** (2020) 833.
- [8] C. Hu *et al.* Nat. Commun. **12** (2021) 1356.
- [9] M. Horio *et al.* UVSOR activity report 2021 **49** (2021) 79.

BL5U

## Polarization Dependent Orbital States in $\text{Mn}_{3-x}\text{Ga}$ Studied by angle-resolved Photoemission Spectroscopy

J. Okabayashi<sup>1</sup>, Y. Miura<sup>2</sup>, K. Tanaka<sup>3</sup>, K. Z. Suzuki<sup>4</sup> and S. Mizukami<sup>4</sup>

<sup>1</sup>Research Center for Spectrochemistry, The University of Tokyo, Bunkyo-ku, Tokyo 113-0033, Japan

<sup>2</sup>National Institute for Materials Science (NIMS), Tsukuba, 305-0047, Japan

<sup>3</sup>UVSOR Synchrotron Facility, Institute for Molecular Science, Okazaki 444-8585

<sup>4</sup>WPI Advanced Institute for Materials Research, Tohoku University, Sendai 980-8579, Japan

Magnetic ordered alloys have attracted significant attention for use as spintronics materials because they are highly likely to exhibit perpendicular magnetic anisotropy (PMA). Tetragonal  $\text{Mn}_{3-x}\text{Ga}$  alloys are widely recognized as hard magnets which exhibit highly anisotropic, ferrimagnetic, and metallic properties [1]. We have investigated the mechanism of PMA and large coercive fields in  $\text{Mn}_{3-x}\text{Ga}$  by x-ray magnetic circular and linear dichroisms (XMCD / XMLD) [2]. The origin of PMA in  $\text{Mn}_{3-x}\text{Ga}$  alloys can be explained by the quadrupole contribution along the  $z$ -axis by the charge distribution. The specific crystalline structures provide the elongated  $c$ -axis direction, which induces the anisotropic chemical bonding, resulting in the anisotropy of electron occupancies in  $3d$  states. However, orbital magnetic moments in the Mn sites are almost quenched because of the half-filled occupation.

Although the site-specific charge distributions can be accessed by x-ray absorption spectroscopies, the origin of quadrupole-induced PMA from the viewpoint of the band structures in  $\text{Mn}_{3-x}\text{Ga}$  alloys is not fully understood. Here, we employ the angle-resolved photoemission spectroscopy (ARPES) to unveil the anisotropic band structures in  $\text{Mn}_{3-x}\text{Ga}$  by the comparison with the density-functional theory (DFT) calculations. Especially, in order to clarify the anisotropic electronic structures, the polarization dependent APRES are necessary.

30-nm-thick  $\text{Mn}_{3-x}\text{Ga}$  samples were prepared on MgO (001) substrate using sputtering technique. On the surface of  $\text{Mn}_{3-x}\text{Ga}$  layer, the Mg and MgO capping layers were deposited. The MgO layer was removed by Ar-ion sputtering and the Mg layer was removed by annealing just before the ARPES measurements. We construct the method to remove the Mg layer which does not react chemically with Mn atoms at the interface. Clear low-energy electron diffraction (LEED) patterns were also obtained.

ARPES was performed at BL5U, UVSOR, where the photoemission chamber is connected to the sample preparation chamber. The measurement conditions were set at 15 meV energy resolution and 10 K. Linear polarized beams of  $s$ - and  $p$ -polarization were used to detect the orbital symmetry. We employ the photon energy ranges of 60 – 80 eV to enhance the Fe  $3d$

photo-ionization cross section, where the  $\Gamma$ -X(M) line is scanned by the angular mode of  $\pm 15^\circ$ .

Figure 1 shows the Fermi surface mapping taken at photon energy of 70 eV. Assuming the inner potential of 10 eV and the work function of 5 eV with the lattice constant along  $c$ -axis as 3.90 Å,  $\Gamma$  point can be accessed at 70 eV photon energy. Figures 1(a) and 1(b) show the vertical ( $s$ -polarized) and horizontal ( $p$ -polarized) cases in  $\text{Mn}_3\text{Ga}$ . Four-fold symmetric lines are detected. High intensity spots appear at the  $\Gamma$  point and they have a character of  $yz$  orbital because it can be detected by the  $s$ -polarized beam in vertical geometry and reproduced by the density-functional-theory (DFT) calculations.

We discuss the quadrupole formation. In the DFT calculations, the virtual spin-flip transitions from occupied up-spin  $yz$  to down-spin  $z^2$  orbitals correspond to the finite matrix element to the PMA in the perturbation. Therefore, occupied  $yz$  orbitals detected by ARPES contribute to spin-flipped  $yz$ - $z^2$  oblate quadrupole charge distribution, resulting in the PMA. Our finding explains the origin of PMA in  $\text{Mn}_{3-x}\text{Ga}$  comes from not orbital moment anisotropy but elongated charge distribution through the spin-flipped transition in specific orbitals [3], whose results are also supported by XMCD and XMLD [2].

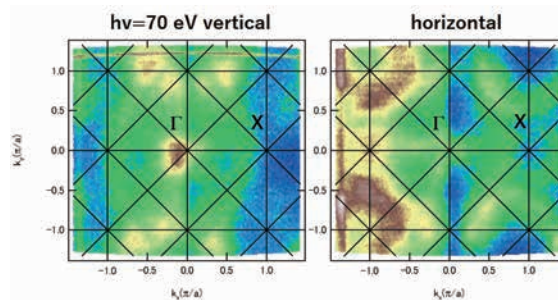


Fig. 1. ARPES images of  $\text{Mn}_3\text{Ga}$  taken at  $h\nu=70$  eV using (a)  $s$ -polarized beam and (b)  $p$ -polarized beam.

[1] S. Mizukami *et al.*, *Scr. Mater.* **118** (2016) 70.

[2] J. Okabayashi *et al.*, *Sci. Rep.* **10** (2020) 9744.

[3] Y. Miura and J. Okabayashi, *J. Phys.: Cond. Mater* **34** (2022) 473001.

## Impact of Electron Scattering on Seebeck Coefficient

K. Kandai<sup>1</sup>, K. Kuga<sup>1,3</sup>, M. Matsunami<sup>1,2,3,4</sup> and T. Takeuchi<sup>1,2,3,4</sup>

<sup>1</sup>Toyota Technological Institute, Nagoya 468-8511, Japan

<sup>2</sup>Research Center for Smart Energy Technology, Toyota Technological Institute, Nagoya 468-8511, Japan

<sup>3</sup>CREST, Japan Science and Technology Agency, Tokyo 102-0076, Japan

<sup>4</sup>MIRAI, Japan Science and Technology Agency, Tokyo 102-0076, Japan

The thermoelectric power generation has been considered as one of the most important technologies for constructing a sustainable society. The thermoelectric devices can directly convert heat and electricity using Seebeck and Peltier effects. The maximum efficiency of thermoelectric generator at an absolute temperature  $T$  is expressed as an increasing function of the dimensionless figure of merit  $ZT = S^2T/\rho\kappa$ , where  $S$ ,  $\rho$ , and  $\kappa$  are the Seebeck coefficient, electrical resistivity, and thermal conductivity, respectively, of constituent materials [1].

In the research field of thermoelectric materials, the thermoelectric properties, particularly for Seebeck coefficient, are frequently interpreted and predicted on the basis of electronic structure calculated with density function theory (DFT). However, the Seebeck coefficient of the materials with unconventional electronic structures, such as strongly correlated electron systems (SCES), cannot be accurately described in terms of only the electronic density of states obtained with first-principles DFT calculations. In the theoretical point of view, the main reason is that the energy dependence of relaxation time in the scattering process of conduction electrons is not considered [2, 3]. Although the first principles calculations incorporating dynamical effects are now in progress, it is still difficult to accurately treat an electron correlation effect. In any case, it is necessary to experimentally evaluate the energy dependence of the relaxation time to verify how it affects the Seebeck coefficient. The strong electron correlation is considered as one of the key concepts for developing next-generation thermoelectric materials because some SCES materials possess superior thermoelectric performance. Therefore, for constructing the guiding principle to develop high-performance thermoelectric materials using SCES, it is very important to identify the origin of the preferable thermoelectric properties.

The main purpose of this research is to establish a methodology for experimentally evaluating the energy dependence of the relaxation time of conduction electrons using angle-resolved photoemission spectroscopy (ARPES). As a first step toward achieving this purpose, we select the elemental Cu metal as a sample because the Cu can be expected to show no significant energy dependence of relaxation time of conduction electrons based on its simple electronic

structure and band dispersion.

Clean (110) surface of single crystalline Cu was prepared by *in-situ* Ar sputtering and subsequent annealing under ultra-high vacuum condition. The ARPES measurements were performed in the energy range of 32-160 eV at the undulator beamline BL5U of UVSOR facility.

Figure 1 shows the ARPES image of Cu (110) surface at 9 K measured with the photon energy of 100 eV. The free electron-like parabolic dispersion of the (bulk) conduction band is clearly observed in the energy range down to -3 eV below the Fermi level. The energy dependent relaxation time of conduction electrons can be estimated from the peak width both of energy distribution curves and momentum distribution curves. As expected, we confirmed that the energy dependence of the relaxation time shows less significant variation across the Fermi level.

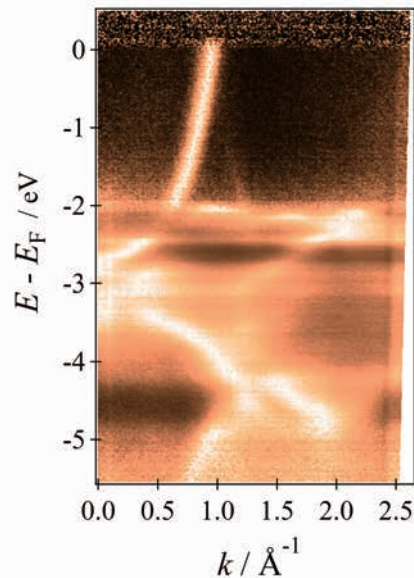


Fig. 1. ARPES image of Cu (110) surface at 9 K measured with 100 eV.

- [1] T. Takeuchi, J. Thermoelectrics Soc. Jpn. **9** (2012) 1.  
 [2] Y. Xia *et al.*, Phys. Rev. Applied **11** (2019) 024017.  
 [3] B. Xu *et al.*, Phys. Rev. B **102** (2020) 155128.

BL5U

## Temperature Dependence of the Band Folding in TiSe<sub>2</sub>

S. Tanaka<sup>1</sup>, K. Ueno<sup>2</sup>, K. Fukutani<sup>3</sup> and K. Tanaka<sup>3</sup>

<sup>1</sup>Sanken, Osaka University, Ibaraki 567-0047, Japan.

<sup>2</sup>Graduate School of Science and Engineering Saitama University, Saitama 338-8570, Japan.

<sup>3</sup>UVSOR Synchrotron Facility, Institute for Molecular Science, Okazaki 444-8585, Japan.

Layered material TiSe<sub>2</sub> is one of the Transition-Metal-Dichalcogenide (TMDC) and has extensively studied for decays as a typical system of Charge-Density-Wave (CDW) transition. Although excitonic condensation is considered to be the most important factor in the CDW transition in TiSe<sub>2</sub> thanks to many experimental and theoretical studies, there are still many unanswered concerns regarding the electrical and atomic structure upon the CDW transition at ~200K. In this article, we use angle-resolved photoelectron spectroscopy (ARPES) to examine how TiSe<sub>2</sub>'s electronic structures change with temperature. We focus on the specifics of the band folding brought on by the reconstruction of the (2x2x2) superstructure as a result of the CDW transition.

Figs.1 displays the ARPES spectra at 190K (a) and 8K (b) with photon energies of 46eV. The electron pocket at M-points (commonly referred to as the conduction band) and the hole pocket at  $\Gamma$  points (commonly referred to as the valence band) combine to form bands close to the Fermi level in TiSe<sub>2</sub>. As a result of the CDW transition, where the M point of the original lattice is folded to the  $\Gamma$  point in the rebuilt lattice, our measurements show that the replica of the valence band at the  $\Gamma$  point is clearly visible at the M point at 8K. This is in agreement with how the Brillouin zone was recreated when the CDW transition created the (2x2x2) superlattice. The replica of the conduction band at the M point, on the other hand, is faintly visible even at 8K. We discovered that this replica's intensity greatly fluctuates with photon energy and is quite low at  $h\nu=46\text{eV}$ . Moreover, the intensity distribution at the M point significantly changes at two temperatures (see the third panel from the top). This can be explained by the Fermi surface modulation along the  $k_z$  line due to the CDW transition.

Together with the production of replicas and changes in the intensity distribution, the energetic profile of the band changes with temperature. At low temperatures, the valence band's energy location is visibly moved downward (see the second panel from the top). This is a defining trait of the bigger gap development brought on by the CDW transition's associated excitonic condensation. The replica located at M at 9K is also energetically displaced to the original valence band at the same temperature. Although the specifics are still

being examined, it might also be linked to the modulation of the band along the  $k_z$  line.

It should be noted that the replica at M can be dimly detected at 190K, which is considerably lower than the reference's CDW transition temperature. We looked more closely at how the ARPES spectra change with temperature and discovered that the reported temperature of the CDW transition is around the transition temperature determined by energetic profile, which is substantially higher than that determined by replica intensity. Investigations are currently ongoing to determine the physical cause of this behavior.

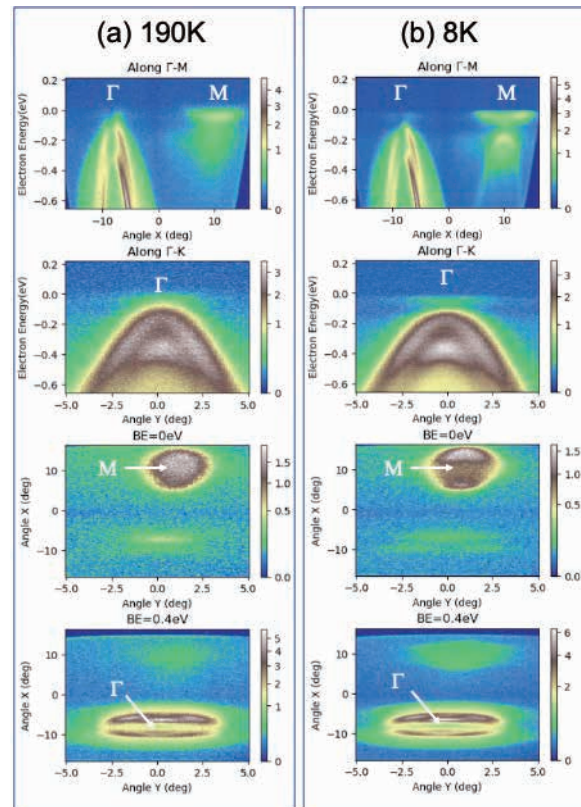


Fig. 1. ARPES spectra of TiSe<sub>2</sub> taken at 190K (a) and 8K (b). Upper two panels for (a) and (b) show the intensity maps along the energy-angle axes. Lower two show the iso-energy intensity maps along the x- and y-angles at the binding energies of 0eV and 0.4eV.

## Doping-Dependent ARPES Study of Nodal Dirac Semimetal Candidate LaTeSb and LaTeBi

R. Saitou<sup>1</sup>, N. Kataoka<sup>1</sup>, T. Wakita<sup>1</sup>, H. Kageyama<sup>1</sup>, R. Kondo<sup>1</sup> and T. Yokoya<sup>1,2</sup>

<sup>1</sup>Graduate School of Natural Science and Technology, Okayama University, Okayama 700-8530, Japan

<sup>2</sup>Research Institute for Interdisciplinary Science, Okayama University, Okayama 700-8530, Japan

LnTe<sub>1+x</sub>Sb<sub>1-x</sub> (Ln: lanthanides) is a layered material consisting of alternative stack of a layer of LnTe and a layer of a single Sb square lattice. It is theoretically predicted as a nodal line semimetal [1]. In addition, by selecting a magnetic element as Ln, it is possible to break the time-reversal symmetry. Therefore, it is a material that has the potential to access novel topological phases [2-5]. Our research group are making an effort to control the physical properties of related materials by introducing magnetic elements, substituting Sb with Bi, and changing carrier concentration [6] for the purpose of observing the exotic transport properties peculiar to Dirac electrons. In the present study, we have performed synchrotron angle-resolved photoemission spectroscopy (ARPES) to experimentally observe the electronic structure of the non-magnetic phase and check whether the carrier concentration can be controlled by changing the Te concentration.

LaTe<sub>1+x</sub>Sb<sub>1-x</sub> ( $x = -0.1$  and  $0.2$ ) and LaTe<sub>1+x</sub>Bi<sub>1-x</sub> ( $x = 0.2$ ) single crystal samples were prepared by a self-flux method. ARPES measurements were performed at BL5U of UVSOR III. Linear polarized light of 70-110 eV energies were used. The energy resolution was set to  $\sim 40$  meV. All samples were cleaved in situ on the (001) plane in an ultrahigh vacuum of less than  $5.0 \times 10^{-9}$  Pa and were measured at 20 K.

Figure 1(a) shows the valence band dispersion of LaTe<sub>1.2</sub>Bi<sub>0.8</sub> along the  $\Gamma$ -M direction in the Brillouin zone (BZ), measured with the photon energy of 94 eV. White regions, which are the higher-intensity regions, correspond to band dispersions. The band dispersions of the two samples are symmetric with respect to the high symmetry points:  $\Gamma$  and M of the bulk BZ of LaTe<sub>1+x</sub>Bi<sub>1-x</sub>. This indicates that the band dispersions reflect intrinsic electronic structure of the sample.

Figure 1(b) is the valence band dispersion of LaTe<sub>1.025</sub>Bi<sub>0.975</sub> measured with the same experimental condition. Although there are small differences in the intensity distribution between the two ARPES maps, which may originate from the difference in the condition of the measured surface, the band dispersions of the two maps look very similar with each other. On the other hand, from a careful comparison, it was found that the energy positions of the structures in the  $x = 0.2$

sample shift to the higher binding energy side by  $\sim 100$  meV. Two guidelines to demonstrate the energy shift of structures at the  $\Gamma$  point were shown with orange dotted lines. This indicates that increasing Te concentration works as electron doping and one can control the relative energy between the Dirac nodal line and the Fermi level ( $E_F$ ) by changing the relative concentration between Te and Bi. Since the energy position of the Dirac nodal line in the  $x = 0.025$  sample was found to be located above  $E_F$ , the Dirac nodal line in the  $x = 0.2$  sample may be located closer to  $E_F$  or just at  $E_F$ . Further ARPES studies along the X-R line in the Brillouin zone, where the Dirac nodal line is expected to be located by band structure calculations, is planned to confirm this anticipation.

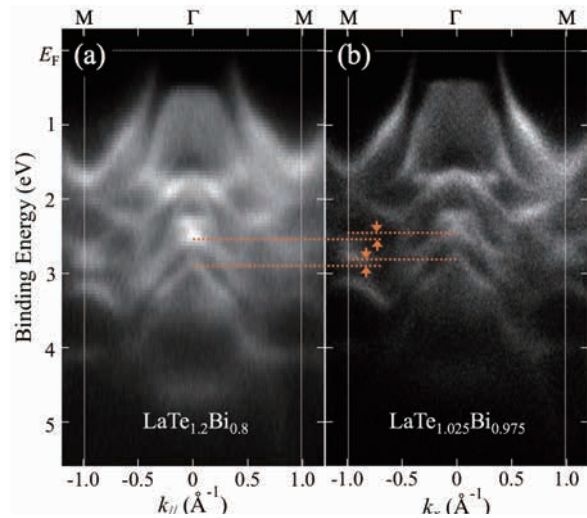


Fig. 1. Comparison of ARPES intensity maps along the  $\Gamma$ -M direction of LnTe<sub>1+x</sub>Bi<sub>1-x</sub> between (a)  $x = 0.2$  and (b)  $x = 0.025$ , measured with 94 eV photons and at 20 K.

- [1] A. Weiland *et al.*, APL Mater. **7** (2019) 101113.
- [2] Y. Wang *et al.*, Phys. Rev. B **103** (2021) 125131.
- [3] S. Yue *et al.*, Phys. Rev. B **102** (2020) 155109.
- [4] P. Gebauer *et al.*, Chem. Mater. **33** (2021) 2420.
- [5] L. M. Schoop *et al.*, Sci. Adv. **4** (2018) eaar2317.
- [6] R. Kondo, in preparation.

BL5U, 7U

## Symmetry Reduction of the Electronic Structure in Heavily Overdoped Pb-Bi2201 Observed by Angle-resolved Photoemission Spectroscopy

Y. Miyai<sup>1</sup>, T. Kurosawa<sup>2</sup>, M. Oda<sup>3</sup>, M. Arita<sup>4</sup>, K. Tanaka<sup>5</sup>, S. Ideta<sup>4</sup> and K. Shimada<sup>4</sup>

<sup>1</sup>Graduate School of Science, Hiroshima University, Higashi-Hiroshima 739-8526, Japan

<sup>2</sup>Faculty of Science and Engineering, Muroran Institute of Technology, Muroran, 050-8585, Japan

<sup>3</sup>Department of Physics, Hokkaido University, Sapporo 060-0809, Japan

<sup>4</sup>Hiroshima Synchrotron Radiation Center, Hiroshima University, Higashi-Hiroshima 739-8526, Japan

<sup>5</sup>UVSOR-III Synchrotron, Institute for Molecular Science, Okazaki, 444-8585, Japan

High transition-temperature ( $T_C$ ) cuprate superconductors have attracted much interest since their discovery in 1986 for their high superconducting transition temperature as well as unusual physical properties such as a pseudogap state and a nematic phase [1, 2]. Superconductivity occurs in the  $\text{CuO}_2$  plane and the  $\text{Cu } 3d_{x^2-y^2}$  state forms the Fermi surface (FS). One can expect a four-fold symmetry of the FS because the  $\text{CuO}_2$  plane is tetragonal. However, symmetry reduction of the electronic structure has been reported in Bi-based cuprate superconductors recently [2, 3]. Similar symmetry reduction or *nematicity* was found in iron-based superconductors, the electronic states break the four-fold rotational symmetry of the lattice [4, 5]. Although nematicity in electron liquids has attracted much interest, the rotational symmetry breaking in the electronic states for high- $T_C$  cuprate superconductors has not been clarified yet.

Here, we have examined the symmetry of the electronic structure of heavily overdoped  $(\text{Bi,Pb})_2\text{Sr}_2\text{CuO}_{6+\delta}$  (Pb-Bi2201) ( $T_C < 2.5$  K) using high-resolution angle-resolved photoemission spectroscopy (ARPES). We selected Bi2201 because it has a single  $\text{CuO}_2$  plane and one can exclude the complexity of the electronic structure such as bilayer splitting derived from two  $\text{CuO}_2$  planes. Furthermore, the pseudogap disappears in the heavily overdoped sample and one can clearly see the entire FS in the normal state without Fermi arc.

Figures 1(a) and 1(b) show the FS obtained by rotating the sample around the two nodal directions taken at  $h\nu = 60$  eV and  $T = 20$  K with the  $s$ -polarization geometry. We have found that the value of  $2k_F$  ( $k_F$ : Fermi momentum) for the two nodal directions are different;  $2k_F^{(1)} = (7.996 \pm 0.003) \times 10^{-1} \text{ \AA}^{-1}$  (Fig. 1(a)) and  $2k_F^{(2)} = (8.572 \pm 0.003) \times 10^{-1} \text{ \AA}^{-1}$  (Fig. 1(b)). This difference independent of temperature from  $T = 20$  K to 260 K. In addition, we reveal that the energy dependence of the quasiparticle lifetime broadening is also different for these two nodal directions. The situation is similar for the samples with  $T_C = 4, 6,$  and 10 K. Our results indicate  $C_4$  symmetry breaking of the electronic structure in the  $\text{CuO}_2$  plane in the heavily

overdoped Pb-Bi2201, which might be related to a charge order formation in the heavily overdoped Pb-Bi2201 as observed by resonant inelastic X-ray scattering [6], and/or the nematic phase associated with the Pomeranchuk instability as suggested by Raman scattering measurements on Bi2212 [7].

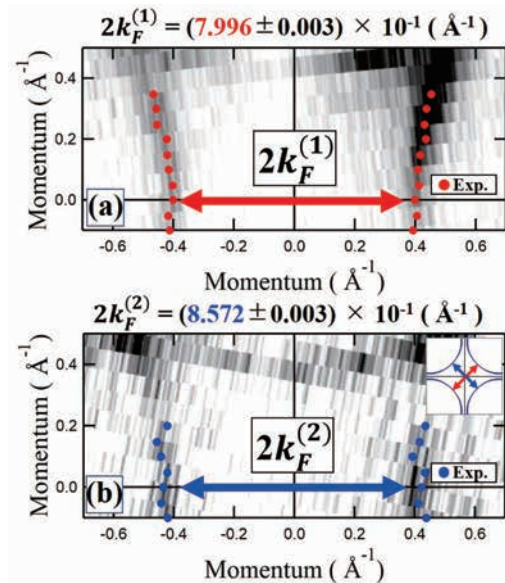


Fig. 1. (a), (b) Fermi surface mapping obtained by rotating around the two nodal directions taken at  $h\nu = 60$  eV and  $T = 20$  K with the  $s$ -polarization geometry. Red and blue markers indicate the Fermi surface points determined from the peaks of the momentum distribution curves. We determine  $2k_F$  values ( $2k_F^{(1)}$  and  $2k_F^{(2)}$ ) for the two nodal directions as shown in the inset of panel (b).

- [1] M. Hashimoto *et al.*, Nat. Phys. **10** (2014) 483.
- [2] S. Nakata *et al.*, npj Quantum Mater. **6** (2021) 86.
- [3] Y. Zheng *et al.*, Sci. Rep. **7** (2017) 8059.
- [4] H. C. Xu *et al.*, Phys. Rev. Lett. **117** (2016) 157003.
- [5] J-H. Chu *et al.*, Science **329** (2010) 824.
- [6] Y. Y. Peng *et al.*, Nat. Mater. **17** (2018) 697.
- [7] N. Auvray *et al.*, Nat. Commun. **10** (2019) 5209.

## Far- and Mid-infrared Absorption on the Single-crystal Pentacene

Y. Nakayama<sup>1,2</sup>, K. Yamauchi<sup>1</sup>, Y. Baba<sup>1</sup> and J. Miyamoto<sup>1</sup>

<sup>1</sup>Department of Pure and Applied Chemistry, Tokyo University of Science, Noda 278-8510, Japan

<sup>2</sup>Institute for Molecular Science, Okazaki 444-8585, Japan

Electronic coupling with molecular vibrations and/or lattice phonons is one of the key issues for the consideration of charge carrier transport in organic semiconductor solids. In the present work, we conducted infrared absorption measurements on the pentacene single-crystal (PnSC) samples as a model case of high-mobility organic semiconductors for the elucidation of the electron-vibration coupling in well-defined solid-state molecules.

Infrared absorption measurements were carried out at BL6B. A Si bolometer or a HgCdTe detector was used for the signal detection in a wave number range of 100 – 700  $\text{cm}^{-1}$  (FIR) or 700 – 7000  $\text{cm}^{-1}$  (MIR), respectively. Details of the PnSC samples and measurement geometry were the same as reported previously [1]. The data were collected by changing the sample azimuthal angle by 180° in 15° and 45° intervals for the FIR and MIR measurements, respectively. In this report, angularly averaged spectra were used for the analyses. Spectra measured through a diamond plate were adopted as blank spectra ( $I_0$ ) to derive the absorbance of PnSCs.

Figure 1 shows a typical FIR spectrum of PnSC in a region where prominent peaks were observed. A persistent background modulation of a “frequency” at  $(5.9 \pm 0.2) \text{ cm}^{-1}$  is filtered out for further analyses. The spectral feature can be attributed to two vibration modes predicted to be at 476.9  $\text{cm}^{-1}$  and 491.7  $\text{cm}^{-1}$ . In the present measurements, twenty vibration modes were assignable in the spectra. Energy deviations of the experimental vibration peaks with respect to the theoretical values calculated in the B3-LYP/6-31g(d) level are plotted in Fig. 2, where a recommended “scale factor” for the calculated wavenumbers [2] is indicated as a standard. As the vibration mode #88 (in-plane scissoring of the backbone) exhibited the best match, the relative intensity for each spectral peak is derived with respect to the mode #88 intensity and plotted as a function of the corresponding calculated relative intensity in Fig. 3. Further discussion on the results is yet under consideration.

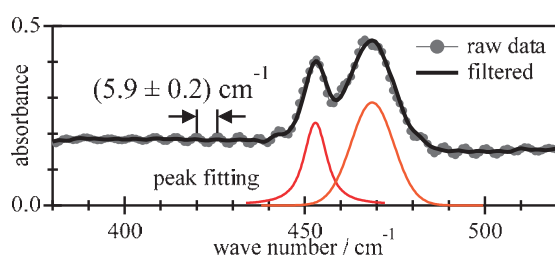


Fig. 1. FIR absorption spectrum on the PnSC.

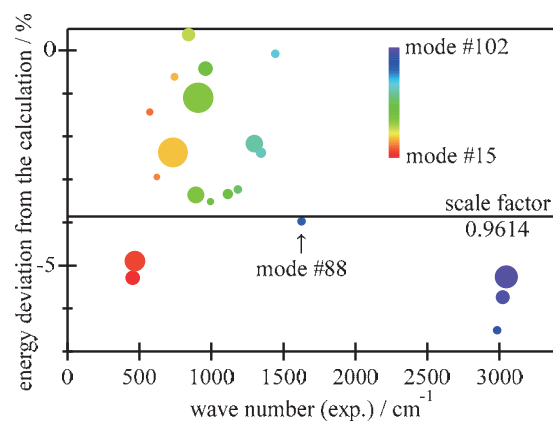


Fig. 2. Energy deviation of the experimental peak positions with respect to the calculated values. The size of the symbols indicates the peak intensity.

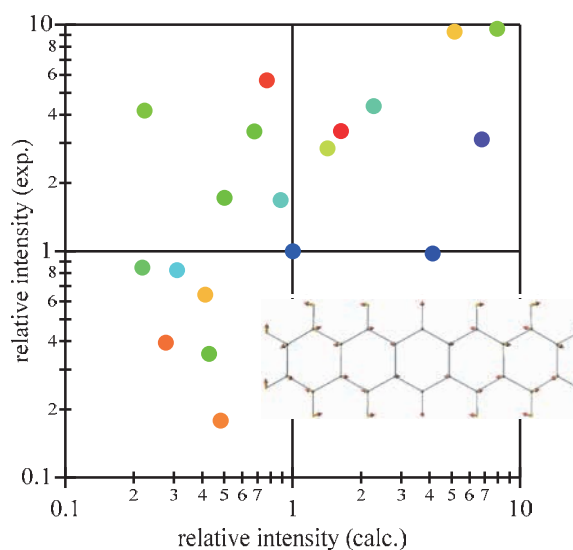


Fig. 3. Experimental relative peak intensity plotted as a function of the calculated magnitudes. The color of the symbols corresponds to the mode number indicated in Fig. 2. The inset image shows the mode #88 vibration of the pentacene molecule.

[1] Y. Nakayama and J. Miyamoto, UVSOR Activity Report 2020 (2021) 83.

[2] J. P. Merrick, D. Moran and L. Radom., J. Phys. Chem. A **111** (2007) 11683.

BL7U

## ARPES Study of a chalcopyrite-type Topological Insulator Candidate

T. Iwaya<sup>1</sup>, A. Honma<sup>1</sup>, K. Nakayama<sup>1</sup>, K. Sugawara<sup>1,2</sup>, S. Souma<sup>2,3</sup>, K. Tanaka<sup>4,5</sup>,  
T. Takahashi<sup>1</sup>, K. Segawa<sup>6</sup> and T. Sato<sup>1,2,3,7</sup>

<sup>1</sup>Department of Physics, Graduate School of Science, Tohoku University, Sendai 980-8578, Japan

<sup>2</sup>Advanced Institute for Materials Research (WPI-AIMR), Tohoku University, Sendai 980-8577, Japan

<sup>3</sup>Center for Science and Innovation in Spintronics (CSIS), Tohoku University, Sendai 980-8577, Japan

<sup>4</sup>UVSOR Synchrotron Facility, Institute for Molecular Science, Okazaki 444-8585, Japan

<sup>5</sup>School of Physical Sciences, The Graduate University for Advanced Studies (SOKENDAI),  
Okazaki 444-8585, Japan

<sup>6</sup>Department of Physics, Kyoto Sangyo University, Kyoto 603-8555, Japan

<sup>7</sup>International Center for Synchrotron Radiation Innovation Smart (SRIS), Tohoku University,  
Sendai 980-8577, Japan

Three-dimensional topological insulators (3D TIs) are a novel quantum state of matter where the bulk band gap induced by a strong spin-orbit coupling leads to the appearance of gapless Dirac-cone surface states protected by time-reversal symmetry. The discovery of 3D TIs has further stimulated the search for novel topological materials. From the viewpoint of the crystal symmetry, most of the 3D TIs so far discovered, e.g., Bi<sub>2</sub>Se<sub>3</sub>, Bi<sub>2</sub>Te<sub>3</sub>, and TlBiSe<sub>2</sub>, have the spatial inversion symmetry in the crystal. On the other hand, there are several theoretical proposals of TI candidates with broken inversion symmetry. There is a demand to experimentally discover such symmetry-broken phase because a peculiar phenomenon which cannot be realized in inversion-symmetric TIs is predicted to emerge.

Here we focus on CdGeAs<sub>2</sub> which crystalizes in a chalcopyrite structure with  $\bar{I}42d$  space group. As seen from Fig. 1(a), the crystal consists of a stack of zinc blend structure and hence breaks the inversion symmetry. Recent theoretical study predicted CdGeAs<sub>2</sub> to be a topological insulator [1]. Owing to the inversion symmetry breaking, CdGeAs<sub>2</sub> can have nontrivial Fermi arc surface states and lead to a giant magnetoelectric effect. To establish a material platform of such exotic phenomena, experimental elucidation of the topological properties in CdGeAs<sub>2</sub> is highly desired.

In this study, we have performed high-resolution angle-resolved photoemission spectroscopy (ARPES) of CdGeAs<sub>2</sub> at BL7U. Single crystals of CdGeAs<sub>2</sub> were grown by the vapor-phase growth method. Clean surfaces for ARPES were obtained by *in situ* cleaving of the crystals. By x-ray laue diffraction, the cleaved surface was determined to be (101) plane. ARPES measurements were performed by using a MBS-A1 spectrometer at BL7U with linearly-polarized energy-tunable photons.

Figure 1(b) shows the ARPES intensity plot along a momentum cut crossing the  $\Gamma$  point of the bulk Brillouin zone. We observed several highly dispersive hole-like bands centered at the  $\Gamma$  point. These bands are reproduced by the band calculations shown by red

curves and attributed to the bulk valence bands with dominant As 4*p* orbital character. We further performed detailed measurements over the entire Brillouin zone with tuning photon energies to find a signature of the topological surface states.

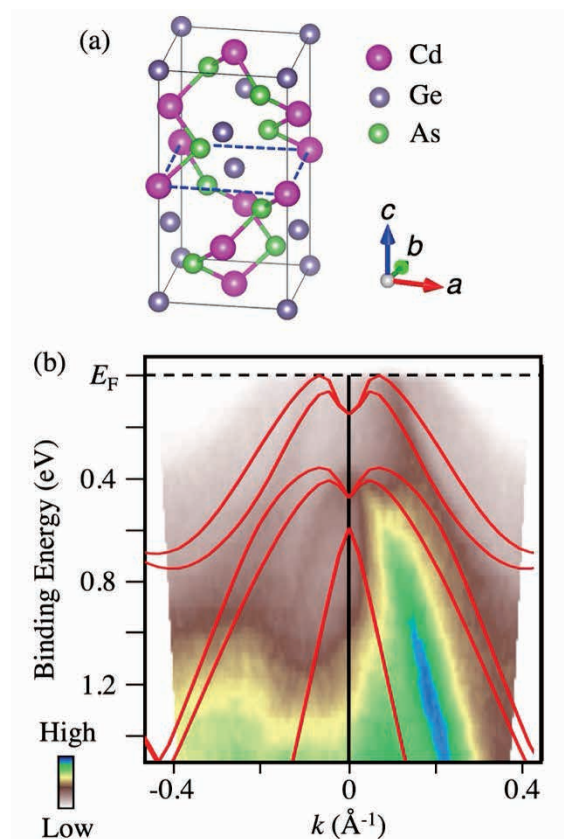


Fig. 1. (a) Three-dimensional view of the crystal structure of CdGeAs<sub>2</sub>. (b) ARPES intensity plotted as a function of binding energy and wave vector measured in CdGeAs<sub>2</sub>. Red curves are the result of first-principles band structure calculations.

[1] K. Osumi *et al.*, Commun. Phys. **4** (2021) 211.

## Electronic Structure of the five-fold oxygen-coordinated Cuprate Superconductor

M. Horio<sup>1</sup>, M. Miyamoto<sup>1</sup>, X. Peiao<sup>2</sup>, K. Tanaka<sup>3</sup>, T. Taniguchi<sup>2</sup>, M. Fujita<sup>2</sup> and I. Matsuda<sup>1</sup>

<sup>1</sup>*Institute for Solid State Physics, The University of Tokyo, Kashiwa, Chiba 277-8581, Japan*

<sup>2</sup>*Institute for Materials Research, Tohoku University, Katahira, Sendai 980-8577, Japan*

<sup>3</sup>*UVSOR Facility, Institute for Molecular Science, Okazaki 444-8585, Japan*

Structural isomers of so-called 214-type cuprates provide a unique platform for studying the effect of oxygen coordination on the electronic structure of cuprate superconductors. The local oxygen coordination around copper can be varied from a six-fold octahedron (T-type) to a four-fold square plane (T'-type). It is known that a decrease in the oxygen coordination number leads to a decrease in the charge-transfer gap and hence electron correlation [1]. However, while the T-type cuprates can be doped only with holes, the T'-type cuprates do not usually accept hole doping [2], preventing direct comparisons. On the other hand, T\*-type cuprates with five-fold pyramidal oxygen coordination can be hole-doped and are directly comparable to the T-type one [3]. Optical conductivity studies of the parent compound suggest that T\*-type cuprates have a smaller charge transfer gap than T-type [1]. As-grown samples of the T\*-type cuprates are known to have oxygen defects in the apical site, and in order to induce superconductivity, post-growth high-pressure oxygen annealing is required [3,4]. Recent oxygen K-edge x-ray absorption spectroscopy (XAS) studies [5] found a dramatic increase in doped holes upon oxygen annealing, consistent with compensation of oxygen defects. The  $T_c$  of O<sub>2</sub>-annealed T\*-SmLa<sub>1-x</sub>Sr<sub>x</sub>CuO<sub>4</sub> (SLSCO) monotonically increases with decreasing Sr concentration [6], in contrast to the dome-like behavior of the T-type La<sub>2-x</sub>Sr<sub>x</sub>CuO<sub>4</sub> (LSCO). The different superconducting properties between T\*- and T-type cuprates suggest a significant difference in the electronic structure associated with a change in the coordination number of oxygen. However, the electronic structure of T\*-type cuprates, including its evolution by annealing, is still largely unknown [7], even 35 years after its discovery. In this work, we performed angle-resolved photoemission spectroscopy (ARPES) measurements on the T\*-type cuprates T\*-SLSCO.

Single crystals of T\*-SLSCO ( $x = 0.25$ ) were grown by the travelling-solvent floating-zone method. After post-growth O<sub>2</sub> annealing at 500 °C and 45 MPa for 72 hours, the sample showed superconductivity below  $T_c = 17$  K. ARPES measurements were performed at BL7U of UVSOR at  $T = 7$  K and  $h\nu = 18$  eV.

Fig. 1 presents ARPES spectra obtained from T\*-SLSCO. While the spectral weight becomes

diminishingly small as approaching the Fermi level, Fermi crossing is observed for the nodal spectrum (#1). As moving away from the nodal region, the band become gapped with a strong suppression of the spectral weight, signifying the opening of a pseudogap. According to a previously reported phase diagram for T\*-SLSCO,  $x = 0.25$  corresponds to deep in the overdoped region. This is apparently incompatible with the present observation of the robust pseudogap, which is typical of underdoped or optimally doped samples. The result suggests a potentially unique phase diagram of T\*-type cuprates, which deserves further systematic investigations with varying hole concentrations.

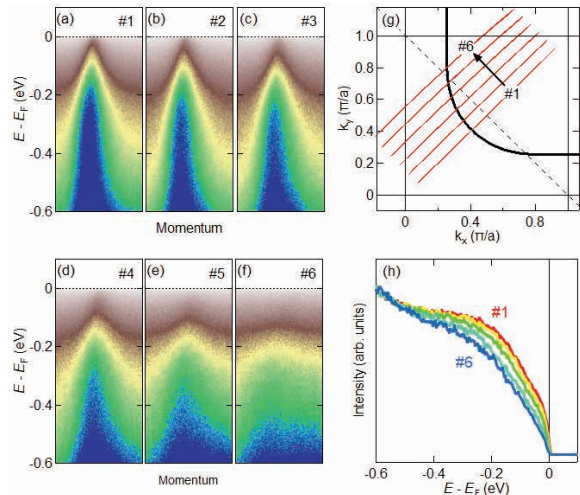


Fig. 1. ARPES spectra of O<sub>2</sub>-annealed T\*-SLSCO ( $x = 0.25$ ). (a)-(f) Energy-momentum maps from the nodal to antinodal regions. Cut positions are indicated in (g). (h) Energy distribution curves at each  $k_F$  point.

- [1] Y. Tokura *et al.*, Phys. Rev. B **41** (1990) 11657.
- [2] N. P. Armitage *et al.*, Rev. Mod. Phys. **82** (2010) 2421.
- [3] J. Akimitsu *et al.*, Jpn. J. Appl. Phys. **27** (1988) L1859.
- [4] F. Izumi *et al.*, Physica C **158** (1989) 440.
- [5] S. Asano *et al.*, J. Phys. Soc. Jpn. **89** (2020) 075002.
- [6] T. Kakeshita *et al.*, J. Phys.: Conf. Ser. **150** (2009) 052089.
- [7] A. Ino *et al.*, Physica B **351** (2004) 274.

BL7U

## Angle-Resolved Photoemission Study of Solid Electrolytes $\text{Li}_x\text{La}_{2/3-x}\text{TiO}_3$ Bulk Single Crystal

S. Koyama<sup>1</sup>, M. Nakatake<sup>2</sup>, S. Takakura<sup>3</sup>, K. Tanaka<sup>4,5</sup>,Y. Fujiwara<sup>6</sup>, T. Taishi<sup>6</sup>, H. Moriwake<sup>7</sup>, Y. Iriyama<sup>1</sup> and T. Ito<sup>1,3</sup><sup>1</sup>Graduate School of Engineering, Nagoya University, Nagoya 464-8603, Japan<sup>2</sup>Aichi Synchrotron Radiation Center, Seto, 489-0965, Japan<sup>3</sup>Synchrotron radiation Research center, Nagoya University, Nagoya 464-8603, Japan<sup>4</sup>UVSOR Facility, Institute for Molecular Science, Okazaki 444-8585, Japan<sup>5</sup>The Graduate University for Advanced Studies, Okazaki 444-8585, Japan<sup>6</sup>Faculty of Engineering, Shinshu University, Nagano 380-8553, Japan<sup>7</sup>Nanostructures Research Laboratory, Japan Fine Ceramics Center, Nagoya 456-8587, Japan

With the recent expansion of the use of lithium-ion secondary batteries, development of all-solid-state batteries using lithium-ion conductive inorganic solid electrolytes has been progressing to realize further safety, high energy density, and high output, etc. On the other hand, the valence-band electronic structure, which is essential to understand the relation between lithium-ion and electron conductivity in inorganic solid electrolytes, has not been well elucidated yet, though the chemical analysis using operando X-ray photoemission has intensively been applied on the system [1,2]. In this study, we have performed angle-resolved photoemission spectroscopy (ARPES) measurements on  $\text{Li}_x\text{La}_{2/3-x}\text{TiO}_3$  (LLTO) bulk single crystals to clarify the effect of lithium on the electronic structure of solid electrolytes. The results were compared with the ARPES study on  $\text{Li}_x\text{La}_{(1-x)/3}\text{NbO}_3$  (LLNbO) in which relatively lower Li ion conductivity has been reported [3].

ARPES measurements were performed at the UVSOR-III BL7U. Data were acquired with  $h\nu = 18$  eV at room temperature. To minimize spectral modification due to photo-irradiation, photon flux was sufficiently reduced ( $<3\text{E}+10$  photons/s) during all measurements. Single crystals were cleaved in situ along (100) plane, where La/Li rich (A1) and La/Li poor layers (A2) appear alternately (inset: Fig.2 (a)).

Figure 1 (a) and (b) show ARPES spectra and band structure along the  $\Gamma\text{X}$  line of LLTO, respectively. The observed band structure mainly consists of two peaks around 4 and 7 eV with the band gap about 3 eV. From the comparison with DFT calculation (Fig. 2(a)) [4], we found that the valence band width ( $\sim 5$  eV) seems to be similar between the ARPES and calculation.

When we compare the ARPES band structure between LLTO and LLNbO bulk single crystals [3], we found that the valence band width of LLTO becomes about 1 eV narrower than LLNbO, while the band gap size observed as almost the same. In Fig. 2(a) and (b), the observed differences of band width as well as the spectral features between LLTO and LLNbO are qualitatively reproduced by the DFT calculations. The results indicate the applicability of ARPES to study the electronic structure of solid electrolytes single-crystal.

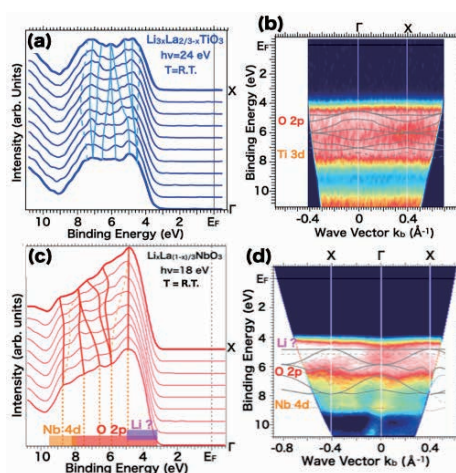


Fig. 1. ARPES spectra (a,c) and band structures (b,d) along the  $\Gamma\text{X}$  line of  $\text{Li}_x\text{La}_{2/3-x}\text{TiO}_3$  (a,b) and  $\text{Li}_x\text{La}_{(1-x)/3}\text{NbO}_3$  (c,d), respectively. Solid and dashed lines are guides for eyes.

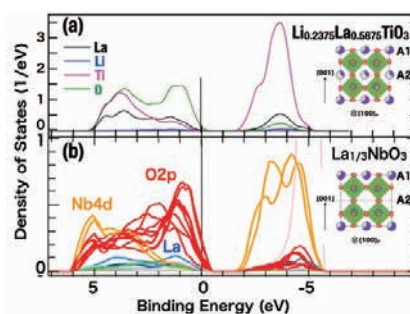


Fig. 2. The partial density of states of  $\text{Li}_{0.2375}\text{La}_{0.5875}\text{TiO}_3$  [4] (a) and  $\text{La}_{1/3}\text{NbO}_3$  (b), respectively. Inset of each panel shows average crystal structures of LLTO and LLNbO, respectively.

- [1]K. Hikima *et al.*, *Comm. Chem.* **5** (2022) 52.
- [2]K. N. Wood *et al.*, *Nature Commun.* **9** (2018) 2490.
- [3]Y. Fujiwara *et al.*, *J. Cryst. Growth* **433**, 48-53 (2016); Y. Fujiwara *et al.*, *Jpn. J. Appl. Phys.* **55**, 090306 (2016).
- [4]K. Dai *et al.*, *J. Mater. Sci.* **57** (2022) 2825.

## Electronic Structure of Layered Nitride Chloride ZrNCl by ARPES

N. Kataoka<sup>1</sup>, R. Saitou<sup>1</sup>, M. Tanaka<sup>2</sup> and T. Yokoya<sup>1,3</sup>

<sup>1</sup>Graduate School of Natural Science and Technology, Okayama University, Okayama 700-8530, Japan

<sup>2</sup>Graduate School of Engineering, Kyushu Institute of Technology, Kitakyushu 804-8550, Japan

<sup>3</sup>Research Institute for Interdisciplinary Science, Okayama University, Okayama 700-8530, Japan

Electron-doped layered nitride chloride ZrNCl shows superconductivity of  $T_c \sim 16$  K by intercalating alkali metals between the layers[1]. Observed exotic properties have suggested that its superconducting properties are difficult to be explained by the BCS theory[2]. Theoretical studies have proposed a model mediated by spin fluctuations[2] and a superconducting mechanism with a BCS-BEC crossover[3]. However, there are no experimental observations of the electronic structure by ARPES measurements, and the superconducting mechanism has remained undetermined. This is due to the fact that alkali metal-inserted ZrNCl is easily oxidized in the atmosphere and that it is difficult to obtain large single-crystal samples. In this study, we prepare electron-doped ZrNCl by depositing alkali metals in vacuum on a relatively large parent material. The electronic structure of ZrNCl before and after alkali metal deposition is studied by ARPES.

Samples were prepared by vacuum evaporation on cleaved ZrNCl single crystals at room temperature in ultrahigh vacuum using a Potassium(K) deposition source. The samples were transferred from the evaporation chamber to the measurement chamber. ARPES measurements were performed at BL7U of UVSOR III with 28–40 eV photons and an energy resolution of 15~20 meV. The measurement temperature was 40 K.

Figures 1(a) and 1(b) show the band dispersion of  $\Gamma$ -M line in ZrNCl before and after K deposition. Before deposition, the top of the valence band was located at  $\sim 3.0$  eV at the  $\Gamma$  point and the bottom of the valence band was located at  $\sim 8.3$  eV at the M point. After K deposition, the band near the  $\Gamma$  point, the top of the valence band, is shifted to the higher binding energy side by about 100 meV. The energy position of the bottom of the valence band at the M point did not change significantly. A theoretical study predicted a bandwidth of 6.1 eV[4] for ZrNCl and significant expansion of the valence band width by alkali metal intercalation. This is different from nearly the same band width between before and after K deposition. Regarding the change of the bandwidth by K evaporation, it is possible that the result is not an intrinsic change in electronic structure, but rather reflect an effect of the surface state formed by the deposition. For near the Fermi energy ( $E_F$ ), after deposition, a clear dispersive band was not observed at the K point, where electron pockets are expected to appear theoretically. On the other hand, angle integrated

spectrum near  $E_F$  shows a small structure, whose energy position and spectral shape are similar to the structure before K deposition (Figure 2), although the intensity increases after K deposition. Based on previous studies, the structure before evaporation may be a state caused by hydrogen impurities[5]. Further studies, including comparison with theoretical studies that also take the surface state into account, are necessary to understand these observations.

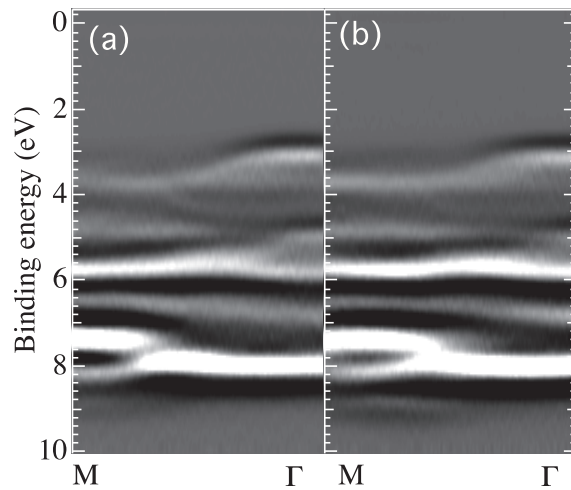


Fig. 1. 2nd-derivative ARPES intensity maps along  $\Gamma$ -M of ZrNCl before (a) and after (b) K deposition.

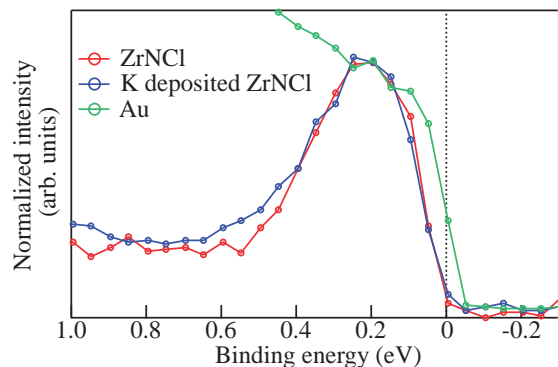


Fig. 2. Angle-integrated spectra near  $E_F$  of ZrNCl before and after K deposition, compared with Au.

- [1] Y. Kasahara *et al.*, *Physica C* **514** (2015) 354.
- [2] K. Kuroki, *Phys. Rev. B* **81** (2010) 104502.
- [3] Y. Nakagawa *et al.*, *Science* **372** (2021) 190.
- [4] Z. P. Yin *et al.*, *Phys. Rev. X* **3** (2013) 021011.
- [5] T. Yokoya *et al.*, *Phys. Rev. B* **70** (2004) 193103.

BL7U

## Low-Energy ARPES Study on the Electronic Structure of $\text{Cr}_2\text{Se}_3$

C.-W. Chuang<sup>1</sup>, T. Kawakami<sup>1</sup>, T. Kato<sup>1</sup>, K. Sugawara<sup>1,2</sup>, K. Nakayama<sup>1</sup>, S. Souma<sup>2,3</sup>,  
K. Tanaka<sup>4,5</sup>, A. Chainani<sup>6</sup>, T. Takahashi<sup>1</sup>, K. Segawa<sup>7</sup> and T. Sato<sup>1,2,3,8</sup>

<sup>1</sup>Department of Physics, Graduate School of Science, Tohoku University, Sendai 980-8578, Japan

<sup>2</sup>Advanced Institute for Materials Research (WPI-AIMR), Tohoku University, Sendai 980-8577, Japan

<sup>3</sup>Center for Science and Innovation in Spintronics (CSIS), Tohoku University, Sendai 980-8577, Japan

<sup>4</sup>UVSOR Synchrotron Facility, Institute for Molecular Science, Okazaki 444-8585, Japan

<sup>5</sup>School of Physical Sciences, The Graduate University for Advanced Studies (SOKENDAI),  
Okazaki 444-8585, Japan

<sup>6</sup>National Synchrotron Radiation Research Center, Hsinchu, 30077, Taiwan ROC

<sup>7</sup>Department of Physics, Kyoto Sangyo University, Kyoto 603-8555, Japan

<sup>8</sup>International Center for Synchrotron Radiation Innovation Smart (SRIS), Tohoku University,  
Sendai 980-8577, Japan

Transition metal chalcogenides (TMCs) are a group of materials that have been intensively studied for long time because of a wide variety of physical properties depending on their crystal structure and composition, including superconductivity, metal-insulator transition, and three-dimensional topological insulators. Recently, TMCs have attracted even more attention because their atomic layer films show dramatically different properties from those of bulk counterparts, such as Ising superconductivity, spin-valley Hall effect, two-dimensional topological insulators. To understand and control these exotic properties, an experimental study on the electronic structure of TMCs is of crucial importance.

Here we focus on a chromium-based TMC,  $\text{Cr}_2\text{Se}_3$  with the two-dimensional rhombohedral crystal structure (NiAs type;  $P6_3/mmc$ ). Bulk  $\text{Cr}_2\text{Se}_3$  is known as a thermoelectric material with a large figure of merit. This material is attracting attention because of intriguing magnetic properties; bulk  $\text{Cr}_2\text{Se}_3$  exhibits a collinear antiferromagnetic order with  $T_N \sim 45$  K, followed by a successive transition to a non-collinear antiferromagnetic phase [1], whereas monolayer  $\text{Cr}_2\text{Se}_3$  was predicted to be a ferromagnet which potentially hosts a half metallic ground state [2]. To clarify the interplay between these magnetic orders and the electronic structure, we have performed angle-resolved photoemission spectroscopy (ARPES) measurements of bulk and monolayer  $\text{Cr}_2\text{Se}_3$ .

High-quality bulk  $\text{Cr}_2\text{Se}_3$  was grown by flux method. Monolayer  $\text{Cr}_2\text{Se}_3$  was grown on graphene/SiC by molecular-beam epitaxy method. High-resolution ARPES measurements were performed by using a MBS-A1 spectrometer at BL7U with linearly-polarized energy-tunable photons.

Figure 1 shows representative ARPES results in the antiferromagnetic state of bulk  $\text{Cr}_2\text{Se}_3$ , i.e. ARPES spectra measured along a momentum cut crossing the  $\Gamma$  point [Fig. 1(a)] and the corresponding intensity plot as a function of binding energy and wave vector [Fig. 1(b)]. We observed several band dispersions in the energy range of the Fermi level ( $E_F$ ) to 5 eV, such as a

relatively flat hole-like band near  $E_F$  and a highly dispersive hole-like band topped at 2 eV below  $E_F$  at the  $\Gamma$  point. Upon increasing the temperature, we found a finite change in spectral intensity across  $T_N$ , indicative of magnetism-induced electronic reconstructions. We also measured the photon-energy dependence of the band dispersion and determined the three-dimensional bulk band structure. In addition, we found a clear difference in the band structure and its temperature dependence between bulk and monolayer  $\text{Cr}_2\text{Se}_3$ . The obtained ARPES results were compared with first-principles band structure calculations to understand the temperature- and thickness-dependent changes in the band structure.

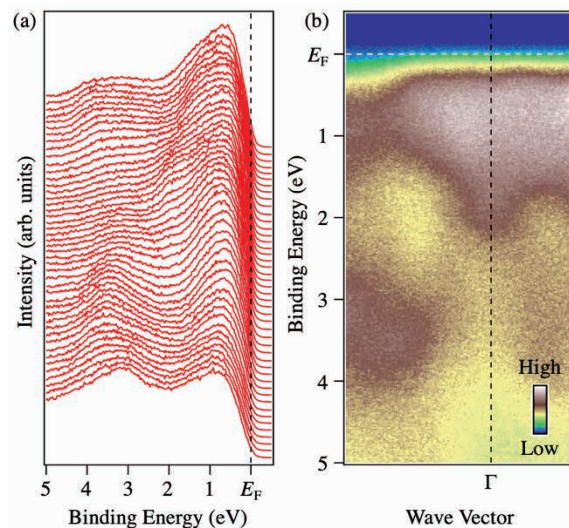


Fig. 1. (a) ARPES spectra in the valence band region of bulk  $\text{Cr}_2\text{Se}_3$  measured at  $T = 30$  K with 21-eV photons, and (b) corresponding intensity plot as a function of binding energy and wave vector.

[1] Y. Adachi *et al.*, J. Phys. Soc. Jpn. **63** (1994) 1548.

[2] J.-Y. Chen *et al.*, Adv. Electron. Mater. **6** (2020) 2070001.

## Polarization-Dependent Photoemission from the Folded Band of $\text{TiSe}_2$

S. Tanaka<sup>1</sup>, K. Ueno<sup>2</sup>, K. Fukutani<sup>3</sup> and K. Tanaka<sup>3</sup>

<sup>1</sup>*Sanken, Osaka University, Ibaraki 567-0047, Japan.*

<sup>2</sup>*Graduate School of Science and Engineering Saitama University, Saitama 338-8570, Japan.*

<sup>3</sup>*UVSOR Synchrotron Facility, Institute for Molecular Science, Okazaki 444-8585, Japan.*

It is crucial for the creation of symmetry-broken collective phases, such as charge density waves and topological and superconducting states of matter, that crystalline solids have a momentum-dependent orbital structure. Measurements with the polarization-dependent angle-resolved photoelectron spectroscopy (ARPES) can provide important details on the material's orbital texture. Layered material  $\text{TiSe}_2$ , one of the transition-metal-dichalcogenide (TMDC) and known as a model system of the charge-density wave (CDW) transition, is a good candidate to make such a study, since  $\text{TiTe}_2$ , which has a similar electronic structure to  $\text{TiSe}_2$  but does not exhibit the CDW transition, has been recently well studied by similar method[1].

Fig. 1 shows ARPES spectra near the  $\Gamma$  point at 10K taken using the vertically polarized photon of 7eV. The cutting plane along the  $k_x$  (at  $k_y=0$ ) and  $k_y$  (at  $k_x=0$ ) axes is shown in the lower panels, while the upper panel displays the photoelectron intensity map along the  $k_x$ - $k_y$  plane at the Fermi level. The band below the  $\text{BE} \sim 0.07\text{eV}$  is the  $\text{Se}4p/\text{Ti}3d$  valence band, and the band near the Fermi level is the replica of the  $\text{Ti}3d$ -derived conduction band originally located at the M point, which is caused by the formation of the  $(2 \times 2 \times 2)$  superlattice as a result of the CDW transition. The assignment can be confirmed by the observation of the extinction of this feature at higher temperatures. The photoelectron intensity distribution, however, is different from the original  $\text{Ti}3d$  conduction band at M. White dot lines represent the replica's anticipated traces, which originate from the six nearby M points, and only a portion of them have photoelectrons visible. This must be due to the matrix element effect, which relates to the orbital texture and also discerning structural and collective phases of the material in the CDW transition.

We measure the polarization-dependent ARPES by rotating the sample along the surface normal to provide information about the matrix element effect (azimuthal rotation). The vertically-polarized photon was used, and the polarization vector is always parallel to the sample surface. The variation in the photoelectron distribution as a result of azimuthal angle is depicted in Figure 2. Shiny branches shift as the polarization vector's angle with the sample axis changes. It makes it evident that the matrix element is crucial, and the in-depth research, currently underway, will yield information regarding the orbital texture of the replica band formed by the CDW transition.

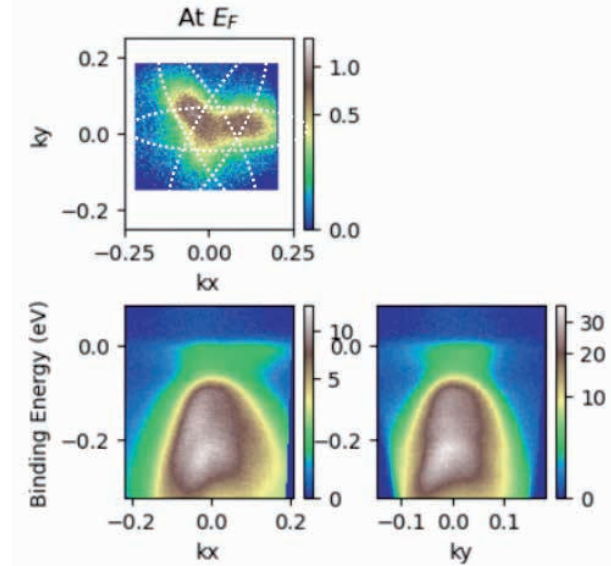


Fig. 1. ARPES spectra of  $\text{TiSe}_2$  at 10K. The photon energy taken was 7eV of vertical polarization.

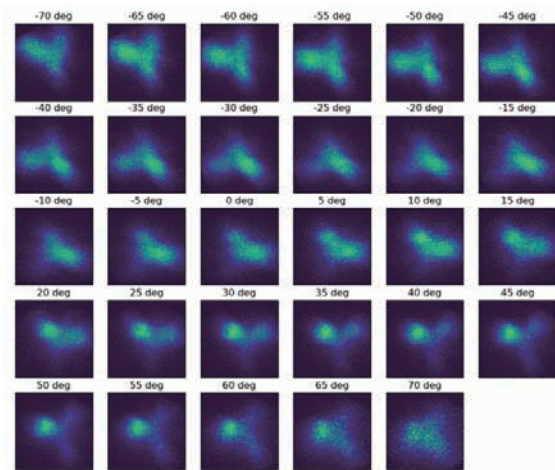


Fig. 2. ARPES intensity maps near the Fermi level as a function of the azimuth rotation. The photon of 7eV with a vertical polarization is used.

[1] S. Beaulieu *et.al.*, npj Quantum Materials **6** (2021) 93.

BL7U

## Momentum Dependence of the Spectral Weight in the Single Layer High- $T_c$ Cuprate $\text{Bi}_2\text{Sr}_2\text{CuO}_{6+\delta}$ Studied by ARPES

Y. Onishi<sup>1</sup>, Y. Miyai<sup>1</sup>, Y. Tsubota<sup>1</sup>, S. Kuma<sup>2</sup>, M. Atira<sup>2</sup>, K. Tanaka<sup>3</sup>, H. Eisaki<sup>4</sup>, S. Ishida<sup>4</sup>, K. Shimda<sup>1,2</sup> and S. Ideta<sup>1,2</sup>

<sup>1</sup>Graduate School of Advanced Science and Engineering, Hiroshima Univ., Japan

<sup>2</sup>Hiroshima Synchrotron Radiation Center (HiSOR), Hiroshima Univ., Japan

<sup>3</sup>UVSOR-III Synchrotron, Institute for Molecular Science (IMS), Japan.

<sup>4</sup>National Institute of Advanced Industrial Science and Technology (AIST), Japan

Spectral weight (SW) directly observed by angle-resolved photoemission spectroscopy (ARPES) has the information of the electronic structure which is related to the mechanism of high-transition temperature ( $T_c$ ) cuprate superconductivity [1-3]. Nonetheless extensive experimental and theoretical studies have been reported, the mechanism of high- $T_c$  cuprates have not been clear yet, why their  $T_c$  exceeds above  $\sim 40$  K which cannot be explained by the BCS theory [4]. To understand the mechanism of high  $T_c$  in cuprate superconductivity, one of the essential physical parameters is superfluid density ( $\rho_s$ ) which plays an important role in determining  $T_c$  and might be proportional to SW observed by ARPES [1,2,5,6]. In this study, we have performed an ARPES study to investigate the relationship between coherent spectral weights (SW) on the Fermi surface directly and  $T_c$  in cuprates, which seem to correspond to the magnitude of  $\rho_s$  and  $T_c$  [5].

We measure the electronic structure of the single-layer Bi-based high- $T_c$  cuprate superconductor,  $\text{Bi}_2\text{Sr}_2\text{CuO}_{6+\delta}$  (Bi2201), which has one  $\text{CuO}_2$  layer in the unit cell and shows a high  $T_c$  of 35-40 K at optimal doping [7]. We have performed ARPES measurements systematically to directly investigate the electronic structure of the optimally doped ( $T_c \sim 35$  K) and overdoped ( $T_c \sim 30$  K) Bi2201. ARPES were carried out at BL7U, and temperature was set at  $\sim 10$  K ( $< T_c$ ) and  $1.5T_c$  to measure the electronic structure in the superconducting and normal states, respectively. The photon energy was  $h\nu = 17$  eV. High-quality single crystals of Bi2201 were cleaved *in-situ* in the ultrahigh vacuum  $\sim 5 \times 10^{-9}$  Pa.

In this study, We have clearly observed Fermi surface (FS) on Bi2201 in the  $s$  polarization above and below

$T_c$ . Energy distribution curves (EDCs) are symmetrized and we have estimated the Fermi momentum ( $k_F$ ) on the entire FS, where the  $k_F$  is determined by minimum gap locus method. Compared with EDC in the superconducting and normal states, we have successfully observed difference of the spectral weight even though the nodal region in contrast with the previous study [6]. We will systematically measured doping dependence of SW in the nodal direction. From the present study, we found that the even in the nodal region which shows the zero superconducting gap, the nodal region should contribute to the superconductivity in cuprates. As a next step, we will measure the momentum dependence on the entire FS and discuss the distribution of SW on FS. We will also study the relationship between pseudogap and the distribution of SW.

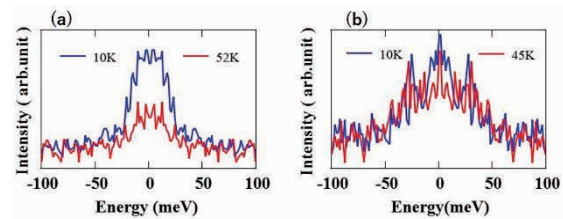


Fig. 1. Symmetrized EDC of OPT35K (a) and OD30K (b).

- [1] D. L. Feng *et al.*, Science **289** (2000) 277.
- [2] H. Ding *et al.*, Phys. Rev. Lett. **87** (2001) 227001.
- [3] K. M. Shen *et al.*, Science **307** (2005) 901.
- [4] W. L. McMillan, Phys. Rev. **167** (1968) 331.
- [5] Y. J. Uemura *et al.*, Phys. Rev. Lett. **66** (1991) 2665.
- [6] T. Kondo *et al.*, Nature **457** (2009) 296.
- [7] A. Iyo *et al.*, J. Phys. Soc. Jpn. **76** (2007) 094711.

## Excitation Spectra of Plastic Scintillators in the Vacuum Ultraviolet Region

M. Koshimizu<sup>1</sup>, Y. Fujimoto<sup>2</sup> and K. Asai<sup>3</sup>

<sup>1</sup>Research Institute of Electronics, Shizuoka University, Hamamatsu 432-8011, Japan

<sup>2</sup>Department of Applied Chemistry, Graduate School of Engineering, Tohoku University, Sendai 980-8579, Japan

Plastic scintillators consist of host polymer and organic phosphor molecules and are widely used owing to their fast response and easy fabrication at large scale. The scintillation process in the plastic scintillators is roughly described as initial formation of ionization and electronic excitation and subsequent transfer of the excitation energy to the phosphor molecules. In the consideration of the scintillation process, we have to consider two kinds of electronic excitations: singlet and triplet states. The triplet states are formed in two processes: one is the intersystem crossing from the singlet to the triplet states, and the other is the direct formation of the triplet states upon recombination of ionization. To analyze the contribution of the latter process, we consider that the excitation in the vacuum ultraviolet (VUV) light may be a convenient tool, because the excitation by the VUV light produces ionization at higher probability with the excitation photon energy. In this study, we measured the excitation spectra of the plastic scintillators at 50–200 nm.

Plastic scintillators were fabricated using polystyrene as the host polymer and DPO and POPOP as the primary and secondary phosphors, respectively. The samples having different phosphor concentrations were fabricated. The photoluminescence spectra of the samples were obtained with VUV excitation at BL7B, UVSOR. The excitation spectra were obtained as the emission intensity in the photoluminescence spectra as functions of the excitation wavelength.

The photoluminescence spectra of the samples are presented in Figure 1. The emission bands are derived from the singlet excitation of POPOP. The spectra were similar at different excitation wavelengths. The excitation spectra of the samples with different DPO-POPOP concentrations are presented in Figures 2 and 3. The photoluminescence intensity increased and subsequently decreased as the excitation wavelength became shorter. The increase in the intensity down to 150 nm can be attributed to production of secondary excitation. The decrease in the intensity can be attributed to the enhanced probability of the triplet formation.

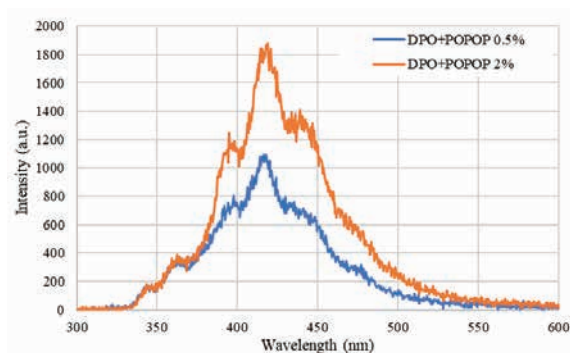


Fig. 1. Photoluminescence spectra of the plastic scintillators with excitation at 150 nm.

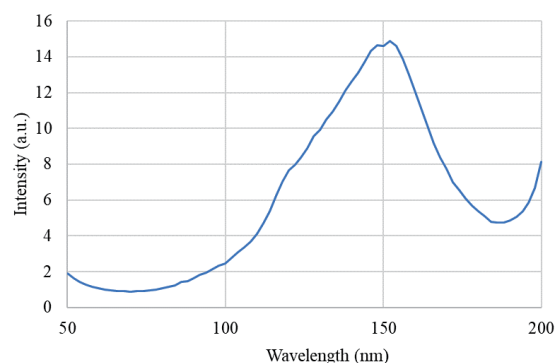


Fig. 2. Excitation spectrum of the plastic scintillators having DPO-POPOP concentration of 0.5 wt%.

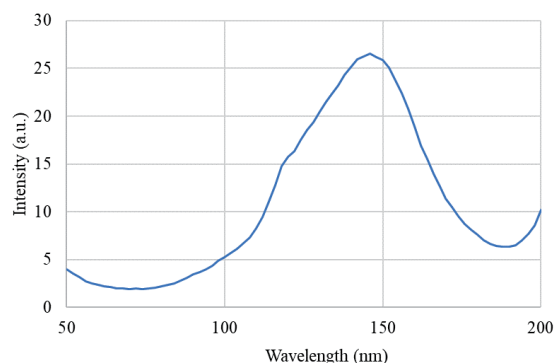


Fig. 3. Excitation spectrum of the plastic scintillators having DPO-POPOP concentration of 2 wt%.

BL7B

## Mineral Analysis for Resource Exploration by Deep Ultraviolet Spectroscopy

T. Shimizu, K. Shinohara, K. Yamanoi and N. Sarukura

*Institute of Laser Engineering, Osaka University, 2-6 Yamadaoka Suita, Osaka 565-0875 Japan*

Vacuum ultraviolet (VUV) light has important technological applications in photochemical processing, surface treatment, optical cleaning of semiconductor substrates, and sterilization. In particular, it has been suggested that non-contact sterilization, treatment, and processing may be advanced by using VUV in the current coronavirus pandemic. To keep pace with the rapid progress in VUV research and application, it is essential to develop detectors in the short wavelength range. Conventional detectors are mainly sensitive only to visible light, and therefore VUV scintillators based on rare-earth ions and wide bandgap materials have been investigated for the detection of VUV. In our research group, we have developed scintillators with rare-earth ions doped in fluoride materials using wide bandgap materials and have achieved good results.

Currently, there is a need to develop a spectrometer for two-dimensional analysis of broadband light, which is required in the fields of industrial technology, energy, and the environment. Imaging spectroscopy is widely used for the identification of molecular species of gases and nondestructive analysis of liquids and solids, and is beginning to be applied to environmental measurements and resource surveys. In addition to the sorting by visible light imaging called color sorting, multi-wavelength imaging measurement is becoming a key to solving social problems in the future. In addition, the non-destructive nature of the measurement reduces the environmental burden, and research that integrates the humanities and sciences, such as the non-contact analysis of cultural assets, is also expected. If this imaging spectroscopic measurement can be performed in a large space, it is expected to make it possible to estimate the location of buried resources without digging, and to analyze tiles and paints on the walls of valuable old temples and shrines.

In the case of resource survey as one of the goals, the deep ultraviolet region, such as VUV, is compatible with the absorption and emission of quartz, the most common mineral on earth, for observation, and its characteristics are well represented. On the other hand, the practical application of imaging spectroscopy systems, for which technology has been accumulated in the visible light region, has not progressed due to the lack of optical elements that are compatible with non-visible light. The applicant has focused on the applicability of imaging spectroscopy measurement and has so far succeeded in developing a lens that can be applied up to deep UV, also using UVSOR [1][2].

Since the preparation of the elements around the measurement device has progressed significantly up to this point, the next step is to start evaluating the VUV properties of the actual minerals.

Typical minerals are known to exhibit fluorescence. Minerals contain a variety of impurities, which are the active factors that give rise to fluorescence. In other words, by observing fluorescence, it is possible to evaluate the quality of a mineral, making it a powerful tool for resource exploration and environmental measurement. However, fluorescence observation requires excitation in the deep ultraviolet. In this study, we used UVSOR-BL7B to demonstrate whether typical mineral impurities can be evaluated by PL (photo luminescence) spectra and PLE (photo luminescence excitation) spectra.

Fig. 1 shows the measurement results of fluorite. It is conventionally believed that europium is contained in fluorite as an impurity. The measurement data this time shows a peak that is certainly derived from europium. Although the data shown here are for general fluorite, other minerals were also analyzed in the same way, and impurities were confirmed. It was found that the deep ultraviolet analysis technique is effective for mineral evaluation. In the future, we will combine this technique with our spectroscopic technology and put it to practical use as a new technology for resource exploration and environmental measurement.

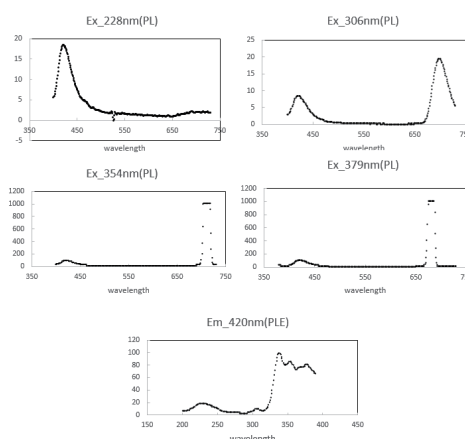


Fig. 1. PL spectra and PLE spectra of fluorite.

[1] T. Shimizu *et al.*, *UVSOR Activity Report 2019*, **47** (2020) 100.

[2] Y. Minami *et al.*, *Phys. Status Solidi B*, **257**(2020) 1900480.

## Optical Reflectivity Study of Au-Al-Yb Quasicrystals

H. Okamura<sup>1</sup>, A. Kamiki<sup>1</sup>, K. Namba<sup>2</sup>, S. Hirokawa<sup>2</sup> and K. Deguchi<sup>2</sup>

<sup>1</sup>Department of Applied Chemistry, Tokushima University, Tokushima 770-8506, Japan

<sup>2</sup>Graduate School of Science, Nagoya University, Nagoya 464-8602, Japan

Since its discovery, quasicrystals (QCs) have attracted a lot of interest for their unique properties [1]. For example, they do not have a translational symmetry in the crystal structure but show a clear rotational order in the measured diffraction pattern. Recently, Yb-containing QCs have been studied in detail [2,3], and they have revealed a singular behavior of the average Yb valence as a function of  $a_{6D}$ , a six-dimensional lattice parameter of the QC [3]. Namely, the average Yb valence of a series of Au-Al-Yb QC samples showed a sudden and steep drop, from 2.82 to 2.31, when  $a_{6D}$  of the sample was increased through a critical value of 0.74 nm by about 0.01 nm. Valence transitions or crossovers have been observed in many Yb-containing crystalline materials such as heavy fermion and intermediate-valence compounds. It is quite interesting whether or not the singular behavior of the Yb valence in QCs shares any common feature with the Yb-based heavy fermion compounds.

To investigate the interesting electronic structures of Yb-containing QCs, we have been measuring the optical reflectivity spectra [ $R(\omega)$ ] of Au-Al-Yb QCs that show the above-mentioned valence-transition-like behavior. In our experimental method,  $R(\omega)$  of a sample is measured over a wide spectral range between infrared and vacuum UV, and the Kramers-Kronig (KK) analysis is used to obtain the dielectric function  $\epsilon(\omega)$  or the optical conductivity  $\sigma(\omega)$  from the measured  $R(\omega)$ . At BL7B of UVSOR, we have measured  $R(\omega)$  between 40 and 600 nm on the six samples indicated in Table 1. Note that Sample C has the critical value of  $a_{6D}$ , and that the average Yb valence rapidly decreases from Sample C to F.

Figure 1 indicates the  $R(\omega)$  spectra of Samples A-F measured at room temperature. All the samples show increase of  $R(\omega)$  toward longer wavelength, with an onset at around 150-200 nm. Samples C, D and E also show a clear minimum of  $R(\omega)$  at 160-200 nm range. Samples A, B and F, on the other hand, do not show a clear minimum. Namely, there seems to be some qualitative difference between the two groups of samples. The difference in the onset wavelength between Samples B and C is particularly clear, although they are next to each other in Table 1. An onset of high reflectivity in a metallic compound is usually associated

with the plasma frequency, and is related with the density of free electrons. However, to make a detailed analysis on the electronic structures, we need to obtain  $\epsilon(\omega)$  and  $\sigma(\omega)$  via the KK analysis of  $R(\omega)$ . To do so, we are currently extending the measurement to the infrared range, since a wide spectral range of  $R(\omega)$  is required to perform a reliable KK analysis. The spectra in Fig. 1 will be connected to those in the infrared range to obtain  $R(\omega)$  in a wide spectral range, and will be used for the KK analysis.

Table 1. Measured QC samples.

Sample label	Chemical formula	Average Yb valence
A	(Au <sub>0.5</sub> Cu <sub>0.5</sub> ) <sub>49</sub> Al <sub>34</sub> Yb <sub>17</sub>	2.90
B	(Au <sub>0.9</sub> Cu <sub>0.1</sub> ) <sub>49</sub> Al <sub>34</sub> Yb <sub>17</sub>	2.83
C	Au <sub>49</sub> Al <sub>34</sub> Yb <sub>17</sub>	2.82
D	Au <sub>49</sub> (Al <sub>0.9</sub> Ga <sub>0.1</sub> ) <sub>34</sub> Yb <sub>17</sub>	2.73
E	Au <sub>49</sub> (Al <sub>0.7</sub> Ga <sub>0.3</sub> ) <sub>34</sub> Yb <sub>17</sub>	2.66
F	Au <sub>56</sub> Ga <sub>28</sub> Yb <sub>16</sub>	2.31

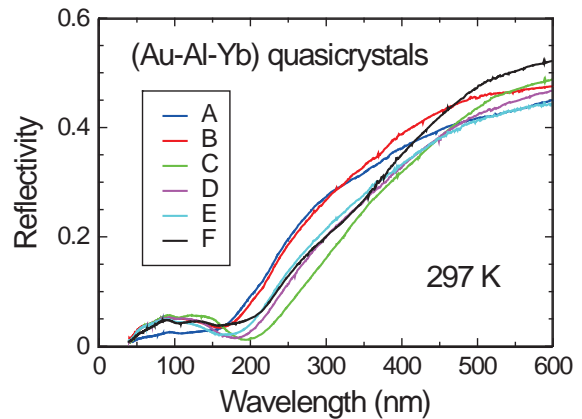


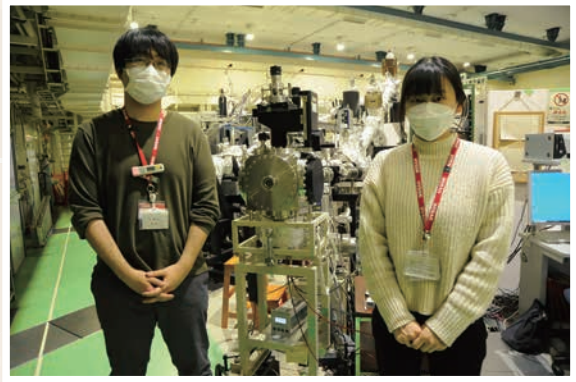
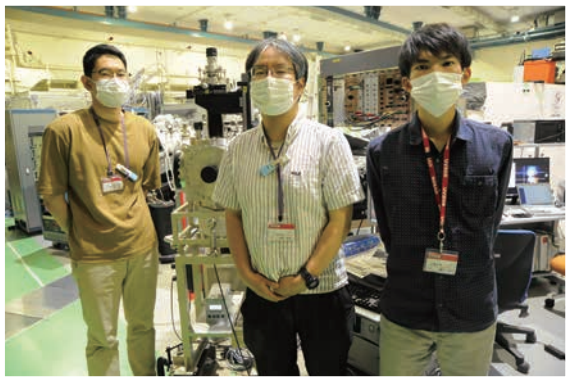
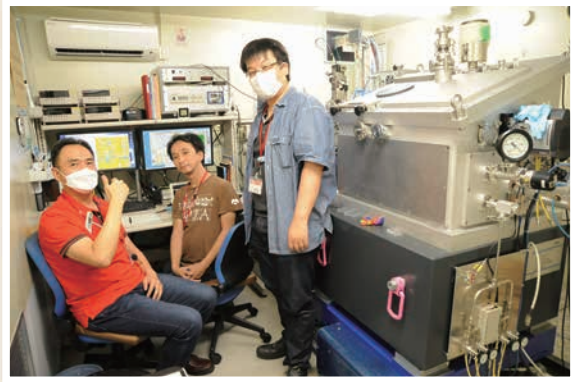
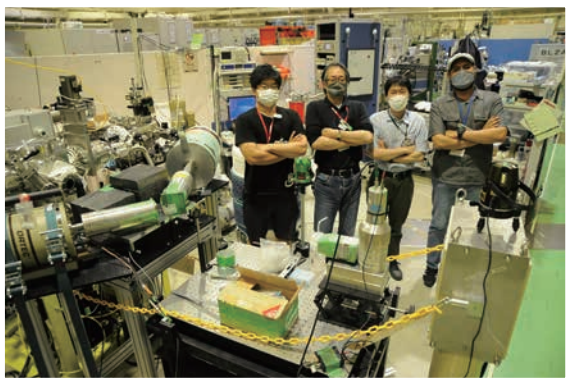
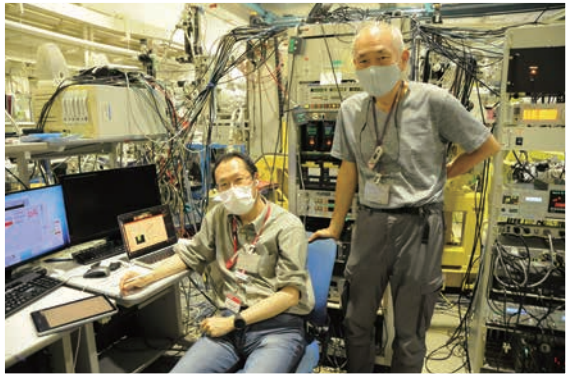
Fig. 1. Optical reflectivity spectra of Au-Cu-Yb quasicrystal samples A to F at room temperature measured at BL7B.

[1] D. Shechtman *et al.*, Phys. Rev. Lett. **53** (1984) 1951.

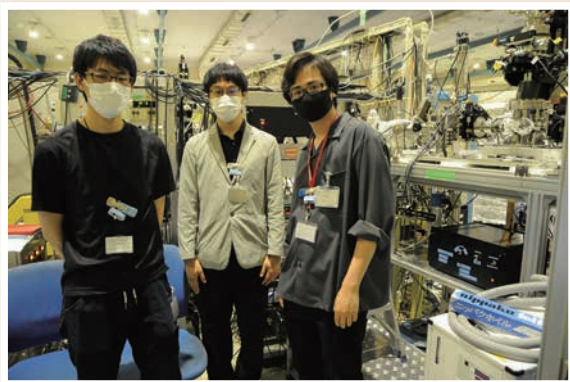
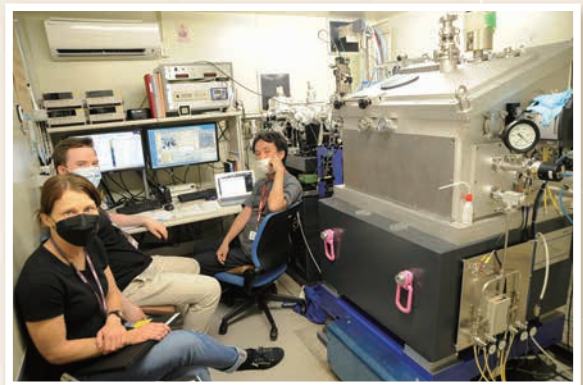
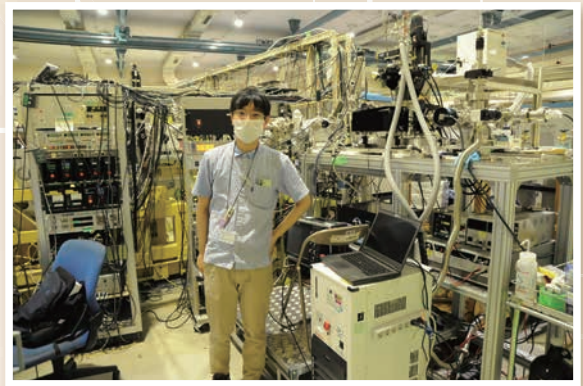
[2] K. Deguchi *et al.*, Nat. Mater. **11** (2012) 1013.

[3] K. Imura *et al.*, Sci. Rep. **10** (2020) 17116.

# UVSOR User 4

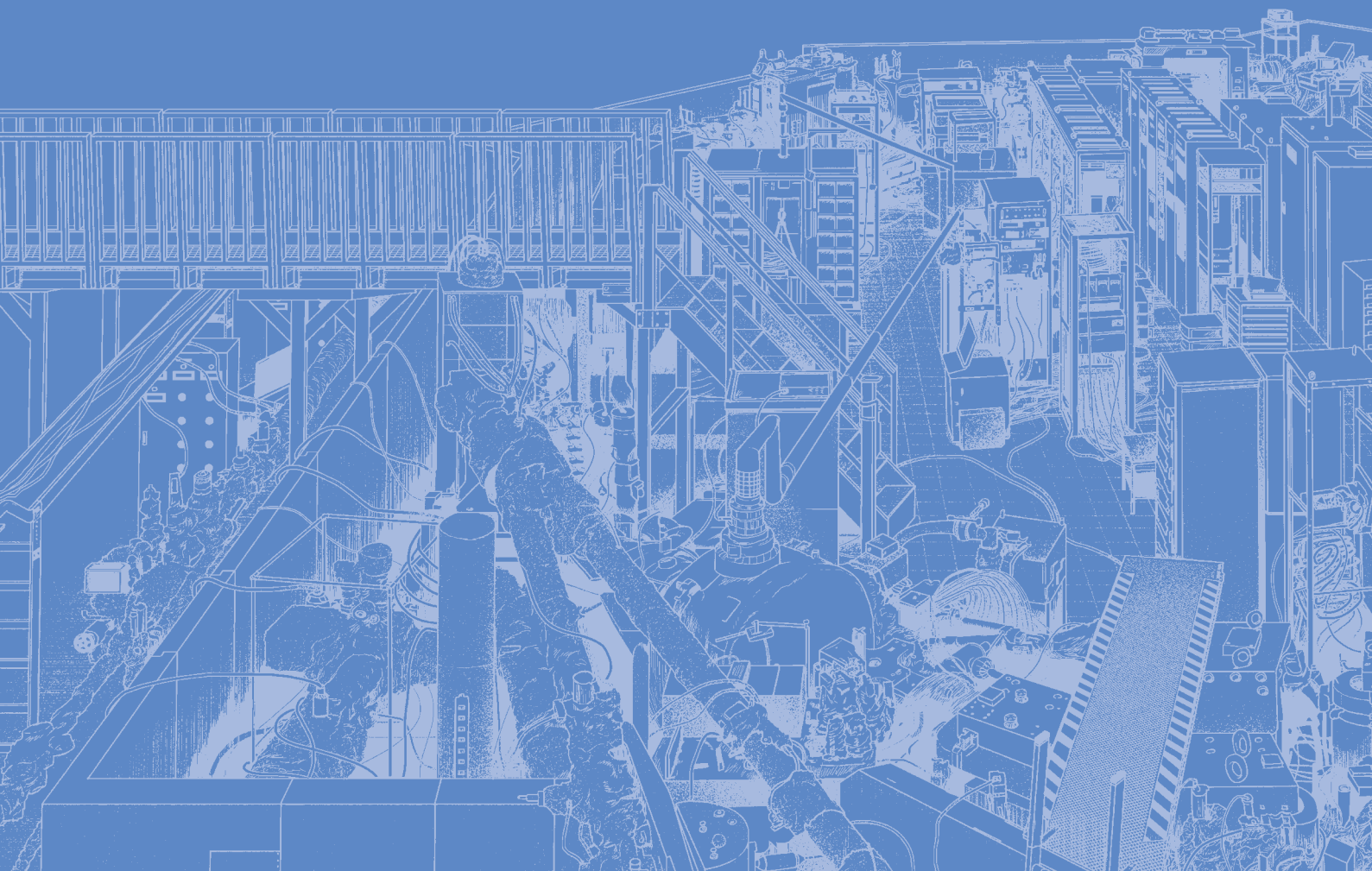


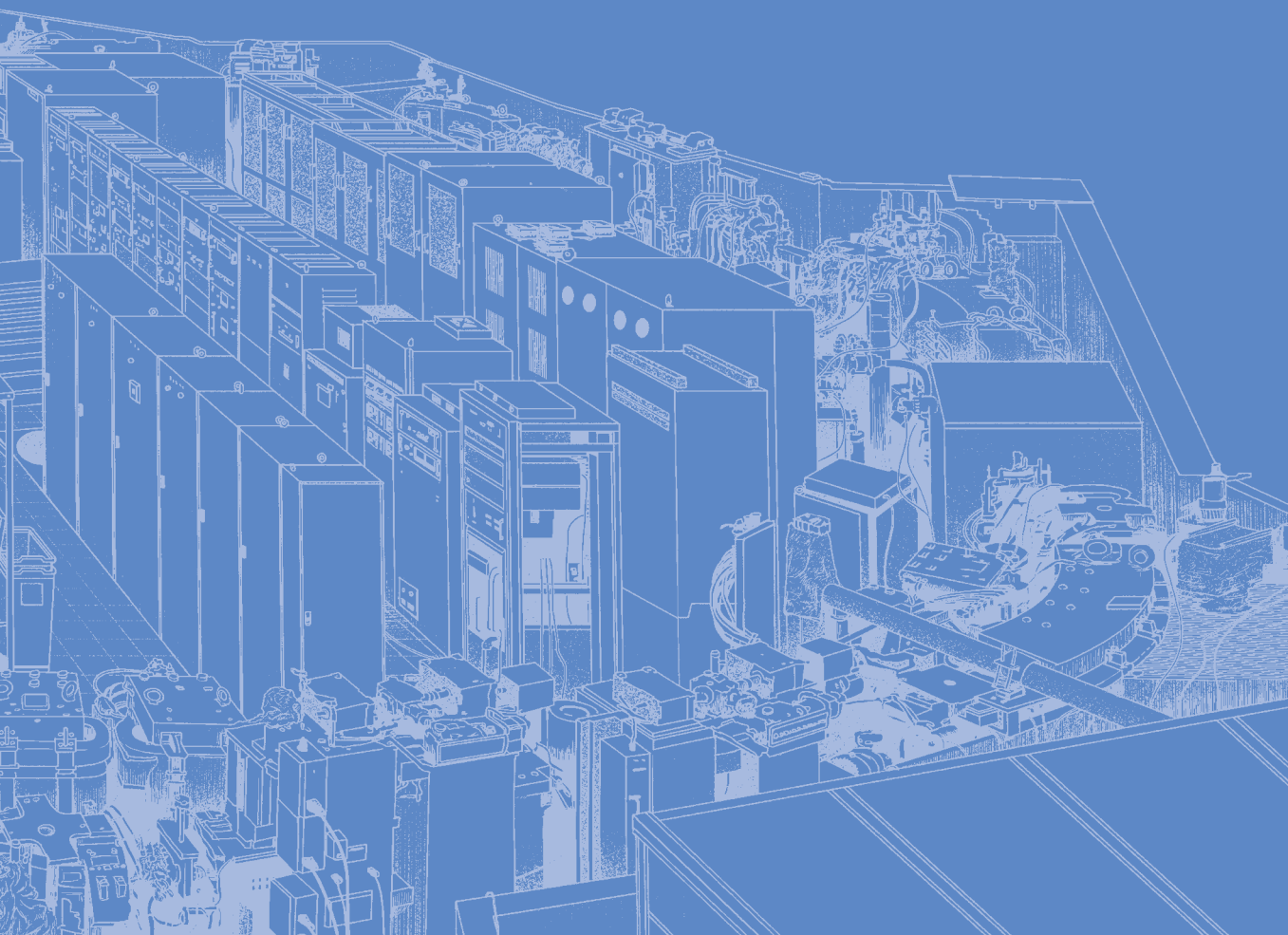
# UVSOR User 5



# III-3

Chemistry





BL4B

## Ligand Field in Fe-based spin-crossover Coordination Polymer Revealed by Soft x-ray Absorption Spectroscopy

K. Yamagami

Japan Synchrotron Radiation Research Institute (JASRI), 1-1-1, Sayo-cho, Sayo-gun, Hyogo 679-5198, Japan

The 3d transition metal elements have many attractive physical phenomena in solid-state materials such as unconventional superconductivity, metal-insulator transition, and spin transition involving magnetism due to their high charge, spin, and orbital degrees of freedom. Since the 3d electronic states in solids are controlled by “ligand field effects” due to the type and symmetry of ligands and “charge transfer interactions” between transition metal ions via ligands, experimental exploration of element-specific electronic states provides fundamental information for understanding macroscopic properties involving 3d electrons.

In this study, I focus on “spin crossover,” which is strongly related to ligand field effects and spin degrees of freedom. Spin crossover is a phenomenon in which a change in the splitting width of the 3d orbital level causes an electron spin transition. In particular, the spin crossover transition that appears in transition metal coordination polymers exhibits thermal hysteresis. Since the transition temperature and the shape of the hysteresis depend on the guest molecules encapsulated in the coordination polymer, it is attracting attention as a new adsorption material along with activated carbon and silica gel. However, spectroscopic element-specific analysis of the 3d orbital levels associated with thermal spin-crossover transitions in coordination polymers is challenging due to their low chemical stability against light source irradiation.

In this work, I performed the soft x-ray absorption spectroscopy (XAS) for the Fe-based spin-crossover coordination polymer  $\text{Fe}(\text{pyrazine})_2[\text{Pt}(\text{CN})_4]$  to investigate the contribution of ligand field effect for  $\text{Fe}^{2+}$  ions under the tetragonal symmetry related to the thermal spin crossover transition.

The XAS measurement was done at UVSOR BL4B. The Fe  $L_{2,3}$ -edge XAS spectra was recorded by the total electron yield (TEY) and partial fluorescence yield (PFY) modes obtained by the drain current for TEY and SDD detector for PFY, respectively. The powder samples were thinly expanded on the carbon tape and its temperature was controlled by the liq.  $\text{N}_2$  and ceramic heaters. During measurement, the x-ray irradiated damage of the samples was checked from the position and irradiation time dependence of the XAS spectra. The energy calibration was done by the Fe  $L_{2,3}$ -edge XAS spectra of  $\text{Fe}_3\text{O}_4$ . All XAS spectra were normalized by the incoming x-ray flux.

In this report, I show the XAS results in PFY mode since the huge noise was observed in TEY mode. Fig. 1 shows the temperature dependent Fe  $L_{2,3}$ -edge XAS spectra. During one cycle of temperature change, I

observed a spectral change corresponding to the transition between the high-spin (HS) state at high-temperature and the low-spin (LS) state at low-temperature and found that the transition temperature differs between the heating and the cooling processes. According to the simplest  $\text{Fe}^{2+}$  ionic model calculations, the  $\text{Fe}^{2+}$  ions have only HS state at 320 K and only LS state at 240 K. Therefore, I carried out the linear fitting analysis by the spectra at 320 K and 240 K to estimate the spin state weight around spin-crossover transition. The fitting results reproduce the experimental spectra and plotted as the function of the temperature together with the macroscopic magnetometry result of  $\text{Fe}(\text{pyrazine})_2[\text{Pt}(\text{CN})_4]$  (Fig. 2). I found that the transition temperature between XAS spectra and magnetization is quite different, seemingly linking to the different thermal stability between the electronic state and structural distortion.

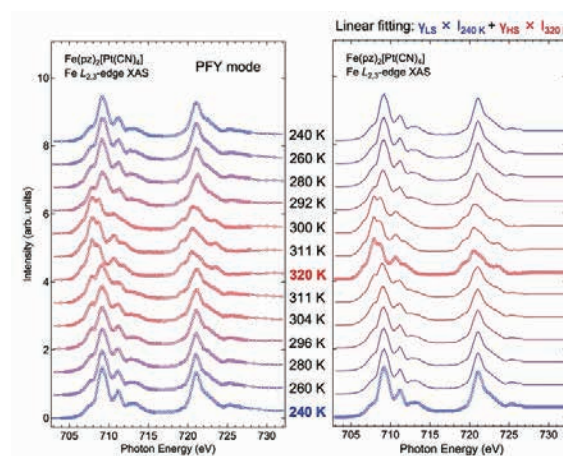


Fig. 1. The temperature dependent Fe  $L_{2,3}$ -edge XAS spectra and fitting analysis result of  $\text{Fe}(\text{pyrazine})_2[\text{Pt}(\text{CN})_4]$ .

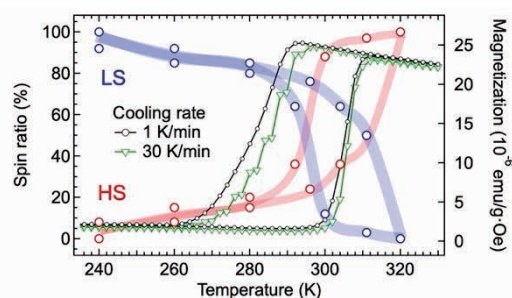


Fig. 2. The spin state weight of  $\text{Fe}^{2+}$  ions as the function of the temperature.

## Monitoring Phase Difference between Magnetic Substates in Helium Atom

T. Kaneyasu<sup>1,2</sup>, Y. Hikosaka<sup>3</sup>, M. Fujimoto<sup>2,4</sup>, H. Iwayama<sup>2,5</sup> and M. Katoh<sup>2,6</sup>

<sup>1</sup>SAGA Light Source, Tosu 841-0005, Japan

<sup>2</sup>Institute for Molecular Science, Okazaki 444-8585, Japan

<sup>3</sup>Institute of Liberal Arts and Sciences, University of Toyama, Toyama 930-0194, Japan

<sup>4</sup>Synchrotron Radiation Research Center, Nagoya University, Nagoya, 464-8603, Japan

<sup>5</sup>The Graduate University for Advanced Studies (SOKENDAI), Okazaki 444-8585, Japan

<sup>6</sup>Hiroshima Synchrotron Radiation Center, Hiroshima University, Higashi-Hiroshima 739-0046, Japan

Quantum manipulation of populations and reaction pathways in matter using the coherence properties of light, so-called coherent control, is currently one of the hottest research areas in optical physics and photochemistry. We have recently shown that synchrotron light is a new tool for achieving coherent control in the XUV and attosecond regimes [1–3]. This method is based on the use of the longitudinal coherence of individual light wave packets comprising incoherent radiation pulses. In all of these experiments, a pair of light wave packets was used to produce a pair of electron wave packets that interfere in a single atom. The quantum phase difference between the electron wave packets determines the behavior of the controlled (or probed) quantum state, and can be precisely controlled by varying the time delay between the light wave packets at the attosecond level. In this report, we present another approach to orbital alignment control of helium atoms [2] to monitor the phase difference between the interfering wave packets. The quantum phase difference between coherently excited magnetic substates is visualized as a quantum beat that appears in the fluorescence decay curve [4].

The experiment was performed at undulator beamline BLIU of the UVSOR-III synchrotron. A tandem undulator consisting of twin APPLE-II type variable polarization devices was operated in helical mode, providing pairs of 10-cycle left- and right-circularly polarized light wave packets. The central frequency of the fundamental radiation was set to about 24 eV. To measure the fluorescence decay curve of helium atoms, the UVSOR-III synchrotron was operated in the single bunch mode. The fluorescence photons emitted from helium atoms were detected by a photomultiplier tube. A magnetic field of approximately 20 G was applied parallel to the light propagation axis in the interaction region to induce Zeeman splitting between the magnetic substates of helium atoms.

Figure 1 shows fluorescence decay curves of  $1s6p$  excited state of helium atoms measured at eight different settings of the time delay  $\tau$  between the light wave packets. The quantum beat oscillations superimposed on the exponential decay with a lifetime of 13.1 ns are visible and the initial phases of the oscillations shift by varying the time delay. The

theoretical curves well reproduce the quantum beat structures observed in the measurement. Quantum beat measurement thus enables visualization of the quantum phase that has been used as a control knob for quantum manipulation of atomic systems

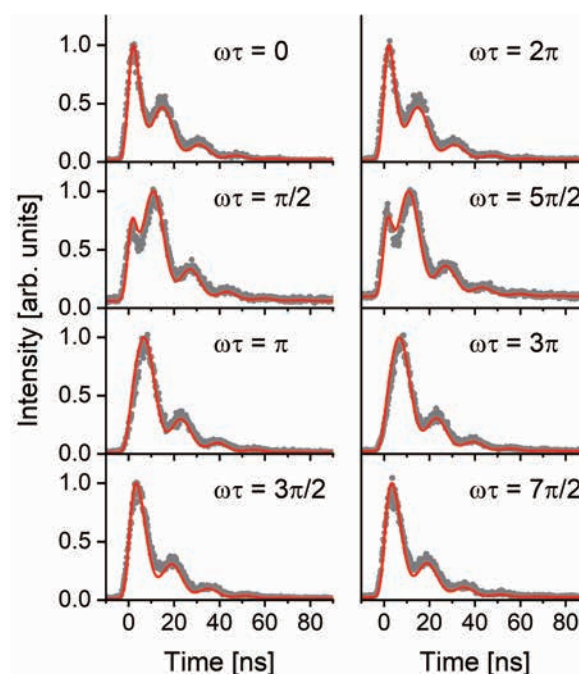


Fig. 1. Zeeman quantum beat in fluorescence decay of helium atoms [4]. The quantum phase  $\omega\tau$  is set to increase from 0 to  $7\pi/2$  with a step size of approximately  $\pi/2$  where  $\omega$  is the resonance frequency from the ground state to the  $1s6p$  state. The experimental data points are shown by gray circles and the red curves represent the calculation results

[1] Y. Hikosaka *et al.*, Nat. Commun. **10** (2019) 4988; *ibid.* **12** (2021) 3782.

[2] T. Kaneyasu *et al.*, Phys. Rev. Lett. **123** (2019) 233401.

[3] T. Kaneyasu *et al.*, Phys. Rev. Lett. **126** (2021) 113202.

[4] T. Kaneyasu *et al.*, J. Phys.: Conf. Ser. **2380** (2022) 012115.

BL1U

## High-Resolution Measurement of State-Resolved Photoelectron Circular Dichroism with Varied Photoionization Energies

H. Kohguchi<sup>1</sup>, Y. Hikosaka<sup>2</sup>, T. Kaneyasu<sup>3</sup>, S. Wada<sup>1</sup>, H. Ota<sup>4</sup>, M. Katoh<sup>1,4</sup> and Y-I. Suzuki<sup>5</sup>

<sup>1</sup>Graduate School of Advanced Science and Engineering, Hiroshima University,  
Higashi-Hiroshima 739-8526, Japan

<sup>2</sup>Institute of Liberal Arts and Sciences, University of Toyama, Toyama 930-0194, Japan

<sup>3</sup>SAGA Light Source, Tosu 841-0005, Japan

<sup>4</sup>UVSOR Synchrotron Facility, Institute for Molecular Science, Okazaki 444-8585, Japan

<sup>5</sup>School of Medical Technology, Health Sciences University of Hokkaido, Tobetsu, 061-0293, Japan

Measurements of photoelectron circular dichroism (PECD) require high-quality radiation for ionizing chiral molecules. One-photon photoionization in the vacuum ultraviolet region provides a fundamental understanding of the physical origin of PECD. Thus, we launched the PECD measurements at BL1U on February 2020. In the beginning of the feasibility test, the undulator conditions for circularly polarized light were optimized for a particular electron beam orbit, which was not used in regular beam time operation. In 2022, the normal electron beam orbit applicable to BL1U was developed so that the PECD measurements were possible in regular beam time. With the alternation of the electron beam orbit, the arrangement of the BL1U line was reformed.

We have employed a monochromator to reduce the spread of photon energy to measure the state-resolved PECD of chiral systems. The monochromator line with two mirror chambers is inserted between the BL1U port and our velocity-map imaging (VMI) apparatus (Fig. 1). We also modify the imaging device in this beam time. Our original setup used a resistive anode backed by an MCP detector to obtain the photoelectron images. We have replaced an imaging system consisting of a phosphor screen and a CCD camera with the anode type imager. The benefit of the optical camera system is real-time imaging during the measurement, which is expected to be advantageous in efficient searching for experimental conditions. Improved performance due to the renewal of the electron beam condition and the imaging system is evaluated in comparison with the previous PECD data [1].

We measured the PECD of methyl oxirane ( $\text{CH}_3\text{-C}_2\text{H}_3\text{O}$ ) in the new experimental setup. The PECD appears as asymmetric forward/backward intensity with respect to the circularly polarized light propagation. The result almost reproduced the previous data in that the forward-backward asymmetry (red/blue in Fig. 2) exhibited distinct state-dependence. The quality of the PECD data is the contrast of the forward/backward asymmetry, which is presented by blue/red contrast in the difference images of the right and left circular polarization in Fig. 2. The imaging system with the

camera provides an analog (Fig. 2(a)) and a counting (Fig. 2(b)) integration modes. The better PECD data was obtained by analog integration, although it is generally inferior to the counting mode in accuracy. This can be due to the too-slow counting integration of the software compared to the photoelectron counting rate. The renewal of the setup potentially improve our PECD measurements; however more detailed examination of several signal properties is necessary.

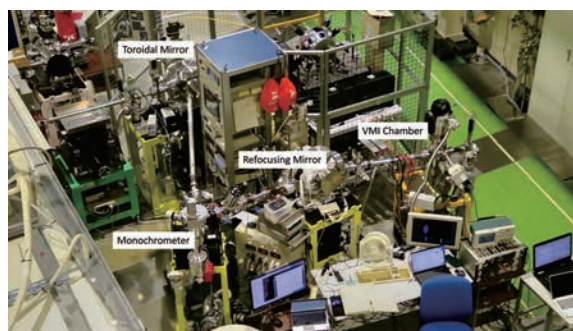


Fig. 1. New arrangement of the VMI apparatus for PECD measurements with a monochromator at the BL1U beamline.

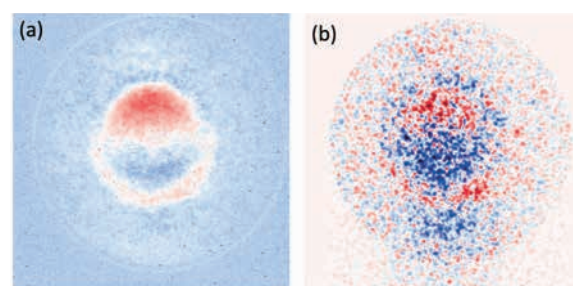


Fig. 2. Photoelectron circular dichroism (PECD) images of *s*-methyl oxirane measured with (a) analog integration mode and (b) counting integration mode. The propagation direction of the photoionization radiation is vertical in the figures.

[1] H. Kohguchi, Y. Hikosaka, T. Kaneyasu, S. Wada, H. Ota, M. Fujimoto, M. Kato and Y-I. Suzuki, UVSOR Activity Report **49** (2021) 106.

## M<sub>4,5</sub>-edge XANES Spectra of La and Nd Complex Oxides

H. Asakura<sup>1</sup>, M. Konno<sup>1</sup> and K. Nanakarage<sup>1</sup>

<sup>1</sup>Department of Applied Chemistry, Faculty of Science and Engineering, Kindai University, Kowakae, Higashiosaka, Osaka 577-8502, Japan

The areas of the pre-edge region at the lanthanide (Ln) L<sub>1</sub>-edge XANES spectra and the full with half maximum of the white line at the Ln L<sub>3</sub>-edge XANES spectra have been found to be good indicators of the local structure or symmetry of Ln elements in complex oxides [1-3]. However, it is usually difficult to obtain detailed electronic and/or geometric information of the Ln elements because of the inherent low energy resolution of Ln L-edge XANES spectra. Then, the M-edge XANES spectra, which are potentially much more sensitive to electronic structure, are employed to obtain more detailed information on the local structure. However, there are very few reports on the measurement of M-edge XANES spectra of Ln elements. In this study, we measured the M-edge XANES spectra of La or Nd complex oxides to investigate whether they can be used as indicators of local structure.

We prepared various La and Nd complex oxides by a polymerized complex method and confirmed that single phase polycrystalline powders were obtained by their XRD patterns. Nd M<sub>4,5</sub>-edge XANES spectra were obtained at BL2A, UVSOR using a Beryl double-crystal monochromator. We put each powder sample onto indium (In) foil bonded to the sample holder with carbon tape for total electron yield method measurement. To the best of our knowledge, there are no well-established data analysis procedure on the M-edge XANES spectra even for basic background removal or normalization. On the present data, we performed background removal in the pre-edge region below the M<sub>5</sub>-edge and normalization in the post-edge region above the M<sub>4</sub>-edge with Athena included in the Demeter package [4].

The Nd M<sub>4,5</sub>-edge XANES spectrum of Nd<sub>2</sub>O<sub>3</sub>, NdAlO<sub>3</sub>, NdMnO<sub>3</sub>, and Nd<sub>2</sub>CoO<sub>4</sub> was very similar to each other (Fig. 1), which indicated the oxidation state of Nd was the same, trivalent. By a closer look into the spectra, we found difference in relative absorbance at around 1006, 1008, and 1010 eV marked as peak A, B, and C at the Nd M<sub>4</sub>-edge XANES region (Fig. 2). The main contribution for the peak A and B is ascribed to the transition obeying the selection rule  $\Delta J = 0$ , and peak C is to  $\Delta J = -1$ , respectively [5]. In addition, theoretical simulation of Pr M<sub>4,5</sub>-edge XANES of Pr<sup>3+</sup>, [PrF<sub>6</sub>]<sup>3-</sup>, [PrCl<sub>6</sub>]<sup>3-</sup>, and [PrBr<sub>6</sub>]<sup>3-</sup> indicates possible sensitivity to the local structure of Pr [5]. However, at present, we do not have plausible interpretation of these characteristic features.

On the other hand, there are some questions as to whether the validity of the spectra can be guaranteed. For example, it is possible that differences due to

charge-up or slight variations in X-rays may be reflected into the spectra. In fact, on NdAlO<sub>3</sub>, significant difference was observed at another facility when the energy sweep direction was from the low energy to the high energy and from high to low, and the effect of charge-up was suspected. Thus, further careful study is needed.

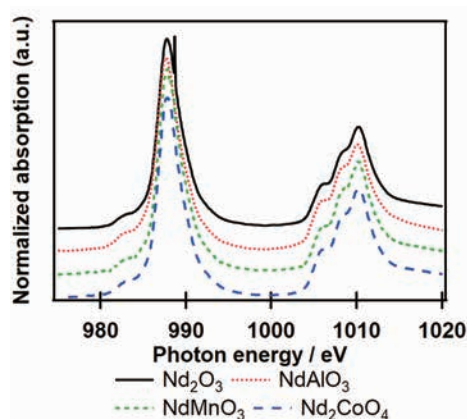


Fig. 1. Nd M<sub>4,5</sub>-edge XANES spectra of Nd complex oxides

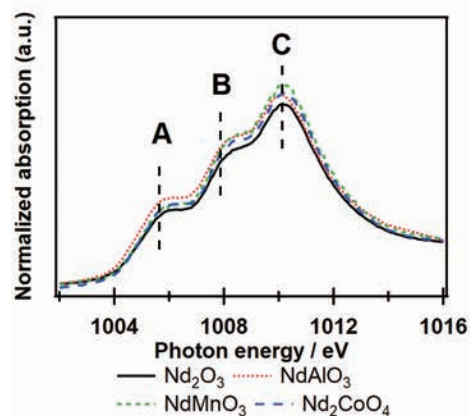


Fig. 2. Nd M<sub>4</sub>-edge XANES spectra of Nd complex oxides

- [1] H. Asakura *et al.*, *Inorg. Chem.* **53** (2015) 6048.
- [2] H. Asakura *et al.*, *J. Phys. Chem. C* **118** (2014) 20881.
- [3] H. Asakura *et al.*, *Inorg. Chem.* **60** (2021) 9359.
- [4] B. Ravel, M. Newville, *J. Synchrotron Rad.* **12** (2005) 537.
- [5] H. Ramanantoanina, *J. Chem. Phys.* **149** (2018) 054104.

BL3U

## O K-edge XAS of Photoreactions in Dissolved Oxygen on Lipid Bilayer

F. Kumaki<sup>1,2</sup>, M. Nagasaka<sup>3,4</sup>, Y. Kinjo<sup>5</sup>, R. Tero<sup>5</sup>, Y. Okano<sup>3</sup>, M. Fujimoto<sup>3,4</sup> and J. Adachi<sup>1,2</sup>

<sup>1</sup>*Institute of Materials Structure Science, High Energy Accelerator Research Organization, Tsukuba 305-0801, Japan*

<sup>2</sup>*School of High Energy Accelerator Science, The Graduate University for Advanced Studies (SOKENDAI), Tsukuba 305-0801, Japan*

<sup>3</sup>*Institute for Molecular Science, Okazaki 444-8585, Japan*

<sup>4</sup>*School of Physical Sciences, The Graduate University for Advanced Studies (SOKENDAI), Okazaki 444-8585, Japan*

<sup>5</sup>*Toyohashi University of Technology, Toyohashi 441-8580, Japan*

Porphyrim dyes form triplet states by the photoexcitation and relaxation process due to light absorption. Singlet oxygen ( $^1\text{O}_2$ ) is generated by the energy transfer from the triplet state of the porphyrin to the surrounding oxygen molecule with ground triplet state ( $^3\text{O}_2$ ). Singlet oxygen is highly reactive, and the generation of singlet oxygen by photosensitizers such as porphyrins is used for a cancer treatment as a photodynamic therapy [1]. The experimental research of the elementary processes of singlet oxygen production in a wet environment like in vivo conditions or in liquid is important for the development of chemistry and medicine.

From O K-edge X-ray absorption spectroscopy (XAS), we planned to measure the electronic state of singlet oxygen generated in solution directly via laser excitation of photosensitizers. We have recently developed and demonstrated the time-resolved XAS system for optical reactions in liquid samples by a synchronizing synchrotron radiation pulse and a laser pulse at KEK Photon Factory [2]. At the UVSOR, we have been developed a similar time-resolved XAS system by synchronizing soft X-ray pulses (530 eV, 128 ps) and visible laser pulses (400 nm). Since the lifetime of singlet oxygen in liquid is  $\sim 3 \mu\text{s}$  [3], the synchrotron radiation pulse whose pulse duration is about 100 ps, is suitable to observe its dynamics. In this report, the change of XAS spectra between the ground state and the state under laser irradiation was measured.

The O K-edge XAS spectra were measured by using the liquid flow cell at BL3U. The liquid cell consists of a liquid layer sandwiched between two  $\text{Si}_3\text{N}_4$  membranes on which lipid bilayers were prepared. The buffer solution (NaCl 100 mM, HEPES 25 mM) bubbled with oxygen gas was continuously pumped into the cell at a flow rate of 100  $\mu\text{l/hr}$  to keep the dissolved oxygen on the lipid bilayer. The emphasized peak of dissolved oxygen on the lipid bilayers can be measured by thinning the liquid layer to the limit [4].

For the formation of singlet oxygen with a photoreaction, the chlorophyll-*a* was used as a photosensitizer and was added to the lipid bilayer. By irradiating the visible laser (400 nm, 0.5mW) which is second order harmonic generation (SHG) of Ti:sapphire laser to the cell, the chlorophyll-*a* was photoexcited.

We attempted to observe singlet oxygen produced from dissolved oxygen by the energy transfer from the triplet state of chlorophyll-*a* caused by the photoexcitation and the relaxation process. The O K-edge XAS spectra of dissolved oxygen in the ground state and during laser irradiation were compared, and the difference was observed.

Figure 1 shows the O K-edge XAS spectra of lipid bilayer. The peak around 531 eV is assigned as dissolved oxygen molecules adsorbed on lipid bilayers. The spectrum of the state during laser irradiation (laser on) shows the lower photon energy shift compared to that in the ground state (laser off). We will discuss the formation mechanism of singlet oxygen from the difference spectrum with the help of the inner-shell calculations.

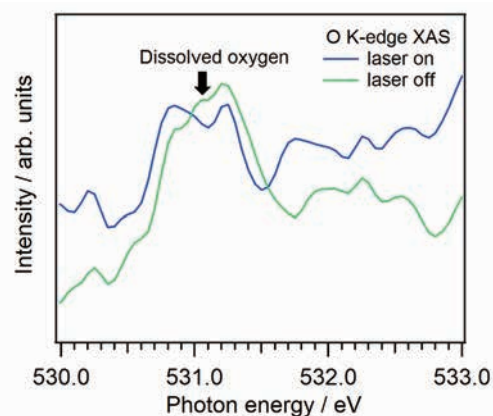


Fig. 1. O K-edge XAS spectra of dissolved oxygen, whose peak positions are around 531 eV, on lipid bilayers. The green and blue lines are the ground state (laser off) and the state under laser irradiation (laser on), respectively.

- [1] M. Ethirajan *et al.*, *Chem. Soc. Rev.* **40** (2011) 340.
- [2] F. Kumaki *et al.*, *J. Chem. Phys.* **158** (2023) 104201.
- [3] C. A. Long and D. R. Kearns, *J. Am. Chem. Soc.* **97** (1975) 2018.
- [4] F. Kumaki *et al.*, *UVSOR Activity Report*, **49** (2022) 118.

## Carbon K-edge X-ray Absorption Spectra of Liquid Ethanol Reproduced by Quantum Chemical Calculations and Molecular Dynamics Simulations

M. Nagasaka<sup>1,2</sup>

<sup>1</sup>Institute for Molecular Science, Okazaki 444-8585, Japan

<sup>2</sup>The Graduate University for Advanced Studies (SOKENDAI), Okazaki 444-8585, Japan

Liquid ethanol (EtOH) shows complicated liquid structures with the continuous formation and decay of hydrogen bond networks including the hydrophobic interactions between ethyl groups. Soft X-ray absorption spectroscopy (XAS) has potential to investigate the structures of liquid EtOH separating the contributions of the hydrogen bond interactions and hydrophobic interactions between ethyl groups. Recently, we have measured C K-edge XAS of liquid EtOH by using a transmitted-type liquid cell [1]. However, the inner-shell spectra of the model structures did not reproduce the spectral shapes of liquid EtOH since the liquid structures reconfigured continuously. In this study, we have performed C K-edge inner-shell calculations of liquid EtOH by the summation of the calculated spectra of excited EtOH molecules with neighbor molecules extracted from the liquid structures obtained by the molecular dynamics (MD) simulations [2].

MD simulations of liquid EtOH were conducted by using the program package GROMACS [3]. The equilibrium structure including one thousand EtOH molecules were obtained after a simulation time of 101 ns at 25 °C and 1 atm in the isobaric-isothermal ensemble. The inner-shell calculations were conducted by using the program package GSCF3 [4]. The ground and core excited states were calculated within the Hartree-Fock method, namely,  $\Delta$ SCF (self-consistent field). As shown in the inset of Fig. 1, we have extracted one thousand small liquid structures that consist of excited EtOH molecules and neighbor EtOH molecules within the  $\text{CH}_2$ - $\text{CH}_2$  distance of 6 Å from the excited EtOH molecules. The inner-shell spectrum of liquid EtOH was obtained by the summation of one thousand calculated spectra of small liquid structures.

Figure 1(a) shows the experimentally obtained C K-edge XAS spectrum of liquid EtOH [1]. The spectrum shows four peaks: The peak at 287.311 eV is the transition of the  $\text{CH}_3$  C 1s electron to the 3s-type Rydberg orbital ( $\text{CH}_3$  3s). The peaks at 288.025 eV and 288.760 eV are assigned as the transition of the  $\text{CH}_3$  C 1s electron to the 3p-type Rydberg orbitals ( $\text{CH}_3$  3p1 and 3p2). The peak at 289.710 eV is assigned to the transition of the  $\text{CH}_2$  C 1s electron to the 3s-type Rydberg orbital ( $\text{CH}_2$  3s). Figure 1(b) shows the calculated inner-shell spectrum of liquid EtOH from the summation of one thousand calculated spectra of small liquid structures. The calculated spectra well reproduced four Rydberg peaks and spectra shapes

obtained by the experiments. However, the calculated higher energy shifts from gas to liquid phases are overestimated compared to the experimental values. It is because the induced polarization of the surrounding EtOH molecules above the  $\text{CH}_2$ - $\text{CH}_2$  distance of 6 Å is ignored, which causes the lower energy shifts of the XAS peaks. We have also calculated C K-edge inner-shell spectra of liquid methanol and confirmed that the calculated spectra well reproduced the experimental results [5].

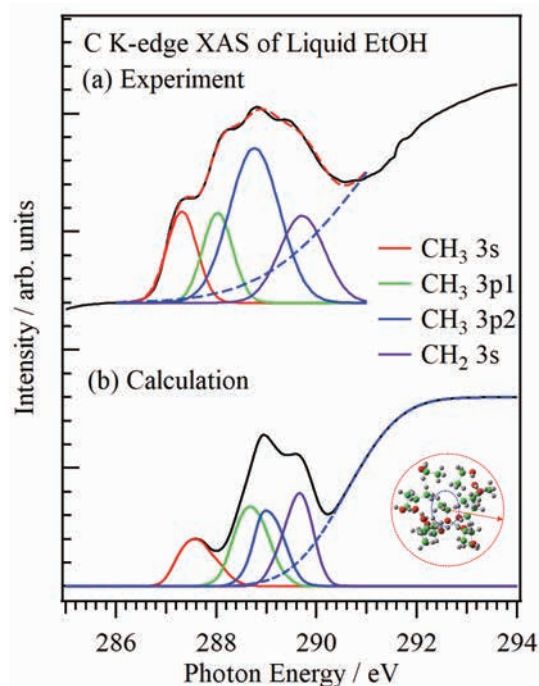


Fig. 1. C K-edge XAS spectra of liquid EtOH from (a) experiments and (b) calculations. The inset shows one of the liquid structures used for the inner-shell calculations, where EtOH molecules were extracted from the liquid structure within the  $\text{CH}_2$ - $\text{CH}_2$  distance of 6 Å from the central EtOH molecule.

- [1] M. Nagasaka *et al.*, J. Phys. Chem. B **126** (2022) 4948.
- [2] M. Nagasaka, J. Chem. Phys. **158** (2023) 024501.
- [3] M. J. Abraham *et al.*, SoftwareX **1-2** (2015) 19.
- [4] N. Kosugi, Theor. Chim. Acta **72** (1987) 149.
- [5] M. Nagasaka *et al.*, J. Phys. Chem. B **118** (2014) 4388.

BL3U

## Observation of the Behavior of Sumanene in Organic Solvents by C K-edge XAS Experiment

Y. Uetake<sup>1,2</sup>, K. Sugimura<sup>1</sup>, R. Ihsan<sup>1</sup>, M. Nagasaka<sup>3</sup> and H. Sakurai<sup>1,2</sup>

<sup>1</sup>Division of Applied Chemistry, Graduate School of Engineering, Osaka University, Suita 565-0871, Japan

<sup>2</sup>Innovative Catalysis Science Division, Institute for Open and Transdisciplinary Research Initiatives (ICS-OTRI), Osaka University, Suita, 565-0871, Japan

<sup>3</sup>Institute for Molecular Science, Okazaki 444-8585, Japan

Sumanene, a bowl-shaped  $\pi$ -extended molecule, has been found to exhibit a unique columnar packing structure in the crystalline state due to the intermolecular CH- $\pi$  interactions between them[1]. Such interactions are expected to occur in the solution state. Previously, our group reported the infrared spectroscopy of sumanene in *para*-H<sub>2</sub> matrix. However, there are still few reports on the dynamic behavior of  $\pi$ -conjugated molecule, including sumanene, in solution state. In this study, we performed solution-phase X-ray absorption spectroscopy (XAS) of  $\pi$ -extended molecules to investigate dynamic behavior, such as intermolecular interactions, in organic solvents.

The solution-phase C K-edge XAS experiments were performed at soft X-ray beamline BL3U using a transmission-type liquid flow cell[2]. Sumanene (**1**), corannulene (**2**), and triphenylene (**3**) were dissolved in tetrahydrofuran, respectively, to give sample solutions (10 mmol/L). The thus-prepared solution was injected to the cell by syringe. After adjusting the optical path length by controlling helium pressure, XAS experiment was conducted.

Fig. 1 shows C K-edge XAS data of sumanene, corannulene, and triphenylene, respectively. In the case of sumanene, relatively sharp peak was observed at 285.2 eV, which is assigned as the transition of C 1s electron to C=C  $\pi^*$  orbitals. Meanwhile, two peaks were observed at 284.8 and 285.3 eV. This result indicated the difference of the electronic structure between sumanene and corannulene. Inner-shell calculations were performed using GSCF3 program[3,4] and it was found that the simulated peak pattern was matched with experimental spectra in the case of sumanene and corannulene, although these calculations did not reproduce the relative energy value (Fig. 2). From this calculation, it was found that the peak at 284.8 eV corresponds to the internal carbons of corannulene. Interestingly, XAS data for triphenylene showed two split peaks, unlike the case of sumanene. Since the inner-shell calculations of sumanene and corannulene exhibited almost the same spectral shape, the spectroscopic difference is thought to represent the difference in the behavior in solution.

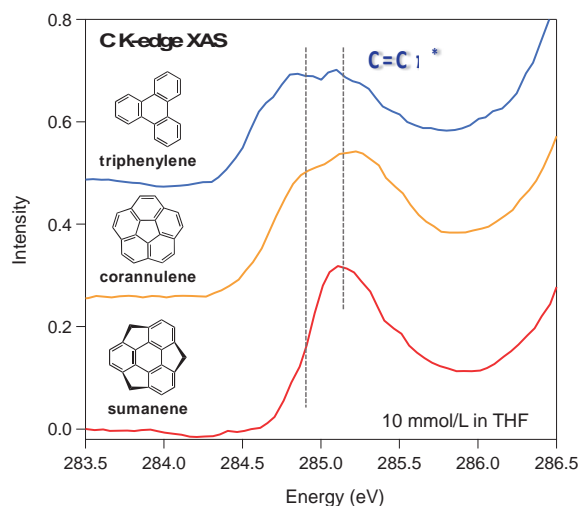


Fig. 1. C K-edge XAS data of sumanene, corannulene, and triphenylene.

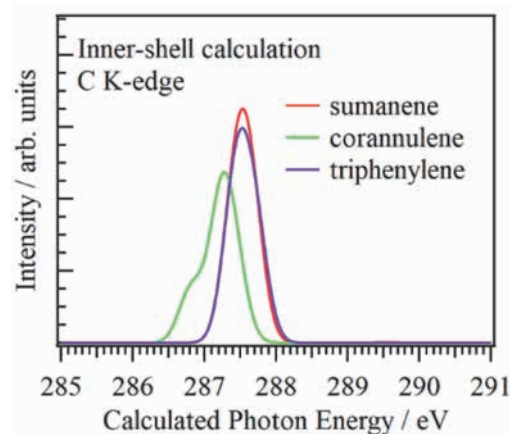


Fig. 2. Inner-shell calculations of sumanene, corannulene, and triphenylene.

[1] H. Sakurai, T. Daiko, H. Sakane, T. Amaya and T. Hirao, *J. Am. Chem. Soc.* **127** (2005) 11580.

[2] M. Nagasaka and N. Kosugi, *Chem. Lett.* **50** (2021) 956.

[3] N. Kosugi and H. Kuroda, *Chem. Phys. Lett.* **74** (1980) 490.

[4] N. Kosugi, *Theor. Chim. Acta* **72** (1987) 149.

## Operando Observation of Adsorbed Anions on the Surface of Nickel Catalysts by Soft X-ray Absorption Spectroscopy

A. Sakai<sup>1</sup>, Z. Li<sup>1</sup>, K. Harada<sup>1</sup>, S. Tsunekawa<sup>1</sup>, M. Nagasaka<sup>2</sup> and M. Yoshida<sup>1,3</sup>

<sup>1</sup>Yamaguchi University, Tokiwadai, Ube, Yamaguchi 755-8611, Japan

<sup>2</sup>Institute for Molecular Science, Myodaiji, Okazaki 444-8585, Japan

<sup>3</sup>Blue Energy Center for SGE Technology (BEST), Ube, Yamaguchi 755-8611, Japan

Recently, electrochemical hydrogen production from water has been attracting attention to develop a sustainable society. In this system, nickel oxides electrodeposited in carbon electrolyte solution are known to be one of the efficient electrocatalyst for oxygen production [1-2]. Thus, various operando spectroscopic analyses have applied to the nickel catalysts in order to reveal the physical properties and functions. However, the role of carbonate anion in the electrolyte solution is still not fully understood. From this background, in this study, the role of adsorbed carbonate anion was investigated for the nickel electrocatalysts by X-ray absorption fine structure (XAFS) measurements using hard X-ray and soft X-ray under operando conditions.

The handmade electrochemical cell was used with a Pt wire counter electrode and an Ag/AgCl reference electrode (NaCl). The nickel electrocatalysts were prepared by electrodeposition on Au thin film in a solution containing Ni<sup>2+</sup> and carbonate anion (Ni-C<sub>i</sub> catalyst). The operando Ni K-edge XAFS were carried out by fluorescence mode in the SPring-8 BL01B1, and the operando C K-edge XAFS were performed by transmission mode at BL3U in the UVSOR synchrotron.

First, SEM, EDX, UV-vis and XPS measurements were also measured to investigate the surface morphology and chemical states of electrodeposited catalysts. Next, we tested the electrochemical activity of oxygen evolution reaction (OER), suggesting that the prepared Ni-C<sub>i</sub> functioned as highly efficient OER electrocatalyst. Moreover, the electrolyte solution was exchanged from potassium carbonate solution (K-C<sub>i</sub>) to potassium phosphoric solution (K-P<sub>i</sub>) during monitoring the OER activity, indicating that the water splitting activity of the Ni-C<sub>i</sub> catalyst was preserved in the K-P<sub>i</sub> electrolyte solution.

The operando Ni K-edge XAFS measurements were performed to investigate the electronic state and local structure of the Ni-C<sub>i</sub> catalyst. The result of EXAFS analysis showed that the peaks of Ni-O and Ni-Ni bonds were observed at similar positions compared to the  $\gamma$ -NiOOH reference sample, suggesting that the local structure of Ni in the catalyst was consistent with that of  $\gamma$ -NiOOH. Moreover, the local structure of the catalyst in the K-P<sub>i</sub> solution was also maintained that of  $\gamma$ -NiOOH.

Finally, the operando C K-edge XAFS measurements were carried out for the Ni-C<sub>i</sub> catalyst under the catalytic reaction (Fig. 1). The result showed that carbonate anions were adsorbed on the catalyst surface. The adsorbed peak was remained even after exchanging the electrolyte solution from K-C<sub>i</sub> to K-P<sub>i</sub>. Thus, this result suggests that the carbonate anions are strongly adsorbed on the Ni-C<sub>i</sub> catalyst. The adsorbed carbonate anions are likely to contribute to stabilize the  $\gamma$ -NiOOH structure with high oxidation number Ni. On the basis of these discussions, we concluded that the  $\gamma$ -NiOOH structure stabilized by adsorbed carbonate anions could efficiently decompose water molecule to oxygen gas due to the high oxidation number Ni of active site.

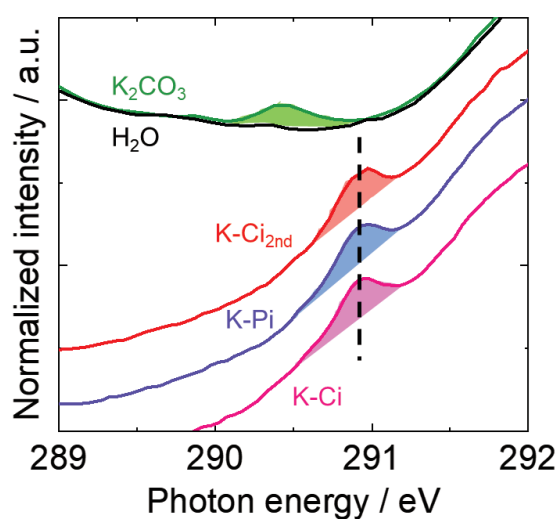


Fig. 1. Operando C-K edge XAFS spectra for Ni-C<sub>i</sub> electrocatalyst with exchanging the electrolyte solution between K-C<sub>i</sub> and K-P<sub>i</sub> by transmission mode at BL3U in the UVSOR synchrotron. The electrolyte aqueous solution of potassium carbonate was measured as reference compounds.

- [1] K. S. Joya, Y. F. Joya, and H. J. M. de Groot, *Adv. Energy Mater.*, **4** (9) (2014) 1301929.
- [2] T. Shinagawa, M. T. Ng and K. Takahashi, *Angew. Chem. Int. Ed. Eng.*, **56** (18) (2017) 5061.
- [3] A. C. Garcia, T. Touzalin, C. Nieuwland, N. Perini and M. T. M. Koper, *Angew. Chem. Int. Ed. Eng.*, **58** (37) (2019) 12999.

BL3U

## Temperature Effects on the X-ray Absorption Spectrum of Aqueous $\text{Ca}(\text{NO}_3)_2$ Recorded at the Ca $L$ -edge

D. Céolin<sup>1</sup>, T. Saisopa<sup>2</sup>, Y. Rattanachai<sup>2</sup>, H. Yuzawa<sup>3</sup> and N. Kosugi<sup>3</sup>

<sup>1</sup>Synchrotron SOLEIL, l'Orme des Merisiers, Saint-Aubin, F-91192 Gif-sur-Yvette Cedex, France

<sup>2</sup>Department of Applied Physics, Faculty of Sciences and Liberal Arts, Rajamangala University of Technology Isan, Nakhon Ratchasima 30000, Thailand

<sup>3</sup>UVSOR Synchrotron Facility, Institute for Molecular Science, Okazaki 444-8585, Japan

Calcium dication is frequently studied due to its abundance in human body and its importance in biological processes. Thus, its local structure determination is the subject of number of investigations, both experimental (XRD, EXAFS, MD, etc.) and theoretical (QM/MM, MD). In aqueous solutions, X-ray absorption spectroscopy (XAS) was used to probe the effect of the concentration on e.g., the hydration number, but the influence of the temperature was not investigated, despite some information was reported on other techniques [1].

In this context, we performed XAS measurements at the BL3U beamline on aqueous  $\text{Ca}(\text{NO}_3)_2 \cdot 4\text{H}_2\text{O}$ , using the liquid cell in transmission mode. The setup offers the possibility to monitor its temperature (T). We choose a high concentration close to the solubility limit of this salt in water at 0°C, that is 1050 g/L. The results are presented in the Figure 1. Each spectrum has its background removed.

A full attribution of the different structures was given in a previous paper [2]. The  $2p^{-1}$  spin-orbit contributions are located below (above)  $\sim 351$  eV for  $L_3$  ( $L_2$ ), respectively. The temperature change from 0 to 60°C do not influence the splitting between the two main lines, nor the position of the smaller peaks. The intensity ratio between peaks 1 and 2, which gives information on the crystal field 10Dq value, is small. Despite we observe a slight modification of this ratio with T, we consider it as not relevant as it does not follow the T variation and is attributed to the background removal procedure.

A more precise analysis shows a slight blue-shift of the right side of the peaks toward the high photon energies following the temperature increase (see insert in Fig. 1 corresponding to a zoom of the main  $L_3$  line), whereas the low energy sides remain quasi-unchanged. The width of peak 1 for each T is shown in Fig. 2. The photon bandwidth and the detector contribution are constant and lead to an experimental resolution of 166 meV, whereas the Lorentzian broadening contribution shows a slight increase roughly from 200 to 250 meV within the T going from 0 to 60°C.

Temperature effects were already probed by XAS in electrolyte aqueous solutions at the O K-edge. For a 5 M LiCl aqueous solution [3], a redshift of the pre-edge resonance maximum was observed when T increases. It was attributed to the change of the distance between the

bulk water molecules with T, whereas molecules in the first hydration shell of lithium ion are more strongly bonded to it and less sensitive to T variations. In the present case, the sample concentration is high and close to the solubility limit at 0°C. We can argue that thermal motion at low T is reduced and slightly increases in this T range. These observations should be confirmed by complementary measurements.

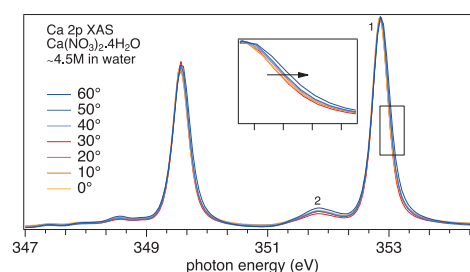


Fig. 1. X-ray absorption spectra of a 4.5 M  $\text{Ca}(\text{NO}_3)_2 \cdot 4(\text{H}_2\text{O})$  aqueous solution, recorded in the vicinity of the Ca  $2p$  ionization threshold, for temperatures in the 0-60°C range.

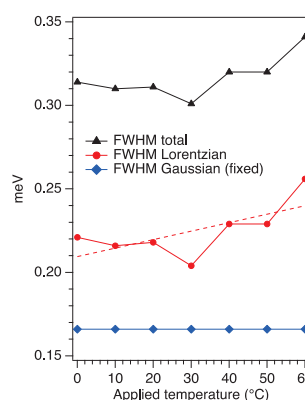


Fig. 2. Influence of temperature on the width of the main line (full width at half maximum: FWHM). The Gaussian and Lorentzian contributions are extracted.

[1] A. A. Zavitsas, *J. Phys. Chem. B*, **109** (2005) 20636.

[2] T. Saisopa *et al.*, *J. Electron Spectrosc. Relat. Phenom.*, **244** (2020) 146984.

[3] M. Nagasaka *et al.*, *J. Phys. Chem. B*, **121** (2017) 10957.

## Self-Assembled Hierarchical Nanosegregated Chiral Intermediate Phases Composed of Two Different Achiral Bent-Core Molecules

F. Araoka<sup>1</sup>, Y. Takanishi<sup>2</sup>, S-W. Choi<sup>3</sup> and H. Iwayama<sup>4,5</sup>

<sup>1</sup>RIKEN Center for Emergent Matter Science (CEMS), Wako, Saitama 351-0198, Japan

<sup>2</sup>Faculty of Science, Kyoto University, Sakyo, Kyoto 606-8502, Japan

<sup>3</sup>Department of Advanced Materials Engineering for Information and Electronics, Kyung Hee University, Yongin 17104, Republic of Korea

<sup>4</sup>UVSOR Synchrotron Facility, Institute for Molecular Science, Okazaki, Aichi 444-8585, Japan

<sup>5</sup>School of Physical Sciences, The Graduate University for Advanced Studies (SOKENDAI), Okazaki, Aichi 444-8585, Japan

Chirality is fascinating because of its fundamental importance in nature. As we presented in the activity report of the previous year, achiral BC molecules are well-known for spontaneous chiral resolution at the macroscopic scale despite the chiral-carbon-atom-free (hence, achiral) molecules (Fig. 1a). The so-called B4 phase—often the lowest temperature phase of BCs—is one such chiral mesophase in which a helical nanofilament superstructure is spontaneously self-assembled. In this case, structural chirality, observed as helical handedness, originates from the layered chirality of tilted smectic layers twisting along the filaments. Another very similar type of chiral phase formed by achiral bent-core molecules is the dark conglomerate (DC) phase. The DC also exhibits optically resolved domains with strong optical activity, but it looks more isotropic. The fundamental morphology of DCs comprises disordered sponge-like structures of tilted smectic layers. Although sponge-like structures do not have morphological chirality, it is understood that the observed macroscopic optical activity is attributed to the layered chirality of the tilted smectic layers.

Recently, we explored some interesting chirality-related phenomena in nano-separated intermediate phases composed of two achiral bent-core liquid crystalline molecules, one of which is circularly polarized luminescence (CPL) in the nano-separated intermediate phase blended with a luminescent dye [1]. Following up this work, we further extended this concept to realize dual-chiral intermediate phase (as illustrated in the right panel of Fig. 1a) of coexisting B4 and DC phases, using nanophase segregation between two bent-core molecules and hierarchical self-organization. Interestingly, the luminescence dissymmetry factor of CPL from the nano-separated dual-chiral phase of the B4 and DC was one order of magnitude higher than that of the previously reported chiral phases of the bent-core system [2].

Thus, the present dual-chiral phase system looks promising. However, its structure has not yet been confirmed. Since the system is consisting of two mesophases, direct observation methods such as using transmission electron microscope aren't usable.

Therefore, for this sake, we performed resonant soft X-ray scattering (RSoXS) experiment to identify the nano-separated phases. Our RSoXS setup was prepared in BL3U of UVSOR at IMS – A homemade vacuum chamber equipped with a cooled CCD camera (Newton, Andor) was used for small angle detection ( $2\theta \sim 1-15^\circ$ ). In the present study, the X-ray photon energy was chosen as 284.5 eV, corresponding to the carbon K-edge absorption of the present sample mixtures. The sample mixture was sandwiched between two SiN membrane films and then sealed not to exposed to vacuum. The sample chamber also equips a furnace to heat up the sample.

The RSoXS profile of the dual chiral phase (Fig. 1b) was compared with those of the only-B4 (Fig. 1c) and only-DC (Fig. 1d) phases. The RSoXS result clearly shows that the patterns of two chiral phases are superimposed in the dual chiral phase. In addition, we carefully examined the dual chiral phase with circular dichroism spectroscopy, polarizing light microscopy, and differential scanning calorimetry, we concluded that the model proposed in Fig. 1a is reasonable in the present dual chiral system.

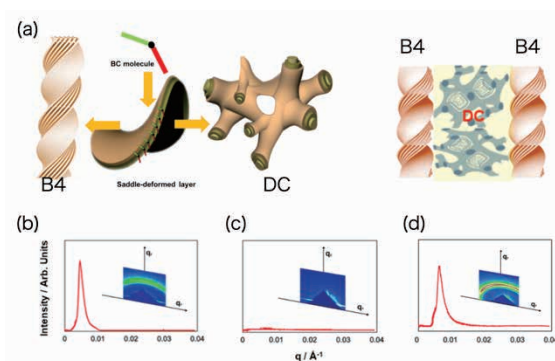


Fig. 1. (a) Schematics of the nanoscopic structures of the B4 and DC phases, and the nano-separated dual chiral phase. (b, c, d) RSoXS patterns obtained for (b) B4, (c) DC, and (d) dual chiral phases. [2]

[1] Kim *et al. Adv. Funct. Mater.* **29** (2019) 1903246.

[2] Lee *et al. Int. J. Mol. Sci.* **23** (2022) 14629.

BL3U

## X-ray Absorption Spectra of Metal Carbonyl Solutions

T. Sasaki and H Xu

Department of Complexity Science and Engineering, Graduate School of Frontier Sciences,  
The University of Tokyo, Kashiwa 277-8561, Japan

XAS measurements for liquid samples have been enabled at UVSOR BL3U, giving new insights for physicochemical properties of materials [1]. We have studied O-K edge XAS measurements for cellobiose aqueous solutions and found that XAS signals can be simulated with CP2K and hydrogen bonding with water molecules affect the relative intensity of XAS peaks. In this study metal carbonyl solutions were examined for XAS measurements to gain information of metal carbonyls dissolved in liquid phase, since metal carbonyls can be regarded as good models for both homogeneous and heterogeneous catalysts. Therefore we can expect XAS method will act as a new characterization tool for chemical and catalytic processes in liquid phase. In this study  $\text{Mo}(\text{CO})_6$  and  $\text{Ru}_3(\text{CO})_{12}$  were chosen as target molecules.

XAS measurements for liquid samples were conducted at UVSOR BL3U using facilities developed by Nagasaka et al. [1]. The liquid sample cell with  $\text{Si}_3\text{N}_4$  membranes was adopted, where the thickness of the liquid layer was controlled by the He gas pressure around the cell.

Fig. 1 shows O-K XAS spectrum for  $\text{Mo}(\text{CO})_6$  (40 mg) in 10 ml  $\text{CH}_3\text{CN}$  at room temperature. Concentration is 15 mM. This condition is close to the saturated solution. A sharp peak at 531.25 eV was observed and can be attributed to excitation to  $\text{C}=\text{O}$   $1\pi^*$  level. Broad features above 534 eV can be associated with sigma bonding of C-O ligand.

Fig. 2 shows O-K XAS spectrum for  $\text{Ru}_3(\text{CO})_{12}$  (3 mg) in 5 ml  $\text{CHCl}_3$  at room temperature. Concentration is 0.94 mM. This condition is also close to the saturated solution. It is noticed that peak intensity for Fig. 2 is weaker than that for Fig. 1, because of the low solubility of  $\text{Ru}_3(\text{CO})_{12}$ . A peak was found at 531.65 eV and can be attributed to excitation to  $\text{C}=\text{O}$   $1\pi^*$  level. Broad features above 534 eV can be associated with sigma bonding of C-O ligand.

Due to the limitation of rather low concentration C-K edge measurements are difficult since overlap with absorption peaks by solvent molecules affect the peaks associated with CO ligand.

For the precise peak assignments MD calculation for carbonyl species dissolved in solvent molecules and

core excitation simulation are now in progress. It is expected to conduct measurements of other metal carbonyls and observation of ligand exchange. Whether site discrimination, for example atop coordination and bridging coordination is possible or not is also interesting point to be clarified.

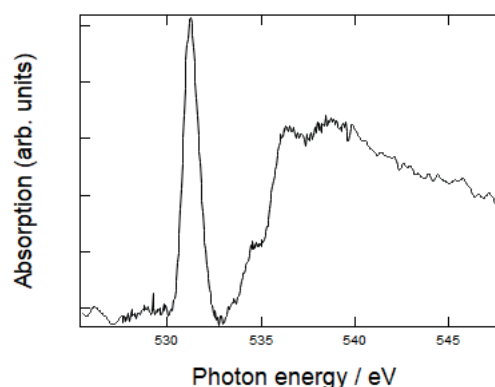


Fig. 1. O-K XAS spectrum for  $\text{Mo}(\text{CO})_6$  (40 mg) in 10 ml  $\text{CH}_3\text{CN}$  at room temperature.

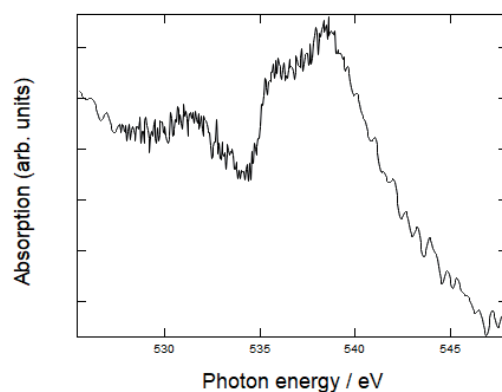


Fig. 2. O-K XAS spectrum for  $\text{Ru}_3(\text{CO})_{12}$  (5 mg) in 5 ml  $\text{CHCl}_3$  at room temperature.

[1] M. Nagasaka *et al.*, *J. Electrosc. Relat. Phenom.* **200** (2015) 293.

[2] D. Akazawa *et al.*, *J. Chem. Phys.* **156** (2022) 044202.

## Soft X-ray Absorption of Photocatalysts for Artificial Photosynthesis: Ultraviolet Light Irradiation in Water

H. Onishi<sup>1,2</sup>, Yi Hao Chew<sup>1</sup>, K. Matsui<sup>1</sup>, N. Ichikuni<sup>3</sup> and T. Yoshida<sup>4</sup>

<sup>1</sup>*School of Science, Kobe University, Kobe 657-8501, Japan*

<sup>2</sup>*Division of Advanced Molecular Science, Institute for Molecular Science, Okazaki 444-8585, Japan*

<sup>3</sup>*Graduate School of Engineering, Chiba University, Chiba 263-8522, Japan*

<sup>4</sup>*Reserch Center for Artificial Photosynthesis, Osaka Metropolitan University, Osaka 558-8585, Japan*

Sodium tantalate ( $\text{NaTaO}_3$ ) and strontium titanate ( $\text{SrTiO}_3$ ) provide a class of semiconductor photocatalysts which produce hydrogen–oxygen mixed bubbles in the overall water splitting reaction, when properly doped with metal cations [1, 2]. We are conducting a series of studies to answer the question of why doping with metal cations raised the quantum yield of the reaction [3]. Here, soft X-ray absorption is applied for characterizing the electronic structure of the photocatalysts in the presence and absence of ultraviolet (UV) light for bandgap excitation.

$\text{NaTaO}_3$  particles doped with Sr cations (2 mol%) were prepared through a solid-state reaction, and characterized with EDX and XRD in Kobe University. The particles were suspended with water ( $5 \text{ g l}^{-1}$ ) and sent to a liquid film cell for transmission absorption by a syringe pump (Figure 1). To avoid sedimentation of the particles, pH of the suspension was tuned at 13, far from isoelectric point of the particles.

An Hg–Xe lamp (200 W) was used to irradiate UV light for photocatalyst excitation. The photodiode detecting transmitted X-ray was capped with a nickel filter to minimize stray UV light from the lamp and higher-order X-ray passing through the monochromator.

Figure 2 shows an oxygen K edge absorption spectrum of Sr-doped  $\text{NaTaO}_3$  photocatalyst particles suspended in water. It was not straightforward to place a significant amount of the photocatalyst particles in the water film pinched with two SiN membranes. An

absorption band appeared at 531.5 eV was ascribed to the photocatalyst particles but to be further examined, since the oxidized layer of the membranes may provide an absorption band at 530–531 eV.

Purin Sathirathai, an undergraduate student of Sirindhorn International Institute of Technology, Thammasat University in Thailand, assisted us in photocatalyst preparation under Sakura Science Exchange Program by Japan Science and Technology Agency. This study was supported by JSPS KAKENHI (grant numbers 18KK0161 and 22H00344).

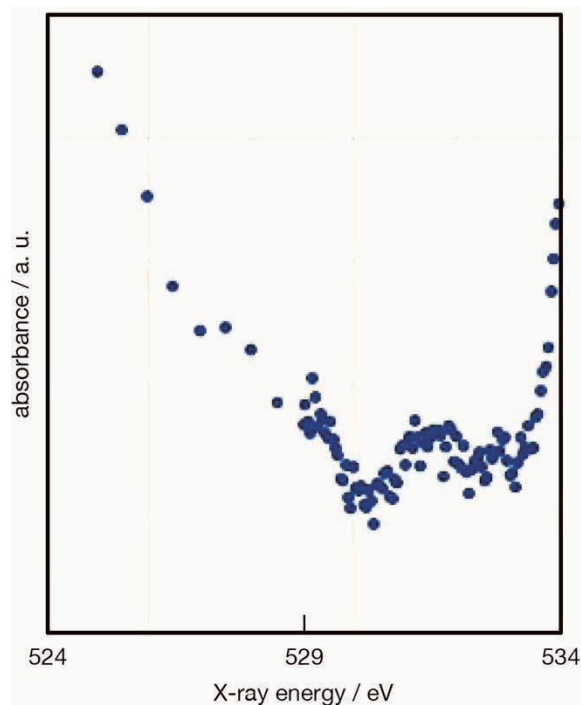


Fig. 2. Oxygen K edge absorption spectrum of  $\text{NaTaO}_3$  photocatalyst particles doped with Sr cations observed in water without UV light irradiation. The absorbance spectrum is shown in an arbitrary unit as a function of X-ray energy.



Fig. 1. Strontium-doped  $\text{NaTaO}_3$  photocatalyst particles suspended in water. White suspension in the syringe was sent to the liquid film cell for transmission XAFS measurements.

[1] H. Kato, K. Asakura, A. Kudo, *J. Am. Chem. Soc.* **125** (2003) 3082.

[2] T. Takata, J. Jiang, Y. Sakata, M. Nakabayashi, N. Shibata, V. Nandal, K. Seki, T. Hisatomi, K. Domen, *Nature* **581** (2020) 411.

[3] H. Onishi, *ChemSusChem* **12** (2019) 1825.

BL3U

## Hydration of Dimethyl Sulfoxide Probed by Liquid-Phase Soft X-ray Absorption Spectroscopy

C. Sugahara<sup>1</sup>, K. Okada<sup>1</sup> and H. Iwayama<sup>2,3</sup>

<sup>1</sup>Graduate School of Advanced Science and Engineering, Hiroshima University,  
Higashi-Hiroshima 739-8526, Japan

<sup>2</sup>Institute for Molecular Science, Okazaki 444-8585, Japan

<sup>3</sup>School of Physical Sciences, The Graduate University for Advanced Studies (SOKENDAI),  
Okazaki 444-8585, Japan

Soft X-ray absorption spectroscopy offers information on the local atomic environment of a molecular system under study by the resonant excitation of the local site. Different characters of water in solution, i.e. bulk and hydrated water, can be detected by the spectroscopy. The subtle differences in character, however, prevent us from clear distinction from one another without a useful analysis method. We have proposed a new quantity, called the excess absorption coefficient, for the analysis of absorption spectra of solutions and applied to the acetone–water binary system [1]. The analysis gives a successful extraction of the hydrated component.

This study is intended for generalization by the application of the method to another solution. The system of interest for this purpose is dimethyl sulfoxide (DMSO) aqueous solution. The DMSO molecule is more polarized than acetone. This is shown by the difference in the values of excess molar enthalpy. The acetone–water mixture has negative values only in the dilute region [2], while the DMSO–water mixture has negative values at all fractions and has greater absolute values [3]. We expect that more intensity in the absorption component of hydrated water for the latter mixture.

The experiments were performed on the soft X-ray beamline, BL3U. The photoabsorption spectra were measured in the oxygen K-edge region, with sample cell windows made of silicon nitride with a thickness of 150 nm. The incident photon energy was calibrated to the peak at 530.88 eV of a polymer film [4]. The absorption coefficient was evaluated so as to match the value at 547.85 eV to that tabulated in the database [5]. The sample solutions were prepared by mixing liquid DMSO with purified water to give the molar fraction of DMSO,  $x_D$ , in the range 0–0.35.

Observed absorption spectra of DMSO aqueous solutions are shown in Fig. 1. The spectrum for pure DMSO ( $x_D = 1$ ) has peaks at 532.6 and 534.0 eV. The former peak, assigned to the  $\pi^* \leftarrow O\ 1s$  transition of DMSO, is clearly dependent on  $x_D$ . The  $4a_1 \leftarrow O\ 1s$  absorption peak of water at 534.7 eV seems to shift to lower energies with  $x_D$ . The behavior is, however, not conclusive due to the overlap with the hump at about

534 eV which is assigned to another resonance transition of DMSO. This fact indicates that in this system the distinction of hydrated water from the bulk water requires a physicochemical analysis method: The system is a perfect system for testing our method of analysis. The results of the analysis will be published elsewhere.

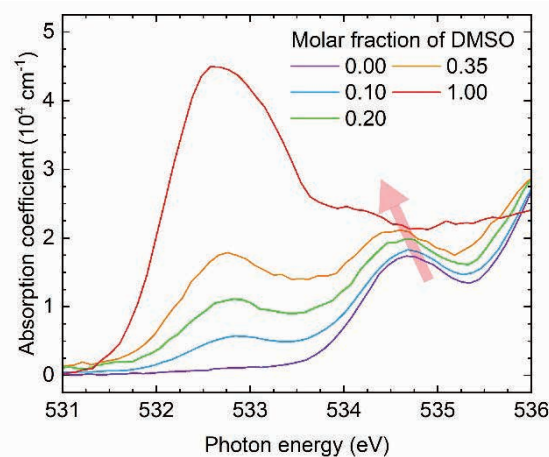


Fig. 1. The soft X-ray absorption spectra of liquid water and DMSO aqueous solutions measured for a series of molar fractions of DMSO. The spectrum of the liquid DMSO is also shown for comparison.

- [1] K. Okada, C. Sugahara, H. Iwayama and M. Nagasaka, *UVSOR Activity Report 2021*, **49** (2022) 117.
- [2] B. Löwen and S. Schulz, *Thermochim. Acta* **262** (1995) 69.
- [3] T. Kimura and S. Takagi, *Netsu Sokutei* **13** (1986) 2.
- [4] M. Nagasaka, H. Yuzawa, T. Horigome and N. Kosugi, *J. Elec. Spectrosc. Relat. Phenom.* **224** (2018) 93.
- [5] C. T. Chantler *et al.*, NIST Standard Reference Database 66 (1995; last update in 2005), available at <https://www.nist.gov/pml/x-ray-form-factor-attenuation-and-scattering-tables>.

## Multielectron-ion Coincidence Spectroscopy of I 4d inner-shell Photoionization of CH<sub>3</sub>I and CH<sub>2</sub>I<sub>2</sub> Molecules

M. Fushitani<sup>1</sup>, Y. Hikosaka<sup>2</sup> and A. Hishikawa<sup>1,3</sup>

<sup>1</sup>Graduate School of Science, Nagoya University, Furo-cho, Chikusa, Nagoya, Aichi, 464-8602, Japan

<sup>2</sup>Institute of Liberal Arts and Sciences, University of Toyama, 2630 Sugitani, Toyama, Toyama, 930-0194, Japan

<sup>3</sup>Research Center for Materials Science, Nagoya University, Furo-cho, Chikusa, Nagoya, Aichi, 464-8602, Japan

Inner-shell photoionization of molecules often leads to formation of highly charged states followed by fragmentation processes. Identifying which ion species are generated from which electronic states is of great importance for the basic understanding of ultrafast processes associated with inner-shell ionization. Among others, multielectron-ion coincidence spectroscopy using a magnetic bottle type electron spectrometer is a powerful approach to obtain such information [1-3]. Here, we applied it to I 4d inner-shell ionization of CH<sub>3</sub>I and CH<sub>2</sub>I<sub>2</sub> molecules to investigate fragmentation processes occurring from doubly charged states.

Electrons generated by photoionization with a synchrotron radiation at 100 eV were guided from the interaction region into a time-of-flight (TOF) tube (1.5 m) by magnetic fields from a permanent magnet and solenoid coil while ions were pushed into the tube by applying pulsed voltages to ion-collecting electrodes [1]. These electrons and ions were detected by a microchannel plate placed on the opposite side of the TOF tube.

Figure 1 shows Auger electron spectra obtained in coincidence with I 4d photoelectrons, I<sup>+</sup> ions and selected counterpart ions for (a) CH<sub>3</sub>I and (b) CH<sub>2</sub>I<sub>2</sub>. These Auger peaks provide information on the location of excited electronic states producing the fragment ion pairs. In Fig.1(a), the pair of I<sup>+</sup> and CH<sub>3</sub><sup>+</sup> ions are mainly generated together with Auger electrons having kinetic energies around 20-30 eV which correspond to doubly charged states associated with outer-valence configurations [4,5]. On the other hand, Auger signals are observed below 20 eV for the (I<sup>+</sup>, CH<sub>2</sub><sup>+</sup>), (I<sup>+</sup>, CH<sup>+</sup>), and (I<sup>+</sup>, C<sup>+</sup>) ion pairs, showing that these ion pairs are formed preferentially from higher excited states related to inner-valence configurations [4].

In the case of CH<sub>2</sub>I<sub>2</sub> (Fig.1(b)), the (I<sup>+</sup>, CH<sub>n</sub>I<sup>+</sup>) ion pair reflecting the single C-I bond cleavage is produced mostly with Auger electrons having 25-32 eV kinetic energies. By contrast, Auger signals appear in the lower energy region for other ion pairs associated with two C-I bond fissions, indicating the dissociations occur in excited doubly charged states.

The present study shows a promising approach for applications and fundamental understanding of nonlinear inner-shell ionization of iodine-containing molecules by intense free-electron lasers.

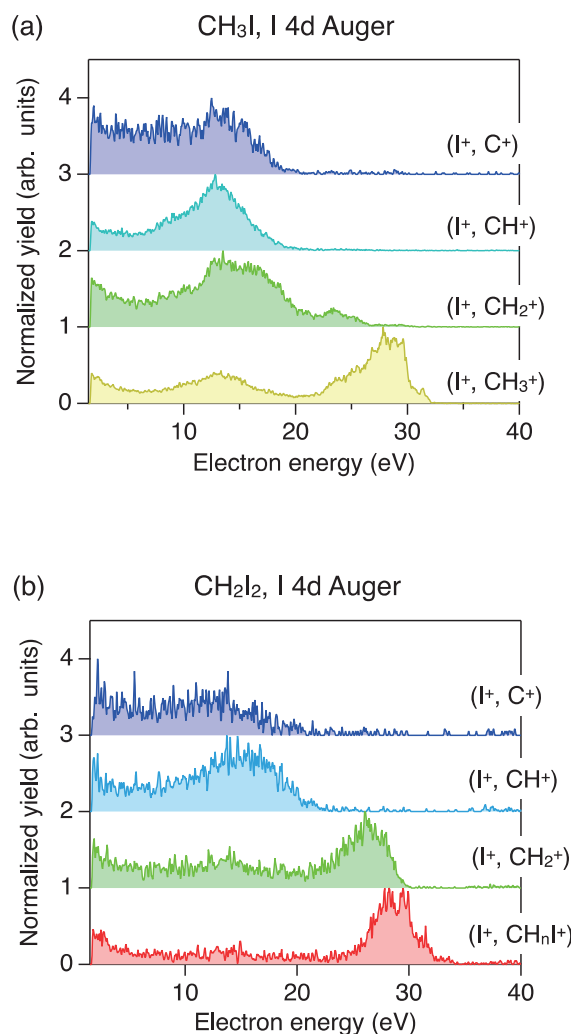


Fig. 1. PEPEPIPICO spectra of I 4d inner-shell photoionization at 100 eV for (a) CH<sub>3</sub>I and (b) CH<sub>2</sub>I<sub>2</sub>.

[1] Y. Hikosaka, *J. Electron Spectrosc. Rel. Phenom.* **255** (2022) 147158.

[2] Y. Hikosaka and E. Shigemasa, *Int. J. Mass Spectrom.* **439** (2019) 13.

[3] M. Fushitani *et al.*, *Phys. Rev. A (Letter)* **107** (2023) L021101.

[4] A. Hult Roos *et al.*, *Chem. Phys.* **491** (2017) 42.

[5] A. Bodi *et al.*, *Phys. Chem. Chem. Phys.* **25** (2023) 7383.

BL4B

## Quadruple Auger Decay from Xe 4s Core-Hole State Studied by Multi-Electron-Ion Coincidence Spectroscopy

Y. Hikosaka

*Institute of Liberal Arts and Sciences, University of Toyama, Toyama 930-0194, Japan*

Emissions of multiple Auger electrons, following inner-shell photoionization of atoms in the soft X-ray region, can occur within the permitted limits of the energetics. Multi-electron coincidence spectroscopy using a magnetic bottle electron spectrometer is a powerful means for studying multiple Auger decay. Discrimination of multiple Auger processes against dominant single Auger decay can be improved by filtering multi-electron coincidences with the additional detection of product ions relevant to the multiple Auger processes. By adding such ion detection capability to a magnetic bottle electron spectrometer, multi-electron-ion coincidence measurements can be performed very efficiently [1-3].

In this study, quadruple Auger decay of the Xe 4s core-hole state is investigated by multi-electron-ion coincidence spectroscopy with a magnetic bottle electron spectrometer [4]. Figure 1(a) shows the total electron spectrum (black curve) and the spectrum filtered by coincidence with  $\text{Xe}^{5+}$  ions (red curve), where the 4s photoelectron peak is observed around a kinetic energy of 180 eV. From the net intensities of the 4s peaks observed in the total and coincidence spectra, the fraction of the quadruple Auger path in the 4s decay was determined to be 16%.

The two-dimensional map in Fig. 1(b) displays the correlation between the fastest electron's energy and the sum of the energies of the other four electrons, determined from the six-fold coincidence including  $\text{Xe}^{5+}$  ion. It is possible to recognize structures running diagonally. The diagonal structures correspond to the formation of  $\text{Xe}^{5+}$  levels, resulting from the energy conservation (photon energy) - (binding energy of the  $\text{Xe}^{5+}$  state) = (fastest electron's energy) + (the sum of the energies of the other four electrons). Enhancement of  $\text{Xe}^{5+}$  formation is observed at the 4s photoelectron energy, corresponding to quadruple Auger decay from the  $4s^{-1}$  state.

Figure 2 shows the  $\text{Xe}^{5+}$  distribution populated by the quadruple Auger decay from the  $4s^{-1}$  state. The distribution is obtained by integrating the coincidence counts in Fig. 1(b) along the direction (fastest electron's energy) + (the sum of the energies of the other four electrons) = const., where the fastest electrons were restricted to be of the 4s photoelectron energy range. In addition to the formation of the  $5p^{-5}$  levels, both histograms show substantial formation of excited  $\text{Xe}^{5+}$  levels. The final formation fractions of the  $5p^{-5}$ ,  $5s^{-1}5p^{-4}$ , and  $5s^{-2}5p^{-3}$  levels by the quadruple Auger decay are estimated to be 7%, 7% and 2% of the 4s decay, respectively.

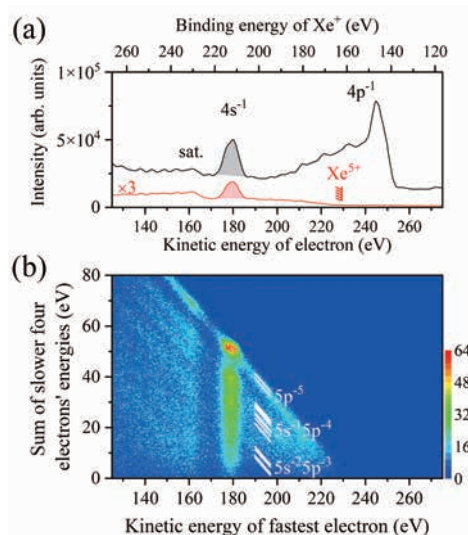


Fig. 1. (a) Inner shell photoelectron spectra of Xe observed at a photon energy of 391.7 eV, obtained for total events in the coincidence dataset (black) or by filtering with the detection of a  $\text{Xe}^{5+}$  ion (red). (b) Two-dimensional map showing the correlation between the fastest electron's energy and the sum of the energies of the other four electrons.

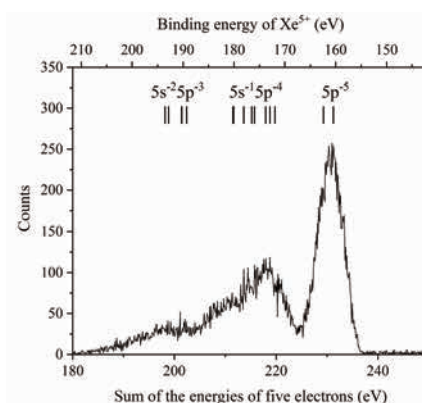


Fig. 2.  $\text{Xe}^{5+}$  distribution populated by the quadruple Auger decay from the  $4s^{-1}$  state.

- [1] Y. Hikosaka and E. Shigemasa, *Int. J. Mass Spectrom.* **439** (2019) 13.
- [2] Y. Hikosaka, *J. Electron Spectrosc. Relat. Phenom.* **255** (2022) 147158.
- [3] Y. Hikosaka and S. Fritzsche, *Phys. Chem. Chem. Phys.* **24**, (2022) 17535.
- [4] Y. Hikosaka, *Phys. Rev. A* **106** (2022) 062814.

## Metastable $\text{OCS}^{3+}$ States Investigated by Multi-Electron–Ion Coincidence Spectroscopy

Y. Hikosaka

*Institute of Liberal Arts and Sciences, University of Toyama, Toyama 930-0194, Japan*

Triply charged molecular ions are always energetically unstable due to Coulomb repulsion between the three positive charges. However, low-lying trication states in some limited molecules are known to be stable for more than  $\mu\text{s}$  due to the presence of deep minima on the potential energy surfaces. In this study, metastability of  $\text{OCS}^{3+}$  states populated by the S 2p double Auger decay has been investigated by multi-electron–ion coincidence spectroscopy. A magnetic bottle electron spectrometer with ion detection capability [1-4] was employed for this investigation, and the high detection efficiencies for electrons enabled to derive the information of stability of  $\text{OCS}^{3+}$  electronic states.

The double Auger decay of the  $\text{S}2\text{p}^{-1}$  states in OCS can be isolated by inspecting electron triple coincidences including a  $\text{S}2\text{p}$  photoelectron. The two-dimensional map in Fig. 1 is derived from the electron triple coincidences, displaying the energy correlation between the two electrons other than the  $\text{S}2\text{p}$  photoelectron. On this map, several diagonal stripes are identified in (faster electron's energy) + (slower electron's energy) = 95–115 eV, which are formed by double Auger decay. The population of the  $\text{OCS}^{3+}$  states formed by the  $\text{S}2\text{p}$  double Auger decay is revealed by projecting the coincidence yields on the diagonal axis of (faster electron's energy) = (slower electron's energy). The resultant  $\text{OCS}^{3+}$  spectrum is shown in Fig. 2 as black curve. Several peaks are observed in the kinetic energy range of 95–115 eV, corresponding to the diagonal structures seen on the two-dimensional map in Fig. 1. Moreover, a broad structure is seen in the binding energy range of 80–95 eV. These spectral profiles agree with the previous investigation by Eland et al. [5].

Metastability of  $\text{OCS}^{3+}$  states can be investigated by inspecting the ion species detected in further coincidence with  $\text{S}2\text{p}$  photoelectron and two Auger electrons. The double Auger spectrum filtered by further coincidence with parent  $\text{OCS}^{3+}$  ion is presented in Fig. 2 as red shaded spectrum. Only the peak for the ground  $3\pi^{-3}{}^2\Pi$  state at a binding energy of 60 eV is exhibited in the spectrum, revealing that the ground state is metastable in the  $\mu\text{s}$  regime. An MRCI/CASSCF calculation [5] predicts the ground  $3\pi^{-3}{}^2\Pi$  state has a potential surface with a potential well along both directions lengthening the CS and CO bonds, although excited  $\text{OCS}^{3+}$  states are all unbound to lengthening the

CS bond. The present observation is in consistent with the calculation results.

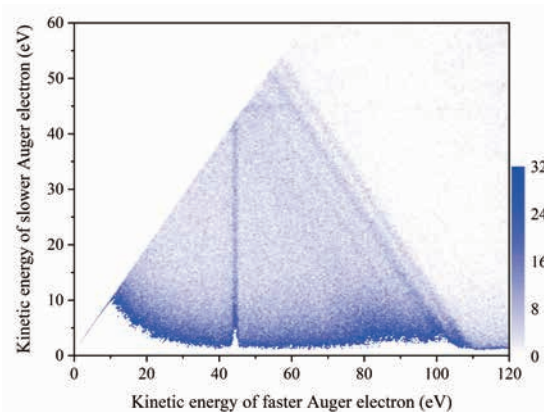


Fig. 1. Two-dimensional map showing the energy correlations between two Auger electrons emitted in the S 2p double Auger decay of OCS, which was derived from electron triple coincidence.

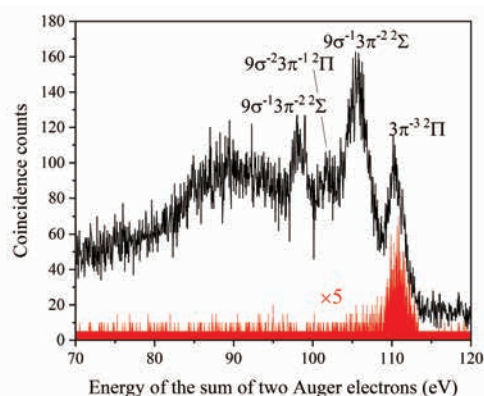


Fig. 2.  $\text{OCS}^{3+}$  spectra formed by the  $\text{S}2\text{p}$  double Auger decay of OCS: total spectrum (black solid curve) and the one filtered with further coincidence with parent  $\text{OCS}^{3+}$  ions (red shaded spectrum).

- [1] Y. Hikosaka and E. Shigemasa, *Int. J. Mass Spectrom.* **439** (2019) 13.
- [2] Y. Hikosaka, *J. Electron Spectrosc. Relat. Phenom.* **255** (2022) 147158.
- [3] Y. Hikosaka and S. Fritzsche, *Phys. Chem. Chem. Phys.* **24**, (2022) 17535.
- [4] Y. Hikosaka, *Phys. Rev. A* **106** (2022) 062814.
- [5] J.H.D. Eland et. al, *J. Chem. Phys.* **132** (2010) 014311.

BL4B

## Soft X-ray Absorption Study of Semiconductor Photocatalysts for Highly Efficient Oxidation of Water

T. Yoshida<sup>1</sup>, N. Ichikuni<sup>2</sup>, H. Onishi<sup>3,4</sup> and Yi Hao Chew<sup>3</sup>

<sup>1</sup>Reserch Center for Artificial Photosynthesis, Osaka Metropolitan University, Osaka 558-8585, Japan

<sup>2</sup>Graduate School of Engineering, Chiba University, Chiba 263-8522, Japan

<sup>3</sup>School of Science, Kobe University, Kobe 657-8501, Japan

<sup>4</sup>Division of Advanced Molecular Science, Institute for Molecular Science, Okazaki 444-8585, Japan

A number of metal oxides including gallium oxide, ( $\text{Ga}_2\text{O}_3$ ), sodium tantalate ( $\text{NaTaO}_3$ ) and strontium titanate ( $\text{SrTiO}_3$ ) provide a class of semiconductor photocatalysts highly efficient for the overall water splitting reaction, when properly doped with foreign metal cations. [1-3]. We are conducting a series of studies to answer the question of why metal-cation doping raised the quantum yield of the reaction [4]. Here, soft X-ray absorption is applied for characterizing the electronic structure of the photocatalysts in the presence and absence of ultraviolet (UV) light for bandgap excitation.

Sub-micrometer-sized  $\text{Ga}_2\text{O}_3$  particles were prepared in Osaka Metropolitan University, while  $\text{NaTaO}_3$  doped with  $\text{Sr}^{2+}$  cations and  $\text{SrTiO}_3$  doped with  $\text{Al}^{3+}$  cations were prepared in Kobe University. Oxygen K edge absorption spectrum of the photocatalysts particles was observed under vacuum in the presence and absence of UV light provided by a Hg–Xe lamp (200 W).

In XAFS measurement of oxygen K edge, the photocatalyst particles were molded as disks of 7-mm diameter. The disks were placed in a vacuum chamber, irradiated with incident X-ray, and fluorescent X-ray was detected with a silicon drift detector (SDD). The detector was capped with a 150-nm-thick aluminum film (LUXEL, TF110) to minimize contribution of stray UV light to detector response (Fig. 1).

Figure 2 shows a set of oxygen K edge spectra observed on Sr-doped  $\text{NaTaO}_3$  photocatalyst disk. The low energy band, which was assigned to the electronic transition from the oxygen 1s to oxygen 2p levels hybridized with tantalum 5d orbitals, appeared at 531.2

eV in the absence of UV light irradiation. The band shifted by 0.4 eV to the low-energy side under UV irradiation.

A possible reason of the band shift is the conduction band partially filled with bandgap-excited electrons. The density of vacant states, the final states of the K edge absorption, should have modified with the electrons excited from the valence band. The oxidation state of Ta cations decreased from 5+ to 4+ by the bandgap excitation.

This study was supported by JSPS KAKENHI (grant numbers 18KK0161 and 22H00344).

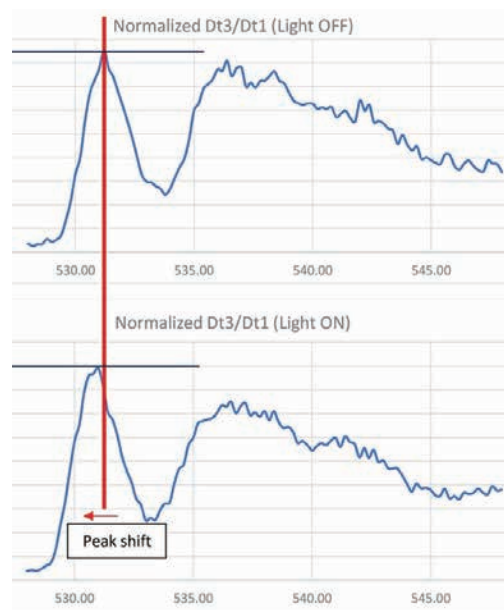


Fig. 2. Oxygen K edge absorption spectrum of a Sr-doped  $\text{NaTaO}_3$  photocatalyst disk in the absence (upper panel) and presence (lower panel) of UV-light irradiation.

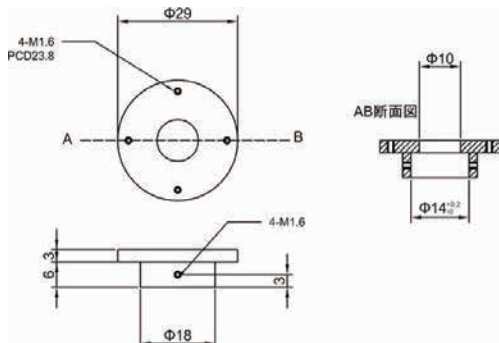


Fig. 1. A devise capping the SDD with the aluminum filter for fluorescence yield detection of oxygen K edge absorption spectrum under UV-light irradiation.

[1] Y. Sakata, T. Hayashi, R. Yasunaga, N. Yanaga, H. Imamura, *Chem. Commun.* **51** (2015) 12935.

[2] H. Kato, K. Asakura, A. Kudo, *J. Am. Chem. Soc.* **125** (2003) 3082.

[3] T. Takata, J. Jiang, Y. Sakata, M. Nakabayashi, N. Shibata, V. Nandal, K. Seki, T. Hisatomi, K. Domen, *Nature* **581** (2020) 411.

[4] H. Onishi, *ChemSusChem* **12** (2019) 1825.

## High-Resolution Photoelectron Spectroscopy of Unexplored Chiral Systems for Demonstration of the Photoelectron Circular Dichroism

H. Kohguchi<sup>1</sup>, Y. Hikosaka<sup>2</sup>, T. Kaneyasu<sup>3</sup>, S. Wada<sup>1</sup> and Y-I. Suzuki<sup>4</sup>

<sup>1</sup>Graduate School of Advanced Science and Engineering, Hiroshima University,  
Higashi-Hiroshima 739-8526, Japan

<sup>2</sup>Institute of Liberal Arts and Sciences, University of Toyama, Toyama 930-0194, Japan

<sup>3</sup>SAGA Light Source, Tosu 841-0005, Japan

<sup>4</sup>School of Medical Technology, Health Sciences University of Hokkaido, Tobetsu, 061-0293, Japan

Photoelectron circular dichroism (PECD) has attracted attention as a novel molecular chirality detection method. One of the remarkable attributes of PECD is that the asymmetric photoelectron angular distribution is generated from isotropically oriented molecules in the gas phase. In addition, PECD depends on the final ionic states so that the PECD data can be related to the chirality of the molecular orbitals. We have been conducting state-resolved PECD measurements with the UVSOR BL1U beam line. Although the circularly polarized light supplied by the BL1U undulator is indispensable for detecting the state-dependence of PECD [1], the narrower photon energy spread is desired for resolving the electronic structure of the observed photoelectron spectra. The width of the experimental photoelectron spectra is limited by our VMI apparatus as well as the light source. High-resolution photoelectron spectra provide unambiguous assignment of the electronic states which is applicable to the PECD image data. For combining the narrow band spectra with the PECD results measured in BL1U, we have developed the VMI apparatus and inspected the performance in the BL7B beam line.

We adopt two types of imaging systems in our VMI apparatus employs: a resistive anode and a CCD camera. The total resolution was evaluated in measurement of Ar photoelectron images in BL7B. The photoelectron images measured with the resistive anode imager exhibited sufficiently high resolution that the spin-orbit dual ring was resolved, as shown in Fig. 1 (a)-(d). The same measurement with the camera system yielded the image data with a comparable resolution but with a poor signal-to-noise ratio (Fig. 1 (A)-(D)). This is because the numerical operation determining the photoelectron positions of the camera system was found to be less efficient by 10 % of the resistive anode imager. The performance of these two imaging systems was directly examined with the narrow band light source, providing necessary improvement toward the state-resolved PECD measurements.

The photoionization experiments of chiral compounds with a heat nozzle were conducted as another evaluation of the machine developments. An increase of the photoelectron in a particular photon energy region was

measured with the elevated nozzle temperature, which was ascribed to the vaporized chiral molecules (Fig. 2). The photoelectron emitted in the shorter wavelength than 100 nm was regarded to be due to contaminated water, which is generally hard to eliminate. This result indicates that the density of the vapor in the irradiation volume needed to be increased for the state-resolved PECD measurements of new chiral systems. The machine developments should be reconsidered based on the results of the BL7B measurements.

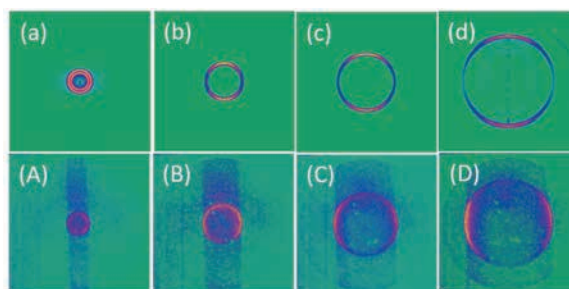


Fig. 1. Photoelectron images of Ar measured at various photon energy from 75 nm to 50 nm; (a)-(d) with a resistive anode imager, (A)-(D) with a CCD camera capturing a phosphor screen image.

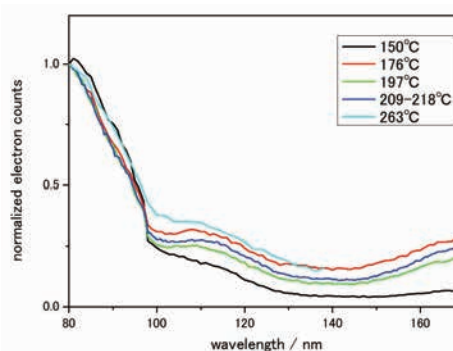


Fig. 2. Photoelectron yield spectrum of binaphthol at various nozzle temperatures near the ionization threshold.

[1] H. Kohguchi, Y. Hikosaka, T. Kaneyasu, S. Wada, H. Ota, M. Fujimoto, M. Kato and Y-I. Suzuki, UVSOR Activity Report **48** (2020) 93.

BL7B

## The Challenge of Photoionization Plasma Generation Using Synchrotron Radiation Source for Study of Plasmas in Interstellar Space and in Nuclear Fusion Devices

M. Kobayashi<sup>1</sup>, H. Iwayama<sup>2</sup>, J. Takahashi<sup>3</sup>, S. Yoshimura<sup>1</sup>, H. Ota<sup>2</sup>, K. Kobayashi<sup>3</sup>,  
M. Katoh<sup>2,4</sup>, H. Nakamura<sup>1</sup>, I. Sakon<sup>5</sup>, K. Sawada<sup>6</sup> and Y. Kebukawa<sup>3</sup>

<sup>1</sup>National Institute for Fusion Science, 322-6 Oroshi-cho, Toki 509-5292, Japan

<sup>2</sup>UVSOR Synchrotron Facility, Institute for Molecular Science, Myodaiji, Okazaki 444-8585, Japan

<sup>3</sup>Yokohama National University, 79-5 Tokiwadai, Hodogaya-ku, Yokohama 240-8501, Japan

<sup>4</sup>Hiroshima Synchrotron Radiation Center, Hiroshima University, 739-0046, Japan

<sup>5</sup>Department of Astronomy, Graduate School of Science, University of Tokyo, Tokyo 113-0033, Japan

<sup>6</sup>Graduate School of Engineering, Shinshu University, Nagano, Japan

An interstellar space is filled with interstellar plasmas, which is generated by ionization by cosmic rays or by interstellar radiation field [1]. In nuclear fusion devices [2], it is considered that neutral atoms and molecules in the divertor region are photoionized by a light coming from the confinement region and the scrap-off layers, where hot plasmas emit light in various energy ranges, from EUV through visible to infrared ranges. Characteristics and roles of the photoionized plasmas are, however, not yet fully understood: What is the dependency of the density and temperature of the photoionized plasmas on the energy range of the light? How the plasma transport under an influence of space magnetic field affects chemical evolution of organic molecules in the interstellar space? How the photoionization process affects the atomic/molecular processes in the divertor region of the nuclear fusion devices, which plays important roles on a device wall heat load mitigation?

To address these issues, we attempt to generate photoionized plasmas by using the Synchrotron Radiation Source UVSOR-III. There has been substantial works on the photoionization by using laser light with relatively high power source. In the present work, however, we are interested in photoionization by the radiation field (continuum light) in order to mimic the interstellar radiation field and the radiation in the fusion devices, such as Bremsstrahlung. It is expected that the photoionization by the continuum light is significantly different from those by the laser, because of the continuous energy distribution that can excite and ionize at various energy levels simultaneously.

The beamline BL7B is used to generate a continuum light from 30 to 400 nm with 0th order emission. A gas cell has been installed inside the irradiation chamber to maintain high pressure of the sample gas while keeping a good vacuum condition for the beamline. A high gas pressure is necessary to enhance the photoionization events through an interaction between the photons and neutral atoms/molecules. Fig.1 shows the gas cell based on a ICF34 cube. Holes of diameter of 1 to 2 mm are made for the injection of the light into the cell as well as for a gas outlet. Optical fibers are installed at the gas

cell for measurements of spectra of VUV, visible and mid infrared range from the photoionized plasmas. The gas is fed to the cell through the pipe at the top of the cell. An electrode is situated at the bottom of the cell and is biased up to +30V with respect to the ground to measure electron saturation currents of the plasmas.

As a sample gas, Ar and hydrogen were introduced respectively. The ionization potentials of the gaseous are 14.5 and 13.6 eV, respectively. The light from the BL7B beamline has a peak intensity at around 50 nm, which corresponds to a photon energy of 24.8 eV. The gas pressure inside the gas cell could be increased to an order of 1 Pa while the ambient pressure outside of the cell was kept at an order of  $10^{-4}$  Pa and the pressure at the upstream of the beamline was at an order of  $10^{-6}$  Pa.

A beam of a few mm diameter could be injected into the gas cell through the holes. The photon flux of the beam was measured with a photodiode, and was estimated at an order of  $10^{11}$  photons/s/mm<sup>2</sup>. However, no significant signal of photoionization was obtained this time. More challenges to come by optimizing the gas cell shape and the measurement system.

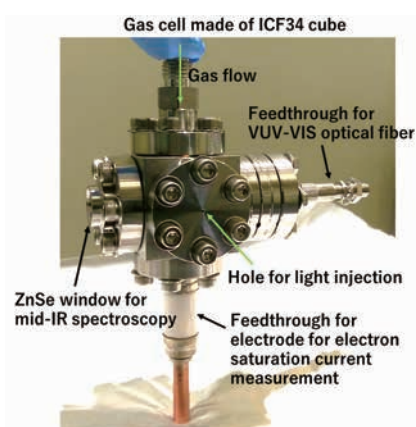
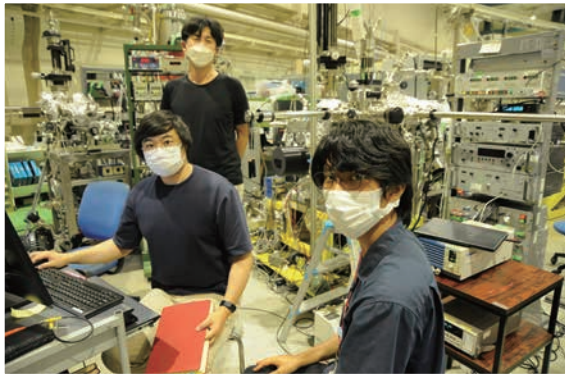
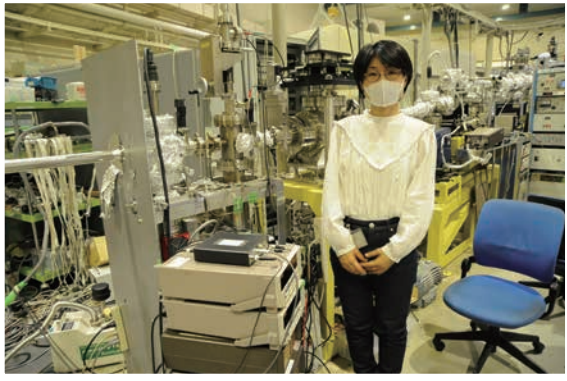
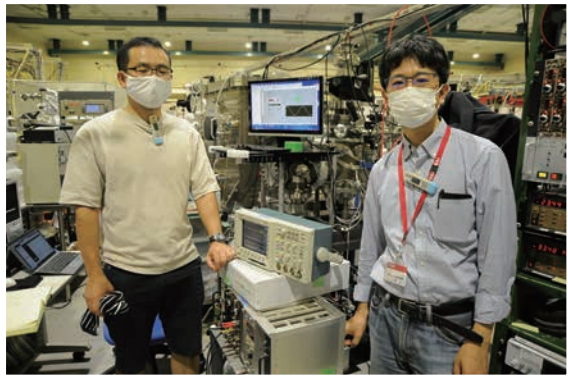
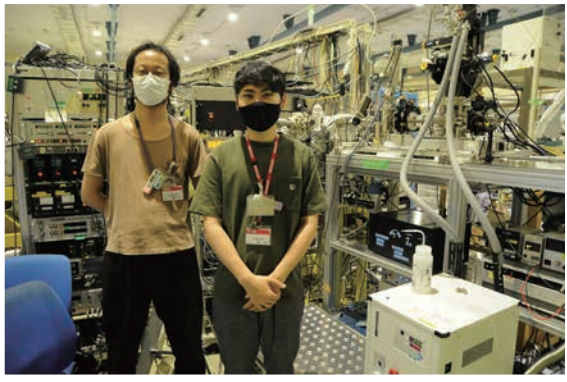
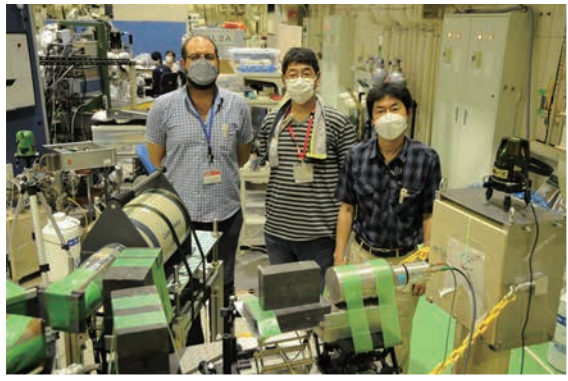
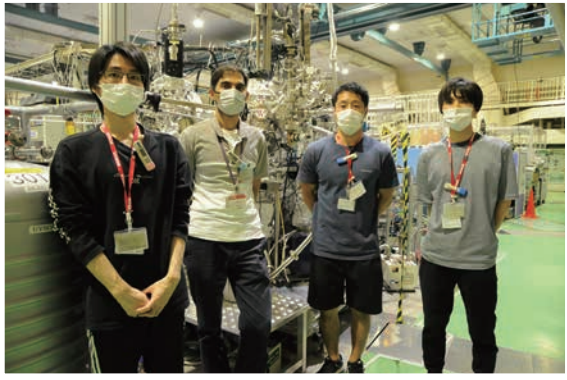


Fig. 1. A gas cell for the photoionization experiments.

[1] E.F.van Dishoeck *et al.*, *Faraday Discuss* **133** (2006) 231.

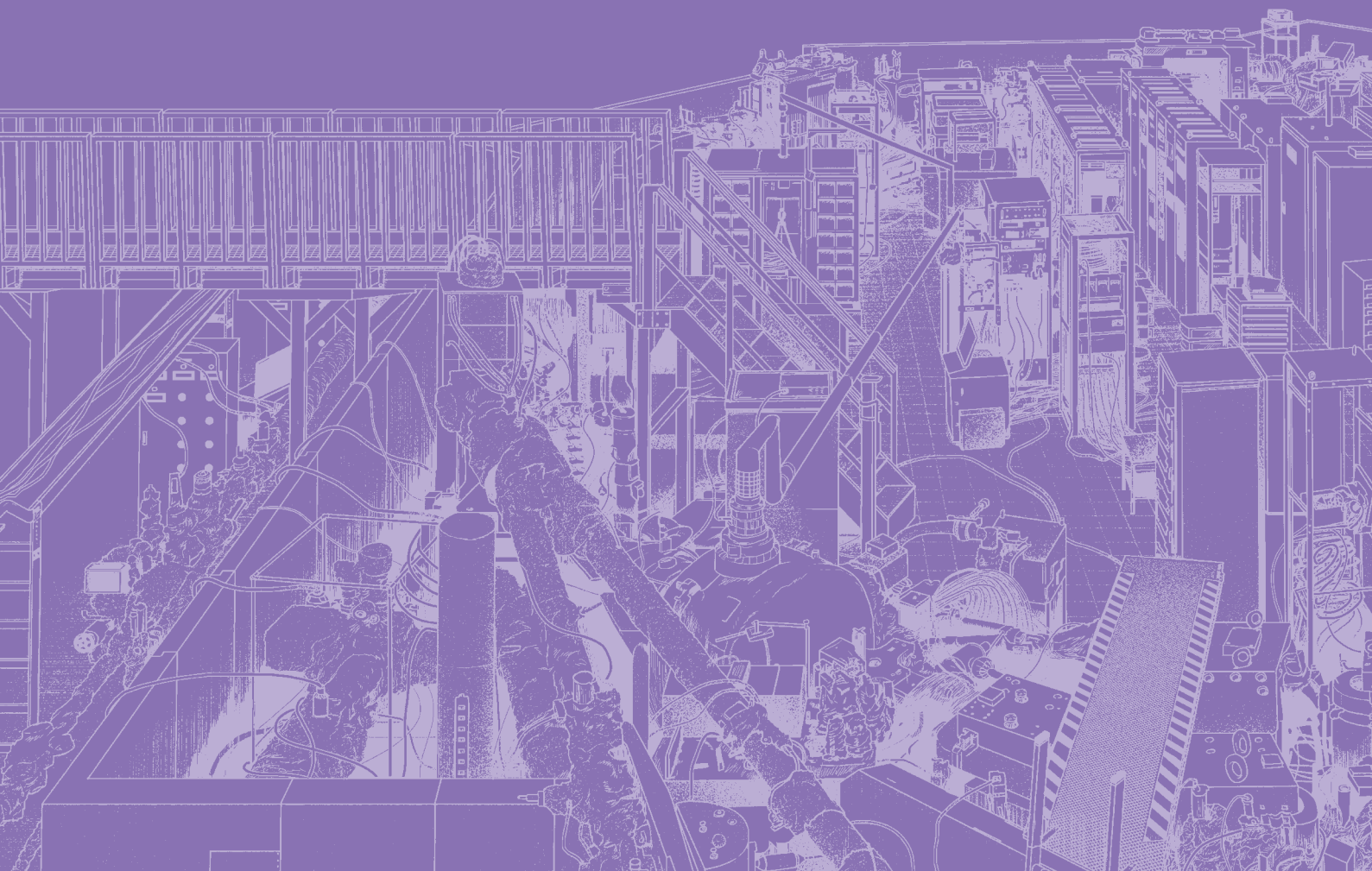
[2] M. Kobayashi *et al.*, *Nucl. Fusion* **62** (2022) 056006.

# UVSOR User 6



# III-4

Surface,  
Interface and  
Thin Films





BL6U

## Fermiology of a Kagome Superconductor $\text{Cs}(\text{V}_{1-x}\text{Nb}_x)_3\text{Sb}_5$ Revealed by Momentum Microscope

T. Kato<sup>1</sup>, K. Nakayama<sup>1</sup>, Y. Li<sup>2,3,4</sup>, Z. Wang<sup>2,3,4</sup>, S. Souma<sup>5,6</sup>, F. Matsui<sup>7</sup>,  
T. Takahashi<sup>1</sup>, Y. Yao<sup>2,3</sup> and T. Sato<sup>1,5,6,8</sup>

<sup>1</sup>Department of Physics, Graduate School of Science, Tohoku University, Sendai 980-8578, Japan

<sup>2</sup>Centre for Quantum Physics, Key Laboratory of Advanced Optoelectronic Quantum Architecture and Measurement (MOE), School of Physics, Beijing Institute of Technology, Beijing 100081, P. R. China

<sup>3</sup>Beijing Key Lab of Nanophotonics and Ultrafine Optoelectronic Systems, Beijing Institute of Technology, Beijing 100081, P. R. China

<sup>4</sup>Material Science Center, Yangtze Delta Region Academy of Beijing Institute of Technology, Jiaxing, 314011, P. R. China

<sup>5</sup>Advanced Institute for Materials Research (WPI-AIMR), Tohoku University, Sendai 980-8577, Japan

<sup>6</sup>Center for Science and Innovation in Spintronics (CSIS), Tohoku University, Sendai 980-8577, Japan

<sup>7</sup>UVSOR Synchrotron Facility, Institute for Molecular Science, Okazaki 444-8585, Japan

<sup>8</sup>International Center for Synchrotron Radiation Innovation Smart (SRIS), Tohoku University, Sendai 980-8577, Japan

Recently,  $\text{AV}_3\text{Sb}_5$  compounds (where  $A$  represents an alkali metal K, Rb, or Cs) have been discovered to host an ideal two-dimensional kagome lattice formed by V atoms [Fig. 1(a)]. These materials undergo a charge density wave (CDW) transition below the critical temperature ( $T_{\text{CDW}}$ ) of 78-103 K. The CDW transition is characterized by lattice distortions with the star-of-David or inverse star-of-David patterns. Notably, the CDW phase exhibits intriguing properties, including the coexistence with superconductivity, time-reversal symmetry breaking, and nematicity. Understanding the origin of the CDW in  $\text{AV}_3\text{Sb}_5$  and its interplay with other properties is currently a hot topic in condensed matter physics. One useful approach to study this issue is to perturb the CDW phase by varying key physical parameters such as pressure and carrier concentrations. In this regard, chemical substitution in the crystal, which can adjust chemical pressure and/or carrier concentrations, is a promising strategy.

In this study, we performed an angle-resolved photoemission spectroscopy (ARPES) study on Nb-substituted  $\text{CsV}_3\text{Sb}_5$ ,  $\text{Cs}(\text{V}_{1-x}\text{Nb}_x)_3\text{Sb}_5$ , with  $x = 0, 0.03$ , and  $0.07$  [1]. The substitution of V with isovalent Nb results in a reduction of  $T_{\text{CDW}}$ , while simultaneously enhancing the superconducting transition temperature ( $T_c$ ) [Fig. 1(b)].

High-quality single crystals of  $\text{Cs}(\text{V}_{1-x}\text{Nb}_x)_3\text{Sb}_5$  were synthesized by the self-flux method. ARPES measurements were carried out by using momentum microscope KREIOS 150 MM (SPECS) at BL6U [2].

In Fig. 1(c), we present the experimentally determined Fermi surface in the normal state at  $T = 120$  K (above  $T_{\text{CDW}}$ ) for the highest Nb concentration ( $x = 0.07$ ). The use of a momentum microscope allowed to collect photoelectrons over a wide momentum space, enabling a comprehensive observation of multiple Fermi surfaces. Specifically, we observed a circular pocket centered at  $\Gamma$ , which is derived from the  $p$  orbital of Sb atoms embedded in the kagome lattice plane, and a

large hexagonal pocket at  $\Gamma$  and triangular pockets at K, both of which originate from the  $3d$  orbitals of the V kagome lattice. A comparison of the Fermi surface at  $x = 0.07$  with that at  $x = 0$  reveals intriguing trends: the circular pocket expands with increasing  $x$ , while the triangular pocket shrinks. The significant impact of the observed band shift is a lifting of the saddle point near the M point away from the Fermi level. Since  $T_{\text{CDW}}$  becomes higher when the saddle point is located at closer to the Fermi level, a large density of states of the saddle point plays a key role in stabilizing CDW. Additionally, our findings suggest that the enhancement of  $T_c$  through Nb substitution is partly attributed to the expansion of the circular pocket.

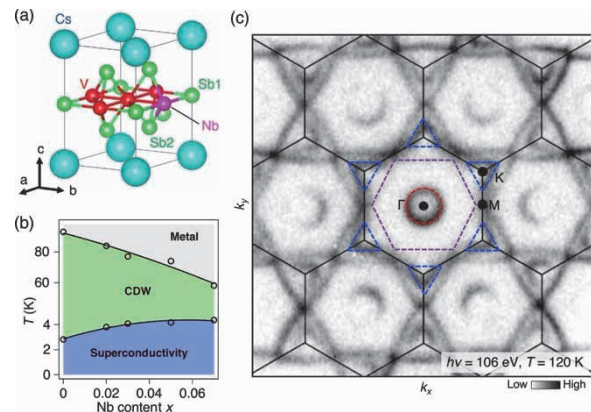


Fig. 1. (a) Crystal structure and (b) phase diagram of  $\text{Cs}(\text{V}_{1-x}\text{Nb}_x)_3\text{Sb}_5$ . (c) ARPES intensity at the Fermi level plotted as a function of two-dimensional wave vector. Red, purple, and blue dashed lines are guides for the eyes to trace the experimental Fermi surfaces.

[1] T. Kato *et al.*, Phys. Rev. Lett. **129** (2022) 206402.

[2] F. Matsui *et al.*, Jpn. J. Appl. Phys. **59** (2020) 067001.

## Mg K-edge NEXAFS of MgO, Mg(OH)<sub>2</sub> and MgCO<sub>3</sub>

E. Kobayashi<sup>1</sup>, S. Yoshioka<sup>2</sup> and K. K. Okudaira<sup>3</sup>

<sup>1</sup>Kyushu Synchrotron Light Research Center, 8-7 Yayoi-gaoka, Tosu, Saga 841-0005, Japan

<sup>2</sup>Graduate School of Engineering, Kyushu University, 744 Motoooka Nishi-ku Fukuoka 819-0395 Japan

<sup>3</sup>Graduate School of Science and Engineering, Chiba University,  
1-33 Yayoi-cho Inage-ku, Chiba 263-8522, Japan

In recent years, organic photovoltaic (OPV) has been attracting attention as a low-cost, lightweight battery that replaces conventional solar cells. Metal oxides play an essential role as an electron and a hole transport layer (ETL and HTL) material. [1,2] In order to further improve the characteristics of these charge transport layers, it is necessary to understand the band structure. Near-edge x-ray absorption fine structure (NEXAFS) spectroscopy is a powerful tool for investigating the unoccupied state of band structure of materials. When discussing the band structure, information on the position of the unoccupied bottom is important. It is necessary to know the effects on the bottom of the unoccupied band when metal oxides are contaminated by atmospheric component such as OH and CO<sub>2</sub>. Therefore, we measured the unoccupied state of MgO, Mg(OH)<sub>2</sub> and MgCO<sub>3</sub> · xH<sub>2</sub>O generated by the adsorption of OH and CO<sub>2</sub> on the MgO surface.

NEXAFS spectra of the MgO, Mg(OH)<sub>2</sub> and MgCO<sub>3</sub> · xH<sub>2</sub>O powders using both total electron yield (TEY) and partial fluorescence yield (PFY) modes were measured at the beamline 2A of the UVSOR in the Institute of Molecular Science. For TEY, the drain current from the sample was measured. For PFY, fluorescence X-rays were collected using an energy dispersible silicon drift detector (SDD). All experiments were performed at room temperature.

Figure 1 shows the Mg K-edge NEXAFS spectra of MgO, Mg(OH)<sub>2</sub> and MgCO<sub>3</sub> · xH<sub>2</sub>O powder obtained from TEY mode. The peak positions of MgO, Mg(OH)<sub>2</sub> and MgCO<sub>3</sub> · xH<sub>2</sub>O spectra are different. This suggests that their structures are different. On the other hand, the rising positions of the spectra of MgO, Mg(OH)<sub>2</sub> and MgCO<sub>3</sub> · xH<sub>2</sub>O are very similar. This suggests that the bottom of the unoccupied band is the same. Figure 2 shows the Mg K-edge NEXAFS spectra of MgO, Mg(OH)<sub>2</sub> and MgCO<sub>3</sub> · xH<sub>2</sub>O powder obtained from PFY mode. The rising positions of the spectra of MgO, Mg(OH)<sub>2</sub> and MgCO<sub>3</sub> · xH<sub>2</sub>O are very similar. It was

found that the bottom of the unoccupied state of MgO was not affected by contamination by atmospheric component such as OH and CO<sub>2</sub>.

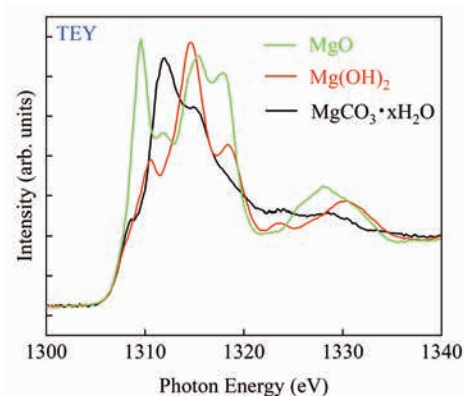


Fig. 1. Mg K-edge NEXAFS spectra of MgO, Mg(OH)<sub>2</sub> and MgCO<sub>3</sub> · xH<sub>2</sub>O powder obtained from TEY mode.

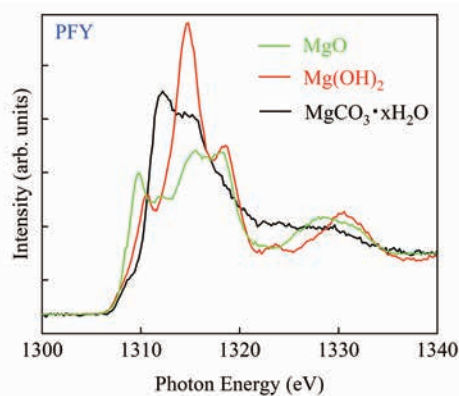


Fig. 2. Mg K-edge NEXAFS spectra of MgO, Mg(OH)<sub>2</sub> and MgCO<sub>3</sub> · xH<sub>2</sub>O powder obtained from PFY mode.

- [1] I. Ierides *et al.*, *J. Mater. Chem. C* **9** (2021) 3901.  
[2] Y. -J. Lee *et al.*, *Adv. Energy Mater.* **2** (2012) 1193.

BL2A

## Structural Analyses of Silicon Atoms in a Zero-dimensional Metal-atom Encapsulating Silicon Cage Clusters by X-ray Absorption Spectroscopy

A. Nakajima and T. Inoue

Department of Chemistry, Faculty of Science and Technology, Keio University, 3-14-1 Hiyoshi, Kohoku-ku, Yokohama 223-8522, Japan

Since silicon (Si) element belongs to the same group as carbon, it has been highly expected to create novel low-dimensional compounds as fullerene and carbon nanotube. In zero-dimensional silicon nanoclusters, it has been found that metal-atom encapsulating silicon cage,  $M@Si_{16}$  superatom (SA), can be generated in a gas-phase synthesis [1, 2]. In this study, the X-ray absorption fine structure analysis (XAFS), especially the extensive X-ray absorption fine structure analysis (EXAFS), has been applied to thin films of  $M@Si_{16}$  SA deposited on a solid surface to reveal the structural information, compared with the structure obtained by quantum chemical calculations.

The  $Ta@Si_{16}$  SA, composed of tantalum (Ta) and Si, was generated using a pulsed magnetron sputtering system, and  $Ta@Si_{16}$  SA cations were deposited on a highly oriented pyrolytic graphite (HOPG) substrate that was set on a wobble stick, as ten layers with a spot of 6-8 mm in diameter. The deposited substrate was kept in vacuum with an ion pump and transported from Keio University to UVSOR, where an ion pump was used with a nickel hydride battery (pumping speed 20L/s). The battery (24 V, 2000 mA h) can work in 10 hours, which covers the transportation time, and XAFS measurements of the Si K-edge were performed at the BL2A beamline (Fig. 1). Absorption of Si atoms was measured by the fluorescence method. The structure was identified by comparing the obtained EXAFS spectrum with the theoretically calculated FEFF spectrum of three structural isomers ( $T_d$ ,  $D_{4d}$ , and  $C_{3v}$ ).

For the deposited  $Ta@Si_{16}$  SA samples, XANES and EXAFS measurements were performed for the Si K-edge at 1800 to 2400 eV in the soft X-ray region (Fig. 2). For monitoring the incident light intensity, the scattered intensity of the copper mesh was used instead of gold mesh, because there is no XAFS of copper in the measurement energy region. However, the optics in the beamline inevitably contain gold-coated ones, and then X-ray absorption based on gold appears above 2000 eV; the light intensity decreases, where Si K-edge signals should be observed from the thin  $Ta@Si_{16}$  SA films. Although proper normalization of the incident light intensity had been tried with the scattered fluorescence from the measurement sample itself, the incident light intensity could not be accurately evaluated, and then the measurement energy range was squeezed to 1800-2000 eV ( $k = 3 - 7 \text{ \AA}^{-1}$ ). The EXAFS vibrations in the soft X-ray region were compared

between the obtained spectra and the theoretically calculated FEFF spectra of structural isomers to obtain the structural information.



Fig. 1. Photo of the connected chamber transported from Keio University.

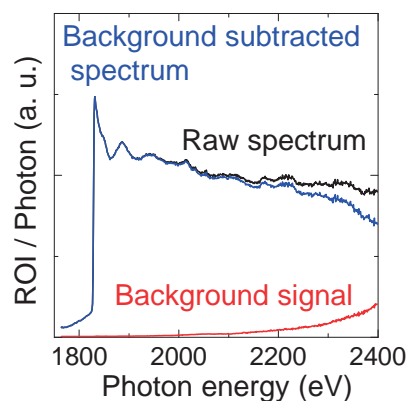


Fig. 2. Si K-edge XAFS Spectra for the deposited  $Ta@Si_{16}$  SA samples. The spectrum in blue was obtained by subtracting background signal in red from raw spectrum in black. The spectrum in 1800-2000 eV was used for the structural analyses.

[1] H. Tsunoyama, H. Akatsuka, M. Shibuta, T. Iwasa, Y. Mizuhata, N. Tokitoh and A. Nakajima, *J. Phys. Chem. C* **121** (2017) 20507.

[2] H. Tsunoyama, M. Shibuta, M. Nakaya, T. Eguchi and A. Nakajima, *Acc. Chem. Res.*, **51** (2018) 1735.

## Annealing Effects on Surface Electronic Structure of MoO<sub>3</sub> Nanoparticles by UPS

K. K. Okudaira<sup>1</sup> and S. Ishii<sup>2</sup>,

<sup>1</sup>Graduate School of Engineering, Chiba University, 1-33 Yohoi-cho, Inage-ku Chiba 263-8522, Japan

<sup>2</sup>Graduate School of Science and Engineering, Chiba University,  
1-33 Yohoi-cho, Inage-ku Chiba 263-8522, Japan

Organic photovoltaic (PV) cells have been the hot research topic in recent years due to their advantages of low-cost manufacturing, light weight and good flexibility. Among these PV cells, solution-processed bulk heterojunction PV cells with donor–acceptor (D–A) blends sandwiched between the anode and cathode are the most promising alternative to realize large-scale production. In bulk heterojunction PV cells, the charges generated in the active layer upon light absorption are transported via D–A networks and collected by the electrodes to realize light-electricity conversion. Recently, the transition metal oxides (TMOs) were inserted between the electrodes and organic active layer to prevent the leakage of undesired charged carrier to electrode as well as to promote the charged carrier transfer. [1] The efficiency of these electron transfer layer (ETL) and hole transfer layer (HTL) largely depend on the surface electronic structure of the TMO layer.

In this work we prepared MoO<sub>3</sub> nanoparticles (NPs) films with different annealing atmosphere and estimated the electronic structure of MoO<sub>3</sub> NPs by ultraviolet photoelectron spectroscopy (UPS) measurements to estimate the effect of annealing on the surface electronic structure and the work function.

UPS measurements were performed at the beam line BL2B of the UVSOR storage ring at the Institute for Molecular Science at the photon energy ( $h\nu$ ) of 28 eV. MoO<sub>3</sub> NPs were synthesized via solvothermal method. [2] The thin films of MoO<sub>3</sub> NPs were deposited on ITO by spin casting (denoted as “non”). The films were annealed at 500°C in air and hydrogen atmosphere (denoted as “in air” and “in H<sub>2</sub>”, respectively). The mean size of synthesized MoO<sub>3</sub> NPs was about 10 ~ 30 nm using TEM measurements.

The whole spectral structure of MoO<sub>3</sub> thin films by annealing in H<sub>2</sub> atmosphere is almost same as that of non annealing as shown in Fig. 1 (a). On the contrary, by annealing in air, the position of valence band top (VBT) is shifted to higher binding energy by about 0.3 ~ 0.4 eV. It is expected that the Fermi level leaves from VBT due to the formation of defect states just

above the Fermi level by annealing in air. Furthermore, the work function of MoO<sub>3</sub> films by annealing in air is larger than that of non annealing MoO<sub>3</sub> films by about 0.2 eV. This vacuum level shift is considered by the interfacial dipole formation due to the introducing the hydroxyl group to the surface of the MoO<sub>3</sub> film by annealing in air.

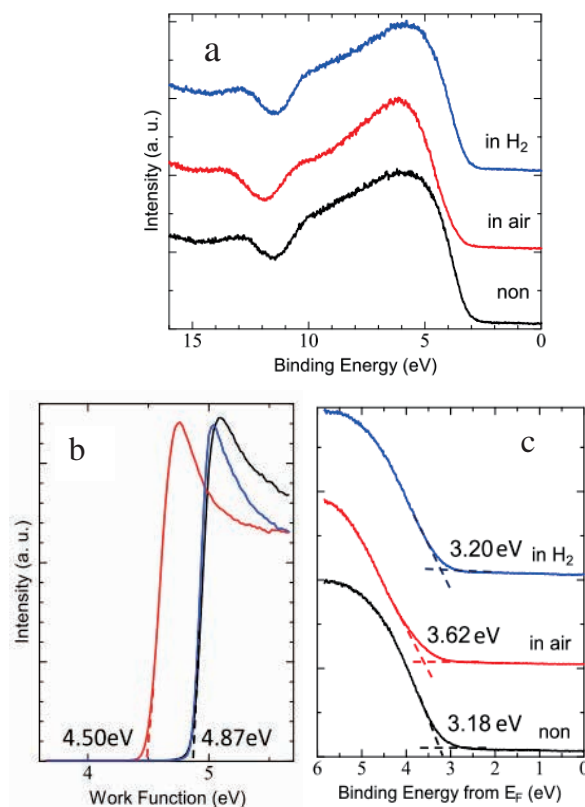


Fig. 1. UPS of MoO<sub>3</sub> NPs at  $h\nu = 28\text{eV}$  (a) in the valence band region (b) in the secondary cut-off and (c) in the valence top region.

[1] F. Liu *et al.*, Sol. Energy Mater. Sol. Cells **94** (2010) 842.

[2] W.-S. Kim *et al.*, J. Nanopart. Res. **12** (2010) 1889.

BL3U

## X-ray Absorption Spectroscopy Study of 4-MBA and Cysteine on Gold Surfaces

F. Sato<sup>1</sup>, I. Sakaida<sup>1</sup>, S. Ohno<sup>1</sup> and M. Nagasaka<sup>2</sup>

<sup>1</sup>Graduate School of Engineering Science, Yokohama National University, Yokohama 240-8501, Japan

<sup>2</sup>Institute for Molecular Science, Okazaki 444-8585, Japan

It is important to understand the behavior of biomolecules on solid surfaces for the application to medical device, biosensor and biocompatible material. It is essential to study the adsorption and desorption behavior of biomolecules and their response to the applied electric fields. It is of particular importance to analyze the dynamic behavior of biomolecules on a surface in electrolyte solutions, which is close to the realistic condition in the body of living creatures [1,2].

In the present study, potential-dependent adsorption/desorption behavior of 4-mercaptobenzoic acid (4-MBA) and cysteine on Au membrane surfaces have been investigated using soft X-ray absorption spectroscopy (XAS) in the transmission mode. The experiments were performed on the soft X-ray undulator beam line at UVSOR-III, BL3U. We used H<sub>2</sub>SO<sub>4</sub> and KOH as the electrolyte solution. For the adsorption of 4-MBA molecules, the samples were immersed in 1mM 4-MBA/ethanol solution for more than 30 min. For the adsorption of cysteine molecules, the samples were immersed in 1mM cysteine/K-OH solution for more than 1 hour.

In our previous study, we have studied the adsorption/desorption behavior of 4-MBA on Au films using surface differential reflectance spectroscopy (SDRS) combined with cyclic voltammetry (CV) [3]. The key issue was the interaction between functional group (-COOH) and Au films through Coulomb interaction depending on the applied biases and pH conditions. Redox processes involving charge transfer were clearly observed with CV and the relation between the change in the reflectance spectra and the peaks in CV was investigated in detail. Interestingly, we found some precursor phenomena to cause significant changes in the reflectance spectra with no corresponding signal in CV. This indicates that such changes in the reflectance spectra are not due to the charge-transfer-type reactions but rather to the subtle change in the orientation/conformation of 4-MBA molecules. We also observed similar effects for cysteine.

To our knowledge, there has been no serious effort to study the 4-MBA/Au and cysteine/Au systems using XAS in terms of the aforementioned precursor phenomena. At the initial stage, we have tried to observe the effects on Au(111). However, we could not obtain the clear data showing the adsorption/desorption behavior of 4-MBA, though they are

confirmed with CV measurements.

Here, we used an Au membrane as the substrate which has polycrystalline structure. Our CV data reveal that there should be Au(111) part on the surface, and that clear feature for adsorption/desorption for both 4-MBA and cysteine are confirmed.

In our previous XAS measurements, we have succeeded in obtaining the absorption peak of carbonyl group (-COOH) for 4-MBA. In this case, we observed two distinct features at 532 and 535 eV in the O K-edge region. These are assigned as due to the transition to the  $\pi^*$  orbital in the C=O double bond. Here, we observed a rather weak feature at 533 and 536 eV for cysteine, as shown in Fig. 1. We expect that these are the slightly shifted components, similarly assigned to the C=O double bond.

As a result, we could have established the measurement set up for the transmission mode for both 4-MBA and cysteine. We now plan to investigate a series of alkanethiol molecules to form self-assembled monolayer (SAM), and compared their behavior with 4-MBA and cysteine.

The next step should be the observation of the change in the orientation/conformation depending on the applied bias to the electrode (Au membrane). We expect that the precursor phenomena be proved more clearly.

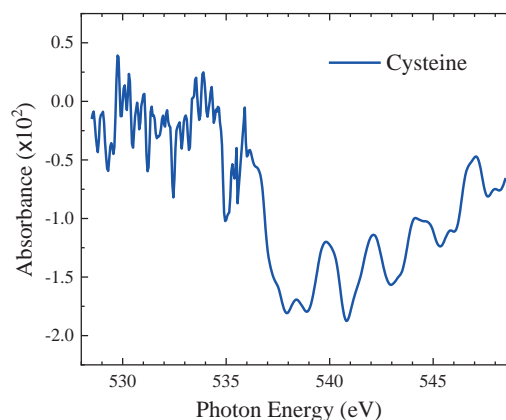


Fig. 1. O K-edge XAS spectrum for cysteine.

- [1] R. LeParc *et al.*, *Langmuir* **22** (2006) 3413.
- [2] C. I. Smith *et al.*, *J. Electrochem. Soc.* **150** (2003) 1.
- [3] N. Ikeda *et al.*, *ALC'19* (2019) 22.

## Evaluation of Growth Orientation and Crystallinity of Deep UV Emitting Zinc Aluminate Thin Films

H. Kominami<sup>1,2,3</sup>, K. Inoue<sup>1</sup>, N. Uesugi<sup>1</sup>, K. Nie<sup>1</sup>, A. Adachi<sup>1</sup>, R. Isihara<sup>1</sup>, K. Yabe<sup>1</sup>, J. Kamikawa<sup>2</sup>, T. Sadamori<sup>2</sup>, D. Takeya<sup>2</sup>, N. Miyazaki<sup>2</sup>, A. Dorokhina<sup>3</sup> and S. Kurosawa<sup>4,5</sup>

<sup>1</sup>Graduate School of Integrated Science and Technology, Shizuoka University,

<sup>2</sup>Faculty of Engineering, Shizuoka University,

<sup>3</sup>Graduate School of Science and Technology, Shizuoka University,

<sup>1-3</sup>3-5-1 Johoku, Naka-ku, Hamamatsu, 432-8651 Japan

<sup>4</sup>New Industry Creation Hatchery Center (NICHe), Tohoku University

6-6-10 Aza-Aoba, Aramaki, Aoba-ku, Sendai, Miyagi, 980-8579, Japan

<sup>5</sup>Faculty of science, Yamagata University, 1-4-12, Kojirakawa-machi, Yamagata, 990-8560, Japan

The UV light is used for various applications depending on the wavelength as well as the sterilization described above. Recently, from the viewpoint of consideration to the environment, the mercury free UV emission devices have been demanded for the application of catalyst and medical situations. In our previous work, it was clarified that ZnAl<sub>2</sub>O<sub>4</sub> phosphor was suitable for the UV field emission lamp because of its stability and luminescent property. It shows strong UV emission peaked around 250 nm which suitable for sterilization.

In this research, ZnAl<sub>2</sub>O<sub>4</sub> thin film layer were prepared by thermal diffusion of ZnO and sapphire substrate for new UV devices. In order to evaluate the inside of the film, an etching treatment was performed using hydrochloric acid.

XRD measurement was performed on the prepared sample. As a result, diffraction peaks of (220)(311)(400)(333) were observed. XRD measurement was performed on the prepared sample. As a result, diffraction peaks of (220)(311)(400)(333) were observed.

$\phi$  scan results of ZnAl<sub>2</sub>O<sub>4</sub>(220)(422)(533) and c-Al<sub>2</sub>O<sub>3</sub> (110)(300) where diffraction peaks were observed in  $2\theta/\phi$  scans around the a- and m-planes, a total of six diffraction peaks were observed every 60°. The results are shown in Fig.1. This is a diffraction peak with six-fold symmetry derived from  $\alpha$ -Al<sub>2</sub>O<sub>3</sub>, which is a hexagonal system. ZnAl<sub>2</sub>O<sub>4</sub> is a cubic substance, and ZnAl<sub>2</sub>O<sub>4</sub> (220)(422)(533) also had a total of six diffraction peaks at intervals of 60°.

In ZnAl<sub>2</sub>O<sub>4</sub>{220}{422}, there are 6 planes perpendicular to ZnAl<sub>2</sub>O<sub>4</sub> (333) every 60°. There is a face. From this, the diffraction peaks of ZnAl<sub>2</sub>O<sub>4</sub> (220)(422)(533) with six-fold symmetry in the  $\phi$  scan are considered to be the diffraction peaks of a crystal in which ZnAl<sub>2</sub>O<sub>4</sub> (333) is oriented on the c-plane of c-Al<sub>2</sub>O<sub>3</sub>.

The six planes of ZnAl<sub>2</sub>O<sub>4</sub>{220} and {422} each form an angle of 30°, and the m-plane and a-plane of c-Al<sub>2</sub>O<sub>3</sub> also form an angle of 30°. ZnAl<sub>2</sub>O<sub>4</sub>(220) and (422) are oriented along the m-plane and a-plane of c-Al<sub>2</sub>O<sub>3</sub>, respectively, from the measurement results of

$2\theta/\phi$  scans around the m-plane and a-plane of c-Al<sub>2</sub>O<sub>3</sub>, so ZnAl<sub>2</sub>O<sub>4</sub>{422} and the a-plane of c-Al<sub>2</sub>O<sub>3</sub>, and the m-plane of ZnAl<sub>2</sub>O<sub>4</sub>{220} and c-Al<sub>2</sub>O<sub>3</sub> are parallel to each other.

From Fig.1, there is a large peak of 6-fold symmetry and a small peak of 6-fold symmetry at 30° shift (▼). In addition, ZnAl<sub>2</sub>O<sub>4</sub>(220) is also oriented on the a-plane of c-Al<sub>2</sub>O<sub>3</sub> from the measurement result of  $2\theta/\phi$  scan around the a-plane of c-Al<sub>2</sub>O<sub>3</sub>. These diffraction peaks are thought to be due to crystals formed by a phase relationship in which ZnAl<sub>2</sub>O<sub>4</sub> is rotated 30° about ZnAl<sub>2</sub>O<sub>4</sub>[333], where the planes of ZnAl<sub>2</sub>O<sub>4</sub> and c-Al<sub>2</sub>O<sub>3</sub> are parallel to each other. Since almost no diffraction peaks other than the above two models are observed, it is considered that the sample is formed by the relationship between the phases of c-Al<sub>2</sub>O<sub>3</sub> and ZnAl<sub>2</sub>O<sub>4</sub> in these two models.

$\phi$  scans of ZnAl<sub>2</sub>O<sub>4</sub>(220) samples whose thin film surface was etched by hydrochloric acid showed that the sample etched about 400 nm lost some of its internal orientation, while the sample etched about 450 nm lost its orientation largely. lost part.

From the CL measurement results of this sample, the sample etched about 400 nm maintained the UV emission intensity, but then the emission intensity dropped sharply, and the sample etched about 450 nm did not obtain UV emission. From these results, it is considered that a uniform ZnAl<sub>2</sub>O<sub>4</sub> thin film is formed from the sample surface to about 400 nm, but the formation of ZnAl<sub>2</sub>O<sub>4</sub> is insufficient inside.

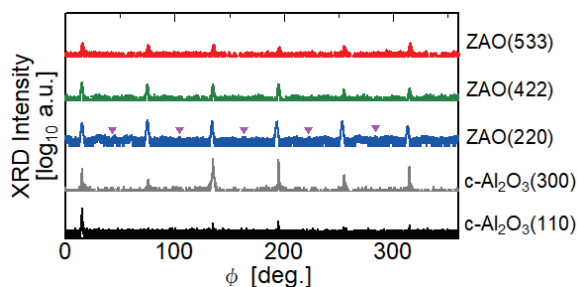


Fig. 1.  $\phi$  - scan XRD spectra of ZnAl<sub>2</sub>O<sub>4</sub> and c-Al<sub>2</sub>O<sub>3</sub>.

BL4U

## Application of atomically-thin Graphene to X-ray Astronomy: Soft X-ray Transmission Measurements

I. Mitsuishi<sup>1</sup>, K. Kashiwakura<sup>1</sup>, Y. Niwa<sup>1</sup>, T. Ogawa<sup>1</sup>, M. Hirota<sup>1</sup>, Y. Tawara<sup>1</sup>, R. Kitaura<sup>2</sup>,  
H. Yuzawa<sup>3</sup>, T. Ohigashi<sup>3</sup> and K. Tanaka<sup>3</sup>

<sup>1</sup>Graduate School of Science, Division of Particle and Astrophysical Science, Nagoya University, Furo-cho,  
Chikusa-ku, Nagoya, Aichi 464-8602, Japan

<sup>2</sup>Department of Chemistry, Nagoya University, Nagoya 464-8602, Japan

<sup>3</sup>UVSOR Synchrotron Facility, Institute for Molecular Science, Okazaki 444-8585, Japan

Thin-film devices have been used in a large variety of fields including astronomy. In X-ray astronomy, thin-film devices have been prepared for payloads such as detectors and telescopes and playing a key role as, e.g., optical and contamination blocking filters and thermal shields [e.g., 1, 2]. For such thin film devices, severe launch and space environmental tolerance and high transmission are essential at the same time for high-sensitivity space observations in the limited observing time. Plastic films such as polyimide have often been adopted as thin films. However, there is still room for improvement especially in transmission of a soft energy range below 1 keV. Thus, we have proposed to make use of graphene which is an atomically-thin material but has excellent mechanical strength. Our idea is to apply graphene to thin film devices in X-ray astronomy [3].

As a first step, we conducted rough X-ray transmission measurements from 100 to 500 eV and confirmed very high transmission for both single- and five-layer graphene sample [3]. As a next step, we performed detailed X-ray transmission measurements to understand systematic errors for the observed values in this experimental setup and aging degradation as shown in Fig. 1. We used the same quartz substrates with large tapers with an angle of 30 degrees to avoid the shadowing effect by the substrate for focused X-ray photons by the Fresnel zone plate. Consequently, very high transmission, specifically 94-99% and 95-101% for single- and five-layer graphene samples in nominal values except the C K-edge structure, was obtained. The systematic errors are estimated to be 3% for our sample in this experimental setup considering short- and long-term time variability and spatial dependence and thus, there is no significant differences in the transmission between the samples within the systematic errors in our current experimental setup. This suggests that very high transmission is expected even for five-layer graphene films with much stronger mechanical strength which allows us to fabricate free-standing structures with larger diameter much easier. The results are shown in Fig. 2. We confirmed that there is no significant aging degradation at least for the single-layer graphene sample for 9 months. The paper including these results is being prepared (Kashiwakura, Mitsuishi *et al.*, in prep.).

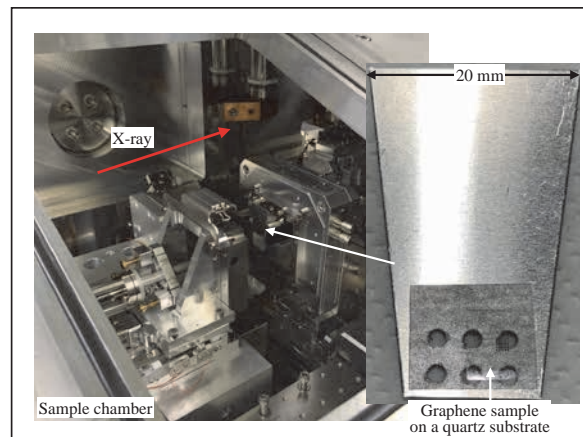


Fig. 1. Sample chamber and a close-up view of the graphene sample on the quartz substrate with a taper structure.

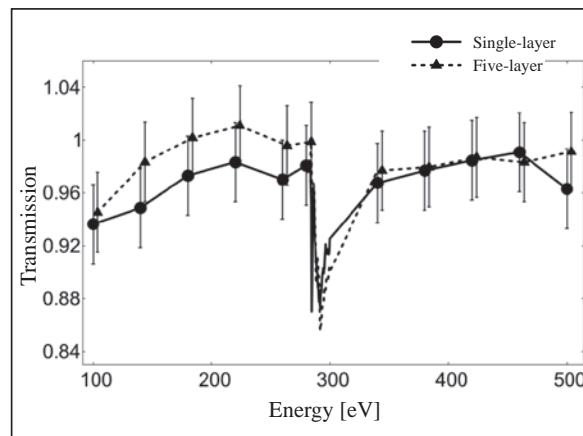


Fig. 2. Resultant transmission from 100 to 500 eV for single- (filled circle) and five-layer (triangle) graphene samples (Kashiwakura, Mitsuishi *et al.*, in prep.). Systematic errors are +/- 3%.

[1] P.J. Serlemitsos *et al.*, Publ. Astron. Soc. Japan **47** (1995) 105-114.

[2] P.J. Serlemitsos *et al.*, Publ. Astron. Soc. Japan **59** (2007) S9-S21.

[3] I. Mitsuishi *et al.*, UVSOR Activity Report 2021 **49** (2022) 45.

## Tuning Magnetic Properties of Atomic Layer Materials by organic-inorganic Interfacial Magnetic Coupling

H. Ono<sup>1</sup>, Y. Umeda<sup>1</sup>, K. Yamamoto<sup>3,4</sup>, O. Ishiyama<sup>3,4</sup>,  
T. Yokoyama<sup>3,4</sup>, M. Mizuguchi<sup>1,2</sup> and T. Miyamachi<sup>1,2</sup>

<sup>1</sup>Department of Materials Science and Engineering, Nagoya University, Aichi, 464-8603, Japan.

<sup>2</sup>Institute of Materials and Systems for Sustainability (IMaSS), Nagoya University, Aichi, 464-8601, Japan.

<sup>3</sup>Institute for Molecular Science, Myodaiji-cho, Okazaki 444-8585, Japan

<sup>4</sup>The Graduate University for Advanced Studies, Myodaiji-cho, Okazaki 444-8585, Japan

Organic materials are expected to be useful to spintronics devices due to their low spin current dissipation derived from weak spin-orbit interaction. Organic-inorganic hybrid interface has been studied because of its controllable interfacial spin state via the proximity effect. Spin-dependent electron transport properties depend on the electronic interaction between organic and inorganic materials and local interface structures. Thus, understanding structural, electronic and magnetic properties of the organic-inorganic interface on the level of single molecules is important for realizing molecular spintronics devices. However, microscopic details of the hybrid interface have not been clarified so far.

In this study, we fabricate organic-inorganic hybrid films and investigate their intrinsic electronic and magnetic properties on the level of single molecules. For this purpose, ferromagnetic iron nitride atomic layers with  $\gamma'$ -Fe<sub>4</sub>N stoichiometry were chosen as an inorganic material, which uniformly grow and show high surface quality on the atomic scale [1,2]. Molecular layers composed of planer cobalt phthalocyanine (CoPc) were chosen as an organic material. Structural, electronic and magnetic properties of the hybrid interface composed of CoPc with the thickness of 1, 2 and 3 molecular layers and a bilayer  $\gamma'$ -Fe<sub>4</sub>N were investigated by scanning tunneling microscopy (STM), low energy electron diffraction (LEED) and x-ray absorption spectroscopy/magnetic circular dichroism (XAS/XMCD).

A bilayer  $\gamma'$ -Fe<sub>4</sub>N was prepared by iron deposition on Cu (001) with N<sup>+</sup> ion bombardment and subsequent annealing at 620 K. Then, CoPc/ $\gamma'$ -Fe<sub>4</sub>N hybrid thin films were fabricated by depositing CoPc on the  $\gamma'$ -Fe<sub>4</sub>N at room temperature. In combination with results of STM and LEED, the impact of thickness-dependent structural properties of CoPc layers on the interfacial Fe and Co spin states were investigated by XMCD.

XAS/XMCD measurements were performed at BL4B in UVSOR by total electron yield mode at B = 0 ± 5 T and T = 7.3 K. The XMCD spectra are obtained at the normal (NI:  $\theta = 0^\circ$ ) and the grazing (GI:  $\theta = 55^\circ$ ) geometries by detecting  $\mu_+ - \mu_-$ , where  $\mu_+$  ( $\mu_-$ ) denotes the XAS recorded at Fe and Co L adsorption edges with the photon helicity parallel (antiparallel) to the sample magnetization. Note that  $\theta$  is the angle between the sample normal and the incident x-ray [3].

We confirm the magnetic coupling for CoPc(1ML)/ $\gamma'$ -Fe<sub>4</sub>N from the finite of Co XMCD signal. The perpendicular magnetic anisotropy of  $\gamma'$ -Fe<sub>4</sub>N, which is proportional to the difference between out-of-plane and in-plane Fe orbital magnetic moment obtained by XMCD sum rule, becomes larger after the deposition of CoPc molecules on the  $\gamma'$ -Fe<sub>4</sub>N. This result indicates the magnetic coupling with CoPc enhances the perpendicular magnetic anisotropy of  $\gamma'$ -Fe<sub>4</sub>N. As for magnetic properties of CoPc, we find that Co out-of-plane and in-plane XMCD signals show different behaviors with increasing the amount of CoPc. While the out-of-plane Co XMCD signal gradually decreases with increasing CoPc thickness, the strong Co XMCD is maintained in the in-plane direction. Taking the random stacking of CoPc layers revealed by STM and LEED, these results indicate that the orbital dependent magnetic coupling between CoPc layers, i.e., the magnetic coupling via the in-plane Co 3d orbitals is weak, but that via the out-of-plane Co 3d orbitals relatively robust.

[1] Y. Takahashi *et al.*, Phys. Rev. Lett. **116** (2016) 056802.

[2] Y. Takahashi *et al.*, Phys. Rev. B **95** (2017) 224417.

[3] S. Nakashima *et al.*, Adv. Funct. Mater. **29** (2019) 1804594.

[4] P. Bruno, Phys. Rev. B **39** (1989) 865.

BL4B (XMCD)

## X-ray Magnetic Circular Dichroism Study of Chiral Antiferromagnetic $\text{Co}_{2-x}\text{Pd}_x\text{Mo}_3\text{N}$ Thin Films

B. Qiang<sup>1,2</sup>, M. Togashi<sup>3</sup>, T. Fukasawa<sup>1</sup>, T. Hajiri<sup>1</sup>, M. Kuwahara<sup>3,4</sup>, H. Asano<sup>1,5</sup> and T. Ito<sup>6</sup><sup>1</sup>Department of Materials Physics, Nagoya University, Nagoya, Japan, 464-8603<sup>2</sup>Department of Materials Design Innovation Engineering, Nagoya University, Nagoya, Japan, 464-8603,<sup>3</sup>Department of Applied Physics, Nagoya University, Nagoya, Japan, 464-8603<sup>4</sup>Institute of Materials and Systems for Sustainability, Nagoya University, Nagoya, Japan, 464-8603<sup>5</sup>Research Department, Nagoya Industrial Science Research Institute, Nagoya, Japan, 464-0819<sup>6</sup>Synchrotron Radiation Research Center, Nagoya University, Nagoya, Japan, 464-8603

Dzyaloshinskii-Moriya (DM) interaction-induced magnetic skyrmions [1,2] have been observed in many chiral magnets with broken space reversal symmetry [3,4]. Recently, filled  $\beta$ -Mn-type  $\text{Fe}_{2-x}\text{Pd}_x\text{Mo}_3\text{N}$  [5] and  $\text{Co}_{2-x}\text{Pd}_x\text{Mo}_3\text{N}$  (CPMN) [6,7] have been reported to host small size skyrmions at room-temperature, which are a good playground for skyrmion device applications. X-ray magnetic circular dichroism (XMCD) is known as a very powerful tool to detect the element-specific spin and orbital states in each site. In this study, we have applied XMCD on filled  $\beta$ -Mn-type CPMN to elucidate the relation between its magnetism, especially ferromagnetic skyrmions at the low-temperature (Spiral-II) phase [6], and spin and orbital magnetic moment of Co.

CPMN ( $x=1.01$ ) thin film (30 nm in thickness, without capping layer) was prepared using magnetron sputtering technique grown on C-sapphire substrates. Measurements of XAS/XMCD were performed at the BL4B in UVSOR by total electron yield mode at  $T = 4$  K (Spiral-II phase). The external magnetic fields  $H$  up to  $\pm 1$  T were applied in parallel to the surface normal axis. The circularly polarized x-ray beam was induced nearly parallel to  $H$ . It should be noted that each  $\text{Co } L_{2,3}$  XAS spectra at  $H = +0.5 \sim +0.1$  T ( $-0.5 \sim -0.1$  T) were obtained after the magnetization due to canted antiferromagnetism being saturated at  $H = -1$  T ( $+1$  T), since the magnetic skyrmions in this system is expected to be generated around  $H = \pm 0.2$  T asymmetrically with respect to the zero field (see inset of Fig. 1(b))[6].

Figures 1(a) and 1(b) show the magnetic field dependence of the  $\text{Co } L_{2,3}$  edge-XAS spectra of CPMN ( $x = 1.01$ ) and the XMCD spectrum obtained by subtracting XAS spectra between  $H = +1$  T ( $\sim +0.1$  T) and  $H = -1$  T ( $\sim -0.1$  T), respectively. It can be seen that a clear XMCD is observed at  $H = \pm 1$  T, where the spin state associated with the formation of canted antiferromagnetism is expected from the magnetic and transport measurements at the low temperature region. With decreasing magnetic field, the observed XMCD intensity gradually decreases, and a opposite sign of the XMCD intensity near the  $L_3$  edge at 778 eV appears in the region of  $H < \pm 0.25$  T, where magnetic skyrmion

formation is expected from the topological Hall effect measurement (Fig. 1(b), inset). We expect that the observed magnetic field dependence of XMCD near the low-energy edge might suggest the change in the magnetic structure associated with the formation of magnetic skyrmions on CPMN.

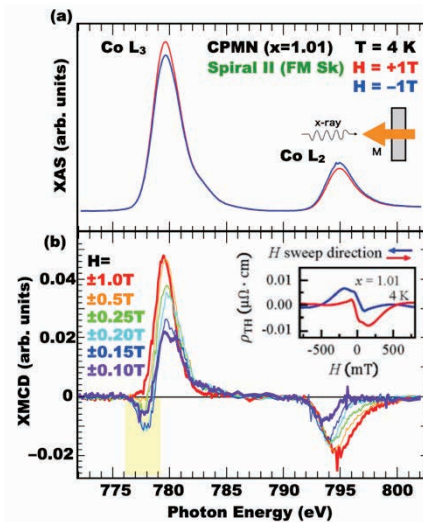


Fig. 1. (a) XAS spectrum at the  $\text{Co } L_{2,3}$  edge obtained by using the photon helicity parallel ( $\mu^+$ , red) and antiparallel ( $\mu^-$ , blue) to the external magnetic field  $H$ , respectively. (b) External magnetic field dependence of XMCD spectra ( $\mu^+ - \mu^-$ ) for CPMN ( $x=1.01$ ) at  $T = 4$  K. Inset shows the field dependence of topological Hall effect [6].

[1]T. Jo, J. Phys. Soc. Jpn. **62** (1993) 1814.[2]Y. Teramura, A. Tanaka, and T. Jo, J. Phys. Soc. Jpn. **65** (1996) 1053.[3]C. Papas *et al.*, Phys. Rev. Lett. **102** (2009) 197202.[4]V. Kumar *et al.*, Phys Rev B **101** (2020) 014424.[5]B. W. Qiang *et al.*, Appl. Phys. Lett. **117** (2021) 142401.[6]B. W. Qiang *et al.*, Jpn. J. Appl. Phys. **61** (2022) 120901.[7]B. W. Qiang *et al.*, AIP Advances **13** (2023) 025138.

## Controlling Magnetic Anisotropy of Magnetic Thin Film Heterostructures

Y. Umeda<sup>1</sup>, H. Ono<sup>1</sup>, K. Yamamoto<sup>3,4</sup>, O. Ishiyama<sup>3,4</sup>,  
T. Yokoyama<sup>3,4</sup>, M. Mizuguchi<sup>1,2</sup> and T. Miyamachi<sup>1,2</sup>

<sup>1</sup>Department of Materials Science and Engineering, Nagoya University, Aichi, 464-8603, Japan.

<sup>2</sup>Institute of Materials and Systems for Sustainability (IMaSS), Nagoya University, Aichi, 464-8601, Japan.

<sup>3</sup>Institute for Molecular Science, Myodaiji-cho, Okazaki 444-8585, Japan

<sup>4</sup>The Graduate University for Advanced Studies, Myodaiji-cho, Okazaki 444-8585, Japan

3d transition metal ordered alloy thin films with L1<sub>0</sub> crystal structure are attracting attention as rare-earth free magnetic materials due to their large perpendicular magnetic anisotropy, large magnetic moment, and high Curie temperature. Using pulsed laser deposition, the growth of FeCo thin films with alternating Fe and Co atomic layers was investigated [1]. Although much effort has been made to realize uniaxial anisotropy in the L1<sub>0</sub>-FeCo phase, the L1<sub>0</sub> structure is a non-equilibrium state of the FeCo phase and hence the method for achieving the out-of-plane magnetization has not been established. The main problem could be caused by atomic-scale disorder at the Fe/Co interface during growth processes, which highlights the importance of microscopic characterizations of the structural, electronic, and magnetic properties of L1<sub>0</sub>-FeCo. Therefore, we intend to fabricate high-quality FeCo alloy thin films on Cu(001) substrates by utilizing the nitrogen surfactant effect of a monatomic layer nitride. The high surface lattice stability of a monatomic layer nitride and the nitrogen surfactant effect that effectively suppresses the interdiffusion at the heterointerface could lead to the growth of FeCo alloy thin films with atomically flat and uniform interfaces [2,3]. The important role of the nitrogen surfactant effect in the preparation of high-quality L1<sub>0</sub>-type alloy thin films has been demonstrated for FeNi alloy thin films [2].

In this study, FeCo ordered alloy thin films in the initial growth stage were prepared using the nitrogen surfactant effect. The correlation between the structural changes at the FeCo interface and magnetic properties upon sample heat treatment was investigated using low-energy electron diffraction (LEED) and X-ray absorption spectroscopy/X-ray magnetic circular dichroism (XAS/XMCD). FeCo alloy multilayer thin films were grown on Cu(001) using the following process: (1) a bilayer iron nitride (Fe<sub>2</sub>N/Fe) was first grown on Cu(001), (2) 1 monolayer (ML) of Co was deposited at a low temperature (~150 K), (3) annealing was carried out at 300, 570, and 670 K, and (4)

additional 1 ML of Fe was deposited at a low temperature (~150 K) for samples heated at 570 K (FeN/Co/Fe/Fe). The annealing temperature dependence of electronic and magnetic properties was investigated by XAS/XMCD. XAS/XMCD measurements were performed at BL4B in UVSOR by total electron yield mode at  $B = 0 - \pm 5$  T and  $T = 7.9$  K. The XMCD spectra are obtained at the normal (NI:  $\theta = 0^\circ$ ) and the grazing (GI:  $\theta = 55^\circ$ ) geometries. Note that  $\theta$  is the angle between the sample normal and the incident x-ray. Element specific magnetization curves were also recorded by plotting the L<sub>3</sub>/L<sub>2</sub> Fe and Co XAS intensities as a function of the magnetic field.

The XMCD signal of the bilayer iron nitride is greater in the GI geometry than in the NI geometry, revealing its strong in-plane magnetic anisotropy as previously reported [3]. Adding 1 ML Co activates the nitrogen surfactant effect [2], which leads to the formation of CoN in the topmost layer (CoN/Fe/Fe). Accordingly, we observed an increase in the out-of-plane magnetization of the Fe layer from Fe magnetization curves. The perpendicular magnetic anisotropy of the Fe layer is further enhanced by annealing at 570 K. However, at an annealing temperature of 670 K, a decrease in the coercivity of the Fe layer is observed. Taking into consideration the annealing temperature dependence of the LEED pattern, the enhancement of the out-of-plane magnetization could be due to improved ordering of the Co/Fe interface up to annealing temperatures of 570 K. At 670 K, surface N atoms start to desorb, which induces the interdiffusion of interfacial Co and Fe atoms and consequently lowers the coercivity. In the sample with additional Fe layers (FeN/Co/Fe/Fe), the perpendicular magnetic anisotropy of Fe is further enhanced.

[1] H. Ito *et al.*, AIP Adv. **9** (2019) 045307.

[2] K. Kawaguchi *et al.*, Phys. Rev. Mater. **4** (2020) 054403.

[3] Y. Takahashi *et al.*, Phys. Rev. B **95** (2017) 224417.

BL4B

## X-ray Photoemission Spectroscopy and X-ray Absorption Spectroscopy Measurement of the Chiral Molecule on the Metal Substrate

F. Nishino<sup>1,2</sup>, K. Fukutani<sup>1,2</sup>, P. I. Jaseela<sup>1,2</sup>, H. Iwayama<sup>1,3</sup>, S. Makita<sup>3</sup> and S. Kera<sup>1,2,3,4</sup>

<sup>1</sup>Institute for Molecular Science, Okazaki 444-8585, Japan

<sup>2</sup>The Graduate University for Advanced Studies (SOKENDAI), Okazaki 444-8585, Japan

<sup>3</sup>UVSOR Synchrotron Facility, Institute for Molecular Science, Okazaki 444-8585, Japan

<sup>4</sup>Graduate School of Science and Engineering, Chiba University, Chiba 263-8522, Japan

Chirality-induced spin selectivity (CISS) is a phenomenon in which the spin of an electron is polarized/filtered in the process of electron transfer (transmission) in a system with broken mirror symmetry. The spin polarization by chiral molecular CISS in the gas phase was studied from 1980's. Since it was reported that the spin polarization was less than 0.5%, CISS has not attracted wide attention at this time. However, in 1999, R. Naaman *et al.* reported that spin-unpolarized electrons that transmitted through the chiral molecular film on solids exhibited spin polarization as high as 60% at room temperature [1]. While the CISS does not require magnetic materials or external magnetic fields, it exhibits higher spin polarization than the spin filters using magnetic metals. These features are expected to be applied to magnetic storage media with high storage density. Therefore, CISS by organic chiral molecules has been actively studied both theoretically and experimentally to elucidate its mechanism and for the purpose of device applications. Presently, however, the details of mechanism why chiral molecular film on solid exhibits spin polarization larger than 1000 times that of gas-phase molecules remains unsolved. For this reason, the gap between the theory and the application research is growing. In order to elucidate the mechanism, it is necessary to rigorously observe the interaction between the travelling electrons and the chiral molecules. In order to understand the CISS processes in chiral molecules, it is important to investigate how CISS effect depends on the relative orientations among the chiral molecules, the substrate, and the direction of electron transmission. Also, the difference of electronic structure and structure between the gas phase and the chiral molecular film on substrate.

In this study, the chiral molecule 2,2'-Bis(diphenylphosphino)-1,1'-binaphthyl (BINAP hereafter) shown in Fig. 1(a) were deposited on a clean Au(111) substrate, and *in-situ* X-ray photoemission spectroscopy (XPS) measurements were performed to investigate the interactions between BINAP molecules and Au(111) substrate.

Figure 1(b) shows the results of XPS from the phosphorus (P) 2*p* core orbital of BINAP molecules, acquired at the nominal coverages of 0.4 monolayer (ML) and 2 ML of (*R*)-BINAP on Au(111).

Interestingly, while the molecules at the sub-

monolayer coverage (0.4 ML) are expected to interact more strongly with the substrate than the multi-layer coverage (2 ML), we find that the P2*p* core peaks appear very similar, as can be seen from the peak fitting results for the two peaks [labelled A and B in Fig. 1(b)]. This likely signifies that the intermolecular interactions are much stronger (which determines the chemical shift of the atomic orbitals) than the molecule-substrate interactions. This view is indeed consistent with the later measurements in our project using the low-energy electron diffraction (LEED) and scanning tunnelling microscopy (STM), which clearly reveals the weakly-interacting incommensurate molecular overlayer structures.

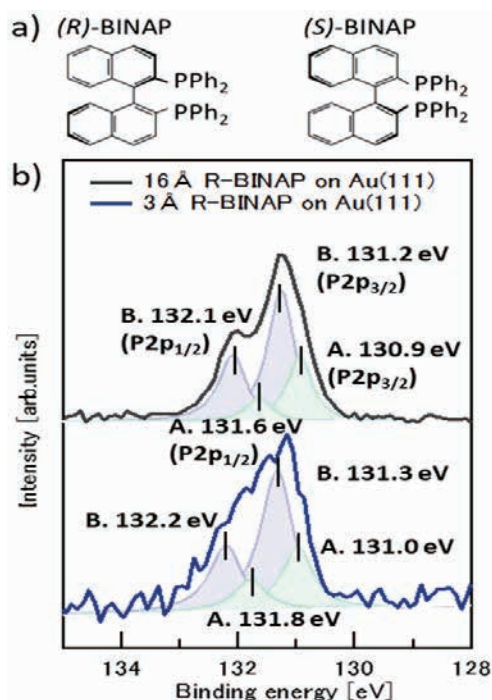


Fig. 1. (a) Molecular structures of (*R*)- and (*S*)-BINAPs. (b) P2*p* core level peaks of (*R*)-BINAP on Au(111) measured by XPS at the nominal coverages of 0.4 ML (bottom) and 2 ML (top). The spectra at each coverage are fitted with the two spin-orbit doublets [labelled A (green) and B (blue)] with Doniach-Sanjic lineshape.

[1] K. Ray, S. P. Ananthavel, D. H. Waldeck and R. Naaman, *Science* **283** (1999) 814.

## Observation of Heat Treatment Effects of Amorphous Selenium Thin Film by Vacuum Ultraviolet Transmission Spectrum

K. Hayashi

*Department of Electrical, Electronic and Computer Engineering, Gifu University, Gifu 501-1193, Japan*

It is well-known that various photoinduced phenomena [1,2] such as changes in optical band gap, conductivity, and volume occur in chalcogenide amorphous semiconductors by light irradiation. Although many studies have been done on the photoinduced phenomena of these materials, little is known about the details of these mechanisms. These phenomena were studied by exciting outer core electrons with the irradiation of light with the energy corresponding to the optical bandgap or sub-bandgap. The interest has been attracted for the change of the optical properties in the energy region of the visible light. We are interesting for the changes of the optical properties in the higher energy region. To obtain a wide knowledge of the photoinduced phenomena, it is necessary to investigate to the photoinduced and heat treatment effects on wide energy region. In this report, we report heat treatment effects on the vacuum ultraviolet (VUV) transmission spectra of amorphous selenium thin film.

Sample used for the measurement of the VUV transmission spectra was amorphous selenium thin film prepared onto thin aluminum film by conventional evaporation technique. The sample thickness was about 180nm. The aluminum film of the thickness of 200 nm was used to eliminate the higher order light from the monochromator in the VUV region. These measurements were carried out at room temperature on the BL4B beam line of UVSOR. The spectrum was measured by using the silicon photodiode as a detector. Two pinholes of 1.5mm in a diameter were inserted between the monochromator and sample to remove stray light. The intensity of the VUV light was monitored by measuring the TPEY of a gold mesh. The positions of the core levels for the samples were calibrated by referencing to the 2p core level absorption of the aluminum film. Observation of the heat treatment effect in the VUV transmission spectrum was carried out by performing heat treatment for one hour at each temperature up to 363K.

Figure 1 shows heat treatment effects on the VUV transmission spectrum of an amorphous selenium thin film. Main absorption peaks around 22nm corresponds to the 3d core level of Se atom. The absorption spectrum observed in the amorphous selenium thin film is roughly consistent with the previous report [3]. Although the spin-orbit splitting of the 3d<sub>5/2</sub> and 3d<sub>3/2</sub> level of Se atom is not clearly resolved in this amorphous selenium thin film. I don't know the cause, but there may be differences in the preparation

conditions of the film. As can be seen from the figure, a significant change in the VUV transmission spectrum is observed by heat treatment at temperatures above 343K. We are also studying the effect of heat treatment on the photoconductivity of amorphous selenium thin films in our laboratory. There is a correlation between the heat treatment effect on photoconductivity and VUV transmission spectrum, and it is thought that this change is due to the crystallization of the amorphous selenium thin film. From the VUV transmission spectrum change of selenium thin films by heat treatment, it can be seen that the broad peak around 20nm in the VUV transmission spectrum of amorphous selenium thin films is composed of about three absorption peaks. It is not clear about the origin of broad spectra and several peaks. I think that these origins are related to the local structures of the amorphous network. The detailed experiments and analysis will be done in the next step. More detailed experiments are necessary to clarify the origin of the VUV transmission spectra.

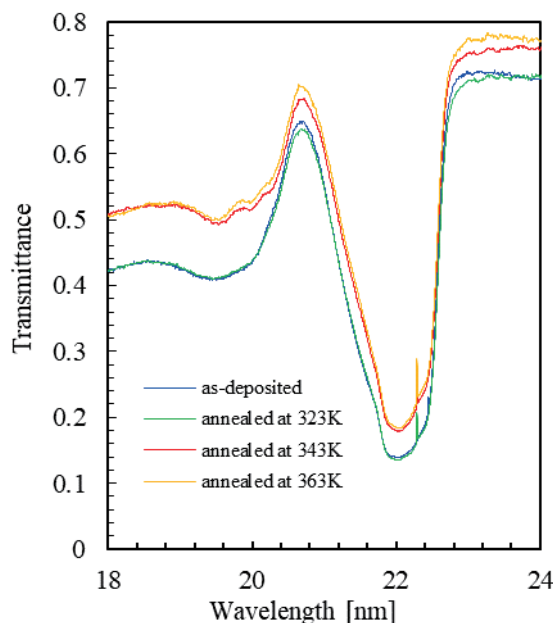


Fig. 1. Heat treatment effects on the VUV transmission spectrum of amorphous selenium film.

- [1] K. Tanaka, *Rev. Solid State Sci.* **4** (1990) 641.
- [2] K. Shimakawa, S. Inami, and S. R. Elliott, *Phys. Rev. B*, **42** (1990) 11857.
- [3] J. Bordas and J. B. West, *Phil. Mag.* **34** (1976) 501.

BL4B

## UV-X-ray Transmission Measurements of Atomically Thin Graphene Astronomical Applications

I. Mitsuishi<sup>1</sup>, K. Kashiwakura<sup>1</sup>, Y. Niwa<sup>1</sup>, T. Ogawa<sup>1</sup>, R. Kitaura<sup>2</sup>, E. Nakamura<sup>3</sup>,  
M. Nagasaka<sup>3</sup> and K. Tanaka<sup>3</sup>

<sup>1</sup>Graduate School of Science, Division of Particle and Astrophysical Science, Nagoya University, Furo-cho,  
Chikusa-ku, Nagoya, Aichi 464-8602, Japan

<sup>2</sup>Department of Chemistry, Nagoya University, Nagoya 464-8602, Japan

<sup>3</sup>UVSOR Synchrotron Facility, Institute for Molecular Science, Okazaki 444-8585, Japan

Thin-film devices have been utilized in a great variety of uses as not only ground-based but also space-based applications such as optical and contamination blocking filters and thermal shields [e.g., 1, 2]. Recently, polyimide films have often been used as thin films considering relatively stronger mechanical strength in plastic films. However, there is still room of improvement in sensitivity of the thin films (= transmission) below 1 keV including UV region although such energy ranges are very informative for understanding, e.g., stellar coronae and large-scale structure of the Universe [e.g., 3, 4]. Thus, we have proposed to make use of graphene which is an atomically-thin material but has excellent mechanical strength. Our idea is to apply graphene to thin film devices in X-ray astronomy [5].

As a first step, we measured reflectivity at a soft X-ray range between 100 and 500 eV successfully for single- and five-layer graphene samples at BL4U and confirmed very high transmission above 90% except C K-edge structure [5]. Thus, as a next step, we tried to measure transmission in UV region below 100 eV and construct our original experimental setup at BL4B. Our experimental setup is shown in Fig. 1 and we prepared a five-layer graphene sample with a diameter of 300  $\mu\text{m}$  on a quartz substrate to obtain larger photon statistics. To check the consistency of transmission between the beamlines of BL4U and BL4B, we used the same sample and measured transmission from 100 to 250 eV as well. Consequently, we measured transmission from 30 to 100 eV successfully and confirmed very high transmission from 91 to 101% in nominal values with systematic errors of 5% due to short- and long-term time variability. We confirmed that there are no significant differences in 100-250 eV between the results obtained from BL4B and BL4U. The results are summarized in Fig. 2. A slight decreasing trend can be seen toward 30 eV even though the systematic errors are high (5%). This trend is the same as the expected from a database for bulk carbon. In order to verify the trend, we need additional measurements with smaller measurement accuracy of <2% down to 10 eV. The paper including these results is being prepared (Kashiwakura, Mitsuishi *et al.*, in prep.).

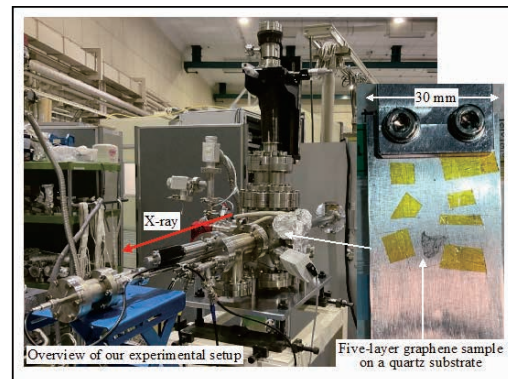


Fig. 1. Sample chamber and a close-up view of the graphene sample on the quartz substrate.

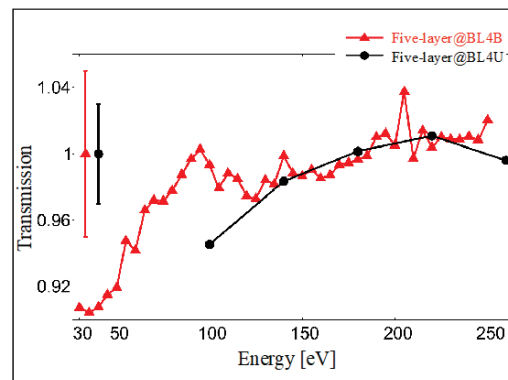


Fig. 2. Resultant transmission from 30 to 250 and from 100 to 250 eV for five-layer graphene samples measured at BL4B (filled triangle) and BL4U (filled circle) (Kashiwakura, Mitsuishi *et al.*, in prep.). Systematic errors are 5% / 3% at BL4B / BL4U.

- [1] P.J. Serlemijos *et al.*, Publ. Astron. Soc. Japan **47** (1995) 105.
- [2] P.J. Serlemijos *et al.*, Publ. Astron. Soc. Japan **59** (2007) S9.
- [3] I. Mitsuishi *et al.*, Publ. Astron. Soc. Japan **64** (2012) 18-1.
- [4] S. Takasao, I. Mitsuishi *et al.*, The Astrophys. J. **901** (2020) 70.
- [5] I. Mitsuishi *et al.*, UVSOR Activity Report 2021 **49** (2022) 45.

## Si *L*-edge NEXAFS Spectra of Native Oxide Si Wafer with Different Crystal Surface

K. K. Okudaira<sup>1</sup>, S. Yoshioka<sup>2</sup> and E. Kobayashi<sup>3</sup>

<sup>1</sup>Graduate School of Engineering, Chiba University, 1-33 Yahooi-cho, Inage-ku Chiba 263-8522, Japan

<sup>2</sup>Graduate School of Engineering, Kyushu University, 744 Motoooka Nishi-ku Fukuoka 819-0395 Japan

<sup>3</sup>Kyushu Synchrotron Light Research Center, 8-7 Yayoi-gaoka, Tosu, Saga 841-0005, Japan

Silicon dioxide is one of the most popular substrate for inorganic semiconductor devices as well as organic devices such as self-assembled monolayers, which is useful for organic field effect transistors. [1] One important advantage of the silicon substrate over the metal substrate is that conductive currents are eliminated. The leakage current is relatively large by using native oxide Si wafer as dielectric layer due to the thinness and inhomogeneous of oxide layer of native oxide Si wafer. The application of self-assembled monolayer to SiO<sub>2</sub>/Si substrate depress the leakage current. [2] The electrical properties such as insulation characteristics depends on the structure of surface silicon dioxides layer, which is considered amorphous. It is expected that the properties of native oxide layer on Si substrates would be affected by the underlying crystalline Si.

In this report, we investigate the effect of crystal structure of underlying crystalline Si on the surface structure of silicon dioxide by means of NEXAFS of native oxide Si(001) and Si(111) wafers.

NEXAFS spectra of the native oxide Si(001) and Si(111) wafers were measured at the beamline 4B of the UVSOR in the Institute of Molecular Science. In the total electron yield (TEY), the drain current of the sample was measured. All experiments were performed at room temperature.

Figure 1 shows the TEY Si *L*<sub>2,3</sub> edge NEXAFS spectra of native oxide of Si(111) and Si(001) wafers. In the observed fine structure two region are identified. The absorption features observed from 100 to 104 eV are attributable to Si<sup>0</sup> (crystalline Si under native oxide layer) and those from 104 to 110 eV are associated with Si<sup>4+</sup> (SiO<sub>2</sub>) [3]

In the hv range from 100 eV to 104 eV due to the Si crystalline layer, the spectral structure of Si(001) is identical with the one of Si(111). On the contrary, the spectral feature of native SiO<sub>2</sub>/Si(001) is different from that of SiO<sub>2</sub>/Si(111) in the hv range from 104 to 110 eV,

which is attributed to native oxide layer (SiO<sub>2</sub>). By closed comparison the relative intensity of the peak a<sub>1</sub> at hv of 106 eV to that of the peak a<sub>2</sub> at hv of 106.8 eV for the SiO<sub>2</sub>/Si(001) is different from that of SiO<sub>2</sub>/Si(111). The peak a<sub>1</sub> disappears in the observed Si *L*-edge NEXAFS of native oxides Si(111) wafer. The peaks a<sub>1</sub> and a<sub>2</sub> can be assigned to 2p<sub>3/2</sub> and 2p<sub>1/2</sub> → the antibonding orbital of Si 3s character. [4] Harp *et al.* shows the peak positions of a<sub>1</sub> and a<sub>2</sub> depend on not only the oxidation state but also the thickness of native oxide layer [5]. These differences indicate that the properties of surface native oxide layer such as bonding structure as well as oxidation states are affected by underlying crystalline Si layer.

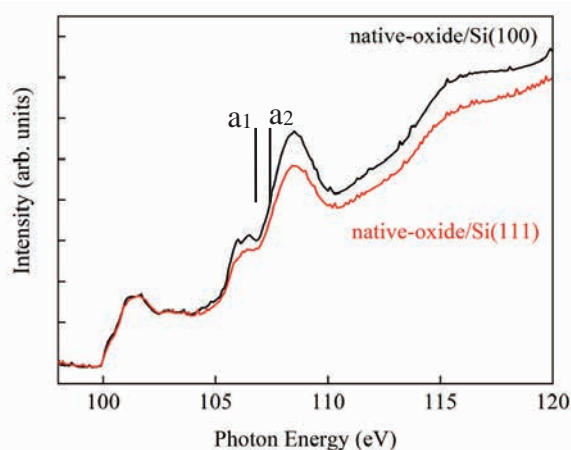


Fig. 1. Si *L*-edge NEXAFS of native oxide Si(001) and Si(111) wafers in TEY mode

[1] M. McDowell *et al.*, Appl. Phys. Lett. **88** (2006) 073505.

[2] M. -H. Yoon *et al.*, PNAS **102** (2005) 4678.

[3] M. Kasrai *et al.*, Appl. Surf. Sci., **99** (1996) 303

[4] M. Kasrai *et al.*, J. Vac. Sci. Tech. **A11** (1993) 2694.

[5] G. R. Harp *et al.*, J. Vac. Sci. Tech. **A8** (1990) 2566.

BL5U

## ARPES from $\text{Si}\{111\}\sqrt{3} \times \sqrt{3}$ -Ag ultra-thin Film on Artificially Designed three-dimensional Si facet-line Structure with $\{111\}$ Facet Surfaces on $\text{Si}(001)$ Substrates

K. Hattori<sup>1</sup>, Ni'matil Mabarroh<sup>1</sup>, Juharni<sup>1</sup>, Y. Ida<sup>1</sup>, W. Imayama<sup>1</sup>, Y. Kimoto<sup>1</sup>, Y. Kitagawa<sup>1</sup>, S. Tanaka<sup>2</sup>, A. N. Hattori<sup>2</sup>, S. Suga<sup>2</sup> and K. Tanaka<sup>3</sup>

<sup>1</sup>Nara Institute of Science and Technology, Ikoma 630-0192, Japan

<sup>2</sup>SANKEN, Osaka University, Ibaraki, 567-0047, Japan

<sup>3</sup>UVSOR Synchrotron Facility, Institute for Molecular Science, Okazaki 444-8585, Japan

Highly densified device like 3D FET has been required by information society to break the limitation of miniaturizing 2D planar-type devices. Control of 3D structure device is indispensable to improve the specification, such as carrier mobilities on any direction surfaces of the 3D structures.

Recently, our group has successfully created 3D-Si surfaces by combining lithography and surface treatment techniques [1-4], and reported a successful creation of  $\text{Si}\{111\} 7 \times 7$  clean facet surfaces showing surface and bulk electronic bands on  $\text{Si}(110)$  substrates using laboratory based angle-resolved photoelectron spectroscopy (ARPES) [5], aiming for a future 3D-surface band-engineering. Here, we first demonstrated the creation of ultra-thin film on 3D Si clean facet surfaces indicating characteristic film band structures, essential for the 3D surface control.

In our experiment, 3D Si facet-lined structures with  $(111)$  and  $(\bar{1}\bar{1}1)$  facet surfaces and  $[\bar{1}10]$ -direction face edges on  $(001)$  substrates with the facet pitch of  $4 \mu\text{m}$  period, were prepared by using a photo-lithography and wet etching (Fig. 1). After degassing and flashing the sample in ultra-high vacuum,  $\{111\} 7 \times 7$  reconstruction was confirmed by low-energy electron diffraction (LEED). Subsequently Ag was deposited on the sample at  $\sim 770 \text{ K}$ , showing  $\sqrt{3} \times \sqrt{3}$  reconstruction in both

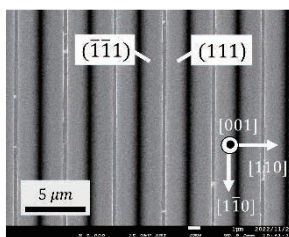


Fig. 1. SEM image of 3D Si facet-lined structure.

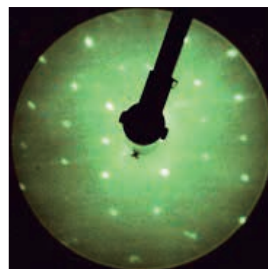


Fig. 2. LEED pattern of  $\{111\}\sqrt{3} \times \sqrt{3}$ -Ag facet surfaces (120 eV).

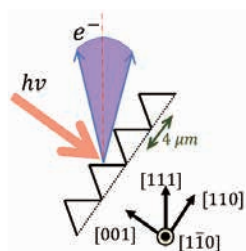


Fig. 3. ARPES geometry. 60 eV photons (pink) result in electron emission (purple) from  $(111)$  facet surfaces.

$(111)$  and  $(\bar{1}\bar{1}1)$  facet surfaces. Note that the superposition of the LEED patterns from the two facet surfaces are seen in Fig. 2.

ARPES was also performed in UVSOR at BL5U. Valence band dispersion was measured mainly at 70 eV photons with the  $(111)$  facet surface normal to the analyzer at 6 K, by optimizing the sample orientation (Fig. 3). We obtained the specific band structures caused by  $\sqrt{3} \times \sqrt{3}$ -Ag ultra-thin film on the  $(111)$  facet surface (Figs. 4a and 4c), which was almost the same as those of the  $\sqrt{3} \times \sqrt{3}$ -Ag on a 2D planar surface (Figs. 4b and 4d) measured under the same condition.

We confirmed that ARPES under optimizing 3D geometries informs us band structures of artificially designed 3D structure surfaces and “created films”. This will shed the light on future band engineering of 3D devices.

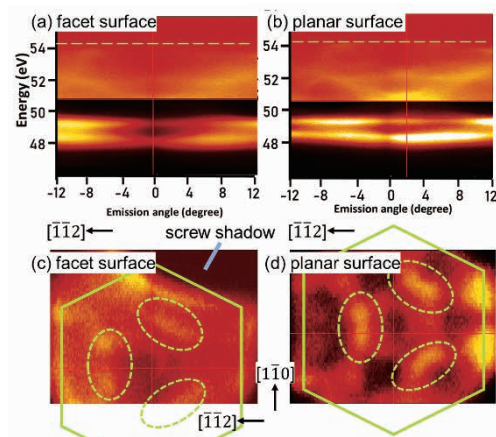


Fig. 4.  $E$ - $k$  along  $[\bar{1}\bar{1}2]$  (a, b) and  $k_x$ - $k_y$  near Fermi level (dashed lines in a and b) (c, d) for facet (a, c) and planar (b, d)  $(111)\sqrt{3} \times \sqrt{3}$ -Ag surfaces.

[1] A.N. Hattori, K. Hattori, *et al.*, Surf. Sci. **644** (2016) 86.

[2] A.N. Hattori, K. Hattori, *et al.*, Appl. Phys. Express **9** (2016) 085501.

[3] A.N. Hattori and K. Hattori, *21st Century Surface Science* (IntechOpen, London, 2020).

[4] S. Nakatsuka, T. Abukawa, A.N. Hattori, K. Hattori, *et al.*, e-J. Surf. Sci. NanoTechnol. **19** (2021) 13.

[5] K. Hattori, A. N. Hattori, *et al.*, e-J. Surf. Sci. Nanotechnol. **30** (2022) 214.

## Sizable Rigid Shift of the Valence Band of h-BN by Cs-doping

S. Ichinokura<sup>1</sup>, A. Hemmi<sup>2</sup>, H. Cun<sup>2</sup>, K. Tanaka<sup>3</sup>, T. Greber<sup>2</sup> and T. Hirahara<sup>1</sup>

<sup>1</sup>Department of Physics, Tokyo Institute of Technology, Tokyo 152-8551, Japan

<sup>2</sup>Physik-Institut, Universität Zürich, Winterthurerstrasse, 190, Zürich CH-8057, Switzerland

<sup>3</sup>UVSOR Facility, Institute for Molecular Science, Okazaki 444-8585, Japan

Hexagonal boron nitride (h-BN) is a two-dimensional semiconductor with a wide bandgap. Its gap size of around 5.9 eV corresponds to deep ultraviolet light, making h-BN a promising material for the development of energy-efficient optical disinfection devices. To reduce the working voltage of electroluminescence through tunneling carrier injection, it is required to develop p- and n-doping near the electrodes. However, the wide gap in h-BN poses a challenge for carrier doping through conventional substitution methods, which limits its use in electroluminescence devices.

To address this challenge, we are exploring an alternative approach known as chemical gating, which involves surface adsorption or intercalation of alkali metals (AMs) to the substrate interface. This creates an electrical dipole by facilitating charge transfer from the AMs to the substrate. Cs-doping has been shown to induce the largest electron doping in h-BN/Ir, where the valence band maximum (VBM), specifically the top of the  $\pi$  band at the K point, was indirectly estimated to be at 5.9 eV from the shift of the  $\sigma$  band at the  $\Gamma$  point, assuming a rigid band shift [1]. However, the limits of doping remain unclear until the direct observation of the band structure in a wide wavenumber range from  $\Gamma$  to K point.

In the present study [2], we conducted an analysis of the complete valence band structure of monolayer h-BN on Rh substrate before and after Cs doping via angle-resolved photoemission spectroscopy (ARPES) utilizing synchrotron radiation as a light source. The h-BN/Rh was grown by means of chemical vapor deposition. The doping of Cs was carried out via vacuum deposition at room temperature in the preparation chamber of the BL5U end station, followed by *in-situ* measurements of ARPES utilizing linear polarized light with  $h\nu = 72$  eV at 200 K. Figures 1(a) and (b) depict the valence band spectra before and after Cs doping obtained by horizontally polarized (H-pol.) light, respectively, whereas Figures 1(c) and (d) show the same as Figs. 1(a) and (b), respectively, obtained by vertically polarized (V-pol.) light. The uppermost portion of the  $\pi$  band is located at the K point with a higher binding energy than the top of the  $\sigma$  band at the  $\Gamma$  point, making it possible for us to evaluate the VBM.  $E_{\text{VBM}}$  and  $E'_{\text{VBM}}$  are defined as the binding energy of the VBM before and after doping, as denoted by dashed black lines. The shift of the VBM,  $\Delta E = E'_{\text{VBM}} - E_{\text{VBM}}$  is

observable to be 2.5 eV, identical to the  $\sigma$  band at the  $\Gamma$  point (refer to Figs. 1(c) and (d)). This clearly suggests a rigid shift of both the  $\pi$  and  $\sigma$  bands. Notably, Cs doping lowers the VBM to 5.7 eV. Considering the bandgap of h-BN is known to be 5.9 eV, the conduction band should lie only 0.2 eV above the Fermi surface. Thus, h-BN experiences significant electron doping.

As a concluding remark, for both Rh and Ir substrates, the VBM attained binding energy nearly equated to the band gap. This can be elucidated by the vacuum level alignment model when Cs is adsorbed on both sides of h-BN. This indicates that Cs with the lowest work function is the most efficacious, and this method can be implemented on an electroluminescence device using h-BN with any electrode.

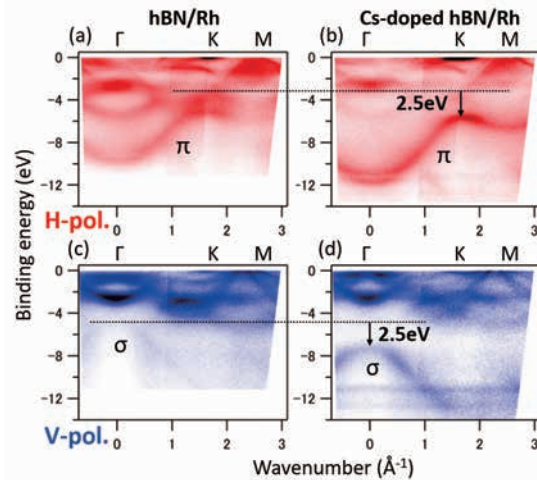


Fig. 1. ARPES spectrum of hBN along  $\Gamma$ -K-M line in the Brillouin zone. Panels (a) and (c) display the spectrum before Cs-deposition, while (b) and (d) show the spectrum after Cs-deposition. The spectra were obtained with  $h\nu = 72$  eV at a temperature of 200 K. Panels (a) and (b) were obtained with horizontally-polarized light, while panels (c) and (d) were obtained with vertically-polarized light. In panels (a) and (b), the shift of VBM is indicated by black dashed line and arrow. In panels (c) and (d), the shift of  $\sigma$  band is denoted by black dashed line and arrow.

[1] J. Cai *et al.*, Phys. Rev. B **98** (2018) 195443.

[2] S. Ichinokura *et al.*, Appl. Phys. Lett. **122** (2023) 071601.

BL5U

## Growth of Transition Metal Phosphide Thin Film on Au(111)

N. Maejima<sup>1,2</sup>, K. Inaoka<sup>1</sup> and K. Edamoto<sup>1,2</sup>

<sup>1</sup>*Coll. Sci., Rikkyo Univ., Tokyo 171-8501, Japan*

<sup>2</sup>*Research Center for Smart Molecules, Rikkyo Univ., Tokyo 171-8501, Japan*

The Ni<sub>12</sub>P<sub>5</sub>@Au core-shell catalyst has attracted attention because of its high catalytic activity for oxygen evolution reactions [1]. Novel functions of core-shell catalysts arise from the interaction between the core and the shell at the interface [2]. Direct observation of the electronic states formed through the interactions between core and shell is difficult, and thus the fabrication of the Ni phosphide thin film on an Au substrate is desirable as a model system that allows the investigation using photoelectron spectroscopy. In this report, we will show that a nickel phosphide thin film can be grown on Au(111) by Ni deposition on a P-covered Au(111).

Experiments were performed at BL5U of the UVSOR facility. The Au(111) surface was cleaned by cycles of Ar<sup>+</sup> ion sputtering (0.5 keV) and annealing (750 °C). P atoms were deposited on the Au(111) surface at 400°C (AuP/Au(111)). The prepared Au(111) and AuP/Au(111) samples showed 1x1 and 5x5 LEED patterns, respectively. Ni was subsequently evaporated onto AuP/Au(111) at 400°C to form a Ni<sub>x</sub>P thin film on Au(111)(Ni<sub>x</sub>P/Au(111)). This LEED pattern of this sample consisted of 1x1 spots arising from the Au(111) substrate and the additional 12 spots which are assigned as the spots from the Ni<sub>x</sub>P crystal thin film. Au 4f, P 2p, Ni 3p and valence band photoelectron spectroscopy (PES) measurements were performed by an MBS A-1 analyzer. The ratio of the amount of Ni and P atoms on the Au substrate were determined by the ratios of the peak areas of Ni 3p and P 2p photoelectron spectra to be Ni : P = 2:1.

Au 4f<sub>7/2</sub> spectra obtained from Au(111) clean surface, AuP/Au(111), and NiP/Au(111) samples are shown in Fig. 1. In the Au 4f<sub>7/2</sub> spectra of Au(111) clean surface, two bulk and surface components were observed at binding energies of 84.0 and 83.7 eV, respectively.[3] The spectrum obtained from P deposited sample contain the bulk and surface Au-P component at 84.0 eV and 84.4 eV, respectively.[4] The surface component observed in the spectra of Au(111) clean surface has disappeared, indicating that the whole surface is covered with P. In the spectrum of the Ni deposited sample, peaks of bulk and surface components were observed at 84.0 eV and 83.7 eV, respectively. The disappearance of the peak at 84.4 eV corresponding to Au-P bonds indicates the cleavage of all Au-P bonds.

Though the P 2p spectrum obtained from Ni<sub>x</sub>P/Au(111) contains multiple peak components, the component that is ascribed to P atoms bonded to Au was disappeared. In addition, the surface component observed in the spectrum of the Au(111) clean surface reappears in the spectrum of Ni<sub>x</sub>P/Au(111). These results imply that the interaction between the thin film and the substrate is weak or the nickel phosphide film congregates to form islands. The Ni 3p peak position in the spectrum of Ni<sub>x</sub>P/Au(111) was higher than that obtained from Ni<sub>2</sub>P(10-10) single crystal by 0.3 eV [5], whereas the spectral shape was almost the same. These results suggested that a Ni phosphide whose composition was Ni : P = 2:1 can be formed on Au(111).

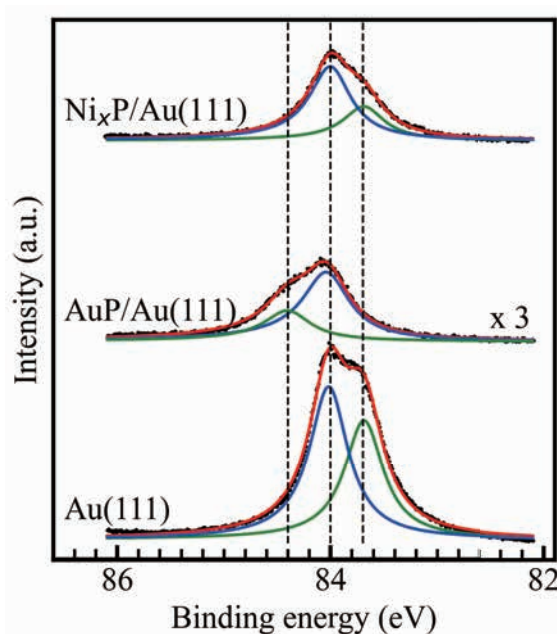


Fig. 1. Au 4f<sub>7/2</sub> photoelectron spectra of clean Au(111), AuP/Au(111) and NiP/Au(111) samples.

- [1] Lee, Jong-Soo *et al.*, JACS **130** (2008) 9673.
- [2] Xu, Yingying *et al.*, Nano research **10** (2017) 3103.
- [3] Citrin, Ph. H. *et al.*, Phys. Rev. Lett. **41** (1978) 1425.
- [4] Zhang, Wei *et al.*, Small **14** (2018) 1804066.
- [5] N. Maejima *et al.*, UVSOR Activity Report **48** (2020) 115.

## Heavy-Fermion in a Mono-Atomic Layer YbCu<sub>2</sub>/Cu(111)

H. Sugihara<sup>1</sup>, T. Nakamura<sup>2,1</sup>, Y. Chen<sup>1</sup>, K. Nishihara<sup>1</sup>

M. F. Lubis<sup>1</sup>, K. Tanaka<sup>3</sup> and S. Kimura<sup>2,1,4</sup>

<sup>1</sup>Department of Physics, Graduate School of Science, Osaka University, Toyonaka 560-0043, Japan

<sup>2</sup>Graduate School of Frontier Biosciences, Osaka University, Suita, 565-0871, Japan

<sup>3</sup>UVSOR Synchrotron Facility, Institute for Molecular Science, Okazaki 444-8585, Japan

<sup>4</sup>Department of Materials Molecular Science, Institute for Molecular Science, Okazaki 444-8585, Japan

The Kondo effect leads to exotic physical phenomena due to hybridization between localized *f*-electrons and conductive carriers at low temperatures. Especially, heavy-fermion (HF) systems, in which massive effective carriers appear due to the Kondo effect, have fascinated many researchers [1,2]. Recently, two-dimensional (2D) HF systems have been realized using a molecular beam epitaxy method and it was shown that dimensionality is also important for the character of the HF system [3,4]. However, two-dimensional mono-atomic layer HF material has never been reported. Here, we have studied the electronic structure of a mono-atomic layer HF material, YbCu<sub>2</sub>/Cu(111), which is a novel perfect two-dimensional HF system, measured by angle-resolved photoelectron spectroscopy (ARPES).

Clean Cu(111) substrates were prepared by the cycle of Ar<sup>+</sup> sputtering with an acceleration of 0.5 eV and annealing at a temperature up to 800 K. After checking the sharp peaks and low background of the streak electron diffraction pattern appearing in the reflection high-energy electron diffraction (RHEED), Yb-metal was evaporated with a homemade Knudsen cell. The fabricated YbCu<sub>2</sub> mono-atomic layer has a fractional pattern suggesting a small lattice mismatch of YbCu<sub>2</sub> from the Cu(111) substrate. VUV-ARPES measurement was carried out at BL7U ( $h\nu = 37$  eV) at temperatures of 7 – 130 K.

Figure 1 shows the ARPES intensity plot of YbCu<sub>2</sub>/Cu(111) surface along  $\bar{\Gamma}-\bar{K}$  of the surface Brillouin zone of YbCu<sub>2</sub>/Cu(111). To see the band dispersion above the Fermi level, the ARPES spectra were divided by the Fermi-Dirac distribution function convoluted with the instrumental resolution. A flat band near the Fermi level and several highly dispersive bands are visible. The flat band is attributed to the Yb<sup>2+</sup> 4*f*<sub>7/2</sub> final state after the photoexcitation process. The highly dispersive conduction bands are hybridized with the flat Yb 4*f* band near the  $\bar{\Gamma}$  point suggesting the appearance of the *c-f* hybridization, which is the spectral evidence of the appearance of HF. Furthermore, angle-integrated photoelectron spectra of YbCu<sub>2</sub>/Cu(111) taken at  $h\nu = 37$  eV ( $T = 10 - 130$  K) are shown in Fig. 2. The appearing steep peak, pointed by an arrow, is grown and moves to the low energy with decreasing temperature. The peak can be attributed to a Kondo resonance peak usually observed in HF materials [5], therefore, the results suggest the HF formation in

the mono-atomic layer YbCu<sub>2</sub>/Cu(111).

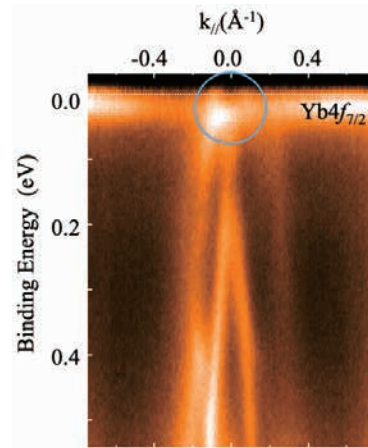


Fig. 1. ARPES band dispersion of YbCu<sub>2</sub>/Cu(111) surface along  $\bar{\Gamma}-\bar{K}$  taken at  $h\nu = 37$  eV ( $T = 7$  K). The photoelectron intensities were normalized by the Fermi-Dirac distribution function convoluted with the instrumental resolution.

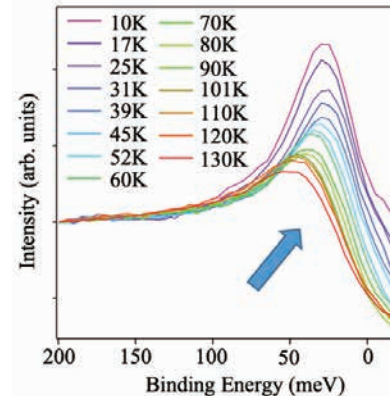


Fig. 2. Angle-integrated photoelectron spectra of YbCu<sub>2</sub>/Cu(111) taken at  $h\nu = 37$  eV ( $T = 10 - 130$  K). The arrow indicates the Kondo resonance peak.

- [1] A. C. Hewson, *The Kondo Problem to Heavy Fermions* (Cambridge Univ. Press, Cambridge, 1993).
- [2] P. Coleman, *et al.*, *J. Phys.: Condens. Matter* **13** (2001) R723.
- [3] L. Fernandez *et al.*, *Nanoscale* **12** (2020) 22258.
- [4] M. Ormaza *et al.*, *PRB* **88** (2013) 125405.
- [5] S. Chatterjee *et al.*, *Nat. Commun.* **8** (2017) 852.

BL6U

## Region and Element-specific Surface Observation of CVD Graphene on Ir(111)/ $\alpha$ -Al<sub>2</sub>O<sub>3</sub>(0001) by Photoelectron Momentum Microscopy

E. Hashimoto<sup>1</sup>, Y. Onuma<sup>1</sup>, F. Matsui<sup>2</sup> and S. Koh<sup>1</sup><sup>1</sup>Aoyama Gakuin University, 5-10-1, Fuchinobe, Chuo-ku, Sagami-hara, 252-5258, Japan<sup>2</sup>UVSOR Synchrotron Facility, Institute for Molecular Science, Okazaki, 444-8585, Japan

A photoelectron momentum microscopy (PMM) is a complementary characterization tool to conventional methods, e.g. Raman spectroscopy and atomic force microscopy (AFM), for comprehensive and element-specific characterization of 2D materials owing to its multifunctionality. We have demonstrated by valence-band photoelectron spectroscopy (VB-PES) using PMM that graphene grown by low-pressure chemical vapor deposition (LP-CVD) on Ir(111)/ $\alpha$ -Al<sub>2</sub>O<sub>3</sub>(0001) had high single-crystallinity for several 100  $\mu\text{m}^2$  [1]. In this study, we performed region and-specific surface observation for graphene by photoemission electron microscopy (PEEM).

Graphene was grown on Ir(111)/ $\alpha$ -Al<sub>2</sub>O<sub>3</sub>(0001) substrates by LP-CVD using H<sub>2</sub> and CH<sub>4</sub> gases. Fig. 1(a) shows an AFM image (1.0  $\mu\text{m}^2$ ) of the graphene surface on Ir(111). Continuous step terraces of the Ir(111), which were the nucleation sites of graphene, were observed. The average step height corresponded to the one-atomic step height of the Ir(111) surface. Wrinkles, which were formed due to the mismatch of the thermal expansion coefficients between graphene and Ir(111), were formed across the step terraces, indicating that graphene domains coalesced and continuous graphene films were formed.

Real space images for graphene/Ir(111) were obtained by PEEM at the linearly polarized soft X-ray beamline BL6U of the UVSOR-III synchrotron [2]. The electronic structure for graphene/Ir(111) were determined by VB-PES. The PEEM images of graphene/Ir(111), which have non-uniformity, are shown in Figs. 1(b) and 1(c). In Fig. 1(b), the photon energy was 85 eV and photoelectron corresponding to the binding energy from 2.0 to 3.5 eV was integrated. Intensity of graphene *M* points contributes the most. Thus, the bright areas in Fig. 1(b) correspond to the areas where graphene exists. The iso-energy cross section of the 2D band dispersion for the bright area in Fig.1(b) by VB-PES is shown in Fig. 1(d). The 6-fold symmetry pattern is attributed to the  $\pi$  band dispersion of graphene connecting the *M* points. Fig. 1(c) shows the PEEM image at the same observation area as Fig.1(b). The photon energy was set to 100 eV. Photoelectron corresponding to the binding energy from 0 to 0.2 eV was integrated. The density of states at the Fermi level of Ir dominates in this condition. Therefore, the bright areas correspond to the area where the Ir surface was exposed. The iso-energy cross section of the 2D band dispersion for the bright areas in Fig.1(c) is shown in Fig.1(e). The pattern with 6-fold symmetry, which corresponds to the energy dispersion of Ir(111),

was observed. The pattern of graphene was not observed, which confirmed that the Ir surface was exposed. We identified areas where covered by graphene and where Ir(111) is exposed, by region and element-specific PEEM for Gr/Ir(111) samples with low single-crystallinity.

In this study, we observed surface irregularities of Gr/Ir(111) samples that were not captured by conventional measurement methods such as Raman spectroscopy and AFM observation, by performing region and element-specific PEEM using PMM. Element-specific measurements using PMM on practical samples are very promising, and the characterization of detailed properties for high-quality Gr/Ir(111) samples is expected.

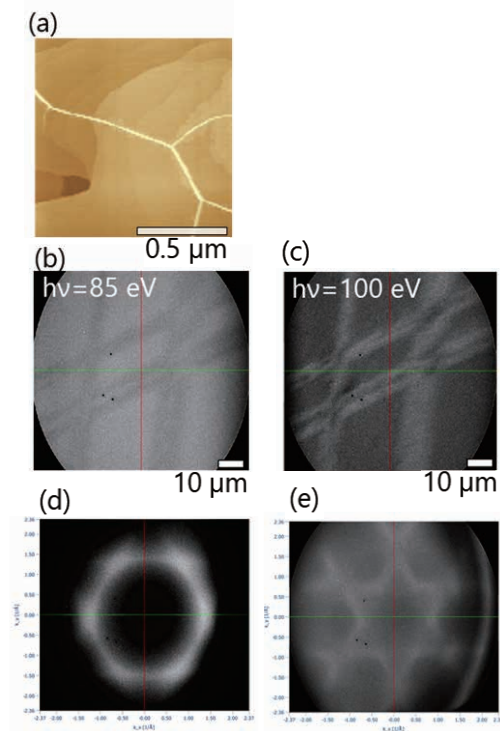


Fig. 1. (a) AFM image and (b)-(c) PEEM images of graphene/Ir(111). Iso-energy cross sections of 2D band dispersion of graphene/Ir(111), with photon energy of (d) 85 eV and (e) 100 eV.

[1] E. Hashimoto *et al.*, Jpn. J. Appl. Phys. **61** (2022) SD1015.

[2] F. Matsui *et al.*, Jpn. J. Appl. Phys. **59** (2020) 067001.

## High-resolution angle-resolved Photoemission Study on MnBi<sub>2</sub>Te<sub>4</sub>/MnBi<sub>2</sub>Te<sub>4</sub>/Bi<sub>2</sub>Te<sub>3</sub> Heterostructure

K. Ishihara<sup>1</sup>, H. Nishimichi<sup>1</sup>, K. Ide<sup>1</sup>, S. Ichinokura<sup>1</sup>, K. Tanaka<sup>2</sup> and T. Hirahara<sup>1</sup>

<sup>1</sup>Department of Physics, Tokyo Institute of Technology, Tokyo 152-8551, Japan

<sup>2</sup>UVSOR Facility, Institute for Molecular Science, Okazaki 444-8585, Japan

Topological insulators (TI) are extensively studied recently due to its peculiar properties [1]. The Dirac-cone surface states of TI are protected by time-reversal symmetry (TRS) and backscattering among these surface states is prohibited. But when TRS is broken by application of a magnetic field or incorporating magnetic materials, a gap opening in the Dirac cone is expected and an intriguing phase called the quantum anomalous Hall state can be realized [2]. This phase is expected to show even more exotic phenomena such as the topological magnetoelectric effect. To realize such state, two types of sample fabrication techniques have been employed up to now: (1) magnetic doping while growing the single crystal or thin film of TI [3], and (2) magnetic impurity deposition on the surface of TI [4]. While method (1) was successful and showed evidence of the TRS violation, no one has succeeded using method (2), which should be a more direct way to examine the interaction between the topological surface states and magnetism. We have previously found another novel technique to induce magnetism into TI, namely the magnetic extension effect [5]. By depositing Mn and Se on Bi<sub>2</sub>Se<sub>3</sub>, we found that Mn and Se are incorporated in the topmost Bi<sub>2</sub>Se<sub>3</sub> layer and a novel heterostructure MnBi<sub>2</sub>Se<sub>4</sub>/Bi<sub>2</sub>Se<sub>3</sub> is formed [5]. This heterostructure showed a clear Dirac cone gap of 85 meV and the gap persisted up to room temperature. From magnetic measurements it was revealed that ferromagnetism also persists up to room temperature in this system. Taking all these facts into account, it can be said that this system is promising to observe the quantum anomalous Hall effect at room temperature. However, the Dirac cone gap is not at the Fermi level and there is no systematic method to control the Fermi level position in Bi<sub>2</sub>Se<sub>3</sub>. Thus, we employed Bi<sub>2</sub>Te<sub>3</sub> as the parent TI and have deposited Mn and Te on Bi<sub>2</sub>Te<sub>3</sub> to see if magnetic extension can also occur for this system. However, it was revealed that the Dirac cone gap is absent in this MnBi<sub>2</sub>Te<sub>4</sub>/Bi<sub>2</sub>Te<sub>3</sub> system [6], in contrast to the theoretical prediction [7].

Therefore, in the present study, we have measured the band structure of the MnBi<sub>2</sub>Te<sub>4</sub>/MnBi<sub>2</sub>Te<sub>4</sub>/Bi<sub>2</sub>Te<sub>3</sub> system to verify whether an addition of another MnBi<sub>2</sub>Te<sub>4</sub> layer would influence the magnetic property

as well as the Dirac Cone gap opening. The experiments were performed at BL 7U of UVSOR with the photon energy of 19 eV. Figure 1 shows the measured band dispersion at different temperatures.

We found that in addition to the Dirac cone gap opening which was observed from 6.6 K up to room temperature, the lower Dirac cone showed some splitting at 6.6 K. Furthermore, this splitting disappeared once at 160 K, but revived at 250 K. Since the state at higher binding energy showed photon energy dependence, it can be regarded as a bulk state, although our preliminary *ab initio* calculation suggested that it can also be a surface state. This puzzling behavior is unexpected from theory and calls for a comprehensive study on the atomic structure as well as magnetism of the system, which we hope to clarify in the future.

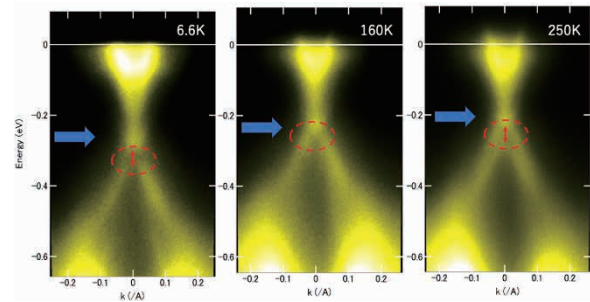


Fig. 1. Band dispersion image of the MnBi<sub>2</sub>Te<sub>4</sub>/MnBi<sub>2</sub>Te<sub>4</sub>/Bi<sub>2</sub>Te<sub>3</sub>/MnBi<sub>2</sub>Se<sub>4</sub> hetero structure measured at 6.6 K, 160 K, and 250 K, respectively.

- [1] M. Hasan and C. Kane, Rev. Mod. Phys. **82** (2010) 3045.
- [2] X.-L. Qi and S.-C. Zhang, Rev. Mod. Phys. **83** (2011) 1057.
- [3] For example, C. Z. Chang *et al.*, Science **340** (2013) 167.
- [4] For example, M. Ye *et al.*, Phys. Rev. B **85** (2012) 205317.
- [5] T. Hirahara *et al.*, Nano Lett. **17** (2017) 3493.
- [6] T. Fukasawa *et al.*, Phys. Rev. B **103** (2021) 205405.
- [7] M. Otrokov *et al.*, Phys. Rev. Lett. **122** (2019) 107202; 2D Mater. **4** (2017) 025082.

BL7B

## Electrochemical Attenuated Total Reflectance Ultraviolet (EC-ATR-UV) Spectroscopy Applied for Organic Semiconductor / Ionic Liquids Interface

I. Tanabe, Y. Hanamori and K. Fukui

Department of Materials Engineering Science, Graduate School of Engineering Science, Osaka University, 1-3, Machikaneyama, Toyonaka, Osaka 560-8531, Japan

Electric double-layer organic field-effect transistors (EDL-OFETs) have attracted much attention due to their significantly low operating voltage (<1 V) compared to conventional SiO<sub>2</sub>-gated OFETs (>10 V). In EDL-OFETs, a high electric field is generated in the EDL that accumulates in the interfacial region between the organic semiconductor and electrolyte, resulting in a low operation voltage. Therefore, the organic semiconductor/electrolyte interface is of particular importance. Recently, we developed a new spectroscopic system, namely electrochemical-attenuated total reflectance (EC-ATR) ultraviolet-visible spectroscopy, which can access the interfacial area [1, 2].

In this study, we fabricated ionic liquid gated organic field-effect transistors (IL-gated OFETs) on the ATR prism. A two-layer single crystalline film of C9-DNBDT-NW was used as an organic semiconductor, and two kinds of ionic liquids (EMIM-TFSI and HMIM-TFSI) were cast on the film. The only difference between EMIM-TFSI and HMIM-TFSI is the length of the carbon chain: two for EMIM and six for HMIM. Au films were evaporated to a thickness as the source and drain electrodes (working electrodes) on both sides of the ATR prism, and a Pt coil and a Pt wire were placed in the ionic liquids as pseudo counter and reference (gate) electrodes, respectively. In our previous study [2], we found that in response to the applied gate voltage, the spectral peaks of the organic semiconductor shifted and bleached, which was correlated with the drain current.

The IL-gated OFETs fabricated on the ATR prism were placed in the sample chamber in BL7B at UVSOR. Figure 1 shows the difference spectra of C9-DNBDT-NW films with EMIM-TFSI or HMIM-TFSI as a function of the applied voltage. Despite the very slight difference in the carbon chain length between EMIM-TFSI and HMIM-TFSI, their spectral behaviors were significantly different.

In the case of HMIM-TFSI (Fig. 1b), spectral bleachings at ~300, 220, 210, 190, and 170 nm were observed. According to TD-DFT calculations, these absorbances are mainly due to electronic excitations in the C9-DNBDT-NW molecule for ~300 nm and in HMIM-TFSI for ~220, 210, 190, and 170 nm. There is a positive relationship between the amount of spectral changes and applied voltage. On the other hand, in the case of EMIM-TFSI (Fig. 1a), no obvious spectral changes were detected. These results indicate a difference in the interaction between the organic

semiconductor and ionic liquid species under electrochemical environments.

The development of the EC-ATR spectroscopic system has the potential to greatly impact the field of electrochemical devices by enabling researchers to access and study the interfacial area between films and ILs, leading to improved understanding of device performance and the development of new, high-performance materials.

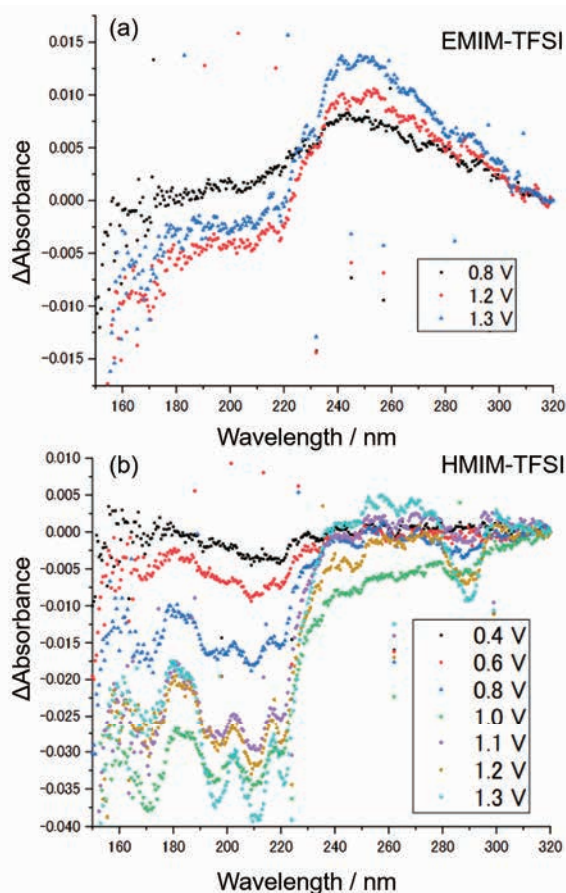
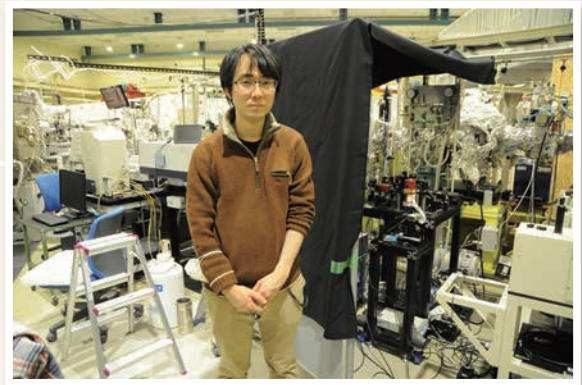
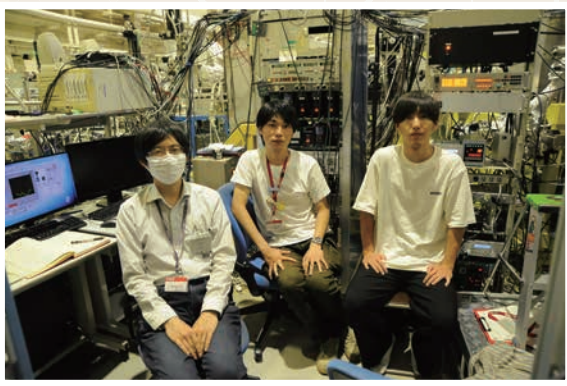


Fig. 1. Difference spectra of C9-DNBDT-NW films with (a) EMIM-TFSI and (b) HMIM-TFSI as a function of the applied voltage.

[1] I. Tanabe, A. Suyama, T. Sato and K. Fukui, *Anal. Chem.* **91** (2019) 3436.

[2] I. Tanabe, I. Imoto, D. Okaue, M. Imai, S. Kumagai, T. Makita, M. Mitani, T. Okamoto, J. Takeya and K. Fukui, *Commun. Chem.* **4** (2021) 88.

# UVSOR User 7



# III-5

Life, Earth and  
Planetary Sciences





BL3U

## X-ray Absorption Spectra of Lipid Bilayer Membranes in Aqueous Solutions

R. Tero<sup>1</sup>, Yu Kinjo<sup>1</sup> and M. Nagasaka<sup>2</sup><sup>1</sup>Toyohashi University of Technology, Toyohashi, 441-8580, Japan<sup>2</sup>Institute for Molecular Science, Okazaki 444-8585, Japan

The lipid bilayer is a self-assembled structure of amphiphilic lipid molecules. It is the fundamental structure of biomembranes such as cell membranes, which are the fields for the transportation of materials, information, and energy into and out of cells. All these physiological reactions proceed in the presence of electrolytes. Ions in the aqueous solution significantly influence to physical properties and structures of lipid bilayers. Phosphatidylcholine (PC) is the most abundant lipid of eukaryotic cell membranes. Cations bind to the phosphate and carbonyl groups of PC. However, affinity of cations to PC and effects of cations to molecular orientation are still controversy especially in the fields of theoretical simulations. We aim to determine the binding affinity of cations to lipids in aqueous solutions experimentally, by means of X-ray absorption spectroscopy (XAS) [1, 2].

Supported lipid bilayers (SLBs) of dioleoyl-PC (DOPC) were formed on the  $\text{Si}_3\text{N}_4$  membranes of the XAS flow cell [1] by the vesicle fusion method in a buffer solution (NaCl 100 mM, HEPES 25 mM/ pH 7.4 NaOH). The  $\text{Na}^+$  concentration ( $[\text{Na}^+]$ ) was varied by exchanging the buffer solution in the flow cell in the range of  $[\text{Na}^+] = 2.1 - 510.4$  mM. The O-K edge XAS spectra of SLB were obtained at the energy range of 527 – 535 eV at the Xray incident angle of  $35^\circ$ . The XAS spectrum of the  $\text{Si}_3\text{N}_4$  membrane without SLB was subtracted from that with SLB.

The O-K-edge spectrum of DOPC appeared at 531 – 533 eV (Fig. 1). It is consisted of  $1s \rightarrow \pi^*$  transitions of double-bond oxygens in the phosphate and carbonyl groups on the PC headgroup: two components attributed to the P=O in the former, and one component attributed to the latter [3]. We measured XAS spectra at the X-ray incident angle ( $T$ ) of  $35^\circ$  to obtain the intensity of each component independently of the molecular orientation. We obtained a specific dependence of the P=O peak at the lower energy (P=O<sub>low</sub>) on  $[\text{Na}^+]$ : its position was identical at  $[\text{Na}^+] = 2.1 - 10.4$  mM, shifted to higher energy by 0.4 eV above  $[\text{Na}^+] = 10.4$  mM, and little independent of  $[\text{Na}^+]$  above 110.4 mM. The results show the  $\text{Na}^+$  coordination to the phosphate group of PC and its dependence of  $[\text{Na}^+]$ . The inner-shell quantum chemical calculation [4] of O K-edge spectrum of P=O indicated that coordination of  $\text{Na}^+$  to the phosphate group causes higher-energy shift of P=O peaks. The dependence of the P=O peak intensity as well as the P=O intensity on  $[\text{Na}^+]$  is investigated in

detail. The effects of the cation species on the XAS components will be investigated.

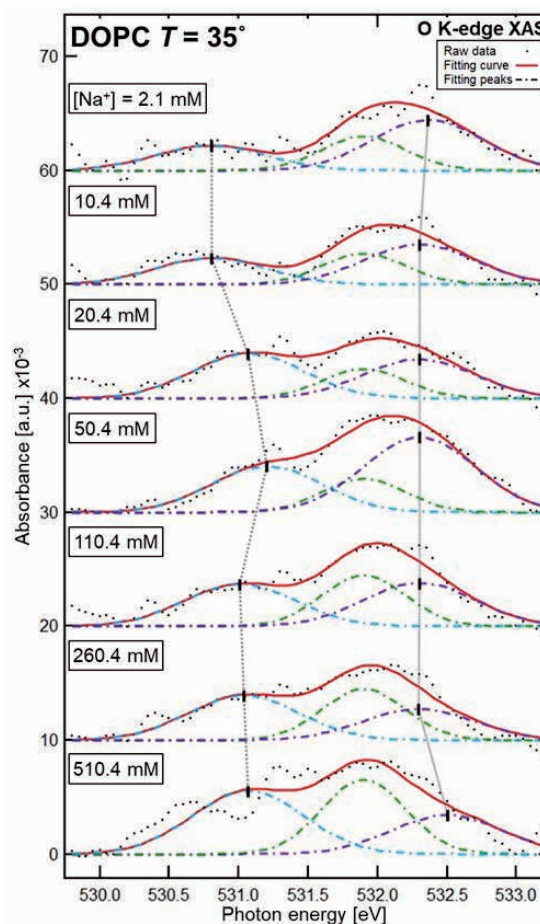


Fig. 1. O K-edge XAS spectra of DOPC-SLB at  $[\text{Na}^+] = 2.1 - 510.4$  mM obtained at the X-ray incident angle of  $35^\circ$ . Black dotted curves represent raw data. Dashed curves and red solid curves show deconvoluted components and their summation, respectively.

[1] M. Nagasaka, H. Yuzawa, T. Horigome, and N. Kosugi, *J. Electron Spectros. Relat. Phenomena* **224** (2018) 93.

[2] R. Tero, Y. Kinjo and M. Nagasaka, *UVSOR Activity Report* **49** (2021) 151.

[3] R. Tero, W.-Z. Goh and M. Nagasaka, *UVSOR Activity Report* **48** (2020) 129.

[4] M. Nagasaka, *J. Chem. Phys.* **158** (2023) 024501.

## Study on Chirality Emergence of Amino Acid Molecules Induced by Circularly Polarized Lyman- $\alpha$ Light Irradiation

M. Kobayashi<sup>1</sup>, J. Takahashi<sup>2</sup>, H. Ota<sup>3</sup>, G. Fujimori<sup>2</sup>, K. Kobayashi<sup>2</sup>, K. Matsuo<sup>4</sup>, Y. Taira<sup>3</sup>,  
M. Katoh<sup>3,4</sup>, H. Nakamura<sup>1</sup> and Y. Kebukawa<sup>2</sup>

<sup>1</sup>National Institute for Fusion Science, 322-6 Oroshi-cho, Toki 509-5292, Japan

<sup>2</sup>Yokohama National University, 79-5 Tokiwadai, Hodogaya-ku, Yokohama 240-8501, Japan

<sup>3</sup>UVSOR Synchrotron Facility, Institute for Molecular Science, Myodaiji, Okazaki 444-8585, Japan

<sup>4</sup>Hiroshima Synchrotron Radiation Center, Hiroshima University, 2-313 Kagamiyama,  
Higashi-Hiroshima 739-0046, Japan

The origin of homochirality in terrestrial biomolecules (L-amino acid and D-sugar dominant) remains one of the most mysterious problems in the research for the origins of life. One of the most attractive hypotheses in the context of astrobiology is “Cosmic Scenario” [1, 2]; Asymmetric reactions of prebiotic molecules on interstellar dust surfaces in molecular cloud circumstances were introduced by polarized quantum radiation sources in space, that is “chiral radiations”. Among the polarized quantum radiation sources, circularly polarized light (CPL) in the space environment is thought to be one of the most likely causes of the enantiomeric excesses of terrestrial bioorganic molecules. In this study, we focused on a hydrogen Lyman- $\alpha$  wavelength of 121.6 nm, where strong emission lines are observed in star-forming regions.

Alanine is selected as a chiral prebiotic molecules in the interstellar space. We formed thin solid film samples of racemic mixture of alanine (DL-alanine) on quartz substrates from crystal powders of DL-alanine by using a thermal-crucible vacuum-evaporation system at HiSOR in Hiroshima university. A schematic of the irradiation system of BL1U is shown in Fig.1. The 121.6 nm wavelength radiation from the undulator is reflected by a gold-coated mirror (M0 focusing mirror) located in the mirror chamber directly beam upstream of the irradiation chamber and then enters the irradiation chamber. On the beam entrance side of the vacuum sample chamber, a gate valve with an MgF2 vacuum sealing window (0.5 mm in thickness) was mounted. The use of gold-coated mirror reflections has made it possible to suppress high-energy higher order light from the undulator source, expecting to reduce the transmittance loss of the MgF2 window due to high-energy radiation induced defects. The sample substrate was set in the sample holder in the irradiation chamber, in which magnetic and electric fields can be applied to perpendicularly to the sample surface. The total photon beam intensity irradiated on the sample was monitored with photoelectron current of a silicon photodiode settled at the beam downstream side of the sample holder.

CD spectra of the CPL irradiated films were measured using the SR-CD beam line BL-12 of HiSOR to clarify

the optical activity emergence by CPL irradiation. Figure 2(a) shows spectra of DL-alanine films irradiated for 30 min with L- or R-CPL at 121.6 nm in wavelength. We clearly observe optical activity induced by the CPL irradiation, which shows opposite sign in the CD between right CPL and left CPL. In addition, we have also examined the additional effect of applying a magnetic field to the sample to investigate the effect of the magnetic field in interstellar space (Fig. 2(b)). The application of the magnetic field seems to alter the CD spectra, suggesting a certain impact of symmetry breaking of the optical activity caused by the CPL irradiation. Detailed analysis of CD spectra is in progress supported by quantum chemical calculations.

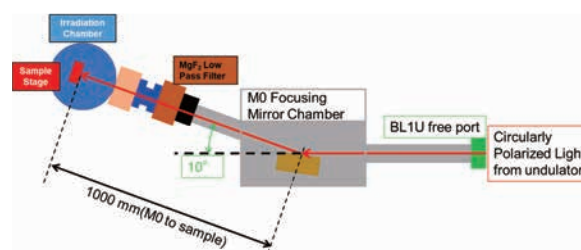


Fig. 1. A schematic of the CPL irradiation system at BL1U.

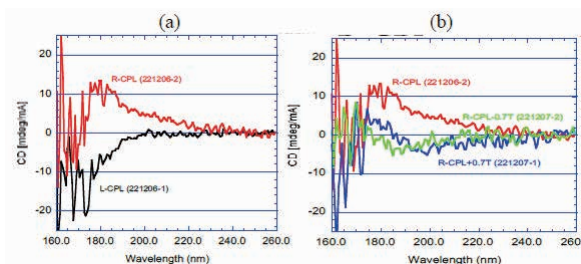


Fig. 2. CD spectra of alanine sample after irradiation of (a) right (red) and left (black)-CPL, and (b) right CPL with magnetic field application (blue:+0.7T, green:-0.7T).

[1] W. A. Bonner, Orig. Life Evol. Biosph. **21** (1991) 407.

[2] J. Takahashi and K. Kobayashi, Symmetry **11** (2019) 919.

BL3U

## Attempts at Structural Analysis of Biological Macromolecules Using Resonant Soft X-ray Scattering

Y. Sugimoto<sup>1</sup> and H. Iwayama<sup>1,2</sup>

<sup>1</sup>UVSOR Synchrotron Facility, Institute for Molecular Science, Okazaki 444-8585, Japan  
<sup>2</sup>School of Physical Sciences, The Graduate University for Advanced Studies (SOKENDAI), Okazaki 444-8585, Japan

Resonant soft X-ray scattering (RSoXS) is a powerful technique to probe the nano-to-mesoscopic structure of molecules. Since this method observes scattered waves due to resonance processes, RSoXS can reveal structures with enhanced or tunable scattering contrast. In particular, since soft X-ray regions include K-edge energies of light elements such as carbon, nitrogen, and oxygen, RSoXS is a suitable tool for investigating soft matters. In UVSOR, the development of the RSoXS instrument has begun since 2019, and we have successfully measured the mesoscopic structure of liquid crystal molecules [1].

Biomacromolecules, such as proteins, are also mainly composed of light-element atoms. Studying biomacromolecule structures is crucial for elucidating biological functions and developing therapeutic drugs. Conventional electron microscopy (EM) and small-angle X-ray scattering (SAXS) are well-established methods for investigating the structure of biological macromolecules. The RSoXS method is expected to complement conventional methods due to its features, such as the selectivity of elements and functional group orientations. In this work, we performed RSoXS measurements for protein samples.

Our RSoXS measurements were performed at UVSOR BL3U. Our sample is bovine milk casein as the typical protein sample. Casein forms micelles with calcium phosphate dispersed inside [2]. We prepared the bovine milk samples in the following step. First, we dissolved the bovine milk powder sample in water, then dropped samples onto a  $\text{Si}_3\text{N}_4$  membrane and dried them naturally. We set the samples in the vacuum chamber and irradiated them with soft X-rays. We measured the scattering intensity with a soft X-ray CCD camera (Andor BN940P). The photon energies were set to 270, 285, 348, and 350 eV. The measured Q-range was  $0.035\text{--}0.35\text{ nm}^{-1}$  at 270 eV and  $0.055\text{--}0.45\text{ nm}^{-1}$  at 350 eV. The Guinier plot of the scattering intensity yields the radius of gyration of  $\sim 55\text{ nm}$ ,

measured at 270 eV below the carbon K-edge absorption. This value is close to the structure of casein micelles obtained in previous studies. The scattering intensity measured at 350 eV, near the calcium L absorption edge, showed a different scattering intensity than that at 348 eV (Fig. 1). The resonance-enhanced structure of the spectrum suggests that RSoXS gives insight into a more detailed structure of calcium phosphate in casein micelles, compared to conventional SAXS.

On the other hand, some structural changes in biomolecules may come from the drying process of the sample preparations. In addition, our equipment is difficult to measure small scattering-angle regions due to the direct beam. We will introduce a new sample cell for wet samples and improve our RSoXS spectrometer for small scattering angle measurements.

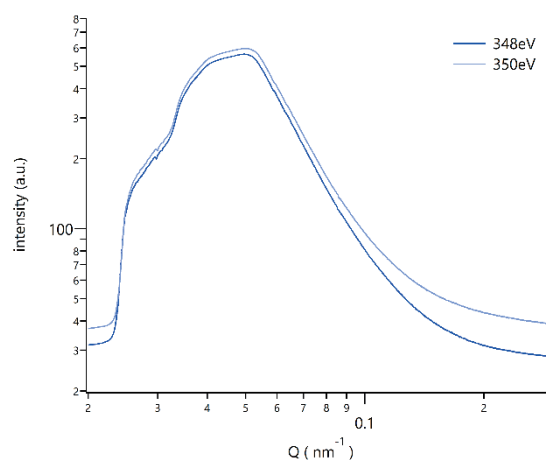


Fig. 1. Q-spectra for casein at the calcium L absorption edge.

- [1] Y. Takanishi *et al.*, RSC Adv. **12** (2022) 29346.  
 [2] H. Takagi *et al.*, Food Chem. **393** (2022) 133389.

## Water-Ion Interactions in Natural Lake Brines

Y. Hao<sup>1</sup>, N. Fauré<sup>2</sup>, Y. Qiu<sup>1</sup>, M. Nagasaka<sup>3</sup>, E. Thomson<sup>2</sup>, S. Wang<sup>1</sup> and X. Kong<sup>2</sup>

<sup>1</sup>Department of Environmental Sciences, College of Urban and Environmental Sciences, Northwest University, Xi'an, China

<sup>2</sup>Department of Chemistry and Molecular Biology, Atmospheric Science, University of Gothenburg, SE-412 96 Gothenburg, Sweden

<sup>3</sup>Institute for Molecular Science, Okazaki 444-8585, Japan

Under climate change and enhanced water use demands, arid regions are undergoing faster transformations compared to humid areas due to their greater susceptibility to changes in precipitation. As a consequence, the number and area of saline lakes are being impacted. Depending on the local circumstances, some saline lakes are being desiccated and transforming to playa covered by evaporite salts, while others are forming and expanding, such as the lakes in the Qinghai-Tibet Plateau [1]. The increases volume and surface area of saline lakes are expected to have impacts on local environment and climate.

In this beamtime, we carried out Near Edge X-ray Absorption Fine Structure (NEXAFS) measurements on brines from various saline lakes in the Qaidam Basin, which is situated in the Qinghai-Tibet Plateau. The sampling sites include eight saline lakes: Mang'ai Feicui Lake (MA), Dalangtan Playa (DLT), West Taijinar Lake (XT), East Taijinar Lake (DT), Qarhan Lake (QH), Dezongmahai Lake (DZMH), Dachaidan Lake (DCD), and Xiaochaidan Lake (XCD) (Figure 1). The brine samples were taken 2 – 5 cm below the lake surface, and then were stored in polyethylene bottles, sealed with Parafilm membranes, and stored at 4 °C.

The NEXAFS measurements were performed at the soft X-ray undulator beamline BL3U at UVSOR-III Synchrotron. In the liquid flow cell, a liquid layer is sandwiched between two 100 nm thick  $\text{Si}_3\text{N}_4$  membranes with the windows size of  $2 \times 2 \text{ mm}^2$ . Teflon spacers with the thickness of 100  $\mu\text{m}$  are set between the support plates of the  $\text{Si}_3\text{N}_4$  membranes. Liquid samples are exchangeable *in situ* by using a tubing pump. The temperature of all the liquid samples were controlled at approx. 25 °C. The  $\text{Si}_3\text{N}_4$  membrane window was set to  $200 \times 200 \mu\text{m}^2$  to allow for suitable photon fluxes.

In Figure 2, the O K-edge NEXAFS results are presented, with 8 brines displayed in two panels for better visibility. The pure water case is also included in both panels for comparison purposes. The spectra exhibit three features: pre-edge (~535 eV), main-edge (~537 eV), and post-edge (~540 eV), with the spectrum lines normalized to the maximum at the main-edge. The post-edge intensities of the brines are lower than those of pure water, which is consistent with existing literature [2]. The pre-edges have been zoomed in and displayed in the insets. Apart from the DZMH brine, the other brines exhibit reduced and shifted pre-edge

peaks, which will be analyzed in more detail. The DZMH brine displays a notably high pre-edge, likely resulting from contamination.

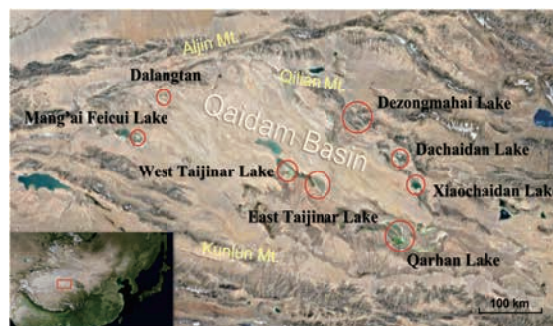


Fig. 1. Eight saline lakes, as marked by red circles, were sampled in the Qaidam Basin.

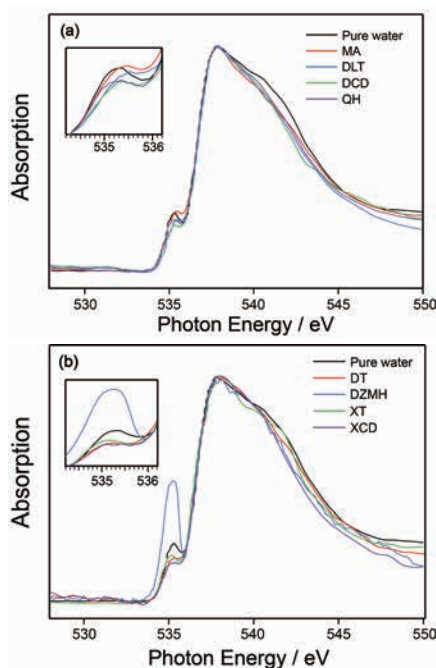


Fig. 2. O K-edge NEXAFS spectra of (a) pure water and brines from MA, DLT, DCD, and QH lakes; (b) pure water and brines from DT, DZMH, XT, and XCD lakes. The temperatures are around 25 °C. The insets zoom in the pre-edge regions.

[1] Zhang, G. *et al.*, *Earth Sci. Rev.* **208** (2020) 103269.

[2] Nagasaka, *et al.*, *J. Phys. Chem. B*, **121** (2017) 10957-10964.

BL4U

## Drug Administration Concepts Involving Redox Nanocarriers Affect the Spatial Distribution of Topically Applied Formulations in Human Skin

G. Germer<sup>1</sup>, T. Ohigashi<sup>2</sup>, H. Yuzawa<sup>2</sup>, K. Rajes<sup>3</sup>, R. Haag<sup>3</sup>, F. Rancan<sup>4</sup>, A. Vogt<sup>4</sup> and E. Rühl<sup>1</sup>

<sup>1</sup>Physical Chemistry, Freie Universität Berlin, Arnimallee 22, 14195 Berlin, Germany

<sup>2</sup>UVSOR Synchrotron Facility, Institute for Molecular Science, Okazaki 444-8585, Japan

<sup>3</sup>Organic Chemistry, Freie Universität Berlin, Arnimallee 22, 14195 Berlin, Germany

<sup>4</sup>Charité Universitätsmedizin, 10117 Berlin, Germany

Different drug administration concepts involving redox-sensitive polymer nanocarriers topically applied to human skin *ex vivo* have been investigated by scanning transmission X-ray microscopy (STXM). The goal of this research is to understand how single and repeated use of drug formulations containing nanocarriers affects the drug and nanocarrier distribution in the top skin layers of inflamed skin. Especially, the repeated use of drug formulations is frequently used in therapy. STXM probes sensitively and label-free the distribution of topically applied formulations [1]. The results are of importance to understand the transport and penetration routes of actives. Polymer nanocarriers are used for transporting drugs that are barely penetrating the skin barriers [2, 3]. The present studies compare different topical drug delivery concepts of a single dose and repeated drug administrations, reaching up to five days, respectively. The skin barrier was initially modified for all samples by topically applying the oxidizer di-benzoyl peroxide (DBPO) for 16 h prior to topical application of rapamycin-loaded oxidation-sensitive nanocarriers (osCMS [2]). The osCMS samples (5 mg/mL,  $\leq 2\%$  drug loading) were formulated in HEC gel.  $40 \mu\text{L}/\text{cm}^2$  of this formulation were applied once for up to 1000 min to the skin samples *ex vivo*. In case of repeated treatments, the skin was four times treated every 24 h with  $40 \mu\text{L}/\text{cm}^2$  of a 1% rapamycin-osCMS formulation with a final drug concentration of  $8 \mu\text{g}/\text{cm}^2$ . The STXM experiments were performed at the BL4U beamline of UVSOR III at the O 1s regime (520 – 565 eV). Key is the acquisition of stacks of images by concentrating on the top skin layers, i.e., the stratum corneum (SC) and the viable epidermis (VE). Fig. 1 shows selected results, where a comparison is made between the single treatment (Fig. 1(a)) and multiple treatments (Fig. 1(b)). At the top of each Figure an X-ray micrograph recorded at 532 eV is shown, indicating the skin structure of the vertical cuts of EPON-fixed skin, where the skin surface is located at the right hand side. Each Figure also contains the local concentrations of rapamycin ① and osCMS ②, derived from the experimental results and subsequent singular value decomposition, similar to recent work [1]. Single treatment shows primarily the species of interest in the stratum corneum (Fig. 1(a)), where the nanocarriers are

mostly found in narrow spatial distribution in the lipids separating the corneocytes, whereas the drug is found in the corneocytes. Multiple treatments (Fig. 1(b)) show a different distribution of both species: Most of the drug has been transported in deeper skin layers, only some of the rapamycin remains in corneocytes. Nanocarriers are primarily found in the viable epidermis, and there they are localized near the cell nuclei. This deep penetration of osCMS into the viable parts of skin is likely the result of a damaged tight junction barrier in the stratum granulosum due to initial treatment by DBPO, as nanocarriers were not observed before in the viable parts of intact skin after single treatment [3]. These differences in drug and nanocarrier distributions provide evidence that in inflamed skin the drug is efficiently transported via nanocarriers to the sites of action, where it is needed for therapeutic success, considering that the drug dissolved in ethanol is barely taken up by intact skin [1].

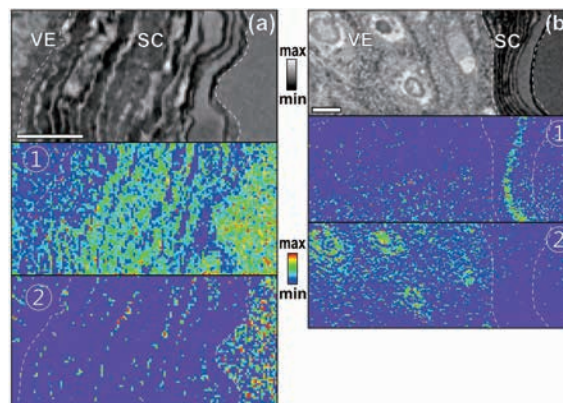


Fig. 1. Results from STXM on different drug delivery concepts of human skin *ex vivo* initially treated by DBPO: (a) single drug application (1000 min); (b) repeated use of drug administration (5 d). Top: X-ray micrograph recorded at 532 eV, below: local concentrations of ① rapamycin and ② osCMS. Scale bar: 5  $\mu\text{m}$ .

[1] G. Germer *et al.*, ACS Omega **6** (2021) 12213.

[2] K. Rajes *et al.*, Pharmaceutics **13** (2021) 37; K. Rajes *et al.*, Biomater. Sci. Engin. **7** (2021) 2458.

[3] K. Yamamoto *et al.*, J. Control. Release **242** (2016) 64.

## Absorption- Image and Spectra of Apoptosis Nuclei in P-L Edge

T. Ejima<sup>1</sup> and S. Tone<sup>2</sup>

<sup>1</sup>SRIS, Tohoku University, Sendai 980-8577, Japan

<sup>2</sup>Sch. of Sci & Technol., Tokyo Denki University, Hatoyama 350-0394, Japan

Apoptosis is programmed death of cells that is an important physiological function for the recycling of cellular components and characterized by chromatin condensation in the cell nucleus. Detailed studies of the chromatin condensation process in isolated cell nuclei have shown that this condensation process occurs in three stages from the normal state of the cell nucleus (Stage 0) to ring condensation (Stage 1), necklace condensation (Stage 2), and cell nuclear collapse/disassembly (Stage 3) [1]. It has been suggested that among the transitions from Stage 0 to 3, Stage 1 to 2 is caused by cleavage of phosphodiester bonds in DNA, while protein kinases such as MST1 may be the cohesive factor in the transition from Stage 2 to 3 [1].

To investigate the change from Stage 0 to Stage 1, infrared absorption experiments were performed, focusing especially on the change in the vibrational structure of  $\text{PO}_2^-$ , which is sensitive to the helical structure of DNA. As a result, the helical structure, which was predominantly B-DNA in Stage 0, decreased as the step progressed, and changed to A-DNA or Z-DNA. This result suggests that the helical structure of DNA changes from Stage 0 to 1, DNA is cleaved in Stage 1 to 2, and phosphate groups are transferred from DNA in Stage 2 to 3. In this study, we focused on this change in the phosphate group of DNA and thought that we could capture the changes in DNA at each stage by measuring the P-L<sub>2,3</sub> absorption edge structure of the cell nucleus.

The samples used in the experiments were obtained according to the method reported by Tone et al [1]. The isolated nuclei of each stage obtained were embedded and sectioned into approximately 100 nm-thick section samples using an ultramicrotome. The sectioned samples were imaged under an optical microscope and cell nuclei showing representative shapes of each stage were selected in the images. Isolated nuclei of Stage 0 and Stage 2 were selected for measurement due to time limitations, and STXM measurements of the C-K and P-L absorption edges were performed for each. The obtained STXM images were analyzed by PCA and reconstructed after removing noise components from the PCA component images, and cluster analysis was performed to the reconstructed images [2]. Figure shows the STXM image of a Stage 2 isolated nucleus at the P-L absorption edge and the obtained absorption spectrum. The spectra show two peak structures, P-L<sub>2</sub> and L<sub>3</sub>, split by spin-orbit interaction. We believe that

the spectral shape of each peak is similar to that of  $\text{PO}_4$ . In combination with the image, it is considered that DNA was degraded and transformed into  $\text{PO}_4$  clusters as apoptosis progressed. This interpretation is consistent with the result of IR absorption results.

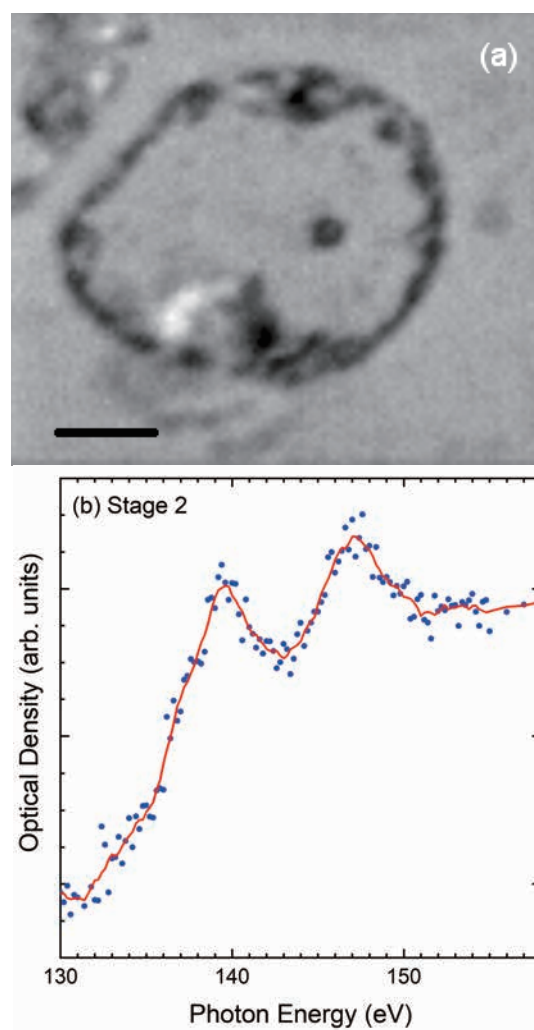


Fig. 1. X-ray absorption image, (a), and X-ray absorption spectrum, (b), of apoptosis nucleus in stage2 at P-L absorption edge. Bar is 2  $\mu\text{m}$  in length.

### References:

- [1] S. Tone *et al.*, *Exp. Cell Res.* **313** (2007) 3635.
- [2] M. Lerotic *et al.*, *JESRP* **144-147** (2005) 1137.

BL4U

## Embracing Natural and Anthropogenic Aerosol Particle Complexity

P. A. Alpert<sup>1</sup>, L. Li<sup>2</sup>, L. F. Escusa Dos Santos<sup>2</sup>, F. Mahr<sup>1</sup>, M. Ammann<sup>1</sup>, L. Wu<sup>3</sup>, W. Hu<sup>3</sup>,  
P. Fu<sup>3</sup>, M. Hallquist<sup>2</sup>, E. Thomson<sup>2</sup> and X. Kong<sup>2</sup>

<sup>1</sup>Laboratory for Environmental Chemistry, Paul Scherrer Institute, Villigen PSI, 5232, Switzerland

<sup>2</sup>Atmospheric Science Research Group, Department of Chemistry and Molecular Biology,  
University of Gothenburg, 41296 Gothenburg, Sweden

<sup>3</sup>School of Earth Systems Science, Tianjin University, 300072 Tianjin, China

A considerable fraction of the global population lives in coastal urban centers. People in these regions are exposed to some of the most complex aerosol particles containing mixtures of natural and anthropogenic compounds. The chemical composition and morphology of these particles are key for their environmental impacts, but remain poorly understood. We have investigated particles taken from ambient air that was influenced by the ocean and mixed ocean-anthropogenic sources to better understand their cloud-forming potential, chemical reactivity and light-scattering properties.

Sea spray aerosol particles contain sea-salts and organic matter [1]. When mixed with anthropogenic air, these particles can uniquely undergo acid displacement reactions forming organic salts and producing inorganic acids, which evaporate from the particles [2]. Mixed anthropogenic and natural aerosol particles aerosolized from saline lakes have previously been shown to act as cloud nuclei [3]. Additionally, anthropogenic emissions from ships are known to have a variable ability to nucleate clouds depending on the type of fuel used and its sulfur content [4].

To better understand such complex processes we collected ambient particles from contrasting sources, *i*) the Indian Ocean with minimal anthropogenic influence, *ii*) the Indian Ocean with significant anthropogenic influence and *iii*) Sanya Port, a coastal city in China. At the Ultraviolet Synchrotron Orbital Radiation Facility, we probed individual particles at the carbon, oxygen and nitrogen K-edges, and the sulfur, chlorine and calcium L-edges using scanning transmission X-ray microscopy coupled to near-edge X-ray absorption fine structure spectroscopy (STXM/NEXAFS). We quantified how inorganics and organics were mixed in individual particles and determined the organic volume fraction (OVF) [5]. The OVF was calculated from high spatial resolution images at 280 eV, 285.4 eV, 288.7 eV and 320 eV with a pixel size of  $0.05 \times 0.05 \mu\text{m}^2$ .

Figure 1 shows optical density measured at 280 eV and OVF for the same field of view of Indian Ocean particles without anthropogenic influence. The optical density image shows X-ray absorption primarily due to elements that are not carbon, such as Na and Cl, as well as other sea salts and inorganic matter. Particle morphology is largely cubic with submicrometer sized

needle-like structures, as expected for sea spray aerosol particles. Based on our STXM/NEXAFS measurements, these needles were confirmed to be dominated by calcium sulfate. The OVF image reveals a considerable fraction of organic material close to salt cores. Carbon K-edge spectra were dominated by carboxyl functional groups, similar to sea spray aerosol particles found over various ocean environments [1, 2, 5].

These data suggest that these particles will likely be highly hygroscopic and act as cloud condensation and ice nuclei due to their high salt content and similar carbon spectra as other ice nucleating particles [1]. Additionally, morphology and composition determined from STXM/NEXAFS are similar to laboratory-generated ice nucleating sea spray particles, implying a role for atmospheric ice particle production [1]. The highest OVF appears close to the salt at values around 0.6 and decreases with distance away from the crystal. This implies a small degree of aging, i.e., that organic salts dominate likely due to acid displacement reaction rather than pure organic coatings. Further work is ongoing to identify differences in particles from various sources and their importance for cloud microphysics and aerosol chemistry.

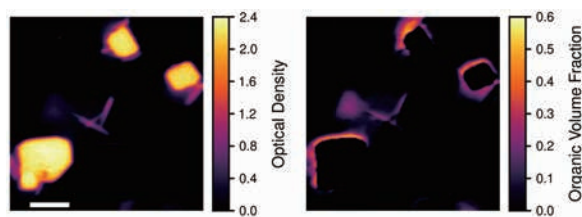


Fig. 1. Optical density at 280 eV indicating X-ray absorption primarily due to compounds other than carbon. Organic volume fraction of the same particles calculated for particles collected over the Indian Ocean. Scale bar is  $2 \mu\text{m}$ .

- [1]P. A. Alpert *et al.*, *Sci. Adv.* **8** (2022) eabq6842.  
[2]A. Laskin *et al.*, *J. Geophys. Res.-Atmos.* **117** (2012) D15302.  
[3]J. Li *et al.*, *Atmosphere* **12** (2021) 1203.  
[4]L. F. E. d. Santos *et al.*, *Environ. Sci.: Atmos.* **3** (2023) 182.  
[5]M. Fraund *et al.*, *Atmos. Meas. Tech.* **12** (2019) 1619.

## STXM in Characterizing Lysosomal Storage Materials in a Mouse Model

T. Mansikkala<sup>1,2</sup>, T. Ohigashi<sup>3</sup>, H. Yuzawa<sup>3</sup>, I. Miinalainen<sup>2</sup>, S. M. Kangas<sup>4</sup>, M. Salo<sup>4,5</sup>,  
N. Kosugi<sup>3</sup>, J. Uusimaa<sup>4</sup>, M. Huttula<sup>1</sup>, R. Hinttala<sup>4,5</sup> and M. Patanen<sup>1,2</sup>

<sup>1</sup>Nano and Molecular Systems Research Unit, PO Box 3000, 90014 University of Oulu, Finland

<sup>2</sup>Biocenter Oulu, PO Box 5000, 90014 University of Oulu, Finland

<sup>3</sup>UVSOR Synchrotron Facility, Institute for Molecular Science, Okazaki 444-8585, Japan

<sup>4</sup>Research Unit of Clinical Medicine and Medical Research Center, Oulu University Hospital and University of Oulu, 90014 Oulu, Finland

<sup>5</sup>Transgenic and Tissue Phenotyping Core Facility, University of Oulu, Finland

In this work, we used scanning transmission X-ray microscopy (STXM) technique at BL4U beamline to study lysosomal storage disease (LSD) mouse model liver and kidney tissues. LSDs are a large family of diseases where e.g. enzymatic dysfunction leads to accumulation of macromolecules in the tissues. This study was part of a project to better understand them. STXM hold promise to be a good tool to study LSDs if the natural chemical contrast of accumulating material and rest of the tissue is high enough. In our previous beamtimes at UVSOR both human and mouse model samples have been studied (Patanen 2018, Mansikkala 2020). This time our aim was to differentiate the storage material within the lysosomes. Liver and kidney tissue samples were used. They both had clear ultrastructural differences compared control samples in form of large number of vacuoles, presumed to be lysosomes fitting the description of the LSDs. Our preliminary studies showed a distinct spectrum from lysosomes compared to the rest of the tissue. This study was to verify the finding in larger number of samples.

The tissue samples were fixed in 4% paraformaldehyde and 2.5% glutaraldehyde in 0.1 M phosphate-buffered saline and then embedded in TTE:MMHA. The 150 nm thick sections were imaged with TEM to find areas with lysosomes on the samples. The same area was then measured with STXM from the subsequent thin sections.

We were able to find and image lysosomes in both tissue types, an example shown in Fig. 1. When analyzing the samples with aXis2000, we noticed that the spectrum from the lysosomes was very similar to that of the TTE:MMHA resin (Fig. 2). To evaluate the result, we subtracted the measured pure resin spectrum from the measured lysosome spectrum shown in Fig. 3 (green). There is only a small peak around 289 eV differentiates the lysosome spectrum from a resin spectrum. However, the spectrum from the extracellular space (blue) is almost identical with just intensity differences. The spectrum of cytosol differs clearly, indicating that the contents of the lysosomes are mostly TTE:MMHA resin. While there is a small difference between the resin and lysosomes and extra cellular space, the spectra are overwhelmed by the resin signal, and we were not able to differentiate the accumulation material spectrum in the lysosomes. Our hypothesis is that the sample preparation has substituted the accumulation material in lysosomes with resin instead of preserving it.

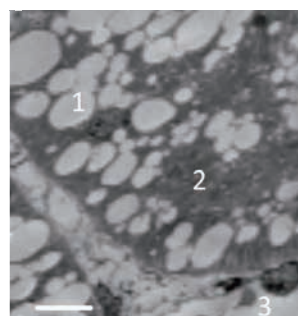


Fig. 1. STXM image of disease model mouse kidney with visible ultrastructural changes. Lysosomes are marked with 1, cytosol with 2 and extracellular space with 3. Scale bar is 5  $\mu$ m.

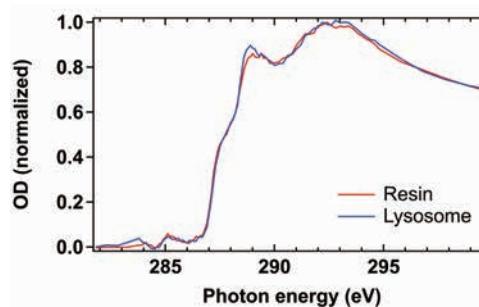


Fig. 2. Comparison of spectra from lysosome (blue) and pure resin (red).

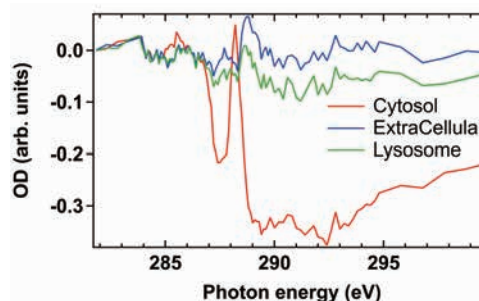


Fig. 3. Spectra from lysosome (green), the extracellular space (blue) and cytosol (red).

[1] T. Mansikkala *et al.*, *UVSOR Activity report 2019* (2020) 155.

[2] M Patanen *et al.*, *UVSOR Activity report 2018* (2019) 166.

BL4U

## Determination of Spectral Changes in NEXAFS of Biomolecules Caused by Radiation Effects for Molecular Mapping of Biological Specimens

A. Ito<sup>1</sup>, K. Shinohara<sup>2</sup>, A. Matsuura<sup>3</sup>, S. Toné<sup>4</sup>, K. Tohya<sup>5</sup>, H. Yuzawa<sup>6</sup> and T. Ohigashi<sup>6,7</sup>

<sup>1</sup>*School of Engineering, Tokai University, Hiratsuka 259-1292, Japan*

<sup>2</sup>*Graduate School of Health Sciences, Fujita Health University, Toyoake, 470-1192, Japan*

<sup>3</sup>*Research Integrity Office, Fujita Health University, Toyoake, 470-1192, Japan*

<sup>4</sup>*School of Science and Engineering, Tokyo Denki University, Hatoyama, 350-0394, Japan*

<sup>5</sup>*Kansai University of Health Sciences, Kumatoricho, 590-0482, Japan*

<sup>6</sup>*UVSOR Synchrotron Facility, Institute for Molecular Science, Okazaki 444-8585, Japan*

<sup>7</sup>*School of Physical Sciences, The Graduate University for Advanced Studies, Okazaki 444-8585, Japan*

We have been working on a quantitative mapping of nucleic acids (DNA and RNA) and proteins (histone and bovine serum albumin abbreviated as BSA) in chromosomes, cultured mammalian cells, and isolated apoptotic nuclei using combined NEXAFS spectra at the C, N and O *K*-edges [1-3]. The molecular mapping is based on the NEXAFS profiles of constituent biomolecules obtained independently. However, increased exposure dose required for X-ray imaging will modify NEXAFS profiles of biomolecules as reported previously [4]. For the precise molecular mapping of biological specimens, spectra measured at the same exposure as that used in the specimen imaging are required. Furthermore, the knowledge of the exposure dependence of NEXAFS profiles would improve the reliability of molecular mapping of biological specimens whose images are taken at any exposure time.

In our previous report, we detected a slight change of NEXAFS profiles of DNA at C, N and O *K*-edges, depending on the exposure time [4]. In the present study, we extended our analysis to the absorbed dose dependence of the mass absorption coefficient for all the energy points of NEXAFS, where absorbed dose is calculated from the exposure.

We prepared dry thin films of DNA, RNA, histone, BSA, actin, actin monomer and nucleosome on SiN membrane. Each one micrometer square area in the specimens was scanned with 10 x 10 pixels at the energy of C, N and O *K*-edge regions mainly in this order with a dwell time of 6, 12 and 20 msec in addition to 2 msec for DNA. For each dwell time the scanned area was shifted to the different area to avoid additional radiation effects to molecules.

Examples of the absorbed dose dependence of mass absorption coefficient are shown in Figure 1 at the lowest energies in the NEXAFS measurements of DNA at the C, N and O *K*-edges. All data in the repeated experiments for several times were compiled in the figures. The linear regression lines showed a slight decrease with increasing absorbed dose, which means that radiation affects the spectra of molecules. Estimation of NEXAFS profiles at a given absorbed dose is in progress.

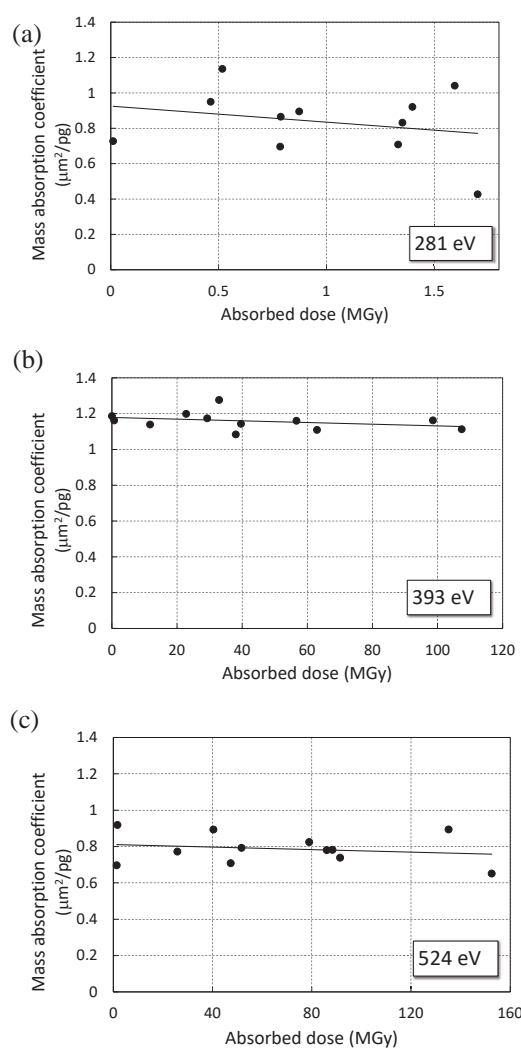


Fig. 1. Effects of soft X-rays on mass absorption coefficients in DNA at (a) C *K*, (b) N *K*, (c) O *K*-edges. The solid lines show linear regression.

- [1] K. Shinohara *et al.*, *Ultramicrosc.* **194** (2018) 1.  
 [2] K. Shinohara *et al.*, *J. X-Ray Sci. Technol.* **26** (2018) 877.  
 [3] K. Shinohara *et al.*, *Cells* **8** (2019) 8.  
 [4] A. Ito *et al.*, *UVSOR Activity Report* **49** (2021) 152.

## Attempt to Constrain the Initial Condition of Aqueous Alteration on Cometary Organic Matter

H. Yabuta<sup>1</sup>, N. Nishii<sup>1</sup>, T. Araki<sup>2</sup> and H. Yuzawa<sup>2</sup>

<sup>1</sup>Department of Earth and Planetary Systems Science, Hiroshima University, Kagamiyama 1-3-1, Hiroshima 739-8526 Japan

<sup>2</sup>UVSOR Synchrotron Facility, Institute for Molecular Science, Okazaki 444-8585, Japan

This study aims to understand the chemical evolution of organic matter in the early stage of aqueous alteration of icy small bodies, through the freeze-thaw experiment of analogues of cometary organic matter.

As a starting material, HCN polymer was synthesized by heating formamide (0.3 ml) at 185°C for 72 hours [1]. The HCN polymer in the same volume of Milli-Q water was frozen with liquid nitrogen (-196°C), kept in the freezer (-18°C), and thawed under room temperature. This freeze-thaw cycle experiment was conducted 10, 20, 30, and 40 cycles. Each experimental products were filtered to remove the residual formamide and once dried.

For the scanning transmission x-ray microscopy (STXM) measurements, each experimental products were suspended in methanol and dropped in SiO<sub>2</sub>-supported Cu transmission electron microscopy (TEM) grids. C- and N-XANES spectra of the samples were acquired by STXM-XANES, beamline 4U, UVSOR. Cody *et al.* (2008) [2] was referred to for the absorption peak assignment.

Figure 1 shows the C-XANES spectra of the products obtained from the freeze-thaw cycle experiments of HCN polymer. The spectrum of the starting material (0 cycle) contains the developed peak derived from nitrile or N-heterocycles with the other three peaks derived from aromatic carbon, carbonyls, and alcohol/ether. Except for the freeze-thaw 10 cycle product showing the high peaks of aliphatic and carbonyl carbons, the spectra of the other products are relatively similar to that of the starting material, but peak intensities of nitrile /N-heterocycles and carbonyls in the spectra of the freeze-thaw 30 and 40 cycles products are lower than those in starting material and the 20 cycle products. The result shows that HCN polymer is likely hydrolyzed and altered with the progress of low temperature freeze-thaw processes. In addition, the freeze-thaw 30 and 40 cycles products showed similar C-XANES spectra to those of ultracarbonaceous Antarctic micrometeorites

(UCAMM) [3], supporting the formation of the UCAMM with a very small amount of fluid on a cometary body.

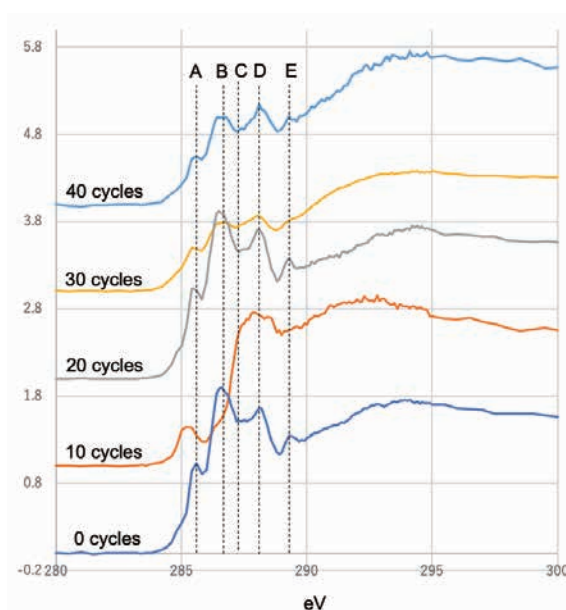


Fig. 1. C-XANES spectra of the products obtained from the freeze-thaw cycle experiments of HCN polymer (0, 10, 20, 30, and 40 cycles). Peak A:  $1s-\pi^*$  transition for aromatic carbon ( $C=C^*$ ) at 285.6 eV, peak B:  $1s-\pi^*$  transition for nitrile ( $C\equiv N^*$ ) or N-heterocycles ( $C-N^*=C$ ), at 286.6 eV, peak C:  $1s-3p/s^*$  transition for aliphatic carbon ( $CH_x$ ) at 287.5 eV, peak D:  $1s-\pi^*$  transition for carbonyl carbon ( $OR(C^*=O)-C$ ) at 288.4–288.7 eV, and peak E:  $1s-3p/s^*$  transition for alcohol or ether ( $CH_x-OR$ ) at 289.3 eV.

[1] F. Cataldo, G. Patanè and G. Compagnini, *J. Macromol. Sci. Part A* **33** (2009) 1039.

[2] G. D. Cody *et al.*, *Meteorit. Planet. Sci.* **43** Nr 1/2 353.

[3] H. Yabuta, *et al.*, *Geochim. Cosmochim. Acta* **214** (2017) 172.

BL4U

## Organics in Asteroid Ryugu Samples: Analytical Approach Utilizing Micro and Multi Beam Techniques.

M. Ito<sup>1</sup>, N. Tomioka<sup>1</sup>, M. Uesugi<sup>2</sup>, A. Yamaguchi<sup>3,4</sup>, N. Imae<sup>3,4</sup>, N. Shirai<sup>5</sup>, T. Ohigashi<sup>4,6</sup>, M. Kimura<sup>3</sup>, M-C, Liu<sup>7</sup>, R.C. Greenwood<sup>8</sup>, K. Uesugi<sup>2</sup>, A. Nakato<sup>9</sup>, K. Yogata<sup>9</sup>, H. Yuzawa<sup>6</sup>, Y. Kodama<sup>8</sup>, A. Tsuchiyama<sup>10</sup>, M. Yasutake<sup>2</sup>, R. Findlay<sup>8</sup>, I.A. Franchi<sup>8</sup>, J.A. Malley<sup>8</sup>, K.A. McCain<sup>7</sup>, N. Matsuda<sup>7</sup>, K.D. McKeegan<sup>7</sup>, K. Hirahara<sup>11</sup>, A. Takeuchi<sup>2</sup>, S. Sekimoto<sup>12</sup>, I. Sakurai<sup>13</sup>, I. Okada<sup>13</sup>, Y. Karouji<sup>14</sup>, T. Yada<sup>9</sup>, M. Abe<sup>9</sup>, T. Usui<sup>9</sup>, S. Watanabe<sup>13</sup> and Y. Tsuda<sup>4,9</sup>  
<sup>1</sup>JAMSTEC Kochi, <sup>2</sup>JASRI/SPring-8, <sup>3</sup>NIPR, <sup>4</sup>SOKENDAI, <sup>5</sup>Tokyo Met. Univ.,  
<sup>6</sup>UVSOR/IMS, <sup>7</sup>UCLA, <sup>8</sup>Open Univ., <sup>9</sup>JAXA/ISAS, <sup>10</sup>Ritsumeikan Univ.,  
<sup>11</sup>Osaka Univ., <sup>12</sup>Kyoto Univ., <sup>13</sup>Nagoya Univ., <sup>14</sup>JAXA/JSEC, <sup>5</sup>Toyo Corp.

How the Earth gained its water and organics remains an outstanding question in planetary science. While a small fraction may have been inherited from the cloud of gas and dust present when the Solar System formed, most was likely delivered to the inner Solar System region by water- and carbonaceous-rich materials i.e., asteroids, meteorites, interplanetary dust particles and comets that may be originated beyond the orbit of Jupiter. To better understand the origin of primitive water- and carbonaceous-rich asteroids, JAXA sent the Hayabusa2 spacecraft to asteroid Ryugu and returned surface and subsurface samples from it in December 2020.

In June 2021, following the initial characterization phase conducted at JAXA curation facility, a subset of Ryugu materials were the subject of investigations by separate research teams of six initial analysis and two curation teams [1-8]. Based on the investigations of bulk O isotopes, major elemental abundances and their mineralogical characteristics [1-3,9], the samples returned from Ryugu have shown that they closely match the rare, water rich, Ivuna type (CI) chondritic meteorites.

Analysis of the organic component in Ryugu particles has been a major theme during this first intensive phase of research activity. One of the successes of the work carried out on the Ryugu materials has been the identification of a clear relationship between coarse grained phyllosilicates and organics indicating of water-mineral-organics interaction under a reducing environment on the asteroid [1]. This was confirmed by a STXM (UVSOR-BL4U), NanoSIMS (JAMSTEC, Kochi) and TEM (JAMSTEC, Kochi) coordinated microanalysis [1]. Approximately 20,000 organic species consisting of carbon, hydrogen, nitrogen, oxygen, and/or sulfur, and at least 20 amino-acids have been identified by using high-sensitivity mass spectrometry [1,6,7]. Studies of chiral amino acids in Ryugu have shown that the abundance of the D- and L-enantiomers are approximately equal (D/L = 1),

indicating nonbiological origins [6]. The diversity of organic matter found in Ryugu samples shows some similarities with that previously reported in primitive carbonaceous chondrite groups [1,6,7].

Isotope analyses of the Ryugu particles have provided clues to the original provenance of these Ryugu-derived materials [1,10-12]. This indicates that materials from Ryugu display similarities to other postulated outer Solar System materials, including interplanetary dust particles, returned cometary materials and spectroscopic observations of comets. These results suggest that Ryugu, and by inference other type asteroid, could have formed in outer Solar System regions, such as are now occupied by Uranus and Neptune. A finding of CO<sub>2</sub>-bearing water in a Ryugu pyrrhotite is also another evidence of outer Solar System origin [4]. Ryugu-like C-type asteroidal bodies may be present in the inner Solar System as a result of giant planet migration [13].

The success of the Hayabusa2 mission and subsequent analytical campaign [1-8] demonstrates the importance of using state-of-the-art analytical techniques when investigating spacecraft returned samples.

- [1] M. Ito *et al.*, *Nat. Astron.* **6** (2022) 1163.
- [2] E. Nakamura *et al.*, *Proc. Jpn. Acad., Ser. B* **98** (2022) 227.
- [3] T. Yokoyama *et al.*, *Science* **379** (2023) eabn7850.
- [4] T. Nakamura, *et al.*, *Science* **379** (2023) eabn8671.
- [5] R. Okazaki *et al.*, *Science* **379** (2023) eabo0431.
- [6] H. Naraoka *et al.*, *Science* **379** (2023) eabn9033.
- [7] H. Yabuta *et al.*, *Science* **379** (2023) eabn9057.
- [8] T. Noguchi *et al.*, *Nat. Astron.* **7** (2023) 170.
- [9] R. C. Greenwood *et al.*, *Nat. Astron.* **7** (2022) 29.
- [10] N. Kawasaki *et al.*, *Sci. Adv.* **8** (2022) eade2067.
- [11] D. Nakashima *et al.*, *Nat. Commun.* **14** (2023) 532.
- [12] T. Hopp *et al.*, *Sci. Adv.* **8** (2022) eadd8141.
- [13] A. Morbidelli, *et al.*, *Meteorit. Planet. Sci.* **35** (2000) 1309.

## Chemical Morphology of Biomass-Burning Particles Generated from Different Fuels under Varied Burning Conditions

J. Chen<sup>1</sup>, N. Faure<sup>2</sup>, Y. Hao<sup>3</sup>, Z. Kanji<sup>1</sup>, E. S. Thomson<sup>2</sup>, S. Wang<sup>3</sup> and X. Kong<sup>2\*</sup>

<sup>1</sup>Institute for Atmospheric and Climate Science, ETH Zürich, Zurich, 8092, Switzerland

<sup>2</sup>Department of Chemistry and Molecular Biology, University of Gothenburg, SE-412 96 Gothenburg, Sweden

<sup>3</sup>Department of Environmental Sciences, College of Urban and Environmental Sciences, Northwest University, Xi'an 710127, China

Biomass burning aerosols (BBA) from fires worldwide have the potential to greatly disrupt the atmosphere-Earth climate system, as they directly absorb solar radiation and also indirectly affect the radiative properties of clouds. However, due to the intricate chemical composition of BBA produced from a variety of fuels under different burning conditions, the environmental and climatic repercussions of BBA remain highly uncertain.

In this study, BBA generated from laboratory burning experiments were examined by scanning transmission X-ray microscopy (STXM), in order to understand the factors influencing the chemical morphologies of BBA. Various types of biomasses (softwood, hardwood, leaves, peat) were burned under controlled conditions, including flaming and smoldering conditions. The generated BBA particles were transferred to the aerosol chamber and collected onto the TEM grid for chemical morphology analysis by. The STXM measurements were performed at the BL4U beamline in UVSOR-III [1].

The images of example particles are shown in Fig. 1, including the BBA particles from softwood under flaming condition (Fig. 1a), and softwood, peat, leaves BBA particles from smoldering condition (Fig. 1b-1d). The morphologies of particles varied between burning conditions: particles formed under flaming condition exhibit a chain-like structure (Fig. 1a), which is typical for fresh soot particles. As for particles collected under the smoldering condition (Fig. 1b-1d), they display a core-shell structure, implying a mixture of organics and soot particles.

The carbon K-edge near edge X-ray absorption fine structure (NEXAFS) spectra of individual particles from different cases were shown in Fig. 2, where the corresponding particles are displayed on the right. All spectra show the absorbance around 285 eV (arising from the  $C\ 1s \rightarrow \pi^*_{R(C^*=C)_R}$  transition) and a broader peak at 290 eV (attributing by  $C\ 1s \rightarrow \sigma^*$  aromatic  $C=C$  transitions). This is one of the identifying features of soot particles. Thus, the strong absorbance at 285 eV of wood-burning particles (softwood flaming and smoldering) indicates the origin of soot particles. This peak is relatively lower in peat and leaves smoldering cases, implying less contributions from soot particles. Two specific peaks at 297.1 eV and 299.8 eV due to the transitions of  $K\ L2\ 2p_{1/2} \rightarrow \sigma^*$  and  $K\ L2\ 2p_{3/2} \rightarrow \sigma^*$  were observed in the leaves smoldering case. The spectra feature in the energy range from 285 eV to 290 eV varied with samples, which is associated with oxygen-

containing organic functional groups and needs further investigation.

These results show that the BBA has distinct chemical morphology depending on biomass types and burning conditions, and the STXM serves as a useful tool to study the morphology and chemical natures of these BBA particles.

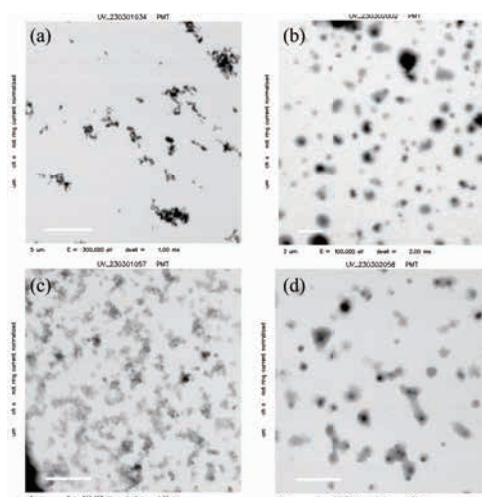


Fig. 1. The morphology of BBA particles from burning different biomasses: (a) Softwood burned under flaming condition; (b-d) softwood, peat and leaves burned under smoldering conditions, respectively. The used photon energy was 300 eV.

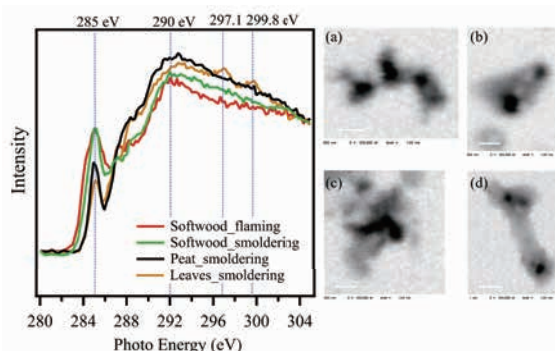


Fig. 2. Left: NEXAFS C K-edge spectra of example particles. Right: (a) softwood burned under flaming condition; (b-d) softwood, peat and leaves burned under smoldering conditions, respectively.

[1] T. Ohigashi *et al.*, J. Phys. Conf. Ser., **463** (2013) 012006.

BL5B

## Heat Resistance of SiC/Mo/Si Multilayer Mirrors at 30.4nm

S. Teramoto<sup>2</sup>, K. Inoue<sup>1</sup>, A. Yamazaki<sup>1</sup>, T. Matsumoto<sup>2</sup>, S. Liu<sup>2</sup>, K. Yoshioka<sup>1,2</sup> and I. Yoshikawa<sup>1,2</sup>

<sup>1</sup>Development of Earth and Planetary Science, Graduate School of Science,  
The University of Tokyo, Tokyo 113-0033, Japan

<sup>2</sup>Development of Complexity Science and Engineering, Graduate School of Frontier Sciences,  
The University of Tokyo, Chiba 277-8561, Japan

Optical observations of planetary atmospheres are conducted over a wide range of wavelengths. In particular, ultraviolet light is useful for obtaining various information about planetary upper atmospheres. For example, by detecting the emission of He II (30.4 nm), the distribution of plasma surrounding the Earth can be observed. The behavior of plasma is related to solar activity and is the key to understanding the physics and evolution of the environment within the solar system. However, the problem is that the signal-to-noise ratio is small due to the low light intensity in UV observations.

Therefore, technology using periodic multilayer for the normal incidence optics in the EUV wavelength ranges has been developed for many planetary science missions, such as Nozomi [1], Kaguya, and EQULEUS [2]. The normal incidence optics is necessary to determine the distribution of plasma. However, the problem is that the normal incidence optics have low reflectance. We can solve this problem by using multilayer mirrors.

Multilayer mirrors can dramatically improve reflectance due to the interference of reflected light at each interface. In particular, the development of high-reflectance multilayer mirrors for He II radiation at 30.4 nm is progressing. A Mo/Si mirror is widely used due to its high stability.

Previously, we demonstrated the performance of a new multilayer mirror consisting of 40 pairs of Mg and SiC, achieving a maximum reflectivity of over 30%. However, it was found that the Mg/SiC mirror had a critical flaw. The reflectivity decreases in high-temperature and high-humidity environments. In actual observations, multilayer mirrors are exposed to high-temperature and humid environments before launch and extremely cold environments in space. Therefore, it is necessary to develop observation equipment that is resistant to such environmental changes.

Since a combination of Mo/Si is stable [3], we designed a new multilayer mirror (SiC/Mo/Si). The new mirror is manufactured by depositing the three different materials periodically. To evaluate its resistance to high-temperature environments, we

conducted a heat environment test in a constant-temperature oven (50 degrees Celsius for 24 hours) and compared the reflectances of the mirrors before and after heating.

The synchrotron radiation was spectroscopic with G3M5. It was led to the calibration chamber. EUV light was irradiated onto the multilayer mirror, and its wavelength dependence was evaluated. The measurement was conducted three times.

Fig. 1 shows the reflectances for the S-polarization of the mirror before and after high-temperature exposure (50 degrees Celsius for 24 hours). The reflectance decreased by approximately 5% after the high-temperature exposure. The irregularity of the interface may have affected the result.

In the future, changing the manufacturing process will make it possible to create a more stable mirror with higher reflectance. We plan to improve the performance of the mirror that is more resistant to environmental changes and have higher reflectance in the next year.

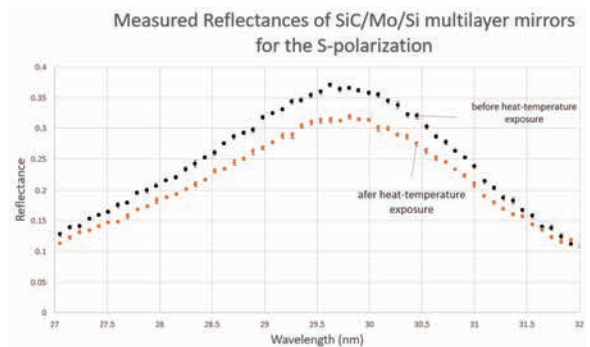


Fig. 1. Reflectances of SiC/Mo/Si mirrors before (black dots) and after (orange dots) heat-temperature exposure.

[1] I. Yoshikawa *et al.*, *Earth Planets Space* **60** (2008) 407.

[2] M. Kuwabara *et al.*, *JAXA Research and Development Report* (2019).

[3] L. Yunpeng *et al.*, *Appl. Surf. Sci.* **317** (2014) 902.

## Synchrotron-radiation Infrared Microspectroscopy Analysis of Persistent Organic Compounds

T. Kawasaki<sup>1</sup>, F. Teshima<sup>2</sup> and K. Tanaka<sup>2</sup>

<sup>1</sup>Accelerator Laboratory, High Energy Accelerator Research Organization, Tsukuba 305-0801, Japan

<sup>2</sup>UVSOR Synchrotron Facility, Institute for Molecular Science, Okazaki 444-8585, Japan

It is important for absorption of carbon dioxide under atmosphere to manage woody biomass properly. Lignin is a part of ingredients of woods and is composed of many phenolic compounds. It has been known that those aromatic molecules such as coumaryl alcohol and coniferyl alcohol are useful for functional materials. However, it is usually difficult to degrade the lignin construct unless using strong acids with extremely high temperatures. We have found that soluble lignin that was prepared by alkaline treatment can be degraded to produce several aromatic molecules by using infrared free electron laser (IR-FEL) [1]. In this study, an insoluble sulfonated lignin was tested as another model sample for degradation by IR-FEL and far-infrared ray from gyrotron [2]. After those irradiations, the complex structure of the lignin was analyzed by using synchrotron-radiation infrared microspectroscopy. The measurement was performed by reflection mode with 64 scans.

In the FT-IR spectra of lignin in the far-infrared region (Fig. 1, upper), increases of absorption intensity can be observed from 150 to 250  $\text{cm}^{-1}$  in all of samples. The inclinations in the cases of samples after the IR-FEL irradiations at 7.1  $\mu\text{m}$  and 3.5  $\mu\text{m}$  are similar with the case of the sample before irradiation (Non-irradiation). On the other hand, the irradiation by a submillimeter wave at 1.4 mm from gyrotron gave increase of absorption at 150-200  $\text{cm}^{-1}$ . This may indicate that the hydration of the lignin sample can be occurred by the irradiation at longer wavelengths.

In the absorption spectra at mid-infrared region (Fig. 1, bottom), broad bands at 1000-1100  $\text{cm}^{-1}$  can be observed in all of samples. Especially, another peak can be slightly detected after irradiations at 1.4 mm and 7.1  $\mu\text{m}$  compared to that at 3.5  $\mu\text{m}$  and the non-irradiation sample (dotted line). This region contains carbon-oxygen stretching vibrational modes, and the lignin is constructed by many ether bonds (C-O-C). Therefore, it can be considered that the structure of lignin can be modified and partial cleavage of the ether bonds can be induced by the submillimeter wave and the IR-FEL irradiations. We are planning to perform mass analysis to confirm the structural modification of the lignin.

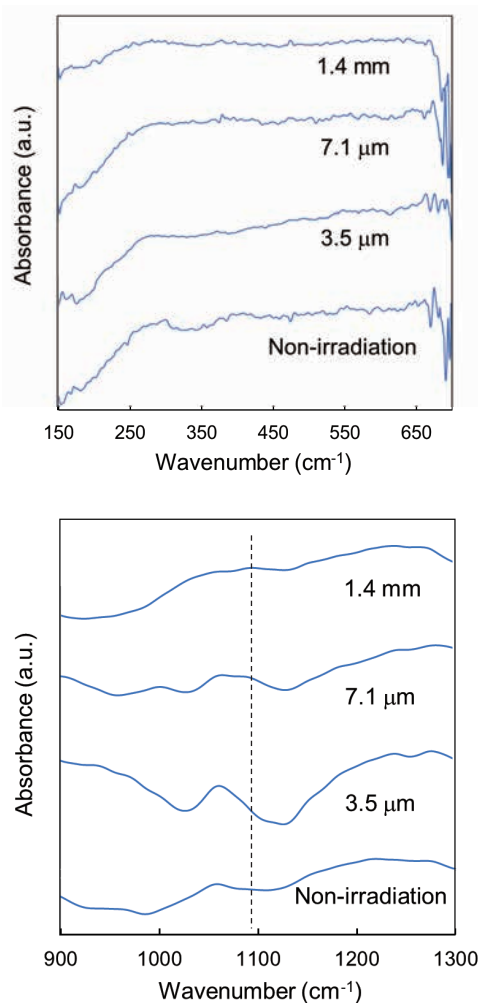


Fig. 1. Infrared absorption spectra of lignin in the far- (upper) and mid- (bottom) infrared regions. “1.4 mm” means the wavelength of submillimeter wave from gyrotron. Both of “7.1  $\mu\text{m}$ ” and “3.5  $\mu\text{m}$ ” are wavelengths of IR-FELs.

[1] T. Kawasaki *et al.*, *Polymers* **14** (2022) 2401.

[2] T. Kawasaki *et al.*, *Biomolecules* **12** (2022) 1326.

BL6B

## Development of an Infrared Spectro-Microtomography Using a Mid-IR Supercontinuum Laser: Preliminary Report

H. Yabuta<sup>1</sup>, Y. Ikemoto<sup>2</sup>, F. Teshima<sup>3</sup> and K. Tanaka<sup>3</sup>

<sup>1</sup>*Department of Earth and Planetary Systems Science, Hiroshima University, Kagamiyama 1-3-1, Hiroshima 739-8526 Japan*

<sup>2</sup>*Japan Synchrotron Radiation Research Institute (JASRI) 1-1-1, Kouto, Sayo-cho, Sayo-gun, Hyogo 679-5198 Japan*

<sup>3</sup>*UVSOR Synchrotron Facility, Institute for Molecular Science, Okazaki 444-8585, Japan*

This study aims to develop a three-dimensional infrared spectro-microtomography using a mid-infrared supercontinuum laser, for investigating the three-dimensional spatial distributions of micron-sized organic materials and hydrous minerals of extraterrestrial samples and for understanding the chemical history in the early Solar System.

In the previous beamtime, an alignment procedure has been established to guide the laser source to the microscope for micro-spectroscopy. The activities of this beamtime were the following three points. The first was to adjust the beam size at the microscope focal point, the second was to confirm the sample holding technique, and the third was to confirm the IR imaging measurement technique by rotating the sample. The details are described in this order.

Fig. 1 shows the schematic illustration of the optical path. The IR beam emitted from the laser are reflected by BaF<sub>2</sub> and reduced to about 1/100 of its original intensity. The IR beam is further attenuated through an ND filter to an intensity that does not damage the optical components of the FTIR spectrometer, and then a spectrum is measured. The microscope at BL6B has 16 elements HgCdTe (MCT) linear array detector. In previous experiments, it was found that due to the small source size, the IR spot on the microscope was small and the IR light was only on a part of the element. In order to increase the number of elements that are illuminated by IR light, a beam expander was installed in front of the FTIR to adjust the spot size.

Samples are glued to the tip of a glass capillary and mounted on a goniostage. Figure 2(a) shows a photograph of the goniostage mounted on the microscope. Figure 2(b) shows a micrograph of a sample glued to the tip of the capillary. The sample was a milled breadcrumb and the size was approximately 90 micrometers in longitudinal.

In the previous beamtime, the mapping measurements were performed in the multipoint measurement mode of microscopy programs, but there is a problem of not being able to access integral intensity plots. In addition, the program is not equipped with a mode to extract only the part of the linear array detector that are illuminated by IR light. The element shift mapping software solves these problems and is used for the measurement.

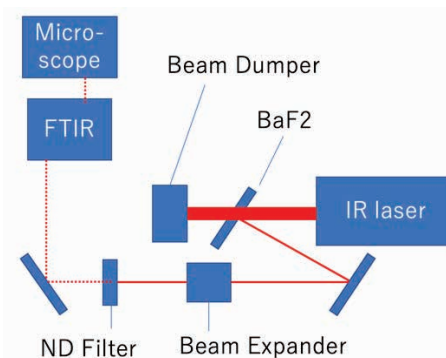


Fig. 1. Schematic illustration of the optical path

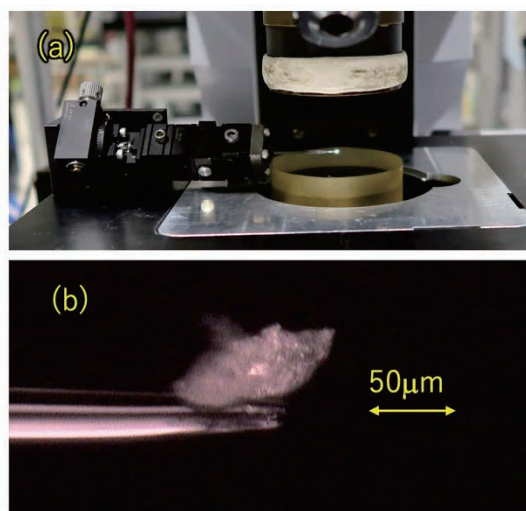
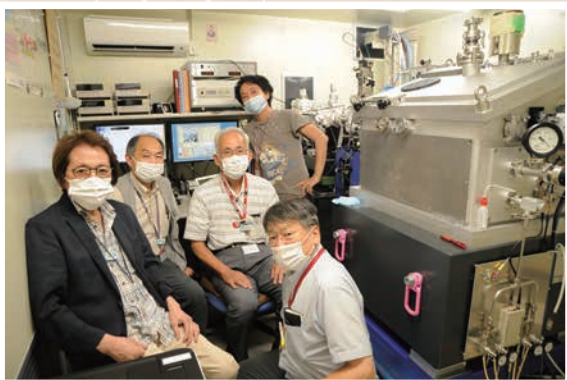
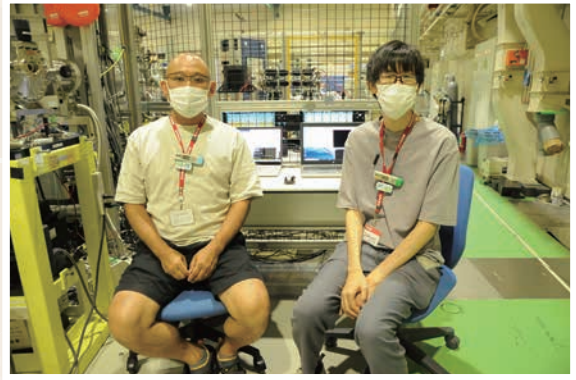
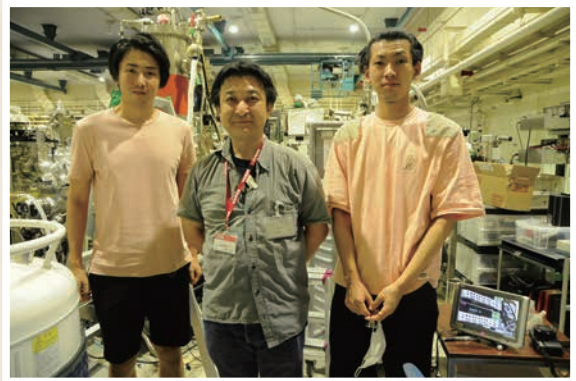
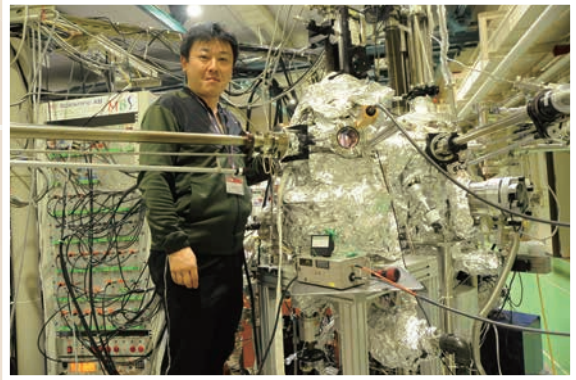
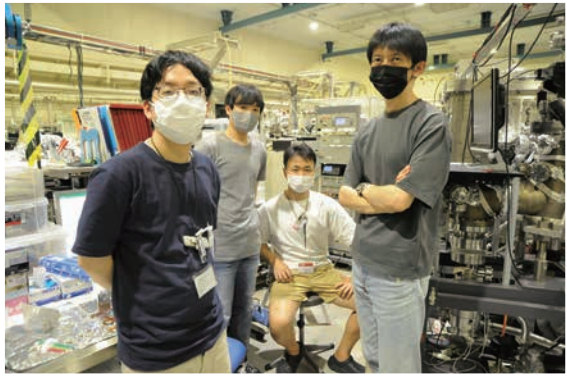


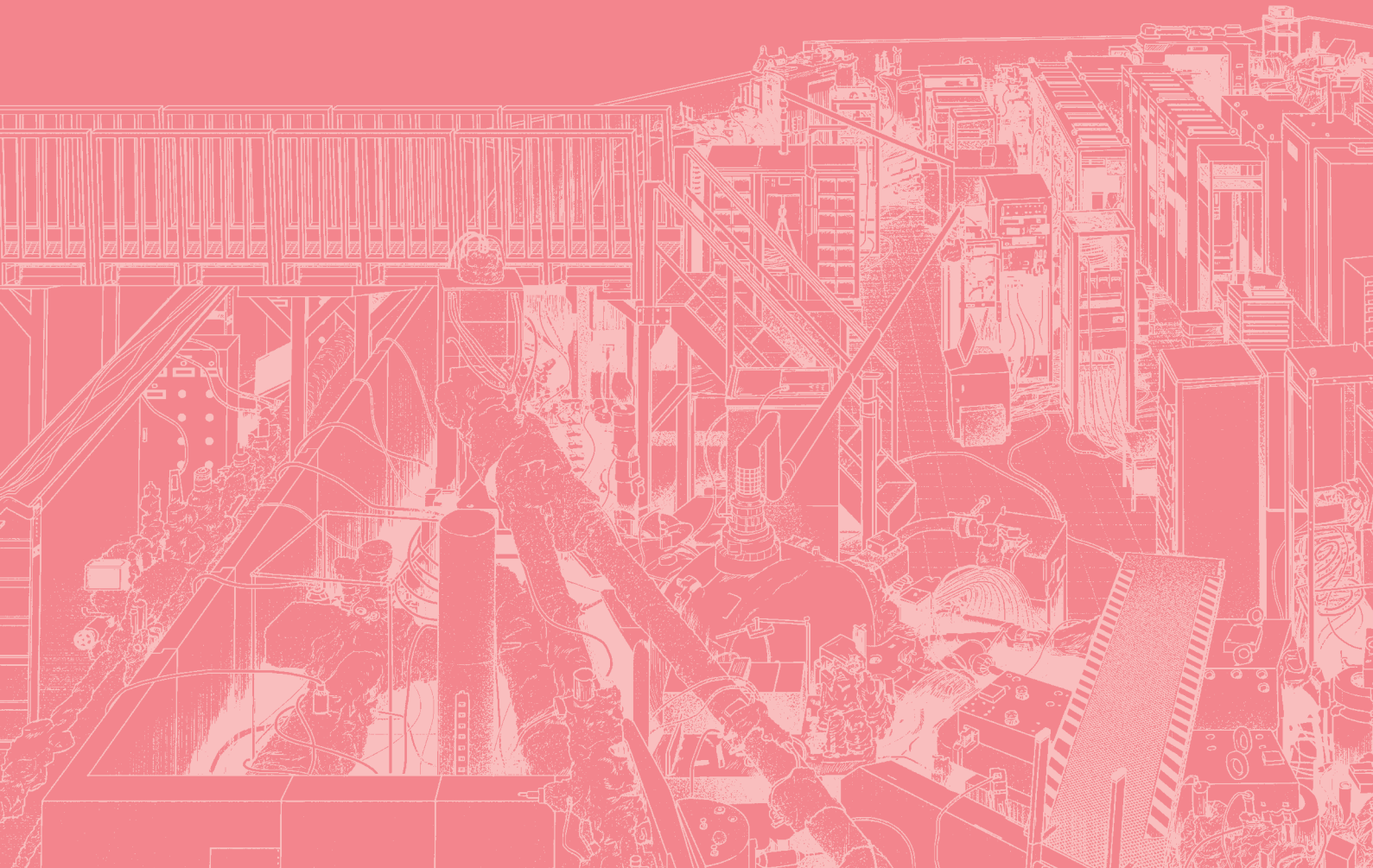
Fig. 2. (a) Photograph of the goniostage mounted on the microscope. (b) Micrograph of a sample glued to the tip of the capillary.

# UVSOR User 8



# IV

## List of Publications





## List of Publications (2022)

D. Asakura, E. Hosono, M. Kitamura, K. Horiba, E. Magome, H. Setoyama, E. Kobayashi, H. Yuzawa, T. Ohigashi, T. Sakai, R. Kanega, T. Funaki, Y. Sato and A. Ohira

**“Redox reaction in Ti-Mn redox flow battery studied by X-ray absorption spectroscopy”**, Chem. Asian J. (2022) e202201047.

A. Dorokhina, R. Ishihara, H. Kominami, V. Bakhmetyev, M. Sychov and T. Aoki, H. Morii

**“Solvothermal Synthesis of LaF<sub>3</sub>:Ce Nanoparticles for Use in Medicine: Luminescence, Morphology and Surface Properties”**, Ceramics 6 (2023) 492.

O. Endo, F. Matsui, S. Kera, W-J. Chun, M. Nakamura, K. Amemiya and H. Ozaki

**“Observation of Hole States at perylene/Au(110) and Au(111) interfaces”**, J. Phys. Chem. C 126 (2022) 15971.

T. Fuji, T. Kaneyasu, M. Fujimoto, Y. Okano, E. Salehi, M. Hosaka, Y. Takashima, A. Mano, Y. Hikosaka, S. Wada, and M. Katoh

**“Spectral phase interferometry for direct electric-field reconstruction of synchrotron radiation”**, Optica 10-2 (2023) 302.

Y. Hasegawa, F. Matsui and S. Kera

**“Resonant Photoemission Spectroscopy of Highly-Oriented-Coronene Monolayer using Photoelectron Momentum Microscope”**, e-J. Surf. Sci. Nanotech. 20 (2022) 174.

E. Hashimoto, K. Tamura, H. Yamaguchi, T. Watanabe, F. Matsui and S. Koh

**“Characterization of Epitaxial CVD graphene on Ir(111)/ $\alpha$ -Al<sub>2</sub>O<sub>3</sub>(0001) by Photoelectron Momentum Microscopy”**, Jpn. J. Appl. Phys. 61 (2022) SD1015.

Y. Hikosaka

**“Sequential Quadruple Auger Decay Pathways from the Xe 4s Core-Hole State”**, Phys. Rev. A 106 (2022) 062814.

Y. Hikosaka and S. Fritzsche

**“Coster–Kronig and Super Coster–Kronig Transitions from the Xe 4s Core-Hole State”**, Phys. Chem. Chem. Phys. 24 (2022) 17535.

M. Ito, N. Tomioka, M. Uesugi, A. Yamaguchi, N. Shirai, T. Ohigashi, M-C. Liu, R. C. Greenwood, M. Kimura, N. Imae, K. Uesugi, A. Nakato, K. Yogata, H. Yuzawa, Y. Kodama, A. Tsuchiyama, M. Yasutake, R. Findlay, I. A. Franchi, J. A. Malley, K. A. McCain, N. Matsuda, K. D. McKeegan, K. Hirahara, A. Takeuchi, S. Sekimoto, I. Sakurai, I. Okada, Y. Karouji, M. Arakawa, A. Fujii, M. Fujimoto, M. Hayakawa, N. Hirata, N. Hirata, R. Honda, C. Honda, S. Hosoda, Y. Iijima, H. Ikeda, M. Ishiguro, Y. Ishihara, T. Iwata, K. Kawahara, S. Kikuchi, K. Kitazato, K. Matsumoto, M. Matsuoka, T. Michikami, Y. Mimasu, A. Miura, O. Mori, T. Morota, S. Nakazawa, N. Namiki, H. Noda, R. Noguchi, N. Ogawa, K. Ogawa, T. Okada, C. Okamoto, G. Ono, M. Ozaki, T. Saiki, N. Sakatani, H. Sawada, H. Senshu, Y. Shimaki, K. Shirai, S. Sugita, Y. Takei, H. Takeuchi, S. Tanaka, E. Tatsumi, F. Terui, R. Tsukizaki, K. Wada, M. Yamada, T. Yamada, Y. Yamamoto, H. Yano, Y. Yokota, K. Yoshihara, M. Yoshikawa, K. Yoshikawa, R. Fukai, S. Furuya, K. Hatakeda, T. Hayashi, Y. Hitomi, K. Kumagai, A. Miyazaki, M. Nishimura, H. Soejima, A. Iwamae, D. Yamamoto, M. Yoshitake, T. Yada, M. Abe, T. Usui, S. Watanabe and Y. Tsuda

**“A pristine record of outer Solar System materials from asteroid Ryugu’s returned sample”**, Nature Astronomy 6 (2022) 1163.

T. Kaneyasu, M. Hosaka, A. Mano, Y. Takashima, M. Fujimoto, E. Salehi, H. Iwayama, Y. Hikosaka and M. Katoh

**“Double-pulsed wave packets in spontaneous radiation from a tandem undulator”**, Scientific reports 12 (2022) 9682.

T. Kaneyasu, Y. Hikosaka, M. Fujimoto, H. Iwayama and M. Katoh  
**“Coherent Control of Atoms in the Extreme Ultraviolet and Attosecond Regime by Synchrotron Radiation”**, J. Phys.:Conf. Ser. 2380 (2022) 012115.

T. Kato, Y. Li, K. Nakayama, Z. Wang, S. Souma, F. Matsui, M. Kitamura, K. Horiba, H. Kumigashira, T. Takahashi, Y. Yao and T. Sato  
**“Fermiology and Origin of Tc Enhancement in a Kagome Superconductor Cs(V<sub>1-x</sub>Nb<sub>x</sub>)<sub>3</sub>Sb<sub>5</sub>”**, Phys. Rev. Lett. 129 (2022) 206402.

H. Kawaguchi, T. Muramatsu, M. Katoh, M. Hosaka and Y. Takashima  
**“Time-Domain Eddy Current and Wake Fields Analysis of Pulsed Multipole Magnet Beam Injector in Synchrotron Radiation Ring”**, IEICE Trans. Electron. E105-C-4 (2022) 146.

T. Kawasaki, Y. Yamaguchi, H. Kitahara, A. Irizawa and M. Tani  
**“Exploring Biomolecular Self-Assembly with Far-Infrared Radiation”**, Biomolecules 12 (2022) 1326.

S. Kimura, H. Watanabe, S. Tatsukawa and H. Tanida  
**“Observation of Electronic Structure Modification in the Hidden Order Phase of CeCoSi”**, J. Phys. Soc. Jpn. 92 (2023) 043704.

M. Kitaura, Y. Taira and S. Watanabe  
**“Characterization of imperfections in scintillator crystals using gamma-ray induced positron annihilation lifetime spectroscopy”**, Optical Materials: X 14 (2022) 100156.

P. Krüger and F. Matsui  
**“Observation and theory of strong circular dichroism in angle-resolved photoemission from graphite”**, J. Electron Spectrosc. Relat. Phenom. 258 (2022) 147219.

K. Kubota and T. Kawai  
**“Optical characteristics of TI+ centers in CsCaCl<sub>3</sub>, KCaCl<sub>3</sub>, and CsCl crystals”**, J. Phys. Chem. Solids 163 (2022) 110592.

S. Kusaka, T. T. Sasaki, K. Sumida, S. Ichinokura, S. Ideta, K. Tanaka, K. Hono and T. Hirahara  
**“Fabrication of (Bi<sub>2</sub>)<sub>m</sub>(Bi<sub>2</sub>Te<sub>3</sub>)<sub>n</sub> superlattice films by Te desorption from a pristine Bi<sub>2</sub>Te<sub>3</sub> film”**, Appl. Phys. Lett. 120 (2022) 173102.

F. Matsui, Y. Okano, H. Matsuda, T. Yano, E. Nakamura, S. Kera and S. Suga  
**“Domain-Resolved Photoelectron Microscopy and micrometer-scale Momentum-Resolved Photoelectron Spectroscopy of Graphite Armchair Edge Facet”**, J. Phys. Soc. Jpn. 91 (2022) 094703.

F. Matsui and S. Suga  
**“Coupling of kz-dispersing  $\pi$  bands with surface localized states in graphite”**, Phys. Rev. B 105 (2022) 235126.

H. Murata, T. Nakamura, R. Kawanabe, Y. Tokudome and A. Nakahira  
**“Reaction of Stoichiometric Hydroxyapatite with Different Crystallinity in Mg<sup>2+</sup> Aqueous Solution”**, J. Ceram. Soc. Jpn. 131 (2023) 8.

D. Nabok, M. Tas, S. Kusaka, E. Durgun, C. Friedrich, G. Bihlmayer, S. Blügel, T. Hirahara and I. Aguilera  
**“Bulk and surface electronic structure of Bi<sub>4</sub>Te<sub>3</sub> from GW calculations and photoemission experiments”**, Phys. Rev. Mat. 6 (2022) 034204.

M. Nagasaka, M. Bouvier, H. Yuzawa and N. Kosugi  
**“Hydrophobic Cluster Formation in Aqueous Ethanol Solutions Probed by Soft X-ray Absorption Spectroscopy”**, J. Phys. Chem. B 126 (2022) 4948.

M. Nagasaka

**“Site Selective Analysis of Water in Hydrogen Bond Network of Aqueous Dimethyl Sulfoxide Solutions by Oxygen K-edge X-ray Absorption Spectroscopy”**, J. Mol. Liq. 366 (2022) 120310.

M. Nagasaka

**“Carbon K-edge X-ray Absorption Spectra of Liquid Alcohols from Quantum Chemical Calculations of Liquid Structures Obtained by Molecular Dynamics Simulations”**, J. Chem. Phys. 158 (2023) 024501.

T. Nakamura, T. Nakaya, Y. Ohtsubo, H. Sugihara, K. Tanaka, R. Yukawa, M. Kitamura, H. Kumigashira, K. Imura, H. S. Suzuki, N. K. Sato and S. Kimura

**“Surface valence transition in SmS by alkali metal adsorption”**, Phys. Rev. B 107 (2023) L041102.

H. Ota, E. Salehi, M. Fujimoto, K. Hayashi, T. Horigome, H. Iwayama, M. Katoh, N. Kondo, S. Makita, F. Matsui, H. Matsuda, T. Mizukawa, A. Minakuchi, E. Nakamura, M. Nagasaka, Y. Okano, T. Ohigashi, M. Sakai, K. Sugita, K. Tanaka, Y. Taira, F. Teshima, J. Yamazaki, T. Yano, H. Yuzawa and S. Kera

**“UVSOR Synchrotron Facility Update”**, J. Phys.: Conference Series. 2380 (2023) 012003.

E. Salehi, Y. Taira, M. Fujimoto, L. Guo and M. Katoh

**“Lattice design of the UVSOR-IV storage ring”**, J. Phys.: Conf. Ser. 2420 (2023) 012062.

K. Sun, O. J. Silveira, Y. Ma, Y. Hasegawa, M. Matsumoto, S. Kera, O. Krejčí, A. S. Foster and S. Kawai

**“On-surface synthesis of disilabenzene-bridged covalent organic frameworks”**, Nature Chemistry 14 (2022) 1071.

I. Suzuki, S. Kawanishi, K. Tanaka, T. Omata, S. Tanaka

**“Contribution of the Sn 5s state to the SnS valence band: direct observation via ARPES measurements”**, Electronic Structure 4 (2022) 025004.

I. Suzuki, S. Kawanishi, K. Tanaka, T. Omata and S. Tanaka

**“Experimental Identification of Atomic Orbital Contributions to SnS Valence Band using Polarization-Dependent Angle-Resolved Photoemission Spectroscopy”**, Phys. Status Solidi B (2023) 2200408.

Y. Taira, R. Yamamoto, K. Sugita, Y. Okano, T. Hirade, S. Namizaki, T. Ogawa and Y. Adachi

**“Development of gamma-ray-induced positron age-momentum correlation measurement”**, Rev. Sci. Instrum. 93 (2022) 113304.

R. Takahashi, A. Hu, P. Gao, Y. Gao, Y. Pang, T. Seo, J. Jiang, S. Maeda, H. Takaya, K. Kubota and H. Ito

**“Mechanochemical synthesis of magnesium-based carbon nucleophiles in air and their use in organic synthesis”**, Nature Commun. 12 (2021) 6691.

Y. Takebuchi, M. Koshimizu, T. Kato, D. Nakauchi, N. Kawaguchi and T. Yanagida

**“Evaluation of Radiation-induced Luminescence Properties of Tb-doped LiCaPO<sub>4</sub>”**, Radiation Physics and Chemistry 197 (2022) 110180.

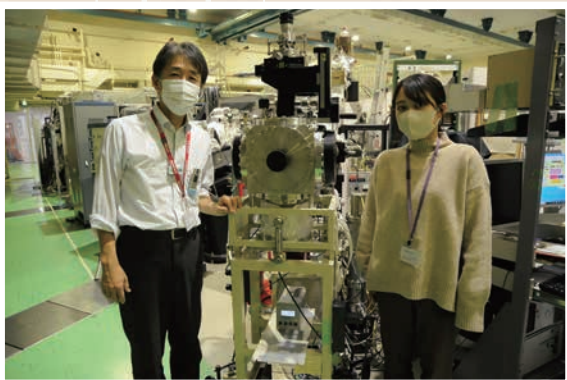
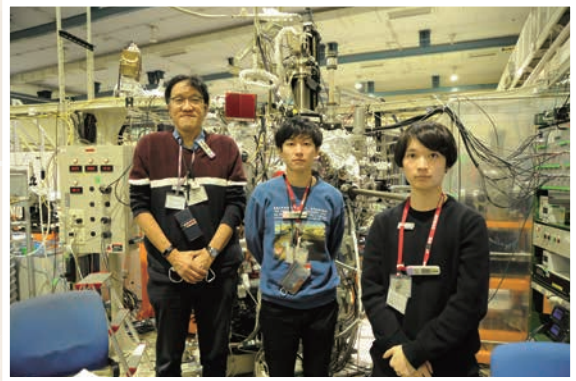
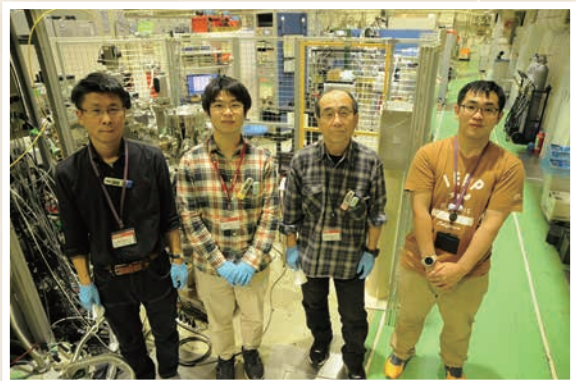
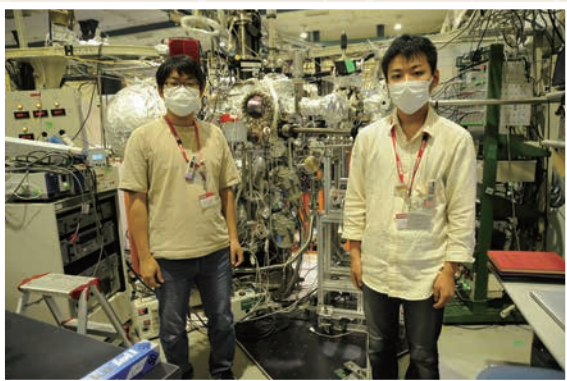
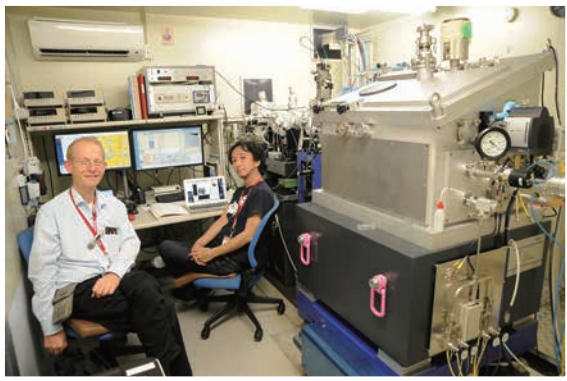
Y. Yamada, K. Morita, T. Sugiura, Y. Toyoda, N. Mihara, M. Nagasaka, H. Takaya, K. Tanaka, T. Koitaya, N. Nakatani, H. Ariga-Miwa, S. Takakusagi, Y. Hitomi, T. Kudo, Y. Tsuji, K. Yoshizawa and K. Tanaka

**“Stacking of Cofacially Stacked Iron Phthalocyanine Dimer on Graphite Achieved High Catalytic CH<sub>4</sub> Oxidation Activity Comparable to that of pMMO”**, JACS Au 3 (2023) 823.

W. Zhang, E. Hosono, D. Asakura, H. Yuzawa, T. Ohigashi, M. Kobayashi, H. Kiuchi and Y. Harada

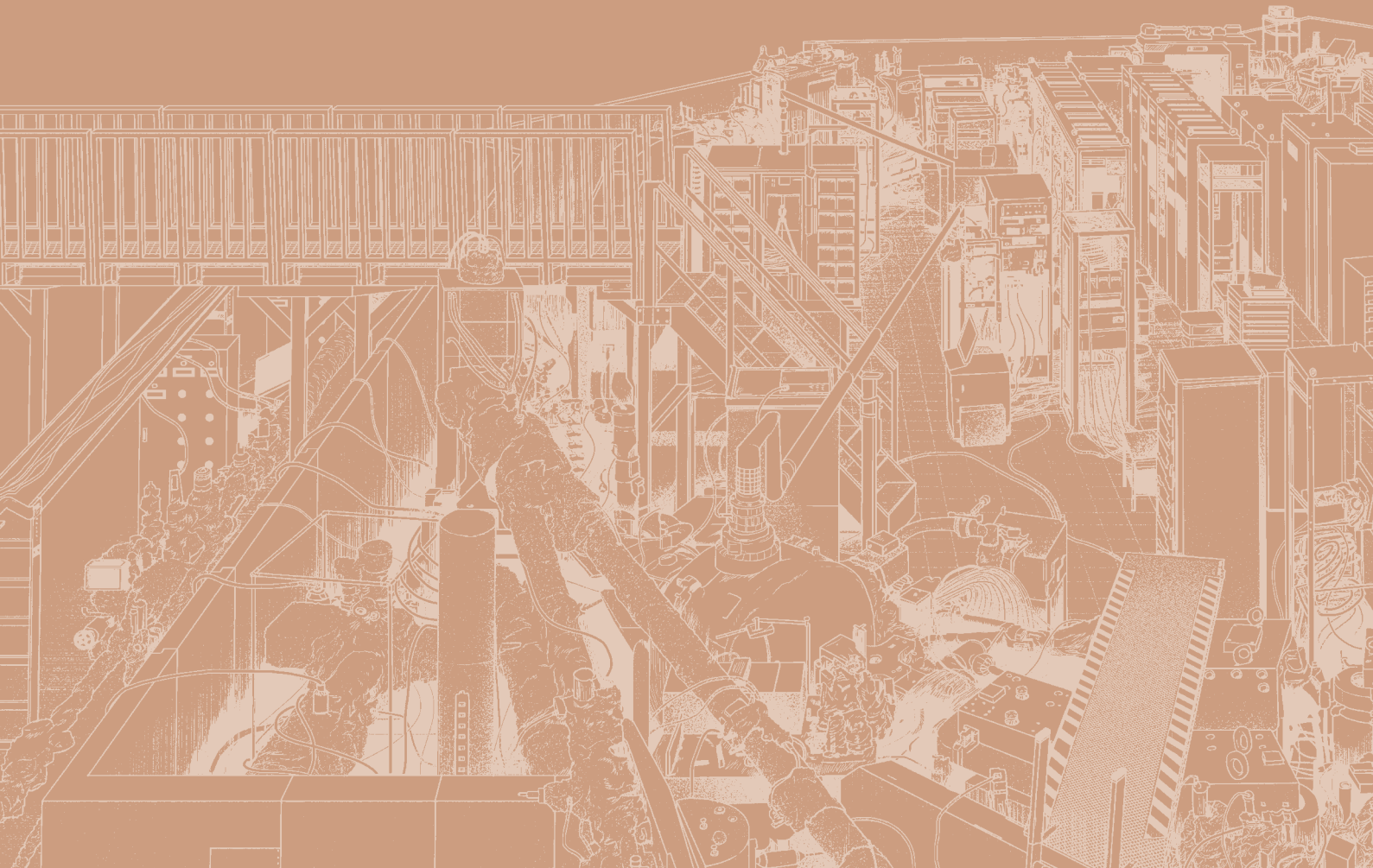
**“Chemical-state distributions in charged LiCoO<sub>2</sub> cathode particles visualized by soft X-rays spectromicroscopy”**, Scientific Reports. 13 (2023) 4639.

# UVSOR User 9





Workshops





## UVSOR Symposium 2022

Date: November 26-27, 2022

Place: Okazaki Conference Center (face-to face), Zoom (online)

### November 26<sup>th</sup> (Sat.)

13:00 – 13:05      Opening remarks

**H. Iwayama** (UVSOR)

<Session 1, Chair: **F. Matsui** (UVSOR)>

13:05 – 13:25      Current status of UVSOR facilities and plans for the next fiscal year

**S. Kera** (UVSOR Director)

13:25 – 13:45      LATTICE DESIGN FOR FUTURE PLAN OF UVSOR

**E. Salehi** (UVSOR)

13:45 – 14:05      Applications of attosecond-controlled double pulses generated by tandem undulator

**T. Kaneyasu** (SAGA LS)

14:05 – 14:35      [Invited Lectures] Coordinated STXM-NEXAFS and TEM analysis of organic materials in samples returned by asteroid Ryugu

**M. Uesugi** (JASRI)

14:35 – 14:50      Break Time

<Session 2, Chair: **M. Kitaura** (Yamagata Univ.)>

14:50 – 15:20      [Invited Lectures] Investigation of Active Organometallic Species by Soft-X-ray XAS

**H. Takaya** (Teikyo Univ. of Science)

15:20 – 15:40      Structural and magnetic properties of FeNi and FeCo alloy thin films on Cu (001) grown by nitrogen surfactant epitaxy

**T. Miyamachi** (Nagoya Univ.)

15:40 – 16:00      Evaluation of X-ray photon counting capability of CMOS sensor aboard FOXSI-4 sounding rocket for solar flare observation

**R. Shimizu** (SOKENDAI)

16:00 – 16:20      Luminescence Properties of NaCl:Tl<sup>+</sup> and NaCl:Au- Crystals

**T. Kawai** (Osaka Metropolitan Univ.)

16:20 – 16:35      Break Time

16:35 – 17:20      Short Presentation for Poster Session (Online video streaming)

17:30 – 18:15      Poster Session (Remo) First half (Odd poster number)

18:15 – 19:00      Poster Session (Remo) Second half (Even poster number)

19:00 – 21:00      Banquet

**November 27<sup>th</sup> (Sun.)**

<Session 3, Chair: **Y. Hikosaka** (Toyama Univ.)>

- 9:00 – 9:20            Exploring biopolymer aggregations with intense infrared radiation  
**T. Kawasaki** (KEK)
- 9:20 – 9:40            Current Status of Spin-Resolved ARPES at BL5U and Development for Automatic  
Measurement at BL5U and BL7U  
**K. Tanaka** (UVSOR)
- 9:40 – 10:00          Surface valence transition in SmS by alkali metal adsorption  
**T. Nakamura** (Osaka Univ.)
- 10:00 – 10:20        Momentum-resolved resonant photoelectron spectroscopy at the Ti2p-3d edge of TiSe<sub>2</sub>:  
interatomic interaction and negative q in Fano resonance.  
**S. Tanaka** (Osaka Univ.)
- 10:20 – 10:50        [Invited Lectures] Spectroscopic study on the topological quantum phenomena of 2D magnets  
**T. Hirahara** (Tokyo Inst. of Tech.)
- 10:50 – 11:00        Break Time
- 11:00 – 12:00        UVSOR USERS' UNION meeting

## The 5<sup>th</sup> workshop on prospects and construction plan of the next generation synchrotron radiation facility: Cooperation between facilities II

Date: November 27, 2022

Place: Okazaki Conference Center (face-to face), Zoom (online)

### November 27<sup>th</sup> (Sun.)

- |               |   |
|---------------|---|
| 13:00 – 13:30 | Present status of NanoTerasu<br><b>H. Yamane</b> ( PhoSiC )   |
| 13:30 – 14:00 | Present status of AichiSR<br><b>T. Okajima</b> ( AichiSR )  |
| 14:00 – 14:30 | Future plan of AichiSR<br><b>H. Sonoeda</b> ( AichiSR )   |
| 14:30 – 15:00 | Progress on the future plan of UVSOR<br><b>S. Kera</b> ( UVSOR Director )   |
| 15:00 – 15:30 | General Discussion: cooperation between NanoTerasu, AichiSR and UVSOR<br>Partnership between NanoTerasu, AichiSR, and UVSOR |

# IMS Symposium

## “Resonant Soft X-ray Scattering and Reflectivity”

Date: November 8th, 2022

Place: Zoom Conference

### November 8<sup>th</sup> (Tue.)

- 10:00 – 10:10      Welcome & Introduction  
**T. Araki** (Diamond Light Source)
- 10:10 – 11:00      Keynote Lecture  
Probing Morphology and Chemistry in Complex Soft Materials with *In Situ* Resonant Soft X-ray Scattering  
**C. Wang** (Advanced Light Source)
- 11:00 – 11:15      Break
- 11:15 – 11:40      Resonant X-Ray Scattering and Reflectivity Measurements of EUV Photoresist at NewSUBARU Synchrotron Light Facility  
**T. Harada** (Univ. of Hyogo)
- 11:40 – 12:05      Development of Resonant Soft X-ray Scattering Equipment at UVSOR and Photon Factory  
**H. Iwayama** (UVSOR)
- 12:05 – 12:30      Concept of Thin Film Analysis Instrument with Soft X-ray Reflectometry and Absorption Spectroscopy Under Wet Conditions  
**N. L. Yamada** (KEK)
- 12:30 – 13:30      Lunch Break
- 13:30 – 13:55      Anomalous Small-angle Scattering of Alloys in Tender X-rays Region  
**H. Okuda** (Kyoto Univ.)
- 13:55 – 14:25      Nano-structure of Polymer Film Analyzed by Small Angle Scattering and Reflectivity Utilizing Tender X-rays at BL15A2 in PF  
**K. Yamamoto** (Nagoya Institute of Technology)
- 14:25 – 14:50      Neutron Analysis of Polymer Electrolyte Fuel Cells  
**M. Harada** (Toyota Central R&D Labs. Inc.)
- 14:50 – 15:05      Break
- 15:05 – 15:30      The Structure Analysis of Liquid Crystals by Resonant Soft X-ray Scattering  
**Y. Takanishi** (Kyoto Univ.)
- 15:30 – 15:55      Solvent-Induced Transition of Polymorphological Chiral Supermolecular Architectures in a Bent-Core Liquid Crystal Dimer  
**F. Araoka** (RIKEN)
- 15:55 – 16:20      Characterizing Self-Assembled Nanoparticles of Drug Delivery by use of Solution Scattering  
**K. Sakurai** (Univ. of Kitakyushu)
- 16:20 – 16:30      Break
- 16:30 – 17:10      Discussion
- 17:10 – 17:15      Closing  
**S. Kera** (IMS)

## IMS Symposium “Symposium on Generation and Advanced Use of Various Quantum Beams in UVSOR-III”

Date: November 28, 2022

Place: Okazaki Conference Center (face-to face), Zoom (online)

### November 28<sup>th</sup> (Mon.)

8:50 – 9:00            Purpose Definition  
                              **Y. Taira** (UVSOR)

<Chair: **Y. Taira** (UVSOR)>

9:00 – 9:30            History of UVSOR light source development beamlines  
                              **M. Katoh** (Hiroshima Univ.)

9:30 – 10:00          Free electron laser development, utilization and future prospects  
                              **H. Zen** (Kyoto Univ.)

10:00 – 10:30        Development of coherent higher harmonic light sources in UVSOR  
                              **F. Sakamoto** (National Inst. of Tech., Akita College)

10:30 – 10:40        Break Time

<Chair: **H. Zen** (Kyoto Univ.)>

10:40 – 11:10        Generation of attosecond controlled double pulses by tandem undulators and their application to atomic and molecular experiments  
                              **T. Kaneyasu** (SAGA LS)

11:10 – 11:40        Control of spatio-temporal structure of synchrotron radiation and its potential applications  
                              **M. Katoh** (Hiroshima Univ.)

11:40 – 12:10        Study on chirality emergence in organic molecules by irradiation of ultraviolet circularly polarized light  
                              **M. Kobayashi** (Natl. Inst. for Fusion Sci.)

12:10 – 13:30        Lunch Time

<Chair: **M. Katoh** (Hiroshima Univ.)>

13:30 – 14:00        Development and utilization of gamma-ray source in UVSOR-III and its future development  
                              **Y. Taira** (UVSOR)

14:00 – 14:30        Current status of the NewSUBARU gamma-ray beamline BL01  
                              **S. Hashimoto** (Univ. of Hyogo)

14:30 – 15:00        Nuclear physics experiments using gamma-rays and their applications  
                              **H. Ohgaki** (Kyoto Univ.)

15:00 – 15:10        Break Time

<Chair: **H. Ohgaki** (Kyoto Univ.)>

15:10 – 15:40      Development and application of polarization detection Compton camera

**K. Shimazoe** (Tokyo Univ.)

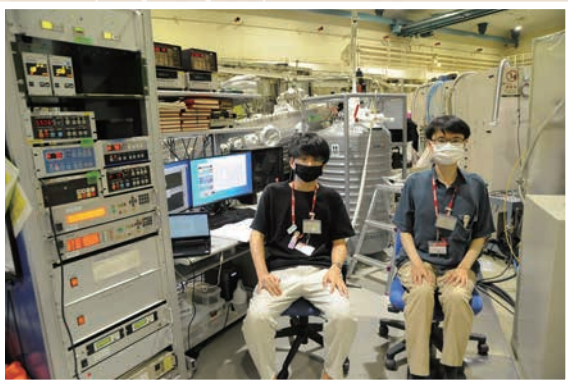
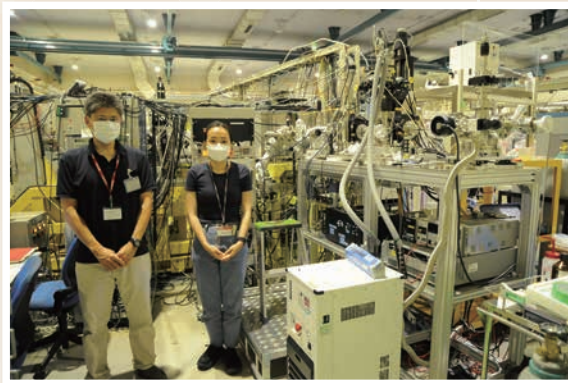
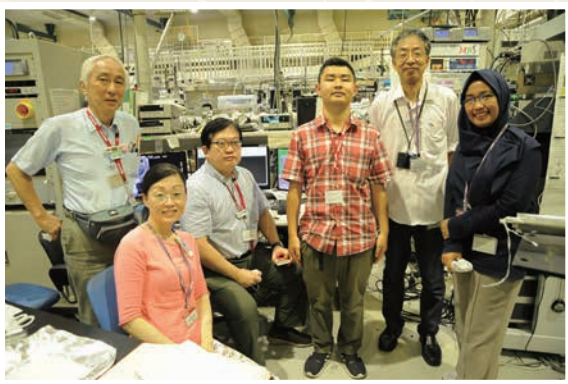
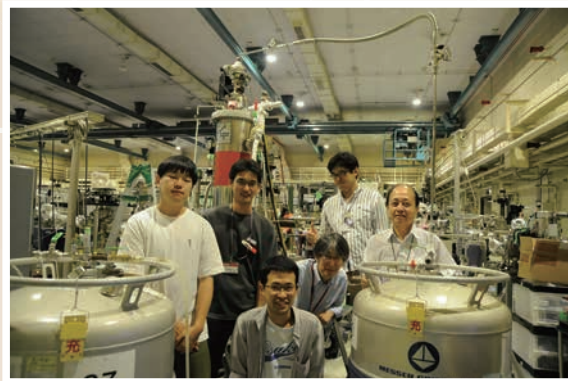
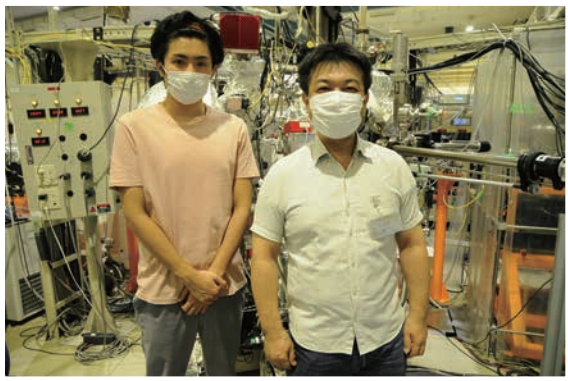
15:10 – 15:40      Fundamentals of positron annihilation method and expectations for pulsed gamma-ray induced positron generator

**M. Fujinami** (Chiba Univ.)

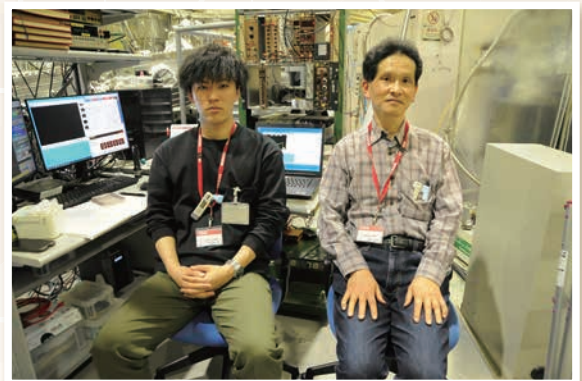
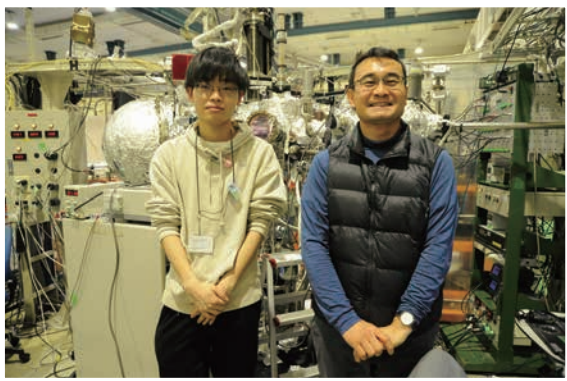
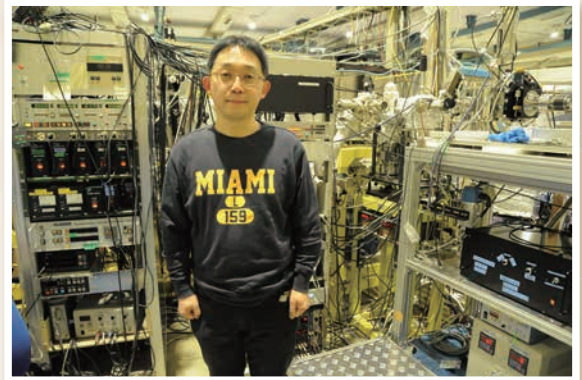
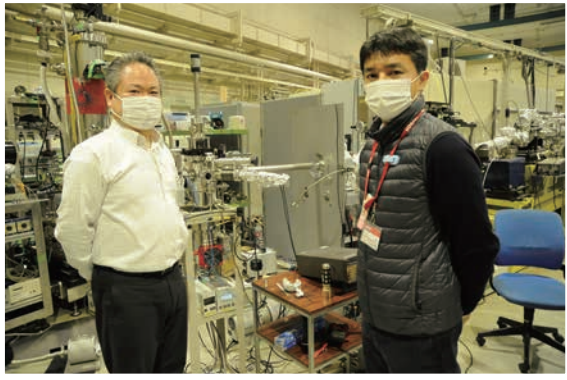
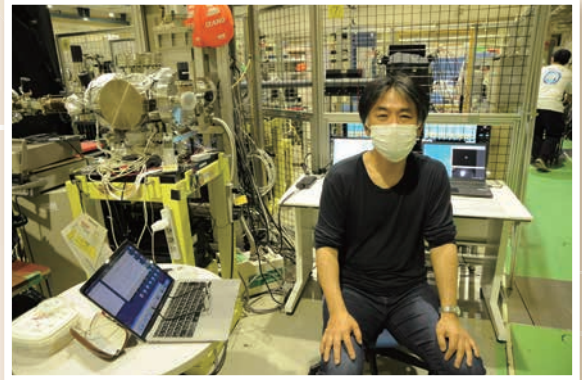
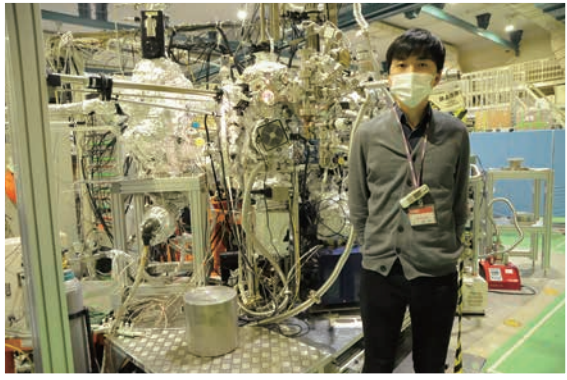
16:10 – 16:40      Probing the effect of impurity addition to luminescent materials by looking at atomic vacancies

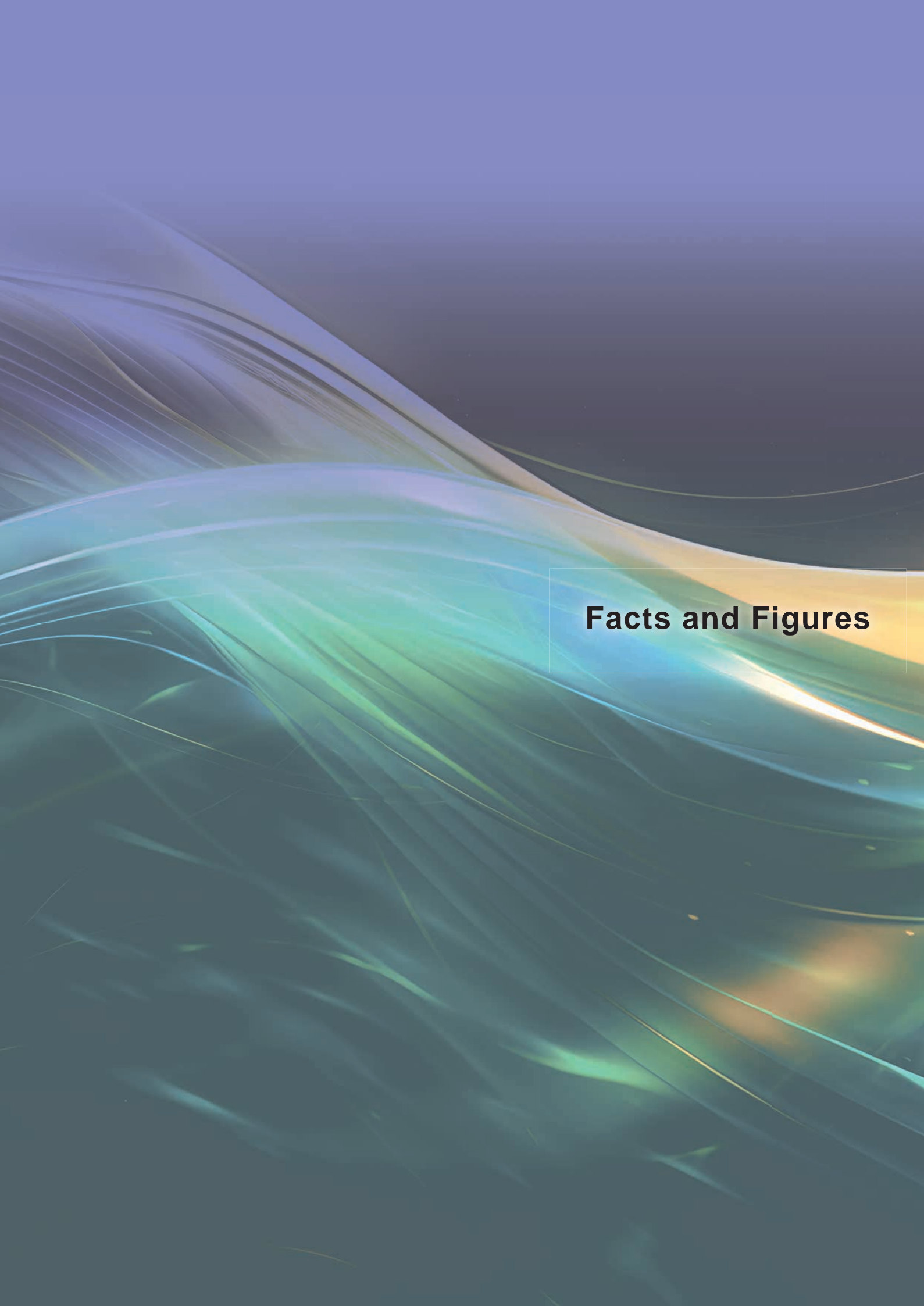
**M. Kitaura** (Yamagata Univ.)

# UVSOR User 10



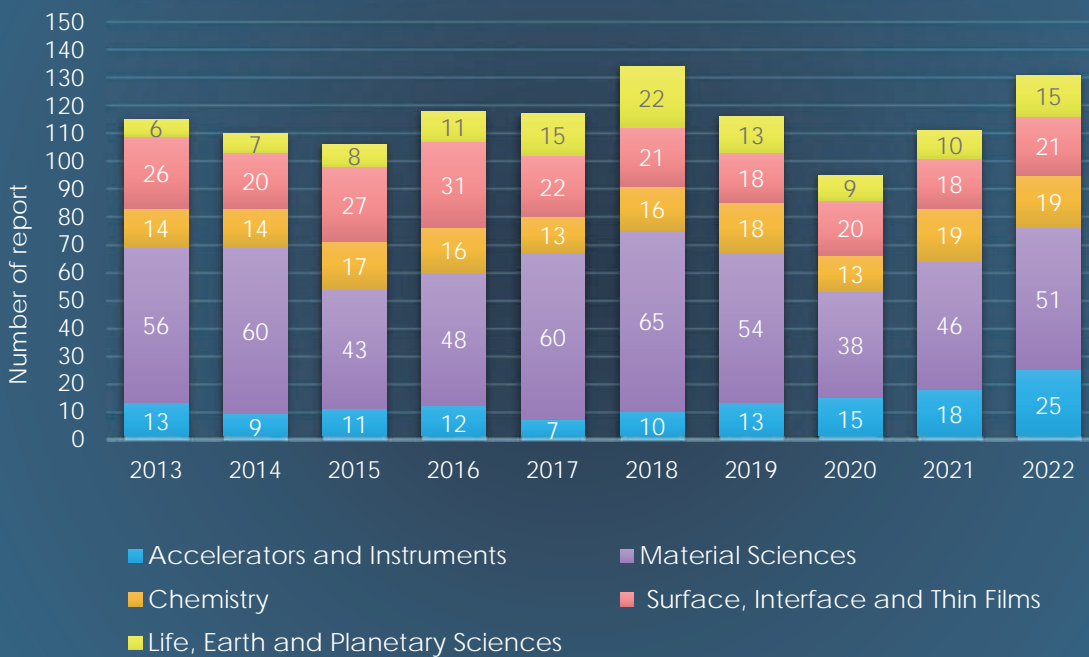
# *UVSOR User 11*



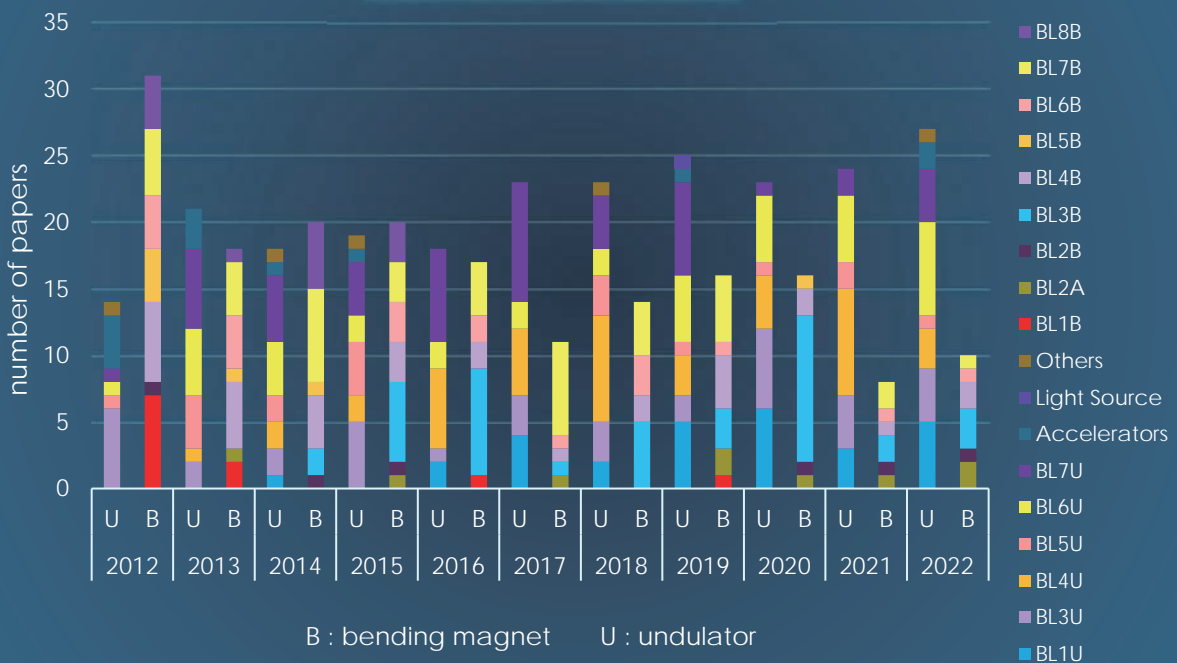


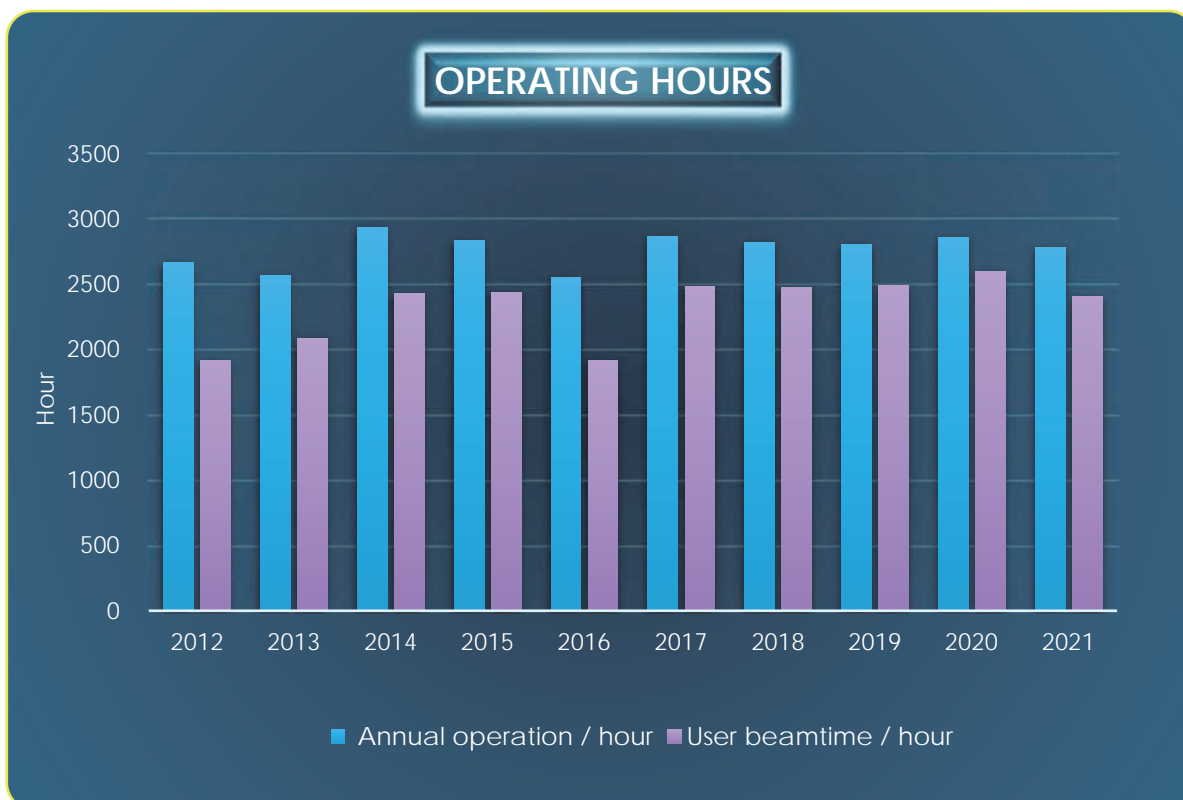
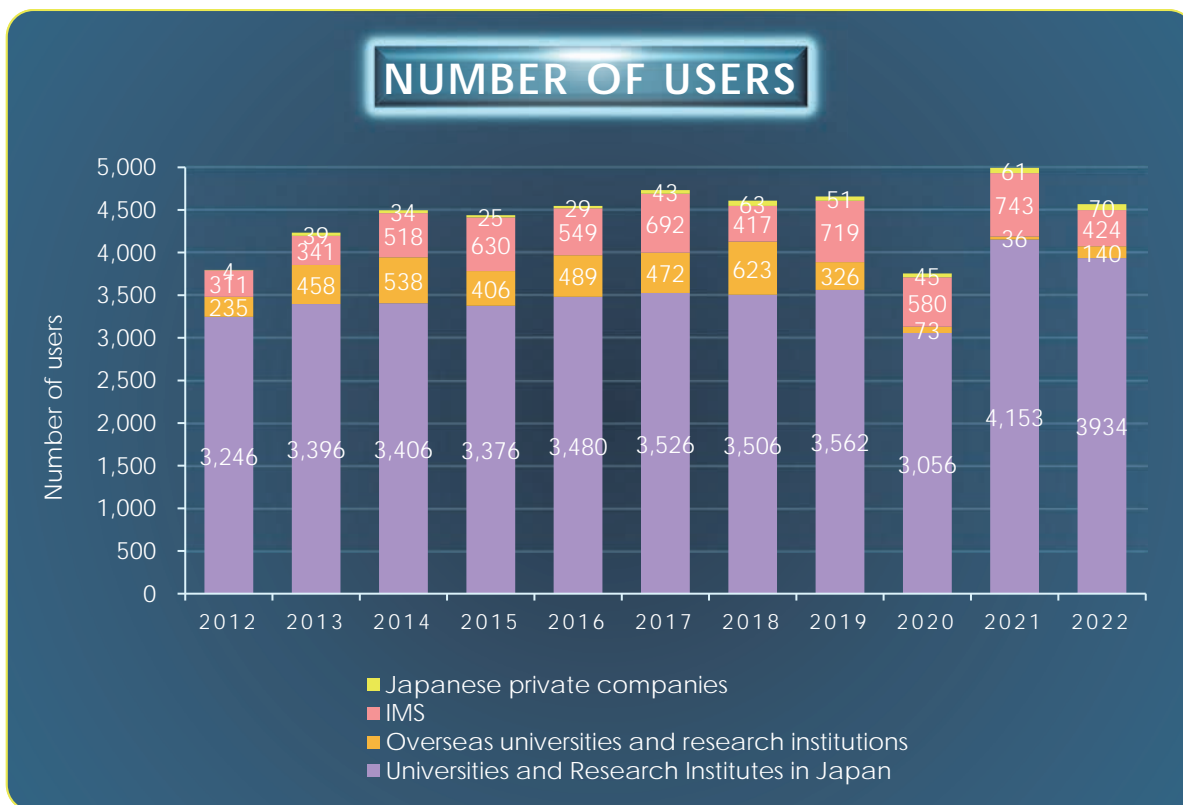
## **Facts and Figures**

## UVSOR ACTIVITY REPORT FIELDS STATISTICS



## NUMBER OF PAPERS







Institute for Molecular Science  
National Institutes of Natural Sciences  
Okazaki 444-8585, Japan

Tel : +81-564-55-7402  
Fax: +81-564-54-7079  
<http://www.uvsor.ims.ac.jp>



Editorial Board: H. Katayanagi, K. Tanaka, H. Iwayama,  
M. Ishihara, K. Kamo

*UNSOR III*  
*since 2012*

